



Provided by the author(s) and University of Galway in accordance with publisher policies. Please cite the published version when available.

Title	Electrical impedance tomography for static lesion detection and identification in the brain
Author(s)	McDermott, Barry James
Publication Date	2020-08-20
Publisher	NUI Galway
Item record	http://hdl.handle.net/10379/16140

Downloaded 2024-04-27T04:59:30Z

Some rights reserved. For more information, please see the item record link above.



Electrical Impedance Tomography for Static Lesion Detection and Identification in the Brain

Presented by:

Barry James McDermott

to:

Electrical and Electronic Engineering,
College of Engineering and Informatics,
National University of Ireland Galway.

in fulfillment of the requirements for the degree of
Doctor of Philosophy.

Supervised by:

Martin O'Halloran and Emily Porter

August 20, 2020

Contents

Contents	i
Declaration of Originality	viii
Abstract	ix
Acknowledgements	xi
List of Figures	xii
List of Tables	xxxvii
Acronyms	xli
Symbols	xlvi
1 Introduction	1
1.1 Motivation	2
1.2 Thesis Contributions	6
1.2.1 Journal Publications	7
1.2.2 Conference Publications	8
1.2.3 Other Publications	8
1.3 Thesis Structure	9
2 Background	11
2.1 Introduction	11
2.2 The Normal and Diseased Brain	12
2.2.1 Anatomy and Physiology of the Head and Brain	13
2.2.2 Cerebrovascular Accident (Stroke)	18
2.2.2.1 Epidemiology of Stroke	18
2.2.2.2 Aetiology and Pathology of Stroke	19
2.2.2.2.1 Haemorrhagic Stroke	20
2.2.2.2.2 Ischaemic Stroke	21

2.2.2.3	Symptoms of Stroke	21
2.2.2.4	Diagnosis of Stroke	22
2.2.2.4.1	Initial Stroke Diagnosis	22
2.2.2.4.2	Neuroimaging of Stroke	24
2.2.2.5	Treatment of Stroke	28
2.2.2.5.1	Treatment of Haemorrhagic Stroke	28
2.2.2.5.2	Treatment of Ischaemic Stroke	28
2.2.2.6	Prognosis of Stroke	32
2.2.2.7	Stroke Patient Pathways	33
2.2.2.7.1	Stroke Overview Pathway	34
2.2.2.7.2	Transient Ischaemic Attack Pathway	34
2.2.2.7.3	Acute Stroke Pathway	35
2.2.3	Traumatic Brain Injury	37
2.2.3.1	Epidemiology of Traumatic Brain Injury	38
2.2.3.2	Aetiology and Pathology of Traumatic Brain Injury	38
2.2.3.3	Symptoms and Diagnosis of Traumatic Brain Injury	40
2.2.3.4	Treatment and Prognosis of Traumatic Brain Injury	41
2.2.3.5	Concussion in Sports Injury	41
2.2.3.6	Traumatic Brain Injury Patient Pathways	41
2.3	Brain Haemorrhage and Clot Static Lesion Detector Need and Re- quirements	43
2.3.1	Brain Haemorrhage and Clot Detector Need and Design Constraints	47
2.3.2	Brain Haemorrhage and Clot Detector Possible Solutions	49
2.3.2.1	Mobile Computed Tomography	49
2.3.2.2	Microwave Imaging	51
2.3.2.3	Electroencephalogram Based Techniques	53
2.3.2.4	Acoustic Wave Based Techniques	54
2.3.2.5	Near Infrared	54
2.3.2.6	Electrical Impedance Tomography	55
2.3.2.7	Brain Haemorrhage and Clot Static Lesion Detector Possible Solutions Summary	59
2.4	Overview of Electrical Impedance Tomography	61
2.4.1	Bioimpedance	61
2.4.2	The Electrical Conductivity of the Tissues of Interest in the Head	64
2.4.3	Principles of EIT Imaging	66
2.4.3.1	EIT Data Acquisition	67
2.4.3.2	The Forward Problem of EIT	69
2.4.3.3	The Inverse Problem of EIT	72

2.4.4	EIT Software	73
2.4.5	EIT Hardware and Test Platforms	74
2.4.6	Existing Modalities of EIT	79
2.5	Conclusions	82
3	Development of Tissue-Mimicking Materials and Phantoms	85
3.1	Introduction	85
3.2	Tissue-Mimicking Material Development	86
3.2.1	Ideal Tissue-Mimicking Materials and Types Used in EIT	87
3.2.2	Tissues of Interest for Head Imaging	89
3.2.3	Tissue-Mimicking Materials Design and Fabrication	90
3.2.3.1	Isopropanol as a Novel Ingredient to Fabricate High Conductivity Tissue Mimicking Materials	94
3.2.4	Tissue Mimicking Material Validation by Conductivity Measurement	97
3.2.4.1	Complex Impedance Spectroscopy to Measure Conductivity	97
3.2.4.2	Selected Tissue Mimicking Material Conductivity Profiles and Comparison to Reference Values	98
3.3	Head Phantom Development	104
3.3.1	Types of Head Phantoms Used in EIT	104
3.3.2	Head Phantom Design Conception	107
3.3.3	Head Phantom Fabrication Process	108
3.3.4	Head Phantom Validation by Time Difference EIT Experiment	114
3.4	Next Steps: 3D-Printable Tissue-Mimicking Materials	117
3.5	Conclusions	123
4	Machine Learning with Electrical Impedance Measurement Frames for Lesion Detection	126
4.1	Introduction	127
4.2	Support Vector Machines Applied to EIT Haemorrhage Static Lesion Detection	128
4.2.1	Machine Learning and EIT	128
4.2.2	Overview of Support Vector Machine Classifiers	129
4.2.3	Classifier Performance Applied to Bleed Detection	133
4.3	Modelling Techniques	134
4.3.1	Numerical Models and Experimental Setup	134
4.3.2	Phantom Model and Experimental Setup	138
4.4	Investigations into Effect of Individual Test Parameters	139
4.4.1	Numerical Studies	139
4.4.1.1	Study 1: Effect of Noise	141

4.4.1.2	Study 2: Effect of Lesion Location	146
4.4.1.3	Study 3: Effect of Lesion Size	148
4.4.1.4	Study 4: Effect of Electrode Positioning	153
4.4.1.5	Study 5: Effect of Normal Variation in Inter-Patient Anatomy	153
4.4.1.6	Study 6: Final Overall Study with All Test Parameters	154
4.4.2	Phantom Studies	156
4.4.2.1	Study 1: Repeatability	157
4.4.2.2	Study 2: Effect of Lesion Location	158
4.4.2.3	Study 3: Effect of Lesion Size	160
4.4.2.4	Study 4: Effect of Electrode Positioning and Varia- tion in Anatomy	163
4.4.2.5	Study 5: Final Overall Study with All Test Parameters	164
4.5	Investigations into Classifier Optimisation	165
4.5.1	Comparison of Performance of Linear SVM, Radial Basis Function SVM, and Neural Network	167
4.5.2	Support Vector Machine Applied to Pre-Processed Electrical Impedance Measurement Frames	170
4.5.2.1	Sub-Frame Means	170
4.5.2.2	Near and Far Sub-Frame Channels	172
4.5.2.3	Laplacian Scores	174
4.5.2.4	Principal Component Analysis	178
4.5.2.5	Ensemble Classifier	180
4.5.3	Investigations into Classifier Optimisation - Key Learnings .	183
4.6	Conclusions	186
5	Symmetry Difference EIT – A Novel Algorithm for Static Per- turbation Detection	188
5.1	Introduction	188
5.2	Symmetry Difference EIT - Algorithm Overview	189
5.3	Symmetry Difference EIT - Initial Development and Proof-of-Concept	192
5.3.1	Modelling Techniques	192
5.3.1.1	Symmetry Difference EIT Simplified Numerical Model	192
5.3.1.2	Symmetry Difference EIT Electrode Layout	193
5.3.2	Symmetry Difference EIT Algorithm and Quantitative Metrics	195
5.3.2.1	Symmetry Difference EIT Step 1 - Lesion Detection and Related Quantitative Metrics	196
5.3.2.2	Symmetry Difference EIT Step 2 - Lesion Identifi- cation and Related Quantitative Metrics	199
5.4	Modelling Techniques	202
5.4.1	Numerical Models and Experimental Setup	202

5.4.2	Phantom Model and Experimental Setup	205
5.5	Investigations into Effect of Individual Test Parameters	207
5.5.1	Numerical Studies	207
5.5.1.1	Study 1: Effect of Lesion Location	207
5.5.1.2	Study 2: Effect of Lesion Size	209
5.5.1.3	Study 3: Effect of Lesion Type	210
5.5.1.4	Study 4: Effect of Noise	213
5.5.1.5	Study 5: Effect of Modelling Errors	215
5.5.1.6	Study 6: More Challenging Lesion Models	217
5.5.2	Phantom Studies	220
5.5.2.1	Study 1: Effect of Lesion Location	220
5.5.2.2	Study 2: Effect of Lesion Size	222
5.6	Conclusions	223
6	Bi-Frequency Symmetry Difference EIT - An Iterative Algorithm for Static Lesion Detection	225
6.1	Introduction	226
6.2	Bi-Frequency Symmetry Difference - Algorithm Overview	227
6.3	Bi-Frequency Symmetry Difference EIT - Initial Development and Proof of Concept	229
6.3.1	Modelling Techniques	229
6.3.1.1	Numerical Models and Experimental Setup	229
6.3.1.2	Phantom Model and Experimental Setup	232
6.3.2	Bi-Frequency Symmetry Difference EIT Algorithm and Quantitative Metrics	233
6.3.2.1	Bi-Frequency Symmetry Difference EIT Example Cases	239
6.3.3	Numerical Studies	243
6.3.4	Phantom Studies	248
6.3.5	Bi-Frequency Symmetry Difference EIT - Initial Development and Proof of Concept Discussion	254
6.4	Bi-Frequency Symmetry Difference EIT - Feasibility and Limitations of Application to Stroke Diagnosis	256
6.4.1	Numerical Model, Data Generation, and Quantitative Metrics	256
6.4.2	Numerical Studies and Investigations into Effect of Individual Test Parameters	259
6.4.2.1	Study 1: Ideal Model Results	259
6.4.2.2	Study 2: Effect of Noise	261
6.4.2.3	Study 3: Effect of Electrode Positioning Errors	262
6.4.2.3.1	Electrode Positioning Errors with Symmetry Lost	262

6.4.2.3.2	Electrode Positioning Errors with Symmetry Maintained	263
6.4.2.4	Study 4: Effect of Electrode Contact Impedance Errors	266
6.4.2.5	Study 5: Effect of Errors in Assumed Conductivity of Tissue	267
6.4.2.5.1	Voxel Level Errors in Assumed Conductivity of Tissue	268
6.4.2.5.2	Whole Tissue Level Errors in Assumed Conductivity of Tissue	268
6.4.2.6	Study 5: Effect of Errors in Assumed Anatomy of the Head	269
6.4.2.6.1	Unilateral Excess of Skull or Brain	269
6.4.2.6.2	Altered Boundary - Shrunk or Dilated Scalp	272
6.4.2.7	Study 6: Effect of a Frequency Dependent Background	273
6.4.2.8	Study 7: Application to Human Data	275
6.4.3	Bi-Frequency Symmetry Difference EIT - Feasibility and Limitations of Application to Stroke Diagnosis Discussion	277
6.5	Conclusions	282
7	Multi-Frequency Symmetry Difference EIT with Machine Learning for Human Stroke Diagnosis	285
7.1	Introduction	285
7.2	Multi-Frequency Symmetry Difference EIT Applied to Stroke Diagnosis	287
7.2.1	The University College London Multi-frequency EIT Human Stroke Dataset	287
7.2.2	Multi-Frequency Symmetry Difference EIT Algorithm and Multi-Frequency GMI	288
7.2.3	Rationale for Application in Stroke	290
7.2.4	Theoretical Ideal Results	291
7.3	Modelling Techniques and Data Generation	292
7.3.1	Numerical Models	292
7.3.2	Multi-Frequency GMI Data Generation	294
7.4	Machine Learning Applied to Multi-Frequency GMI Data	295
7.4.1	Support Vector Machine Classifiers and Classification Protocol	296
7.4.2	Numerical and Human Classification Studies	299
7.4.2.1	Study 1: Normal versus Lesion (Bleed or Clot)	299
7.4.2.2	Study 2: Bleed versus Clot	300
7.4.2.3	Study 3: Normal versus Bleed	301
7.4.2.4	Study 4: Normal versus Clot	302

CONTENTS

7.4.2.5	Study 5: Multi-Class Classification	303
7.4.2.6	Study 6: Effect of Centrally Lying Lesions	304
7.4.2.7	Study 7: Effect of Noise on Classification Performance	305
7.5	Multi-Frequency Symmetry Difference EIT with Machine Learning for Human Stroke Diagnosis Discussion	306
7.5.1	UCL MF EIT Stroke Dataset - Other Remarks	309
7.6	Conclusions	310
8	Conclusions	312
8.1	Summary and Conclusions	312
8.2	Future Work	315
	Bibliography	318

Declaration of Originality

I, the Candidate **Barry James McDermott**, certify that the thesis entitled “**Electrical Impedance Tomography for Static Lesion Detection and Identification in the Brain**”:

- is all my own work;
- has not been previously submitted for any degree or qualification at this University or any other institution;
- and where any work in this thesis was conducted in collaboration, appropriate reference to published work by my collaborators has been made and the nature and extent of my contribution has been clearly stated.

Name:

Barry James McDermott

Abstract

There is a clinical need for a novel approach to the detection of brain haemorrhage and clots. Such static lesions are characteristic of important conditions such as stroke, and traumatic brain injury. In these conditions rapid and definitive detection, and identification of a causative lesion is vital to progressing the patient pathway and ensuring best patient outcomes.

Electrical Impedance Tomography represents an emerging technology that may be capable of translation into a brain haemorrhage and clot detection device. To date Electrical Impedance Tomography has found application in a number of biomedical areas, notably lung monitoring. Electrical Impedance Tomography can detect differences in the electrical conductivity profiles of tissues. As there is notable differences in the electrical conductivity profiles of haemorrhage, clot, and the other tissues of the head this motivates the primary overall research objective: to develop a novel brain haemorrhage and clot static lesion detector using Electrical Impedance Tomography.

Firstly, the clinical need is examined focussing on stroke and traumatic brain injury. The results of this analysis indicate there is a clear need for an efficient, robust, cost-effective, sensitive and specific device for the detection and differentiation of static brain haemorrhage and or ischaemic lesions. Electrical Impedance Tomography is proposed as a solution but key challenges for successful translation are identified such as the acquisition of better real world data, and the development of a dedicated Electrical Impedance Tomography algorithm capable of detecting and identifying static lesions.

Secondly, representative experimental Electrical Impedance Tomography data is generated from numerical models, and then from novel solid phantoms emulating the anatomy and conductivity of tissues of the head. In addition a human Electrical Impedance Tomography stroke data set is leveraged from University College London.

Thirdly, a novel symmetry based algorithm is developed that can detect and identify lesions using Electrical Impedance Tomography data. Machine learning

principles are also applied to the output from the algorithm. The proposed algorithm is tested and refined using synthetic data, and experimental data. The proposed algorithm is then applied to the clinical data from University College London, which includes data from patients both with and without brain lesions. These results suggest that the proposed algorithm can detect and identify stroke lesions in human patients. However, the synthetic data, experimental data, and clinical data all highlight that results are affected by electrode placement errors, and variations in patient anatomy. More work needs to be done to address ways to mitigate against, or improve the robustness of the algorithm to such errors.

In summary, this thesis examines and develops Electrical Impedance Tomography as a technology for detection of brain haemorrhage and clot lesions. A novel algorithm is proposed and tested that could be the basis of translation of Electrical Impedance Tomography into clinical use for such an application.

Acknowledgements

I would like to thank Martin and Emily for being stellar supervisors, and for giving me the opportunity to work with such a fantastic research group. This group included in no particular order Marggie, Eoghan, Niko, Conor, Adnan, Atif, Laura, Adam, Anna B, Anna G, Alessandra, Declan, Bárbara, Bilal, Nadia, Jiss, Saqib, and Nuno. Throughout the PhD journey they have given me support both technically and personally, which I hope I have reciprocated in some way. In addition I would like to thank my collaborators in University College London for being instrumental in catalysing the second part of the PhD, in particular Dr James Avery.

Outside of the Translational Medical Device Lab a special thanks goes to my amazing wife Treasa, my two sons James and Conor, and my parents for their patience, and support before, during, and now after my time doing a PhD. The journey to becoming an Engineer, and now a Doctor of Engineering would simply not have been possible without the help and support of my family.

List of Figures

2.1	The bones of the skull and suture lines. The suture lines are immobile strips that bind the skull bones together as one unit [28]	13
2.2	Parts of the brain as well as lobes of the cerebrae and some functional mapping [26]	14
2.3	Blood supply to the head. The left and right internal carotid arteries as well as the left and right vertebral arteries supply the brain [26] . . .	15
2.4	Anatomy of the cerebral arterial circle (Circle of Willis). The Circle of Willis is formed from the merging of the left and right internal arteries and the basilar artery. From the Circle of Willis, the major paired arteries that serve the brain emerge as the ACA, MCA, and PCA [26] .	16
2.5	Anatomy of the ventricular system. Choroid plexuses in the walls of the ventricles produce CSF. The lateral ventricles drain into the 3 rd ventricle and on into the 4 th ventricle. After this point the CSF flows either into the central canal of the spine or into the subarachnoid space [26]	17
2.6	Normal brain on non-contrast CT. In the case of acute ischaemic stroke an identical image is often seen as ischaemic changes such as oedema may not yet have occurred [66]	25
2.7	Left: Haemorrhagic Stroke seen on non-contrast CT. The presence of a bleed is seen as a hyperdense region with CT having sensitivity and specificity of near to 100 % for haemorrhage in the acute phase [67]. Right: Ischaemic Stroke seen on CT involving MCA territory (arrow). The hypodense regions indicated are due to tissue affected by the presence of a clot becoming oedematous and dying [68]	26
2.8	Left: Haemorrhagic stroke in the right posterior frontal region with dark borders imaged by gradient-echo MRI (arrow) [70]. Right: Ischaemic Stroke seen on diffusion-weighted MRI involving the right insular lobe [71]	27
2.9	NICE Stroke Overview Pathway (adapted from [54])	34
2.10	NICE TIA Pathway (adapted from [34])	35
2.11	NICE Acute Stroke Pathway (adapted from [3])	36
2.12	Simplified Acute Stroke Pathway. The crucial decision to be decided by imaging is to rule in or rule out the presence of a haemorrhagic lesion .	37

LIST OF FIGURES

2.13	Coup contrecoup injury. The coup injury refers to the injury at the point of impact, with the contrecoup injury a result of the rebounding of the brain to the opposite side [96]	39
2.14	NICE Head Injury Overview (adapted from [101])	42
2.15	NICE Investigation for Clinically Important Brain Injuries in Patients With Head Injury (adapted from [4])	43
2.16	An EIT setup with electrodes arranged around a body of interest as a ring. A given channel will be most sensitive to a particular region of the body, with tissues within this region most affecting the voltage reading at the boundary (adapted from [6])	56
2.17	Electrical model of biological tissue for EIT. Tissue is modelled as cells in ECF. The cell is then modelled as a resistor R_i and capacitor C_m in series representing the cell membrane and ICF respectively. The surrounding ECF is represented as another resistor R_e (this figure is adapted from [6])	62
2.18	Current movement thorough tissue at low and high current frequencies. At low frequencies the capacitor like cell membrane prevents current flow through cells with all current forced to flow through the ECF. At higher frequencies, the impedance of the cell membrane will drop allowing current flow through cells with a consequent overall reduction in impedance of the tissue (adapted from [6])	62
2.19	The electrical conductivity profiles of scalp, skull, CSF, brain, bleed and clot tissues across from 20 Hz to 20 kHz (data from [12], [146]) . . .	65
2.20	Channel from a Skip 2 protocol with current injected between electrodes #1 and #4 and voltage measured between electrodes #3 and #6. The electrodes form a 16-member ring around the body of interest with a perturbation present in the interior represented as a red circle	69
2.21	The Forward Problem explained in terms of the sensitivity (Jacobian) matrix (adapted from [6]). Each voxel in the body of interest has an assigned σ . The values of σ are known in the forward problem. The sensitivity matrix of a hypothetical simple body with three elements has three columns, with each column representing the σ of that element. For a given channel, that channel will be ‘sensitive’ to each element to a differing extent. This sensitivity is shown in grey in the sample injection/ measurement pair shown here. Hence the V for that channel will be the sum of the σ for each element multiplied by a weighting (sensitivity to) each element. It is usually the case that the number of elements far exceed the number of channels. The general equation for the voltage measurement of the n^{th} channel (V_n) in a body with m elements is shown	71

LIST OF FIGURES

2.22	Block diagram of the essential components of an EIT system. The digital stimulus is usually a sinusoidal wave form, and is used to drive an analogue current source using a digital-to-analogue converter. Multiplexers connect to and select the current injecting electrodes which are connected to the body of interest. On the other side multiplexers also select the measurement electrodes with the analogue measurement amplified and demodulated into a (usually) digital value with the additional use of an analogue-to-digital converter. A control system (not shown) automates the injection/ measurement protocol and collection of the complete measurement frame (adapted from [6], [10])	76
3.1	Three core component chemicals were used in the TMMs. Polyurethane (VytaFlex 20 from Smooth-On, Easton, PA, USA) (top left) was used as the mechanically stable base matrix into which two conductive fillers were added. These fillers were graphite (Graphite powder general purpose grade from Fisher Scientific, Loughborough, Leics, UK) (top right) and CB (Carbon Black, acetylene 50% compressed, 99.9% + from Alfa-Aesar Ward Hill, MA, USA) (bottom)	91
3.2	Summarisation of the TMM fabrication process. In (1), the two liquid polyurethane precursors ('A' and 'B') are weighed out 1:1 by mass, and homogenously mixed. This mixing begins the polymerisation process which takes 12 to 16 hours to complete. In (2), the conductive fillers of graphite and CB are weighed out before being homogenously mixed. Finally in (3), the graphite/ CB mix is added to the polyurethane steadily with thorough mixing again to achieve homogeneity until all is added. The final mixture is worked into the final desired shape here shown added to a mould, and allowed set overnight. For TMMs with a high percentage of conductive filler, acetone or isopropanol is added to aid mixing as well as boosting conductivity	93
3.3	Rectangular cuboid samples of the TMMs made from polyurethane, graphite, and CB	94

LIST OF FIGURES

3.4	AC Conductivity curves over the 1 kHz–1 MHz band are plotted, demonstrating the effect of isopropanol when added to two of the TMM mixtures: the Blood TMM and the Fat TMM 2. In both cases, the conductivity is dramatically increased when isopropanol is added to the TMM compared to when not. The greatest increase is for the fat mimicking TMM. The reference tissue profiles shown are those of highly conductive biological tissues for which these isopropanol containing mixtures may be useful: CSF and urine (with blood and fat also shown) [148]. The values are plotted on (top) linear frequency scale and (bottom) logarithmic frequency scale. The two different scales are used for clarity	96
3.5	Complex impedance spectroscopy of a TMM sample (labelled as (1)) using a three-electrode setup. The electrodes (crocodile clips) connect to the PARSTAT 2273 potentiostat (not shown)	98
3.6	AC conductivity curves for the reference tissues of blood, Intermediate Brain Hybrid, Outer Hybrid, clot, fat [12], [146], [148], and the selected TMM mixtures that most closely emulate these target tissues across the 1 kHz–1 MHz frequency band. The values are plotted on (top) logarithmic frequency scale and (bottom) linear frequency scale. The two different scales are used for clarity	100
3.7	AC conductivity curves for the reference tissues of blood, Intermediate Brain Hybrid, Outer Hybrid, clot, fat [12], [146], [148], and the selected TMM mixtures that most closely emulate these target tissues across the 50 kHz–250 kHz band. This band of 50 kHz–250 kHz is covered by a commercially available EIT research device, the Swisstom EIT-Pioneer [187]	102
3.8	3D-printed phantom of the 3-layer head model presented in [139]	106
3.9	3D-printed anatomically accurate (in terms of structure and size) head (left) and brain (right). The photographs are not shown with the same scale, i.e., the brain here is shown larger than actual size relative to the head for purpose of illustration	108
3.10	Counter mould of the head made from polyurethane with the impression of the 3D-printed head (left). The 3D brain mould is positioned in the head counter mould cavity with outer layer TMM laid down around the brain mould (right). The positioning of the brain within the cavity is based on anatomical information [225] to ensure the placement is accurate. A wire is placed around the brain, falling into the cerebral fissure on the topside, in order to aid removal of the printed brain after the outer layer TMM sets	109

LIST OF FIGURES

3.11	Removal of the brain mould leaves the completed outer layer in the head counter mould. The impression of the outer brain surface is imprinted on the inner side of this outer layer. In the case of the hollow head phantom, saline is now added to model the brain. In the case of the solid phantom, an inner layer of brain mimicking solid TMM is subsequently added (with cavities for lesion phantoms). See also Fig. 3.15	110
3.12	Cylindrical plugs (labelled in the picture as (1)) used to create the cylindrical cavities in the brain layer of the solid head phantom. Plugs of phantom material are then created using the corresponding mould (labelled in the picture as (2)). Material is packed into the two halves of the cylindrical mould, which are then joined and allowed to set. A completed phantom plug is shown (labelled in the picture as (3)). The plug may be purely healthy brain mimicking TMM, purely haemorrhage (or clot) TMM, or contain discrete blood (or clot) lesions of known size and location embedded in brain TMM. Some examples of blood and clot TMM lesions are shown (labelled in the picture as (4)). These lesion TMMs can be sized and shaped as required. The lesions are then inserted into the mould (labelled in the picture as (5) and (6)) where two lesions are positioned surrounded by brain mimicking TMM in one half of the mould, before the second half of the mould is placed on top, completing the phantom plug. In addition, the discrete haemorrhage or clot lesions shown in (labelled in the picture as (4)) can be used in the hollow phantom when suspended in the saline brain layer	112
3.13	Steps involved in head phantom fabrication process. In (1) the 3D-printed head is used to create an impression in polyurethane which then sets, leaving a head shaped counter mould cavity as shown in (2). Next, the outer layer TMM is packed into the cavity and the 3D-printed brain mould positioned to ensure the outer layer is laid correctly as shown in (3). Once set, removal of the 3D-printed brain leaves a cavity. Removal of the counter mould at this point and filling of the cavity with saline to model brain results in the hollow head phantom (shown in (4a)). Discrete phantom lesions can be suspended in the saline brain to model pathology (shown in (5a)). In the case of the solid head phantom, the cavity is filled with brain TMM with cylindrical rods placed and positioned to leave cavities for plugs (shown in (4b)). Once the brain TMM is set, the counter mould and cylindrical rods are removed leaving the complete solid head phantom with an outer solid layer, inner solid brain layer and cavities that can be plugged with cylindrical plugs that can be made exclusively of brain TMM or can have discrete lesion phantoms at known positions (shown in (5b))	113

LIST OF FIGURES

3.14	Final solid head phantom shown upright (top left, top right and bottom left) and inverted (bottom right). The inverted view shows the three cylindrical cavities, one of which has a cylindrical plastic plug inserted. The cavities are at an oblique angle to maximize the area of the brain into which phantom lesions can be positioned	114
3.15	Left: The designed hollow head phantom shown with electrodes positioned in a ring arrangement. Right: Wooden rods are used to attach and place lesions within the saline brain layer. The electrodes are attached to a Swisstom EIT-Pioneer set which records the measured voltages as part of the measurement frames	115
3.16	Reconstructed tEIT images for the hollow head phantom for the case of phantom haemorrhagic lesions, with the EIT setup having a 16 member electrode ring positioned as shown in Fig. 3.13. In both cases, the baseline measurement frames have the saline brain without a phantom haemorrhagic lesion present (normal case), with these frames averaged to reduce noise. Left: A 35 ml spherical phantom haemorrhagic lesion is placed midway between the sagittal plane of the head and electrode #13 with measurement frames taken (and averaged). Right: A 20 ml rectangular cubic phantom haemorrhagic lesion is placed near electrode #8 with measurement frames taken (and averaged). In both cases the averaged frames with the lesion present are differenced with respect to the averaged baseline frames, and the resulting time-difference image is then reconstructed. The haemorrhagic lesion is more conductive with respect to the saline background and so a positive difference intensity is expected. This result is clearly seen in the expected region where the perturbation is placed. Further, the magnitude of the difference intensity is greater in the case of the larger 35 ml lesion than for the 20 ml lesion	117
3.17	Example of the fabricated 3D-printable TMM	120
3.18	AC Conductivity curves for the reference tissues [148] (blood, fat) shown with dashed lines, and the 3D-printable TMM mixtures containing CB (0 %, 5 %, 6.5 %, and 11 % by mass) shown with solid lines across the 1 kHz–1 MHz frequency band. Note that the trace for 0 % CB overlays the x-axis. The values plotted in (top) are in logarithmic frequency scale and in (bottom) are in linear frequency scale. The two scales are presented for clarity	122
3.19	Successfully 3D-printed rectangular disc made from the 3D-printable TMM mixture containing 6.5 % CB	123

LIST OF FIGURES

4.1 The basis of SVM classification. Here n-dimensional data points are separated by a 2-dimensional hyperplane into +1 or -1 categories depending on what side of the hyperplane they are on. Support vectors are those data points that define the margin about the hyperplane. These support vectors are shown by the circles on the hashed lines . . . 130

4.2 The Confusion Matrix for a binary classifier with classes ± 1 . The expected (true) class and predicted class assigned to cases are compared. A True Positive (TP) is where a case is truly +1 and classified as such. A True Negative (TN) is where a case is truly -1 and classified as such. A False Positive (FP) refers to cases that are truly -1 but misclassified as +1. A False Negative (FN) refers to cases that are truly +1 but misclassified as -1. The performance of a classifier on a test set is often reported as a confusion matrix with the number of cases in each category shown. Many other performance metrics are derived from the confusion matrix 131

4.3 Receiver Operating Curves (ROC) curves are a plot of sensitivity versus (1 - specificity), and show the trade-off possible between sensitivity and specificity. An ideal ROC curve has an Area Under the Curve (AUC) of 1 with an example of this shown as the blue plot. Here an operating point where both sensitivity and specificity are both 100% is at (0,1). The red and orange plots show imperfect ROC curves where $AUC < 1$. In this case it is possible to maximise sensitivity by moving to the operating point shown with the penalty of reduced specificity. Depending on the application this trade off may be acceptable. At any given point the red curve gives a better sensitivity/ specificity trade off compared to the orange curve. The orange curve only offers a sensitivity of 1 where specificity is 0, which would result all observations being classified as +1 132

LIST OF FIGURES

4.4	<p>Numerical model of the head. Left: The base numerical model is an anatomically accurate 2-layer model of the brain and aggregated tissues external to the brain. The 16-member electrode ring is shown with electrode contact areas in green, and white numbering of some electrodes for orientation. Right: Removal of the brain layer to illustrate the size and positioning of the bleeds. The positioning of the electrodes #1-16 is shown as a ring of white numbers. Bleeds of volume 30 ml and 60 ml are positioned in the north, south, east, and west locations as shown. A given model will contain no bleed or only one bleed. The bleeds are positioned towards the exterior of the brain layer, and in the plane of the ring. The different colouring of the layers represents the different electrical conductivities: 0.1 Sm^{-1} for the aggregate outer layer (white), 0.3 Sm^{-1} for the brain (yellow) and 0.7 Sm^{-1} for bleed (burgundy)</p>	137
4.5	<p>Left: The phantom head model with EEG electrodes attached to form a 16-member ring. Right: Wooden rods are used to attach and place lesions inside the saline brain layer. The electrodes are attached to a Swisstom EIT-Pioneer set which records measurement frames</p>	139
4.6	<p>Summary of workflow for the application of SVM classifier to measurement frames studying the effect of individual parameters in both numerical studies (Section 4.4.1) and phantom studies (Section 4.4.2). For a given study the complete experiment is performed with the frames unsorted and then with the frames sorted. In all cases the complete set of n measurement frames has an equal number of normal and lesion models, with a greater number used in the training set compared to the test set (i.e. $x > y$)</p>	141
4.7	<p>Classifier results from test data in numerical model Study 1: Effect of Noise. Separate experiments are done for 80 dB, 60 dB, 40 dB, and 20 dB noise levels. The raw measurement frames used to train and test the linear SVM are unsorted or sorted by numerical value. For both of these resultant classifier models, the performance is given as the AUC of the ROC curve generated from the training data and the sensitivity (Sens.) and specificity (Spec.) of the classifier on the test data at the default operating point and at the adjusted operating point. The adjusted operating point is selected to augment sensitivity, at the expense of specificity. From the plots, it is seen that the classifiers perform well at 80 dB and 60 dB with performance starting to drop at 40 dB and becoming poor at 20 dB. The adjusted operating point does boost sensitivity as expected. This boost in sensitivity has most obvious benefit seen at 40 dB</p>	143

LIST OF FIGURES

4.8	The channels of maximal difference between the normal and lesion cases are reported. The channels suggest the lesion may be at the north location, as electrodes involved in these channels (for example #1 & #16) are adjacent to this location. The 60 ml bleed shows a greater difference relative to the normal than does the 30 ml case. Further, separation is more distinct at a higher Signal to Noise Ratio (SNR) with overlap increasing at 40 dB	145
4.9	Classifier results from test data in numerical model Study 2: Effect of Lesion Location. Separate experiments are done for 80 dB, 60 dB, 40 dB, and 20 dB noise levels with results arranged in the same format as Fig. 4.7. Both using a sorted measurement frame and the adjusted operating point dramatically improve sensitivity at a given SNR. Implementing both of these modifications result in excellent classifier performance at the 80 dB and 60 dB points, indicating that in these cases the classifier still works well even when test data lesion locations differ from training data locations	147
4.10	Classifier results from test data in numerical model Study 3: Effect of Lesion Size. The models are trained using the 60 ml lesion in all possible locations in the base numerical model. Separate testing is then performed on unseen normal frames and separately each of 30 ml, 20 ml, 10 ml, and 5 ml lesion at all locations, with 60 dB noise added in all cases. Training data features all locations, rendering the effect of sorting the frame redundant. Using the adjusted operating point boosts sensitivity in all cases with lesions robustly detectable down to a 10 ml volume	150
4.11	Classifier results from test data in numerical model Study 3: Effect of Lesion Size. The models are trained using the 5 ml lesion in all possible locations in the base numerical model. Separate testing is then performed on unseen normal frames and separately each of 60 ml, 30 ml, 20 ml, and 10 ml lesion at all locations, with 60 dB noise added in all cases. Training data features all locations, rendering the effect of sorting the frame redundant. Sensitivity and specificity in all cases is excellent at the default operating point, while using the adjusted operating point unnecessarily reduces specificity of the classifier that uses unsorted frames but does not appreciably affect performance of the classifier that uses sorted frames	152

LIST OF FIGURES

4.12	Classifier results from test data in numerical model Study 6: Final Overall Study. The classifiers perform well at the 80 dB and 60 dB points. The sorting of the frames developed to compensate for test data featuring lesions in previously unseen locations has little effect as training features cases from all 4 locations. However, there is a noticeable improvement when using sorted frames at the 80 dB point. Using the adjusted operating point increases sensitivity in all cases at the expense of a perhaps unacceptable drop in specificity	156
4.13	Classifier results from test data in phantom model Study 1: Repeatability. Variances are seen in performance of the same experiment on each of the 3 days. Sensitivity approaches 1 in all cases when the adjusted operating point is used, with a variable reduction in specificity depending on the day	158
4.14	Classifier results from test data in phantom model Study 2: Effect of Lesion Location. On average, the best overall performance is seen when the raw measurement frames are sorted, and classification performed at the adjusted point designed to maximise sensitivity. Results are seen to differ from day to day as expected due to variation in electrode positioning and other sources of systematic error	160
4.15	Classifier results from test data in phantom model Study 3: Effect of Lesion Size - detection of lesions smaller than those in the training set. Specificity is high in all cases, which is a consequence of the normal model being the same for the training and test measurement frames. Sensitivity is boosted using the adjusted point reaching about 80% using the results from Day 1 but dropping to under 60% for Day 3	161
4.16	Classifier results from test data in phantom model Study 3: Effect of Lesion Size - detection of lesions larger than those in the training set. Specificity is generally high in all cases, with the exception of Day 1. The use of smaller lesions for training may result in increased false positives. Sensitivity is higher than in Fig. 4.15, and is boosted using the adjusted point reaching 100% on all days	162
4.17	Classifier results from test data in phantom model Study 4: Effect of Electrode Positioning and Anatomy. Any given classifier performs poorly with simultaneous high values of specificity and sensitivity not achieved in any case. Interestingly the classifier trained and tested with unsorted frames give a specificity of 100%, while the classifier trained and tested with sorted frames give a sensitivity of near 100% suggesting that a cascade of classifiers may provide improved results	164

LIST OF FIGURES

4.18	Classifier results from test data in phantom model Study 5: Final Overall Study. The best performance is seen with the sorted frames used at the default operating point, giving a sensitivity and specificity of 75%. Moving to the adjusted operating point improves sensitivity but severely causes a reduction to specificity. The results are between those of the 60 dB and 40 dB numerical study results reported in Fig. 4.12, as expected since the experimental SNR is ~ 50 dB	165
4.19	Nested cross-validation. The complete data set is separated into $k = 10$ folds with 90% as a training set (white) and 10% as a test set (grey). The training set from each of these outer folds is itself divided similarly into $m = 10$ inner folds divided into training (white) and test (grey) sets, with 10-fold cross validation performed on the inner fold to optimise hyper-parameters. These hyper-parameters are then used to train a final SVM model on the entire training set, with performance assessed on the held out test set. This process is repeated over the k folds with a final overall performance reported as the mean \pm standard deviation	167
4.20	Performance results across classifiers. The sensitivity, specificity and accuracy of each of three classifiers (Top: Linear SVM, Middle: RBF SVM, Bottom: NN) is expressed as the mean \pm standard deviation following training and testing of each classifier on the total pooled numerical data across the 10-fold testing, with each dot representing the mean classifier performance and the error bars representing the standard deviation range at the respective noise level (at the four SNR levels of 80 dB, 60 dB, 40 dB and 20 dB). There is a significant improvement in performance when using the RBF kernel, notably at the 60 dB and 40 dB SNR levels	169
4.21	Generating the mean of each sub-frame. Each sub-frame is made up of the 16 channels associated with a given injection pair. Removal of channels involving either of the injection pair electrodes gives 16 sub-frames each with 13 channels. The mean of the voltage measurements from each set of 13 channels in a given sub-frame is used leaving 16 values, the sub-frame means. These subframes are used as inputs to the classifier	171

LIST OF FIGURES

4.22	Performance of the RBF-SVM using sub-frame means as input features. Each dot on the plot denotes the mean classifier performance across the 10-fold testing, with the error bars representing the standard deviation range at the respective noise level. The performance at 80 dB SNR is near the ideal of 1 ± 0 for all metrics, comparable to the performance achieved when using the complete frames. However, performance falls off quickly at lower SNRs, with all metrics below 0.85 at 60 dB and at approximately 0.5 at 40 dB and 20 dB	172
4.23	Near and Far Sub-Frame Channels. Here the injection pair of 1-4 is shown (red). The 7 nearest channels are shown in orange, with the 6 far channels shown in green. Channels involving the measurement pair are not considered. These near sub-frames and far sub-frames channels are then used as inputs to the classifier	173
4.24	Comparison of RBF-SVM classifier performance with using the near (top) and far (bottom) sub-frame channels as input features. Both the near and far sub-frame channels results in perfect (1.00 ± 0.00) performance at 80 dB SNR, and near perfect ($\geq 0.99 \pm 0.01$) at 60 dB SNR. At lower SNR levels of 40 dB and 20 dB the near sub-frames outperform the far sub-frames. Of note, the near sub-frames result in equivalent performance to using full measurement frames at all SNR points	174
4.25	The performance of the RBF-SVM classifier using a different the number of ranked features, measured by the generalised accuracy. The ranked features were determined using the Laplacian Score. The optimal point at a given SNR is that offering the highest accuracy with the lowest number of features	176
4.26	Performance of the RBF SVM Classifier at each SNR level using features based on Laplacian Scores. The number of ranked features offering maximal accuracy is pre-determined with this feature set (selection of channels) used to train and set the classifier. Perfect performance is achieved at 80 dB SNR with 1.00 ± 0.00 in all metrics, with the use of only 25 features. In addition, an accuracy of ≥ 0.97 at 60 dB SNR is achieved using 75 features	177
4.27	A comparison of the generalised accuracy at the four SNR levels as the number of principal components is increased. The optimal number of principal components at each SNR level is that number giving the highest generalised accuracy which is 10, 10, 11 and 31 principal components for 80 dB, 60 dB, 40 dB, and 20 dB SNR levels respectively	179

LIST OF FIGURES

4.28	Comparison of the performance at each of the four SNR levels for the classifier after performing PCA. Perfect performance (1.00 ± 0.00 in all metrics) is given at the 80 dB and 60 dB SNR levels despite using only 10 components at each point. A near 0.1 (10%) improvement in accuracy is seen at the 40 dB SNR level compared to the full measurement frames, but performance is approximately 0.5 in all metrics at 20 dB SNR essentially representing a random classifier	180
4.29	Example of the design and implementation of the ensemble classifier. The measurement frame for a given case can be divided into subframes with the channels from each subframe used as the input for a separate classifier. The complete set of frames are segregated in this way with 16 classifiers trained and tested. Each classifier separately labels a case as ± 1 with the aggregate result calculated according to a threshold which can be adjusted	182
4.30	ROC curves for the Ensemble Classifier at each SNR level. The points on each curve correspond to each discrete threshold value between 1 and 16 from right to left, with the corresponding line interpolated between the points. The curves illustrate the trade-offs between sensitivity and specificity possible at each SNR level by changing the operating points. Both the 80 dB and 60 dB plots offer an operating point of perfect performance (0,1). Performance is reduced at 40 dB and is worst at 20 dB SNR as expected. The 20 dB line is approximately that of a random classifier, being a diagonal line passing through the points (0,0) and (1,1)	183
5.1	Summarised version of the two steps comprising the sdEIT algorithm. In Step 1 the outcome is the detection or no detection of a lesion. After Step 2 the conclusion is either no lesion detection or lesion detection with disambiguation resulting in identification (bleed or clot in this application), as well as localisation. Further details and a thorough description are provided in Section 5.3	191

LIST OF FIGURES

5.2	<p>Left: sdEIT electrode layout on a simplified numerical model of the head (transparent) and brain (burgundy) based on spherical geometry where the natural plane of symmetry, the sagittal plane, is shown as a green dashed line. The view is from the top down with front, left, and right sides of the head marked. The clockwise electrode orientation are shown as red numbered electrodes. The counter-clockwise electrode orientation are shown as green numbered electrodes. Centre: A spherical haemorrhagic lesion inside the now transparent brain layer. The lesion is near to the clockwise orientation Electrode #4, which is the same as counter-clockwise orientation electrode #13. Right: The injection/measurement pattern of a sample channel. The injection pair is shown in light colour, while the measurement pair is in a heavier tone. The clockwise orientation channel is in red while the corresponding counter-clockwise orientation channel is in green. The two respective channels of the same colour are symmetric partners</p>	195
5.3	<p>Left: Symmetry difference image showing a conductive target near Electrode #4 and a non-conductive target near Electrode #13. Right: Surface plot of the symmetry difference image. The z-axis of the surface plot (64 x 64 grid) shows the intensity values of the differences detected (arbitrary units). The topology is dominated by the symmetrical peak and trough caused by the presence of the lesion</p>	196
5.4	<p>Symmetry Difference Image of the normal (no lesion) case is shown on the left with a surface plot (64 x 64 grid) shown on the right. The z-axis of the surface plot shows the intensity values of the differences detected (arbitrary units). The topology is chaotic and of low intensity as compared to the case where a lesion is present and dominates the topology, as shown in the surface plot in Fig. 5.3. The IS metric of +0.14 in the normal case suggests that a lesion likely not present</p>	198
5.5	<p>Thresholded images where the top and bottom 10% (by intensity) of pixels are kept. The difference intensities are mapped to a 0 – 256 scale, the colourbar of which is shown between the figures. Left: Symmetry difference image thresholded. From this thresholded image, the potential targets of a conductive target near Electrode #4 or non-conductive target near Electrode #13 are isolated. Right: Pseudo normal difference image thresholded. The largest high intensity and low intensity regions of interest in both images are compared quantitatively to assess if the high conductivity or low conductivity targets match. It is evident that the true lesion is the high intensity target near Electrode #4</p>	201

5.6 Left: Anatomically accurate 2-layer FEM model of head with brain and outer layer assigned conductivity values of 0.3 Sm^{-1} and 0.1 Sm^{-1} , respectively. A ring of 16 electrodes are represented as green circles. This electrode ring is placed symmetrically across the sagittal plane in a layout analogous to that shown in Fig. 5.2. Right: Locations and sizes of the phantom lesions used. The brain layer is removed for clarity. Locations: (1) near Electrode #4 (Electrode #13 on counter-clockwise orientation); (2) far from Electrode #4 (Electrode #13 on counter-clockwise orientation); (3) near Electrode #8 (Electrode #9 on counter-clockwise orientation); (4) far from Electrode #8 (Electrode #9 on counter-clockwise orientation); (5) midway from the sagittal plane and Electrode #13 (Electrode #4 on counter-clockwise orientation). Sizes: locations (1) and (4) are shown with 2 ml lesions, (2) has a 10 ml lesion, (3) has a 20 ml lesion and (5) has a 30 ml lesion. It should be noted that due to the method of assigning interior elements there is a pixellation effect and thus the lesion shapes are not perfect spheres in the FEM model 204

5.7 Tank experimental setup. Top left: Tank filled with saline and the two electrode rings. The clockwise electrodes are red, and odd numbered. The counter-clockwise electrodes are black, and even numbered. The electrodes from both orientations are co-located on the wingnuts of the bolts. Top right: Samples of the spherical phantoms used. These phantoms proportionally match 30 ml, 10 ml and 2 ml haemorrhages in a realistic-sized human brain. Bottom left: Wooden sticks are used to suspend a phantom at a fixed point in the tank with the aid of graph paper under the tank. Bottom right: Close up of a cuboid phantom next to Electrode #4 on the clockwise ring (Electrode #13 on the counter-clockwise ring) 206

5.8 Symmetry difference images thresholded (left) and pseudo normal difference images thresholded (right) for 10 ml bleed near Electrode #4 (top) and 10 ml bleed far from Electrode #4 (bottom), both at 20 dB SNR. The lesion near the extremity shows a high IS and clear disambiguation favouring the high intensity ROI lesion. For the lesion far from the electrode near the midline of the head, symmetry is very poor. This result should lead to a decision at this point that a lesion cannot be detected. The results of the second step for the near midline lesion shows that ROI analysis fails to determine the true lesion. Quantitative metrics collating with these observations are reported in Table 5.2 . . . 208

LIST OF FIGURES

5.9	Symmetry difference images thresholded (left) and pseudo normal difference images thresholded (right) for small bleed (top) and large bleed (bottom), both at 40 dB SNR. In both cases the lesions are strongly detected, with both images sharing the high intensity ROI (i.e. haemorrhage), as quantified by the metrics reported in Table 5.3	209
5.10	Symmetry difference images thresholded (left) and pseudo normal difference images thresholded (right) for equivalent haemorrhagic (top) and ischaemic (bottom) targets at 40 dB SNR. The symmetry difference technique detects both equally well	211
5.11	Surface plots of the symmetry difference images resulting from a haemorrhagic lesion (left) and ischaemic lesion (right) both of 20 ml located at position (5) with 40 dB SNR. The magnitude of the peak and trough corresponding to the haemorrhage and anti-haemorrhage lesion is 1669 (arbitrary units). For the ischaemic lesion this value is 1372 (arbitrary units). Hence the haemorrhagic lesion is easier to detect. However, the ischaemic lesion is still detectable	212
5.12	Symmetry difference images thresholded (left) and pseudo normal difference images thresholded (right) for in all the cases a 10 ml ischaemic lesion near Electrode #8: Top row images with 80 dB SNR, middle row images with 20 dB SNR, and bottom row images with 10 dB SNR. At 80 dB SNR the target is clearly detected and disambiguated. The lesion is barely detectable at 20 dB. At 10 dB SNR the lesion is undetectable. These visual analyses are quantified in Table 5.6	214
5.13	Symmetry difference images thresholded (left) and pseudo normal difference images thresholded (right) for the cases of (top row) a 20 ml haemorrhagic lesion at position (5) but raised out of the plane of the ring, and (bottom) the case where two haemorrhagic lesions are simultaneously present at both positions (1) and (5) of 10 ml and 20 ml volume respectively. The simulations are performed at a noise level of 80 dB SNR. In the case of the lesion outside the plane of the ring the haemorrhage is readily detected. For the case of two simultaneous lesions the larger bleed is detected. These visual analyses are quantified in Table 5.8	219
5.14	Symmetry difference images thresholded (left) and pseudo normal difference images thresholded (right) of haemorrhagic lesions of equal volume (10 ml equivalent) placed near to clockwise Electrode #4 (top row) and far from Electrode #4 (bottom row). As expected the scenario with the lesion near the electrode is more clearly detectable but the far from Electrode #4 case is also readily identified	221

LIST OF FIGURES

5.15	Symmetry difference images thresholded (left) and pseudo normal difference images thresholded (right) of small ischaemic lesion (top row) and large ischaemic lesion (bottom row) both positioned midway from Electrode #13. The small target, which is equivalent to a 2 ml lesion in a real brain is not detectable and the negative IS score is a clear indicator of this. The large 30 ml equivalent target is easily detectable and robustly disambiguated by the ROI disambiguation metrics	222
6.1	CAD model of the 4-layer head showing the scalp, skull, CSF and brain layers as well the position of the 32 electrodes. The sagittal plane represents a natural plane of symmetry in the head. Lesions in the numerical models were modelled as spheres of volume 10 ml and 50 ml positioned in one of Positions I, II or III. In this figure, 10 ml lesions are shown at Positions I and II, with a 50 ml lesion at Position III. In the phantom, cubic phantoms of equivalent volume were used at the same locations	231
6.2	3D printed phantom of the 3-layer head model with 10 cm ³ potato perturbation at Position III. The perturbations are suspended in place using a wooden pole and small stick as shown	233
6.3	Summarised version of the two steps comprising the BFS-D-EIT algorithm. In Step (1), the outcome is the detection (or lack thereof) of a lesion. After Step (2), the conclusion is either no lesion detection or lesion detection with disambiguation resulting in identification (bleed or clot in this application) as well as localisation	235
6.4	Six electrodes from A-orientation and the symmetrically equivalent B-orientation are shown along with 3 sample electrode pairs from each orientation. Any given pair from A-orientation is the symmetric equivalent of that from B-orientation (for example A11-A12 is the equivalent of B11-B12). In the absence of a perturbation or if there is a perturbation lying on the sagittal plane, the measurement recorded from a given pair should be identical to the respective symmetric partner pair. In this diagram, a 50 ml perturbation is in Position III (highlighted in blue). The perturbation will result in differences in the symmetric partner pair measurements. Also, it is seen that Electrode #6 from both orientations lies on the plane of symmetry (the sagittal plane) and so is its own symmetric partner. Finally, it can be seen that the algorithm used to design the Pair Drive Skip 0 pattern ensures that the distances between each electrodes pair constituting a channel is maximised	237

LIST OF FIGURES

6.5 Reconstructed images and quantitative metrics for a 50 ml clot at Position III. At f_1 the lesion has a conductivity of 0.05 Sm^{-1} and the surrounding brain conductivity is 0.1 Sm^{-1} . The image for this frequency point shows ROIs suggestive of a conductive lesion in the true position and a confounding anti-lesion in the symmetrically opposite position. This result could be caused by a clot in Position III or a bleed in the symmetrically opposite position. Also, artefacts are seen near the mesh surface. At f_2 a clot has a conductivity of 0.09 Sm^{-1} while the brain conductivity is the same as at f_1 . The result is a much noisier image at f_2 than f_1 due to the reduced contrast. A clot is expected to produce this behaviour while the image of bleed at f_2 would give a result identical to the first image (at f_1). Hence the true lesion must be a clot, at Position III. The quantitative metrics support this conclusion with both the GMI and RMI having an “equal but opposite” pattern with larger magnitude in figures at f_1 than at f_2 as a result of more contrast between the tissues at f_1 than at f_2 . The enhanced contrast is also reflected in the increased volume of ROIs at f_1 and smaller DCL, relative to f_2 240

6.6 Reconstructed images and quantitative metrics for a 10 ml bleed at Position II (left) and for a case where no lesion is present (right). For both scenarios, the conductivities of the tissues are the same at both f_1 and f_2 , meaning the results are identical at both frequency points, hence only the results at one f point (arbitrarily f_1) are shown. The case with no lesion is near identical to the case where a 50 ml bleed is at Position I (not shown), since there is no deviation in symmetry between the two sides when a lesion lies on the plane of symmetry and hence no lesion is detectable. Artefacts are seen near the mesh surface but are not part of the brain layer 242

- 6.7 GMI metrics for each of the 13 cases at each of the noise levels. The notation used to describe each case is given in Table 6.2 with ‘1’ corresponding to f_1 and ‘2’ corresponding to f_2 . The blue bars represent a negative intensity value and the red bars a positive intensity value on either the LHS or RHS depending on the case. The normal case (N) and lesions on the sagittal plane (Position I, i.e., cases A/a and B/b) are expected to have near zero values. Bleeds away from the midline (Positions II and III, i.e., cases C-F) are expected to give identical results at each frequency. Clots away from the midline (i.e. cases c-f) will result in values of increased magnitude at f_1 relative to at f_2 as the contrast between clot and the background reduces. Left: Results with noise-free frames (i.e., $\text{SNR} = \infty$). Right: Results with 60 dB and 40 dB SNR. Note the axes correspond to those of the noise-free plot, with the grid lines grouping cases of the same location and nature. At 60 dB the results are still similar to the noise-free scenario, however now the “equal but opposite” property is compromised. At 40 dB, results become excessively noisy with only cases C, D, F clearly detectable. These plots indicate that the presence and disambiguation of a lesion is possible with this metric alone. Larger lesions should have values of greater magnitude than the corresponding smaller lesion. The localisation to the level of whether the lesion is in the LHS or RHS, is also possible to derive 245
- 6.8 The Quantitative ROI metrics: RMI and DCL for the 13 cases at various noise levels. If no ROI is detected in a given case at a given frequency point, then no metric value is listed. Left: The noise-free scenario (i.e., $\text{SNR} = \infty$). Right: The results at 60 dB and 40 dB SNR levels (note the axes correspond to those of the noise-free plot, with the grid lines grouping cases of the same location and nature). The bars represent the RMI for the ROI_H (red bar) and ROI_L (blue bar). The DCL between a ROI_H and ROI_L for a given case is reported in mm to the right of the red bar. Ideally, $\text{DCL} = 0$; therefore, cases with high values indicate failed detection 246

6.9 GMI results for each of the 7 cases with the 1-layer phantom (left) and 3-layer phantom (right). The notation used to describe each case is given in Table 6.3 with ‘1’ corresponding to f_1 and ‘2’ corresponding to f_2 . The blue bars represent a negative intensity value and the red bars a positive intensity value on either the LHS or RHS depending on the case. The potato perturbation is conductive with respect to the saline background at both f_1 and f_2 , with increased contrast expected at f_2 . The normal case (N) and perturbations on the sagittal plane (Position I, i.e., cases A and B) are expected to have near zero values. Position II and III cases (C – F) are expected to result in a negative intensity on the side the perturbation is truly on, with an equal but opposite positive intensity on the other side. Further the magnitude of intensities will increase for the Position II and III cases from f_1 to f_2 . The smaller perturbation will follow the same pattern as the larger perturbation in a given location but result in smaller magnitude of values (C compared to D, E compared to F). Finally, perturbations nearer the exterior (C, D) will give higher magnitude values compared to those further from the exterior (E, F). These expected patterns are borne out for the no skull (1-layer) set of results. *A priori* knowledge of the expected pattern of conductivity change for potato with respect to saline allows the detection, identification, and to an extent localisation of the perturbation. In the case of the 3-layer phantom, the presence of the skull which is a highly insulating layer dampens the signal, indicated with the lower magnitude of values compared to the 1-layer case. The results are as expected for cases D, E, F but the “equal but opposite” principle is violated 250

6.10 The Quantitative ROI metrics: RMI and DCL for the 7 cases with the 1-layer phantom (left) and 3-layer phantom (right). If no ROI is detected in a given case at a given frequency point, then no metric value is listed. The bars represent the RMI for the ROI_H (red bar) and ROI_L (blue bar). The DCL between the ROI_H and ROI_L for a given case is reported in mm to the right of the red bar. The results indicate that lesions are detectable with expected behaviour when no skull is present. However, detection suffers using these metrics when the skull is present 251

LIST OF FIGURES

6.11	Reconstructed images for a 50 cm ³ cubic potato perturbation at Position III in the 1-layer phantom case (left) and the 3-layer case with the skull (right). The images at both 80 kHz (f_1) and 100 kHz (f_2) are shown. Potato is found to become more conductive with respect to saline from f_1 to f_2 with the enhanced contrast at f_2 evidenced by sharper ROIs and more intense ROIs at this point. The skull layer, being highly insulating, reduces the signal rendering images noisier when compared to the simpler 1-layer case. Further, the intensity of the voxels of the ROIs in the skull case is lower than in the no skull case	252
6.12	The fine FEM model used in Section 6.4 viewed from above. This FEM has electrodes in A-Orientation. The sagittal plane is shown as an orange line. The positions of the two model lesions, a 10 ml spherical bleed ('B') and 50 ml spherical clot ('C') are shown. In a given case only one or neither of the lesions are present	257
6.13	Top: Reconstructed images of the ideal model for the three cases at an f point of 25 Hz: No lesion present (N); 10 ml spherical bleed at Position II (B); 50 ml clot at Position III (C). The N case shows noisy artefacts towards the exterior of the FEM whereas when a lesion is present the ROIs corresponding to the perturbation are the dominant feature. Bottom: Quantitative metrics corresponding to the reconstructed images. GMI: The blue bars represent a negative intensity value and the red bars a positive intensity value on either the LHS (negative x-axis) or RHS (positive x-axis). RMI: If no ROI is detected in a given case at a given frequency point, then no metric value is listed, the bars represent the RMI for the ROI _H (red bar) and ROI _L (blue bar) on either the LHS (negative x-axis) or RHS (positive x-axis). IN, MD and DCL are reported if ROIs are detected. The RDR for each case is reported on the x-axis of the IN, MD, DCL plot	260
6.14	Quantitative Metrics for models where noise of 80 dB, 60 dB and 40 dB SNR is added to the measurement frames prior to reconstruction for cases N (no lesion present); B (bleed); C (clot). GMI: The blue bars represent a negative intensity value and the red bars a positive intensity value on either the LHS (negative x-axis) or RHS (positive x-axis). IN, MD and DCL are reported if ROIs are detected. The RDR for each case is reported at each noise level. For the 40 dB models, the RDR is shown, but the excessive noise hinders the ability to detect ROIs	262

LIST OF FIGURES

6.15	Quantitative Metrics for erroneous electrode position models with symmetry lost (top), and symmetry maintained (bottom) between electrode pairs. This study is performed for cases N (no lesion present); B (bleed); C (clot). GMI: The blue bars represent a negative intensity value and the red bars a positive intensity value on either the LHS (negative x-axis) or RHS (positive x-axis). IN, MD and DCL: These metrics are calculated if ROIs are detected and are shown for these situations. The RDR for each case is reported at each electrode deviation	265
6.16	Quantitative Metrics for erroneous electrode contact impedance models. No Symmetry (top two rows): all electrodes have random contact impedances within the range $\pm 20\%$ or $\pm 50\%$. Symmetry (bottom two rows): symmetrical partner electrodes have the same (but erroneous) contact impedance within the range $\pm 20\%$ or $\pm 50\%$. Cases are N (no lesion present); B (bleed); C (clot). GMI: The blue bars represent a negative intensity value and the red bars a positive intensity value on either the LHS (negative x-axis) or RHS (positive x-axis). IN, MD and DCL: These metrics are reported if ROIs are detected. The RDR for each case is reported on the x-axis of the bottom-most IN, MD, DCL plot and was identical (and ideal) in all deviation models tested	267
6.17	Quantitative Metrics for models with errors in assumed conductivity of tissues. Each individual voxel corresponding to a given tissue (left) or the whole tissue (right) is assigned a conductivity corresponding to the ideal conductivity of that tissue \pm up to a maximum of 50% error. The tissues include scalp, skull, brain, CSF, bleed or clot. Cases are N (no lesion present); B (bleed); C (clot). GMI: The blue bars represent a negative intensity value and the red bars a positive intensity value on either the LHS (negative x-axis) or RHS (positive x-axis)	269
6.18	Quantitative Metrics for models with excess skull (top row) or brain (bottom row) on the LHS compared to the RHS. In each model, the CSF encompassed by a sphere of radius 10 mm, 20 mm or 50 mm centred at a point on the LHS of the skull (or brain) is re-assigned as skull (or brain). Cases are N (no lesion present); B (bleed); C (clot). GMI: The blue bars represent a negative intensity value and the red bars a positive intensity value on either the LHS (negative x-axis) or RHS (positive x-axis)	271

LIST OF FIGURES

6.19	Quantitative Metrics for models where the scalp layer is shrunk to 97% of the original volume (top row) and dilated to 105% of the original volume (bottom row). Cases are N (no lesion present); B (bleed); C (clot). GMI: The blue bars represent a negative intensity value and the red bars a positive intensity value on either the LHS (negative x-axis) or RHS (positive x-axis). IN, MD and DCL are reported if ROIs are detected. The RDR for each case is reported on the x-axis of the IN, MD, DCL plot	273
6.20	GMI metric results for the 3 cases at f_1 of 25 Hz and then a f_2 of 25 kHz, demonstrating the effect of a frequency-dependent background	274
6.21	GMI metric results (LHS and RHS) for the 3 cases (N, B, C) across the 25 to 100 Hz band	275
6.22	GMI metric results (LHS and RHS) human ischaemic stroke patient across the 5 to 100 Hz band. Reconstruction is performed onto a patient specific mesh (A), and two patient non-specific meshes (Y and Z). The results from using simulated data onto the patient specific mesh is also shown (C), and represents the ideal case	276
7.1	Illustration of an equivalent channel from A- (green) and B- (blue) orientations. The plane of symmetry is shown as an orange line, with electrodes simultaneously part of A- and B- orientations (for example Electrode #1 in A-orientation is also Electrode #3 in B-orientation). In the sample channel, current is injected between Electrode #2 and #32, with voltage measured between Electrode #3 and #4. The ‘green’ channel represents this channel when A-orientation is used while the ‘blue’ channel is this channel for B-orientation. The channels are equivalent and theoretically give the same voltage measurement in the absence of a perturbation. However, the presence of a perturbation (illustrated as a red circle) upsets the symmetry with this disruption seen as a difference in the voltages recorded between the green and blue channels	290
7.2	Conductivity spectra of ischaemia, bleed and brain across the 5 to 100 Hz band (data from [12], [146]). Ischaemia and bleed are respectively less and more conductive than healthy brain. However, across this band the contrast profile in conductivity between ischaemia and brain is significantly different than that of bleed and brain facilitating disambiguation using MFSD-EIT. The UCL stroke dataset includes measurements taken at 5 Hz, 10 Hz, 20 Hz, and 100 Hz	291

LIST OF FIGURES

7.3	Theoretical MF GMI results for normal (N), bleed (B), and clot (C) cases across the 5 to 100 Hz band at four f points (5 Hz, 10 Hz, 20 Hz, 100 Hz). The GMI for a given case is ideally equally but opposite at each f point and the trend follows the contrast of the tissue with respect to background brain across the band. In the N case the results approach zero as there is no lesion present. The pattern for B differs to that for C leading to differentiation being possible	292
7.4	Left: All the simulated anatomies are derived from CT neuroimaging of stroke patients. A sample CT slice of the anatomy used to create the fine mesh is shown (from resources supplied in [13]). Right: Fine mesh with 50 ml simulated spherical lesion in the north-east position (where the front of the head represents north). The brain layer has been removed in order to show the lesion. The electrode refinement on the scalp layer is also clearly seen	294
7.5	Nested cross-validation. The complete data set is separated into $k = 10$ folds with 90% as a training set (white) and 10% as a test set (grey). The training set from each of these outer folds is itself divided similarly into $m = 10$ inner folds divided into training (white) and test (blue) sets, with 10-fold cross validation performed on the inner fold to optimise hyper-parameters. These hyper-parameters are then used to train a final SVM model on the entire training set, with performance assessed on the held out test set. This repeated over the k folds with a final overall performance reported as the mean \pm standard deviation	298
7.6	Classifier performance for normal (negative class) versus lesion (positive class) for human (~ 48 dB SNR), and simulated (48 dB SNR) data sets. A mean accuracy of 77% is seen for the human data, with a mean sensitivity of 88% and PPV of 81% indicating strong detection of lesion while the mean specificity (51%) and NPV (66%) indicative of a low rate of accurate detection of normal cases. In the case of the simulated results strong performance is indicated by an accuracy of 92% at the 48 dB SNR level	300
7.7	Classifier performance for bleed (negative class) versus clot (positive class) for human (~ 48 dB SNR) and simulated (48 dB SNR) data sets. A mean accuracy of 85% is seen for the human data, with clots strongly detected (mean sensitivity 90% and PPV 85%). Bleeds are slightly less well detected with a mean specificity (77%) and NPV (86%). The simulated results are strong at the 48 dB SNR level, with no metric with a mean less than 99%	301

LIST OF FIGURES

- 7.8 Classifier performance for normal (negative class) versus bleed (positive class) or human (~ 48 dB SNR), and simulated (48 dB SNR) data sets. The classifier performs with a mean accuracy of 87% in both the human and the simulated 48 dB SNR sets 302
- 7.9 Classifier performance for normal (negative class) versus clot (positive class) for human (~ 48 dB SNR), and simulated (48 dB SNR) data sets. The classifier performs with a mean accuracy of 74% with the human data, with a mean accuracy of 95% in the simulated 48 dB SNR set . . . 303
- 7.10 Central lying lesions effect on classifier performance for normal (negative class) versus lesion (positive class), and bleed (negative class) versus clot (positive class) for simulated (48 dB SNR) data sets. The classifier performance is consistently reduced in all metrics when centrally placed lesions are included in the data set compared to when absent 305

List of Tables

2.1	Summary of Brain Haemorrhage and Clot Detector Need and Design Constraints	49
2.2	Overview of Head Phantoms reported in the literature for Electrical Impedance Tomography (or closely related) applications (EIS: Electrical Impedance Spectroscopy, PVC: polyvinyl Chloride, ABS: Acrylonitrile Butadiene Styrene, PLA: Polylactic Acid). Arranged in chronological order of publication	78
2.3	Overview of EIT Algorithms and Modalities reported in the literature for static lesion imaging and detection (or closely related) applications. Arranged by application, and by chronological order of publication . . .	81
3.1	Ideal TMM properties versus classification by physical state. TMMs used in EIT head phantoms are listed by state. An ideal TMM would satisfy all of the criteria listed in the left-most column	88
3.2	Concentrations (as % w/w) of ingredients used in the final mixtures of each TMM. Acetone if added is as 1 ml in addition to each 100 g of mixture	99
3.3	Mean percentage difference in AC conductivity of each TMM mixture and the respective reference tissues values across the 1 kHz–1 MHz, 50 kHz–250 kHz bands, and at the 50 kHz point	103
4.1	The optimum number of ranked features at each SNR level (maximal accuracy with fewest number of features)	176

LIST OF TABLES

4.2 Summary of different classifier performance at 60 dB SNR. All metrics reported as the mean \pm standard deviation of the sensitivity, specificity, and accuracy with a perfect score being 1.00 ± 0.00 . All classifiers used RBF kernel except when labelled ‘Linear’. Linear: Linear kernel with full measurement frames as the classifier input; RBF: RBF kernel with full measurement frames as the classifier input; Mean: Sub-frame means as classifier input; Near: Near sub-frame channels as input; Far: Far sub-frame channels as classifier input; Laplacian: Optimal number of ranked features as determined by Laplacian filtering used as classifier input; PCA: Optimal number of principal components used as classifier input; Ensemble: Ensemble classifier used. Results correspond to the threshold offering maximal sensitivity 184

4.3 Summary of different classifier performance at 40 dB SNR. All metrics reported as the mean \pm standard deviation of the sensitivity, specificity, and accuracy with a perfect score being 1.00 ± 0.00 . All classifiers used RBF kernel except Linear. Nature of the classifier types is consistent with Table 4.2 185

5.1 Results of the Quantitative Metrics applied to the top (high intensity) and bottom (low intensity) ROIs compared from the two images 202

5.2 sdEIT Quantitative Metrics for the separate cases of a 10 ml haemorrhage at 20 dB SNR positioned at (1) near the exterior, and at (4) near the midline 208

5.3 sdEIT Quantitative Metrics for the separate cases of a 2 ml, and 20 ml haemorrhage positioned at (5) at 40 dB SNR 210

5.4 sdEIT Quantitative Metrics for the separate cases of a 20 ml lesion at 40 dB SNR positioned at (5), modelled as either a haemorrhage or an ischaemic lesion 211

5.5 sdEIT Quantitative Metrics for the separate cases of a 10 ml haemorrhage at 20 dB SNR positioned at (1) near the exterior or a 10 ml ischaemic lesion at 20 dB also at position (1) 212

5.6 sdEIT Quantitative Metrics for the separate cases of a 10 ml ischaemic lesion at position (3) at 80 dB, 20 dB and 10 dB SNR 215

5.7 Symmetry Difference Electrical Impedance Tomography (sdEIT) Quantitative Metrics and images for various forward models. In all cases the scenario is that of a 20 ml haemorrhage with no added noise. The first row shows the complete sdEIT result with the ideal forward model. Subsequent rows only show the output from step 2 (as the output of step 1 will be the same as in the first row) for various non-ideal forward models 217

LIST OF TABLES

5.8	sdEIT Quantitative Metrics for the two challenging lesion cases: Lesion out of the electrode plane and multiple simultaneous lesions (both at 80 dB SNR)	220
5.9	sdEIT Quantitative Metrics for the separate cases of a 10 ml haemorrhagic lesion positioned at (1), near the exterior, or at (4), near the midline	221
5.10	sdEIT Quantitative Metrics for the separate cases of a 2 ml and 30 ml ischaemic lesion positioned at (5)	223
6.1	Degree of Asymmetry in the Head Model as (1) Mean \pm Standard Deviation of the Distance Errors of the 32 electrodes; (2) Percentage overlap between the tissues from both sides	232
6.2	Notation for the numerical experimental setups (upper case – bleed; lower case – clot. Position I: centre of the brain; Position II: left side of the mid-height traverse plane towards the exterior of the brain; Position III: right side, below the mid-height traverse plane towards the exterior of the brain)	244
6.3	Notation for the phantom experiments (Position I: centre of the brain; Position II: left side of the mid-height traverse plane towards the exterior of the brain; Position III: right side, below the mid-height traverse plane towards the exterior of the brain)	249
6.4	Mean \pm standard deviation of the distance errors of the 32 electrodes (Symmetry Lost or Symmetry Maintained)	264
6.5	Volume of the increase in Skull or Brain Layer (with reciprocal decrease in CSF Layer) on the LHS with varying sphere radii	271
7.1	Results as Confusion Matrices of Multiclass Classification for Human Data Set (\sim 48 dB SNR). The results are the average \pm standard deviation over 10 iterations as percentages. The cells with bold text are correct classifications, with other cells incorrect. The cells on the rightmost column are the PPV results (dark blue), and the cells on the bottommost row are the sensitivity results (light blue). The cell in the bottom right is the overall classification accuracy (red)	304
7.2	Results as Confusion Matrices of Multiclass Classification for Simulated Data Set (48 dB SNR). The results are the average \pm standard deviation over 10 iterations as percentages. The cells with bold text are correct classifications, with other cells incorrect. The cells on the rightmost column are the PPV results (dark blue), and the cells on the bottommost row are the sensitivity results (light blue). The cell in the bottom right is the overall classification accuracy (red)	304

LIST OF TABLES

7.3	Results as Performance Accuracy reported as the average \pm standard deviation over 10 iterations as percentages for each Binary Classification Problem for the Simulated Data at 80 dB, 48 dB, and 20 dB SNR Noise Levels	306
-----	--	-----

Acronyms

- ABS** Acrylonitrile Butadiene Styrene. 88, 105, 119, 124, 315
- AC** Alternating Current. 61, 63, 87, 97, 98, 99, 101, 104, 107, 120
- ACA** Anterior Cerebral Artery. 15, 30
- ACR** American College of Radiology. 27, 46
- aEIT** Absolute Electrical Impedance Tomography. 3, 4, 56, 79, 192
- AHA** American Heart Association. 31, 45
- AI** Asymmetry Index. 270
- ASPECTS** Alberta Stroke Program Early CT Score. 25, 31
- AUC** Area Under the Curve. 131, 133, 140, 142, 143, 146, 149, 150, 153, 154, 155, 157, 163
- BFSD-EIT** Bi-Frequency Symmetry Difference Electrical Impedance Tomography. 84, 224, 225, 226, 227, 228, 229, 231, 233, 239, 242, 243, 248, 249, 253, 254, 255, 256, 258, 263, 269, 270, 272, 273, 275, 277, 278, 280, 281, 282, 283, 285, 286, 288, 311, 314, 317
- C** Clockwise. 196, 199, 200
- CAD** Computer Aided Design. 74, 106, 229, 230, 257, 292
- CB** Carbon Black. 6, 85, 90, 91, 92, 94, 95, 99, 103, 104, 118, 119, 120, 121, 123, 124, 315
- CC** Counter Clockwise. 196, 200
- CD** Centroid Difference. 200, 209, 210, 212, 213, 215, 217
- CEM** Complete Electrode Model. 75
- CNS** Central Nervous System. 16, 17
- CSF** Cerebrospinal Fluid. 2, 4, 16, 20, 40, 57, 64, 89, 90, 95, 105, 106, 110, 119, 124, 135, 202, 229, 230, 232, 239, 243, 248, 270, 277, 279, 280, 290, 292, 294, 312
- CT** Computed Tomography. 1, 24, 25, 26, 27, 31, 36, 39, 40, 41, 42, 45, 46, 47, 48, 49, 50, 51, 53, 54, 55, 57, 59, 60, 133, 134, 229, 286, 288, 292, 293, 307, 312
- CVA** Cerebrovascular Accident. 18
- DAS** Delay and Sum. 52
- DC** Direct Current. 3, 63, 104

- DCL** Difference in Centroid Location. 239, 241, 243, 248, 249, 253, 254, 258, 259, 260, 261, 272
- DPI** Dots per Inch. 232
- ECF** Extra Cellular Fluid. 3, 58, 61
- ECOC** Error-Correcting Output Code. 298, 299
- EEG** Electroencephalogram. 49, 53, 58, 59, 68, 138, 193, 231, 233, 263, 278, 287
- EICs** Early Ischaemic Changes. 24, 25, 27, 28, 31, 36, 44, 45
- EIDORS** Electrical Impedance Tomography and Diffuse Optical Tomography Reconstruction Software. 74, 116, 135, 136, 142, 192, 202
- EIS** Electrical Impedance Spectroscopy. 83, 104, 105, 128, 189
- EIT** Electrical Impedance Tomography. 1, 2, 3, 4, 5, 6, 7, 9, 10, 11, 12, 49, 55, 56, 57, 58, 59, 60, 61, 63, 64, 65, 66, 67, 68, 69, 70, 71, 72, 73, 74, 75, 76, 77, 79, 80, 82, 83, 84, 85, 86, 87, 88, 89, 90, 97, 98, 99, 101, 103, 104, 105, 106, 109, 114, 115, 117, 119, 123, 124, 126, 127, 128, 129, 132, 133, 134, 135, 136, 138, 141, 144, 153, 156, 157, 167, 186, 187, 188, 189, 191, 192, 193, 196, 213, 215, 223, 224, 226, 227, 228, 232, 237, 238, 248, 254, 255, 256, 268, 277, 278, 281, 282, 285, 286, 287, 288, 296, 306, 307, 308, 309, 310, 311, 312, 313, 314, 315, 316, 317
- F1** F1 Score. 200, 209, 210, 212, 213, 215, 217
- FAST** Face, Arms, Speech, Time. 22, 23, 34, 44
- FDA** Food and Drug Administration. 30, 53
- fdEIT** Frequency Difference Electrical Impedance Tomography. 3, 4, 56, 57, 58, 72, 79, 80, 83, 101, 192, 199, 282
- FEM** Finite Element Method. 70, 71, 73, 74, 116, 135, 136, 137, 140, 165, 186, 189, 197, 202, 207, 229, 230, 232, 235, 256, 257, 269, 275, 279, 286, 288, 292, 293, 294, 309, 311
- FN** False Negative. 130, 181, 200, 296
- FP** False Positive. 130, 181, 200, 296
- FPS** Frames per Second. 115, 249
- GCS** Glasgow Coma Scale. 40, 42, 46
- GMI** Global LHS & RHS Mean Intensity. 238, 239, 241, 242, 243, 246, 247, 249, 252, 253, 254, 258, 259, 260, 261, 263, 268, 270, 272, 273, 274, 275, 276, 278, 279, 280, 281, 283, 285, 286, 287, 289, 290, 291, 294, 309, 310, 311, 314, 316, 317
- GPU** Graphics Processing Unit. 74
- GREIT** Graz Consensus Reconstruction Algorithm for EIT. 116, 193, 196, 203
- HASU** Hyper Acute Stroke Unit. 275, 287
- HSE** Health Service Executive. 19

- ICER** Incremental Cost Effectiveness Ratio. 29
- ICF** Intracellular Fluid. 61
- ICH** Intracerebral Haemorrhage. 20, 28, 29, 57, 78, 105, 111, 193, 203, 229, 230
- ICP** Intracranial Pressure. 54, 60
- IEC** International Electrotechnical Commission. 2, 55, 69
- IHF** Irish Heart Foundation. 33, 44
- IN** Image Noise. 258, 259, 260, 261, 272
- IR** Infrared. 54, 55, 60
- IS** Index of Symmetry. 197, 198, 207, 209, 210, 213, 215, 217, 220, 222
- IT'IS** Foundation for Research on Information Technologies. 65, 90, 99, 316
- IVH** Intraventricular Haemorrhage. 40, 58
- L** Left. 197
- LHS** Left Hand Side. 206, 231, 238, 241, 247, 259, 270, 276, 279, 288, 289, 291
- MCA** Middle Cerebral Artery. 15, 17, 22, 25, 28, 30, 31, 36, 45
- MD** Morphology Deviance. 258, 259, 260, 261, 272
- MERCI** Multi Mechanical Embolus Retrieval in Cerebral Ischemia. 30
- MF** Multi-Frequency. 286, 287, 306, 309
- MF-GMI** Multi-Frequency Global LHS & RHS Mean Intensity. 285, 286, 289, 292, 294, 295, 296, 297, 307, 309, 310, 311, 314, 316
- MFSD-EIT** Multi-Frequency Symmetry Difference Electrical Impedance Tomography. 285, 286, 287, 288, 290, 293, 308, 310, 311, 314, 315, 316, 317
- MID** Mean Intensity Difference. 200, 209, 210, 212, 213, 215, 217
- ML** Machine Learning. 5, 6, 7, 9, 10, 52, 53, 60, 83, 84, 125, 126, 127, 128, 129, 133, 186, 187, 190, 284, 285, 293, 295, 296, 308, 310, 311, 313, 314, 315, 316, 317
- MRI** Magnetic Resonance Imaging. 1, 24, 26, 27, 40, 46, 89, 90, 229, 288, 307, 312
- mRS** Modified Rankin Score. 29, 30, 32
- MSU** Mobile Stroke Unit. 49, 50, 51, 59
- N** normal. 199, 200
- N/A** Not Applicable. 78
- NHS** National Health Service. 29, 34
- NICE** National Institute for Health and Care Excellence. 18, 24, 31, 33, 41, 44
- NIHSS** National Institutes of Health Stroke Scale. 31, 32, 36, 44
- NINDS** National Institute of Neurological Disorders and Stroke. 31
- NN** Neural Network. 168, 170, 184
- NPV** Negative Predictive Value. 297, 298, 299, 300, 301, 306, 307, 309
- NSAID** non-steroidal anti-inflammatory drug. 19
- PCA** Principal Component Analysis. 170, 177, 178, 179, 184, 185

- PCAr** Posterior Cerebral Artery. 15, 30
- PEITS** Parallel EIT Forward Solver. 235, 294
- PLA** Polylactic Acid. 88, 105, 106, 108, 118
- PPV** Positive Predictive Value. 297, 299, 300, 301, 302, 306, 307, 308, 309
- QALY** Quality Adjusted Life Year. 29
- R** Right. 197
- RBF** Radial Basis Function. 168, 170, 171, 173, 178, 183, 184, 185, 187, 296, 311
- RDR** ROI Detection Rate. 258, 261, 263, 272, 278
- RHS** Right Hand Side. 206, 231, 238, 241, 247, 259, 270, 276, 279, 288, 289, 291
- RMI** ROI Mean Intensity. 238, 241, 243, 247, 249, 253, 254, 258, 259, 260
- RMS** Root Mean Square. 2, 69, 255
- ROC** Receiver Operating Characteristic. 129, 131, 133, 134, 140, 146, 181
- ROI** Region of Interest. 197, 200, 201, 207, 209, 210, 212, 213, 215, 216, 217, 218, 220, 222, 238, 239, 241, 242, 243, 247, 248, 249, 253, 258, 259, 260, 261, 263, 270, 277, 278, 280
- ROSIER** Rule Out Stroke in the Emergency Room. 22, 23, 34, 44, 306
- SAH** Subarachnoid Haemorrhage. 20, 40
- sdEIT** Symmetry Difference Electrical Impedance Tomography. xxxviii, 84, 125, 188, 189, 191, 192, 193, 194, 195, 197, 199, 202, 204, 205, 206, 207, 210, 213, 215, 217, 218, 220, 223, 224, 225, 226, 227, 282, 314
- SDH** Subdural Haematoma. 39, 46, 60
- SEBS** Poly(styrene-b-ethylene-butylene-b-styrene). 119, 124, 315
- SNR** Signal to Noise Ratio. xx, 2, 3, 69, 75, 138, 141, 142, 144, 145, 147, 148, 155, 165, 168, 170, 171, 173, 175, 176, 177, 178, 179, 181, 184, 185, 186, 187, 205, 207, 209, 210, 211, 212, 213, 218, 224, 226, 243, 247, 248, 249, 255, 261, 275, 277, 281, 283, 287, 294, 299, 300, 302, 303, 305, 306, 309, 310, 311, 314
- STL** Stereolithography. 108, 135, 136, 154, 202, 203, 232, 292, 293
- SVD** Singular Value Decomposition. 72
- SVM** Support Vector Machine. 127, 128, 129, 130, 132, 133, 134, 139, 140, 141, 142, 143, 145, 149, 154, 155, 157, 165, 166, 167, 168, 170, 171, 173, 175, 178, 185, 186, 187, 285, 286, 295, 296, 297, 298, 308, 311, 313, 314
- TBI** Traumatic Brain Injury. 1, 12, 18, 37, 38, 39, 40, 41, 42, 43, 46, 47, 48, 49, 52, 53, 55, 58, 59, 60, 82, 127, 133, 134, 301, 307, 308, 312, 313
- tdEIT** Time Difference Electrical Impedance Tomography. 3, 4, 56, 58, 72, 77, 79, 80, 86, 101, 105, 106, 114, 115, 153
- TIA** Transient Ischaemic Attack. 12, 18, 21, 22, 23, 24, 28, 32, 33, 34, 35, 45
- TMM** Tissue-mimicking Material. 3, 5, 6, 7, 9, 77, 82, 85, 86, 87, 88, 89, 90, 92, 94, 95, 97, 98, 99, 101, 102, 103, 104, 105, 107, 108, 110, 111, 112, 113, 114, 115, 117, 118, 119, 120, 123, 124, 125, 138, 205, 313, 315

ACRONYMS

TN True Negative. 130, 131, 296

TOAST Trial of Org 10172 in Acute Stroke Treatment. 21

TP True Positive. 130, 131, 200, 296

tPA tissue plasminogen activator. 19, 21, 28, 32, 50

UCL University College London. 4, 10, 74, 84, 281, 286, 287, 288, 289, 292, 306, 309, 310, 311, 317

UCLH University College London Hospital. 275, 287

UK United Kingdom. 19, 22, 24, 29, 33, 34, 38, 44

USA United States of America. 1, 24, 29, 38, 44, 50, 108

w/w mass percentage. 91, 104

Symbols

- A* Area. 63
C Electrical Capacitance. 62, 63
J Electrical Current Density. 69
E Electric Field. 69, 70
I Electrical Current. 62
f Frequency. 61, 63, 255, 282, 283
J Jacobian (Sensitivity) Matrix. 70, 72, 73, 74
L Length. 63
 ϵ_r Relative Permittivity. 63
X Reactance. 63
R Electrical Resistance. 62, 63
 ρ Electrical Resistivity. 63
 σ Electrical Conductivity. 63, 70, 136, 198
V Voltage. 62, 70, 72

Introduction

Brain diseases featuring haemorrhagic or ischaemic lesions are a significant source of morbidity and mortality globally [1], [2]. Stroke is the second most common cause of death globally, with up to 12% of mortality in western nations attributed to the condition [1]. Traumatic Brain Injury (TBI) has 1.6 million incidents annually in the United States of America (USA), consuming 10% of the health care budget [2].

Common to both these conditions is the improvement in patient outcomes associated with timely and robust lesion detection and identification [3], [4]. In stroke for example the treatment indicated is radically different depending on the cause. Neuroimaging with Computed Tomography (CT) or Magnetic Resonance Imaging (MRI) is needed for definitive diagnosis before intervention can be made. However impediments to timely access to these gold standard modalities include the cost and size of the imaging systems, as well as the need for trained staff. Such challenges to rapid imaging access for acute stroke patients can lead to irreversible damage of brain tissue [5]. Hence there is a clinical need for an efficient, robust, cost effective, sensitive and specific device for the detection and identification of brain lesions.

Electrical Impedance Tomography (EIT) represents an emerging technology that may provide a solution to this clinical need, but significant development is needed to achieve translation to clinical use. In EIT, an array of electrodes is placed around a body of interest with current injected through electrode pairs. By analysis of the resulting voltage measurements at other electrode pairs, EIT can potentially detect and image tissues based on differing electrical conductivity [6]. EIT suffers from a low spatial resolution as well as high sensitivity to noise. However, EIT is a low cost, hazard free, non-invasive modality [7]. As such, EIT is an active area of research [8] across a variety of biomedical applications. To date, EIT has been most successful when used to image the thorax, due in part to the high conductivity difference between the inflated and deflated lung, leading to applications such as monitoring of mechanical ventilation and pulmonary function testing [9]. EIT has also shown promise in a range of other areas such as detection of various cancer types, neural imaging and perfusion studies [10].

There is an encouraging and increasing level of research and application of EIT to clinical problems [10]. Crucially however the technology enjoys most success in monitoring applications where there is a time change in the scene [10]. In such cases differencing can be performed based on measurements taken at different times. Areas where there is a static (or quasi-static) scene require the achievement of lesion detection without the benefit of temporal differencing. In such cases, novel approaches are needed for successful application of EIT. Development of such a novel approach and achievement of detection and identification of static brain lesions using EIT motivates the work in this thesis, and the specific challenges are discussed in detail in the following section.

1.1 Motivation

EIT is a promising modality that can be applied to a number of clinical scenarios. In this thesis, the clinical application is that of detection and identification of static intracranial lesions. The use of EIT for this application is not a trivial challenge. EIT can be an ill-posed, ill-conditioned inverse problem, based on the typically under determined nature of the system, and the manner in which electrical current propagates in a dispersive manner throughout the body of interest with concentration near injecting electrodes [8]. These and other challenges including those related to static lesion detection and identification in the brain are now briefly discussed.

As a result of the dispersive pattern of current flow, EIT is relatively insensitive to anatomy or physiology deep in the interior of the imaging domain compared to the surface. This insensitivity is due to the fact that most current resides near the boundary [8]. This non-uniformity of current flow is an even more pronounced issue in the head. In the case of the head, current must first pass through the relatively resistive scalp, before the highly resistive skull layer and meningeal layers attenuate the signal even further. Finally, the Cerebrospinal Fluid (CSF) layer in the subarachnoid space acts to shunt current away from the brain further reducing the amount of current reaching the area of interest [6]. Hence, simply maximising the delivery of current to the brain is a major challenge in EIT [6].

A further challenge is the restrictions on current amplitude under the International Electrotechnical Commission (IEC) 60601-1 standard, which are of the order of μA Root Mean Square (RMS) at frequencies up to 1 kHz [7], [11]. The overall effect is that little of the injected current reaches the brain, which is the true area of interest where lesions may be present. One way to increase the SNR would be to

increase the frequency and hence use the upper allowed limit of injected current. A popular frequency for use in EIT in general is 50 kHz [6]. At 50 kHz most current goes through the Extra Cellular Fluid (ECF) but there is a large reduction in electrode impedance compared to at Direct Current (DC). This reduction in electrode impedance results in less instrumentation errors [6]. The current amplitude allowed increases beyond 1 kHz to a 10 mA limit for frequencies over 100 kHz [6], [7], [11]. However, lower frequencies of the order of 10 to 100 Hz may be of more interest in EIT for detection of bleeds and clots. At these lower frequencies the contrast in the conductivity between brain, bleed and clot tissues is maximised, and frequency dependent changes in conductivity are present (Fig. 2.20) [12], [13]. Bleeds and clots are the lesions of interest in this thesis. These lesions may change in nature over time, but are considered as static in this thesis as acute detection is of interest. Hence, these frequency dependent changes in conductivity are of importance as the leveraging of other properties for detection such as a time change is not possible.

EIT is also highly sensitive to errors in the hardware used and in particularly the electrodes [8]. Again this sensitivity is more of an issue for head EIT where there is a need for systems offering a SNR far higher than that required for thoracic applications [14], and with a relative lack of such hardware available [15].

Another challenge in the field is a lack of good clinical data. The data set presented by Goren *et al.* [13] is the most comprehensive study with EIT data collected from 23 stroke patients and 10 healthy volunteers. An alternative source of real-world data is given by the use of good phantom models. Such data is not a substitute for clinical human data but offers a lower bar of accessibility. As will be discussed in Section 2.4.5 and shown in Table 2.2, there is a lack of anatomically accurate phantoms, and a particular lack of such phantoms with static lesion detection as the final application. For example Tissue-mimicking Materials (TMMs) with frequency-dependent conductivity would be suited to developing phantoms specifically for applications using Frequency Difference Electrical Impedance Tomography (fdEIT) or other modalities for static lesion detection.

Efficacy of algorithm, algorithm design, and algorithm (and also modality) choice is another area of challenge for EIT in the proposed application. The gold-standard modality of EIT is Time Difference Electrical Impedance Tomography (tdEIT), which uses the differencing of before and after EIT measurements in order to detect a change and suppress errors [10]. This gold-standard modality is not applicable to static lesion detection due to the lack of a baseline ‘normal’ frame. As such alternative modalities such as Absolute Electrical Impedance Tomography (aEIT) and fdEIT must be used. However, these modalities do not benefit from the

error cancellation effect of differencing at all (aEIT) or as well (fdEIT) as tdEIT [12].

As such, significant challenges exist in order to realise translation of EIT into a modality that could successfully address the clinical need. However progress is being made. Some of the most interesting and important advances in EIT applied to the stroke diagnostic problem, and other pathologies featuring brain bleeds have been achieved by the group in University College London (UCL). In terms of algorithm design, UCL have focussed on novel approaches related to fdEIT. The first step in this work was a study of frequency dependent changes in conductivity of brain, bleed, and clot tissues.

The work of Dowrick *et al.* indicates frequency-dependent contrasts in conductivity exist between brain, bleed, and clot tissues. Most contrast, and change in contrast, in these tissues is seen at frequencies under 500 Hz (and arguably even under 100 Hz) [5]. These contrasts imply fdEIT may theoretically be applied to the problem. Horesh *et al.* conducted a study into the feasibility of fdEIT for stroke detection with simulation models of normal, ischaemic, and haemorrhagic brain with lesions of varying sizes. They found that detectable changes in voltage at the boundary were on the order of +2% (ischaemic lesion) to -7% (haemorrhagic lesion) in the best cases featuring large lesions. Small lesions gave changes in the order of $\pm 0.1\%$. Significantly, errors such as electrode position, tissue layer thickness, and contact impedance were in the order of 10% (up to 40%). The conclusion of this feasibility study was that sources of error such as electrode positioning errors and noise would put severe constraints on the accuracy needed in equipment [16].

The novel non-linear fdEIT algorithm proposed by the group [17] shows promise and advantages over previous fdEIT approaches [12], [18]. This algorithm may be considered the state of the art as regards EIT applied to static brain lesions. However, the algorithm is not without some challenges. In numerical studies applied to the stroke problem, this spectrally constrained fdEIT algorithm was found to be highly sensitive to electrode positioning errors, reasonably robust to erroneous tissue conductivity spectra (addressed in [19]) and highly robust to contact impedance errors of electrodes. Also of note the CSF layer was not included in the model used, and sensitivity to artefacts due to errors in skull shapes was reported [20]. Further, the algorithm took 5 to 6 hours for image reconstruction implying a high computational cost. Bleed detection was also more challenging than clot detection likely due to the relatively small change in contrast between the bleed and background across the frequency range considered [20].

It is useful to briefly consider the work of Persson *et al.* in the microwave domain

who has attempted to apply microwave imaging to detection and identification of bleeds and clots for stroke [21]. An innovation in this field has been the adoption of Machine Learning (ML) techniques including classification, and a move away from imaging [21], [22]. Such innovations have to date not been seen in EIT applied to static brain lesions.

Hence the application of EIT to static lesion detection and identification in the brain has a number of challenges to overcome in order to be successful. Areas of potential improvement include:

- The data acquisition process, including the frequencies used, and measurement protocols adopted;
- Hardware and test platforms available;
- Software, and the related area of algorithms and modalities. These areas in turn are related to the mathematical underpinnings of EIT which include the forward and inverse problem;
- Robust analysis of the data, with the possibility of adoption of ML principles for example.

These areas of improvement motivate the remainder of this thesis which primarily is focussed on innovations in two of these key areas. These selected areas of improvement are hence the research objectives of this thesis:

1. Designing a test platform (phantom) and acquiring of valuable real world data;
2. Designing a novel algorithm and modality for static lesion detection and identification.

The first research objective is addressed in Chapter 3, where a novel solid TMM is developed and use to create reconfigurable test platforms. Chapters 4 - 7 of the thesis are then dedicated to developing an algorithm for use in static lesion detection and identification. This algorithm development uses computational models, phantoms models, and ultimately uses data from human stroke patients. Two separate approaches are initially used including a ML approach, and an approach based on the analysis of symmetry. These approaches are merged at the end of the thesis with application to the human stroke data.

These opportunities and improvements that form the specific research contributions of this thesis are discussed in the next sections. The journal and conference publications arising from these contributions are now listed.

1.2 Thesis Contributions

Significant contributions are presented in this thesis advancing the application of EIT to brain haemorrhage and clot detection and identification. The specific novel contributions are summarised below, in particular:

- The development of a novel solid TMM for use as an experiment test platform in EIT:
 - This TMM based on polyurethane, graphite, and Carbon Black (CB) covers the biological range of conductivities in the 1 kHz–1 MHz EIT band, and can be used to emulate the electrical conductivity of any tissue or tissue aggregate of interest.
- The designing, building, and testing of modular head phantoms based on this TMM for gathering of valuable real world data for use in EIT head and brain applications:
 - In particular realistic solid haemorrhagic and clot phantom lesions were developed, with such phantom lesions not seen before in EIT.
- The novel application of ML classification algorithms to EIT measurements for brain haemorrhage detection (available from [10.5281/zenodo.1302331](https://doi.org/10.5281/zenodo.1302331)):
 - This exciting new approach was shown to robustly allow detection of lesions without the challenging reconstruction step of EIT, as well as opening up opportunities into intelligent feature selection for use in ML algorithms.
- The initial development and refinement of a novel symmetry based algorithm for static brain lesion detection and identification:
 - Importantly the feasibility of applying this algorithm to stroke was assessed demonstrating significant advances over the existing state of the art in EIT including a tolerance to electrode placement errors of up to ± 30 mm, a potential to mitigate against errors in assumed anatomy, and a reduction in computation time from hours to minutes.
- The application of this symmetry based algorithm to human stroke data for the first time with clear lesion detection demonstrated.
 - The expected pattern of frequency dependent symmetry change was seen in a numerical model of stroke, and then validated with real human data from an ischaemic stroke patient. This latter result using real clinical data represents a significant step in the successful translation of EIT for static lesion detection in the brain.
- The development of a novel quantitative metric from the symmetry based algorithm and use of this metric as an input into ML algorithms for brain lesion detection and identification:
 - This quantitative metric was composed of only two numbers (features)

per frequency point and was shown to be robust to a number of important EIT error sources including noise, electrode positioning, electrode contact impedance, tissue conductivity, anatomy of the head, and the presence of a frequency-dependent background.

- The use of this approach applied to human stroke data:
 - Strong results were achieved for challenging and clinically important classification problems with a mean accuracy of 87% and 85% achieved for normal versus bleed and bleed versus clot scenarios.

These contributions are described in detail in the following chapters, including: the development of solid TMMs and head phantoms in Chapter 3; application of ML approaches to analysis of EIT measurements in Chapter 4; development of a novel symmetry based algorithm in Chapter 5; iteration and improvement of this symmetry based algorithm in Chapter 6; and combining of this algorithm with the earlier explored ML principles with application to human data in Chapter 7. These novel contributions have been published in six journal articles, six conference publications, and one book chapter which are listed in the following sections. Where appropriate, these journal and conference publications are referenced in the relevant chapters of this thesis.

1.2.1 Journal Publications

- **B. McDermott**, B. McGinley, K. Krukiewicz, et al., “Stable tissue-mimicking materials and an anatomically realistic, adjustable head phantom for electrical impedance tomography,” *Biomedical Physics & Engineering Express*, vol. 4, no. 1, pp. 1-13, Nov. 27, 2017;
- **B. McDermott**, M. O’Halloran, E. Porter, et al., “Brain haemorrhage detection using a SVM classifier with electrical impedance tomography measurement frames,” *PLOS ONE*, vol. 13, no. 7, e0200469, Jul. 12, 2018;
- **B. McDermott**, E. Porter, M. Jones, et al., “Symmetry difference electrical impedance tomography—a novel modality for anomaly detection,” *Physiological Measurement*, vol. 39, no. 4, pp. 1-20, Apr. 26, 2018;
- **B. McDermott**, J. Avery, M. O’Halloran, et al., “Bi-frequency symmetry difference electrical impedance tomography – a novel technique for perturbation detection in static scenes,” *Physiological Measurement*, vol. 40, no. 4, pp. 1-19, Feb. 20, 2019;
- **B. McDermott**, M. O’Halloran, J. Avery, et al., “Bi-frequency symmetry difference EIT - feasibility and limitations of application to stroke diagnosis,” *IEEE Journal of Biomedical and Health Informatics*, pp. 1–14, 2019.
- **B. McDermott**, M. A. Elahi, A. Santorelli, et al., “Multi-frequency symmetry difference electrical impedance tomography with machine learning for

human stroke diagnosis,” *Physiological Measurement* - UNDER REVIEW, 2020.

1.2.2 Conference Publications

- **B. McDermott**, E. Porter, M. Jones, et al., “A novel tissue-mimicking material for phantom development in medical applications of EIT,” in *Proceeding of the 18th International Conference on Biomedical Applications of Electrical Impedance Tomography*, Thayer School of Engineering at Dartmouth Hanover, New Hampshire, USA, 2017;
- **B. McDermott**, M. O’Halloran, A. Santorelli, et al., “Classification applied to brain haemorrhage detection: Initial phantom studies using electrical impedance measurements” in *Proceeding of the 19th International Conference on Biomedical Applications of Electrical Impedance Tomography*, Edinburgh, Scotland, Jun. 2018;
- **B. McDermott**, E. Porter, B. McGinley, et al., “Electrical impedance tomography with exploitation of symmetry,” in *Bioengineering in Ireland 2018, DCU: Royal Academy of Medicine in Ireland Section of Bioengineering*, Jan. 27, 2018;
- **B. McDermott**, M. O’Halloran, and E. Porter, “Static lesion detection in symmetric scenes using dual-frequency electrical impedance tomography,” in *Bioengineering in Ireland 2019, UL: Royal Academy of Medicine in Ireland Section of Bioengineering*, Jan. 19, 2019;
- **B. McDermott**, M. O’Halloran, and E. Porter, “Bi-frequency symmetry difference (BFSD) EIT in stroke diagnosis,” in *Proceedings of the 20th International Conference on Biomedical Applications of Electrical Impedance Tomography*, University College London, Jul. 1, 2019;
- **B. McDermott**, M. A. Elahi, A. Santorelli, et al., “Stroke diagnosis using multi-frequency symmetry difference EIT (MFSD-EIT) with SVM classification,” in *Proceeding of the 21st International Conference on Biomedical Applications of Electrical Impedance Tomography* *[Cancelled due to COVID-19 Virus], National University of Ireland Galway, Jun. 2020.

1.2.3 Other Publications

- **B. McDermott**, E. Dunne, M. O’Halloran, et al., “Brain haemorrhage detection through SVM classification of electrical impedance tomography

measurements,” in *Brain and Human Body Modeling: Computational Human Modeling at EMBC 2018*, S. Makarov, M. Horner, and G. Noetscher, Eds., Cham: Springer International Publishing, 2019, pp. 211–244.

1.3 Thesis Structure

The remainder of this thesis describes the background, experimental systems, methods and results used to address the primary research objective.

Chapter 2 provides a thorough review of the normal and diseased brain, presenting a need for a technology that can identify the presence of lesions. Candidate technologies are discussed, before EIT is considered. An introduction to EIT is then presented with an emphasis on application to the proposed need of brain haemorrhage and ischaemic lesion detection.

Chapter 3 presents novel solid TMMs which can be used to develop test platforms. Head phantoms, and phantom lesions are developed from these TMMs. These phantoms are used to generate valuable experimental EIT data which is used throughout subsequent chapters to inform and guide development of algorithms that can be used to detect and identify static lesions.

Chapter 4 presents the application of ML techniques to EIT measurements. In particular ML classification algorithms are used to detect static haemorrhagic lesions. A range of numerical and phantom studies are performed with the phantoms the product of Chapter 3. These studies assess the effect of individual parameters on classifier performance. In addition substantial investigation into optimisation and processing of measurements to boost performance is considered.

Chapter 5 lays out another novel approach to static lesion detection through the use of symmetry. An analysis of EIT measurements from symmetrically opposite orientations can detect deviations caused by the presence of a lesion. Again numerical and phantom studies are performed to study individual parameters. While this novel algorithm can detect lesions, challenges are presented particularly in terms of robust identification of detected lesions.

Chapter 6 refines the symmetry based algorithm from Chapter 5. The use of multiple frequencies in the measured EIT data results in a more robust identification of detected lesions. Numerical and phantom studies are performed, as well

CHAPTER 1. INTRODUCTION

as a complete feasibility study into application of the algorithm to stroke. The chapter concludes with a successful application of the algorithm to EIT data from human stroke patients collected by UCL.

Chapter 7 further extends the symmetry based algorithm. Symmetrical differences if present are captured as a quantitative metric related to the mean intensities on either side of the sagittal plane. This metric offers information on the presence and nature of a lesion if present. Next, the ML principles from Chapter 4 are used with this metric as the input. Both numerical and the UCL human data are used to assess the effectiveness of this combined use of both the novel ML and symmetry based approach to detect and identify static brain lesions.

Chapter 8 summarises the thesis, discussing the main results and conclusions. Future work is also identified that if implemented will further push the successful clinical translation of EIT for brain lesion detection and identification.

Background

In this chapter, a discussion of the normal and then diseased brain both identifies the need for a system of detection and identification of static brain lesions, and frames the ideal technological solution. A candidate solution, EIT, is then focussed on and discussed in terms of the fundamental basis of the technology, the state of the art, and key challenges in the application of EIT to static pathology detection.

Firstly, the normal anatomy and physiology of the head, and relevant brain pathologies are discussed. The overall clinical problem is refined into a validated and justified ‘need’ which centres on the sensitive and specific detection of static lesions in the brain of patients. These lesions specifically included bleeds (haemorrhage) and clots (ischaemia). The hypothetical ideal technological solution that fulfils this need is described and bounded by a series of design constraints. Potential technologies that may meet the constraints and provide a solution are then outlined. One of these technologies is EIT, which is then elaborated on in more detail. This discussion of EIT places particular emphasis on both the success and issues in the application of the technology to date in biomedical applications involving static brain lesions.

2.1 Introduction

The Biodesign methodology described by Yock *et al.* [23], [24] informs this thesis. As part of the Biodesign approach, before finding or developing a solution there should be a well-defined problem or clinical need identified [23], [24]. This need is then captured as a needs statement, with subsequent invention and implementation of a solution. In this thesis, neurology was chosen as the area of strategic focus and in particular brain diseases featuring bleeds and clots were selected as a well-defined problem judged as having significant merit in pursuing. In order to implement this needs based approach effectively, an understanding of the normal and then the abnormal is required, and is presented in Section 2.2. Section 2.2.1 describes the normal healthy anatomy and physiology of the brain and surrounding tissues of the head. Two clinically important brain diseases are then presented in Sections 2.2.2, and 2.2.3 with bleeds and or clots the central aetiology of each. Cerebrovascular

disease refers to any pathology resulting from problems in cerebral blood supply. Cerebrovascular accident (stroke) and Transient Ischaemic Attacks (TIAs) are two examples of these diseases with either a bleed or a clot as the cause. Next, TBI (and the related area of concussion in sports injury) is outlined. For each of these conditions the epidemiology, aetiology, pathology, symptoms, diagnosis, treatment and prognosis are outlined as well as the overall ‘patient pathway’. The need and benefit in robustly detecting the presence of a bleed and or clot is emphasised in each condition. Of these conditions it is proposed that stroke is the most clinically important and hence most emphasis is placed in this thesis on the detection of bleed or clot in stroke patients. The needs and requirements of a technology that would detect bleeds or clots is described in Section 2.3, and summarised as a needs statement. In Section 2.3.1, a series of design constraints a technological solution would need to fulfil are defined. Candidate technologies are then briefly presented in Section 2.3.2 before it is concluded that EIT is a technology worthy of development and application to this clinical problem.

Finally, a more detailed analysis of EIT is presented in Section 2.4 with the basis of the technology and state of the art introduced. A discussion is given of relevant areas such as the bioelectrical basis of the technology which includes areas such as:

- Bioimpedance and the dielectric properties of the head;
- EIT data acquisition;
- The mathematical basis of EIT imaging which can be described in terms of the forward and inverse problems;
- Existing software and hardware, including phantom test platforms;
- Existing modalities of EIT.

Throughout all of these sections emphasis is placed on application of EIT to the head, particularly the use of EIT in static lesion detection with the state of the art as well as challenges and gaps highlighted. Ultimately these challenges and gaps motivate the primary research objectives of this thesis, which help address some of the challenges. These objectives are described in the final section 2.5, and where in subsequent chapters these objectives are met.

2.2 The Normal and Diseased Brain

The brain is the area of focus in this thesis. An appreciation and understanding of the normal anatomy and physiology of this crucial organ is required before exploring the abnormal pathologies and diseases that can affect the brain. Hence, in this section the anatomy and physiology of the normal head and brain is first presented. Next, a thorough analysis of two important clinical conditions with

static brain haemorrhages and/ or clots as the central aetiology is given.

2.2.1 Anatomy and Physiology of the Head and Brain

The human brain is an organ of about 1.5 kg mass and $1,450 \text{ cm}^3$ volume in an adult [25] and can be considered to comprise of three main parts – the cerebral hemispheres, the brain stem and the cerebellum [26], [27]. The entire structure is encased in the bony skull (cranium) for protection [26], [27].

As shown in Fig. 2.1, the cranium consists of a series of main bones (temporal, parietal, frontal, occipital, sphenoid and ethmoid), which in the adult are joined by immobile fibrous strips called sutures. In the neonate, membrane covered soft spots called fontanelles exist that allows space for the developing brain to grow and facilitates the passage of the skull through the birth canal. These fontanelles then ossify, closing over during the first two or so years of life [27].

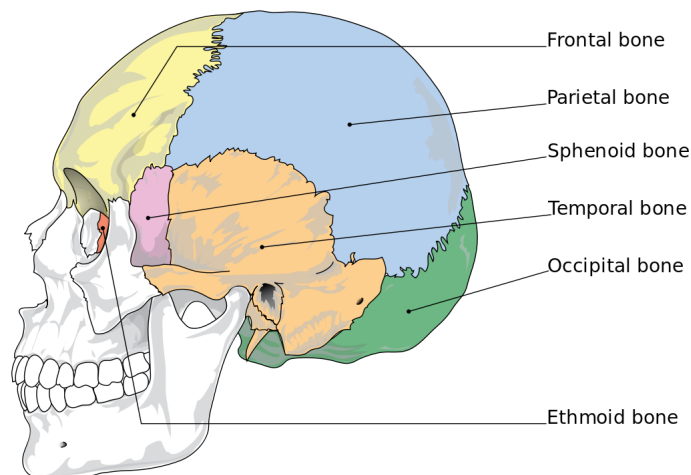


Figure 2.1: The bones of the skull and suture lines. The suture lines are immobile strips that bind the skull bones together as one unit [28].

The brain tissue comprises of grey matter on the outer surface and white matter in the interior. This tissue sub-classification refers to the gross appearance of the tissue and corresponds to the cell bodies and axons of the neurons respectively.

The cerebral hemispheres as shown in Fig. 2.2 perform higher functioning such as

speech, reasoning and learning [29]. They are connected by the corpus callosum and are divided into lobes, which are regions of the cerebrum under different skull bones and have been mapped for different functionalities. As an example, the frontal lobe contains the motor cortex while the occipital lobe has vision centres. The outer surface of the cerebrum is heavily folded into convulsions (gyri) and depressions (sulci) to increase surface area. The brainstem consists of a series of structures like the thalamus, hypothalamus, pons and medulla, and is located deep in the brain. The brainstem connects the cerebrum to the cerebellum and spinal cord as well as performing many lower level functions such as regulation of the autonomic systems including blood pressure, body temperature, respiration, and digestion. The cerebellum is located at the base of the brain and is responsible for balance and coordination.

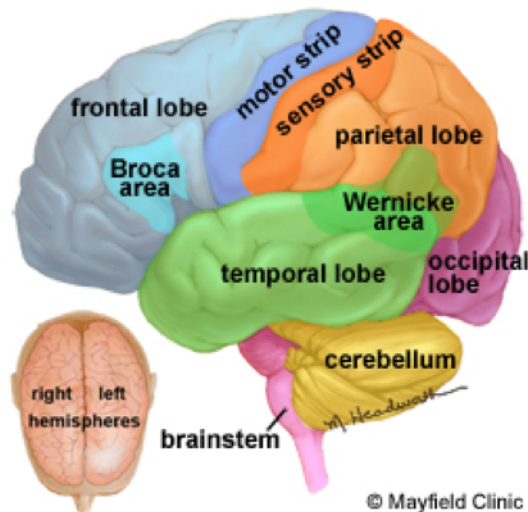


Figure 2.2: Parts of the brain as well as lobes of the cerebrae and some functional mapping [26].

The brain can also be modelled as consisting of collections of neurons (and supporting cells), with different functions depending on region. Like any tissue, nutrients like oxygen and glucose are required as well as the supply of input regulatory signals. Simultaneously waste products must be removed in order for the tissue to function and stay viable. The blood supply to the brain is the key network that performs these functions of supply of nutrients and inputs, and removal of wastes. The neck contains the left and right vertebral arteries, which merge to form the basilar artery, as well as the left and right internal carotid arteries which branch

from the common carotid arteries as shown in Fig. 2.3. This arterial supply merges to form the cerebral arterial circle, or Circle of Willis, at the level of the brain stem deep inside the brain (Fig. 2.4). From this deep location within the brain, the major paired arteries that serve the brain emerge: Anterior Cerebral Arterys (ACAs), Middle Cerebral Arterys (MCAs) and Posterior Cerebral Arterys (PCAr). The ACA serves mainly the front and middle of the cerebra, while the PCAr serves mainly the posterior brain such as the cerebellum and brainstem. The MCA is the largest of the arterial group and serves the frontal lobe, lateral surfaces of the temporal and parietal lobes including primary motor and sensory areas of the face, throat, hand, arm and speech. The MCA is the artery most often occluded in stroke [30].

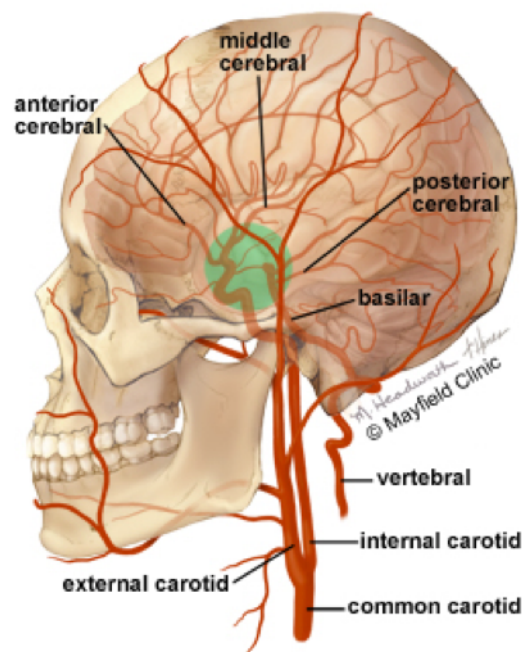


Figure 2.3: Blood supply to the head. The left and right internal carotid arteries as well as the left and right vertebral arteries supply the brain [26].

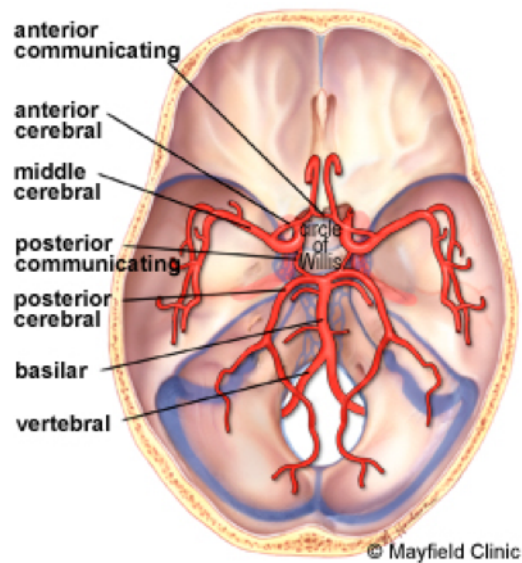


Figure 2.4: Anatomy of the cerebral arterial circle (Circle of Willis). The Circle of Willis is formed from the merging of the left and right internal carotid arteries and the basilar artery. From the Circle of Willis, the major paired arteries that serve the brain emerge as the ACA, MCA, and PCA [26].

Three membranes called the meninges surround the brain and spine. These membranes protect, nourish, and support the Central Nervous System (CNS). The outer most meningeal layer is the dura mater. The dura is comprised of two layers. The tough periosteal outer layer of the dura is continuous with the skull, with the thinner inner layer of the dura extending into major brain fissures to give partitions. These partitions included the falx cerebri between the cerebral hemispheres, and the tentorium cerebelli between the back of the cerebrum and the cerebellum. Inside the dura is the arachnoid mater, a delicate avascular layer. Innermost is the pia mater which is a delicate vascular layer closely linked to the brain and spine. In between the arachnoid and pia there is the subarachnoid space where cerebrospinal fluid (CSF) flows.

CSF is produced by the choroid plexuses which are capillary networks found in the walls of the network of cavities in the brain called ventricles as shown in Fig. 2.5. Two large lateral ventricles are found in each of the two hemispheres and these drain into the 3rd ventricle, which is found at the level of the thalamus before draining via the cerebral aqueduct into the 4th ventricle. From the 4th ventricle CSF then flows out either through the central canal into the spine or through the lateral apertures into the subarachnoid space. CSF acts as a shock absorber for

the CNS as well as having a role in normal maintenance of the CNS.

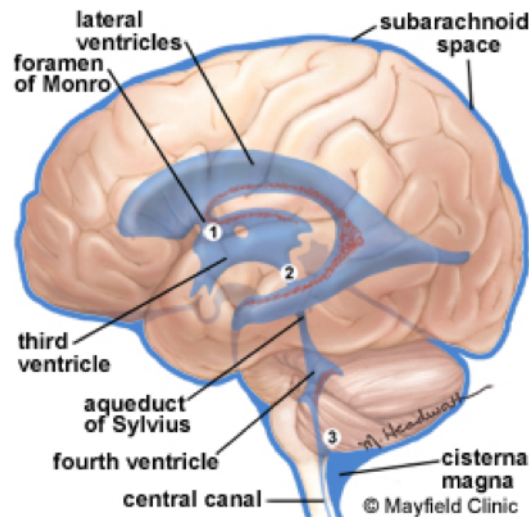


Figure 2.5: Anatomy of the ventricular system. Choroid plexuses in the walls of the ventricles produce CSF. The lateral ventricles drain into the 3rd ventricle and on into the 4th ventricle. After this point the CSF flows either into the central canal of the spine or into the subarachnoid space [26].

Normal physiological functioning and health of a given area of the brain depends on the maintaining of a steady state environment, a phenomenon called homeostasis [29]. If homeostasis cannot be maintained then the result is abnormal physiology or pathology. Pathology is characterised by compromised function and structure. For example, bleeds or clots in an arterial bed will compromise the supply of blood flow distally. The functionality of the distal area served by the affected artery is compromised with the effects on the patient dependent on the area affected and the severity of the breach in homeostasis. An infarction of the MCA will result in symptoms such as hemiparesis (one sided weakness) or hemiplegia (one sided paralysis) of the contralateral face and limbs as well as speech impairment. These consequences logically follows by appreciation of the areas served by the MCA and the functions of these areas.

As well as a loss in function, neurons now not served by an adequate blood supply may begin to undergo necrosis and death, leading to potential permanent loss of function and morbidity or even mortality. Hence an understanding of pathology naturally follows once the normal anatomy and physiology are understood.

This normal anatomy and physiology has been presented in this section.

In the next section, brain diseases are discussed, and in particular brain diseases with bleeds and or clots as the central aetiology. The first of these is Cerebrovascular Accident (Stroke), with TBI then discussed.

2.2.2 Cerebrovascular Accident (Stroke)

Cerebrovascular disease is any brain pathology resulting from a disruption in blood supply. The most common of these is stroke, also known as Cerebrovascular Accident (CVA) [31]. CVA is defined as the sudden loss of neurological function persisting for greater than 24 hours as a result of an interruption in blood flow [32]. Closely related are TIAs which are characterised by blocked blood supply for a period of typically 1-2 hours (but up to 24), and brain damage that is often reversible [33], [34].

A person with a suspected CVA or TIA will follow a series of patient pathways with steps detailing diagnosis, treatment as well as aftercare and prognosis. Various guidelines and pathways exist globally. In this thesis, the pathways studied are those devised by National Institute for Health and Care Excellence (NICE) [35]. These patient pathways are summarised at the end of this section on stroke after sections on the epidemiology, aetiology, symptoms, diagnosis, treatment, and prognosis of stroke.

2.2.2.1 Epidemiology of Stroke

Stroke is responsible for about 9% of deaths globally (10 to 12% in western countries) and is the second most common cause of death after heart disease [1]. Prognosis after having a stroke is poor with 25% of patients dead within a month and 50% within a year [1]. The age-adjusted mortality is in the region of 50-100 per 100,000 [1].

However, there has been a reduction in mortality as stroke risk factors like hypertension are tackled [1]. There has also been a simultaneous increase in morbidity [1]. Survivors of stroke may be left with permanent disability involving paralysis, dysphagia and psychiatric issues directly or indirectly linked to the damage and loss of neurological tissue [1]. It is estimated that about 500 per 100,000 live with the consequences of stroke [32].

In Ireland, approximately 10,000 people are hospitalised with a diagnosis of stroke with 2,000 deaths annually [36]. There are 30,000 stroke survivors in Ireland, many

of whom have disability as a result [36]. Stroke in Ireland is the third most common cause of death and most common cause of physical disability [36].

Globally, stroke consumes about 2 to 4% of health budgets with a total cost to society of about £8.9 billion in the United Kingdom (UK) [37]. The decreasing mortality but increasing morbidity is expected to drive up spending into the future. In Ireland the current cost burden is about 4% of the Health Service Executive (HSE) budget with the total possibly exceeding €1 billion per year [38]. The total direct cost per stroke patient in the first year is about €20,000 [38].

There are great improvements possible in terms of both patient outcomes and also economically by changes in acute and post-acute care. For example, one of the key acute treatments for ischaemic stroke, tissue plasminogen activator (tPA) is underutilised primarily due to delays in differentiating haemorrhagic and ischaemic stroke. A recombinant tPA, alteplase, is a licensed medicinal product approved for a variety of conditions and acts by thrombolysis (dissolution) of blood clots [39].

Achieving a 20% thrombolysis rate could save the lives of about 100 people per year in this country and €3 million [36]. Currently, the thrombolysis rate in Ireland is about 1% [36]. Without implementation of actions either to prevent or treat stroke effectively, the number of cases in Ireland could increase by over 50% by 2021 [36]. This outcome would result in an equivalent percentage rise in economic cost [36]. There is clearly a great need and space in the area of stroke for new research and technological innovation.

2.2.2.2 Aetiology and Pathology of Stroke

The cause of stroke can be due to either an ischaemic (clot) or haemorrhagic (bleed) lesion, with the patient then classed as an ischaemic or haemorrhagic stroke patient [1].

A number of causal risk factors exist for both types of stroke. These risk factors may be fixed or modifiable [1]. Hypertension, diabetes and heart disease are linked to stroke, as well as lifestyle elements such as lack of exercise, poor diet, and smoking [1]. Men are more likely to have a stroke except in the 45-54 age bracket where women are twice as likely to suffer a stroke [32], [40], [41]. There is also a greater chance of fatality in women [32], [40], [41]. Personal and family history is important with an increased risk of stroke if an individual or family member previously has had a stroke [1]. Certain vascular medical conditions also predispose to stroke, for example vasculitis and sickle cell anaemia [32]. Use of drugs including non-steroidal anti-inflammatory drugs (NSAIDs) and cocaine are also linked to

stroke risk [32]. Age is a risk factor with 75 % of strokes occurring in people over 65 years old [32]. While risk factors like gender and age cannot be changed, tackling and reducing modifiable risk factors like hypertension and exercise is an obvious way to reduce stroke incidence [1], [32], [40], [41].

Upon suffering a stroke, treatment is radically different depending on whether an ischaemic or haemorrhagic aetiology is present and so a crucial part of the diagnostic process is absolute differentiation of the patient as an ischaemic stroke or haemorrhagic stroke patient [1], [32]. As a result of this dichotomy in treatment it is worth considering the two stroke types in a little more detail. These two stroke types are described in the next two subsections.

2.2.2.2.1 Haemorrhagic Stroke

Haemorrhagic stroke accounts for 15 % of stroke cases and are associated with higher mortality compared to ischaemic [42]. Haemorrhagic strokes are often linked to hypertension (causing an aneurysm) and vascular malformations. Haemorrhagic strokes can be further subdivided into intracerebral (10 %) and subarachnoid (5 %), depending on the location of the haemorrhage [42].

Intracerebral Haemorrhage (ICH) refers to a bleed into the parenchyma of the brain whereas a Subarachnoid Haemorrhage (SAH) involves a bleed in the subarachnoid space [42]. ICH often occur in deep brain structures like the thalamus, pons and cerebellum as a result of hypertension. Cases of ICH related to other conditions like cerebral amyloid angiopathy may be seen as lobar bleeds at the grey and white matter junction [43]. However, ICHs can and do occur everywhere and in a vast range of volumes [44], [45]. The volume of an ICH is a predictor of outcome and volumes at or above 30 ml have been used as an indicator of increased mortality [46]. However a haemorrhagic stroke can be caused by bleed volumes a lot smaller, with bleeds of down to 1 ml being reported as causing an attack [47].

In a case of SAH, blood pools in the space about the brain normally occupied by CSF. SAHs in common with ICHs have multiple sites of origin and underlying causes. A sample cause is aneurysmal rupture due to haemodynamic stress on arteries especially at branching points like at the Circle of Willis. A potential challenge in imaging a SAH in the diagnostic work-up is the tendency of the blood not to collect in a spherical or ellipsoid mass but rather to spread around the subarachnoid space as a thin flat collection [48].

2.2.2.2.2 Ischaemic Stroke

Approximately 85% of strokes are ischaemic resulting from an arterial thrombus or embolus blocking a vessel [49]. The tissue downstream of the blockage may become permanently damaged, forming a dead core. Surrounding the dead core there will be a volume of impaired but salvageable tissue called the ischaemic penumbra [49]. The penumbra is the tissue that may be saved by timely therapeutic intervention causing reperfusion. The goal of modern treatment is to salvage this tissue leading to better patient outcomes [49].

Ischaemic strokes are classified in a variety of ways with one commonly used system being the Trial of Org 10172 in Acute Stroke Treatment (TOAST) criteria [1]. This classification looks at the origin of the blockage. Major TOAST subtypes include large-artery atherosclerosis (emboli originating from a large artery like the carotid arteries or a cardiac source), lacunar infarction (small local occlusions in deep vessels with a small infarction zone of about 5 to 15 mm diameter) and cardioembolic infarction (due to concurrent conditions like atrial fibrillation, which are a common cause of recurrent stroke and also linked to high mortality) [1], [49]. TOAST classification conveys relevant treatment and secondary prevention information [1], [49]. Although there are sites and areas where blockages are more likely, an ischaemic stroke can occur at any location within the network of arteries in the brain [49]. Haemorrhagic transformation of ischaemic infarction is a recognised condition occurring often days after stroke occurrence and more likely if the patient has received tPA [50]. However this condition does not influence prognosis except in extreme cases, for example a massive haematoma [50].

Finally TIAs, also called mini-strokes, are a closely related condition. TIAs share the same aetiology as ischaemic stroke but in the case of a TIA the blockage is temporary causing transient symptoms and usually no lasting damage to the brain. A clot is naturally dissolved by the body and in the case of a TIA this happens quickly enough to avoid permanent loss in function [51]. This separation of TIA from ischaemic stroke is arbitrary with the cut off time for an event to be labelled a TIA being less than 24 hours. After this point the lesion becomes an ischaemic stroke. Permanent damage is seen in about 25% of TIA patients on MRI indicating that a TIA is often not without effect on a patient [1].

2.2.2.3 Symptoms of Stroke

Stroke caused by a blockage or a bleed can result in a sudden loss of neurological function. Different areas of the brain control different functions and different nerve types are responsible for motor, sensory and autonomic regulation of organs and

systems. Hence, stroke is associated with neurological symptoms in the patient. Localisation of the affected region of the brain is possible based on the symptoms displayed, giving so called stroke syndromes [52]. As an example, blockage of the MCA will result in symptoms like weakness in the contralateral face, arm and legs as well as speech and vision problems. By contrast, a stroke in the brainstem will likely result in vision disturbances, facial weakness, difficulty with balance as well as blood pressure and respiratory dysfunction.

However due to the complexity of the brain and the fact that a stroke can occur anywhere, absolute localisation may be difficult if not impossible based on physical symptoms alone. Common stroke symptoms include numbness, weakness or paralysis on one side of the body, as well as speech and vision problems. Other common symptoms include confusion and impaired balance [53].

2.2.2.4 Diagnosis of Stroke

The diagnosis of stroke typically involves an initial diagnosis based largely on physical examination. Confirmation with the crucial additional diagnosis of the underlying aetiology as haemorrhagic or ischaemic requires subsequent neuroimaging. These diagnostic steps are now discussed.

2.2.2.4.1 Initial Stroke Diagnosis

The first steps of stroke diagnosis are the initial recognition of the disease. Validated tools such as Face, Arms, Speech, Time (FAST) and Rule Out Stroke in the Emergency Room (ROSIER) as well as other preliminary diagnostics are used [54]. Based on these tests the patient will be labelled as a TIA or acute stroke patient and handled accordingly, moving onto neuroimaging for definitive diagnosis [54].

FAST is a public health campaign aiming to inform people as to the common signs seen in stroke:

- Face: Facial weakness;
- Arms: Arm weakness;
- Speech: Speech disturbance;
- Time: Time to call the emergency services.

Since a launch in the UK in 2009, the campaign has been shown to have had a statistically significant impact based on metrics such as information seeking behaviour by the public on stroke, hospital admissions with a primary diagnosis of stroke and (less so) thrombolysis rates [55]. Studies on the impact of the campaign vary in quality but most show positive attributable interventions [56].

ROSIER is designed for use by medically trained personnel to diagnose stroke and also to differentiate stroke mimics such as syncope and seizures. The test is based on results of physical examination aspects such as assessment of degree of facial weakness and consciousness with a scoring system applied. The final score is indicative of stroke as a probable diagnosis or not [53]. Early analysis of ROSIER suggested a sensitivity of 92% and specificity of 86% for stroke diagnosis [53]. More recent studies suggest that while sensitivity is good, specificity may not be as high as first thought being in the vicinity of 40 to 45% [57].

Of interest is the performance of FAST and ROSIER by paramedics and ambulance crews as likely first responders to stroke patient. Studies of this cohort report that the ROSIER (and FAST) tests have a high sensitivity (circa 97%) but again a low specificity (circa 15%) [58].

Hence these initial physical examinations have a high rate of detecting true positives, but may also detect a high rate of false positives. So called ‘stroke mimics’ account for many of these false positives with common mimics including seizures, syncope, sepsis and migraine [53]. Neuroimaging helps differentiate these stroke mimics from true stroke. Other stroke mimics such as hypoglycaemia is easy to diagnose at the initial stages by simple blood testing and thorough history taking [59].

The ROSIER test is not suitable for TIA patients. A TIA patient by definition often has no neurological symptoms at the time of assessment (within 24 hours) [34]. TIA patients are however at risk of a subsequent stroke and are assessed for that risk by another validated scoring system, ABCD². This scoring system is again based on the results of patient history and physical examination:

- A: Age, (1 point if greater than 60);
- B: Blood Pressure (1 point if over a threshold value);
- C: Clinical features of TIA (e.g. unilateral weakness, speech problems);
- D: Duration (greater than or less than 60 minutes);
- D: Diabetes (yes or no).

The scale is from 0-7 with decisions on hospitalisation and the urgency of neuroimaging made based on the result. The system is optimised to give the risk of stroke at two days post TIA but also gives the risk within 90 days [60].

Analogous to the case in stroke, TIA mimics exist. These mimics include migraine, syncope but also significantly haemorrhage [61]. The diagnosis of TIA relies largely on history and assessment, which is not ideal and often fails to rule out

potential mimics. Up to 60% of patients referred to a TIA clinic do not have a final diagnosis of TIA [59]. Haemorrhage is not a frequent TIA mimic. However, the presence of haemorrhage is an important consideration as treatment for TIA often involves starting on clotting inhibitors like aspirin [34]. These medications may have devastating consequences in patients with a haemorrhage. Although NICE does indicate neuroimaging in TIA, the urgency is not as high as for stroke. There is an argument for the use of neuroimaging sooner in a TIA patient's pathway to rule out bleeding [34].

2.2.2.4.2 Neuroimaging of Stroke

Neuroimaging is a crucial step in the pathway of an acute stroke patient [32]. Quick and accurate confirmation of a stroke diagnosis and differentiation of ischaemic from haemorrhagic stroke is vital since these two lesion types are treated in radically different ways. Of fundamental importance is the existence of only one currently approved drug for treatment of acute ischaemic stroke, alteplase, a recombinant human tissue-type plasminogen activator [39]. This “clot busting drug” is licenced only for administration within 3 hours of stroke onset in the USA and within 4.5 hours in the UK. Importantly the drug can be fatal if given to a haemorrhagic stroke patient. Further, haemorrhagic patients often need urgent surgery that can only be completed by specialist hospitals. Hence the need for time-critical imaging to correctly triage stroke patients and give them the best chance of good outcomes.

As noted, neuroimaging is also indicated in TIA patients but unlike acute stroke the urgency is not as high. Depending on the result of the ABCD² score, imaging may be needed within 24 hours or as long as even a week [34]. The two primary imaging modalities used in stroke patients are CT and MRI as well as variants on these modalities. These modalities are discussed in the next two subsections.

Computed Tomography

Non-contrast CT is the primary imaging modality used in acute stroke due to the speed of imaging and availability [62]. In the acute phase CT may detect ischaemic stroke (as characterised by Early Ischaemic Changes (EICs)) but more importantly is the superb sensitivity and specificity of the modality in haemorrhage detection [63]. In the time critical six hour period after stroke onset, CT has a sensitivity and specificity of near to 100% for haemorrhage [63], [64]. Hence CT will definitively rule in or rule out haemorrhage and also may help detect stroke mimics including tumours [62]. If EICs in ischaemic stroke are detected they can

also be quantified. An example is the Alberta Stroke Program Early CT Score (ASPECTS) system which is applied to ischaemic stroke involving the MCA. The ASPECTS system divides the MCA territory into 10 regions and deducts a point from 10 for every region involved based on non-contrast CT imaging [32]. EICs include features like hypodensity, loss of grey/ white differentiation and oedema [65].

It must be emphasised that the power of non-contrast CT lies in the ability of the modality to detect haemorrhage. Often CT will not detect EICs, and an ischaemic stroke patient will have a normal CT in the crucial acute stage [62]. However, the most important role imaging has in the acute stroke workup is to differentiate between ischaemic and haemorrhagic. As described in Section 2.2.2.2, it is on this differentiation that life and death therapeutic decisions are made. The absence of a bleed on CT rules out haemorrhagic stroke and effectively results in a diagnosis of ischaemic stroke, with appropriate treatment to follow. Figs. 2.6 and 2.7 show typical non-contrast CT findings for various acute stroke patients.



Figure 2.6: Normal brain on non-contrast CT. In the case of acute ischaemic stroke an identical image is often seen as ischaemic changes such as oedema may not yet have occurred [66].

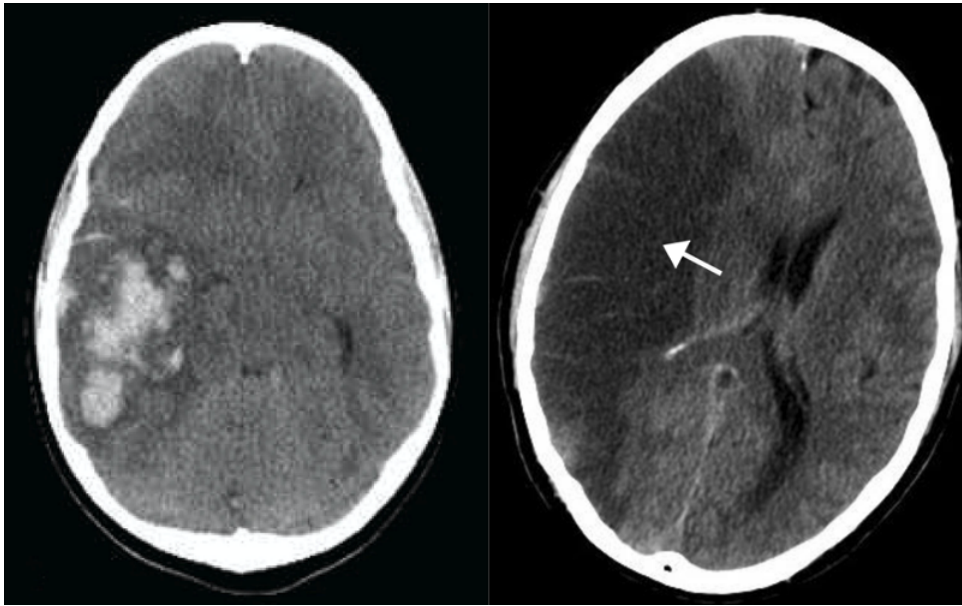


Figure 2.7: Left: Haemorrhagic Stroke seen on non-contrast CT. The presence of a bleed is seen as a hyperdense region with CT having sensitivity and specificity of near to 100% for haemorrhage in the acute phase [67]. Right: Ischaemic Stroke seen on CT involving MCA territory (arrow). The hypodense regions indicated are due to tissue affected by the presence of a clot becoming oedematous and dying [68].

Some variants to conventional non-contrast CT exist and can be used to provide a more complete and accurate picture of stroke [62]. CT Angiography involves the injection of a contrast agent before taking timed images [62]. This modality is especially useful to see stenosis and may for example identify the location of the blockage which is useful for planning mechanical thrombectomy intervention [62]. CT perfusion studies again involve the use of contrast agent and timed imaging [62]. This variant of CT focuses on studying flow metrics such as cerebral blood flow and mean transit time [62]. These metrics help to identify and measure areas of the brain that are unsalvageable and those that are salvageable (penumbra tissue) [62].

Magnetic Resonance Imaging

MRI is a superior imaging modality to CT for stroke diagnosis in the acute phase but the speed, ease of use, availability and lower cost means CT is the primary diagnostic imaging tool used [62]. MRI may also not be suitable for some patients, particularly those with metal implants, pacemakers and those who are claustrophobic [69]. However, an ideal imaging modality should be able to image both ischaemia and haemorrhage in acute stroke patients. While CT is both sensitive and specific to acute haemorrhage, the modality does not detect ischaemia

well in the early period after stroke onset [62].

Gradient-echo MRI is as effective as CT for diagnosis of haemorrhagic stroke while diffusion-weighted MRI is sensitive to ischaemic stroke and EICs within minutes of the stroke occurring. While CT may only detect 10% of ischaemic strokes in the critical first three hours, diffusion-weighted MRI detects 46% of these strokes within that time window [69]. Some studies report even greater levels of performance from MRI compared to CT [69]. MRI detects acute stroke (haemorrhagic or ischaemic), acute ischaemic stroke and chronic haemorrhagic stroke more frequently than CT [69]. Hence MRI is more effective at diagnosing acute stroke than CT. An example of a haemorrhagic and ischaemic stroke imaged using MRI is shown in Fig. 2.8.

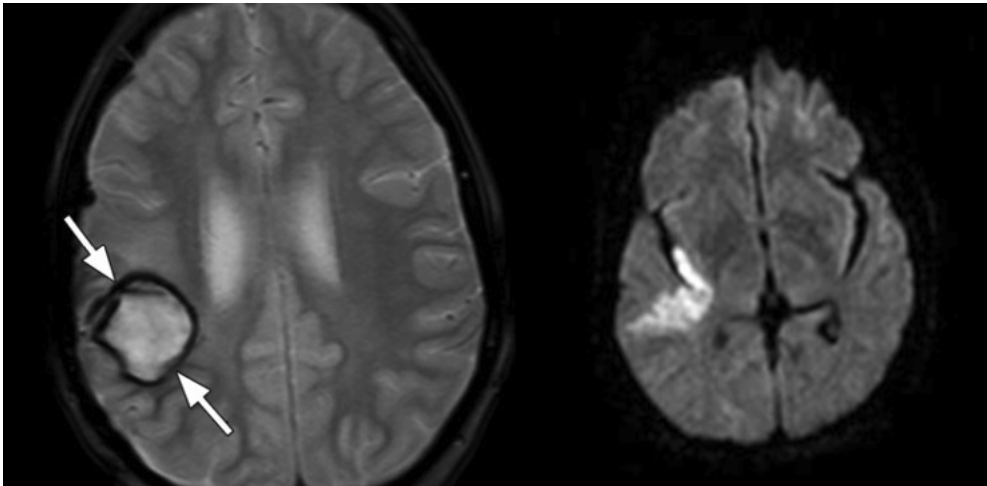


Figure 2.8: Left: Haemorrhagic stroke in the right posterior frontal region with dark borders imaged by gradient-echo MRI (arrow) [70]. Right: Ischaemic Stroke seen on diffusion-weighted MRI involving the right insular lobe [71].

Respected bodies such as the American College of Radiology (ACR) recommend MRI as the primary imaging modality and gold standard but availability, cost and ease of use make this recommendation impractical [62]. Hence, acute ischaemic stroke hence requires imaging (usually CT) to detect the presence or absence of a bleed. Based on this imaging outcome a diagnosis of haemorrhagic or ischaemic stroke is made with treatment initiated. These treatments are now described.

2.2.2.5 Treatment of Stroke

The treatment of acute stroke is radically different depending on the aetiology (ischaemic or haemorrhagic). Common treatments are present in the period after stabilisation of the patient, for example medications to prevent subsequent strokes. In addition, specialist rehabilitation strategies are common regardless of aetiology [54]. However the focus here is the acute treatment strategies for each type of the two types of stroke. These treatments are now discussed.

2.2.2.5.1 Treatment of Haemorrhagic Stroke

Haemorrhagic stroke patients should be hospitalised and observed by specialists in neurosurgery or stroke care in case of deterioration and be ready for immediate imaging and rapid surgical intervention since haemorrhage, and in particular ICH is the most lethal form of stroke. Haemorrhagic stroke patients are primarily treated medically and with the addition of surgery if indicated [3]. Medical treatment for haemorrhagic stroke include anti-hypertensives to reduce blood pressure, diuretics to help relieve intracranial pressure and also medicines to prevent seizures [42]. Treatment is largely aimed at mitigating the symptoms with the aim of stabilising the patient, and not directly targeted at the bleed. Surgical intervention may not be needed for patients with for example small deep bleeds or without evidence of hydrocephalus [3]. Surgery aims to stop bleeding and to reduce pressure in the skull, employing interventions including evacuation of the haematoma to cause decompression and coil embolisation to treat aneurysms [72].

2.2.2.5.2 Treatment of Ischaemic Stroke

Ischaemic stroke is treated by thrombolysis and mechanical clot removal [3]. The surgical intervention, decompressive hemicraniectomy, is indicated if the MCA area is involved [3]. For TIA patients treatment consists of anti-platelet aspirin, specialist assessment to screen for mimics, and measures to prevent subsequent attacks [34]. The ischaemic stroke treatments are of particular interest being more specialist in nature than those for haemorrhagic stroke and are discussed in more depth in the following sub-sections. Finally the treatment of ischaemic stroke in cases where EICs are detected is discussed.

Thrombolysis

Alteplase is a recombinant human tPA that dissolves clots (thrombolysis). The drug is heavily time dependent, with the size of effect a function dependent on the interval between onset of stroke and administration. Cut off times of three

hours post stroke onset in the USA [73] and 4.5 hours in the UK and many other European countries [74], [75] exist as after these time points the risks outweigh the benefits, with an unacceptable risk of morbidity and mortality.

The major adverse effect of alteplase is unsurprisingly bleeding. In 6 to 7% of cases, ICH is seen as a result of the drug [1]. Because of this adverse effect an absolute contraindication for administration of alteplase is the presence of brain haemorrhage. The presence of a bleed must be ruled out by appropriate imaging before alteplase is given as a fixed dose to the patient [39]. Administration is by appropriately trained staff and there should be access to imaging and reimaging with staff to interpret the results.

Evidence for the effectiveness of alteplase looks at patient outcomes and costs. The Modified Rankin Score (mRS) is a scale of disability of a patient after a neurological insult like stroke. The scale ranges from 0 (death) to 6 (no symptoms). Using this metric it is seen that alteplase given within three hours to patients results in better outcomes compared with placebo. With administration within 3 to 4.5 hours there are better outcomes with regards to morbidity (despite an increased risk of haemorrhage in this window [39]) but no statistical differences in mortality compared to placebo [73]. Importantly, alteplase is more effective the sooner administration occurs, coining the expression “time is brain” [76]. Because of this time urgency on initiation of treatment and the need to rule out haemorrhage before administration, guidelines recommend imaging within one hour of arrival at hospital and all hospitals to have round-the-clock imaging facilities [74].

Cost and effectiveness can be judged by metrics such as Incremental Cost Effectiveness Ratio (ICER). This metric is the difference in cost between two possible interventions, divided by the difference in effectiveness of the interventions. Cost can be measured in terms of local currency and effectiveness in terms of Quality Adjusted Life Years (QALYs). A QALY is a measure of disease burden in terms of quality and quantity of life lived. In the UK, the National Health Service (NHS) has a threshold ICER of about £20,000/ QALY, with treatments above that theoretically not approved [77]. Alteplase treatment within the 4.5 hour window was found to dominate standard care (both more effective and cheaper) with an ICER of under £10,000/ QALY depending on the time to treatment window considered [74]. While studies indicate that alteplase is an effective treatment in terms of efficacy and cost within the 3 hour window [78], there is difference of opinion on efficacy within the 3 to 4.5 hour period. Most studies support the use of the agent in this latter window but some controversy still exists in the literature [75], [79].

While debate may exist between jurisdictions as regards cut off times for administration of alteplase what is agreed is that the drug is a proven intervention for ischaemic stroke with use dependent on time critical imaging ruling out the presence of bleed.

Mechanical Thrombectomy

Mechanical removal of the clot is a relatively new treatment strategy for ischaemic stroke. Unlike alteplase, which can take up to two hours to dissolve a clot, physically removing the clot takes minutes [80]. This rapid clot removal translates into a larger window for intervention. Although like alteplase, outcomes are better the sooner after onset thrombectomy is completed, evidence indicates the method is effective within 8 hours of the attack [81], and perhaps even up to 24 hours [82].

The Food and Drug Administration (FDA) currently has approved two device classes: stent retrievers (and variants) and aspiration catheters. Early trials of these devices failed to show efficacy but trials like the Multi Mechanical Embolus Retrieval in Cerebral Ischemia (MERCI) trial showed 55 % recanalisation (i.e. restoration of blood supply) with the first generation concentric retriever device alone, and 68 % if alteplase was used with the device. More recent trials with next generation stent retrievers (including the pivotal MR CLEAN, EXTEND-IA, ESCAPE, SWIFT PRIME, and REVASCAT trials) have established the efficacy of the treatment [83]. The Penumbra trial demonstrated 82 % recanalisation with an aspiration based device [32], with the ASTER trial suggesting comparable efficacy and safety (or at least non-inferiority) of aspiration mediated thrombectomy compared to thrombectomy with stent retrievers [84].

Mechanical thrombectomy is usually indicated for clots in one of the main cerebral arteries (MCA, PCAr, ACA) and needs precise imaging to confirm occlusion and exact lesion location. The optimal treatment strategy is still an area of active research but it is becoming more common in practice to use a multi-modal approach with both alteplase and mechanical thrombectomy. This multi-modal approach is supported by evidence from randomised controlled trials which report better outcomes (based on mRS) for patients who receive both modalities compared to thrombolysis alone [81]. Recanalisation rates of at least 60 % and good clinical outcomes (defined as 90 day mRS 0-2) of at least 30 % are the recommended minimal targets for a modern treatment strategy to achieve [85].

Impact of Presence of Early Ischaemic Changes

There is a subtle dichotomy in how ischaemic stroke patients may be treated depending on if EICs are imaged or not. EICs include hypodensity, loss of grey/white differentiation, oedema and are of particular interest if with MCA involvement [65]. EICs may be quantified using scoring systems like ASPECTS which is used for ischaemic stroke of the MCA. As remarked on in Section 2.2.2.4.2, CT may or may not show the early signs of ischaemia in the acute phase of stroke. If however EICs are imaged than alteplase may not necessarily be indicated for use.

NICE guidelines advise on decompressive hemicraniectomy if at least 50% of the MCA territory as imaged on CT is involved, the patient is over 60 years old, has depressed consciousness and a score of 15 or more on the National Institutes of Health Stroke Scale (NIHSS) (a 15 point neurological examination stroke scale used to assess the effect of the infarction) [3]. Irish thrombolytic guidelines recommend consultation between a stroke consultant and radiologist if greater than one third of the MCA region is affected or if other early infarction signs are seen such as mass effect [86]. In these cases the risks of alteplase may be increased.

This treatment decision pathway is however an area of controversy. As noted intracerebral haemorrhage is an important adverse effect of alteplase seen in about 6% of acute ischaemic stroke patients receiving the drug [86]. Risk factors for bleed have been developed based on studies such as the National Institute of Neurological Disorders and Stroke (NINDS) trials resulting in absolute and relative exclusion criteria such as extreme hypertension, thrombocytopenia, NIHSS scores of over 25, major surgery in the previous 14 days and the presence of EICs on CT [87]. These risk factors form checklists to be completed before administration of the drug. There is an argument that these exclusion criteria are too restrictive in practice and relaxation would benefit patients by allowing increased thrombolysis rates [87]. Some groups feel the presence of EICs alone should not be a reason to exclude patients from alteplase treatment [65]. Indeed, the American Heart Association (AHA) 2013 guidelines recommend administration of alteplase even if EICs are present and regardless of extent [87]. However distinct hypodensity on CT indicates more severe, irreversible damage and an increased risk of bleed if alteplase is given as does an ASPECTS score of less than or equal to 7 [88], but judging the amount and severity of established infarction versus ischaemia may not be easy.

In summary, using EICs to judge whether or not to give alteplase is not an exact science and clear guidelines are lacking resulting in a requirement for discussion with the consultant present to make a judgement on risk versus benefit.

2.2.2.6 Prognosis of Stroke

The prognosis is poor for stroke patients, with a one month mortality rate of 25 % and a one year mortality rate of 50 % [1]. The prognosis is worse for haemorrhagic compared to ischaemic stroke due to issues including potential rapid haematoma expansion in haemorrhagic patients [1]. Stroke is the second most common cause of death and major cause of disability worldwide [1]. Because of the ageing population, the burden will increase greatly during the next 20 years, especially in developing countries.

Neurologic deficits due to permanent damage to regions of the brain include hemiparesis, cognitive impairment, aphasia and sensory problems as well as secondary issues such as depression and social withdrawal. Medical complications due to stroke include cardiac issues, pneumonia, venous thromboembolism and dysphagia [89]. These complications predispose the patient to increased risk of morbidity and even death. Despite the potential severity of the condition, mortality from stroke is decreasing globally but morbidity is increasing as more people survive [1]. Better outcomes, as measured by the mRS and other metrics, can be achieved by both good care and rehabilitation post stroke but also administration of effective treatments in the acute phase and prevention strategies [90].

Predictors of recovery include the age of the patient and the initial extent of the neurological damage, which will depend on the size and location of the stroke and can be scored using tests like the NIHSS. Another issue is recurrent stroke which is frequent and of greatest risk immediately after an initial event. The pooled cumulative risk of stroke recurrence is 3.1 % at 30 days, and 11.1 % at one year [91]. TIA patients as described earlier in Section 2.2.2.4.1 are also at risk of a stroke after an event with the two day and 90 day probability given by the ABCD² score necessitating hospitalisation and more urgent imaging for some patients. For example, a score of 6/7 gives an 8 % risk of stroke at two days for these patients [34], [60].

Advances have occurred in the prevention and treatment of stroke during the past decade. For patients with acute stroke, management in a stroke care unit, intravenous tPA within three hours or aspirin within 48 hours of stroke onset, and decompressive surgery for supratentorial malignant hemispheric cerebral infarction are interventions of proven benefit [1]. Several other interventions are being assessed with mechanical thrombectomy being a notable and efficacious treatment modality [83], [84]. Proven secondary prevention strategies are warfarin for patients with atrial fibrillation, endarterectomy for symptomatic carotid stenosis, antiplatelet agents, and cholesterol reduction [1]. The most important intervention is the management of patients in stroke care units because these units provide a

framework within which further study might be undertaken. These advances have however exposed a worldwide shortage of stroke health-care workers, especially in developing countries [1].

As discussed in Section 2.2.2.1, stroke is a global problem. Taking as an example the situation in Ireland and the UK there is an urgent need to improve how stroke is dealt with. A 2008 audit from the Irish Heart Foundation (IHF) found major flaws in stroke care in Ireland [36]. There was no organised system of care to prevent and manage stroke both at primary care level but also at hospital level with only 1 out of 37 hospitals in Ireland having a full stroke care unit compared with 91 % of UK hospitals having one. Further, only 16 % of Irish hospitals had services for TIA compared to 78 % in the UK [36]. There was also a reported lack of staff as only one third of hospitals had a stroke consultant as well as a shortage of allied healthcare professionals such as stroke nurses [36]. As described, thrombolysis absolutely needs rapid access to imaging before commencement but only 40 % of patients received CT imaging within 24 hours [36]. This rate of imaging negatively affects any attempt to provide an effective thrombolysis service in Irish hospitals and indeed thrombolysis was not routinely available in any Irish hospital, compared to 18 % of UK hospitals according to the report [36]. To further hinder an effective thrombolysis service was the fact that only 5 % of stroke patients were admitted to hospital within two hours of their stroke compared to 39 % in UK [36]. On discharge, only 28 % of patients were assessed as independent in daily activities (39 % in UK) and then faced other issues out of hospital such as a lack of rehabilitation services [36]. Although there are plans for development of stroke services at all levels from primary care through to hospital, as well as at all stages such as primary prevention, acute treatment, hospital care, rehabilitation and secondary prevention; there remains major problems in the stroke care pathway. Especially noted was the lack of availability and inefficiency of services such as access to early neuroimaging and availability of stroke care units. There is a lack of easily accessible gold standard stroke imaging in Ireland. Diagnosis and treatment are time critical and time is being lost – only 4 % of audited patients were scanned within three hours of admission [36]. As part of the 18 point recommendation list was the need for 24 hour availability of neuroimaging and the 24 hour availability of stroke specialists trained in thrombolysis (on-site or via tele-medicine) [36].

2.2.2.7 Stroke Patient Pathways

To complete the picture of stroke and the subtypes (ischaemic, haemorrhagic and TIA) the NICE patient pathways are summarised in Figs. 2.9, 2.10, and 2.11 describing the stroke overview, TIA, and acute stroke pathways respectively. These pathways incorporate aspects of presentation, diagnosis, treatment and after-care

for each disease as well as other relevant points. They are best practice evidence-based guidelines incorporating efficacy and cost-effectiveness for use by the NHS in the UK.

2.2.2.7.1 Stroke Overview Pathway

The initial step of prevention looks at tackling the modifiable stroke risk factors such as hypertension and atrial fibrillation. If a stroke occurs then rapid recognition of signs and symptoms involve use of the early diagnostic tools like FAST and ROSIER to identify a stroke or TIA patient as well as other tests to rule out mimics such as hypoglycaemia. Based on these steps the patient will be triaged as a TIA or acute stroke patient (or indeed not a stroke patient) and funnelled down the appropriate path [54].

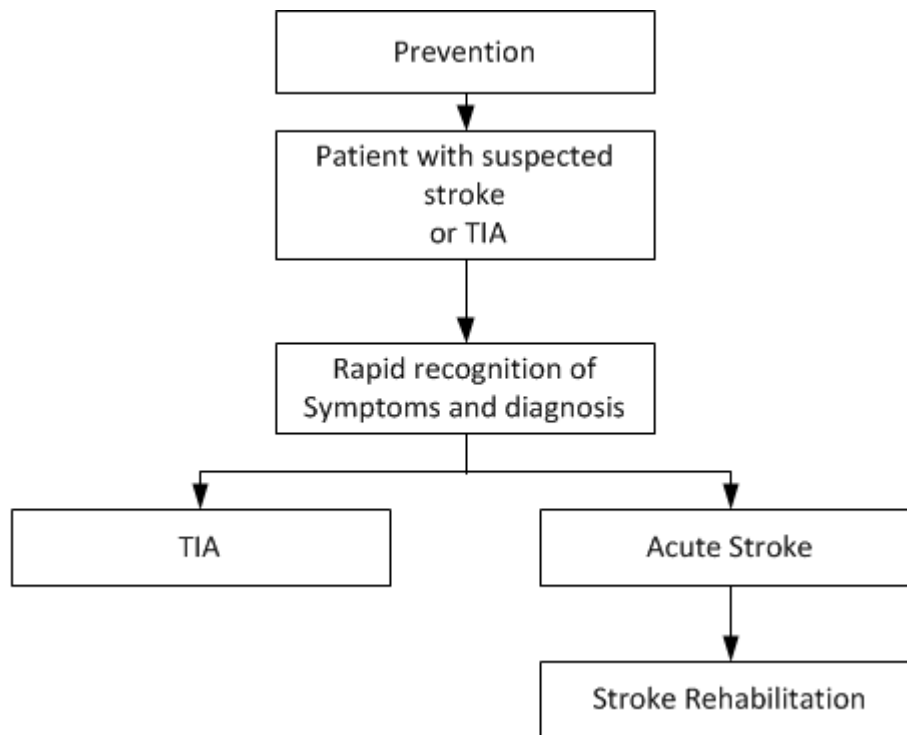


Figure 2.9: NICE Stroke Overview Pathway (adapted from [54]).

2.2.2.7.2 Transient Ischaemic Attack Pathway

TIA patients are assessed for the risk of a subsequent stroke as soon as possible using a system like ABCD² [34]. This system classifies them as high risk

(ABCD² of 4 or above) or low risk patients (ABCD² of 3 or below), and appropriate initial management can be implemented. This treatment will include administration of aspirin, specialist assessment to exclude stroke mimics, investigation of the cause and appropriate treatment (within 24 hours if high risk and within a week if low risk) as well as implementing measures for secondary prevention. In addition, brain imaging is indicated within 24 hours if high risk and within a week if low risk to help in the overall assessment of the patient. Imaging may also help rule out TIA mimics such as migraine, tumour and also crucially haemorrhage [34]. Carotid artery imaging is needed if the patient is a candidate for surgery to relieve narrowing of this vessel [34].

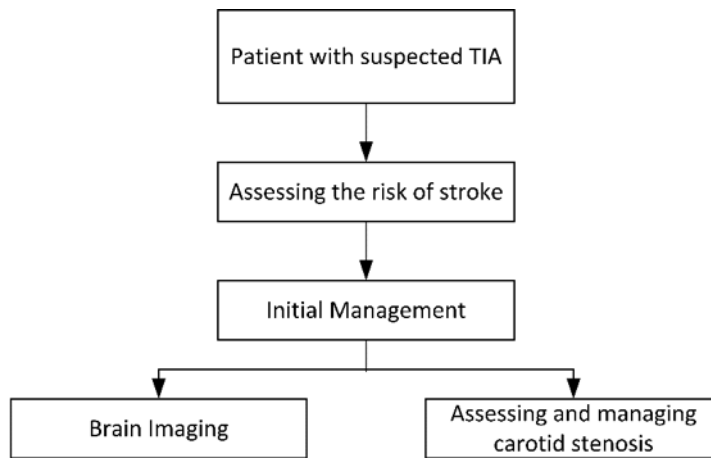


Figure 2.10: NICE TIA Pathway (adapted from [34]).

2.2.2.7.3 Acute Stroke Pathway

After a suspected acute stroke patient is admitted to a stroke unit, imaging is performed [3]. While imaging is always vital and urgent, the decision on precisely when to perform brain imaging is dependent to a degree on indications present. Imaging is performed immediately (within the hour at the latest) for patients with indications such as depressed levels of consciousness or severe headache, and otherwise as soon as possible for patients without such indications (within 24 hours) [3]. Based on the outcome the patient is diagnosed as an ischaemic or haemorrhagic patient and treated accordingly as shown in Fig. 2.11.

Haemorrhagic stroke patients are usually managed medically with surgical intervention implemented if necessary [3]. In ischaemic patients, thrombolysis is indicated if and only if haemorrhage has been ruled out by appropriate imaging,

the patient is within 4.5 hours of ictus and appropriately trained staff are available to administer the thrombolytic medication [3]. For patients with an infarction of the MCA involving greater than 50% of the MCA territory, aged 60 or over and a NIHSS score of 15 or greater, decompressive hemicraniectomy is indicated [3]. As discussed in Section 2.2.2.5.2 the role of alteplase in these stroke patients is controversial especially since the majority of the time CT will fail to detect EICs in the acute phase [87], [88]. In practice, hospitals, and indeed consultants, will have their own protocols for alteplase use in this scenario [3].

If the situation is simplified by removing the uncertainty surrounding EICs then the pathway for acute stroke can be reduced to that as proposed in Fig. 2.12. The crucial decision to be made by imaging is to rule in or rule out the presence of haemorrhage and based on that single piece of information a diagnosis and therapeutic decisions can be made.

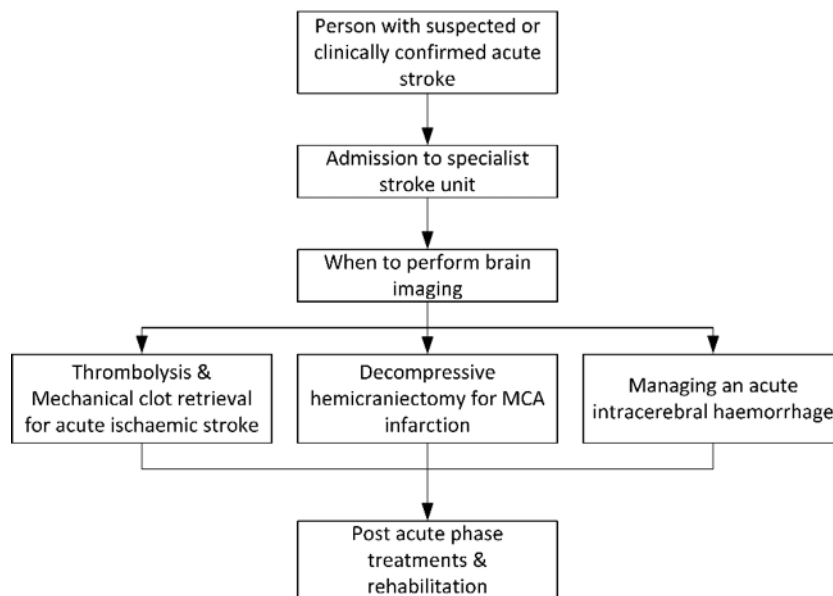


Figure 2.11: NICE Acute Stroke Pathway (adapted from [3]).

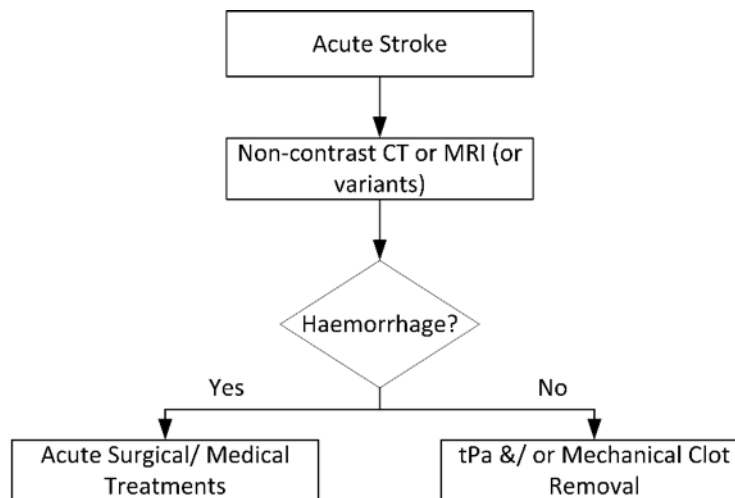


Figure 2.12: Simplified Acute Stroke Pathway. The crucial decision to be decided by imaging is to rule in or rule out the presence of a haemorrhagic lesion.

2.2.3 Traumatic Brain Injury

TBI represents another important pathology of brain with the presence of haemorrhage associated with increased severity and an urgent need for detection if present [2].

TBI refers to the range of injuries resulting from an external mechanical force impacting the head, with consequences for the brain. TBIs may be classified depending on severity, mechanism of the insult as well as by location and nature of the resultant injuries. TBIs are a mixed group of conditions including both primary and secondary insults. Primary injury refers to the result of the force at the moment of impact and can cause fracture, auditory or vestibular disturbance, haemorrhage and other injury types. Secondary injuries occur later and can result in oedema, hydrocephalus and herniation [92]. Treatment involves addressing both the acute and the later injuries to ensure best possible outcomes [93]. In particular neuroimaging is important in the patient assessment to examine the results of the injury, guide treatment choice as well as monitoring in the secondary phase.

Closely related to TBI is concussion, which is a term referring to minor TBI. Concussion is of major concern especially in sport, because of the potential problems associated with a single initial incident of TBI but also the possibility of repeat incidents in a short time frame exacerbating morbidity. Most TBIs (75 to 85%) are classified as concussion [94].

TBI is now discussed in more detail with the following sections detailing epidemiology, aetiology, symptoms, diagnosis, treatment, and prognosis. Finally patient pathways for TBI patients are summarised at the end of this section.

2.2.3.1 Epidemiology of Traumatic Brain Injury

TBI is a common occurrence with an estimated 1.6 million incidents in the USA alone annually resulting in 50,000 deaths and 70,000 patients left with permanent neurological deficits [2]. TBI consumes about 10% the health budget in the USA [93]. The cost of TBI both directly and indirectly through lost productivity, is greater than \$60 billion per annum [93]. In the UK there is approximately one hospital admission every 3 minutes and about 445 per day due to TBI [95].

2.2.3.2 Aetiology and Pathology of Traumatic Brain Injury

A TBI is the result of any external force impacting on the head. Typical examples included road traffic accidents, impacts in sport, or after a fall [93]. In the acute phase, head trauma can result in a range of potential brain and head injuries. These injuries can include fractures, haemorrhage (including haematomas and contusions), and brain swelling which may also result in herniation of the cerebellum for example [93]. Fig. 2.13 shows the example of the classic coup contrecoup injury where the coup injury is seen under the site of impact and the contrecoup occurs on the opposite side due to inertia and rebounding of the brain [93]. These injuries may be seen together or sometimes alone [93]. For example coup is more likely if struck by a moving object and contrecoup is more likely if the head strikes a stationary object) [93].

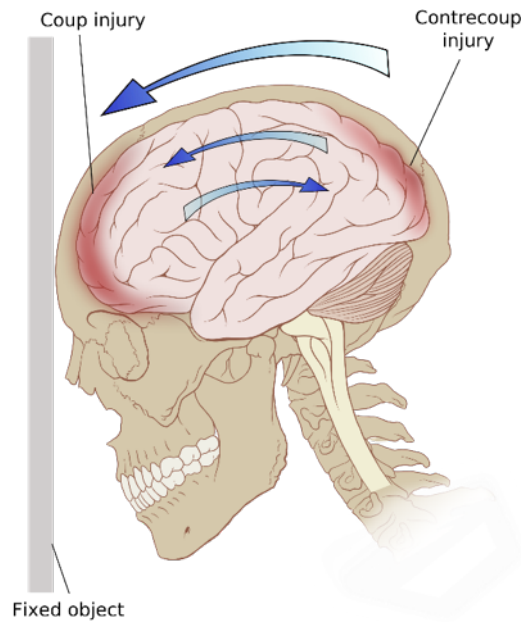


Figure 2.13: Coup contrecoup injury. The coup injury refers to the injury at the point of impact, with the contrecoup injury a result of the rebounding of the brain to the opposite side [96].

Of interest are the TBI injuries involving haemorrhage as patients with haemorrhage tend to be symptomatically worse and need more urgent care than those without [2]. For example, haemorrhage and oedema can cause mass effect, which would require urgent evacuation of the fluid. The various haemorrhages of interest are now listed and discussed:

- Contusion is where blood mixes with brain tissue with the pia intact. A contusion differs from a haematoma, which is a discrete swelling of clotted blood, and a laceration, which is a deep cut. Contusions are common occurring in 43 % of patients following blunt trauma [2]. Intracerebral haemorrhage is sometimes seen secondary to lacerations or severe contusions [93];
- Subdural Haematomas (SDHs) are bleeds beneath the dura mater often due to a vein rupture. SDHs are found in 10 to 20 % of TBI patients and have a high mortality rate of the order of 50 to 85 % [2]. SDH lesions are often found at the coup or (more frequently) contrecoup site. These crescent shape lesions do not cross the midline, usually being located hemi-spherically but may occur along the falx cerebri or tentorium cerebelli. Often they necessitate evacuation depending on thickness as seen on CT. Surgery is indicated if the thickness of the bleed is ≥ 5 mm [97];

- Epidural Haematomas are biconvex lens shaped bleeds occurring between the skull and the dura mater. Usually the location is at the coup site and not crossing cranial suture lines, occurring in about 1 to 4% of patients [2]. Surgery is indicated when the volume exceeds 30 ml [98];
- SAH is seen in about 11% of TBI patients, especially children and the elderly [2]. Unlike in stroke where ruptured aneurysms are often the cause, in TBI a SAH is usually as a result of laceration of vessels. A SAH may be benign or cause hydrocephalus if CSF flow is blocked. Grading of SAH uses metrics such as the Fisher scale, which looks at the volume of bleed on CT. A SAH of thickness ≥ 1 mm is associated with higher severity [99];
- Intraventricular Haemorrhage (IVH) is seen rarely in about 3% of TBI patients [2]. IVH usually occurs in severe injuries and has a poor prognosis [2]. Volumes ≥ 20 ml are particularly associated with poorer outcomes [100].

Also, of note is chronic or delayed haemorrhage, where a bleed can start or continue for days after the initial trauma and indeed after initial evacuation [2]. Monitoring with CT is useful in such cases as well as in cases with more obviously visible deteriorating symptoms. Hence, TBI can feature a range of important brain haemorrhage types the presence of which can affect the symptoms, treatments, and ultimately the patient outcomes.

2.2.3.3 Symptoms and Diagnosis of Traumatic Brain Injury

TBI patients may exhibit typical neurological symptoms such as loss of consciousness, focal neurological deficits, vomiting, seizure or indeed visible trauma such as skull fractures. The presence of any of these symptoms necessitate hospital referral [101].

A commonly used scoring system to assess neurological function is the Glasgow Coma Scale (GCS). This system is based on physical examination looking at eye, verbal, and motor responses to stimuli and scores the patient from 3 (deep coma or dead) to 15 (fully conscious and awake) [101]. The various potential injuries associated with TBI will cause outward physical symptoms in the patient but often imaging is needed to aid treatment decisions.

Imaging is indicated for ‘major’ injuries which are hard to define. Worsening consciousness (low GCS score), seizures, repeated vomiting, and signs of fractures are all indicative of major injuries necessitating urgent CT or MRI imaging [101]. Minor injuries often do not require CT – less than 10% of these group of injuries show findings on CT and only 1% requires neurosurgery. Better initial triage may reduce the number of CT scans required resulting in a savings to the health

system. A 10% reduction in CT to minor TBI patients could save over \$10 million annually [2].

2.2.3.4 Treatment and Prognosis of Traumatic Brain Injury

Mild TBI often does not require special treatment and the patient may be discharged after a period of observation. Major TBI patients will be treated to both initially stabilise, and then to prevent secondary injury to the brain using diuretics, anti-seizure medications and coma-inducing drugs. Surgery may be needed especially in the case of fracture, swelling, or haemorrhage. After discharge, prognosis depends on the nature and extent of the injury and the resultant (if any) neurological damage. Rehabilitation is often needed with treatments including occupational therapy, speech therapy and physiotherapy [102].

2.2.3.5 Concussion in Sports Injury

Concussion refers to mild TBI and is of particular interest in contact sports. Concussion can be considered a functional (as opposed to structural) injury with the patient regaining full consciousness within 24 hours [103]. Of course, an impact in a contact sport involving the head may not be mild and instead feature some of the more severe injuries listed in Section 2.2.3.2.

Because of the high incidence of concussion injury in sports, guidelines have been developed by respected groups (such as the American Academy of Neurology) on how to diagnose, manage and treat these incidents. Diagnosis is by physical examination with tests focussed on neurological markers like cognition and balance. Imaging has a role, contributing little to a standard concussion evaluation but of value if reserved for cases of suspected haemorrhage in more severe TBI. In fact neuroimaging may be underused in this cohort. There is growing evidence that concussion and repeat concussion can result in long-term neurologic sequelae in athletes, and there is therefore a need for better triage, including more frequent use of imaging [94].

2.2.3.6 Traumatic Brain Injury Patient Pathways

Again, NICE produce patient pathways to summarise best practice at each step along the path a TBI patient takes, summarised in Figs. 2.14, and 2.15 which provide both a general overview and pathway for brain injury investigation respectively.

The overview includes pre-hospital management and emergency room assessment. These pathways include the initiation of appropriate trauma care, assessing the

patient for neurological and other signs to grade the severity and nature of the injuries (for example using the GCS), making judgments to rule in or out head or cervical spine involvement as well as the need for neuroimaging to further guide diagnosis and treatment [101], [104].

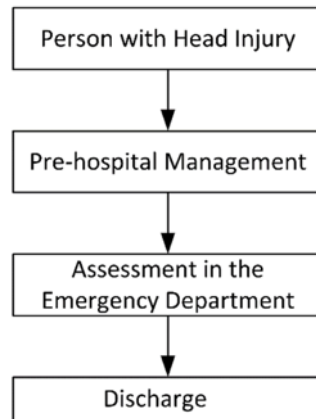


Figure 2.14: NICE Head Injury Overview (adapted from [101]).

The pathway exploring brain injury investigation in TBI starts with neuroimaging, with CT being the imaging modality of choice. Different protocols are followed depending on if the patient is an adult or child, but they have much in common. CT is indicated within one hour if the patient has a GCS score of less than 13 (less than 14 for a child) or fails to improve sufficiently within two hours. Other signs like seizure activity, fracture, vomiting indicate urgent CT is warranted in an adult. CT within eight hours may be sufficient if no indication for urgent imaging is present. In a child observation may be sufficient if the TBI is deemed not serious as assessed using metrics like the GCS. Decisions on the need for surgery and other care are influenced by the initial triage and the results of neuroimaging if performed [4].

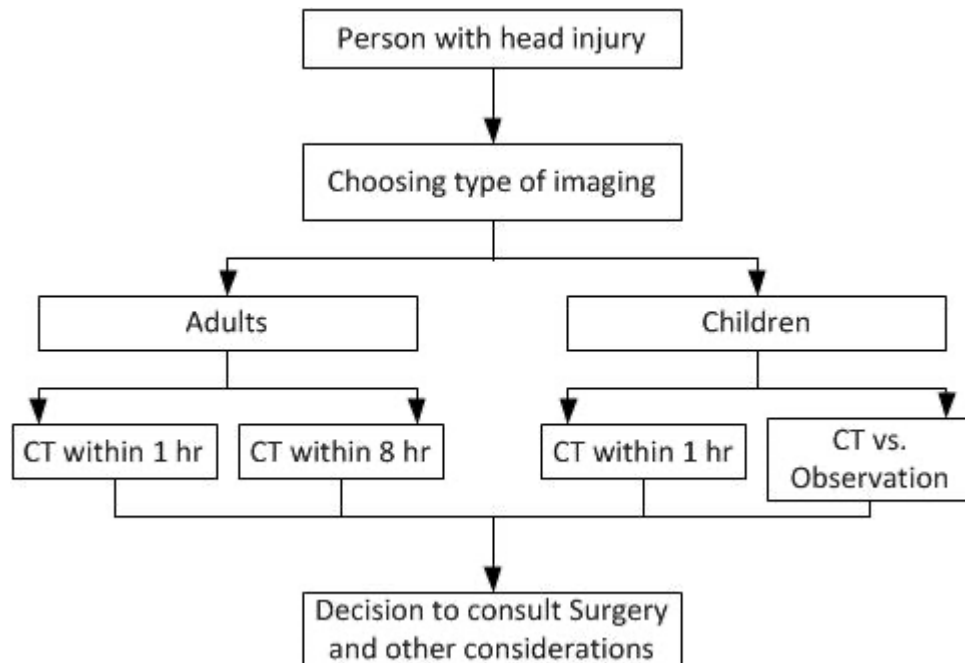


Figure 2.15: NICE Investigation for Clinically Important Brain Injuries in Patients With Head Injury (adapted from [4]).

2.3 Brain Haemorrhage and Clot Static Lesion Detector Need and Requirements

The result of employing the Biodesign needs based approach outlined at the start of this chapter was to identify the brain and in particular conditions involving static bleed and or clot lesions as an area of interest. A firm needs statement was developed capturing the clinical question:

“There is a need for an efficient, robust, cost effective, sensitive and specific device for the detection of (and differentiation between) static brain haemorrhage and ischaemic lesions”.

This statement was validated by examining diseases that have brain haemorrhage or clot as a significant part of the pathology. These diseases include stroke and TBI. The process of thoroughly analysing the diseases in terms of their pathology, patient pathway, treatments, and potential market confirmed that a brain haemorrhage and clot detector could make a major positive impact in healthcare, has definite merit and hence is a viable area to research and develop.

The question arises as to whether such a device needs to have the ability to detect ischaemia or if the ability to solely detect haemorrhagic lesions alone is sufficient. In terms of stroke (the only disease considered that has ischaemia as an aetiology) a major decision made early in the patient pathway and diagnostic workup is to classify the stroke as haemorrhagic or ischaemic [3].

As described in Section 2.2.2.7.3, and shown in Fig. 2.12, imaging needs to only detect the presence or absence of haemorrhage in a stroke patient in order for a decision on whether to initiate treatment with alteplase be made. In ischaemic stroke patients, alteplase administration is time critical. The agent must be given within 3 hours of onset in the USA [73], and 4.5 hours in UK [74] with better patient outcomes the earlier administration occurs.

If a device existed that only detected the presence or absence of haemorrhage (and not ischaemic lesions) would this single extra piece of diagnostic information be sufficient for the decision on alteplase administration be made? The NICE guidelines imply the presence or absence of haemorrhage is the key diagnostic criterion [3] (disregarding the debate about EICs as explained in Section 2.2.2.5.2) but there are other considerations. The IHF thrombolytic guidelines [86] as well as the summary of product characteristics for Actilase (alteplase) [39] list contraindications and exclusion criteria (absolute and relative) that must be checked after making an initial diagnosis of stroke but before administering the drug. Some of these contraindications include severe hypertension, thrombocytopenia, severe stroke symptoms (NIHSS ≥ 25), and history of prior stroke in the last 3 months or a history of diabetes. Importantly all of these parameters can be assessed by a thorough history taking and physical examination by a responding advanced paramedic. More difficult to assess criteria like thrombocytopenia could be assessed with a blood test completed on site also noting that these patients would usually have a history of this condition. An absolute essential feature would be the inclusion of telemedicine to allow consultation with a clinician at a hospital to have the final say on whether to proceed, with administration then potentially possible by the paramedic under the clinician's guidance.

This reduction of stroke diagnostic decision to the presence or absence of a haemorrhage assumes the initial diagnostic tests such as FAST, and ROSIER are 100% specific for stroke. As described in Section 2.2.2.4.1 this assumption is not the case. Although these initial tests are sensitive (92 to 97%), specificity is poor with values of about 40 to 45% reported [57], and some studies showing specificity as low as 15% [58]. Stroke mimics account for these false positives and include conditions

such as seizure and syncope [53]. This reality of frequent false positive diagnosis of stroke by advanced paramedics could theoretically result in patients having a negative haemorrhage test result on the device and so be assumed to be ischaemic stroke patients and given alteplase. An obvious question is to ask whether it safe for a non-haemorrhagic and non-ischaemic (and non-stroke) patient to receive a clot-busting drug. Large studies looking at the outcomes of thrombolysis in stroke mimics have shown that administration to such patients rarely causes issue and is safe - nearly all such patients had no bleeding and were discharged without complications from alteplase. A small number of deaths (two) were reported and were attributed to comorbidities including an epileptic seizure in an elderly man and a brain tumour in another [105], [106].

Hence, a device that detected haemorrhage that could be utilised by paramedics at the site of first contact with a stroke patient would allow earlier administration of the drug and remove the need to first bring the patient to a hospital for CT. Treatment could be started and then the patient brought to hospital for a more thorough work-up. As discussed there is controversy as to whether ischaemic stroke patients with significant EICs (as seen under CT) such as can be present with large involvement of the MCA territory should be given alteplase [3]. Authorities such as the AHA recommend giving the drug even if these EICs are present [65], [87]. Hence, if an early bleed detection device was available there is no doubt the result would be a higher rate of thrombolysis in ischaemic stroke patients.

Further, haemorrhagic stroke patients need medical and or surgical intervention by specialist teams and should be triaged to hospitals providing these facilities. Currently these patients are brought to the nearest hospital with CT for initial diagnosis of the underlying cause and only then can be transferred. For these patients time is also vital and early intervention reduces the chances of significant morbidity or death. Once haemorrhage is detected paramedics could transfer the patient directly to such specialised hospitals and also could start the appropriate medical treatment. This treatment includes lowering blood pressure, reversing anti-coagulants and relieving fluid.

TIA patients are routinely started on the blood thinner aspirin after an attack and may not have imaging performed for up to a week. The majority of TIAs are due to a blockage but TIA mimics like haemorrhage, although rare, should be screened for in this cohort [34], [59]. A bleed detector would fulfil this need allowing easy screening of these patients before commencing aspirin and also resulting in a more complete initial set of examinations.

An issue is that such a device would need to be as sensitive and specific CT at detecting haemorrhage, which is near to 100 % in terms of both sensitivity and specificity in the acute stage [63], [64]. Also haemorrhages are often deep within the brain and can be of volumes as low as 1 ml [47]. These bleeds would need to be robustly detectable to ensure no false negatives are declared that would result in haemorrhagic stroke patients being diagnosed incorrectly as ischaemic and being administered alteplase, which would be potentially lethal in that group. Developing a device with these levels of sensitivity and specificity to haemorrhage may be unrealistic, especially as regards challenging deep small bleeds. It may however be more reasonable to develop a device with high sensitivity to bleed but not necessarily 100 % specificity. A highly sensitive test would capture all patients with bleeds allowing immediate triage to appropriate neurosurgical units, which would be lifesaving. The imperfect specificity would mean some false positives would be present with these patients not in fact having bleeds. CT would be needed at the hospital to ultimately rule in or out bleed. While not ideal the advantage of a highly sensitive device is that theoretically there are zero false negatives and hence the catastrophic scenario of a bleed patient being administered a clot busting drug is avoided. Also, if the device returns a negative result for bleed than the user can have confidence that a this is a true negative with no bleed being present and timely treatment for clot can be commenced. Although the impact of such a device with less specificity to haemorrhage than CT would be less as one that matched the performance of CT, the device would still have sufficient merit to pursue development.

It is noted however that the current standard for neuroimaging in stroke is non-contrast CT, due the speed and availability of the modality [107]. The power of CT lies in the ability to sensitively and specifically rule in or out haemorrhage rather than an ability to robustly detect ischaemia. While a theoretical device would need to match CT in the ability to detect haemorrhage there would be additional benefit if the device could robustly detect ischaemia as this lesion type seems to be an area where innovation is also merited and maybe lacking. Indeed, bodies like the ACR recommend MRI over CT as the neuroimaging modality of choice in stroke due to the superior ability of MRI in detecting both lesion types (Section 2.2.2.4.2).

TBI often involves haemorrhage and that cohort of patients tend to have worse outcomes and have a more urgent need for intervention, especially for example in the case of SDH [97]. The pathway and work-up for TBI involves a triage process initially where a decision is made based on physical examination (using the GCS and other metrics) as to whether to use CT imaging or not and how urgently imaging is needed. Without CT (or indeed MRI) there is no way to

diagnose haemorrhage in a TBI patient [4]. A brain haemorrhage detector could be effectively employed as part of this initial triage to make more informed choices on the need for CT and other treatment decisions. In the case of concussion, and in particular in the area of sports injuries, the examination is usually made at the sports venue without the aid of a hospital and the associated facilities. Decisions are made by the attending medic on whether to allow the athlete continue, rest or indeed to be hospitalised based on in the field set of physical examinations with minimal equipment [94]. A portable brain haemorrhage detector would again facilitate better decisions by these medical personnel on the appropriate course to follow based on objective information.

In this section the clinical need has been distilled into a Biodesign needs statement. Further, the requirements that a solution to this need must meet have been discussed. In the next section further boundaries are established that the solution must also meet.

2.3.1 Brain Haemorrhage and Clot Detector Need and Design Constraints

A firm validation and justification of the need, as described, means the next steps of invention and implementation can be started. Before progressing to the next stages however constraints should be established around the potential device to focus development and establish firm boundaries. Below are the constraints developed and considered for application of a brain haemorrhage clot detection device for stroke and TBI patients, which are the two primary diseases of interest for the application. While haemorrhage detection maybe the more valuable application, there is also significant merit in clot detection. When referring to sensitivity and specificity in following sections, these terms refer to haemorrhage detection unless otherwise indicated.

- What the device needs to do:
 - The device must, with 100 % specificity and sensitivity, detect haemorrhage anywhere in the brain and at volumes down to 1 ml in suspected stroke patients as a definitive test to differentiate ischaemic from haemorrhagic stroke and hence to decide whether or not to administer alteplase;
 - If the above specification cannot be achieved then the device may have less than 100 % specificity, but retain 100 % sensitivity, in order to correctly triage the haemorrhagic patients to appropriate neurosurgical and other specialist units for appropriate care. Further, a patient returning a negative result could be confidently considered as having no bleed allowing treatment for ischaemic stroke to be commenced. Specificity

- should be however as high as possible. Ideally the device would also robustly detect static ischaemic lesions;
- In the case of TBI the device must be sensitive (and as specific as possible) to the various haemorrhages possible in TBI keeping cognisant that most TBI bleeds are towards the surface of the brain and of clinical and surgical significance at volumes usually at or above 10ml. However, the more specific the device is the higher the value as a diagnostic tool.
 - Where the device needs to operate:
 - For stroke the device would be used at the initial point of contact with the patient immediately after physical examination is completed. Hence the device would have to be present in the ambulance and be portable to allow use at the patient’s side;
 - For TBI the device needs to be both useable in the field (in the case of concussion in sport) and also in the hospital as part of the initial workup in a TBI patient.
 - How long the device has to produce a result:
 - “Time is brain” for stroke patients and the time critical urgency of initiation of treatment has been emphasised. The device must take minutes to set up, run and deliver a result;
 - Although time is not as critical in TBI, an extra test as part of an examination would usually be measured in minutes and the quicker the better.
 - Consequences of failure:
 - As a definitive test to rule in or out haemorrhage in stroke the consequences of failure are catastrophic. If the device is a sensitive but not specific test for haemorrhage, then false negatives are minimised at the expense of false positives. Patients diagnosed as haemorrhagic at the site of first contact would need CT at a hospital to confirm diagnosis. However the possibility of incorrectly diagnosing a haemorrhagic stroke patient as ischaemic and administering alteplase which would be fatal is minimised. The ability to detect ischaemia would add to the overall sensitivity and specificity of the device in the application of stroke diagnosis;
 - For TBI the device would be part of the initial patient assessment. The device is envisioned as adding information on the decision to use CT scan or not and the urgency needed. The use of the device would not be a critical test but part of the triage process but should add value and give valid, robust information.
 - Other devices and technologies needed:
 - In the case of stroke there would be a need for the device to be incorpo-

- rated with telemedicine, with relaying of the result to a clinician at the hospital. The clinician could then give the go-ahead on whether or not to start alteplase or to route the patient to an appropriate hospital;
- Telemedicine would be a useful feature to have in the TBI application but not as vital as in the case of stroke as no major clinical decision is being made solely as a result of the test.

These design constraints are summarised in Table 2.1. Once the design constraints are established, candidate solutions can be examined to see if any are capable of meeting the need within the constraints. These candidate technologies are discussed next.

Table 2.1: Summary of Brain Haemorrhage and Clot Detector Need and Design Constraints .

What?	<ul style="list-style-type: none"> • At point of first contact with the patient, usually in the field.
Where?	<ul style="list-style-type: none"> • At point of first contact with the patient, usually in the field.
When?	<ul style="list-style-type: none"> • As soon as possible after the incident.
Consequences of Failure?	<ul style="list-style-type: none"> • Haemorrhagic stroke patients incorrectly given alteplase. • TBI patients with or without haemorrhage wrongly triaged with consequent inappropriate utilisation of CT imaging.
Other Technologies Needed?	<ul style="list-style-type: none"> • Telemedicine to facilitate clinician input.

2.3.2 Brain Haemorrhage and Clot Detector Possible Solutions

The needs statement, requirements, and design constraints for any possible solution is documented in the previous section. In this section potential technologies that could offer a solution are considered. These technologies include mobile CT and emergent technologies such as microwave imaging, Electroencephalogram (EEG) based modalities, acoustic wave-based modalities, techniques involving near infra-red radiation, and EIT. These technologies are discussed in the following subsections.

2.3.2.1 Mobile Computed Tomography

Mobile Stroke Units (MSUs) are modified ambulances consisting of a mobile CT unit as well as a laboratory for blood testing, telemedical systems and specialised crew [108]. MSUs have been in use in Germany since 2003, and today are also

seen in parts of the USA particularly Cleveland, Ohio and Houston, Texas [108]. The CT units developed for use in ambulances are smaller and lighter but do have technological trade-offs notably as regards image quality, which is inferior to that from fixed units [108]. Of importance would be the possibility of missing small haemorrhages and administering tPA to such patients. The images produced however are of adequate diagnostic quality and are not statistically inferior to fixed CT for excluding haemorrhage, but potential problems included motion artefact and issues with telemedicine [108].

The primary purpose of the MSU is to reduce the time to administer alteplase in ischaemic patients. In addition, there is benefit in the care of haemorrhagic patients as initiation of medical treatment and triage to specialist neurosurgical centres are facilitated by the MSU. Exact protocols differ but in general terms on arrival at the scene the patient's history is taken and physical examination completed before blood samples are run and a CT image taken with telemedicine being used to consult with clinicians remotely. The decisions on treatment can then be made.

In an initial study in the Saarland region of Germany the primary outcome, the median time from alarm to decision on treatment, was reduced from 76 minutes to 35 minutes [108]. A later study in the more urban area of Berlin showed a reduction in the time from 77 minutes to 52 minutes with an increase of thrombolysis from 21 % in ischaemic patients to 33 % [108]. Similar impressive results were evident from a study using MSUs in Cleveland, Ohio. In a cohort of 100 patients, 99 were successfully diagnosed with the door to thrombolysis time being reduced from 58 minutes to 32 minutes [109]. Reported benefits of the MSU model to diagnosed haemorrhagic stroke patients in terms of early medical therapy and triage are also present in the literature. In [108], the MSU model reported only 11.3% of haemorrhagic stroke patients were sent to a hospital without a neurosurgical unit compared to 43% if the MSU was not used.

Although impressive, a major issue with MSUs and mobile CT as a solution is cost. The complete initial setup cost for the ambulance with mobile CT unit, laboratory, telemedicine and other equipment was approximately \$600,000 in the case of the MSU in Houston [110]. Of these costings, the mobile CT unit (CereTom®) cost \$375,000 with an additional cost of \$53,000 to customise the ambulance. Significant recurrent annual costs include maintenance and warranty for the CereTom® unit of \$30,000 and leased telemedicine equipment costs of \$24,000 [111]. Savings are possible however. Telemedicine was used exclusively to communicate with clinicians in the Ohio study. In contrast to the German study where a neurologist was in the MSU [108], [109]. The use of telemedicine reduces the onboard staffing

of the MSU with an increase in the benefit-cost ratio [108]. It is also the case that some of the costs associated with a MSU are in common with those for a conventional hospital based CT unit, and so are not additional costs *per se*.

2.3.2.2 Microwave Imaging

Microwave imaging is a technology that has been applied to biomedical diagnostic problems such as stroke with some success [21]. However, the technology is still in the research phase of development and has not achieved widespread clinical use yet [112]. Microwaves are electromagnetic radiation in the frequency range 300 MHz to 300 GHz [112]. If passed through a medium, microwaves are sensitive to changes in the electrical and magnetic properties therein such as permittivity and conductivity. If the medium is homogenous then the waves will not be deflected but if there is a material with different electrical or magnetic properties within the medium then reflection or scatter will occur. Transmitter antennae can be used to generate and send microwaves through a sample. Receiver antennae located around the sample can then detect the microwaves passing through and out along various paths that depend on the makeup of the sample. With the aid of computer processing of the signals received, quantitative and qualitative information can be derived about the sample and images developed of the internal makeup [112].

Biological tissues differ in permittivity and conductivity. These properties are also called dielectric properties, and strongly correlate to the water content of the tissue. High water content tissues like muscle and blood having a high permittivity and conductivity, while low water content tissues like bone and fat have low permittivity and conductivity. Further, these dielectric properties of a tissue will depend on frequency of the microwave radiation used and the pattern of change seen with changing frequency will again depend on the tissue type. Hence microwaves can be used to create images of the body using various techniques such as tomography and radar [112].

Microwave imaging has been applied with some success to breast cancer screening and has the advantages of being non-ionising, relatively cheap, and sensitive and specific to the abnormal tumour tissue within a breast [112]. The nature of the imaging also negates the need for compression of the breast, which is a problem in mammography [112].

There are challenges with microwave imaging. These challenges include attenuation of signal due to conductance of tissue, resolution limitations, tissue motion, and also heterogeneity of tissue. For example breast tissue is a heterogeneous mass of glandular and fat tissues. There is also a limited contrast between healthy and

pathological tissue. While the contrast between fat and a tumour in the breast may be as large as a factor of 10, the contrast between fibro-glandular tissue and tumour in that organ may only be 10 % [113].

These issues make the technology challenging with innovations needed in hardware, software algorithms, and measurement types used in order to realise the promise microwave imaging has shown for a variety of medical applications including neuroimaging. Despite these challenges, progress is being made with respect to microwave imaging applied to lesion detection within the brain.

Mohammed *et al.* developed a wideband (1 to 4 GHz) microwave system with 16 antennae to capture radar backscatter [114]. A realistic head phantom with anatomically realistic different tissue types was created and a realistic blood clot in the shape of an ellipsoid $2 \times 1 \times 0.5 \text{ cm}^3$ (approximately 4.2 ml volume) was positioned at locations near the surface of the head. The processing algorithm incorporated analysing for differences in symmetry between the two sides of the head and was able to accurately detect the simulated haemorrhage location within millimetres [114].

Mobasher *et al.* utilised a microwave system based on backscatter and a Delay and Sum (DAS) algorithm. Intracerebral haemorrhage was modelled using a head phantom with both small $1 \times 1 \times 1 \text{ cm}^3$ (approximately 4.2 ml assuming an ellipsoid) and large $2 \times 2 \times 1 \text{ cm}^3$ (approximately 17 ml if ellipsoid) bleeds. Note was made that the median volume of intracerebral haemorrhages are about 17 ml. The study found that bleeds located deeper in the brain and of smaller volume were harder to detect compared larger more superficial bleeds [115].

Persson *et al.* developed a microwave-based system that used ML in the form of a classifier to differentiate between both haemorrhagic and ischaemic strokes as well as haemorrhagic stroke and normal. The latter differentiation would be useful for some stroke mimic patients. Studies were completed both on models and in real patients with excellent sensitivity for haemorrhage reported [21]. This system was also used for subdural haematoma models, a potential outcome of TBI with a particularly guarded prognosis, with sensitivity of 100 % and specificity of 96 % reported in phantom studies [116].

These results affirm microwave imaging as a candidate technology for brain haemorrhage and clot detection.

2.3.2.3 Electroencephalogram Based Techniques

EEG is a technique involving electrodes placed on a patient's scalp in a certain configuration and the recording of the electrical activity from within brain. The electrical impulses from neuronal activity are detected as voltage fluctuations by the surface electrodes and these signals are recorded, interpreted and related to structural and functional features of the brain.

EEG can be used to assess functional conditions such as epilepsy, and is part of the diagnostic assessment for classification of the epilepsy sub-type and the associated choices for medical or surgical treatment [117], [118]. For epilepsy, the waveforms associated with different seizure types are well documented and recognised. Theoretically many other functional and indeed structural problems like the presence of a bleed or clot would result in abnormal patterns in brain activity with associated characteristic waveforms on EEG.

This potential EEG based classification of different pathology has been researched by the American company Brainscope® and has resulted in a medical device, the Ahead® 300 having obtained 510(K) status by the FDA. This device is a wearable, low-cost, non-invasive unit that uses no radiation and is available to use in the field [119]. Brainscope® have targeted their device primarily at the TBI markets in the areas of military, hospital and sports. A wearable headset with optimally positioned electrodes records EEG signals. These signals are then sent to a handheld device, which uses advanced signal processing to remove artefacts and extract information signals. Big data and ML techniques are then used to classify the signals to a particular pathology (or indeed as normal) [119].

In terms of TBI, the device has been reported to have sensitivity in the region of 96% with specificity of 78% for detecting TBI patients with structural injuries confirmed by CT, and separating them from milder TBI cases like concussion. These studies also demonstrate the ability to differentiate normal patients from concussed or serious TBI patients (sensitivity 81%, specificity 74%) [120]. The Marshall scale is a medical scale used to assess the severity of TBI based on non-contrast CT imaging and examines factors like the status of the cisterns, midline shift and the presence of haemorrhage to assess severity [121]. TBI patients with more severe injuries as measured by metrics like the Marshall scale were detected by the Brainscope® device with a sensitivity of 98% but a lower specificity of 60%, with best performance being in cases of clinically significant haematomas [122].

In terms of being able to detect any abnormality, including concussion, encephalopathy, haemorrhage, seizures or indeed stroke, and hence act as an adjunct tool to

triage patients for CT or other gold standard imaging, the device is found to be very effective with sensitivity of 96 % and specificity of 87 % [123]. As regards stroke the technology has been shown to be effective in diagnosing acute stroke but not at classifying the stroke as ischaemic or haemorrhagic and indeed showed poor specificity at classifying stroke from stroke mimics [124]. When used to detect haematomas in a study that featured a range of different bleed locations and volumes, the device showed a sensitivity of 96 % and a specificity of 44 % as compared to CT. Performance was however independent of the distance between the bleed and the electrodes, or indeed the volume of the bleed [125].

2.3.2.4 Acoustic Wave Based Techniques

A novel technology based on acoustic waves has been proposed and developed into a non-invasive medical device by the company Headsense®. Ear buds are placed into the patient's ears with a low frequency acoustic wave being generated by one ear bud, travelling through the cranium and detected by the ear bud on the far side. This wave will have been altered by passing through the cranium with subsequent signal processing and analysis revealing information on the structure of the brain. The device seems to primarily monitor Intracranial Pressure (ICP) with the company claiming to be able to accurately and continuously monitor various conditions, presumably those related to ICP changes [126], [127]. An increase in ICP is a serious medical problem associated with a range of conditions including haemorrhage but also tumours, hydrocephalus and meningitis. Precise information on the sensitivity and specificity of the technology is not as yet available.

2.3.2.5 Near Infrared

Near Infrared (IR) radiation are electromagnetic waves in the range 700 to 900 nm. These waves can penetrate the scalp, skull and into the brain to a depth of about 2.5 cm [128]. Such radiation is absorbed to differing extents by chromophores found in molecules. Oxyhaemoglobin and deoxyhaemoglobin are biomolecules found in erythrocytes (red blood cells) and contain chromophores that absorb near IR to the greatest extent of any biomolecule found within the brain's various tissues. Further, extravascular blood will absorb near IR better than intravascular blood due to more haemoglobin being present in a haematoma [128].

As such, a device that shines near IR into the brain from the scalp and monitors absorption would be a non-invasive technique to detect intracranial bleeds. Studies have shown devices based on this technology to have high sensitivity and specificity for surface bleeds such as epidural and subdural haematomas (91 % and 96 % respectively) when compared to CT [128]. For any type of intracranial

haemorrhage when compared to CT, a 70% sensitivity and 91% specificity is reported [128]. The major issue with the technology is the depth restriction [128]. Commercial devices based on near IR have been developed such as the handheld Infrascanner-2000® which is used by the American military [129]. This company targets TBI patients in hospitals, and also military in the field which is possible due to the mobility of the device. This mobility would allow application to sports injuries at pitch side and by paramedics at first contact with TBI patients [129].

2.3.2.6 Electrical Impedance Tomography

EIT uses the differing electrical impedance characteristics of different tissues as a way to generate an image. EIT has been studied for a number of different medical applications such as gastrointestinal functional monitoring, breast imaging, and with most success in lung monitoring [7]. Research has also been completed into suitability for application in brain imaging. EIT has the advantages of being cheap, hazard free, quick and with excellent temporal resolution [7].

An EIT system applies alternating current of a particular frequency to a sample with the resultant voltage across the tissue measured. Typically EIT systems operate at frequencies of the order of low Hz to about 1 MHz [7], [15]. The current is limited to 10 mA at 100 kHz with a lower maximal current allowed at lower frequencies as defined by the IEC 60601-1 standard [10], [11]. The voltage recorded will depend on the impedance of the tissue according to Ohm's law. This impedance is characteristic of the tissue and can be used for identification and imaging.

A typical EIT system will consist of electrodes around a tissue or a part of a body. The electrodes typically number between 8-64 and are arranged depending on the application with rings a popular arrangement [10].

Current is injected at a particular frequency through two of the electrodes with voltage measured at two others in the electrode array. The four electrodes involved in the injection and measurement define a 'channel'. The relative locations of the injection and measurement electrodes renders the channel most sensitive to a particular region of the sample as shown in Fig. 2.16. The makeup of the tissue in this region of sensitivity will give the entire region a particular 'bulk' impedance value, and affect the voltage recorded.

Voltage readings can then be taken in sequence for other electrode pairs in the array. Following these measurements, the current injection pair is moved and voltages recorded at different pairs again. In this manner, a complete set of channels are defined by an injection/ measurement 'protocol' with voltages recorded from each

channel resulting in a complete ‘measurement frame’.

The measurement frame can be processed and used to reconstruct an image of the internal makeup of the tissue. Different injection/ measurement protocols exist. In addition, measurement frames can be generated at a number of different current frequencies. The exact setup and protocol depend on the specific application intended.

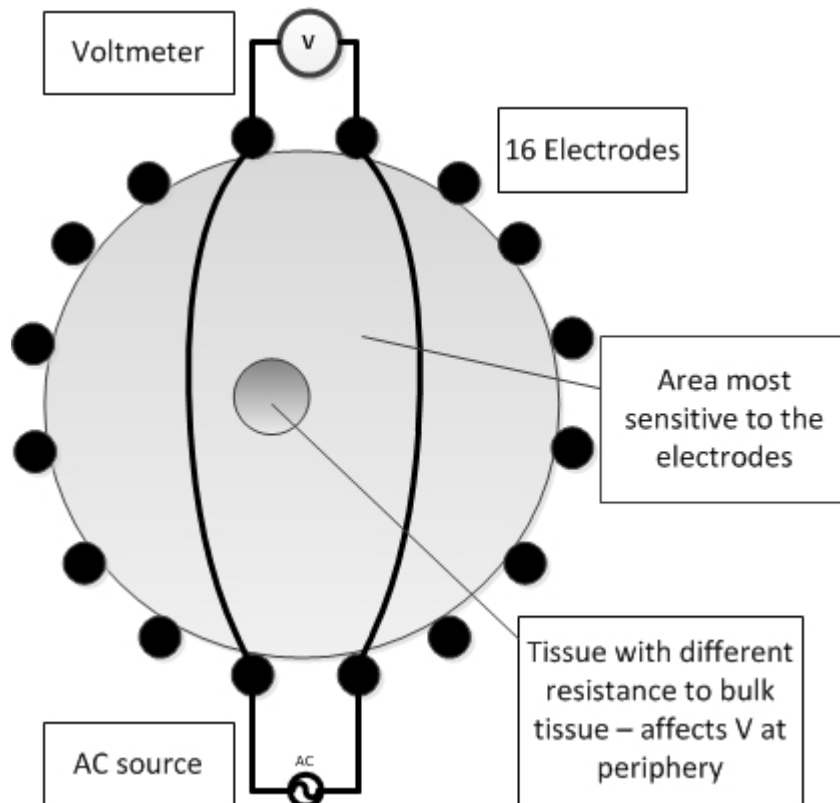


Figure 2.16: An EIT setup with electrodes arranged around a body of interest as a ring. A given channel will be most sensitive to a particular region of the body, with tissues within this region most affecting the voltage reading at the boundary (adapted from [6]).

Major modalities of EIT include aEIT, tdEIT and fdEIT:

- aEIT involves image reconstruction from a single data set, and is known to be very difficult and highly sensitive to errors;
- tdEIT involves comparing an image or data set to a baseline image or data set and detecting changes. This modality is useful for monitoring on-going changes in applications like monitoring lung function;

- fdEIT takes images or data sets at differing current frequencies. Tissues where impedance changes at different rates as the frequencies changes can be distinguished from each other using this technique [10].

Despite being researched for various medical uses, EIT has failed to gain widespread acceptance or use. EIT suffers from a number of problems [8]:

- Typically in EIT the impedance properties of the body of interest occupies a parameter space that exceeds the number of voltage measurements. Reconstruction of an image is hence mathematically an ill-posed inverse problem;
- Reconstruction is also ill-conditioned as EIT is most sensitive to events near the electrodes and not deep in the of the body of interest;
- The diffuse nature of current propagation in the body results in low sensitivity to the phenomenon of interest as typically a lesion is deep inside where little current reaches;
- EIT also has high sensitivity to phenomena not of interest such as imperfections in electrode positioning and contact, as well as to changes in blood flow and temperature in a tissue;
- Good mathematical reconstruction algorithms that focus on the object of interest and reject artefacts are challenging to create [8].

With regards to EIT specifically applied to pathology within the head a further challenge is the high resistance of the skull which severely attenuates the amount of current getting into the brain. The effect of the skull can attenuate a signal by a factor of x50–x100 [16]. Further, the low resistance CSF layer immediately inside the skull tends to shunt current away from the underlying brain proper [6]. Another inherent problem with EIT is the poor spatial resolution of the technology which is typically about 15 % of the diameter of the electrode array [6]. The circumference of a typical human head is 0.55 m giving a diameter of 0.17 m and hence an EIT resolution limit of about 2.62 cm [130]. Assuming a spherical bleed as an approximation for the typical ICH with ellipsoid topology this translates to EIT being able to detect a minimal bleed volume of 9 ml. Deep bleeds would presumably be harder to detect. Even with optimistic estimates applied to future developments in hardware and software it is unrealistic to think EIT will be able to match the resolution of CT, and be able to detect clinically significant bleeds down to 1 ml deep in the brain.

The problem is indeed challenging, but progress has and is being made in applying EIT to the detection of lesions in the brain. Boverman *et al.* tried to detect small bleeds (5 ml) both on the brain surface and deep inside in a simulation. Although the surface bleed was detectable, the deep bleed was not [131]. The

feasibility study of Horesh *et al.* for fdEIT applied to stroke detection examined the acquisition of measurement frames at a range of low frequencies and although a signal was recorded which could be used in a fdEIT algorithm, severe constraints were required on the modelling and hardware used in order to avoid excessive error levels [16].

There is work actively being completed to make EIT more useful and viable in a range of medical areas including in neuroimaging. Key areas focussed on for the development of the technology include the EIT hardware, raw measurement collection protocols, and reconstruction algorithms to analyse the data in robust ways [8].

Specifically as a haemorrhage and clot detector, EIT may have promise. Blood is more conductive than brain parenchyma and so impedance in an area of haemorrhage should be lower than the surrounding tissue. For ischaemia, impedance should increase as cells become oedematous and the amount of ECF drops leading to the possibility of the technology being used to detect ischaemic lesions. These changes relating to ischaemia would be slower to occur however after stroke and so theoretically ischaemia may not be detectable in the acute phase [132]. In both stroke and TBI the lesion is assumed to be established and in effect static in the acute stage [5]. This condition renders tdEIT redundant here, as there are no changes occurring in the brain in these conditions quickly enough to detect. fdEIT however may be of use as different tissues have different patterns of impedance change with respect to frequency of current applied. Dowrick *et al.*, using an *in vivo* rat model, demonstrated a measurable difference in healthy brain tissue and ischaemic tissue at lower frequencies (less than 500 Hz) using EIT and an even greater contrast between blood and these two tissue types. This result would support the argument that EIT may be a viable haemorrhage and clot detector technology in neuroimaging [5].

In the case of an active bleed than tdEIT may be utilised. In both [133], [134], EIT was used as a monitoring modality with an evolving brain haemorrhage with tdEIT being used. Tang *et al.* successfully used an *in vivo* neonatal pig model to detect intraventricular haemorrhage using an EEG layout based EIT to volumes of as low as 0.2 ml [133]. That study built on similar work by Sadlier *et al.* who detected intraventricular bleeds of 0.5 ml with this volume equating to about 2.5 ml in a premature baby which is the typical volume involved in a Grade 2 IVH [134]. These studies focussed on active bleeds are not directly applicable to the proposed static lesion problem but offer evidence for EIT as a technology that can detect brain haemorrhages.

2.3.2.7 Brain Haemorrhage and Clot Static Lesion Detector Possible Solutions Summary

A brain haemorrhage and clot detector that fulfils the need and design constraints described in Section 2.3 is not a trivial device to create.

MSUs perform extremely well and can provide a definitive diagnosis for stroke patients. Although MSUs could be used for TBI cases it would be an excessive use. For TBI the role of the envisioned device is as an aid in the initial assessment to decide the need and level of urgency for CT. Clearly using a mobile CT unit to make a decision on the need for CT is a null argument. The major disadvantage of mobile CT is cost. The CereTom® unit employed by the unit in Houston has a cost in the region of \$375,000 plus additional costs for areas such as ambulance modification [111]. In the future costs may come down but it is expected that the other technologies like microwave imaging or EIT would always be more competitively priced. Also in many regions of the world both CT and mobile CT will remain prohibitively expensive for the foreseeable future. The physically large size of MSU devices is also not seen with the other technologies being considered.

Research into microwave imaging seems an area with promise for the proposed application and has many similarities to EIT. Both technologies share challenges in particular with detection of crucial small deep bleeds. EIT is the older of the two technologies and so the area has less current active research than the more modern microwave imaging technology. However, there is space in EIT to pursue similar avenues of research coupled with the fact EIT has purpose built commercial systems and software which could be studied and extended making EIT perhaps a more desirable area to explore.

EEG is an underutilised modality in acute medical situations due to the relative unavailability of the technology but more importantly the need for skilled technicians and skilled clinicians to take readings and then interpret them respectively [135]. The technology developed by Brainscope® boasts impressive hardware but also the software, which incorporates signal processing and ML to allow reliable mapping of EEG waveforms to various pathologies. The Ahead® 300 device has most success when used to detect and flag the abnormal rather than give a definitive diagnosis, with good specificity of 87% when used in this manner [123]. Studies which give an indication as to the potential application of the device as a detector of more specific pathology show decreased performance results. When applied to the problem of detecting the presence or absence of bleeds excellent sensitivity but low specificity was found (Section 2.3.2.3) [125]. Possibly a two system approach where the Ahead® 300 would be utilised alongside a modal-

ity with good specificity for bleeds would be the most effective use case for the device.

Acoustic waves seem to be limited to monitoring ICP and would not be pathology specific enough for use as a bleed or clot detector. A range of conditions can elevate ICP such as haemorrhage but also meningitis and hydrocephalus. Monitoring of ICP is of value however. For example in haemorrhagic stroke patients monitoring of ICP could be used to direct pressure relieving medical treatment.

Near IR demonstrates good sensitivity and specificity when applied to surface bleeds but the limitation on penetration depth of the radiation to about 2.5 cm into the brain renders near IR less useful for deeper bleeds [128]. Of note however is that the most common and most dangerous bleeds associated with TBI are SDHs, which are located near the surface of the brain. As such near IR is a valuable technology and is, like many of those mentioned, cheap, effective and mobile.

EIT shows some promise as a basis technology in a brain haemorrhage and clot detector. The work of Dowrick *et al.* [5] demonstrates promising frequency difference trends for both bleed and ischaemic tissue with respect to brain. Hence there is the possibility of an EIT based detector being used for both lesion types and application in stroke. As regards TBI, a resolution of 9 ml (and possibly lower with better technology) would be of value in the initial triage process. The disproportionate sensitivity of EIT for phenomena near the surface may be of benefit in TBI as many TBI haemorrhages of significance occur near the surface such as SDH which can occur in 10 to 20 % of TBI cases and has a high mortality (up to 85 %) [2]. With developments possible in terms of hardware, techniques of generating raw data and reconstruction algorithms, as well as the potential to incorporate ML there is every reason to be optimistic that EIT could be an effective diagnostic tool in these conditions. As with the other technologies mentioned excluding mobile CT, EIT would be low-cost, non-invasive, portable and free from concerns related to dangerous radiation. Hence this technology shows potential as a possible solution for application in a brain haemorrhage and clot detector. Additionally, this technology remains relatively unexplored compared to the other candidates listed and as such represents a potentially exciting area of novel research.

The next section gives a more detailed analysis of EIT and highlights the state of the art in the area. Also highlighted are challenges and gaps, particularly in the application of EIT to static lesion detection in the brain. The work presented in this thesis seeks to address and improve upon some of these key challenges and gaps, as will be discussed in Section 2.5.

2.4 Overview of Electrical Impedance Tomography

EIT is an imaging modality based on the fundamental material property of electrical conductivity, and the differences in the flow of current under induced voltage through such materials [6], [7], [10]. This section extends upon the brief introduction given in Section 2.3.2.6 with the technology described in more detail, and with emphasis on application to the head and brain. Relevant areas discussed and fundamental to EIT include the concept of bioimpedance, the dielectric properties of the head, principles of EIT measurement acquisition, the mathematical basis of EIT (including the forward and inverse problems), existing software and hardware (including phantom test platforms), and existing modalities of EIT. Emphasis is placed on the description of the current state of the art and application of EIT to the detection of static haemorrhagic or ischaemic lesions in the head.

2.4.1 Bioimpedance

Biological tissues feature electrical properties which can be measured, characterised, and utilised [6]. A key electrical property is that of impedance. Impedance is an extension of the concept of electrical resistance incorporating a phase as well as a magnitude component. Bioimpedance is simply the impedance of biological tissues, and it is this property that is utilised by EIT [6].

A typical biological tissue can be modelled as a collection of cells in ECF. The significant components of the cell in this model are the membrane and the Intracellular Fluid (ICF). Both the ECF and ICF can be thought of as resistors while the membrane can be modelled as a capacitor. This model is shown in Fig. 2.17 where R_e is the resistance of the ECF, R_i is the resistance of the ICF, and C_m is the capacitance of the cellular membrane. If low frequency (f) Alternating Current (AC) is passed through such a circuit then the cell membrane does not allow the current to pass, resulting in all the current flowing through the ECF. The impedance of the system in this setup is hence effectively the impedance of the ECF. In most tissues this impedance will be high as the ECF usually makes up 20% or less of the tissue volume. At higher frequencies current can pass through both the ECF and the cell as the membrane is conductive at higher frequencies [6]. In this now parallel circuit, the overall impedance of the system will be reduced compared to the low frequency case. The flow of current in these two scenarios is shown in Fig. 2.18.

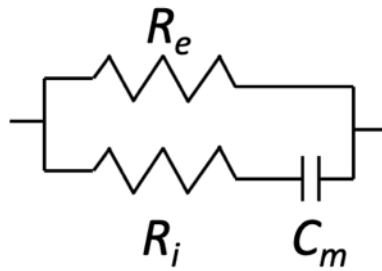


Figure 2.17: Electrical model of biological tissue for EIT. Tissue is modelled as cells in ECF. The cell is then modelled as a resistor R_i and capacitor C_m in series representing the cell membrane and ICF respectively. The surrounding ECF is represented as another resistor R_e (this figure is adapted from [6]).

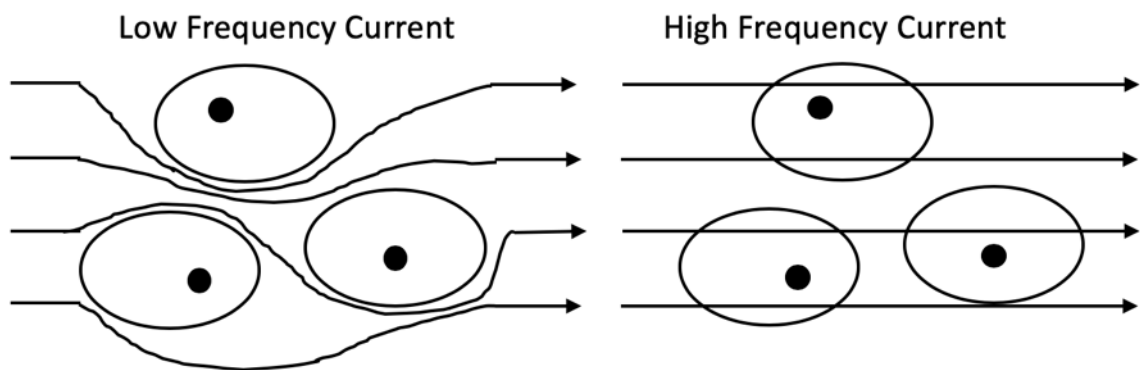


Figure 2.18: Current movement through tissue at low and high current frequencies. At low frequencies the capacitor like cell membrane prevents current flow through cells with all current forced to flow through the ECF. At higher frequencies, the impedance of the cell membrane will drop allowing current flow through cells with a consequent overall reduction in impedance of the tissue (adapted from [6]).

Bioimpedance is hence dependent on the frequency of electrical current used as well as the histology (cell makeup) of the tissue of interest [6]. Further, as described by the model shown in Fig. 2.17, impedance can be described in terms of resistance R and capacitance C . R is the ability of a tissue to oppose current flow while C measures the ability of a tissue to retain and store electrical energy [136]. The discrete impedance contributions of the individual resistors and capacitor in Fig. 2.18 can be calculated mathematically as the R and C respectively. These individual contributions (as opposed to the impedance of the entire circuit) are shown in Equations 2.1 and 2.2. R can be expressed mathematically by Ohm's law, where V is the applied voltage, I is the current and R is the resistance:

$$V = IR. \quad (2.1)$$

The contribution of C to the overall impedance can be expressed in terms of reactance X , related to C by the expression:

$$X = \frac{1}{2\pi fC}, \quad (2.2)$$

where f is the frequency of the applied current. Impedance is hence composed of R and X with the former the real part and the latter the imaginary part [6]. For EIT it is usually the real part, R , that is of interest as this part dominates at the lower frequencies typically used in EIT [10], [136]. Hence, for this thesis it is the real part that is of interest and not the imaginary part.

Furthermore, the R of a material can be generalised in terms of area (A) and length (L) of a material by the term electrical resistivity (ρ) which is given by:

$$\rho = \frac{RA}{L}. \quad (2.3)$$

In addition the electrical conductivity (σ) of a material is often used, which is the inverse of ρ :

$$\sigma = \frac{1}{\rho}. \quad (2.4)$$

It follows that electrical conductivity is a function of the f of the applied current and for precision the term ‘AC conductivity’ is occasionally used to differentiate from the DC conductivity. In this work, the term ‘conductivity’ refers to ‘AC conductivity’ unless otherwise indicated, and the two terms are used interchangeably throughout. It is also noted that the σ of a tissue (or material) also constitutes a dielectric property of that material and hence bioimpedance directly relates to dielectric properties.

Finally, while it is the real part of impedance that is of interest in this thesis it is noted that each property described has a corresponding imaginary counterpart with ‘reactivity’ corresponding to resistivity, and ‘susceptance’ corresponding to conductivity. Further, it can be shown that the other important dielectric property of relative permittivity (ϵ_r) relates to the capacitance and hence the imaginary part of the impedance of the material [10], [137], [138]. While EIT in biological systems is possible using ϵ_r signals, the small signal size relative to σ and the need to strictly minimise system errors means it is electrical conductivity that is the dielectric property generally of more interest in EIT [6]. The next section discusses the electrical conductivity properties of the tissues of the head.

2.4.2 The Electrical Conductivity of the Tissues of Interest in the Head

EIT relies on differences in the bioimpedance of tissues and hence differences in the dielectric properties of the tissues. Further, at the low frequencies of interest in EIT it is the real part of the bioimpedance that is usually of more interest as the effects of stray capacitance often renders the imaginary component inaccurate, and the imaginary component is usually much smaller compared to the real part at EIT frequencies [6]. Hence the conductivity of the tissues is the property focussed on [10], [136]–[138]. These principles apply to EIT in relation to any part of the body, with the head of interest in this thesis. The conductivity of the tissues of the head are now discussed.

In EIT applied to the head it is a common simplification to only consider those tissues above the level of theinion-nasion line [139], [140]. This simplification results in inclusion of most of the brain and surrounding tissues with the removal of structures such as the ear, eye, oral cavity and neck. While not representative of the true anatomy the removed structures are considered challenging to model, and the effect of these tissues on head EIT is questionable [139]. The tissues above the chosen line however are of fundamental importance in the application of EIT to the head in particular the scalp, skull, subarachnoid CSF, and brain layers [6], [141]. The electrodes lie on the scalp surface with current passed through this layer to the highly resistive skull, next the highly conductive (and hence shunting) layer of CSF in the subarachnoid space before reaching the brain parenchyma and then back out again to the second electrode of the injecting pair [6].

It is these tissues as well as the pathological tissues of bleed and clot that are of interest in this thesis. However, it is conceded that further simplifications are inevitable. The skull for example is often modelled as a single homogenous bone [141]–[144], when in fact the skull is comprised of a series of fused bones (as described in section 2.2.1) each with a distinct conductivity profile [145]. More intricate modelling is therefore possible taking this skull heterogeneity into account [139], [140]. There is always a trade-off as regards the degree of realism in a model which correlates to the needs of a proposed study. For example the intricate skull modelled in [140] was part of a head model that lacked an inner CSF layer before the brain, with the focus of the study being the skull. In terms of the brain this organ is in truth composed of a number of regions differing in histology and conductivity (for example grey and white matters, the CSF filled ventricles). However, it is common practice to model the brain as one uniform homogenous organ in EIT [20], [139]–[143]. Hence in this work the level of discretisation extends to that of scalp, skull, CSF, brain, bleed and clot tissues. The conductivity profile of these tissues

across the EIT band is shown in Fig. 2.19 [12], [146].

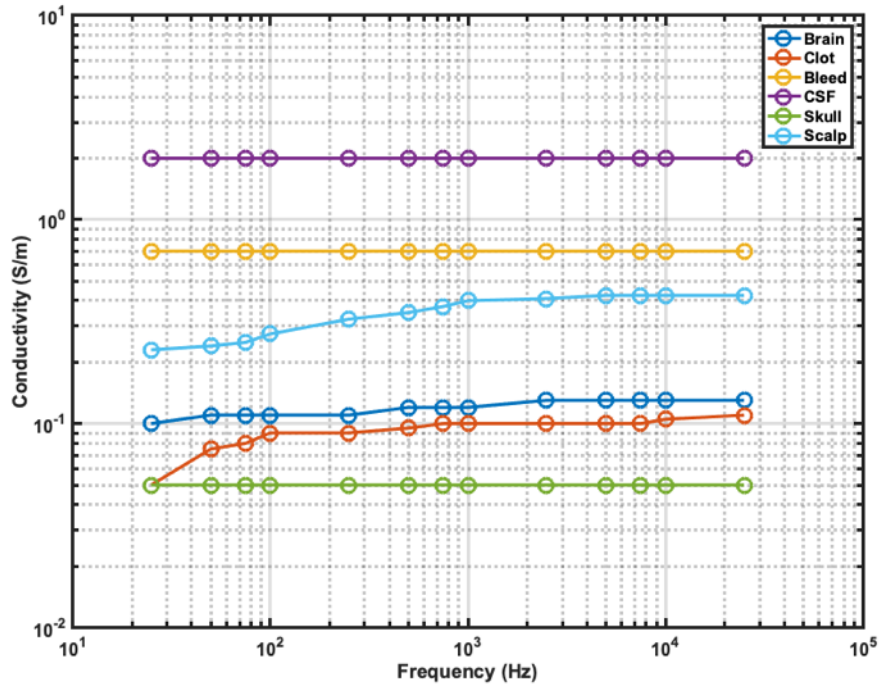


Figure 2.19: The electrical conductivity profiles of scalp, skull, CSF, brain, bleed and clot tissues across from 20 Hz to 20 kHz (data from [12], [146]).

The values presented in Fig. 2.19 are approximations and have an associated band of variance, as is the case with any quoted value of a dielectric property of a biological tissue [147]. The Foundation for Research on Information Technologies (IT'IS) database [148] provides a comprehensive collection of tissue properties including the dielectric properties which are derived largely from the studies of Gabriel *et al.* [149], [150]. The work of Gabriel *et al.* provided an extensive literature review of studies measuring the dielectric properties of a wide variety of tissues over an extensive frequency range. The study also reported new dielectric measurement data. The selected data was biased towards *in vivo* human data near body temperature. The resulting database is an invaluable resource for researchers in the field of tissue dielectrics. However the database has some limitations, for example by providing only mean values and without an indication of the range of variation that exist around those values. Variations exist in the dielectric properties of tissues due to intrinsic and extrinsic factors. For example, tissues are naturally heterogeneous [147] with a spread of values between subjects and indeed within

a given sample depending on the tissue location studied. Other intrinsic factors such as age, metabolic activity and pathology can also affect the properties [151], [152]. Extrinsically, variance is introduced both by the measurement technique, as well as the measurement error and sampling technique [147]. The result of all of these sources of variation in the dielectric data is a band of uncertainty around the reference values. Of note, a study by Gabriel *et al.* on the variation of dielectric properties due to age in rats over 30 kHz–300 MHz found a variation of about 20 % for the skull and skin and 10 % for the brain tissues [151].

With respect to the dielectric properties of tissues at frequencies under 1 MHz (the band of interest in EIT) further uncertainty is present. Most of the reference values in this band are derived from measurements of excised tissue and the overall amount of data is scarce. As a result, the database often provides a “best guess” on values [153]. However, for the reasons listed above one can assume that variance from reference values is more pronounced at lower frequencies. Indeed measurements completed on *in vivo* porcine samples at 40 Hz and 70 Hz showed significant variability in conductivity of $\pm 24\%$ for fat, $\pm 35\%$ for blood and $\pm 118\%$ for skull bone [153]. This potentially wide band of variance must be kept in mind when using any reference value for a dielectric property of a tissue.

The presence of this uncertainty and variance is further demonstrated by studying the conductivity values assigned to the tissues of the head in Section 3.3.1 where a review of head phantoms used in EIT is presented. For example the brain reported at approximately 0.1 Sm^{-1} in Fig. 2.19 [12], [146] has been modelled as 0.15 Sm^{-1} in [154], and up to 0.4 Sm^{-1} in [139].

These dielectric properties are intimately related to the concept of bioimpedance with conductivity the usual property EIT systems indirectly measure when current is passed through an electrode pair and voltage measured on other pairs during the collection of a measurement frame. In the next section the process by which these principles are used to generate an image are discussed. This discussion starts with the collection of measured voltages which collectively give a measurement frame. The collection of measurements is referred to as the data acquisition process.

2.4.3 Principles of EIT Imaging

In this section the data acquisition process involved in EIT is first outlined. After this the forward and inverse problems of EIT are discussed which form the mathematical basis of the technology. These areas collectively facilitate EIT imaging.

2.4.3.1 EIT Data Acquisition

As described in Section 2.3.2.6, EIT measurement frames are the collective term for the voltages measured from a set of channels defined according to a prescribed injection/ measurement protocol from an electrode array arranged usually externally around the body of interest [10]. These measurement frames (also simply referred to as ‘frames’ in this thesis) are the basic EIT data used in subsequent steps to derive information about the interior of the body and to reconstruct an image. The intended application will determine to an extent the choice of electrode arrangement, protocol, allowable electrical current, as well as other parameters. Each parameter choice features trade-offs as to the nature and quality of information gathered on the interior encoded in the recorded frames as briefly now discussed.

As an example, a 16-member ring arrangement around the perimeter of a body of interest is shown in Fig. 2.20. The ring arrangement is a classic EIT layout used frequently in arguably the most successful biomedical application of the technology to date, that of lung function monitoring [9], [155].

A common example of an injection/ measurement system is that of ‘pair-drive’ with current passed between one pair of electrodes and voltage measured between another pair resulting in a ‘channel’ [10]. An illustrative example of a protocol developed using a pair-drive system in a 16-electrode ring arrangement is a Skip 2 protocol with a channel shown in Fig. 2.20. In this protocol, each electrode is paired to another the skip-distance away (e.g. electrode #1 paired with #4, #2 paired with #5 and so on). For a given injecting pair, voltage is measured between every other pair. The injecting pair is then moved, and the voltage measurements taken again over the other electrode pairs and so on until every injecting pair has been iterated over. In this way, for N_e electrodes and avoiding measurements on the injecting electrodes as is conventional [156], there are

$$N_m = N_e(N_e - 3) \quad (2.5)$$

channels in a complete measurement frame (where N_m is the number of channels) [10]. Further, due to reciprocity, the number of independent measurements (N_i) is given by

$$N_i = \frac{1}{2}N_e(N_e - 1) \quad (2.6)$$

[156]. Also, in this work the term ‘sub-frame’ is used to refer to the sub-set of a measurement frame comprised of the measurements from a single (specified) injecting pair.

While the possible permutations of electrode arrangements and protocols are theoretically infinite any given selection will have trade-offs. A single ring for example offers limited information away from the plane of the ring and while multiple rings can be used this adds to the complexity for the setup [155]. Given a single electrode ring arrangement and using a skip patterns, the two extreme protocols are the ‘adjacent’ and ‘opposite’ patterns where electrodes are paired to the immediate neighbour and the neighbour furthest away respectively. The adjacent protocol results in poor sensitivity to changes in the interior while the opposite protocol has a low number of independent measures [157]. It is for this reason that many modern systems adopt an intermediate skip distance as a compromise between the two extreme cases [10]. Specifically for application to the head, protocols should aim to maximise current density in the centre of the head to obviate the shunting effects of the anatomy surrounding the brain [158]. Hence protocols that feature current injection between diametrically opposite electrodes are preferred with measurement between adjacent pairs, excluding the injecting electrodes [158]. Further, adoption of the international EEG 10-20 system for electrode placement maximises coverage of the scalp [158]. Although a given protocol is study dependent and may be restricted by factors such as the available hardware, an optimal protocol based on these principles has been proposed for head EIT by Malone *et al.*, where the distance between injecting electrode pairs is maximised while acquiring the maximal number of independent measurements [20].

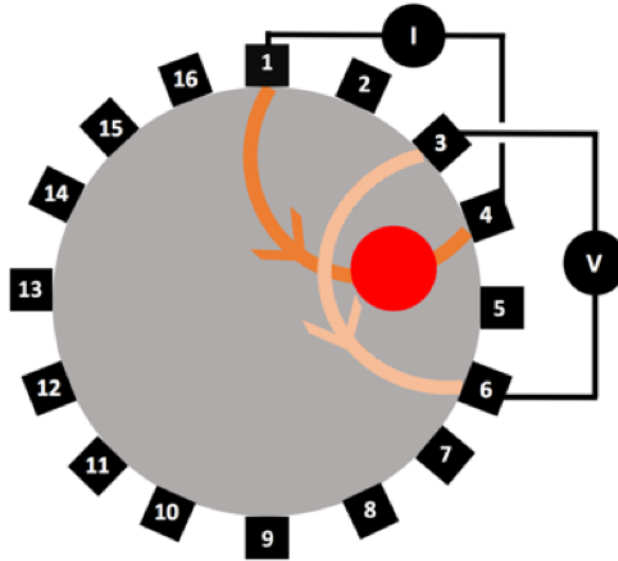


Figure 2.20: Channel from a Skip 2 protocol with current injected between electrodes #1 and #4 and voltage measured between electrodes #3 and #6. The electrodes form a 16-member ring around the body of interest with a perturbation present in the interior represented as a red circle.

The frequency of current used in EIT is typically in the kHz or lower ranges [7], [10], [13] with the current usually delivered as a sinusoid [10]. Limitations on the permissible current amplitudes at these frequencies are governed by the IEC 60601-1 standard, with a $100\ \mu\text{A}$ RMS limit on frequencies up to 1 kHz rising to a 10 mA limit for frequencies over 100 kHz [7], [11]. In order to maximise the SNR it is desirable to operate at the higher frequency of the band in order to maximise current, which may or may not be feasible depending on the application [10], [13]. These measurements are collected using physical hardware systems, or computer simulations with computer derivation of measurement frames involving solving of the forward problem of EIT. It is the forward problem that is discussed in the next section.

2.4.3.2 The Forward Problem of EIT

The forward problem refers to the prediction of the voltage distribution within the body of interest (and in particular at the electrodes) given knowledge of the conductivity of the body as well as the applied current passed through the boundary electrodes. Further, the forward problem relates to the sensitivity of the voltages to any changes in the pattern of conductivities in the body [10]. Within the body of interest there is a current density \mathbf{J} and electric field \mathbf{E} which are related by Ohm's law,

$$\mathbf{J} = \sigma \mathbf{E}, \quad (2.7)$$

where σ is the electrical conductivity of the tissue(s) in the body. The low frequencies used in EIT mean a quasi-static approximation is valid and so the magnetic field is considered negligible [10], [159], [160] with \mathbf{E} related to a voltage V according to

$$\mathbf{E} = -\nabla V. \quad (2.8)$$

The solution to the forward problem now reduces to the solving of Laplace's (Poisson's) equation:

$$\nabla \bullet \sigma \nabla V = 0. \quad (2.9)$$

Equation 2.9 can be solved analytically for simple regular geometries but for more complex geometries numerical models are needed with the Finite Element Method (FEM) commonly used [10], [136]. In a FEM model the body is divided into discrete elements, with each element assigned a conductivity. A FEM model is alternatively called a mesh. The FEM approach allows the generation of a 'sensitivity matrix' (Jacobian matrix, \mathbb{J}) to solve the forward problem (Fig. 2.21). As shown in a hypothetical channel in Fig. 2.21 for a body with 3 elements, although current flows throughout the interior, the flow is more concentrated in some elements than in others. The quantity of current flowing through a given element is a function of the conductivity of a given element, the distance from the electrodes, and the surrounding elements affecting current reaching the element. Hence, each element affects the voltage measurement of a given channel to a different extent with this effect quantified as a sensitivity or weighting. The voltage measurement of a given channel is the sum of the conductivity value of each element, with each conductivity multiplied by the sensitivity of that element for that channel (Fig. 2.21) [6].

The values of the \mathbb{J} are pre-calculated using methods including differentiation of the FEM system and adjoint-field methods, with the approaches equivalent [161]. Hence, the \mathbb{J} represents the sensitivity of a given measurement to a conductivity change in any given voxel.

Careful calculation of the \mathbb{J} is essential to ensuring an accurate solution of both the forward, and as will be shown inverse problems of EIT [10], [162]. An example of the improvements that are possible in order to ensure a precise \mathbb{J} is the refinement of element size in the vicinity of electrodes and an increase in the total number of FEM elements. In EIT, the \mathbf{E} is most concentrated in the region around the electrodes with a resultant high sensitivity in the area. Refinement of the model in these regions gives better results and can be easily achieved using the FEM [162].

In terms of total number of elements, denser meshes improve the overall quality of result but at the cost of computational expense [163], [164]. It is recommended for example that FEM nodes of $> 10^6$ elements are needed for good results when using EIT applied to stroke with the consequent need for software and hardware capable of efficient computation times with models of that size and density [164].

The voltage measurements obtained either through solving of the forward problem using a computational FEM model, or recorded on a physical phantom or animal or human, are then used to reconstruct an image of the interior of the body as a map of the internal conductivity distribution. This reconstruction refers to the inverse problem of EIT, now described in Section 2.4.3.3.

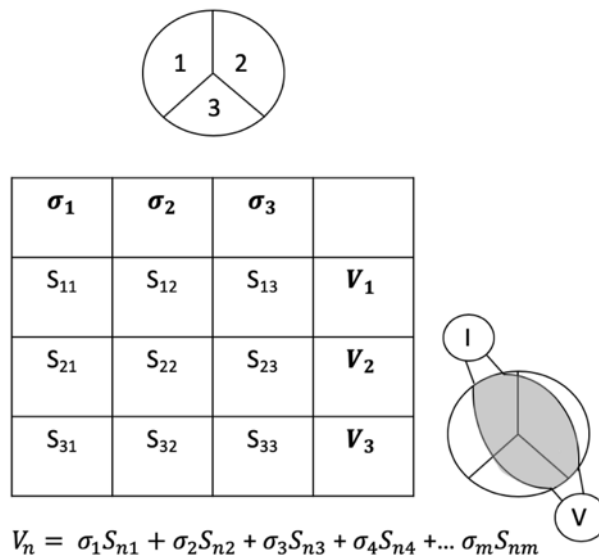


Figure 2.21: The Forward Problem explained in terms of the sensitivity (Jacobian) matrix (adapted from [6]). Each voxel in the body of interest has an assigned σ . The values of σ are known in the forward problem. The sensitivity matrix of a hypothetical simple body with three elements has three columns, with each column representing the σ of that element. For a given channel, that channel will be ‘sensitive’ to each element to a differing extent. This sensitivity is shown in grey in the sample injection/ measurement pair shown here. Hence the V for that channel will be the sum of the σ for each element multiplied by a weighting (sensitivity to) each element. It is usually the case that the number of elements far exceed the number of channels. The general equation for the voltage measurement of the n^{th} channel (V_n) in a body with m elements is shown.

2.4.3.3 The Inverse Problem of EIT

The inverse problem of EIT refers to the calculation of the conductivity distribution of the body given knowledge of the voltage measurements and the applied current. The inverse problem is also referred to as reconstruction. Theoretically this calculation can be achieved by inversion of the \mathbb{J} . In practice this inversion is not possible as the data must be infinitely accurate and the number of elements would need to equal the number of channels, neither of which is the case [6]. A problem is described as well-posed only if it meets the Hadamard criteria [165], [166]:

- A solution exists;
- The solution is unique;
- The inverse mapping is continuous.

The inverse problem of EIT is termed an ill-posed problem due to the system being under determined. The number of elements is larger than the number of channels, with the resultant absence of a unique solution [10]. Further the problem is ill-conditioned as a result of the third Hadamard criterion being violated. There is a lack of continuity in the inverse mapping with for example EIT being more sensitive to changes near the boundary as compared to in the interior. Hence a large change in the conductivity profile of the interior can result in only nominal changes in recorded measurements [10], [166].

A commonly used approach to solving the inverse problem and giving a ‘reasonable’ or ‘smooth’ result is by regularisation [10]. Regularisation refers to the stabilising of the recovery process against confounders such as modelling errors and measurement noise [6], [166]. Regularisation effectively results in pseudo-inversion of the \mathbb{J} and requires *a priori* information be combined with the measurement data. Many different regularisation techniques exist that as a fundamental requirement seek to ensure that the worst-case error in reconstruction is minimised in the asymptotic limit case of low noise levels [166]. Examples of regularisation techniques include Tikhonov regularisation and truncated Singular Value Decomposition (SVD) [6]. Tikhonov regularisation is used throughout this thesis.

A further approximation that aids the solving of the inverse problem is the use of a linear approximation. The reconstruction of the conductivity distribution inside a body from voltage measurements as well as being severely ill-posed and ill-conditioned is also non-linear [167]. A linear assumption can be made, particularly when applied to difference modalities of EIT such as tdEIT, and fdEIT. An assumed linear relationship between the conductivity of an element and effect on the V recorded and is valid for small changes in conductivity. A suggested limit of 20% between the ‘update’ and ‘reference’ scenarios is given in the literature [12],

[167].

The simplified view of the forward and inverse problems for difference modalities of EIT are given equations 2.12 and 2.13 respectively where \mathbf{y} the vector of change in voltage measurements between an ‘update’ (\mathbb{V}_u) and ‘reference’ frame (\mathbb{V}_r),

$$\mathbf{y} = \mathbb{V}_u - \mathbb{V}_r, \quad (2.10)$$

and \mathbf{x} the corresponding vector of conductivity change values for the elements comprising the geometry of the FEM model,

$$\mathbf{x} = \sigma_u - \sigma_r. \quad (2.11)$$

The Jacobian (sensitivity) matrix is represented as \mathbb{J} with the pseudo-inverse of the \mathbb{J} achieved through regularisation represented as \mathbb{J}^{-1} :

$$\mathbf{y} = \mathbb{J}\mathbf{x}, \quad (2.12)$$

$$\mathbf{x} = \mathbb{J}^{-1}\mathbf{y}. \quad (2.13)$$

The \mathbf{x} vector is then traditionally used to reconstruct an image. Each value in \mathbf{x} is mapped onto a particular element of the FEM model resulting in a map of the interior showing the change in conductivity between the update and reference. In order to avoid an ‘inverse crime’ it is standard practice to have a fine FEM model when solving the forward problem, and then using a coarse mesh to reconstruct an image onto. Hence the number of elements in the forward model is larger than the inverse model with a corresponding difference in the dimensions of \mathbb{J} and \mathbb{J}^{-1} [168], [169].

Given the challenging nature of the inverse problem it stands to reason that the steps in EIT preceding the implementation of reconstruction should be as accurate and error free as possible. This includes the acquisition of good measurement frame data necessitating the use of robust hardware, as well as the use of good software with accurate FEM models, careful \mathbb{J} calculation, and strong implementation of forward and inverse solvers. The software and hardware needed for EIT are discussed next.

2.4.4 EIT Software

Computational tools are essential for research into EIT. While hardware is clearly needed to record measurement frames in real world setups including in phantoms

and with patients, software is needed for most of the other steps and is entirely used in simulation studies. The work in this thesis leveraged the tools available from the Electrical Impedance Tomography and Diffuse Optical Tomography Reconstruction Software (EIDORS), which is commonly used by most groups working in EIT [164], [170]. EIDORS provides algorithms for solving of the forward and inverse problems as well as using other software, for example Netgen [171] and GMSH [172] for FEM model generation. EIDORS is primarily designed for use with MATLAB [173]. Despite providing an extensive range of tools EIDORS does have limitations, for example a lack of parallelisation when dealing with large and dense models which results in lengthy computation time [164].

For EIT applied to the head and the stroke problem, FEM models of the order of 10^6 elements are recommended for the forward model [174]. With models of this level of complexity comes a heavy computational overhead. For example, the most computationally expensive step is calculation of the \mathbb{J} , which for a model of 500,000 elements with 2430 measurements per frame can be shown to require 3.9 GFlops for \mathbb{J} computation (15.9 GFlops for complex value problems) [175]. The use of Graphics Processing Units (GPUs) in modern machines has helped overcome some of these computational challenges [175].

Further contributions to the range of software tools available for EIT, and in particular head EIT are being actively developed by the group in UCL which have produced fast parallel forward solvers [164] as well as FEM model generation and reconstruction tools [176].

In this thesis, EIDORS and the UCL tools were the main software used. These tools were added to and built upon primarily through MATLAB scripts. Additional software packages and tools used are noted in relevant sections. For example in the area of Computer Aided Design (CAD) of head and stroke numerical models packages such as Blender [177] and Autodesk Fusion 360 [178] were used, with dense FEM models produced using COMSOL [179].

2.4.5 EIT Hardware and Test Platforms

For the collection of EIT data in the real world good hardware is needed. An EIT system typically is made up of:

- A current source;
- A voltage measurement system;
- Switching circuitry (i.e. multiplexers) to select the injecting/ measurement electrode;

- A controller to automate the delivery of the protocol and collection of the overall measurement frame [6], [10], [15].

These components are illustrated in Fig. 2.22.

EIT is highly sensitive to any hardware imperfections. Although all components in the system should and must achieve high levels of performance, it is worth in particular emphasising the key role of the electrodes in an EIT system [8]. It is through the electrodes that current is transduced to the body of interest and voltage measured from the body. Parameters related to electrodes where EIT is highly sensitive include:

- Electrode positioning errors, including movement during a recording session;
- Electrode contact impedance errors, for example as contact gel dries out;
- The concentrating of current density in the vicinity of the electrodes;
- Poor modelling of electrodes.

Imperfections in the above listed parameters result in challenges in recovering high quality measurement frames with resulting artefacts in reconstructed images [7], [8], [162], [180]–[182].

Modalities of EIT based on differencing help to cancel out errors such as those in electrode contact impedance, electrode area, and boundary shape. However taking precautions such as a minimising contact impedance to maximise measurement sensitivity, and using accurate electrode models such as the Complete Electrode Model (CEM) help maximise the quality of results [10], [181].

A number of EIT systems have been developed for both research [14], [15], [183]–[185] and commercial [186], [187] use. The latter set of systems are largely designed for thoracic applications. Of fundamental importance to any of these systems is the ability to repeatedly produce accurate and precise measurement frames to the standard required by the specific application. Familiarity with, and characterisation of a system is essential in order to discover if the hardware is suitable and can be used effectively in a particular application. Parameters of interest in EIT hardware include knowledge of the achievable SNR, the noise floor, the reciprocity error, as well as drift characteristics and time to equilibrate following a change [188], [189]. As an example relating to SNR, applications such as thoracic imaging may be successful even with a system offering a SNR of 30 to 40 dB [14] whereas more demanding neural applications that may involve smaller changes and face issues such as the skull dampening signals require systems capable of 80 dB and higher [14]. In terms of electrode number and layout, the ring arrangement is often

used in thoracic applications. For neural applications of EIT, irregularly spaced electrodes, a greater number of electrodes (32–128), and irregular protocols are frequently seen [15], [20]. Knowledge of the parameters possible, and limits of a system allow the development of effective protocols for use with the device, and optimum application to the particular need.

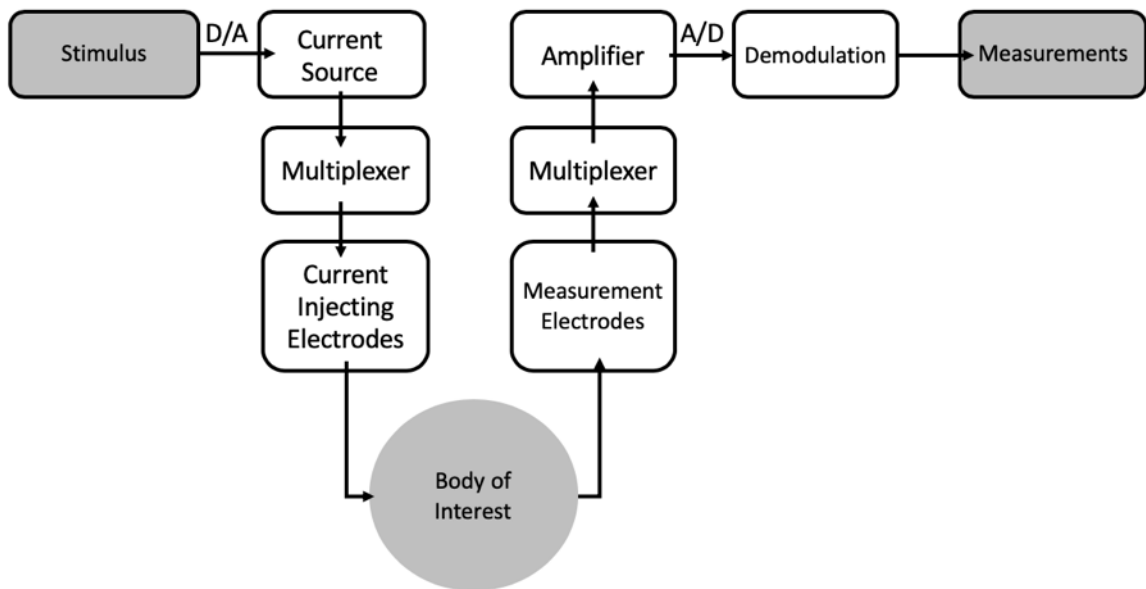


Figure 2.22: Block diagram of the essential components of an EIT system. The digital stimulus is usually a sinusoidal wave form, and is used to drive an analogue current source using a digital-to-analogue converter. Multiplexers connect to and select the current injecting electrodes which are connected to the body of interest. On the other side multiplexers also select the measurement electrodes with the analogue measurement amplified and demodulated into a (usually) digital value with the additional use of an analogue-to-digital converter. A control system (not shown) automates the injection/ measurement protocol and collection of the complete measurement frame (adapted from [6], [10]).

An important part of a real world EIT data collection setup not typically considered a piece of hardware is the ‘body of interest’ which is in fact central as shown in Fig. 2.22. In the case of this work the body of interest is the human head. Before applying the surrounding hardware to a human head a common precursor step in the development of any system is application to a physical phantom of the head. This phantom emulates the conductivity of the anatomy of interest acting as a real world ‘forward model’, and as an intermediate test platform between purely computational modelling and animal or human studies. A good phantom will

be realistic in terms of anatomy and conductivity, allow modelling of pathology. Simultaneously the phantom should not be excessively complex and hence allow incremental development of the technology. A brief comparison of these head phantoms used in EIT is given in Table 2.2. Some important points from a study of Table 2.2 include:

- There has been a gradual shift from phantoms with relatively simple geometries to those with more anatomical realism. This increased anatomical complexity has been aided by the advent of 3D printing with this technology offering the ability to produce intricate moulds and even direct printing of TMMs;
- The reported head phantoms have largely not been tested in applications involving static lesion imaging despite the presence of such lesions in many important pathologies. Most of the phantoms listed in Table 2.2 were used or validated in tdEIT including all of the phantoms modelling realistic anatomy;
- There is lack of realistic phantom lesions, with the most commonly reported being saline-based haemorrhage phantoms (with the saline added to a space) [132], [154]. There are no realistic clot phantoms reported, the nearest being non-conducting plastic cylinders [144].

Head phantoms for EIT, and the materials used to fabricate them (TMMs) are discussed in more detail in Chapter 3. This is an area of improvement focussed on in this thesis with the development of novel phantoms based on solid TMMs. The improvements offered over the current state of art include mechanical and dielectric stability, and ease of fabrication of realistic modular anatomical structures.

Table 2.2: Overview of Head Phantoms reported in the literature for Electrical Impedance Tomography (or closely related) applications (EIS: Electrical Impedance Spectroscopy, PVC: polyvinyl Chloride, ABS: Acrylonitrile Butadiene Styrene, PLA: Polylactic Acid). Arranged in chronological order of publication.

Reference	Tissues Involved	TMMs	Anatomical Structure	Lesion/ Perturbation Involved and TMM Used	Application Tested	EIT Modality Used	Other Notes
Gamba <i>et al.</i> 1999, [142]	3-Layer: Scalp, Skull, Brain.	Saline (Scalp and Brain), Plaster of Paris (Skull).	✗ Phantom was cylindrical Perspex tank as exterior, skull as interior cylinder with gaps for scalp, brain.	✗	Measurement of Current Distribution (as a precursor for use in EIT studies).	N/A	<ul style="list-style-type: none"> • Saline but also Ca/ CuSO₄ aqueous solution given as liquid TMM. • Scalp and Brain identical.
Bonmasser <i>et al.</i> 2010, [132]	1-Layer: Brain.	Agarose and Saline (various concentrations) (Brain).	✗ Anthropomorphic head model used.	✓ Haemorrhage Saline	Brain haemorrhage detection using EIS.	EIS	<ul style="list-style-type: none"> • 3D printed anthropomorphic head used as mould. • Space carved out and filled with saline to model haemorrhagic lesion.
Sperandio <i>et al.</i> 2012, [141]	4-Layer: Scalp, Skull, CSF, Brain.	Agar and Saline (various concentrations) (Scalp, Skull, CSF); Saline (Brain).	✗ Phantom was 4 hemispherical shells, one inside the other.	✗	Paper focussed on phantom development. Measurements taken to validate TMMs compared to simulation.	Not Applicable (N/A)	<ul style="list-style-type: none"> • Each layer separated by thin impermeable conductive polymer sheet. • Outer exterior of PVC.
Li <i>et al.</i> 2014, [140]	3-Layer: Scalp, Skull, Brain.	CaSO₄ aqueous solution (Scalp and Brain). Water and Dental Grade Plaster (CaSO₄) in varying ratios to adjust conductivity (Skull).	✓ Anatomically realistic skull.	Cylindrical perturbation (material not reported).	Paper focussed on phantom development. Phantom validated with cylindrical perturbation.	tdEIT	<ul style="list-style-type: none"> • 3D printed anatomically realistic moulds used to cast skull bones. • Each skull bone modelled with different conductivity. • Exterior resin tank. • Skull modelled above the inion-nasion line.
Nissinen <i>et al.</i> 2016, [144]	3-Layer: Scalp, Skull, Brain.	Saline (Scalp and Brain), Plaster of Paris (Skull).	✗ Phantom was cylindrical tank as exterior (material unknown), skull as interior cylinder with gaps for scalp, brain.	Non-conducting cylindrical perturbation (plastic).	Enhancement of the contrast of EIT brain imaging compensating for the shielding effects of the skull	aEIT	<ul style="list-style-type: none"> • Cylindrical plastic rod used as low conductivity target perturbation in brain. • Scalp and Brain identical.
Wang <i>et al.</i> 2016, [143]	3-Layer: Skull, CSF, Brain.	ABS with conductive powder (Skull); Cotton Wool and Saline (CSF). Agar and saline (Brain).	✓ Anatomically realistic skull (based on work of [140]).	✓ Haemorrhage blood	Developing ICH modelled by injection of blood into balloon over time.	tdEIT	<ul style="list-style-type: none"> • Electrodes appear to have been placed through the skull layer. • ICH modelled by injection of blood into balloon embedded in the brain layer. • Skull modelled above the inion-nasion line.
Avery <i>et al.</i> 2017, [15]	3-Layer: Scalp, Skull, Brain.	Saline (Scalp and Brain), PLA with Saline (Skull).	✓ Anatomically realistic skull	Sponge perturbation with reported 20% contrast	Paper focussed on phantom development. Phantom validated with sponge perturbation	tdEIT	<ul style="list-style-type: none"> • 3D printed anatomically realistic skull phantom. • Skull permeated with saline filled holes. • Scalp and Brain identical. • Exterior PLA tank with embedded electrodes.
Zhang <i>et al.</i> 2017, [154]	4-Layer: Scalp, Skull, CSF, Brain.	Saline (Scalp and CSF), ABS with Carbon Black (Skull and Brain).	✓ Anatomically realistic skull and brain.	✓ Haemorrhage Saline	Paper focussed on phantom development. Phantom validated with saline	tdEIT	<ul style="list-style-type: none"> • 3D printed anatomically realistic skull and brain phantoms. • Exterior ABS tank with embedded electrodes.

2.4.6 Existing Modalities of EIT

EIT as an imaging modality has found use in domains ranging from originally geophysical through to industrial, and relatively recently biomedical [7], [10], [190]. Biomedical applications can be roughly divided into anatomical or functional imaging. Differing modalities of EIT are available with a given application often best served by a particular modality. The best described modalities of EIT are aEIT, fdEIT and tdEIT [10].

aEIT seeks to reconstruct an image from a single set of measurements at a single time point [10]. As such, it is theoretically useful for anatomical imaging of static (or quasi-static) scenes. While aEIT has been successfully applied to geophysical problems, successful implementation in the biomedical space has proved more challenging [8], [190]. The relative failure of aEIT lies in the sensitivity of EIT in general to noise, modelling errors, and the inherent non-linear nature of the inverse problem [10], [191]. Recently, innovative variants of aEIT have been developed. These variants include for example the D-bar method which directly solves the non-linear problem and has shown promise to date in 2D simulation and phantom studies as well as with the application of deep neural networks [191], [192]. However, EIT is most successful especially in biomedical applications when difference imaging techniques are used. The sensitivity of EIT to errors is mitigated to an extent by the differencing of frames [10], [17], [180].

The gold standard modality of EIT is tdEIT with this modality the most used in biomedical applications [10], [17]. tdEIT is primarily of use in functional imaging such as the monitoring of pulmonary and cardiac physiology [7]. In tdEIT ‘update’ frames from different time points are differenced against a baseline frame. The use of a baseline frame cancels out many time constant errors. The major requirement for the success of tdEIT is a change in the tissues within the area of interest over time. Examples include the change in the conductivity profile of the lungs between expiration and inspiration, or of the heart from systole to diastole [10]. Hence while a valid modality in such applications with detectable changes over time, tdEIT cannot be used in static (or quasi-static) scenes as is the case in imaging the anatomy in acute stroke diagnosis due to the probable lack of a ‘normal’ baseline being available [16], [17], [20], [193].

If the tissues in the area of interest show differences in response to the electrical stimulation at different frequencies then the remaining modality of fdEIT may be used to attempt imaging of the anatomy [194]. In fdEIT, measurements are taken at two or more frequencies with differencing of the frames and reconstruction then performed. Error suppression is achieved due to the differencing, and imaging

achieved if the electrical properties of the tissues differ between the frequencies [10]. fdEIT techniques have been used to image static (or quasi-static) biomedical scenes but the technique is more challenging than the gold-standard modality of tdEIT [17]. The error suppression achieved by differencing in fdEIT is not as complete as per tdEIT due to the presence of different errors at different frequencies [12]. Simple frequency-difference methods using linear reconstruction work well in the case of homogenous frequency-independent backgrounds with a frequency-dependent perturbation [12]. Weighted frequency-difference algorithms overcome some of these limitations and are capable of anomaly detection in simple inhomogeneous backgrounds, but performance degrades with more complex backgrounds particularly when the background conductivity changes by more than 20% [12], [18]. Progress in the fdEIT domain is ongoing with for example a novel algorithm described in [17] with an increased degree of robustness, using nonlinear methods and spectral constraints to achieve image reconstruction in complex anatomical scenes. It is suggested that this algorithm based on fdEIT is the current state of the art as regards EIT applied to the stroke problem.

A comparison of EIT algorithms and modalities applied to areas of static imaging and lesion detection are shown in Table 2.3.

The information presented in Table 2.3 implies progress but as yet a relative lack of success when applying EIT to biomedical problems featuring static or quasi-static scenes. There is a paucity of options in terms of algorithms. These issues are particularly the case for static lesion detection and imaging in the brain.

Table 2.3: Overview of EIT Algorithms and Modalities reported in the literature for static lesion imaging and detection (or closely related) applications. Arranged by application, and by chronological order of publication.

Reference	Motivating Clinical Example	Algorithm	EIT Modality Used	Other Notes
Romsauerova <i>et al.</i> 2006, [195]	Stroke (Ischaemic versus Haemorrhagic)	Examined the most sensitive channels from the FEM; non-linear imaging constrained to known site of the lesion.	fdEIT	<ul style="list-style-type: none"> Data collected and analysed from human subjects with brain tumours, arteriovenous malformations, chronic stroke. All as models for ischaemic or haemorrhagic stroke. No reproducible changes between the pathologies were found.
Packham <i>et al.</i> 2012, [12]	Stroke (Ischaemic versus Haemorrhagic)	tdEIT used as gold standard with frequency difference (FD), FD adjacent (FDA), weighted FD (WFD), and weighted FDA (WFDA) linear algorithms compared.	fdEIT	<ul style="list-style-type: none"> Model used was 3D head-shaped tank with potato and carrot perturbations. Perturbation detected if frequency independent background for all. If frequency dependent background, perturbation only detected for tdEIT, WFDA, WFD (WFDA best fdEIT algorithm overall).
Malone <i>et al.</i> 2014, [17]; 2014 [20]	Stroke (Ischaemic versus Haemorrhagic)	Non-linear fraction reconstruction method using spectral constraints.	fdEIT	<ul style="list-style-type: none"> Tested feasibility using numerical model of stroke [20]. Highly sensitive to electrode positioning and shape. Spectra of tissues of interest must be sufficiently distinct. Robust to errors in contact impedance. Better performance with haemorrhage compared to ischaemia.
Cherepenin <i>et al.</i> 2001, [196]	Breast Cancer Screening	Weighted Back Projection	aEIT	<ul style="list-style-type: none"> 256 electrodes in a flat square plate pressed against the breast. Tested on $n = 21$ women with unilateral breast cancer, compared to results of mammography. Detection of tumours in $n = 18$ cases (but not-blinded, subjective image interpretation).
Choi <i>et al.</i> 2001, [197]	Breast Cancer Screening	3D reconstruction with regularised linear equation used to solve the inverse problem.	aEIT	<ul style="list-style-type: none"> Simulation study validated with phantom tank. Simple rectangular box geometry. Detection of 5 mm metal and 6 mm agar target at 15 mm depth in tank with 32 electrode system.
Murphy <i>et al.</i> 2018, [198]	Prostate Cancer Screening	Test measurement compared to reference measurement of homogeneous conductivity.	Variant of tdEIT	<ul style="list-style-type: none"> Electrodes placed on transrectal ultrasound probe and biopsy probe. Simulation and phantom studies performed. Metal and plastic perturbations detected in phantom studies.
Trepte <i>et al.</i> 2016, [199]	Quantification of Pulmonary Oedema	EIT measurements taken as thorax is rotated and fluid redistributes. These redistributions can be difference imaged.	Variant of tdEIT	<ul style="list-style-type: none"> $n = 30$ pigs used with one of no injury, injury using saline lavage, injury with oleic acid injection ($n = 10$ in each group). Correlation found between extravascular lung water as measured by post-mortem gravimetric analysis and EIT.

In this section, the technology of EIT has been introduced in detail with an emphasis on application to the detection and identification of static brain lesions. A reading of this section indicates that while EIT is a promising modality, significant challenges exist. As described in Section 1.1, the work of this thesis seeks to address some of these challenges and help move forward the translation of EIT for clinical use.

2.5 Conclusions

In this chapter, the need for a brain haemorrhage and clot detection system was presented. First in Section 2.2, the normal and then diseased brain was introduced. The anatomy and physiology of the normal brain was initially discussed. Next the epidemiology, aetiology, pathology, symptoms, diagnosis, treatment, prognosis, and finally patient pathways for the important conditions of stroke and TBI were considered. From a reading of this section, it was argued that the development of a brain haemorrhage and clot detection system would have significant merit, and a high potential for impact in the pathways and ultimately outcomes for patients with conditions such as stroke and TBI.

Next in Section 2.3, the requirements of a technology that meets the need were discussed. A number of candidate technologies are available that may translate into such a system, one of which is EIT. It is this technology of EIT that is the focus of this thesis, with the intention of moving towards successful application of EIT to this clinical need. Hence the technology of EIT was thoroughly examined in Section 2.4, and how the technology may be applied to application of brain haemorrhage and clot detection.

It can be concluded from a reading of Section 2.3 and also Section 1.1 that improvements are possible in many areas of EIT when applied to detection of static brain haemorrhage and clot lesions in the head. As described in Section 1.1 the areas of improvement focussed on in this thesis are:

- Test platform (phantom) design and better real world data acquisition;
- Novel algorithm and modality design for static lesion detection and identification.

With regards the former, development of emergent technologies such as EIT involves testing and improvement on computational models followed by the use of phantoms as an intermediary step to *in vivo* testing. In Chapter 3, the development of a novel TMM and phantom test platform for EIT is discussed which offers advantages such as tailoring of dielectric properties, modularity of anatomical areas, mechanical

and dielectric stability, and ease of fabrication. The end result is the acquisition of better, more robust and accurate EIT data.

These phantoms and the acquired data in turn facilitate the development of advances in the latter area of algorithm and modality design. The development of novel algorithms and modalities of EIT for the detection of static (or quasi-static) lesions in the brain, specifically bleeds and clots is the main area of interest in this thesis. There is a lack of algorithms available for EIT particularly when applied to static lesion imaging and detection in the brain, with the majority based on fdEIT (which has limitations as described in Section 2.4.6) as shown in Table 2.3. In this thesis novel algorithmic approaches are proposed based on the inherent symmetry of the head, and on the application of ML to measurement frames. Initially these two approaches of utilising symmetry and ML are developed independently but then integrated and applied to both simulated and human data. Such a modality or algorithm, according to the constraints described in Section 2.3.1, needs to:

- Detect the presence or absence of a lesion;
- Identify the nature of the lesion (bleed or clot) if present.

A key point is an acceptance of some of the limitations of EIT. For example, the inverse problem of EIT is ill-posed and often computationally expensive [164], [175]. Perhaps reconstruction is not necessary for lesion detection and identification, with analysis of the measurement frames sufficient. This is similar to the basis of the related technology of Electrical Impedance Spectroscopy (EIS) which involves analysis of the conductivity profile of materials from a multi-frequency sweep and which has been used in some biomedical applications, including some work related to stroke diagnosis [132], [200]–[202]. A further limitation of EIT is the inherent low resolution of the reconstructed imaging [8], [10]. An image may not in fact be needed, or perhaps a crude image or a key metric derived from the reconstruction result. For example the presence of a lesion may upset the inherent symmetry in the brain with detection of this disturbance in symmetry enough to detect and identify the lesion. The related area of microwave imaging has seen success in using the measurement data in conjunction with ML for brain bleed and clot detection [21], which may in the future be also the case for EIT. Further, Atefi *et al.* have demonstrated the possibility of using EIS data taken from across the sagittal plane of the brain with ML for classifying normal from stroke patients [203].

In Chapter 4, for the first time, EIT measurement frames without reconstruction are directly used in conjunction with ML techniques to detect brain bleeds. Chapters 5 and 6 deal with the development and evolution of a novel algorithm and modality of EIT for lesion detection and identification using the inherent symmetry

present in the brain across the sagittal plane. sdEIT is introduced in Chapter 5 which provides an initial implementation using the symmetry principle for lesion detection and identification, with Chapter 6 describing the iterative Bi-Frequency Symmetry Difference Electrical Impedance Tomography (BFSD-EIT) both in terms of implementation, proof of concept and limitations when applied to the stroke diagnostic problem. Then, Chapter 7 examines the application of a variant of the BFSD-EIT algorithm on the UCL human stroke data set [13] with the application of ML techniques. In all of these chapters, analysis of the data with derivation of novel metrics is performed alongside algorithm development. Finally, Chapter 8 concludes the dissertation and provides a discussion of future possible work on this topic. These contributions help advance the field of EIT, and in particular the application of EIT to the area of static lesion detection in the brain by addressing some challenges faced by the current state of the art in the technology.

Development of Tissue-Mimicking Materials and Phantoms

Work from this chapter featured in two peer-reviewed publications. Early work and results on tissue-mimicking material development, fabrication and characterisation was published as part of the Proceedings from the 18th International Conference on Biomedical Applications of Electrical Impedance Tomography, Thayer School of Engineering at Dartmouth, Hanover, New Hampshire, United States of America, 2017 as a conference paper entitled “A Novel Tissue-Mimicking Material for Phantom Development in Medical Applications of EIT” [204]. In addition, a journal paper which described the creation of the solid head phantom was published in the Institute of Physics publication Biomedical Physics & Engineering Express in 2017, with the work entitled “Stable tissue-mimicking materials and an anatomically realistic, adjustable head phantom for electrical impedance tomography” [205].

This chapter documents the development, fabrication, and characterisation of a set of dielectrically accurate, easy to mould, novel solid TMMs, and head and lesion phantoms based on these materials for use in EIT, as well as a description of a proof-of-concept study on the possibility of automating and improving the fabrication process using 3D-printing.

3.1 Introduction

As discussed in Chapter 2, there is a need for the development of phantoms for EIT in order to acquire better experimental data. Phantoms bridge the gap between computational models and *in vivo* platforms used to test emergent technologies. In this context, phantoms are physical objects that emulate tissues, organs and indeed the entire anatomy of interest providing a controlled environment for testing. These phantoms are constructed from TMMs.

In this chapter, solid TMMs fabricated based on polyurethane, graphite, and CB compositions are presented. These materials have been investigated previously for microwave imaging studies, particularly in the field of breast imaging [206],

[207]. However, the TMMs that are used at the higher microwave frequencies may not be directly applicable to the lower frequency EIT range. This unsurety is because the dielectric properties of the materials may not match biological tissues at these lower frequencies. Therefore, here and for the first time, the development of novel TMMs to model tissues of interest for the EIT frequency range is described.

Once these TMMs are created, they are then used to fabricate two anatomically and dielectrically accurate 2-layer head phantoms. In addition, the TMMs are used to create phantom bleed and clot lesions. Collectively these phantoms provide reconfigurable test platforms for EIT. These platforms included a simple hollow head phantom, and a solid head phantom. Both of the head phantoms enabled the addition of phantom lesions, allowing the modelling of test scenarios. Significantly, these head phantoms are reconfigurable for a wide range of distinct test scenarios. In this way, head phantoms based on these solid TMMs provide an excellent, realistic test platform for EIT applied to brain imaging. The head phantoms introduced in this chapter are used in subsequent chapters of this thesis.

The structure of this chapter is as follows: TMMs are considered in Section 3.2. The properties of an ideal TMM are discussed before reviewing existing TMMs used in EIT based on classification of TMMs by physical state. Next, the target tissues of interest are described. The ingredients and fabrication process of the novel solid TMMs are presented. Finally, validation of the TMMs by dielectric characterisation and comparison to reference values is discussed. Next in Section 3.3 head phantoms are considered. First a review of the current state-of-the-art of head phantoms in EIT is provided, before the design and fabrication of the two head phantoms based on the solid TMMs is described, along with phantom haemorrhagic and clot lesions. The TMMs and their use in head phantoms are validated through EIT measurements, with a simple tdEIT experiment using the hollow head phantom and a haemorrhagic phantom lesion. Finally, an iterative improvement of both the material and manufacturing process by developing a 3D-printable variant of the TMMs is reported in 3.4. The chapter concludes with Section 3.5, which highlights the expected advantages of using these TMMs in experimental EIT studies.

3.2 Tissue-Mimicking Material Development

This section provides a thorough discussion of the TMMs used in this thesis. The next sub-section discusses the properties of an ideal TMM, and the types of TMM used in EIT based on a classification by physical state. Next, the target tissues to be mimicked by the TMMs are discussed. Then, the ingredients and fabrication

protocol of the novel solid TMM developed in this work are documented. The effect of a novel ingredient, isopropanol, on the conductivity of the TMMs is outlined at the end of this subsection. Finally, the TMMs are characterised by profiling of the AC conductivity.

3.2.1 Ideal Tissue-Mimicking Materials and Types Used in EIT

The primary requirement of a TMM is to emulate a tissue of interest. The nature of this emulation is dependent on the needs of the study and technology of interest. As described in Section 2.4.2 while either conductivity or permittivity can be used for EIT, it is generally conductivity that the primary property of interest and is the sole property focussed on in this thesis. Hence, it is especially important that the TMMs emulate the conductivity profiles of the target tissues over a frequency band. The 1 kHz-1 MHz band is representative of the frequencies of most EIT studies [7]. The properties that an ideal TMM or phantom should possess include:

- Low-cost;
- Easy to Fabricate;
- Mechanically Stable;
- Electrically accurate and stable;
- Easy to mould and shape;
- Cover the biological range in terms of conductivity over the 1 kHz-1 MHz band;
- Match the conductivity profile of any tissue or tissue aggregate.

TMMs can further be classified based on physical state as liquid, semi-solid (e.g. gel) or solid [208]. These differing types of TMMs each have advantages and disadvantages, with no phantom fully having all the characteristics of the ideal TMM. These types of TMMs are now briefly discussed.

Liquid TMMs are usually based on aqueous solutions, often involving saline [208]. Suspensions or emulsions combining oily components are also reported in the literature [208]. Since the dielectric properties of tissues are closely related to tissue water content, liquid TMMs facilitate easy adjustment of the dielectric properties. However liquid based TMMs tend to dehydrate causing a change in dielectric properties. Liquid TMMs also need a container to hold shape. Hence, liquid based TMMs are not dielectrically or mechanically stable. Further, creating discrete layers to mimic different tissue types while preventing the mixing of layers is a challenge.

CHAPTER 3. TMM AND PHANTOM DEVELOPMENT

Gel and semi-solid TMMs based on materials such as agar seek to address the limitations of liquid TMMs. Hence, these materials are more dielectrically and mechanically stable compared to liquids, and can be used to create more realistic anatomy without the need necessarily for a containing vessel. However, semi-solid TMMs tend to still suffer from issues including dehydration over time, stability in dielectric properties, and mechanical stability [208].

Solid TMMs do not commonly include water and therefore do not dehydrate, rendering them dielectrically stable. Further, phantoms based on solid TMMs hold their shape resulting in the possibility of creating more anatomically realistic and mechanically stable phantoms. The materials and fabrication process of solid TMMs tends to be more specialised and expensive compared to other TMMs types [208]. Examples of solid TMMs used in EIT include Plaster of Paris [142], and polymers such as Polylactic Acid (PLA), Acrylonitrile Butadiene Styrene (ABS) with or without conductive fillers [139], [154] (Table 2.2, Table 3.1).

The ideal properties of a TMM [206], [209], and the classification by physical state is summarised in Table 3.1. It should be noted that a complete phantom can be composed of a variety of TMMs, of varying physical states.

Table 3.1: Ideal TMM properties versus classification by physical state. TMMs used in EIT head phantoms are listed by state. An ideal TMM would satisfy all of the criteria listed in the left-most column.

	Liquid	Semi-Solid (Gel)	Solid
Materials Used	Saline [132], [139], [141], [142], [144], [154]; Other water soluble salts (e.g. CaSO ₄ [140])	Agar; Agarose base with conductivity adjusted with saline [132], [141]	Plaster of Paris [142]; Polymers (PLA, ABS) with or without conductive fillers to adjust conductivity [139], [154]
Low Cost	✓	Intermediate	✗
Ease of Fabrication	✓	Intermediate	✗
Mechanically Stable	✗	Intermediate	✓
Dielectrically Stable	✗	Intermediate	✓
Ease of Moulding and Shaping	✓	Varies	✗
Emulation of the conductivity profile of the tissues of interest	✓	✓	✓

As can be seen from Table 3.1, existing TMMs do not meet all of the charac-

teristics of an ideal TMM. Therefore, the work in this chapter focusses on the design and development of a novel solid set of TMMs for EIT. The advantages of these solid TMMs include mechanical, anatomical, and dielectric long-term stability, making them a valuable tool for EIT researchers. Further, the developed TMMs are relatively low cost, easy to fabricate, and easy to mould and shape. The dielectric profile of the TMMs are designed to cover the conductivity profile of biological tissues at typical EIT frequencies with the 1 kHz–1 MHz range used as a band of interest in EIT [7]. In the next section, the head tissues of interest for this study that the TMMs need to emulate are discussed.

3.2.2 Tissues of Interest for Head Imaging

In this work the goal is to design TMMs that emulate the conductivity profile of several key tissues. These targets are now discussed which include tissues that bound the biological range of conductivity, and tissues of the head. As the TMMs are ultimately used to fabricate phantoms, the nature of the proposed phantoms is relevant here as these phantoms have areas that represent aggregates of head tissues. The TMMs must model these tissue aggregates.

Specifically blood and fat are targeted as representative high and low water content tissues respectively. These tissues hence represent bounds on the biological range of conductivity. The tissues of the head are also of interest in order to fabricate the two planned head phantoms. These tissues and the anatomical layout is described in Section 2.2.1. The desired solid head phantom was to be a 2-layer model with an outer layer and inner brain layer. The outer layer was modelled as a weighted aggregate of the tissues external to the brain (skin, skull, meninges and CSF), and the inner layer modelled as an aggregate of the tissues of the brain. The desired hollow head phantom was envisioned to be identical to the solid phantom but lacking the inner solid brain layer, with saline instead being used to emulate brain. The TMMs involved in each of the two layers of the head phantoms are hence composites of the multiple tissues present in each of these layers. It is hence these constituent tissues that are of interest in this study.

In terms of the outer layer, Makris *et al.* produced an MRI study demonstrating the proportions of the tissues external to the brain as 33% skin, 34% skull cortical bone, 17% skull cancellous bone, 14% meninges and 2% subarachnoid CSF [210]. These proportions were used to weight reference data for these tissues to produce an ‘Outer Hybrid’ model of the outer layer.

The inner layer model was produced from values intermediate to two independent models of the brain. The first brain model was derived from another MRI study

by Luders *et al.* which reported the dominant tissues of the brain to be 55% grey matter, 27% white matter, and 18% CSF [211]. Therefore, a brain model can be produced by combining these ratios with the discrete tissue reference data. A second brain model is provided directly from the IT'IS database which is based on the data from Gabriel *et al.* for the cerebellum [148]. The cerebellum lacks CSF and is comprised of grey matter and white matter in the ratio 84:16 [210]. As such this cerebellum model is a simplification of the brain, yet the model may be adequate depending on the nature of a given study. For the purposes of this study the reference brain model, here denoted as the 'Intermediate Brain Hybrid', is calculated as the mean of the respective values from the MRI derived brain model and the cerebellum model.

In addition, blood is used to model brain haemorrhage, and uniquely clot is also modelled using a solid TMM. The values for blood is directly available from the IT'IS database [148]. The work of Packham *et al.* [12] and Horesh *et al.* [146] describe the conductivity profile for clot and the data from these works is used in this study. The conductivity profiles of the tissues are shown in Fig. 3.6 as part of Section 3.2.4.2.

With the tissues of interest selected and the respective conductivity profiles derived from literature, the next step is the targeting of these tissues using various mixtures of TMM. First however the TMMs need to be fabricated. The materials in the TMM and fabrication process is next presented.

3.2.3 Tissue-Mimicking Materials Design and Fabrication

In this subsection, the materials used in the proposed solid TMMs are described. This description includes the proportions used in order to produce an initial thirteen member test set of candidate TMM mixtures, and the method of manufacture. A risk assessment was performed before working with the materials involved in the TMMs with this risk assessment kept in the laboratory.

The presented solid TMMs are a mixture of polyurethane, graphite and CB composites varying in proportions of ingredients. As described in [206], [207] polyurethane provides a mechanically strong and flexible base matrix. Graphite and CB in varying proportions can next be used to adjust the dielectric properties of the material, and to emulate those of biological tissues [206], [207]. Both graphite and CB act to increase conductivity. The safety data sheets were studied before work with these materials commenced and informed the risk assessment, with these safety statements available from the suppliers [212]–[214]. In this study, a variety of these mixtures were developed and then tested in the EIT range of 1 kHz–1 MHz.

CHAPTER 3. TMM AND PHANTOM DEVELOPMENT

Polyurethane (VytaFlex 20) provided a stable and flexible base matrix into which graphite (Graphite powder, general purpose grade) and CB (Carbon Black, acetylene 50% compressed, 99.9%+) were added. The conductivity profile of the mixture is altered depending on the proportions of each ingredient used. These three component chemicals are shown in Fig. 3.1.

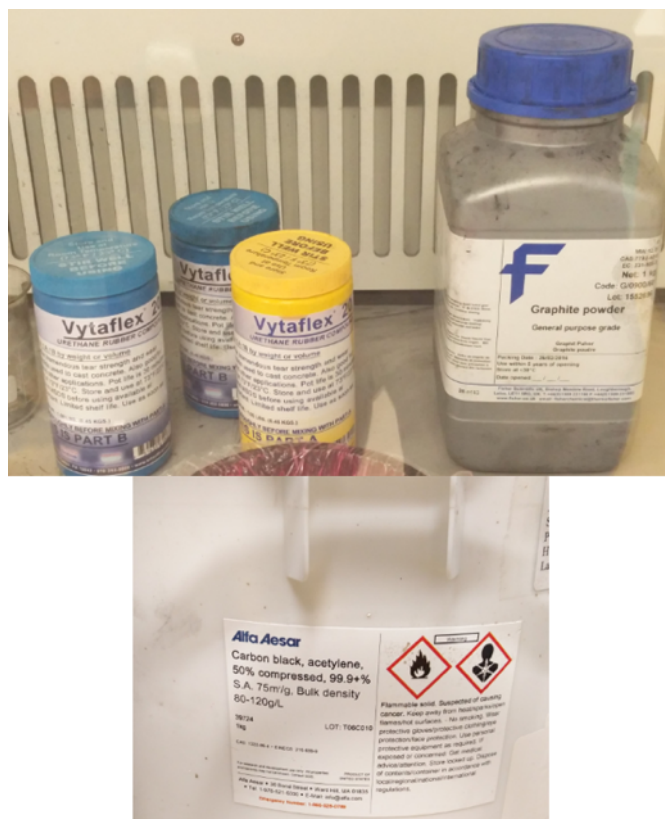


Figure 3.1: Three core component chemicals were used in the TMMs. Polyurethane (VytaFlex 20 from Smooth-On, Easton, PA, USA) (top left) was used as the mechanically stable base matrix into which two conductive fillers were added. These fillers were graphite (Graphite powder general purpose grade from Fisher Scientific, Loughborough, Leics, UK) (top right) and CB (Carbon Black, acetylene 50% compressed, 99.9% + from Alfa-Aesar Ward Hill, MA, USA) (bottom).

In total, a set of thirteen mixtures were prepared. Over all of the mixtures, the graphite used was in the range of 7.5 to 45% mass percentage (w/w) and CB used was in the range 3 to 7% w/w.

It was found that tissues of a relatively high conductivity such as blood, could not be accurately emulated using only these components. Even with the higher

CHAPTER 3. TMM AND PHANTOM DEVELOPMENT

percentages of graphite and CB the conductivity profile of blood was not matched. Further, it was not possible to exceed the mass percentages of these conductive fillers beyond the limits used as mixing became difficult and full incorporation of the filler into the matrix not achievable. For the targeting of these high water content tissues higher amounts of graphite and CB were used, with the addition of 1 ml of acetone for every 100 g mixture. Acetone acted as a thinning agent and also was found to boost conductivity. The fabrication protocol for the TMMs is now described, with a summarised version depicted in Fig. 3.2.

To create the TMMs, two liquid polyurethane precursors (which comprise the Vytaflex 20 product) are weighed and mixed thoroughly. Combining these materials begins the polymerisation process, ultimately setting fully and curing over the course of 12 to 16 hours. These two precursors are mixed in a 1:1 ratio by mass. The mixing is done manually using a glass pestle and mortar. In a separate vessel the graphite and CB are measured before being mixed together thoroughly. This thorough mixing ensures that these two powder components are homogeneously blended. Next, this powder blend is gradually added to the polyurethane in the mortar and blended thoroughly with the pestle before more powder is added. Homogeneity is assessed visually at this stage.

For mixtures with high powder content, additional ingredients were added to ensure mixability and to achieve the desired electrical properties. As described, small volumes of acetone were added to thin mixtures seeking to replicate high water content tissues. These tissues required higher percentages of graphite and/or CB to be used. This addition of acetone also results in an increase in conductivity, an effect also seen in [215] which used mixtures using similar ingredients for application in the microwave band. In this work, small volumes of isopropanol were uniquely used to achieve the same result but giving a more exaggerated increase in conductivity compared to acetone. This increase in conductivity is postulated to be a result of enhanced dispersion of graphite and CB in isopropanol. Alcohols are known to prevent agglomeration of these materials resulting in more conducting pathways [216].

Once all the ingredients are thoroughly mixed together, each TMM is cast into shape using a mould and let set overnight. It was found that higher powder content samples were progressively more difficult to shape: a lower percentage of graphite and CB mixtures could be poured into a mould, while higher percentage mixtures needed to be pressed and kneaded. For the initial thirteen samples, rectangular cuboids of $50 \times 20 \times 20 \text{ mm}^3$ were made from the mixtures using a mould (Fig. 3.3). These cuboid samples were later cut to produce multiple specimens of a given

sample and then the conductivity was measured across the 1 kHz–1 MHz band using complex impedance spectroscopy.

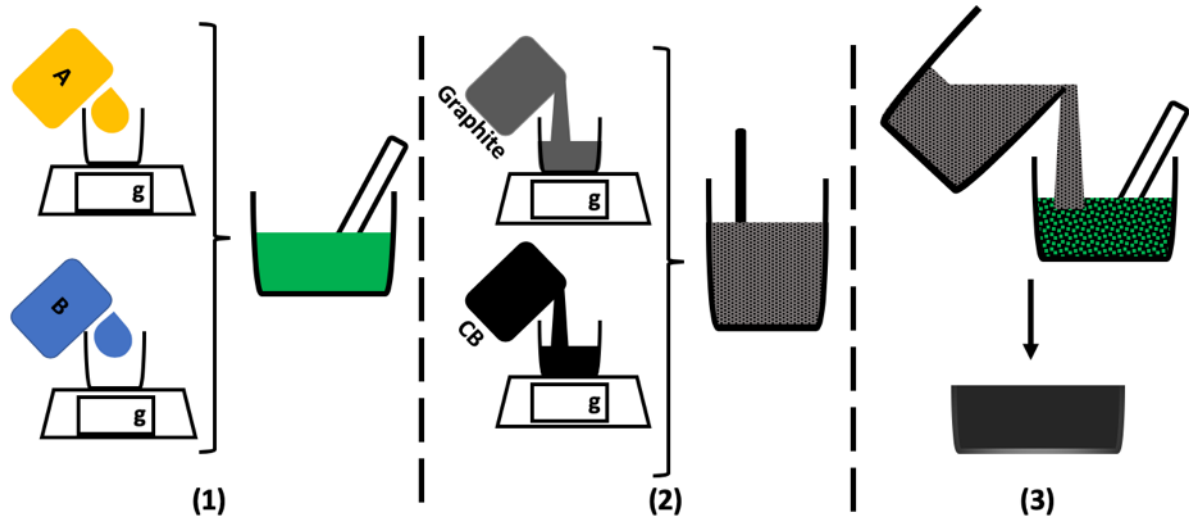


Figure 3.2: Summarisation of the TMM fabrication process. In (1), the two liquid polyurethane precursors ('A' and 'B') are weighed out 1:1 by mass, and homogenously mixed. This mixing begins the polymerisation process which takes 12 to 16 hours to complete. In (2), the conductive fillers of graphite and CB are weighed out before being homogenously mixed. Finally in (3), the graphite/ CB mix is added to the polyurethane steadily with thorough mixing again to achieve homogeneity until all is added. The final mixture is worked into the final desired shape here shown added to a mould, and allowed set overnight. For TMMs with a high percentage of conductive filler, acetone or isopropanol is added to aid mixing as well as boosting conductivity.



Figure 3.3: Rectangular cuboid samples of the TMMs made from polyurethane, graphite, and CB.

This section has described the materials used in the TMMs and the fabrication process. Once fabricated, the conductivity profiles of the members of the test set needed to be characterised. The method for this characterisation is presented next. First however, the effect of isopropanol as a novel ingredient is briefly considered.

3.2.3.1 Isopropanol as a Novel Ingredient to Fabricate High Conductivity Tissue Mimicking Materials

As discussed in Section 3.2.3, acetone is needed to aid mixing when using higher concentrations of graphite and CB. In [215], acetone was also found to increase the conductivity of the mixtures as well as acting as a mixing aid.

The effect of a novel ingredient on the conductivity of the TMMs is outlined in this subsection. The addition of isopropanol to a base TMM mixture was found to significantly increase the conductivity beyond that achieved with acetone. This effect may be of use depending on the target value.

In this study for the first time isopropanol was also examined in place of acetone at the same mixing ratio of 1 ml per 100 g mixture. Using isopropanol resulted in mixtures that were more friable than those that contained acetone or no mixing aid. Significantly however the use of isopropanol was found give a marked increase in conductivity for any given TMM. In the case of the targeted tissues of the head, no TMM with isopropanol was needed. However, the increase in conductivity may be required to emulate some unusually highly conductive biological materials, for

example CSF and urine.

The conductivity profiles of CSF and urine are plotted in Fig. 3.4, with blood and fat also shown for reference. Also plotted in Fig. 3.4 are the profiles of a blood TMM and a fat TMM, both with and without isopropanol. The fat TMM was one of two fabricated with the one shown here referred to as fat TMM 2. These blood and fat TMMs are discussed separately in Section 3.2.4.2. It is clearly seen the isopropanol gives a large increase in conductivity compared to the equivalent TMM without isopropanol. The precise increase in conductivity is frequency dependent. For example at 50 kHz the conductivity of blood TMM increases in by 60% with the addition of isopropanol compared to without. These increases in conductivity allows the conductivity of CSF and urine to be successfully emulated. Although these high conductivity tissues were not a focus for this study, this result proves the versatility of these TMMs in reaching extremely high conductivities. Future work is needed to optimise the amount of isopropanol that can be added to each TMM in order to achieve higher conductivity values without compromising the mechanical stability of the material. This increase in conductivity compared to acetone is postulated to be a result of the dispersion effect of the alcohol on graphite and CB, resulting in more conducting pathways in the material [216]. The enhanced effect on the fat TMM compared to the blood TMM is postulated to be a result of the ease of mixing of the isopropanol through the fat TMM with less solid material used in the former.

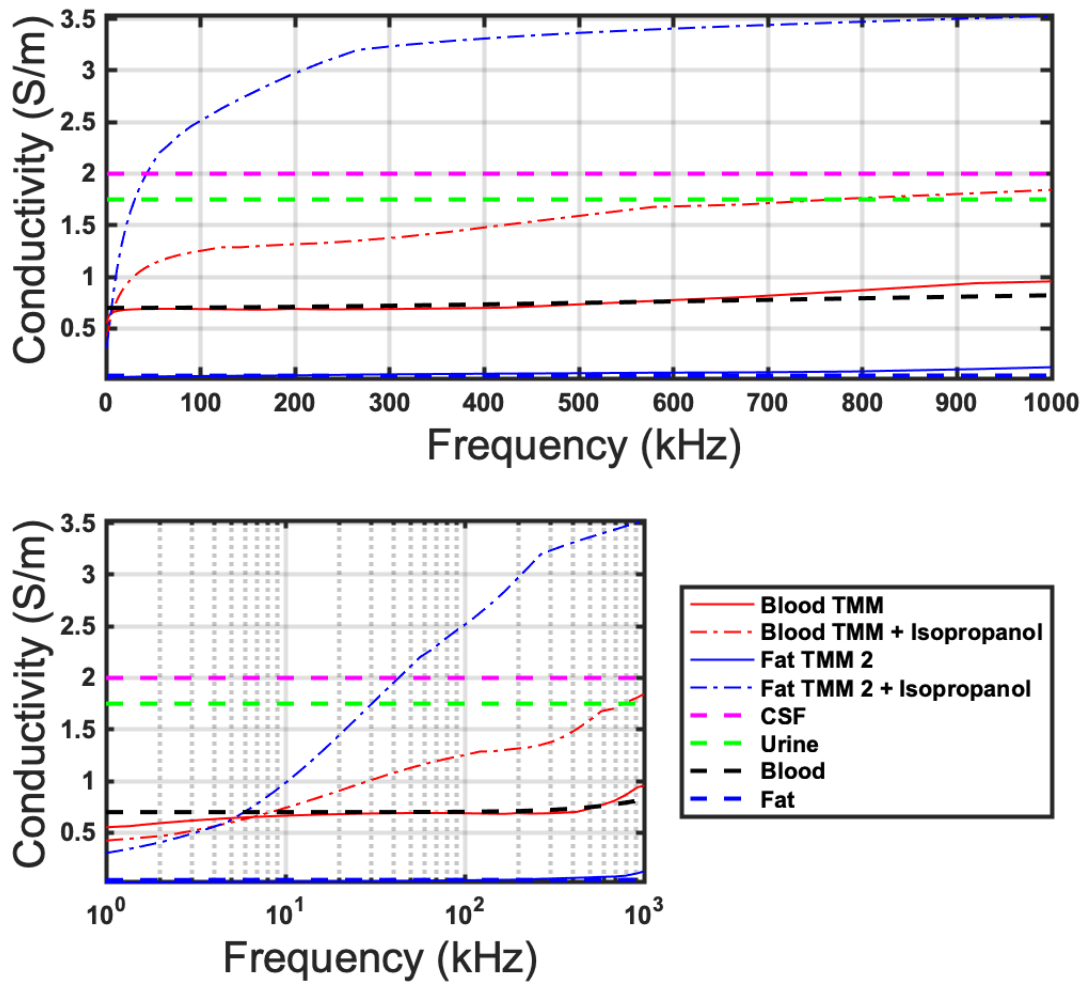


Figure 3.4: AC Conductivity curves over the 1 kHz–1 MHz band are plotted, demonstrating the effect of isopropanol when added to two of the TMM mixtures: the Blood TMM and the Fat TMM 2. In both cases, the conductivity is dramatically increased when isopropanol is added to the TMM compared to when not. The greatest increase is for the fat mimicking TMM. The reference tissue profiles shown are those of highly conductive biological tissues for which these isopropanol containing mixtures may be useful: CSF and urine (with blood and fat also shown) [148]. The values are plotted on (top) linear frequency scale and (bottom) logarithmic frequency scale. The two different scales are used for clarity.

3.2.4 Tissue Mimicking Material Validation by Conductivity Measurement

In this subsection validation of the TMMs for use in EIT is performed by profiling of the conductivity over the 1 kHz-1 MHz band using complex impedance spectroscopy. These conductivity profiles are then compared to reference values for the tissues of interest.

3.2.4.1 Complex Impedance Spectroscopy to Measure Conductivity

Complex impedance spectroscopy is an established technique for the dielectric characterisation of materials [217]–[220]. As such the technique was used to characterise the conductivity profiles of the TMM mixture test set over the 1 kHz–1 MHz band. Only the conductivity was profiled, not the permittivity. The technical details now described.

Complex impedance spectroscopy of the TMMs was performed using a PARSTAT 2273 Advanced Electrochemical System in a three-electrode cell arrangement in a 0.1 M KCl aqueous solution. An Ag /AgCl (3 M KCl) electrode and a platinum wire were used as the reference and counter electrodes, respectively. The PARSTAT 2273 potentiostat is designed to operate within the 10 μ Hz-1 MHz range with errors in impedance modulus measurement occurring beyond a 1 % level at higher frequencies, and at impedances that are at the lower or higher end of the operating range. For example at 100 kHz, Z of the order of $\leq 1 \Omega$ or $\geq 1 \times 10^8 \Omega$ are beyond the range of optimal measurement accuracy [221]. The impedance measurements were completed over a frequency range of 1 kHz–1 MHz, with an AC voltage amplitude of 40 mV. The impedance profiles were then used to calculate the AC conductivity of TMMs according to the relation [218], [219]:

$$\sigma = \frac{t}{ZA}, \quad (3.1)$$

where t is the thickness of the specimen (between 5×10^{-3} m and 1×10^{-2} m in the samples used), A is the area of the cross section (0.283×10^{-4} m²) and Z is the impedance modulus (Ω).

In Fig. 3.5, a TMM sample is shown attached to the electrodes which in turn connect to the PARSTAT 2273 potentiostat (not shown).

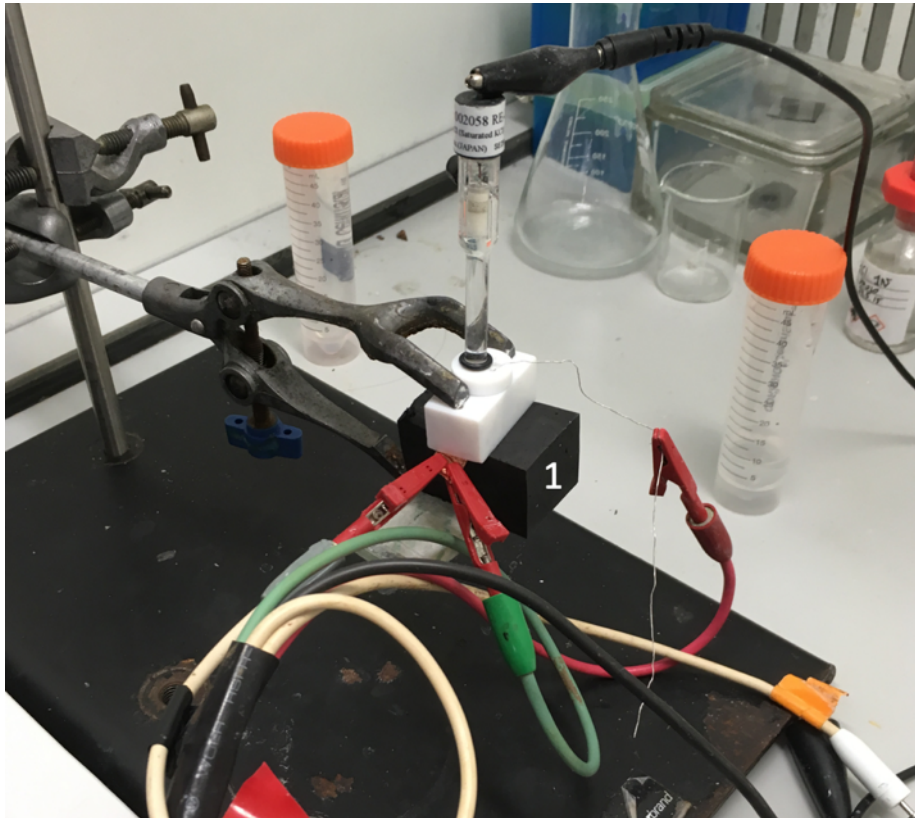


Figure 3.5: Complex impedance spectroscopy of a TMM sample (labelled as (1)) using a three-electrode setup. The electrodes (crocodile clips) connect to the PARSTAT 2273 potentiostat (not shown).

The conductivity profiles of the candidate mixtures once characterised were compared to the conductivity profiles of the target tissues. These tissues of interest are discussed next.

3.2.4.2 Selected Tissue Mimicking Material Conductivity Profiles and Comparison to Reference Values

In this subsection the developed TMMs mixtures that best emulate the target tissues are discussed. As the emulation of AC conductivity between the TMM and the tissues of interest is of primary interest in EIT, this property is focussed on and quantified.

From the initial thirteen-member test set fabricated, five mixtures were selected as best matching the target tissues. The AC conductivity profiles of these five selected TMM mixtures are shown in Fig. 3.6 across the 1 kHz–1 MHz band. The

CHAPTER 3. TMM AND PHANTOM DEVELOPMENT

profiles are shown in both logarithmic and linear frequency scales for clarity. The AC conductivity profiles of the target tissues are also shown in Fig. 3.6. These target tissues are blood, fat, Outer Hybrid, Intermediate Brain Hybrid, and clot. The reference values of the conductivity profiles of these target tissues are obtained as described in Section 3.2.2. As discussed in Section 2.4.2, these reference values are presented as a single trace but in actuality there is variance and uncertainty due to a range of intrinsic and extrinsic factors, and particular uncertainty at the frequencies of interest in EIT [153]. However, this variance and uncertainty exists with any reference for the dielectric properties of biological tissues. The values used are largely derived from the widely used IT'IS database [148].

It is seen that the biological range of conductivity from fat to blood is covered by the profiles of the two fat mimicking TMM mixtures, and the blood mimicking TMM. Further, these TMMs are found to be successfully able to target discrete conductivity profiles, including the Intermediate Brain Hybrid as a model of the brain and the Outer Hybrid as a model of tissues external to the brain. Table 3.2 describes the ingredients used to fabricate the selected TMM mixtures. In the table, there are two fat mimicking TMM mixtures documented. These two different mixtures are found to each be a better match to the fat reference profile depending on the points selected across the 1 kHz–1 MHz band. It is also noted from Fig. 3.6 that the profiles of Outer Hybrid and clot are remarkably similar. It was found that the average difference in between the two profiles is 0.025 Sm^{-1} across the 1 kHz–1 MHz band. As such, one TMM was used to simultaneously emulate both the Outer Hybrid and clot tissues.

Table 3.2: Concentrations (as % w/w) of ingredients used in the final mixtures of each TMM. Acetone if added is as 1 ml in addition to each 100 g of mixture.

Target Tissue	Graphite	CB	Polyurethane	Acetone
Blood	45	4	To 100 %	Yes
Brain	42.5	4	To 100 %	Yes
Outer/ Clot	42.5	3.5	To 100 %	Yes
Fat(1)	35	5	To 100 %	No
Fat(2)	30	5.7	To 100 %	No

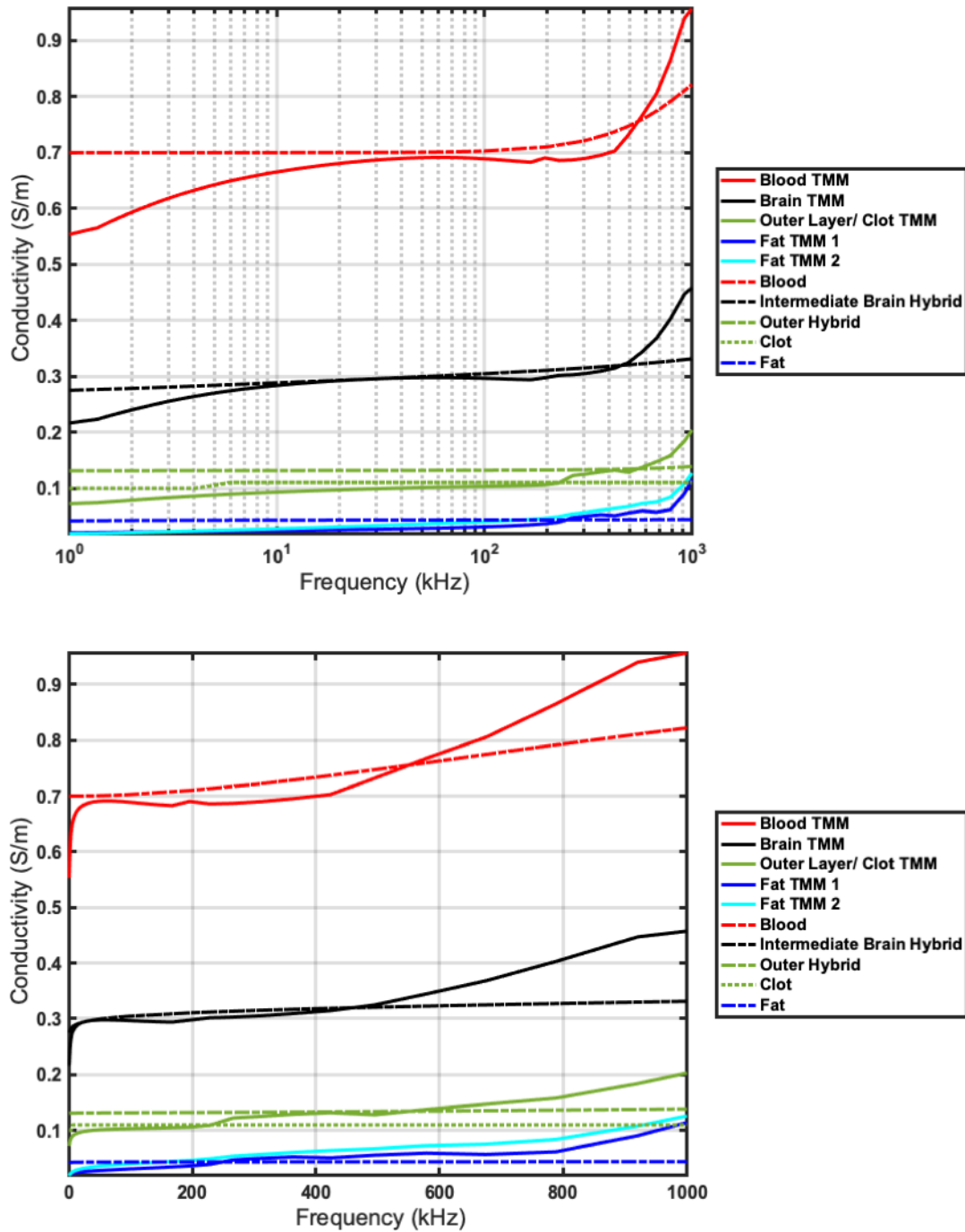


Figure 3.6: AC conductivity curves for the reference tissues of blood, Intermediate Brain Hybrid, Outer Hybrid, clot, fat [12], [146], [148], and the selected TMM mixtures that most closely emulate these target tissues across the 1 kHz–1 MHz frequency band. The values are plotted on (top) logarithmic frequency scale and (bottom) linear frequency scale. The two different scales are used for clarity.

CHAPTER 3. TMM AND PHANTOM DEVELOPMENT

EIT often does not use broadband measurements. Instead discrete frequencies are frequently used with 50 kHz being a common point [6]. In tdEIT, for example update measurement frames are compared to a baseline measurement frame but typically all frames are taken at a single frequency value [6]. In fdEIT, measurements are taken at different frequencies but each frame is usually recorded at a discrete frequency point [6]. Hence, for a given experiment if the frequency or frequencies of interest are known then a TMM set could be designed to target the reference tissue values specifically for that frequency or discrete set of frequencies as opposed to a general matching over a broadband. In this way, a more specialised, and more accurate phantom can be developed.

In this study, the aim was to create TMM mixtures that would emulate the reference values over the full range from 1 kHz–1 MHz. However it is of interest to focus on the range covered by a commercial EIT research device. The Swisstom EIT-Pioneer is such a device, and covers the range 50 kHz–250 kHz [187]. As the Swisstom EIT-Pioneer was used in all the phantom experiments documented in this thesis, the AC conductivity profiles of the selected mixtures and the respective reference values in this range were important. These profiles are shown in Fig. 3.7.

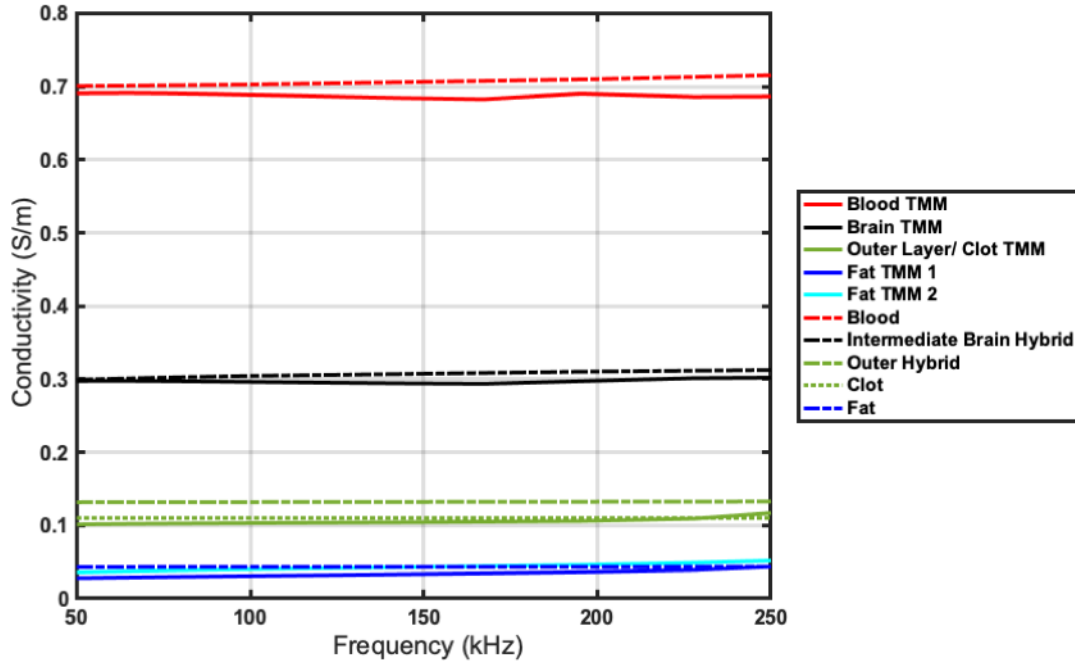


Figure 3.7: AC conductivity curves for the reference tissues of blood, Intermediate Brain Hybrid, Outer Hybrid, clot, fat [12], [146], [148], and the selected TMM mixtures that most closely emulate these target tissues across the 50 kHz–250 kHz band. This band of 50 kHz–250 kHz is covered by a commercially available EIT research device, the Swisstom EIT-Pioneer [187].

The degree to which the selected TMM mixtures successfully emulated the target tissues was measured across the band, and quantified. The absolute difference between the mixture value conductivity value and the reference conductivity value of the target tissue was calculated at each frequency point. This difference value was converted to a percentage of the reference conductivity value at this frequency point to normalise the difference with respect to the reference value. Finally, the mean of these percentage differences were reported in Table 3.3. These mean percentage differences were calculated across the 1 kHz–1 MHz band and across the 50 kHz–250 kHz band covered by the Swisstom EIT-Pioneer. The error at the commonly used 50 kHz point was also shown in this table.

CHAPTER 3. TMM AND PHANTOM DEVELOPMENT

Table 3.3: Mean percentage difference in AC conductivity of each TMM mixture and the respective reference tissues values across the 1 kHz–1 MHz, 50 kHz–250 kHz bands, and at the 50 kHz point.

Target Tissue	Conductivity Error (%) (1 kHz–1 MHz)	Conductivity Error (%) (50 kHz–250 kHz)	Conductivity Error (%) (at 50 kHz)
Blood	7	2	1
Brain	8	2	0.5
Outer	27	20	23
Clot	27	7	8
Fat(1)	47	27	35
Fat(2)	52	14	16

The data shown in Fig. 3.6 and Table 3.3 demonstrates that the TMMs cover the biological range of conductivity values from fat to blood, and also emulate the target tissues of fat, blood, Outer Hybrid, clot, and Intermediate Brain Hybrid. The differences between the TMMs and the target tissues presented in Table 3.3 are within reported biological variance of conductivity discussed in Section 2.4.2.

It is seen in Table 3.3 that one of the two fat TMM models give closer alignment to the fat reference profile depending on the band chosen. It is also seen that the TMM mixtures for fat have errors higher relative to other TMMs. This outcome is due to the method of error calculation. A given absolute difference between a candidate TMM and a reference results in a bigger percentage difference for fat compared to blood, as the former is being expressed as a percentage of a much smaller number compared to the latter. Despite these larger error values for the fat TMMs the values are still within variance values reported in the literature [153], and discussed in Section 2.4.2.

Of note is the finding that the mass percentages of graphite and CB used in this study to achieve the high conductivity target of blood here are similar to those used by Santorelli *et al.* [215] to match the high conductivity target of tumour in the microwave frequency range. However, the lower percentages of graphite (15 to 25 %) and CB (0 %) used successfully by Santorelli *et al.* to model fat in the microwave range are not sufficient in the EIT range, as shown in Table 3.2, where much higher concentration mixtures of graphite and CB are needed to emulate fat. The consequence is that the concentration range of graphite (30 to 45 %) and CB (3.5 to 5.7 %) that covers the biological range of conductivity in this EIT study is narrower than that used in microwave studies. Hence the conductivity profiles are more sensitive to small changes in concentrations of the constituent chemicals. This sensitivity is demonstrated by the fact the outer layer TMM only contains 2.5 %

w/w less graphite and 0.5 % w/w less CB than the blood TMM. Therefore, the AC conductivity profiles and patterns of such TMMs may not directly translate from one study to another if the frequency bands differ. Thus TMMs should be developed and characterised based on the desired properties for a given frequency range.

This section has quantitatively characterised the degree to which the selected TMMs emulate the AC conductivity profiles of the target tissues over the 1 kHz–1 MHz band, and also other narrower bands such as the 50 kHz–250 kHz band used by the Swisstom EIT-Pioneer [187]. It has been shown that the TMM can cover the biological range of conductivity and successfully target tissues. These selected TMMs were used to fabricate the head and lesion phantoms described in the next section.

3.3 Head Phantom Development

Head phantoms were fabricated from the TMMs to further demonstrate the value of these TMMs for use in EIT applications. These phantoms were utilised as test platforms for later chapters. First, a review of head phantoms currently used in EIT is first described. Next the design and fabrication of two anatomically precise, mechanically stable, robust, and dielectrically accurate head phantoms is presented. After this, a validation of the developed phantoms is discussed.

3.3.1 Types of Head Phantoms Used in EIT

A comprehensive review of head phantoms for application in EIT and related technologies such as EIS is presented now as the current state-of-the-art of phantoms and TMMs used in the field. Phantoms are found to range in complexity, with the degree of realism needed dependent on the proposed study. Table 2.2 in Chapter 2 provides a summary of these phantoms and TMMs, which are discussed in more detail here. These phantoms can be roughly divided into those based on simpler idealised geometry such as cylinders and hemispheres, and those that had more anatomical realism. The more simple shaped phantoms are initially reviewed.

Gamba *et al.* developed a 3-layer head phantom to measure the current distribution in the brain as a precursor for use in EIT studies [142]. The experiments were performed at DC [142]. The phantom featured an external Perspex tank of simple cylindrical geometry used to house a cylindrical Plaster of Paris skull layer with a conductivity of 0.9 Sm^{-1} at DC. A saline, CaSO_4 , CuSO_4 mixture with a conductivity equal to 30 times that of the skull was used on both sides of the skull to model both scalp and brain [142].

CHAPTER 3. TMM AND PHANTOM DEVELOPMENT

Nissinen *et al.* used a similar phantom, to study the shielding effect of the skull on electrical current. A Plaster of Paris skull layer with reported ‘low conductivity’, and saline of conductivity 0.156 Sm^{-1} were used to model both scalp and brain. The experiments were performed with a current of 5 mA and a frequency of 10 kHz [144].

Sperandio *et al.* presented a relatively complex four shell model which used gel-based TMMs based on agar and various concentrations of saline to independently model scalp (0.5 Sm^{-1}), skull (0.08 Sm^{-1}), and CSF (2 Sm^{-1}) [141]. The brain was modelled as 0.03 M saline (0.3 Sm^{-1}). A film was used to separate the layers to prevent diffusion without interfering with the current travel or measurement data. The layers were constructed as concentric hemispheres, limiting the anatomical realism. This work was focussed on phantom development with measurements taken to validate the phantom. These phantom measurements were compared to measurements from simulations over a 10 kHz-1 MHz band [141].

In terms of more anatomically realistic phantoms, Bonmasser *et al.* utilised an anthropomorphic head model to create a 1-layer brain phantom from a mixture of agarose and saline with a conductivity of 0.1 Sm^{-1} [132]. Cavities were present and filled with saline (conductivity not reported) in order to assess the ability of EIS to detect brain haemorrhage at frequencies in the range 0 kHz-50 kHz [132].

Li *et al.* produced a 3-layer head phantom for EIT with a noteworthy intricate skull layer in which the conductivity profiles of the different skull bones were individually modelled using different water and dental grade plaster powder (CaSO_4) mixtures (conductivity range of 0.005 to 0.017 Sm^{-1}) [140]. The bone phantoms were cast by anatomically realistic 3D moulds. The skull (0.5 Sm^{-1}) and brain (0.3 Sm^{-1}) layers were then created from aqueous solutions of CaSO_4 with a resin tank used form an exterior tank [140]. This work was again focussed on the development of the phantom, with validation performed using a cylindrical perturbation in a tdEIT experiment at 50 kHz [140].

Wang *et al.* presented another 3-layer phantom which used ABS with conductive powder to model an anatomically realistic skull layer based on the work of [140]. Cotton wool and saline was used to model CSF, and agar and saline used to model brain. ICH was modelled by injection of blood into a balloon embedded in the brain layer in a tdEIT study, with the frequency not reported [143].

Avery *et al.* demonstrated the use of a 3D-printed PLA to create anatomically realistic 3-layer head phantoms of both an adult and a neonate. In both phantoms a

CHAPTER 3. TMM AND PHANTOM DEVELOPMENT

solid skull layer modelled a realistic conductivity profile (again based on the values presented in [140]) as a result of a series of intricate holes permeated by saline [139]. The saline formed both the inner brain and outer scalp layers, with conductivity of 0.4 Sm^{-1}). A solid PLA exterior formed a tank to encase the phantom and hold the electrodes, with validation performed using a 20 mm diameter sponge perturbation of reported 10% contrast in conductivity using tEIT at 1.4 kHz [139]. Of note, this phantom is available as an open source repository of 3D-printable CAD models and as such is a readily available head phantom. As part of this work this phantom was printed and used as a test platform in Chapter 6 in part due to a high level of anatomical accuracy afforded as a result of 3D-printing. This phantom as recreated for the work of this dissertation is shown in Fig. 3.8.

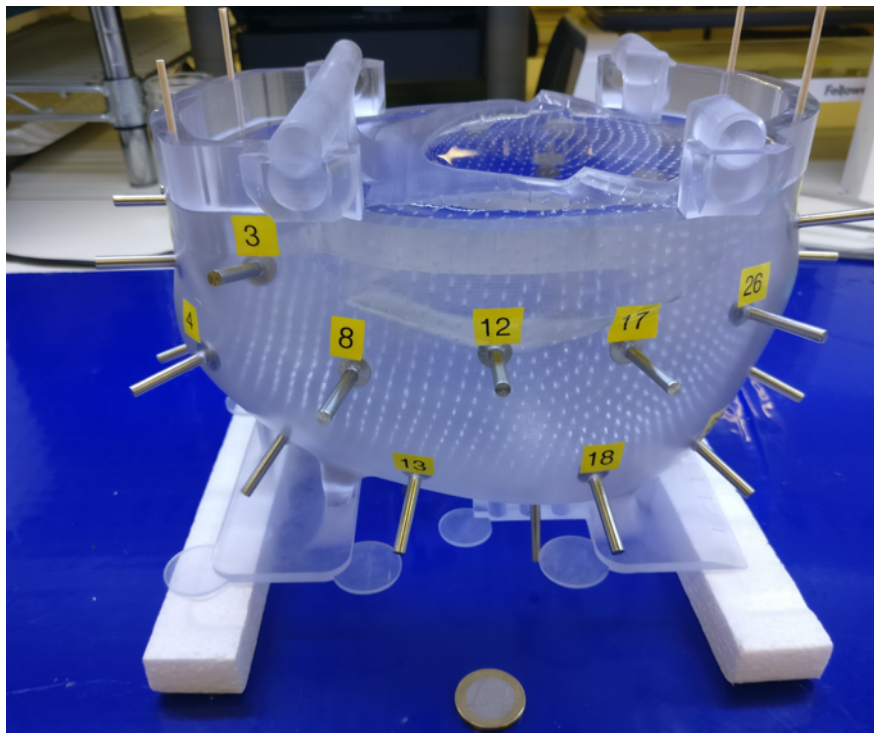


Figure 3.8: 3D-printed phantom of the 3-layer head model presented in [139].

Zhang *et al.* subsequently used a 3D-printable conductive material to produce a 4-layer head phantom with solid and anatomically realistic skull (0.004 to 0.1 Sm^{-1} at 1 kHz) and brain (0.16 Sm^{-1}) layers. Saline was used to model other tissues such as scalp (0.44 Sm^{-1}) and CSF (1.78 Sm^{-1}) [154]. This work of [154] focussed on phantom development, with validation by using saline haemorrhage perturbations (0.6 Sm^{-1}) in cavities within the brain layer with EIT measurements taken at 1 kHz.

As was concluded in Section 2.4.5, this review showed that pace of development in head phantoms for TMM is slow with the studies documented above covering from 1999 to 2017. There is a gradual shift to more anatomical realism facilitated in part by 3D printing. A lack of use of these phantoms in scenarios featuring static lesions, and a lack of realistic phantom lesions is also noted. These are limitations that are addressed and progressed in this chapter, and in subsequent chapters.

3.3.2 Head Phantom Design Conception

The head phantoms developed for this thesis were designed as a simple ‘hollow’ phantom and more complex ‘solid’ variant. Phantom lesions also designed for use with the phantoms.

The phantoms were both designed with two layers. This design demonstrated the ease of creating modular phantoms from the TMMs. In this study, 2-layer models were used as proof of concept and as initial test platforms for the work in later chapters. The models however can easily be extended to include additional layers. An outer and inner layer were modelled in the phantoms. The outer layer was made from the TMM mixture replicating the AC conductivity profile of a weighted aggregate of tissues external to the brain, described as the Outer Hybrid model (see Sections 3.2.2, 3.2.4.2). The inner layer was modelled using the AC conductivity profile of the tissues of the brain, described as the Intermediate Brain Hybrid (see Sections 3.2.2, 3.2.4.2). In the solid head phantom this inner brain layer is fabricated from the brain TMM described in Section 3.2.4.2. In the hollow phantom the inner layer was left vacant and could be filled with a saline that emulated the Intermediate Brain Hybrid model of brain. As shown in Fig. 3.6, the target conductivity was approximately 0.3 Sm^{-1} for the Intermediate Brain Hybrid across the 1 kHz–1 MHz band. This conductivity is achieved using 0.032 M saline, which has a conductivity of 0.3 Sm^{-1} across the 1 kHz–1 MHz [153].

Both of these phantoms are designed to facilitate the modelling of brain lesions of known size and location. In this study, bleed and clot phantom lesions are made from the respective blood and clot mimicking TMM (see Sections 3.2.2, 3.2.4.2). In the case of the hollow phantom, the use of a saline brain layer means that solid bleed or clot phantoms can be made in a range of sizes and suspended anywhere in the saline brain. For the solid phantom, lesion placement is achieved by three cylindrical cavities left in the brain layer at fabrication. These cavities could be later filled with cylindrical plugs containing either solely brain TMM, solely bleed (or clot) TMM, or brain TMM with discrete bleed (or clot) TMM lesions of known size and location. Hence, these plugs provide a way to model lesions, and a variety of plugs ensure the lesions are reconfigurable and adjustable in terms of size and

location.

In this section the high level design of the head phantoms has been presented. The fabrication process is next discussed.

3.3.3 Head Phantom Fabrication Process

In this section, the manufacture of the head phantoms is described. Anatomically accurate Stereolithography (STL) files of the human head [222] and brain [223] were 3D-printed to produce moulds using an Ultimaker 2+ Extended 3D printer with PLA as the print material [224]. The head STL file was developed from a reverse engineered polygon mesh [222] with the brain STL developed from MRI studies [223]. The approximate dimensions of the head STL and 3D-print were:

- Nasion to inion distance of 0.175 m;
- Distance between the left and right sides at the level of the temporal bone of 0.125 m;
- Distance from the crown to the level of the nasion-inion line of 0.07 m.

The corresponding dimensions for the brain STL and 3D-print were 0.155 m, 0.105 m, and 0.055 m respectively. The 3D prints are shown in Fig. 3.9.

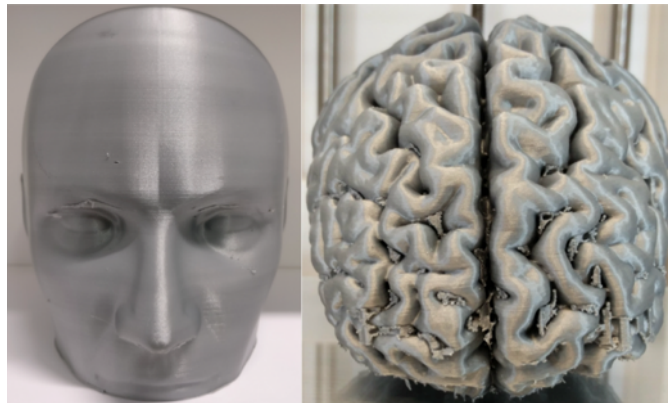


Figure 3.9: 3D-printed anatomically accurate (in terms of structure and size) head (left) and brain (right). The photographs are not shown with the same scale, i.e., the brain here is shown larger than actual size relative to the head for purpose of illustration.

A counter mould was developed for the head by pouring polyurethane into a large box and placing the smaller head mould inside. Once set, the head was removed. The inner surface of the counter mould was thoroughly sprayed with mould release spray (Universal Mold Release from Smooth-On, Easton, PA, USA). The outer layer TMM mixture was then fabricated and laid down evenly on the inner surface

of the counter mould surface, along the crown of the head and down the sides. Details of the position of the brain cortex surface with respect to the scalp [225] was used to ensure that the thickness of the outer layer was anatomically correct. The cortex surface is found to be approximately 15 mm from the scalp on the crown of the head and approximately 11 mm from the lateral, anterior and posterior surfaces of the scalp [225]. Using this information the brain mould was sprayed with mould release spray, and positioned within the head counter mould with the outer layer built up in the gap between the head and brain surfaces. A wire was placed around the brain falling within the cerebral fissure in order to aid removal of the brain mould from the outer layer once set. The head counter mould with the brain mould positioned within the counter mould and the outer layer packed between the counter mould and brain mould are shown in Fig. 3.10.

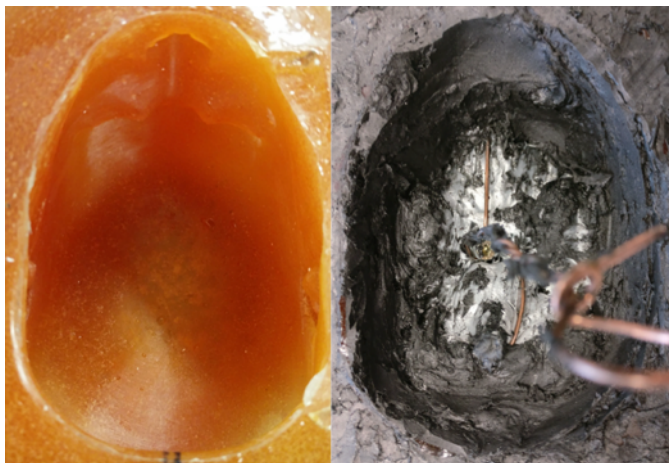


Figure 3.10: Counter mould of the head made from polyurethane with the impression of the 3D-printed head (left). The 3D brain mould is positioned in the head counter mould cavity with outer layer TMM laid down around the brain mould (right). The positioning of the brain within the cavity is based on anatomical information [225] to ensure the placement is accurate. A wire is placed around the brain, falling into the cerebral fissure on the topside, in order to aid removal of the printed brain after the outer layer TMM sets.

When the head is viewed in sagittal section, the brain extends down to approximately the level of the philtrum, with the spinal cord beginning [27]. At this level other structures such as the eye, ear, and nasal cavity are present which are not usually modelled in head EIT [139]. Indeed as described in Section 2.4.2, a common approximation is to only consider those tissues above the level of the inion-nasion line [139], [140]. However, the head phantoms designed in this work were built to extend to the level of the lower lip. This design matches the limits of the counter mould. The result is a cosmetically more realistic head phantom, but with the outer layer only modelling the aggregate of tissues above the inion-nasion line (skin,

CHAPTER 3. TMM AND PHANTOM DEVELOPMENT

skull cortical bone, skull cancellous bone, meninges, and subarachnoid CSF), as described in Section 3.2.2.

Once the outer layer was set approximately 24 hours after initial pouring, the brain mould was removed. The mould release spray, attached wire, and some careful dissection of excess outer layer TMM across the base of the brain was needed to ensure removal without damage to the mould. An impression of the external surface of the brain is left on the inner layer of the outer layer. This step completed the fabrication of the outer layer with the result shown in Fig. 3.11. At this point the hollow phantom was complete, with saline then added to model brain when in use as a test platform.



Figure 3.11: Removal of the brain mould leaves the completed outer layer in the head counter mould. The impression of the outer brain surface is imprinted on the inner side of this outer layer. In the case of the hollow head phantom, saline is now added to model the brain. In the case of the solid phantom, an inner layer of brain mimicking solid TMM is subsequently added (with cavities for lesion phantoms). See also Fig. 3.15.

In the case of the solid head phantom, the brain TMM was then mixed and packed into the cavity left from the removal of the brain mould. Three 3D-printed cylinders of 25 mm diameter were placed at various positions obliquely extending into the brain layer from the surface. The cylinders were pushed into the brain TMM in order to penetrate to as close to the outer layer as possible. The brain layer was

CHAPTER 3. TMM AND PHANTOM DEVELOPMENT

built up and packed around these cylinders. Once the brain layer set, the cylinders were removed to leave a brain layer with three cylindrical cavities. The choice of three cylindrical cavities was a trade-off between maximising the number of test cases and compromising stability of the brain layer. Space also limited the number of cavities possible. The positions of the cavities were selected to enable test cases at the front, middle and rear of the head, with the oblique angles maximising the amount of brain volume that can be filled by test plugs. These cavities can be filled with plugs of phantom material to replicate lesions or indeed with brain TMM. In this study haemorrhagic and clot lesions were used, made from blood and clot TMM. The placing of the cylinders extending the full thickness through the brain layer ensures haemorrhages (and clots) can be modelled at all heights from the surface of the brain through to the base along the line of the cylindrical cavity. The cylinders were chosen to have a 25 mm diameter enabling fabrication of lesions within an expected range of dimensions. For example ICH are typically ellipsoid [226] with the median volume being about 17 ml in the acute stage [115]. A blood TMM lesion shaped as an ellipsoid with dimensions of 20x20x10 mm³ equates to this 17 ml volume. Simplified shapes include for example, a sphere of diameter 25 mm or a cuboid of 20 mm³ both of which model a blood volume of 8 ml. Alternatively a cuboid 20x20x30 mm³ corresponds to a 12 ml volume of blood. Some of these haemorrhagic lesions and corresponding clot lesions are shown in Fig. 3.12.



Figure 3.12: Cylindrical plugs (labelled in the picture as (1)) used to create the cylindrical cavities in the brain layer of the solid head phantom. Plugs of phantom material are then created using the corresponding mould (labelled in the picture as (2)). Material is packed into the two halves of the cylindrical mould, which are then joined and allowed to set. A completed phantom plug is shown (labelled in the picture as (3)). The plug may be purely healthy brain mimicking TMM, purely haemorrhage (or clot) TMM, or contain discrete blood (or clot) lesions of known size and location embedded in brain TMM. Some examples of blood and clot TMM lesions are shown (labelled in the picture as (4)). These lesion TMMs can be sized and shaped as required. The lesions are then inserted into the mould (labelled in the picture as (5) and (6)) where two lesions are positioned surrounded by brain mimicking TMM in one half of the mould, before the second half of the mould is placed on top, completing the phantom plug. In addition, the discrete haemorrhage or clot lesions shown in (labelled in the picture as (4)) can be used in the hollow phantom when suspended in the saline brain layer.

The plugs of phantom material were fabricated using a mould of the same shape and dimensions as the cylinders used to produce the cavities. These moulds were in two halves and are shown alongside the cylinders in Fig. 3.12. Phantom material was worked into each half of the mould with the two halves joined together and kept in place using elastic bands until the plug was set. Filling the cavities with plugs completed the anatomy, and it was found that a little pressure and manipulation was needed to work the plugs into the cavities with a tight seal formed indicating minimal risk of potential air gaps. If the material used to fill the plug was only brain TMM then when the plug was inserted into the head phantom the normal

brain was represented. Alternatively the plug could be entirely of blood (or clot) TMM that resulted in a gross haemorrhagic (or ischaemic) lesion of 25 mm diameter and extended the full thickness through the brain along the line of the cylindrical cavity. Finally, discrete haemorrhagic (or clot) lesions of cuboid, spherical or other shapes could be fabricated and used in the hollow phantom suspended in saline. In the case of the solid phantom these lesions could also be embedded in brain TMM to result in a discrete lesion of known size and location in the plug. Examples of a complete plug and discrete lesions are shown in Fig. 3.12. The complete head phantom fabrication process is summarised in Fig. 3.13.

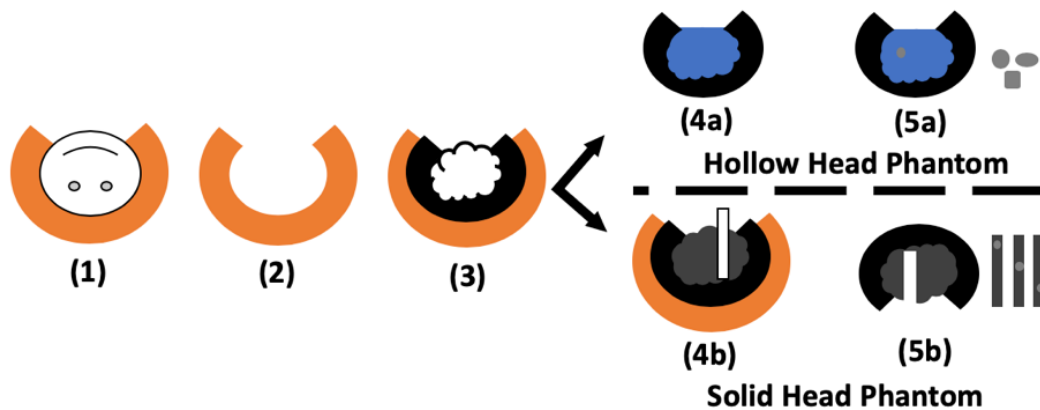


Figure 3.13: Steps involved in head phantom fabrication process. In (1) the 3D-printed head is used to create an impression in polyurethane which then sets, leaving a head shaped counter mould cavity as shown in (2). Next, the outer layer TMM is packed into the cavity and the 3D-printed brain mould positioned to ensure the outer layer is laid correctly as shown in (3). Once set, removal of the 3D-printed brain leaves a cavity. Removal of the counter mould at this point and filling of the cavity with saline to model brain results in the hollow head phantom (shown in (4a)). Discrete phantom lesions can be suspended in the saline brain to model pathology (shown in (5a)). In the case of the solid head phantom, the cavity is filled with brain TMM with cylindrical rods placed and positioned to leave cavities for plugs (shown in (4b)). Once the brain TMM is set, the counter mould and cylindrical rods are removed leaving the complete solid head phantom with an outer solid layer, inner solid brain layer and cavities that can be plugged with cylindrical plugs that can be made exclusively of brain TMM or can have discrete lesion phantoms at known positions (shown in (5b)).

The complete solid head phantom after removal from the counter mould, is shown in Fig. 3.14. The result is a phantom of realistic anatomy, being made in two layers from realistic moulds. Further, the head phantom is mechanically robust as demonstrated by the ability to support its own weight and is dielectrically accurate in terms of electrical conductivity since the electrical conductivity properties of the constituent TMM mixtures are known and appropriately matched to the properties

of the various tissues. Finally, the cylindrical cavities allow the introduction of phantom pathological lesions of known location and size, and the cavities should be filled with a TMM plug before use of the phantom. The complete hollow head phantom is shown in Fig. 3.15. The hollow phantom shares the same realistic anatomy as the solid phantom, and has the same dielectric accuracy in the outer layer. The brain layer is modelled as 0.032 M saline. This liquid brain layer facilitates the placement of phantom lesions of a wider variety of shapes and sizes, as well as at any location within the brain as shown in Fig. 3.15, where a cubic phantom lesion is seen suspended into the saline. As such, these head phantoms provide valuable test platforms for EIT studies related to the head and brain. In the next section a simple tdEIT experiment is described to validate the use of these type of head phantoms in EIT.



Figure 3.14: Final solid head phantom shown upright (top left, top right and bottom left) and inverted (bottom right). The inverted view shows the three cylindrical cavities, one of which has a cylindrical plastic plug inserted. The cavities are at an oblique angle to maximize the area of the brain into which phantom lesions can be positioned.

Following fabrication of the EIT head phantoms, validation was required. In the next section a simple tdEIT experiment is described that validated the use of these type of head phantoms in EIT.

3.3.4 Head Phantom Validation by Time Difference EIT Experiment

In Section 3.2.4 the TMMs were validated in terms of characterising the conductivity profiles of the selected mixtures. These mixtures were designed to cover the

CHAPTER 3. TMM AND PHANTOM DEVELOPMENT

biological range of conductivity, emulate the target conductivity profiles of blood, fat, Outer Hybrid, and Intermediate Brain Hybrid (Fig. 3.6), within the allowed biological variance (Table 3.2, Section 2.4.2). These TMMs were then used to construct head phantoms. In this section the designed head phantoms are further validated through incorporation into an experimental EIT setup.

The hollow head phantom was used with phantom haemorrhagic lesions using a 16-member electrode ring positioned as shown in Fig. 3.15. This phantom test platform was then connected to a Swisstom EIT-Pioneer set used at a frequency of 50 kHz, a 5 mA peak to peak current, with recording of measurement frames performed at 10 Frames per Second (FPS) for a minute and using a Skip 2 Protocol.

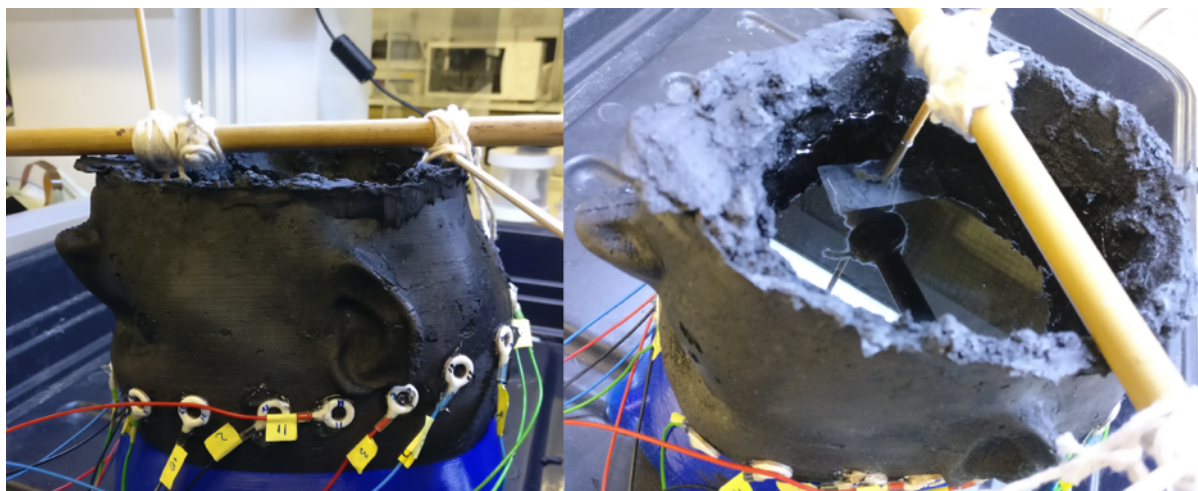


Figure 3.15: Left: The designed hollow head phantom shown with electrodes positioned in a ring arrangement. Right: Wooden rods are used to attach and place lesions within the saline brain layer. The electrodes are attached to a Swisstom EIT-Pioneer set which records the measured voltages as part of the measurement frames.

Two tdEIT experiments were performed. For both, the ‘baseline’ case of the saline brain without any lesion (normal case) was recorded with the measurement frames averaged to reduce noise (denoted as $Frame_N$). Then the ‘update’ case was recorded in which a lesion was placed into the saline brain, again with measurements recorded and averaged (denoted as $Frame_L$). In the first experiment, a spherical haemorrhagic phantom lesion of 35 ml volume was positioned midway between the sagittal plane and Electrode #13. In the second experiment, a rectangular cubic haemorrhagic phantom of 20 ml volume was positioned near Electrode #8.

In order to reconstruct time-difference images from the experimentally collected

data a ‘normal’ FEM model of the head, lacking lesions, was generated using EIDORS and GMSH. This FEM model comprising 268,240 elements had identical geometry to the hollow head phantom. The outer layer of the FEM model was assigned a conductivity of 0.1 Sm^{-1} and the brain layer a conductivity of 0.3 Sm^{-1} , which are equivalent to the conductivity values of these layers in the experimental phantom at the 50 kHz point (Figs. 3.6, 3.7). This FEM model was used to generate a coarse inverse model of 6,846 elements using the Graz Consensus Reconstruction Algorithm for EIT (GREIT) linear reconstruction algorithm. Reconstruction was performed using GREIT with the difference vector ($Frame_L - Frame_N$) as input. The GREIT algorithm is used here since this algorithm is an optimised and well-documented method for time-difference imaging [227].

The reconstructed images for both experiments are shown in Fig. 3.16, which also shows the electrode numbering and positioning used. The haemorrhagic lesion is more conductive with respect to the saline background and so a positive difference intensity is expected. This result is clearly seen in the expected region where the perturbation is placed. Further, the magnitude of the difference intensity is larger in the case of the bigger 35 ml lesion than for the 20 ml lesion. This difference in magnitude is a consequence of a larger lesion resulting in larger changes in recorded voltages, with these larger changes carried into the values of reconstructed conductivity values for each voxel as a result of Equation 2.13.

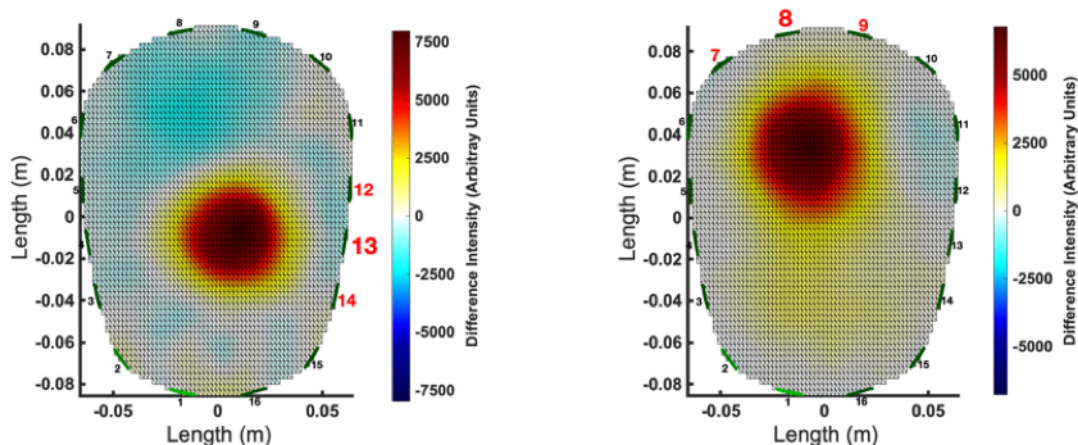


Figure 3.16: Reconstructed tdEIT images for the hollow head phantom for the case of phantom haemorrhagic lesions, with the EIT setup having a 16 member electrode ring positioned as shown in Fig. 3.13. In both cases, the baseline measurement frames have the saline brain without a phantom haemorrhagic lesion present (normal case), with these frames averaged to reduce noise. Left: A 35 ml spherical phantom haemorrhagic lesion is placed midway between the sagittal plane of the head and electrode #13 with measurement frames taken (and averaged). Right: A 20 ml rectangular cubic phantom haemorrhagic lesion is placed near electrode #8 with measurement frames taken (and averaged). In both cases the averaged frames with the lesion present are differenced with respect to the averaged baseline frames, and the resulting time-difference image is then reconstructed. The haemorrhagic lesion is more conductive with respect to the saline background and so a positive difference intensity is expected. This result is clearly seen in the expected region where the perturbation is placed. Further, the magnitude of the difference intensity is greater in the case of the larger 35 ml lesion than for the 20 ml lesion.

In this section the head phantoms constructed for use in EIT were validated, with the results correlating to the expected theoretical outcome. The results shown in Fig. 3.16 demonstrate that the developed phantoms can be used in EIT experiments and operate as expected. Despite working well, further improvements are possible to allow for even more advanced anatomical modelling and more precise matching to conductivity profiles of tissues. The next section describes a proposed next step in phantom development that may achieve such improvements - 3D printing.

3.4 Next Steps: 3D-Printable Tissue-Mimicking Materials

The solid TMMs presented in Section 3.2 and the head phantoms produced in Section 3.3 offer many advantages as experimental platforms for EIT as discussed

CHAPTER 3. TMM AND PHANTOM DEVELOPMENT

in Section 3.3. However, improvements are possible in both the materials and fabrication method, which would translate into improvements in the final phantoms. Presented in this section are the preliminary results of a novel composite material for 3D-printing, which aimed to achieve such improvements.

In terms of materials, the percentages of graphite (30 to 45 %) and CB (3.5 to 5.7 %) needed to cover the biological range with the TMMs presented in Section 3.2.4.2 were relatively narrow compared to the studies of Santorelli *et al.* [215]. The result was sensitivity of the conductivity profile of the material to small changes in concentrations. These percentages were also higher than those used by Santorelli *et al.* [215] and resulted in physical challenges in hand mixing higher mass percentage amounts of solid powder in the polyurethane base.

It is possible that these issues could be overcome by using more conductive grades of the chemicals as well as specialised industrial mixing machinery. The grade of CB used in the initial development of the TMMs, CB (Carbon Black, acetylene 50 % compressed, 99.9 % +), has a surface area of $75 \text{ m}^2 \text{ g}^{-1}$, is 50 % compressed, and has a bulk density of 80 to 120 kg m^{-3} . The electroconductive behaviour of CB is primarily influenced by surface area, structure, and surface chemistry [228]. A grade of CB that offers improvements over the type initially used is Ketjenblack EC-600JD which has a surface area of $1,400 \text{ m}^2 \text{ g}^{-1}$, a highly porous branched structure, and a low concentration of surface oxygen containing moieties ('volatiles') which can hamper electroconductivity [228]. This highly conductive form of CB allows higher values of conductivity to be achieved at much lower concentrations than other forms of CB. Ketjenblack EC-600JD is however significantly more expensive at approximately five times the cost of the Alfa-Aesar product by mass [228].

The fabrication procedure used also presented challenges. The manual nature of mixing and sculpting used in the fabrication of the TMMs was aided by the use of 3D-printed moulds process, but still resulted in an inevitable loss of anatomical accuracy. The TMMs also require relatively large mass percentages of graphite and carbon black, which can make homogenous mixing more difficult. It was postulated that the set of challenges in materials and fabrication could be addressed using 3D printing. There has been recent advancements in 3D printing and in the use of 3D printing in phantom development. To date as in this work, the use of 3D printing has mainly been for the printing of anatomically accurate shells to hold liquid, gel or semi-solid based TMMs or as moulds [208]. However recently, studies have shown incorporation of 3D-printed materials as a part of the phantom proper both indirectly and directly [139], [154]. Avery *et al.* used non-conductive PLA to print a skull as part of a head phantom. Precisely aligned holes placed in the

skull allowed the permeation of conductive saline and emulation of the conductivity of the bones of the skull [139]. Zhang *et al.* doped non-conductive ABS with CB to produce a 3D-printable composite TMM [154]. This material was used to produce anatomically and dielectrically realistic bones of the skull, and brain phantoms [154]. These printed TMMs were then incorporated into a full head phantom with other layers such as the CSF modelled with saline [154]. The range of conductivity achieved in [154] (measured at a frequency of 1 kHz) ranged from 0.16 Sm^{-1} for the solid brain to 0.004 to 0.01 Sm^{-1} for the solid skull bones.

Hence in order to further improve the quality of solid conductive TMMs for EIT, a proof of concept study was performed. This study was to investigate the use of ABS doped with CB to produce 3D-printable TMMs. The use of these materials aimed to overcome some of the limitations of the hand-made and moulded TMMs:

- The use of specialised extrusion machinery would facilitate thorough homogeneous mixing with production of 3D-printable filaments;
- Subsequently by virtue of being 3D-printable the manual nature of the fabrication process would be removed;
- By adjusting the percentage of conductive agent in the ABS a broad range of conductivities would be covered, both covering the biological range and extending beyond the values reported in [154]. Hence this study would build upon the work of [154] in particular by increasing the conductivity range achieved. In [154] the highest conductivity reported using the composite was a brain phantom with a conductivity of 0.16 Sm^{-1} at 1 kHz.

Presented here are preliminary results of this novel composite material for 3D-printing, which aimed to meet these objectives.

The base composite developed in this study consisted of ABS and Poly(styrene-b-ethylene-butylene-b-styrene) (SEBS) in the ratio 4:1 respectively by mass. The thermoplastic ABS is a commonly used material for 3D-printing [154], [229]. However, it was found that direct use of CB with ABS resulted in a very brittle material, particularly at the higher concentrations of CB [229], [230] that are needed to achieve higher levels of conductivity. SEBS is a polymer composed of a tri-block structure, with two hard end blocks and an elastomeric rubbery mid-block [231]. The composite of ABS and SEBS was found to offer good toughness and material strength but also flexibility and malleability even after addition of CB. ABS was obtained as solid pellets with SEBS as flakes, and the CB used being Ketjenblack EC-600JD [228]. The CB was used in concentrations ranging from 5 to 11 % by mass in the base composite.

CHAPTER 3. TMM AND PHANTOM DEVELOPMENT

Four separate mixtures were prepared differing in the percentage of CB in the composite (0 %, 5 %, 6.5 %, and 11 % by mass). Following weighing out of the appropriate masses of each material sufficient to make 450 g of final product, the three constituent materials were first mixed thoroughly by hand. Then, fabrication of the mixtures into 3D-printable filaments was by extrusion using a twin screw co-axial extruder. Prior differential scanning calorimetry gave the melting temperature of the composite at approximately 240 °C. Therefore, a temperature profile of 210 to 240 °C was used over the 5 zones (feed, melting, compression, mixing and metering) with a length to diameter of extrusion screw (L/D) ratio of 20:1, torque profile below 16 Nmm and die pressure of 7 to 21 MPa (higher for higher CB concentrations) [232].

After extrusion the filament was sliced into fragments and re-extruded, with this repeated resulting in three passes through the extruder. Repeat extrusion is performed to ensure homogeneity [233]. The final result was TMMs in the form of 3D-printable filaments of diameter approximately 2.85 mm (the diameter of the die used), with a sample of the filament shown in Fig. 3.17.



Figure 3.17: Example of the fabricated 3D-printable TMM.

Complex impedance spectroscopy of the TMMs was performed, as previously described in Section 3.2.3. In Fig. 3.18 the AC conductivity profiles of these TMMs across the 1 kHz–1 MHz band is shown using both logarithmic and linear frequency scales for clarity, along with the reference values of blood and fat [148]. As expected, the sample with 0% CB was non-conductive. The plots for the CB 11% sample with a relatively high conductivity $\geq 1.1 \text{ Sm}^{-1}$ across the band contain measurement error. This error is as a result of the measured Z values being of the order of 100Ω across the band. The measurement error becoming higher at higher frequencies as evidenced by increasing aberrations at higher frequencies, due to the limitations of the PARSTAT 2273 device as explained in Section 3.2.3 [221].

The profiles demonstrate that the TMMs cover the spectrum of conductivity values

CHAPTER 3. TMM AND PHANTOM DEVELOPMENT

seen in biological tissues (from fat to blood) and can emulate the conductivity profile of a range of tissues by adjusting the content of CB.

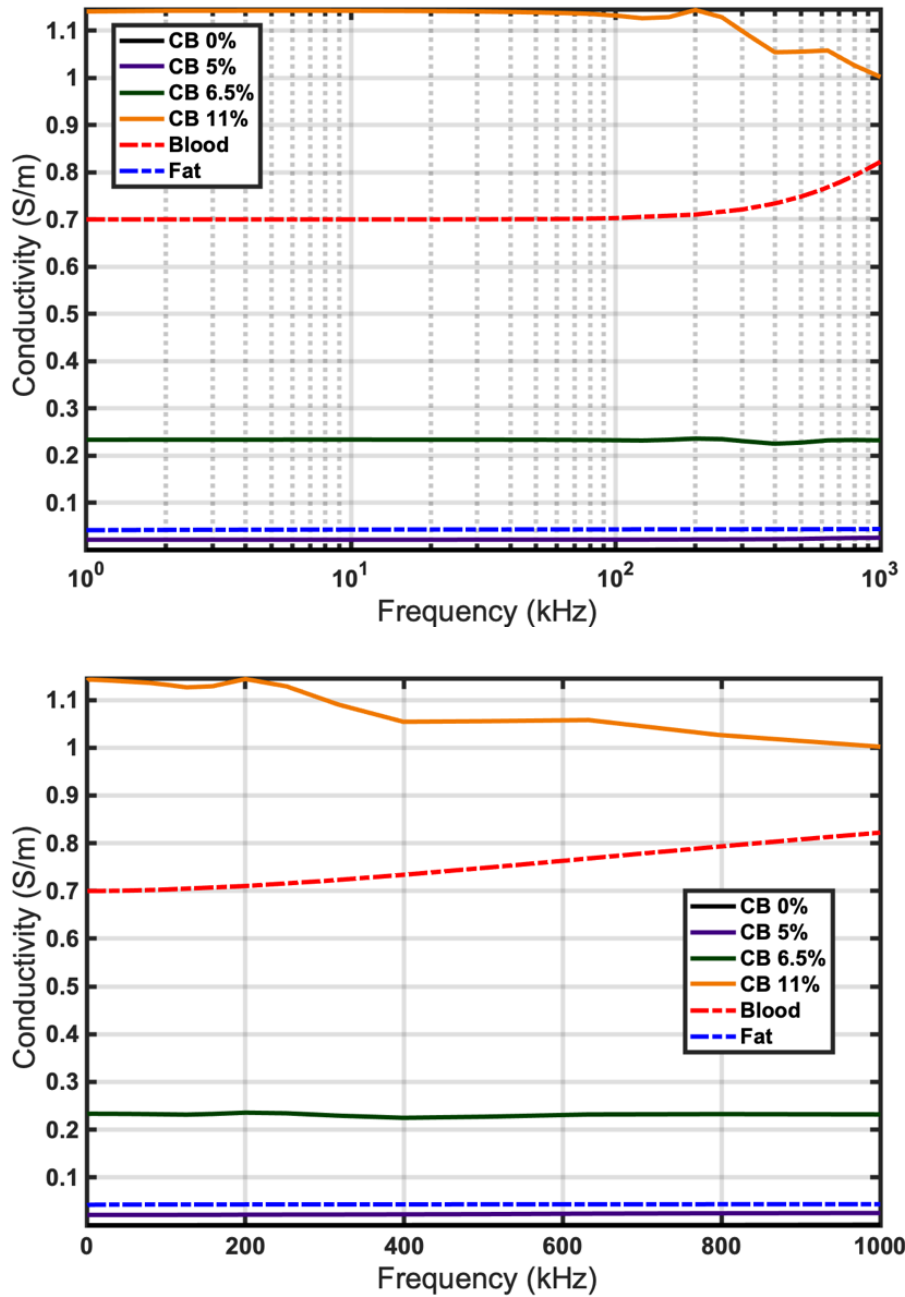


Figure 3.18: AC Conductivity curves for the reference tissues [148] (blood, fat) shown with dashed lines, and the 3D-printable TMM mixtures containing CB (0%, 5%, 6.5%, and 11% by mass) shown with solid lines across the 1 kHz–1 MHz frequency band. Note that the trace for 0% CB overlays the x-axis. The values plotted in (top) are in logarithmic frequency scale and in (bottom) are in linear frequency scale. The two scales are presented for clarity.

These 3D-printable TMMs represent an improvement over the initial handmade solid TMMs in terms of ease of fabrication and assurance of homogeneity. However, the extruder used lacked an automated system for drawing the filament. Hence, the filament was hand drawn and resulted in a tolerance of approximately ± 1 mm from the nominal die diameter of 2.85 mm. This tolerance is beyond that of most 3D printers [224]. A more specialist extruder, or simply one with automated dispensing of the final filament would have helped with this issue. Additionally a 3D printer with higher tolerance allowances may have allowed optimal use of the phantom material. Despite this, a rectangular disc was printed using the material in the Ultimaker 2+ Extended printer. This disc was printed using the 6.5 % CB material as a sample, and is shown in Fig. 3.19. This result demonstrates the material to indeed be 3D-printable. Further, the developed material is a step forward in the field of solid TMMs and one which future researchers may be able to use.

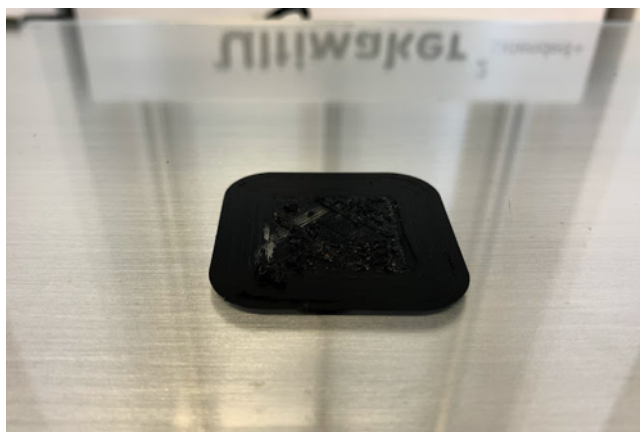


Figure 3.19: Successfully 3D-printed rectangular disc made from the 3D-printable TMM mixture containing 6.5 % CB.

3.5 Conclusions

In this chapter, solid TMMs were developed for use in EIT as test platforms for medical applications. These TMMs and corresponding phantoms fulfil the need for controlled test platforms bridging the gap between computational models and *in vivo* platforms, allowing the generation of valuable real world data. First in Section 3.2 the TMMs were presented with a description of the properties of the ideal TMM before reviewing the different types of TMMs. Next the target head tissues were outlined before the fabrication process, and subsequent validation process for the solid TMMs was described.

The advantages of these TMMs can be summarised as:

- The TMMs have accurate dielectric properties that cover the biological range of conductivity profiles between 1 kHz–1 MHz. The biological range of conductivities is delimited by blood and fat with these two tissues representing a high conductivity and low conductivity target tissue respectively;
- The TMMs can be tailored to match the conductivity of any tissue or aggregate tissue. In this work TMMs were developed for both discrete haemorrhage, fat, and clot tissues; and composite models of the head tissues external to the brain, and the tissues of the brain;
- Highly conductive tissues such as CSF and urine can also be mimicked by the novel use of isopropanol, which increases the conductivity of a mixture;
- Phantoms developed from these TMMs are easy to shape and mould, with a mechanically robust and stable shape;
- Modular, anatomically realistic phantoms can be developed using a selected set of TMMs as building blocks to give a mechanically stable, dielectrically accurate complete phantom structure.

Hence, these TMMs are a valuable addition to the options available for the development of test platforms for EIT applications.

In Section 3.3 novel phantoms based on the materials were fabricated as anatomically accurate solid head phantoms. These phantoms are presented both a demonstration of use, and as a test platform for use in later EIT studies. These phantoms use the TMM mixtures to model the tissues external to the brain, and those of the brain itself in the case of the exclusively solid phantom. The head phantoms also incorporate the ability to model pathologies using the TMMs, demonstrated by the development of unique haemorrhage and clot phantoms. Lesions of known size, shape, and location can be swapped in and out to allow easy implementation of a wide range of reproducible test cases to aid the development of EIT technologies. The range of modularity offers a wide range of phantom choice. The final selection will depend on the needs of a given study.

Although these solid TMMs offer advantages over liquid and semi-solid TMMs, the materials and fabrication process presented challenges that could be improved upon. In Section 3.4 the development of an iterative 3D-printable TMM was presented. The TMM was based on a composite of ABS, SEBS, and a highly conductive form of CB. The material was machine mixed to improve homogeneity, 3D-printable improving anatomical accuracy, and the levels of CB could be adjusted to tailor the conductivity properties. Hence this 3D-printable material offers all

CHAPTER 3. TMM AND PHANTOM DEVELOPMENT

of the advantages of the TMMs described in Section 3.2 as well as the promise of improved anatomical accuracy, and ease of fabrication of phantoms in future studies.

For the subsequent chapters in this thesis, the solid TMMs and the phantoms developed offered valuable real world early test platforms. In Chapter 4 the phantoms were used for real world testing of ML applied to collected impedance data. Specifically the hollow head phantom described in Section 3.3.3, and validated in Section 3.3.4 is used as a test platform with the saline brain offering ease of lesion reconfiguration for a wide variety of test cases. In Chapter 5, the initial development of the symmetry-based algorithm sdEIT utilised the haemorrhagic and clot phantoms in a saline filled cylindrical tank. The idealised geometry and near perfect symmetry of the cylindrical tank was needed in the early stages of algorithm development. Therefore these novel TMMs and phantoms offer many advantages as a test platform, demonstrated in this chapter and in Chapters 4 and 5 to follow, with these advantages envisioned to be improved upon with the future development of the 3D-printable variant.

Machine Learning with Electrical Impedance Measurement Frames for Lesion Detection

Work from this chapter was published in three peer-reviewed articles. The feasibility of using raw measurement frames designed for use in EIT as data sets in machine learning classification algorithms for haemorrhage detection was explored for the first time in terms of numerical and phantom studies in the 2018 PLOS ONE journal paper “Brain Haemorrhage Detection using a SVM Classifier with Electrical Impedance Tomography Measurement Frames” [234]. The preliminary phantom work (which was later extended upon for [234]) was published as part of the Proceedings from the 19th International Conference on Biomedical Applications of Electrical Impedance Tomography, University of Edinburgh, Edinburgh, Scotland, United Kingdom, 2018 as a conference paper entitled “Classification Applied to Brain Haemorrhage Detection: Initial Phantom Studies using Electrical Impedance Measurements”, winning Best Student Paper at this international conference [235]. Finally, the numerical studies were extended to consider the effect of novel pre-processing of the data on classifier performance which was published as a Springer book chapter entitled “Brain Haemorrhage Detection Through SVM Classification of Electrical Impedance Tomography Measurements” as part of “Brain and Human Body Modelling - Computational Human Modelling at EMBC 2018” [236].

In this chapter ML classification algorithms are applied to both unprocessed and minimally processed raw electrical impedance measurement frames: i.e. the voltage measurement frames collected using an EIT injection/ measurement protocol (Section 2.4.3.1). These measurement frames are used without image reconstruction in order to detect the presence or absence of brain haemorrhage in a series of both numerical and phantom studies with the effect of changes in test parameters. These parameters include noise, lesion location, lesion size, electrode location, anatomy, as well as repeatability considered on classifier performance. In addition, investigations into classifier optimisation and the effect of pre-processing of the frames on performance in detection of the presence or absence of brain haemorrhage

is analysed.

4.1 Introduction

As described in Chapter 2, accurate and timely detection and diagnosis of brain lesions is an important medical problem. Such diagnostic challenges are part of the patient pathway in clinical conditions such as stroke and TBI (Sections 2.2.2.7, 2.2.3.6). In such conditions imaging of the lesion is unnecessary. Instead commencement of treatment is dependent on the timely and definitive ruling in or ruling out of the presence of a particular lesion type [236]. As such, if EIT is to be applied to such problems, the question arises as to whether the complexity of reconstructing an image is necessary or useful. This removal of a challenging part of the usual EIT workflow is particularly of interest in such challenging static or quasi-static scenes. In such cases existing EIT algorithms traditionally struggle (Section 2.4.6), and novel approaches are needed.

Thus in this chapter for the first time lesion detection and identification using only unprocessed or minimally processed raw EIT voltage measurement frames is studied for the detection of haemorrhagic lesions in the brain. A series of numerical and phantom models are produced with and without the presence of haemorrhagic lesions. These models are used to produce EIT measurement frames. Then these produced frames are used as inputs to Support Vector Machine (SVM) ML classification algorithms to detect the presence or absence of brain haemorrhage.

The remainder of the chapter is structured as follows: In Section 4.2 the use of ML techniques for similar clinical applications is initially reviewed. Next, SVMs are introduced, along with a description of the performance metrics that are applied to results and reported throughout this study. The performance of a classifier applied to bleed detection is also discussed. In Section 4.3, the numerical and phantom models, and the EIT setups used in the experiments are described. Next, in Section 4.4, a range of experimental conditions each focussed on a key experimental parameter are described and results presented for both numerical and phantom experiments. In Section 4.5, research into feature selection, and selection of the best SVM classifier based on choice of kernel is reported. Finally, the chapter concludes with Section 4.6, which provides a discussion on the relevance of the findings, limitations of the study, and future work. This final section also highlights the significance of this ML approach as a promising way to combine the technology of EIT with classification for important clinical applications.

4.2 Support Vector Machines Applied to EIT Haemorrhage Static Lesion Detection

In this section, a basis for the proposed approach of using SVM ML classification for brain haemorrhage detection using measurement frames is presented. A review of the use of ML algorithms in related applications is first outlined. Next, an overview of SVM classifiers is presented. Finally consideration is paid to the optimisation of classifier performance for this specific application.

4.2.1 Machine Learning and EIT

A logical basis for the approach is first presented. Following this, the prior use of ML in similar biomedical applications is reviewed.

The approach presented in this chapter is that:

1. The EIT measurement frames encode information regarding the nature, and location of the various tissues present including a lesion;
2. It may be possible to elicit this clinical information using an approach other than image reconstruction. The use of ML techniques are such an approach [236].

The series of studies in this chapter are designed as an initial proof of concept of this approach. Specifically, the chapter examines if measurement frames can be directly used as inputs into ML algorithms to detect brain haemorrhages, without the complexity of reconstructing an image. Electrical conductivity or impedance is the physical property indirectly measured with EIT. The property does vary detectably between normal brain parenchyma and haemorrhage [5], [132]. Thus the corresponding measurements frames should have detectable differences.

SVMs are a group of popular ML algorithms commonly employed for binary classification [237]. This use in binary classifications, as well as the extensive use of SVMs in previous studies involving biomedical signals [238]–[244] motivated the choice of using this type of classifier in this work. Examples include microwave measurements applied to breast cancer detection [238], [239], and other electrical impedance paradigms applied to various tissues [240]–[243]. Golnaraghi *et al.* used electrical impedance measurements from a multi-frequency sweep (EIS) of different tissues to train and test a SVM to classify ‘breast’ and ‘not breast’ with sensitivity and specificity reported at approximately 80% [240]. EIS and SVMs was again used by Gur *et al.* to measure impedance properties of breast tissue to identify patients at risk of cancer [241]. In that study, an area under the

Receiver Operating Characteristic (ROC) curve of 0.816 was reported with the author concluding the technique had the potential for use in risk stratification [241]. A similar technique and application was reported by Laufer *et al.* with a conclusion that the concept was ‘feasible’ [242]. Shini *et al.* used SVM models with impedance measurements to improve the sensitivity of prostate biopsies [243], with Khan *et al.* using composite impedance metrics as inputs for SVM classifiers for detection of prostate cancer [245]. Finally, Murphy *et al.* have investigated the use of EIT data with ML algorithms including SVM for use in measuring cardiac output [246].

In summary, there is evidence from the literature that the bleed detection approach suggested in this chapter has merit. In the next subsection, SVMs are described in more detail, followed by a discussion of the clinical requirements of classifier application to bleed detection.

4.2.2 Overview of Support Vector Machine Classifiers

In this subsection the ML classification algorithm of SVMs are discussed. Classification, and a general description of the generation and use of a ML classification model is first described. Next a theoretical background to SVMs is provided, as well as the the metrics used to quantify performance of classifiers like SVMs. Finally in the next subsection, the application of SVMs to EIT data for bleed detection will be introduced.

SVMs are a type of classification algorithm. Classification is one of the major task types in ML [237]. Each case or observation is defined by several features, and belongs to one of a number of designated classes or labels. Initially a classification algorithm is provided with labelled observations as a training set, with these used to produce a trained classification model. This model is then used to assign labels to new observations where only the features are known [237]. Good model generation is an essential prerequisite in order to correctly predict labels for cases.

In the specific case of a SVM classifier, the trained model defines a hyperplane in multidimensional space [247]. This hyperplane best separates the training data, and is used to classify future observations. The nature of the hyperplane is defined by the kernel used by the SVM. Data points are assigned into one of the two categories depending on which side of the plane they lie on. This hyperplane will incorporate the widest margin possible with the data points that form the border of the margin on each of the $+1$ and -1 sides called the support vectors [247]. A linear SVM for example utilises a hyperplane that is linear in nature. This type of kernel is mathematically and computationally light. An example of a linear hyperplane

and separation of classes is shown in Fig. 4.1, with observations consisting of n -dimensional data points separated by a 2-dimensional hyperplane (a line).

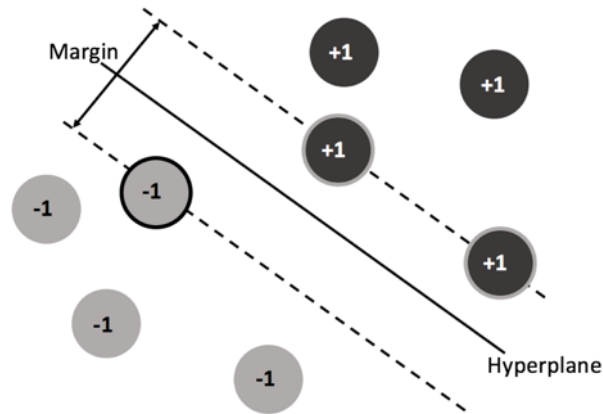


Figure 4.1: The basis of SVM classification. Here n -dimensional data points are separated by a 2-dimensional hyperplane into $+1$ or -1 categories depending on what side of the hyperplane they are on. Support vectors are those data points that define the margin about the hyperplane. These support vectors are shown by the circles on the hashed lines.

The classification results of the trained SVM model on the unseen test data are used to describe performance. The performance of a classifier can be reported by a number of different metrics. A key result is the confusion matrix, which compares the expected and predicted classes. An example of a confusion matrix for a binary classifier is shown in Fig. 4.2. As shown, a True Positive (TP) refers to observations where the expected and predicted classes are $+1$, a True Negative (TN) where the expected and predicted classes are -1 . A False Positive (FP) is where the expected class is -1 but is predicted as $+1$, with a False Negative (FN) the opposite case of misclassification.

		Expected	
		+1	-1
Predicted	+1	TP	FP
	-1	FN	TN

Figure 4.2: The Confusion Matrix for a binary classifier with classes ± 1 . The expected (true) class and predicted class assigned to cases are compared. A True Positive (TP) is where a case is truly +1 and classified as such. A True Negative (TN) is where a case is truly -1 and classified as such. A False Positive (FP) refers to cases that are truly -1 but misclassified as +1. A False Negative (FN) refers to cases that are truly +1 but misclassified as -1. The performance of a classifier on a test set is often reported as a confusion matrix with the number of cases in each category shown. Many other performance metrics are derived from the confusion matrix.

Two key metrics of performance derived from the confusion matrix are the sensitivity and specificity. Sensitivity (TP Rate) is the proportion of observations classified as +1 out of the total that are truly +1. Specificity (TN Rate) is the proportion of observations classified as -1 out of the total that are truly -1. The Accuracy is the proportion of correctly classified cases out of the total number of cases. These metrics are defined in Equations 4.1, 4.2, 4.3:

$$\text{Sensitivity} = \frac{TP}{TP + FN}; \quad (4.1)$$

$$\text{Specificity} = \frac{TN}{TN + FP}; \quad (4.2)$$

$$\text{Accuracy} = \frac{TP + TN}{TP + TN + FP + FN}. \quad (4.3)$$

A further tool used to assess performance is the ROC curve. The ROC curve is a plot of sensitivity versus $(1 - \text{specificity})$ [247]. The ROC curve is a useful tool to illustrate a trade-off between sensitivity and specificity. An example of three ROC curves are shown in Fig. 4.3. An ideal classifier is 100% sensitive and 100% specific, and the ROC curve has an Area Under the Curve (AUC) of 1. Such a classifier features a ROC curve as shown by the blue plot.

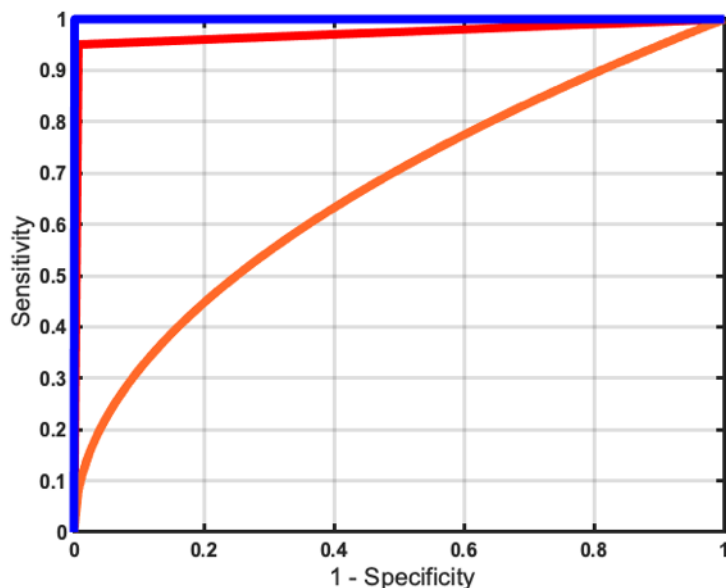


Figure 4.3: Receiver Operating Curves (ROC) curves are a plot of sensitivity versus ($1 - \text{specificity}$), and show the trade-off possible between sensitivity and specificity. An ideal ROC curve has an Area Under the Curve (AUC) of 1 with an example of this shown as the blue plot. Here an operating point where both sensitivity and specificity are both 100% is at $(0,1)$. The red and orange plots show imperfect ROC curves where $\text{AUC} < 1$. In this case it is possible to maximise sensitivity by moving to the operating point shown with the penalty of reduced specificity. Depending on the application this trade off may be acceptable. At any given point the red curve gives a better sensitivity/ specificity trade off compared to the orange curve. The orange curve only offers a sensitivity of 1 where specificity is 0, which would result all observations being classified as +1.

Finally in this subsection, the application of SVMs to EIT data for bleed detection is considered, with a brief overview of how this data is treated in this chapter. Throughout this chapter EIT measurement frames are generated from models with a member 16-electrode ring. These numerical and phantom models are described in Section 4.3. Each measurement frame (observation) will hence be a 208-dimensional data point or vector [7]. The input features to the SVM are thus the channels of the measurement frames, which are voltage values. These measurement frames are raw or minimally processed, and are obtained from numerical simulation and phantom models of the head in which a bleed is or is not present in the brain. The two classes defined in this scenario are ‘bleed’ or ‘no-bleed’ (‘normal’), denoted as +1 and -1 respectively. As there are two classes this is referred to as a binary classification problem.

In Section 4.4, the performance results are reported as the sensitivity and specificity

of the trained classifier on unseen test data never used as part of the training process. Also reported is the AUC of the ROC curve. The AUC values reported are those for the ROC curve of the trained model. This is the ROC curve produced from comparing the true labels of the training data to the predicted labels assigned to the training data by the model. The workflow for Section 4.4 is shown in Fig. 4.6.

In Section 4.5 the performance results are reported primarily as the mean \pm standard deviation of the sensitivity, specificity, and accuracy of the classifier with performance results generated from k-fold testing during cross validation. The workflow for Section 4.5 is shown in Fig. 4.18. The software package MATLAB and the MATLAB statistics and machine learning toolbox is used throughout for the training and testing of the linear SVMs [173].

This last subsection has described the ML task of classification, describing the processes of model generation and model use using testing and training sets of observations. The specific type of ML classification algorithm used in this study, SVMs, were described. Further, the metrics used to assess performance were outlined as well as the basis for the SVM approach for bleed or no bleed classification in EIT. The next subsection continues this discussion of the application of SVMs to bleed detection. This following subsection also includes an analysis of performance trade-offs that are possible when using an imperfect classification model and the clinical relevance of such.

4.2.3 Classifier Performance Applied to Bleed Detection

In the proposed clinical application of bleed detection in stroke and TBI, the key objective is to definitively detect haemorrhage. Ideally, the classifier would be 100% sensitive and 100% specific to haemorrhage. Such ideal classification would be the case where the $AUC = 1$. However, in reality it is not possible to achieve an ideal classification. Therefore, the priority is to maximise sensitivity at the expense of decreased specificity.

As described in Section 2.3, reduced specificity means an increased rate of false positives. These false positives are cases where bleed free patients are incorrectly classified as having a bleed.

Although not ideal, the converse of reduced sensitivity would mean increased false negatives. Such an increase would lead to haemorrhagic patients being misdiagnosed as being bleed-free. In such a scenario potentially haemorrhagic stroke patients would receive alteplase, which may be fatal. In TBI, increased sensitivity means haemorrhagic patients are not missed and are properly referred for CT

scanning. The simultaneous reduction in specificity would result in some non-haemorrhagic patients also receiving CT scans. This outcome is preferable to the alternative of some haemorrhagic TBI patients having false negatives and not receiving an appropriate scan.

The ROC curve can be used to choose an ideal operating point of the SVM classifier, resulting in changes to the sensitivity and specificity balance. As part of the classification process the trained SVM model calculates the posterior probability of the test case belonging to both classes. The default threshold called the ‘default operating point’ here, is 0.5. This means that if the probability of the case belonging to the -1 category is ≥ 0.5 the case is classified as -1 , otherwise the case is classified as $+1$. The threshold point can be changed, with an adjusted operating point selected. This adjusted operating point is found from finding the first point on the ROC curve which has a true positive rate of 1.0. Use of the adjusted operating point effectively increases the threshold to a value greater than 0.5, thus boosting sensitivity to bleeds at a cost to specificity. In Section 4.4 classifier performance is reported at both the default operating point and at an adjusted operating point designed to maximise sensitivity.

Hence this section has described the clinical necessity of maximising sensitivity in the case of bleed detection, and how this can be done even with an imperfect classifier. In the next section the numerical and phantom models used to generate the data used as input features for the SVM models are described.

4.3 Modelling Techniques

Fundamental to the research proposed in this chapter is the use of numerical models and experimental phantoms. These computer and real-world based test platforms allow controlled development of a technology or algorithm. The result is an ability to experiment and test parameters. This testing progresses the technology before translation to patients. This section begins with a description of the numerical model created for this study along with the phantom. In both cases the EIT experiment setup used is also described.

4.3.1 Numerical Models and Experimental Setup

The numerical models and EIT experimental setup used in the studies of this chapter are now described. First, the construction of an anatomically correct 2-layer ‘base model’ is described. Also described is the modelling of EIT electrodes and an EIT injection/ measurement protocol for data acquisition. Next the methods used

to extend this single model to 243 unique models by varying anatomy and electrode positioning are described. Each of these models is in turn extended by adding a single haemorrhagic lesion, varying in size and location, to each to give 1,944 lesion models. The conversion of this set into FEM models suitable for use with EIT software is then outlined. Solving of the forward problem gives EIT measurement frames unique to each model.

The hollow head phantom as described in Section 3.3.3 was used as the physical test platform with the numerical models based on the same geometry. The anatomy of the head model was designed as a 2-layer structure, as described previously in Section 3.3. The layers were anatomically accurate representations of the brain and an aggregate outer layer comprised of the tissues external to the brain. The external layers were the scalp, skull and CSF. These layers were derived from STL files of the head [222] and brain [223]. These two STL files are referred to as the ‘base’ STL files. This simplified numerical model was used as the study was exploratory in nature. Further, the selected numerical model facilitated the use of the anatomically equivalent hollow phantom also described in Section 3.3, allowing comparison between the numerical model results and the phantom results. Finally, the model was computationally light and allowed rapid development of variant test models.

In order to generate a variety of related numerical models, the base STL files were both increased and reduced in size by 5% in each of the X, Y, Z axes, independently, as well in all 3 axes simultaneously. This manipulation was achieved using the Autodesk Fusion 360 CAD package [178]. The $\pm 5\%$ variance was based on work studying adult head circumferences [130] and assumed that variances in circumference will extrapolate to head size and brain size. These variations resulted in 9 different models for each head and brain, with 81 different head and brain combinations created. It is recognised that combinations of, for example, +5% head size coupled with -5% brain size may be unlikely in reality, but such extremes were used here for completeness.

The STL files were meshed into FEM models using EIDORS [170] aided by Netgen [171] and GMSH [172]. During meshing the 16-member electrode ring was also positioned on the exterior of the model with the mesh refined in the areas where the electrodes contact [162]. The electrode ring was placed at three possible heights differing by 2 mm from each other to mimic user error in placing electrodes in repeated experiments. Electrode modelling errors such as these are a key challenge in EIT [180].

CHAPTER 4. MACHINE LEARNING WITH EI MEASUREMENT FRAMES

All possible combinations of head, brain and electrode layout were meshed resulting in 243 normal numerical head models. The head model produced from the base STL files of the head and brain combined with the electrode ring at the middle of the three heights was called the ‘base numerical model’ as it was used as the standard in many of the experiments.

Haemorrhages were modelled as simple spheres, generated using Autodesk Fusion 360. These spheres varied in volume. A 30 ml bleed is often seen as a threshold indicator of worse outcomes in stroke patients [46]. Thus bleeds of 30 ml or larger (60 ml) were chosen for the initial experiment. These correspond to spheres of radius 19.3 mm and 24.3 mm respectively. A second experiment consisted of classifying smaller 5 ml (radius 10.6 mm), 10 ml (radius 13.4 mm), and 20 ml (radius 16.8 mm) more difficult to detect bleeds. The spheres were placed in different locations: the 4 cardinal points of north (front), south (back), east (right side) and west (left side). Further the spheres were in the plane of the electrode rings and inside but towards the exterior surface of and with respect to the FEM model of the brain. Each of the 60 ml and 30 ml bleeds at each of the 4 locations were meshed with each of the 243 possible normal models to form 1,944 separate bleed head models, with each given model having 1 lesion.

Finally, the electrical conductivity of each tissue was assigned with the outer layer given a value of 0.1 Sm^{-1} , the brain layer set at 0.3 Sm^{-1} , and the haemorrhagic lesions 0.7 Sm^{-1} . These are the σ values of these tissues at 100 kHz (Fig. 3.7). The EIT hardware used in the phantom studies further described in Section 4.3.2 operates at the 50 kHz frequency point. Hence this conductivity assignment further facilitates comparison between numerical and phantom results.

After completing the numerical models, EIDORS was then used to solve the forward problem. The EIT setup chosen was a 16-member electrode ring placed symmetrically across the sagittal plane at a one of the three possible heights. Each ring formed a plane from approximately the mid forehead sweeping around to theinion at the rear of the head. The commonly used Skip 2 protocol was adopted, with measurements not taken from the injecting electrodes as is conventional [7], [10] (Section 2.4.3.1). The resultant raw measurement frames are inputted into the classifier. The raw frames are unprocessed or minimally processed by sorting by voltage measurement value. Sorting was undertaken as it was hypothesised that it may improve performance in some scenarios, particularly in those test cases featuring lesions in locations not seen in the training data. The rationale for this sorting is described later in Section 4.4.1.2. This sorting process had not been reported before in the literature.

These computed measurement frames from the models were then used in each numerical study as described later in Section 4.4.1. In Fig. 4.4 the base numerical model with the electrode ring is shown, as well a model with the brain layer hidden and four bleeds illustrating the 60 ml and 30 ml sizes and the four possible locations. The final FEM forward models each comprised approximately 268,240 elements.

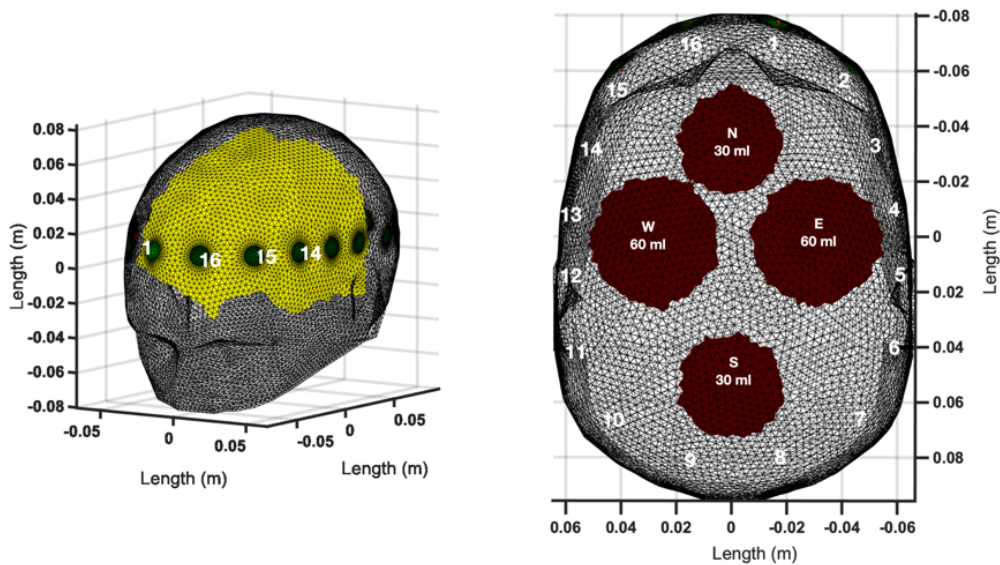


Figure 4.4: Numerical model of the head. Left: The base numerical model is an anatomically accurate 2-layer model of the brain and aggregated tissues external to the brain. The 16-member electrode ring is shown with electrode contact areas in green, and white numbering of some electrodes for orientation. Right: Removal of the brain layer to illustrate the size and positioning of the bleeds. The positioning of the electrodes #1-16 is shown as a ring of white numbers. Bleeds of volume 30 ml and 60 ml are positioned in the north, south, east, and west locations as shown. A given model will contain no bleed or only one bleed. The bleeds are positioned towards the exterior of the brain layer, and in the plane of the ring. The different colouring of the layers represents the different electrical conductivities: 0.1 Sm^{-1} for the aggregate outer layer (white), 0.3 Sm^{-1} for the brain (yellow) and 0.7 Sm^{-1} for bleed (burgundy).

This subsection has outlined the numerical models used in this study and the generation of measurement frames unique to each of the 243 lesion free and 1,944 lesion models. These models allow generation of unique measurement frames. Selections of these measurement frames are used as inputs into the experiments described in Section 4.4.1

4.3.2 Phantom Model and Experimental Setup

The phantom and experimental EIT setup are now outlined. As described in Section 2.4.5, the experimental setup for an EIT study consists of the EIT hardware and the body of interest. Here, the body of interest was the hollow head phantom along with discrete spherical bleed phantoms of 30 ml and 60 ml volume as described in Section 3.3. The conductivity values of the TMMs from which these phantoms were made match those used in the numerical models: 0.1 Sm^{-1} for the outer layer, 0.3 Sm^{-1} for the brain layer (using 0.032 M saline [153]), and 0.7 Sm^{-1} for the bleed phantoms all at 50 kHz. The EIT hardware system used was the Swisstom EIT-Pioneer set, a commercially available system for research [187]. To complete the experimental setup, a ring of 16 EEG electrodes were placed on the head phantom using electrolyte gel [248]. The electrodes are placed symmetrically across the sagittal plane as in the numerical study. These electrodes were connected to the Swisstom EIT-Pioneer set which was connected to a laptop.

Before use the Swisstom EIT-Pioneer set was allowed to warm up for about an hour. Different phantom setups were used as described in each experiment in Section 4.4.2. For each of these experiments, measurements were recorded using the same Skip 2 protocol used in the numerical experiments at 10 frames per second and at 50 kHz. Measurement frames were of about 70 s duration in all setups used. The Swisstom EIT-Pioneer requires 32 electrodes to be connected. By connecting two electrode connections to each EEG electrode in a prescribed manner, and then parsing the frame correctly, the frame for the effective 16-member ring was extrapolated out. Data was collected from the phantom on three consecutive days with the electrodes being repositioned on the phantom head on each day. The saline-filled head without lesions constituted the normal case. Over the course of the daily measurements approximately 24 cases of the normal case were taken. Each of these measurements were of about 70 s each in duration giving ~ 17000 normal frames daily. To further characterise the setup, these measurement frames were used to calculate an approximate figure for the SNR of the system. This SNR was calculated as the ratio of the mean to the standard deviation of the values for each measurement channel for all the frames. The average SNR over the three days was approximately 50 dB.

In Fig. 4.5 the phantom setup with EEG electrodes attached is shown. This figure also shows a phantom lesion being suspended into the saline brain layer, with the aid of wooden rods.

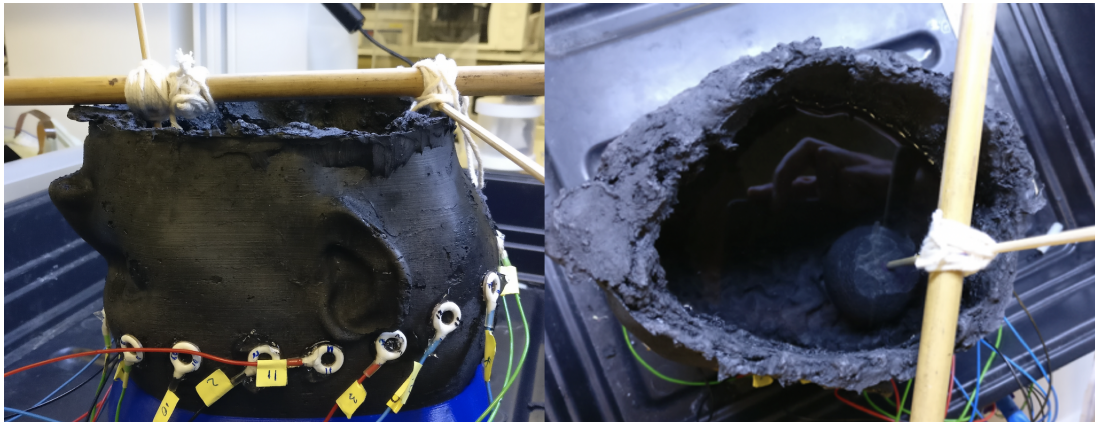


Figure 4.5: Left: The phantom head model with EEG electrodes attached to form a 16-member ring. Right: Wooden rods are used to attach and place lesions inside the saline brain layer. The electrodes are attached to a Swisstom EIT-Pioneer set which records measurement frames.

This section has described both the numerical models, and the corresponding experimental setup used. These test platforms allow the generation of measurement frames under controlled conditions. In the next sections, subsets of these frames are used, with the subsequent assessment of classifier performance when individual parameters are changed.

4.4 Investigations into Effect of Individual Test Parameters

In this section measurement frames collected from the numerical and phantom models, tested with and without a variety of haemorrhagic lesions under a range of experimental conditions each focussed on a key experimental parameter are used to train and test a SVM. The subsequent performance for each experiment is reported and discussed giving an insight as to the effect of each variable. As a final study, the classifier is trained and tested with variants in all of the possible parameters.

4.4.1 Numerical Studies

In this section initial numerical experiments are described. These experiments focussed on the effect of individual parameters such as measurement noise, lesion location, lesion size, electrode position, and anatomy. These parameters constitute important variables. An understanding of the effect they have on measurement frames and consequent performance of the SVM classifier can help inform future

research decisions.

In each of these experiments, raw measurement frames generated from an appropriate subset of FEM models were used to train and test a SVM. The frames were used unprocessed or with minimal processing of the frames performed prior to use of the classifier. Minimal processing constituted sorting the values in the measurement frames in order of numerical value. This simple pre-processing step was empirically found to aid performance in certain scenarios. The specifics of each experiment are given in each subsection that follows. However, the experiments as a whole follow some general principles.

In all cases the training and test sets comprised of an equal number of measurement frames from normal models and models with haemorrhagic lesions present. In both the numerical and phantom studies of this section and Section 4.4.2 a linear SVM classifier was implemented for all experiments. The classifier was trained with data from the training set using nested 10-fold cross validation and hyper-parameter optimisation. Further details on this process are given in Section 4.5. The trained classifier was then tested with the testing set data which comprises frames unseen in the training set. The test data was produced from models having a variant of the parameter under consideration in that particular study unseen in the training data. In all cases the number of frames in the training set was larger than that in the test set [237]. The trained classifier is used at the default operating point to classify the previously unseen test set data. Then the operating point of the classifier was moved to the adjusted point designed to maximise sensitivity with classification of the test set data performed again. The classification results from both the default and adjusted operating points are used to calculate the performance metrics presented in this section. The AUC from the ROC curve is also presented. It should be noted that the reported AUC is a performance metric from the training data, while the other reported metrics are from the unseen test data that has a variant in the parameter under test. Hence the performance results from the training and test sets may not correlate.

This workflow is shown in Fig. 4.6, and is used for the numerical studies in this section as well as for the phantom studies in Section 4.4.2. Each experiment focussing on one particular variable is now described in the following subsections, with the results also presented and discussed. As a final experiment, variants in all of the possible parameters are used to train and test the SVM classifier.

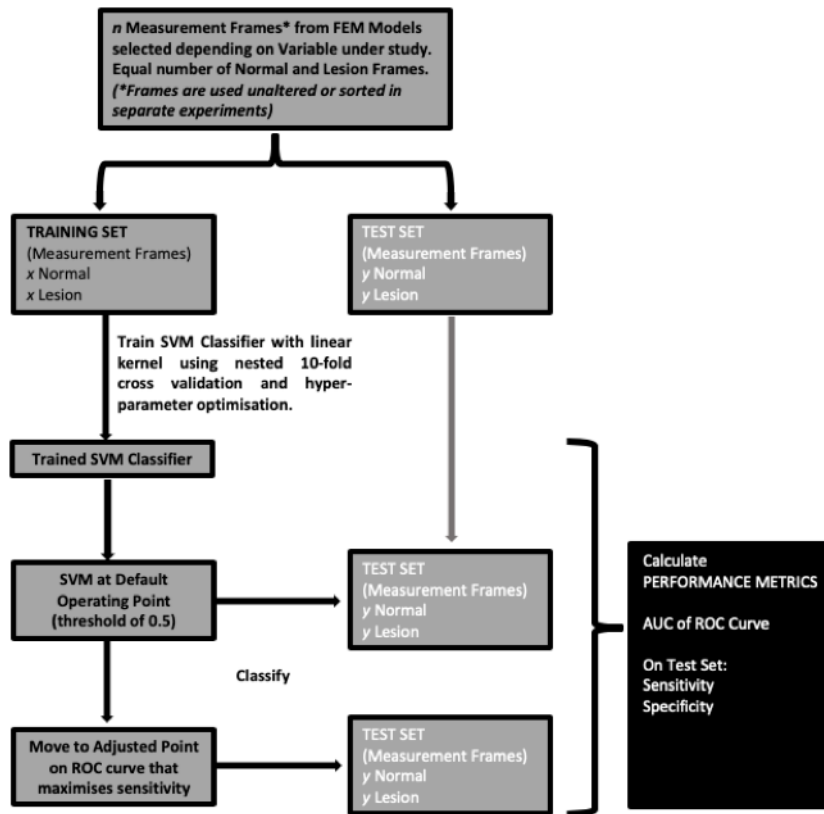


Figure 4.6: Summary of workflow for the application of SVM classifier to measurement frames studying the effect of individual parameters in both numerical studies (Section 4.4.1) and phantom studies (Section 4.4.2). For a given study the complete experiment is performed with the frames unsorted and then with the frames sorted. In all cases the complete set of n measurement frames has an equal number of normal and lesion models, with a greater number used in the training set compared to the test set (i.e. $x > y$).

4.4.1.1 Study 1: Effect of Noise

The level of noise in EIT recordings is an important parameter that can affect performance. Some EIT applications such as thoracic imaging can operate sufficiently well with an SNR of 30 to 40 dB. Other applications require a significantly higher SNR. For example those trying to detect neural signals and facing issues such as the dampening effect of the skull require systems with an SNR of 80 dB or higher [14] (Section 2.4.5). In order to study the effect of noise on data, the performance of each SVM classifier was assessed at different SNR levels selected to cover this range. The levels selected were 80 dB, 60 dB, 40 dB and 20 dB. The base numerical model was used to generate normal measurement frames, with the

30 ml and 60 ml lesions placed in the north location to generate lesion measurement frames. Measurement frames were generated for each of the three models and noise added using tools supplied by EIDORS to achieve each specified SNR [170].

The SNR is defined as:

$$SNR = 20 \log_{10}\left(\frac{Signal}{Noise}\right), \quad (4.4)$$

where the signal and noise are numerical values in Volts.

In order to add random Gaussian noise to a measurement frame, EIDORS generates a vector of same size as the measurement frame of normally distributed random numbers. The values in this vector are then scaled by multiplication by the ratio of the Euclidean norms of the measurement frame and noise vector, before further scaling by division by the desired SNR value. This scaled vector of noise values is added to the measurement frame, resulting in a ‘noisy’ frame.

Next the training and testing of the SVM classifier was performed as now described. A linear SVM was trained with 500 measurement frames with 250 normal and 125 from each of the two lesion models. This trained SVM model was then tested with 200 unseen measurement frames: 100 normal and 50 from the two lesion models. This training and testing was performed at each of 80 dB, 60 dB, 40 dB and 20 dB noise levels. As detailed above in Section 4.4.1, the raw measurement frames are either unsorted or sorted by value (low voltage to high voltage). Hence, each SNR level has two corresponding SVM models trained and tested using these two frame types each with an AUC reported. In addition, the sensitivity and specificity for each classifier at each SNR level has two performance values: that when tested at the default operating point and then when retested at the adjusted operating point designed to maximise sensitivity. These results are shown in Fig. 4.7.

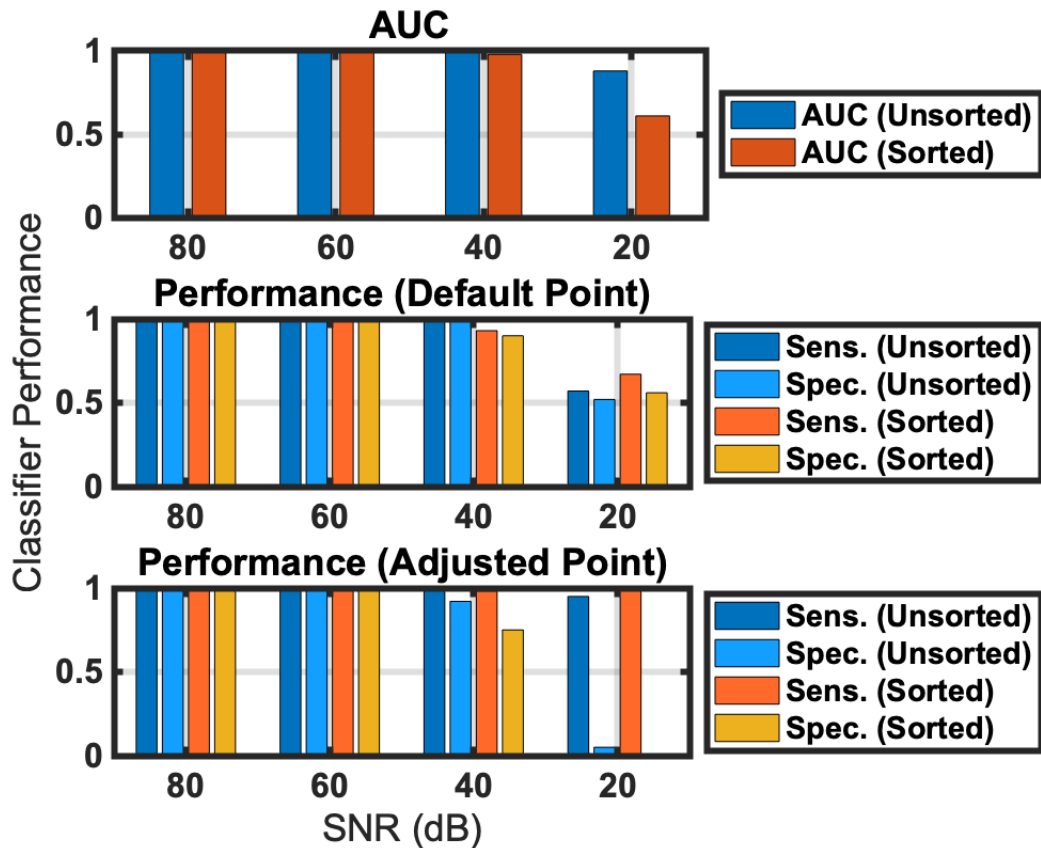


Figure 4.7: Classifier results from test data in numerical model Study 1: Effect of Noise. Separate experiments are done for 80 dB, 60 dB, 40 dB, and 20 dB noise levels. The raw measurement frames used to train and test the linear SVM are unsorted or sorted by numerical value. For both of these resultant classifier models, the performance is given as the AUC of the ROC curve generated from the training data and the sensitivity (Sens.) and specificity (Spec.) of the classifier on the test data at the default operating point and at the adjusted operating point. The adjusted operating point is selected to augment sensitivity, at the expense of specificity. From the plots, it is seen that the classifiers perform well at 80 dB and 60 dB with performance starting to drop at 40 dB and becoming poor at 20 dB. The adjusted operating point does boost sensitivity as expected. This boost in sensitivity has most obvious benefit seen at 40 dB.

The results of Fig. 4.7 show that the SVM classifier performs well with both the unsorted and sorted raw measurement frames with an AUC, as well as sensitivity and specificity at or near 1 for the 80 dB and 60 dB noise levels. At 40 dB, the classifier performance significantly degrades and the benefit of the adjusted operating point compared to the default operating point is apparent, as sensitivity is boosted at the

expense of specificity. For example in the sorted frame results the sensitivity jumps from 0.92 to 1.0 while the specificity drops from 0.9 to 0.78. The performance at 20 dB is poor and there is no significant difference in the performance between using the unsorted or the sorted frames. The SNR value of 20 dB was chosen as an extreme value, significantly lower than that used even in high contrast time changing scenes such as thoracic EIT [14]. As such, the poor performance reported at this value is expected and helps to establish a lower limit on the acceptable SNR range that can be used.

It was also of interest in this part of the study to analyse if the measurement frames could be used to detect lesion location and size. A haemorrhagic lesion has a higher conductivity than the surrounding brain. Hence, a given channel of the measurement frame (i.e. one specific combination of injecting and measurement electrode pairs) would be expected to give a lower measured voltage magnitude for the fixed injection current if the lesion is near to the electrodes involved in the channel. The channel that had the maximal average difference in value between the normal frames and the lesion frames was calculated for both cases of the 30 ml and 60 ml haemorrhage in the north location. The electrode layout used meant that electrodes #1 & #16 lie in front of the north location with #2 & #15 also nearby and so on. These maximal difference channels are shown in Fig. 4.8. These maximal difference channels as expected feature electrodes directly adjacent to the lesion location. It would also be expected that the magnitude of the difference would be greater for the 60 ml bleed than the 30 ml bleed compared to the normal and these differences should be clearer at higher SNR. Fig. 4.8 confirms these hypotheses with plots of voltage measurements at the maximal difference channel shown for the 80 dB and 40 dB cases. The separation is indeed greater for the 60 ml bleed and the separation is more distinct for the 80 dB SNR case. It should be noted that such information on lesion location is lost if sorting of frames is performed, but sorting aids in some cases where lesion detection is challenging as is discussed in subsection 4.4.1.2.

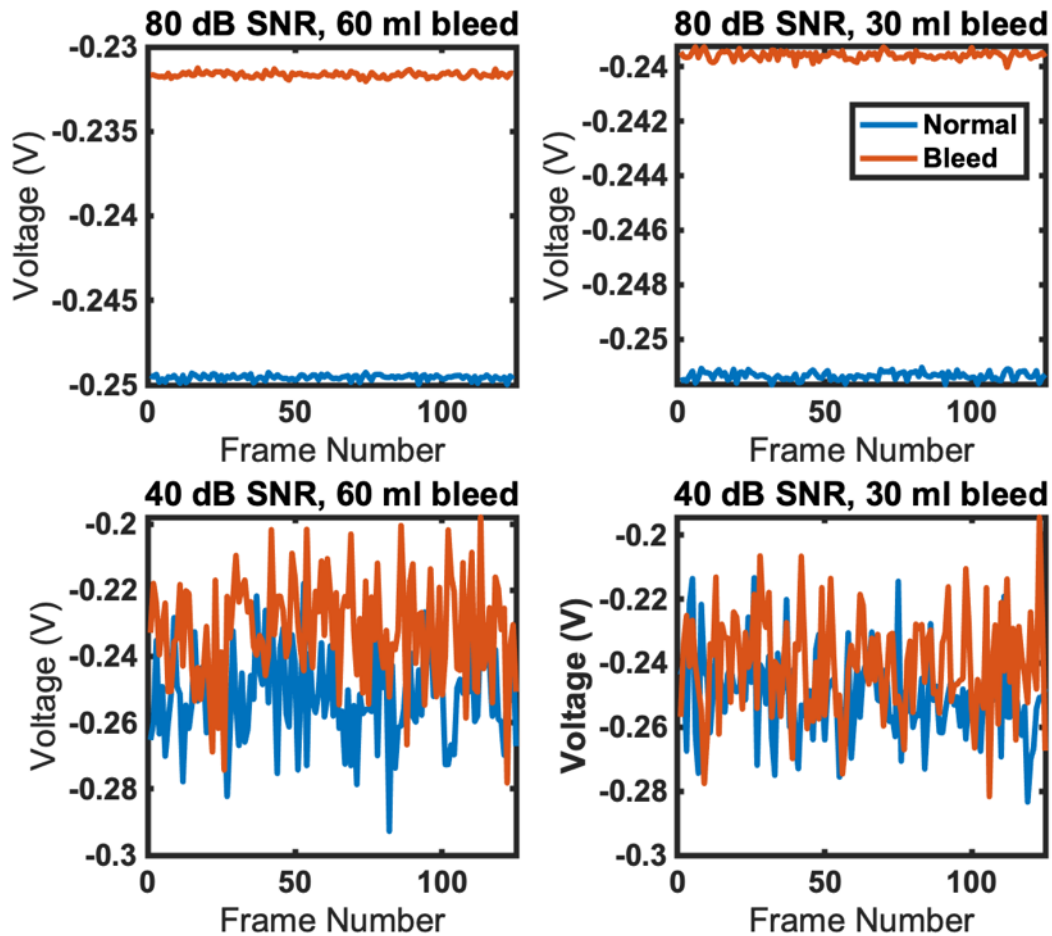


Figure 4.8: The channels of maximal difference between the normal and lesion cases are reported. The channels suggest the lesion may be at the north location, as electrodes involved in these channels (for example #1 & #16) are adjacent to this location. The 60 ml bleed shows a greater difference relative to the normal than does the 30 ml case. Further, separation is more distinct at a higher SNR with overlap increasing at 40 dB.

This study investigating the effect of noise on SVM performance has shown that near perfect performance is maintained down to a SNR of about 60 dB. Further, information on lesion location and size is possible to infer directly from measurement frames based on the pattern of voltages recorded by channels near a given lesion provided the SNR is sufficiently high, as is shown in Fig. 4.8. The next subsection further examines the effect of lesion location.

4.4.1.2 Study 2: Effect of Lesion Location

In this study performance of a trained classifier was assessed with test data from lesions in locations unseen in the training data. In order to implement this experiment the base numerical model was again used as the normal case, with both the 30 ml and 60 ml lesions added to the north location separately. These models were used to train the classifier with 500 measurement frames: 250 from the normal and 125 each from the two lesion models. The performance was then tested with 120 unseen normal measurement frames and 20 measurement frames each from 6 lesion models. These lesion models were created from all individual combinations of lesions of volume 30 ml or 60 ml, in each of the east, south, and west locations. Hence, the classifier was tested on lesions in locations that were not included in the training set.

As before the results are presented with the two classifiers trained with unsorted or sorted raw measurement frames, giving two separate AUC values from the respective ROC curves generated from the training data. Next, the sensitivity and specificity for each classifier on the test data is reported at both the default operating point and at the adjusted operating point selected for better sensitivity. The experiment is repeated for each of 80 dB, 60 dB, 40 dB, and 20 dB simulated noise levels with the results shown in Fig. 4.9.

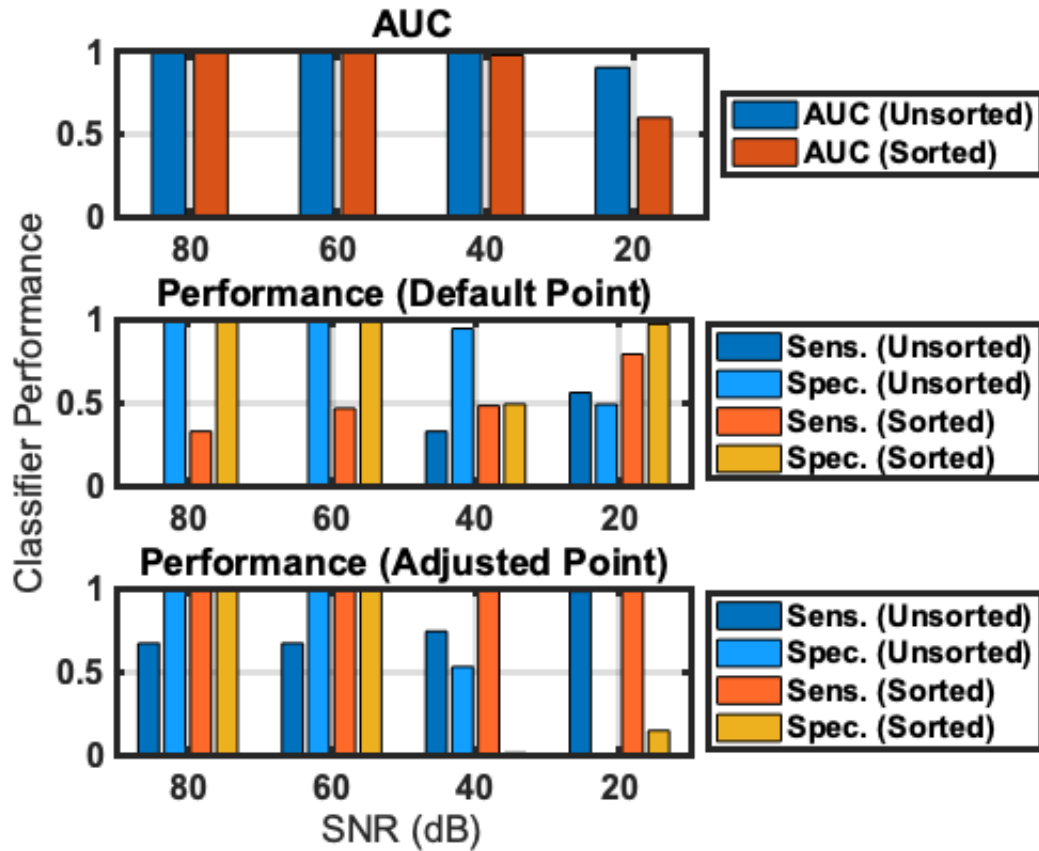


Figure 4.9: Classifier results from test data in numerical model Study 2: Effect of Lesion Location. Separate experiments are done for 80 dB, 60 dB, 40 dB, and 20 dB noise levels with results arranged in the same format as Fig. 4.7. Both using a sorted measurement frame and the adjusted operating point dramatically improve sensitivity at a given SNR. Implementing both of these modifications result in excellent classifier performance at the 80 dB and 60 dB points, indicating that in these cases the classifier still works well even when test data lesion locations differ from training data locations.

The results from Fig. 4.9 show that if the raw measurement frames are left unsorted and classification is performed at the default operating point, then sensitivity is low at all SNRs: at about 0 for 80 dB and 60 dB and at about 0.55 for 20 dB. An explanation for this paradoxical result at 20 dB may be the introduction of general inability to differentiate normal from bleed at lower SNR levels as evidenced by the drop in specificity. Moving to the adjusted operating point with unsorted measurement frames helps to improve sensitivity with values now above 0.6 in all cases. Despite this improvement the sensitivity is still unacceptably low. In this

case, the classifier cannot detect lesions when the location of the test case is one the classifier is not trained on. Specificity is not as affected as this is primarily a measure of ability to detect the -1 class of normal. The classifier is trained and tested on this normal case. However, the simple pre-processing step of sorting the raw measurement frame values from low to high helps boost sensitivity at all SNR levels compared to the respective unsorted case.

The purpose of sorting the frames is to aid the classifier in correctly classifying lesions at locations not seen previously in the test set. As described in Section 4.4.1.1, the presence of the lesion should result in lower magnitude voltage measurements especially for those channels in the locality of the lesion. In the normal case sorting should not overly affect the frame, at least in this simple model where electrode distance and regional differences in tissues are neglected. In the case of a lesion, sorting should result in a similar resultant frame regardless of lesion location. The results shown in Fig. 4.9 provide evidence supporting this hypothesis. The adjusted operating point further boosts sensitivity with excellent performance of sensitivity and specificity both equal to 1, seen at both 80 dB and 60 dB when the measurement frames are sorted.

This section has analysed the effect of lesions in unseen locations on classifier performance. If frames are sorted and the adjusted operating point is chosen, then the classifier seems to be independent of the lesion locations used, for the 60 dB and 80 dB SNR levels. The next subsection examines the effect of lesion size.

4.4.1.3 Study 3: Effect of Lesion Size

As described in Section 4.4.1.1, the voltage measurements will deviate more from the normal values with a larger size of lesion. To investigate this effect of lesion size, measurements were taken from the base numerical normal model, and then from models with lesions of 60 ml, 30 ml, 20 ml, 10 ml, and 5 ml at each of the 4 locations (i.e. one normal model, and 20 lesion models). Measurement frames at a noise level of 60 dB SNR were produced from each of these 21 models. The methodology of this study was to perform two sub-studies:

- Train with measurement frames from the normal, and models using the largest lesion (60 ml), before testing using unseen measurement frames from the normal, and all lesion models with smaller size lesions;
- Train with measurement frames from the normal, and models using the smallest lesion case (5 ml), before testing using unseen measurement frames from the normal, and all lesion models with larger size lesions.

CHAPTER 4. MACHINE LEARNING WITH EI MEASUREMENT FRAMES

In order to perform these studies, 300 noisy measurement frames were generated from the base numerical normal model. Next, 75 measurement frames were generated from each of the four 60 ml lesion models which differ in lesion location. Hence 300 noisy measurement frames in total were generated using the 60 ml lesion. In an identical manner 300 noisy measurement frames were each produced from the 30 ml, 20 ml, 10 ml and 5 ml lesions. This set of normal and lesion measurement frames were used to study the performance of the classifier when tested with lesions of sizes not used in the training set.

In order to perform the first sub-study SVM classifiers were trained using the 300 measurement frames from the normal model, and the 300 frames from the model with the 60 ml lesion, either as unsorted or sorted frames. The resultant classifiers both had an AUC value of 1. Next, the trained classifier models were tested using 80 unseen normal frames and 80 unseen frames from the 30 ml lesion positioned at each of the 4 locations (20 frames from each location). The testing was repeated in an identical way for each of 20 ml, 10 ml and 5 ml model lesions. Hence, the models are trained on the largest lesion and tested sequentially on each of the smaller lesions.

The classifier performance results for sensitivity and specificity are given in Fig. 4.10. These results indicate that when the classifiers are trained using the 60 ml lesion there is an inability to detect smaller test lesions unless the adjusted operating point is used. The best value for sensitivity observed was 0.63 when using unsorted frames when detecting the 30 ml bleed. Again, the specificity is not affected as the normal cases are the same in both the training and test sets. Since training featured cases from all locations the benefit of the sorted frame which was very effective in the previous study on effect of location, is redundant here. If the adjusted operating point is used increasing sensitivity, then robust classification (sensitivity and specificity both of 1) down to a 10 ml volume is achieved.

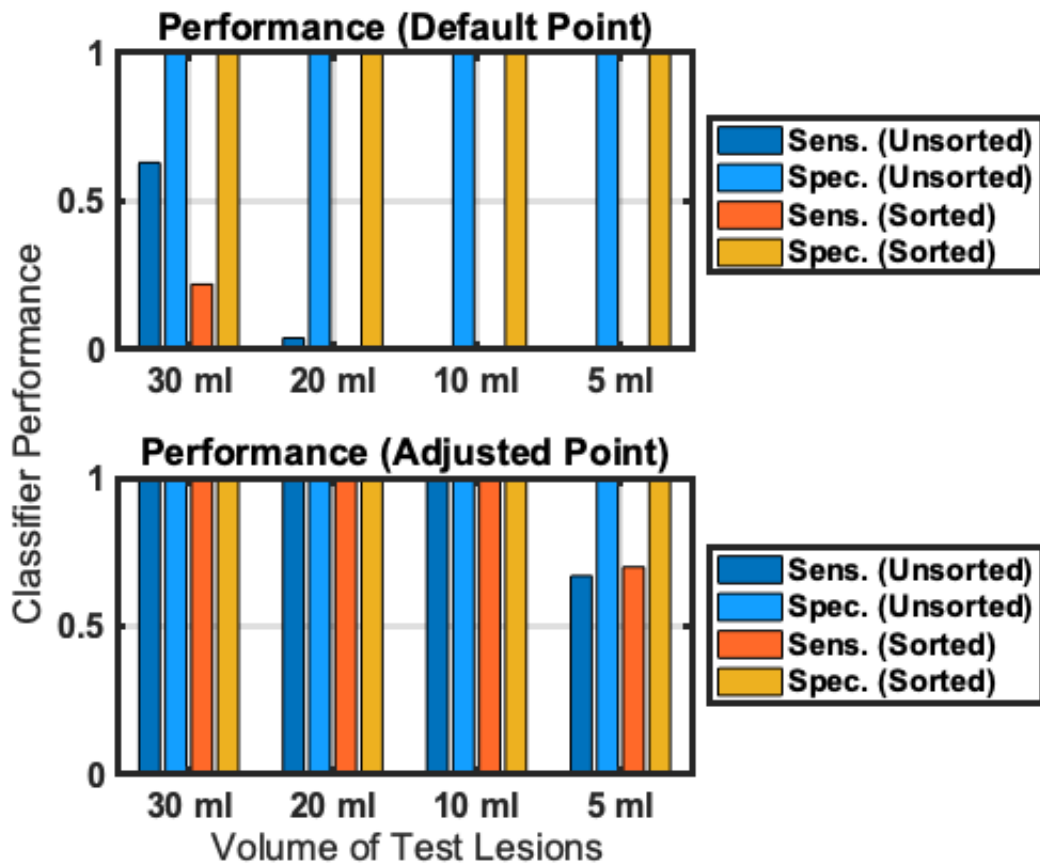


Figure 4.10: Classifier results from test data in numerical model Study 3: Effect of Lesion Size. The models are trained using the 60 ml lesion in all possible locations in the base numerical model. Separate testing is then performed on unseen normal frames and separately each of 30 ml, 20 ml, 10 ml, and 5 ml lesion at all locations, with 60 dB noise added in all cases. Training data features all locations, rendering the effect of sorting the frame redundant. Using the adjusted operating point boosts sensitivity in all cases with lesions robustly detectable down to a 10 ml volume.

Next, the entire experiment was repeated in order to perform the second sub-study. This time training was performed on the smallest lesion (5 ml) and testing on the 60 ml, 30 ml, 20 ml and 10 ml cases. The normal case being used throughout as in the previous experiment. The trained classifiers both reported an AUC of 1 again. These testing results are given in Fig. 4.11 with improved performance compared to Fig. 4.10. All larger test lesion sizes are detected at the default operating point with generally good performance (sensitivity and specificity near 1). As discussed in Section 4.4.1.1, the magnitude of voltage measurements are related to lesion size with larger lesions affecting measurements more than smaller one. Hence,

training with a small lesion ‘sensitises’ the classifier to the lesion type with larger lesions resulting in even more pronounced changes in voltages and hence easier classification as bleeds. Changing to the adjusted operating point unnecessarily decreases specificity with unsorted frames, although sorted frames are more robust to this effect giving nearly the same performance at both operating points. In this case, sensitivity of 1 was achieved at the default operating point using the default threshold. Moving to the adjusted point which forces the threshold up unnecessarily increased the number of false positives with no reduction in false negatives. In cases like here where the default threshold of 0.5 already gives a sensitivity of 1 the adjusted threshold is also 0.5. However, the adjusted threshold now categorises cases with an equal probability of being +1 or -1 as being +1 (bleed) whereas the default threshold categorises these cases as -1 (not bleed). This classifying of 50/50 cases as bleeds is an attempt to err on the side of caution, which is appropriate given the intended clinical application. Hence, this subtle change causes a reduction in specificity in these cases.

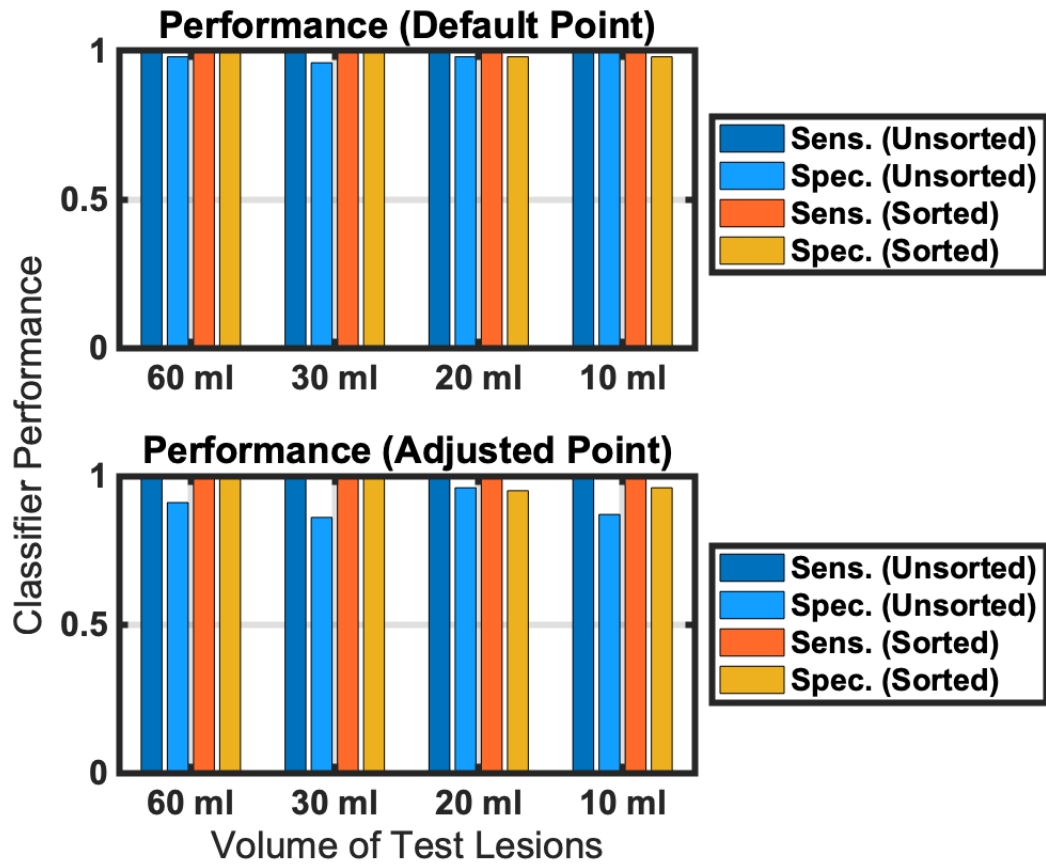


Figure 4.11: Classifier results from test data in numerical model Study 3: Effect of Lesion Size. The models are trained using the 5 ml lesion in all possible locations in the base numerical model. Separate testing is then performed on unseen normal frames and separately each of 60 ml, 30 ml, 20 ml, and 10 ml lesion at all locations, with 60 dB noise added in all cases. Training data features all locations, rendering the effect of sorting the frame redundant. Sensitivity and specificity in all cases is excellent at the default operating point, while using the adjusted operating point unnecessarily reduces specificity of the classifier that uses unsorted frames but does not appreciably affect performance of the classifier that uses sorted frames.

In this section, the effect of lesion size on classifier performance was investigated. The results indicate that performance is best when trained on lesions smaller than those in the subsequent test set. In the next subsection the effect of electrode positioning is investigated.

4.4.1.4 Study 4: Effect of Electrode Positioning

Recent literature suggests that EIT is sensitive to errors in electrode positioning [180]. In order to investigate this effect in this study, the positioning of the electrode ring was varied while all other parameters were kept constant. In all training and test cases 60 dB simulated noise was added to the measurement frames. The classifiers for both raw unsorted and sorted frames were trained on a data set of 640 measurement frames. Each data set comprised 320 measurement frames from the base numerical model and 40 measurement frames from each of the 8 combinations of the 30 ml and 60 ml bleeds at each of the 4 possible locations. Both classifiers, when trained returned an AUC value of 1.

Next these one normal and 8 lesion models had the electrode ring positioned at one of the two locations that deviated from the original training position. This deviated position was ± 2 mm with respect to the original, and such that the plane of the ring was parallel to the original. These position changes mimic user error in positioning of the ring. Further, errors in electrode placement of the order of mm are known to have a significant impact on EIT, particularly when tdEIT is not used [8], [20]. Each new normal model was used to produce 40 measurement frames and each new lesion model used to produce 5 measurement frames giving a testing set of 80 normal, and 80 abnormal measurement frames.

The intention of this study was to mimic a minor error in electrode positioning when placing the ring on a patient's head. Even such a minor movement causes a noticeable drop in performance, with the results falling from 1.0 sensitivity to a sensitivity value of 0.95 in the case of unsorted measurement frames, and 0.97 for the sorted measurement frames when using the default operating point. This reduction in performance demonstrates that even changes in electrode ring position of the order of millimetres can cause challenges in EIT. However, using the adjusted operating point sees sensitivity moving back to 1.0 again without affecting specificity (which in all cases tested remained at 1.0) thus mitigating the effects of the 2 mm positional error. This result demonstrates the value of the adjusted operating point in such scenarios. In the next subsection a study of variation in anatomy is presented.

4.4.1.5 Study 5: Effect of Normal Variation in Inter-Patient Anatomy

This study examined the ability of the classifier to detect lesions in head and brain anatomies different to the anatomy the training data set is recorded from. All frames used in training and testing had 60 dB noise added. The study was designed using training models comprised of the base numerical model as the normal, with 8

lesion models produced from the normal using all 8 combinations of the 30 ml and 60 ml lesion at all locations. In total 5,120 normal and 5,120 lesion (640 from each lesion model) measurement frames were used to train the classifier. The resultant classifiers trained from the unsorted or sorted measurement frames both reported an AUC value of 1. The test set was comprised of measurement frames from 80 other anatomies. These anatomies differ in the size of both the aggregate outer layer and brain layer by $\pm 5\%$ in the three Cartesian axes but had the electrode ring in the same position (as described in section 4.3.1). These anatomies are used to generate measurement frames with and without the equivalent lesions present. Each of the 80 other normal anatomies were each used to create 16 test normal frames each. Each of these normal models were then combined with each of the 8 possible lesions to create 640 lesion cases with 2 frames from each used to complete the test set. Hence, the classifier was trained on lesions in one anatomy but tested on lesions in a variety of 80 different anatomies.

The results indicate the classifier struggles with unseen anatomy, with sensitivity and specificity metrics all < 0.6 for the classifiers trained with both the unsorted and sorted raw measurement frames. This represents a decrease in over 40% from the classifier performance with known anatomies. Further analysis showed that an excess of brain tissue or lack of outer tissue in a test model compared to the training model was often misclassified as a bleed. Conversely, lack of brain tissue or excess outer tissue compared to the training model was often misclassified as normal. In some cases a larger lesion size could be correctly classified despite anatomical differences, but in general the classifiers were excessively sensitive to differences in anatomy of the test models compared to that used to train. This subsection completes the set of numerical studies investigating individual test parameters. A final subsection looks at the effect of variation in all these parameters simultaneously.

4.4.1.6 Study 6: Final Overall Study with All Test Parameters

As a final overall analysis, a series of tests were completed featuring all 243 normal models and 1944 lesion models with all variants in all of the possible parameters used to train and test the SVM classifier. As described in Section 4.3.1, the base STL files of the head and brain were each distorted by $\pm 5\%$ in each of the X, Y, Z axes independently as well as in all 3 axes simultaneously, resulting in 9 distinct head and brain models and hence 81 different combinations. The 16-member electrode ring was then placed at 1 of 3 distinct locations giving 243 models of the normal.

To create the lesion models, each of these 243 normal models were combined

with one the 30 ml or 60 ml haemorrhages at one of the 4 locations. All permutations of these lesion size and locations resulted in the 1,944 lesion models. These models were used to train and test the SVM classifiers with the training and test sets comprised of 139,968 and 15,552 measurement frames, respectively. In each case the sets were evenly divided between frames from the normal and lesion models, with each of these two subsets further divided to ensure an identical number of frames are provided by each model contributing to each set. Hence, each of the 243 normal models each contributed an equal number of frames totalling 69,984 for the training set and 7,776 for the test set. Likewise for each of the 1,944 lesion models contributed equally to the 69,984 lesion measurement frames used for the training set and 7,776 lesion measurement frames used for the test set. Raw measurement frames were again used either unsorted or sorted, resulting in two classifiers. This experimental setup was repeated for each of 80 dB, 60 dB, 40 dB and 20 dB noise levels.

The AUC of the trained classifiers, and the sensitivity and specificity of the classifiers on the test sets are reported in Fig. 4.12. These results show that the classifiers perform well at the 80 dB and 60 dB noise levels. There is a subsequent drop in AUC, sensitivity, and specificity seen at the 40 dB level and the classifier performing little better than random at 20 dB SNR. There is little difference in the results produced from using the unsorted or sorted frames, except at the 80 dB level where the sorted frames result in a small but noticeable improvement. The sorted frames were developed to compensate for the challenges in encountering lesions in the test sets at locations not seen in the training set, but this is not the case in this study. Using the adjusted operating point does boost sensitivity. However use of the adjusted operating point also causes a perhaps unacceptable drop in specificity. The overall effect is a drop in false negatives but maybe an excessive level of false positives.

This overall study indicates the system performs well provided the SNR does not drop below 60 dB, and ideally at 80 dB or better. Further, the sensitivity/specificity balance seems to be the best at the default operating point. However, if the motivation is to eliminate false negatives in order to be confident that bleed cases are not misclassified, then the adjusted operating point may be preferable. It is seen that the performance at the adjusted operating point for the sorted frames at 80 dB has a sensitivity of 1 and a specificity of ~ 0.6 . Presumably moving to 90 dB or higher would increase this specificity, making an even stronger argument for working at the adjusted operating point.

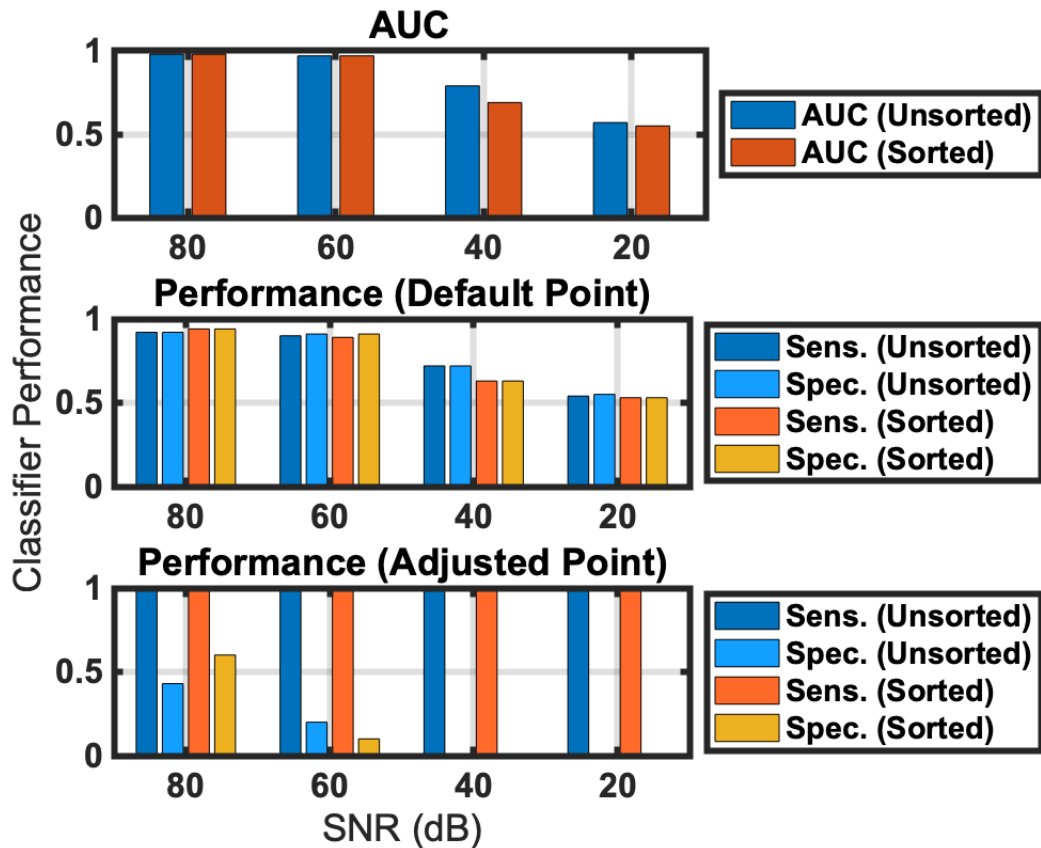


Figure 4.12: Classifier results from test data in numerical model Study 6: Final Overall Study. The classifiers perform well at the 80 dB and 60 dB points. The sorting of the frames developed to compensate for test data featuring lesions in previously unseen locations has little effect as training features cases from all 4 locations. However, there is a noticeable improvement when using sorted frames at the 80 dB point. Using the adjusted operating point increases sensitivity in all cases at the expense of a perhaps unacceptable drop in specificity.

4.4.2 Phantom Studies

This section describes studies completed on the phantom test platform. These studies were analogous to those performed with the numerical models in Section 4.4.1. A hollow head phantom was used with spherical bleed phantoms, and the Swisstom EIT-Pioneer EIT system [187] was used to produce all measurement frames operating at the noise level inherent to the setup. Hence, it was not possible to fully replicate the variety of models and noise levels used in numerical

experiments. However even with this limitation, a series of five experiments were performed. These experiments included an initial study examining repeatability before analysing the effect of location, size, electrode placement variation, and a final overall experiment. The phantom and hardware were described in Section 4.3.2, with each study now outlined and results reported and discussed.

4.4.2.1 Study 1: Repeatability

In this study, the ability to achieve repeatable results on different days was assessed. The ability to reproduce readings with fidelity is an important parameter to consider with any system. In order to investigate this parameter, raw measurement frames were taken using the setup described above in Section 4.3.2. The brain layer was free of lesions (normal) or with either the 30 ml or 60 ml lesion in the north location. Six recording sets were taken of the normal case and three sets taken of each of the two lesion cases. The order of recording the sets was randomised and each recording set was approximately 70 s (700 frames) in length. The experiment was performed on 3 separate days, with the electrode ring placed each day as described in Section 4.3.2 and the phantom re-filled with saline. For the frames produced from each day, linear SVM classifiers were trained with 6,800 randomly selected raw measurement frames either unsorted or sorted (3,400 normal and 1,700 from each of the two lesion cases). The trained SVM was then tested with 800 unseen raw measurement frames again, evenly selected as 400 normal and 200 from each lesion case and either unsorted or sorted.

The AUC of the trained classifiers is reported, along with the performance on the test data. These results are shown for each of the 3 days experiments in Fig. 4.13. The results show a variance in the performance for each of the three days. However, the AUC is always > 0.8 and sensitivity approaches 1 in all cases if the adjusted operating point is used. However using the adjusted operating point has a negative impact on the specificity, the magnitude of which varies between days.

The differences in results over the 3 days show the challenge in achieving repeatability using an EIT system, which is sensitive to effects such as changes in electrode contact and positioning which may vary day to day and over the course of a day as the contact gel dries out [8].

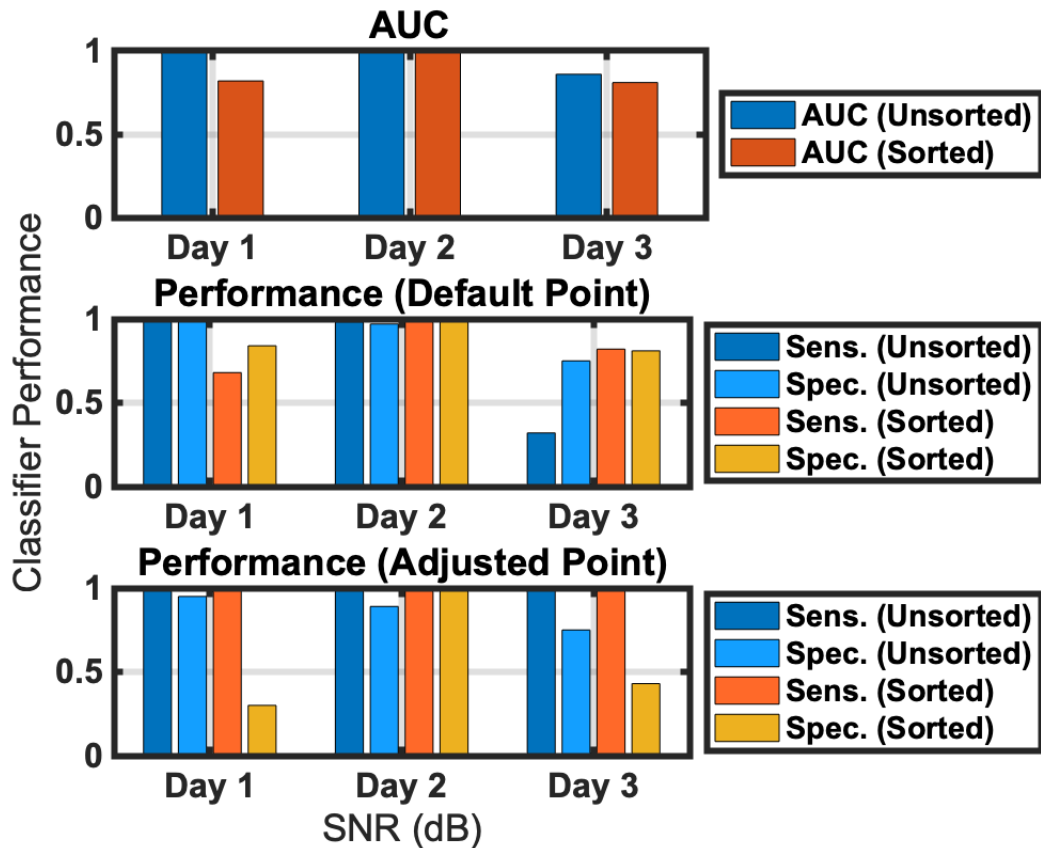


Figure 4.13: Classifier results from test data in phantom model Study 1: Repeatability. Variances are seen in performance of the same experiment on each of the 3 days. Sensitivity approaches 1 in all cases when the adjusted operating point is used, with a variable reduction in specificity depending on the day.

4.4.2.2 Study 2: Effect of Lesion Location

This location effect study is analogous to that described in Section 4.4.1.2, where the performance of the classifier was tested with lesions placed in locations different to those used in the training set. The design of the study was such that the training sets were comprised of 7,800 raw measurement frames made up of equal amounts of normal and lesion phantom models. The lesion models were the 30 ml or 60 ml bleed in the north location, with an equal number of each making up the lesion measurement frames. The test set was comprised of 1,200 raw measurement frames of which 600 were unseen normal measurement frames and the remaining lesion measurement frames composed of 100 each from all combinations of the

CHAPTER 4. MACHINE LEARNING WITH EI MEASUREMENT FRAMES

30 ml and 60 ml bleeds at each of the other 3 locations of east, south and west. The measurement frames sets were taken as 70s recordings of each lesion case, repeated 3 times. The normal case was repeated 24 times. A randomised order of measurements was computed, with random measurements selected for training and testing with no overlap. The complete experiment was repeated on 3 consecutive days. The training and test raw measurement frame sets were again used unsorted or sorted with the results shown in Fig. 4.14.

The results again show the variance in day to day repeatability of the experiments on a real-life phantom. On average over the 3 days, the best overall performance is seen when the frames are sorted by numerical value, and classification is performed at the adjusted operating point to maximise sensitivity. This conclusion is consistent with the results observed in Fig. 4.9. The sorting of the frames should theoretically offer a robustness to differences in lesion location. While this effect is not as pronounced as in the numerical model, it is observed in this equivalent phantom experiment.

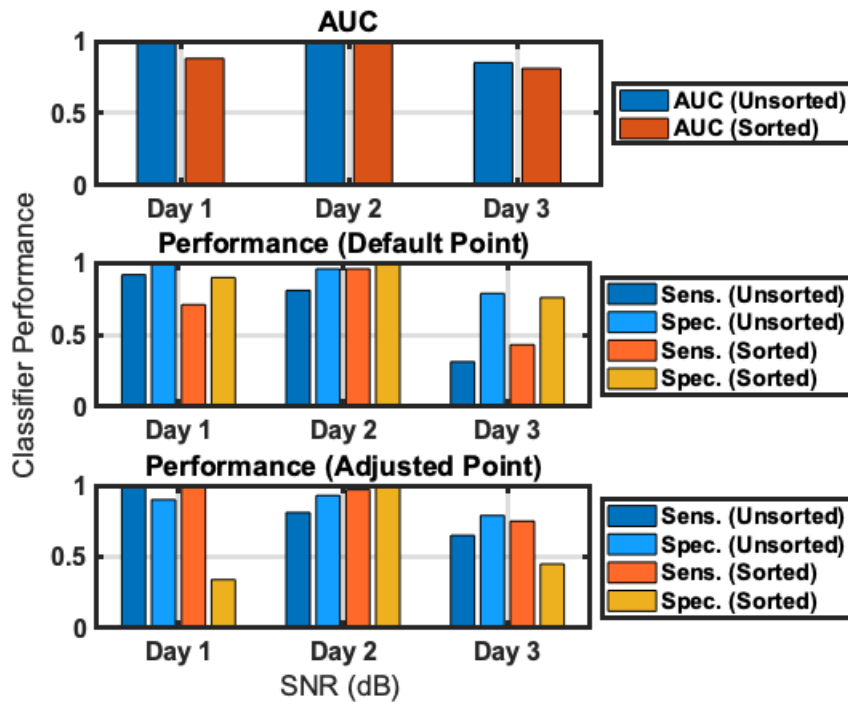


Figure 4.14: Classifier results from test data in phantom model Study 2: Effect of Lesion Location. On average, the best overall performance is seen when the raw measurement frames are sorted, and classification performed at the adjusted point designed to maximise sensitivity. Results are seen to differ from day to day as expected due to variation in electrode positioning and other sources of systematic error.

4.4.2.3 Study 3: Effect of Lesion Size

This study is similar to that described in Section 4.4.1.3. Firstly an examination was performed into classifier performance in detecting lesions smaller than those in the training set. The classifiers were trained with recorded raw measurement frames of both the normal (lesion free) phantom, and from the phantom with the 60 ml lesion at one of the 4 positions. The trained classifiers were then tested on unseen normal measurement frames and measurement frames from when the 30 ml lesion was placed at one of the 4 positions. The training set comprised 14,800 measurement frames and the test set comprised 1,600 measurement frames. Each set was evenly divided between normal and lesion measurement frames with the lesion measurement frames further evenly split between all 4 positions.

The measurement frames were gathered in the same way as described in Section 4.4.2.2. The raw measurement frames were used either unsorted or sorted.

The results are shown in Fig. 4.15. As a result of the normal being the same for both the training and test measurement frames (aside from frame to frame changes in random measurement noise), specificity should be, and is, high. Sensitivity was low if using the default operating point but rises to about 80% when using the adjusted operating point for the data taken on Day 1, dropping to 60% on the Day 3 data. These results imply a challenge in detecting smaller volume lesions in the phantom than those featured in the training set.

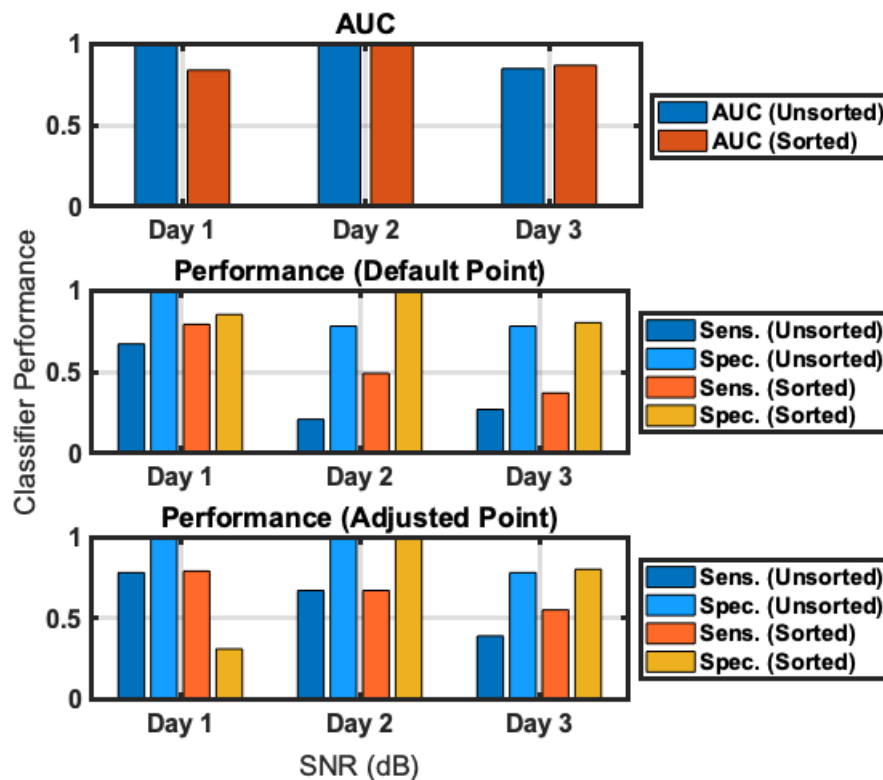


Figure 4.15: Classifier results from test data in phantom model Study 3: Effect of Lesion Size - detection of lesions smaller than those in the training set. Specificity is high in all cases, which is a consequence of the normal model being the same for the training and test measurement frames. Sensitivity is boosted using the adjusted point reaching about 80% using the results from Day 1 but dropping to under 60% for Day 3.

Next, the experiment was repeated in an identical manner except for a reversal in the use of the measurement frames from the 60 ml and 30 ml lesion models. Hence, the performance of the classifier in detecting lesions larger than those in the training set was assessed, analogous to the second sub-study of Section 4.4.1.3.

The results are shown in Fig. 4.16. Specificity is again expected to be high, with this prediction borne out with the exception of the measurements from Day 1. It is postulated that training with the smaller 30 ml lesion may have resulted in miss-classification of some normal cases as lesion cases. This may be as the difference in measurement frame values between the normal and 30 ml lesion is not as pronounced as that in the previous phantom sub-study which used the larger 60 ml lesion size for training. Sensitivity is improved compared to the the results from Fig. 4.15. This result correlates with those of Section 4.4.1.3 with the classifier performing better in detecting lesions larger than those trained with. Again use of the adjusted operating point improves sensitivity with 100% sensitivity being achieved on all days.

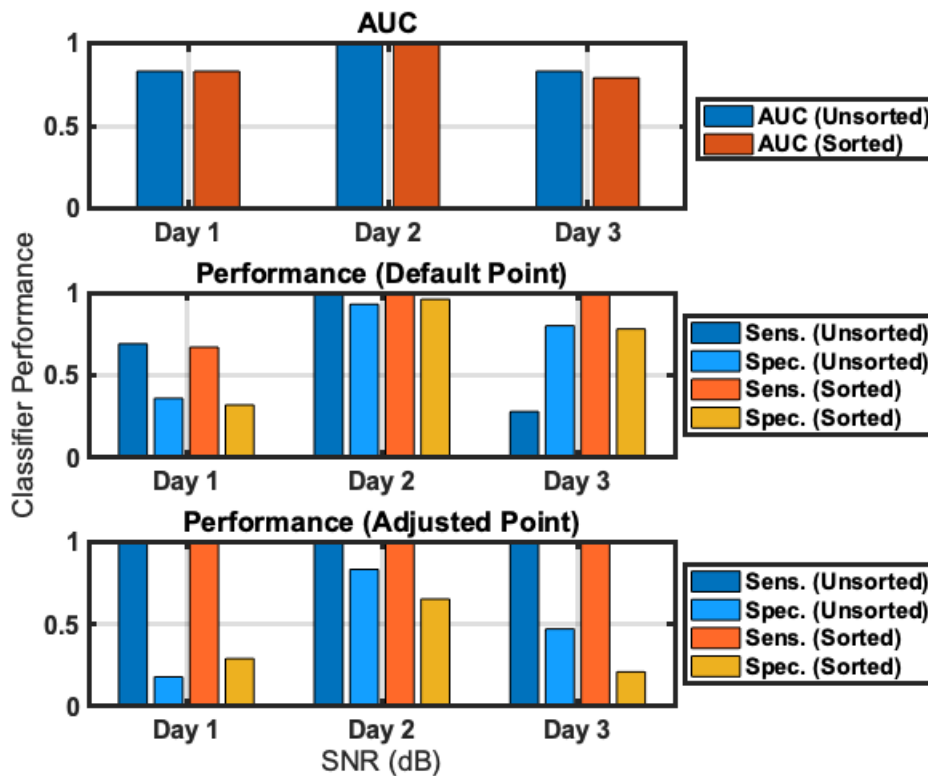


Figure 4.16: Classifier results from test data in phantom model Study 3: Effect of Lesion Size - detection of lesions larger than those in the training set. Specificity is generally high in all cases, with the exception of Day 1. The use of smaller lesions for training may result in increased false positives. Sensitivity is higher than in Fig. 4.15, and is boosted using the adjusted point reaching 100% on all days.

4.4.2.4 Study 4: Effect of Electrode Positioning and Variation in Anatomy

In this study, raw measurement frames from normal and lesion cases taken on a given day were used to train a classifier. Measurement frames from a different day were then used to test. Since the platform was setup anew each day this experiment modelled changes in electrode positioning due to the physical inability to position the electrodes in precisely the same location from day to day. The experiment also investigated different anatomies, since the electrodes were in contact with a different part of the phantom on the different days. On a given day the 8 lesion cases (all combinations of the 30 ml and 60 ml lesions in all 4 locations) had approximately 70s recordings taken 3 times with 24 normal recordings of the empty saline brain also taken. The order of the recording was randomised. Again, the raw measurement frames are used either unsorted or sorted by numerical value. In total, 14,400 measurement frames were used to train with 1,440 used to test. The sets were evenly divided between normal and lesion cases (and evenly divided between the different lesion cases). The trained classifiers reported a AUC value of 1, with the performance results on the test data shown in Fig. 4.17.

The results show that the classifiers failed to give simultaneously high specificity and sensitivity. However, interestingly the classifier trained with unsorted frames gave a specificity of 100% while the classifier trained with sorted frames gave a sensitivity of near 100%. This result opens the future possibility of implementing a cascade classifier approach to give more robust classification in such scenarios.

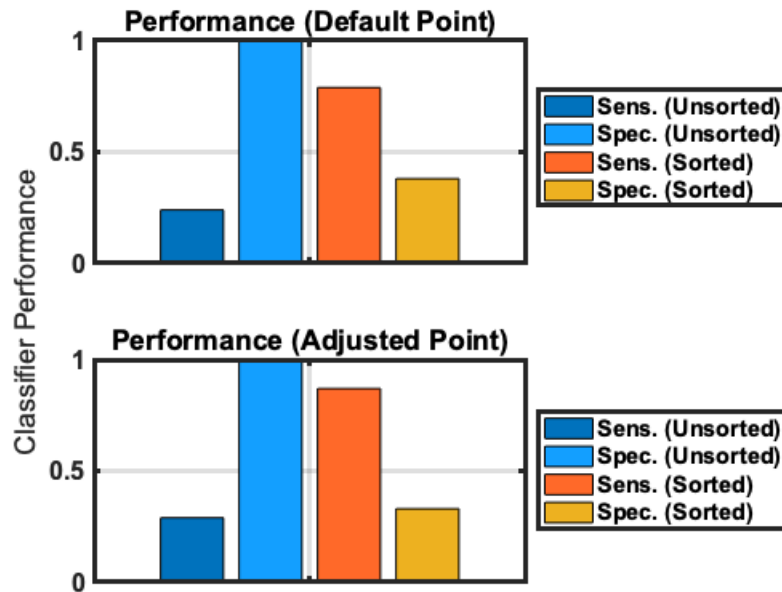


Figure 4.17: Classifier results from test data in phantom model Study 4: Effect of Electrode Positioning and Anatomy. Any given classifier performs poorly with simultaneous high values of specificity and sensitivity not achieved in any case. Interestingly the classifier trained and tested with unsorted frames give a specificity of 100%, while the classifier trained and tested with sorted frames give a sensitivity of near 100% suggesting that a cascade of classifiers may provide improved results.

4.4.2.5 Study 5: Final Overall Study with All Test Parameters

The final study trained and tested from the combined pool of measurement frames from all measurements conducted over all 3 days. This study was analogous to the numerical study described in Section 4.4.1.6: here featuring the complete set of variants from all of the phantom parameters used in the study. The training set comprised of 28,800 raw measurement frames, with the test set comprised of 2,880 raw measurement frames. The frames in each set were evenly selected from each of the 3 days, evenly divided between normal and lesion cases and with the lesion frames evenly split between all 8 lesion scenarios. No frame in the training set was repeated in the test set. As usual, two classifiers were trained and tested – one using unsorted frames and one using sorted frames. The results are shown in Fig. 4.18. The results show that the best achievable performance was about 75% sensitivity and specificity for the case of sorted frames used at the default operating point. Using the adjusted operating point improves sensitivity but causes a significant drop in specificity. Interestingly, the results in Fig. 4.18 lay between

those of the 60 dB and 40 dB numerical results as seen in Fig. 4.12. The SNR of the phantom experimental platform was calculated at about 50 dB, which is in line with these results. Hence the phantom results correlate with those of the numerical study.

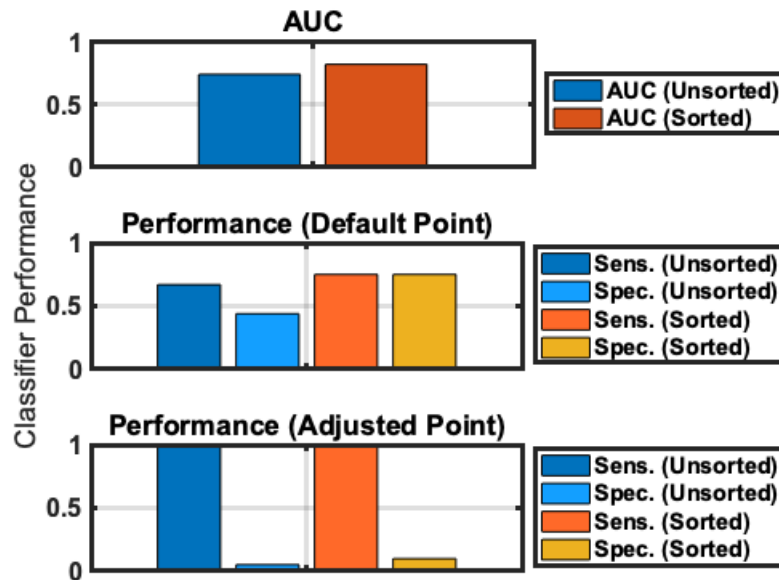


Figure 4.18: Classifier results from test data in phantom model Study 5: Final Overall Study. The best performance is seen with the sorted frames used at the default operating point, giving a sensitivity and specificity of 75%. Moving to the adjusted operating point improves sensitivity but severely causes a reduction to specificity. The results are between those of the 60 dB and 40 dB numerical study results reported in Fig. 4.12, as expected since the experimental SNR is ~ 50 dB.

4.5 Investigations into Classifier Optimisation

Section 4.4 examined the use of a linear SVM classifier to classify FEM models and phantom test platforms of the head and brain as having a ‘bleed’ or ‘no-bleed’ (‘normal’). The emphasis was on the effect of individual parameters such as noise, lesion location and size, electrode positioning and anatomy on classifier performance. These sections constituted an initial exploratory study with minimal attempt to intelligently select features for input to the classifier or indeed in selection of the best type of SVM classifier. Now in this section research into these areas is reported. First the effect of a change of classifier type on performance is investigated. Next

an examination is made of the effect of changing input features from unsorted raw measurement frames to more intelligent input feature selection.

In the experiments in this section, the pool of 155,520 raw measurement frames generated as described in Section 4.4.1.6 from all 243 normal models and 1,944 lesion models are used. The number of frames in both classes were identical, and within each class the number of frames from each unique normal or lesion model was identical. A robust method was applied in this section to optimise the performance of the SVM classifiers, outlined as follows: First, the data was separated into 10 separate folds each with a unique training data set and testing data set that was made up of 90% and 10% of the original data set respectively. This training data set was then used to optimise the SVM classifier hyper-parameters, namely the box constraint and kernel scaling factor. A Bayesian optimisation procedure was implemented to identify the hyper-parameters that lead to the greatest generalised accuracy across 10-fold cross-validation on the training set (i.e. nested cross validation). Once identified, a final trained SVM classifier was created with these optimised hyper-parameters. The hold out testing data set was then used to obtain performance metrics for the final classifier. This procedure was then repeated for all ten of the unique training-testing data pairs, and final classifier performance presented as the mean \pm standard deviation across these ten iterations. This nested cross-validation procedure, which has been used previously in the literature [249], [250], provided a generalised and robust indication of classifier performance. The procedure is shown in Fig. 4.19.

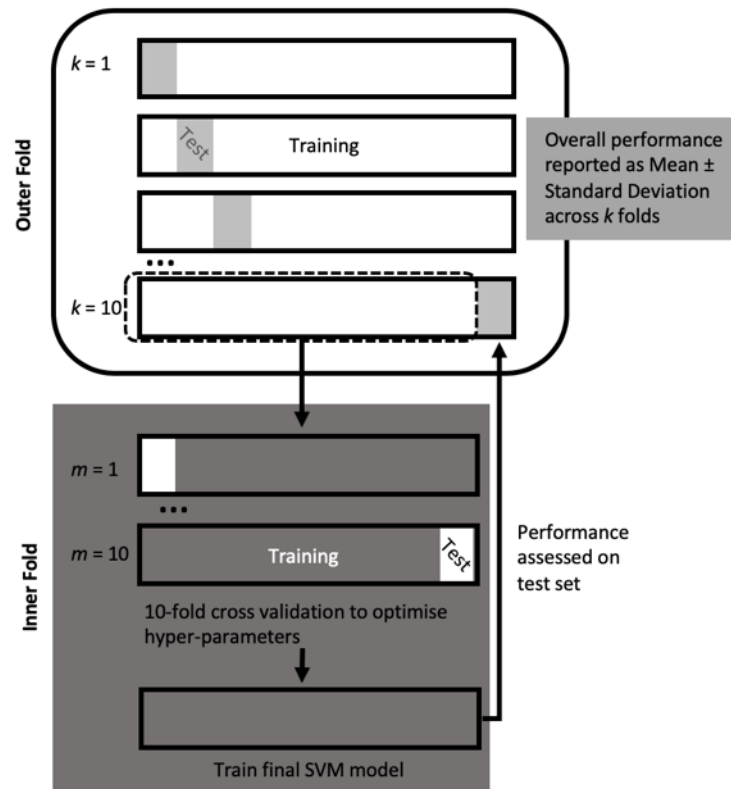


Figure 4.19: Nested cross-validation. The complete data set is separated into $k = 10$ folds with 90% as a training set (white) and 10% as a test set (grey). The training set from each of these outer folds is itself divided similarly into $m = 10$ inner folds divided into training (white) and test (grey) sets, with 10-fold cross validation performed on the inner fold to optimise hyper-parameters. These hyper-parameters are then used to train a final SVM model on the entire training set, with performance assessed on the held out test set. This process is repeated over the k folds with a final overall performance reported as the mean \pm standard deviation.

4.5.1 Comparison of Performance of Linear SVM, Radial Basis Function SVM, and Neural Network

In this section, the performance of the linear SVM is compared to two different classifiers: SVM with Radial Basis Function Kernel and Neural Networks.

A linear SVM offers advantages such as speed, low computational cost and ease of implementation. However, given the nature of EIT and the measurement frames produced, a linear kernel may not be best choice of classifier for the intended application. This classifier choice is an important consideration for future development of the technology and is thus discussed briefly here. In related studies, a popular

kernel for SVMs is that of a Radial Basis Function (RBF) [238], [240] which is a non-linear function that defines the separating hyperplane. Hence, the hyperplane is a “gently varying surface” and is suitable for scenarios where the data points (measurement values) do not change dramatically within a short distance in the n -dimensional hyperspace [251]. The RBF kernel can be used for SVMs when the relationship between the features and labels is non-linear, and further this kernel has less hyperparameters than a polynomial kernel [251]. Another popular machine learning algorithm is Neural Networks (NNs), which unlike SVMs are unsupervised classifiers. NN algorithms are based loosely on a model of the brain and feature ‘neurons’ as processing and learning layers between the input and output [252]. These two alternative classifiers were compared to that of the linear SVM using the data of the final overall numerical study (Section 4.4.1.6). This study featured pooled data with maximisation of parameter variability in both normal and lesion cases. Using this numerical set the classifier comparison study was performed at 80 dB, 60 dB, 40 dB and 20 dB SNR. In these classifier comparison studies, the raw measurement frames were used as unsorted frames and the default operating point was used.

For the linear kernel and RBF kernel SVMs, the results are reported as described in Section 4.5 and Fig. 4.19. In the case of the NN classifier, the data was divided 70% : 15% : 15% into training, validation, and test data. These ratios are the default offered by MATLAB. Ten hidden neurons were used and a scaled conjugate backpropagation algorithm applied. The confusion matrix generated from the test data allows calculation of the sensitivity, specificity and accuracy. This process is repeated ten times with the sensitivity, specificity and accuracy reported as the mean \pm standard deviation across each iteration.

The sensitivity, specificity and accuracy statistics from the three classifier types are compared below in Fig. 4.20. Altogether, there are four types of data compared in each plot of Fig. 4.20 based on the total numerical data with different SNR levels. Each dot in the graphs denotes the mean classifier performance across the 10-fold testing, with error bars representing the standard deviation range.

The results indicate that effective classifier performance (1 ± 0 in all metrics) is given by both SVM kernel types at 80 dB. The NN results in a performance level of 0.99 ± 0 in all metrics. It is observed that in particular the use of the RBF kernel can improve the classifier performance, notably at the 60 dB and 40 dB SNR levels. There is an increase in the mean accuracy of between approximately 3% and 9% respectively, at these SNR levels when using the RBF kernel compared to the linear SVM. When the SNR decreases to 20 dB all classifiers are essentially guessing with the mean accuracy only slightly above 50%, indicating that the changes in

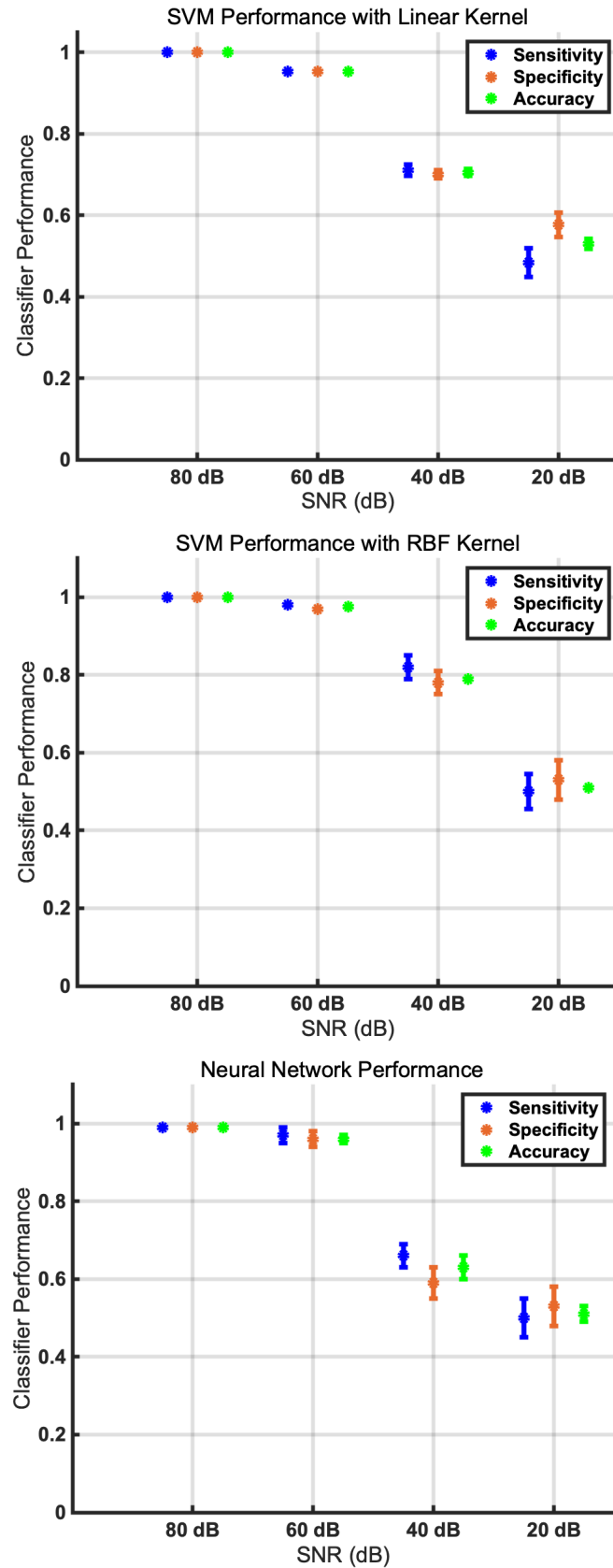


Figure 4.20: Performance results across classifiers. The sensitivity, specificity and accuracy of each of three classifiers (Top: Linear SVM, Middle: RBF SVM, Bottom: NN) is expressed as the mean \pm standard deviation following training and testing of each classifier on the total pooled numerical data across the 10-fold testing, with each dot representing the mean classifier performance and the error bars representing the standard deviation range at the respective noise level (at the four SNR levels of 80 dB, 60 dB, 40 dB and 20 dB). There is a significant improvement in performance when using the RBF kernel, notably at the 60 dB and 40 dB SNR levels.

impedance due to the presence of the bleed are embedded within the noise. This finding suggests that hardware should guarantee an SNR well above 20 dB. In fact from Fig. 4.20 it can be inferred that the SNR for a hardware system should be on the order of 60 dB to expect accurate detection of brain bleeds.

The improvement with the use of the RBF kernel over the linear kernel and above the NN provided the motivation for the use of this kernel in all the following parts of Section 4.5. These sections deal with investigations into pre-processing of frames and intelligent feature selection, and are now presented.

4.5.2 Support Vector Machine Applied to Pre-Processed Electrical Impedance Measurement Frames

In the previous sections the classifier input features were the unprocessed measurement frames, with the injection channels removed. This current section will explore the use of various pre-processing techniques applied to the measurement frames ranging from:

1. Manually chosen feature-extraction methods such as taking the mean of sub-frames;
2. Electrode pair proximity to decide input features;
3. Variance-based methods such as Laplacian scores and Principal Component Analysis (PCA);
4. Use of an ensemble classifier.

These feature extraction methods are carried out on data at all four SNR levels (80 dB, 60 dB, 40 dB, and 20 dB), with the RBF-SVM classifier optimised as described in the introduction to Section 4.5.1. As before, classifier performance is presented as the results across 10-fold testing.

4.5.2.1 Sub-Frame Means

In this study, a sub-frame is defined as the set of measurement channels associated with a given injection pair. A measurement frame from a 16-electrode array using a Skip 2 pattern will have 16 such sub-frames, each with 13 channels (3 channels are removed as these channels include the injecting electrodes). The 13 voltage measurements in each of the 16 subframes are averaged, with the resulting 16 mean-values used as the input features to the classifier. This reduces the dimensionality of the input from 208 features to 16 features. The pre-processing work-flow is shown in Fig. 4.21.

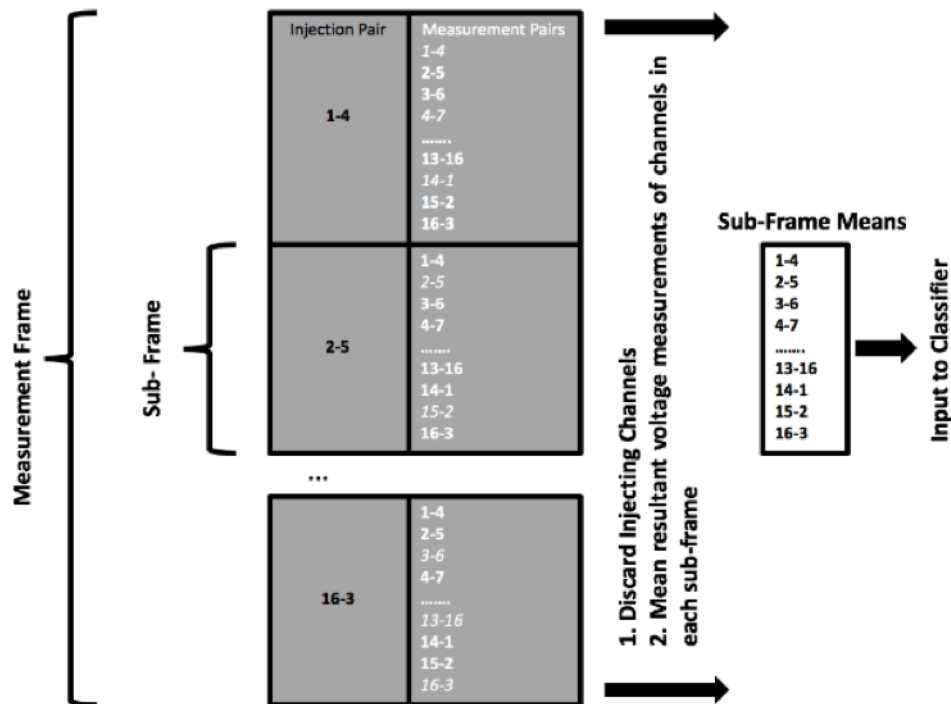


Figure 4.21: Generating the mean of each sub-frame. Each sub-frame is made up of the 16 channels associated with a given injection pair. Removal of channels involving either of the injection pair electrodes gives 16 sub-frames each with 13 channels. The mean of the voltage measurements from each set of 13 channels in a given sub-frame is used leaving 16 values, the sub-frame means. These subframes are used as inputs to the classifier.

The performance of the RBF-SVM classifier using the sub-frame means as inputs is reported in Fig. 4.22 at each SNR level. The mean \pm standard deviation of the sensitivity, specificity, and accuracy after 10-fold nested cross validation and Bayesian optimisation is illustrated. As seen, the performance at 80 dB is excellent, being near 1 ± 0 for all metrics. At lower SNRs there is a fall off in performance with for example sensitivity at approximately 0.71 ± 0.02 at 60 dB, and all metrics at approximately 0.5 at 40 dB and 20 dB. However it is noteworthy that near identical performance is achieved at 80 dB relative to that of using full measurement frames (with a difference of < 0.01 (1%) in all metrics), despite the significant drop in the number of features. Such a reduction in dimensionality, with near no effect on performance would result in a less computationally expensive algorithm.

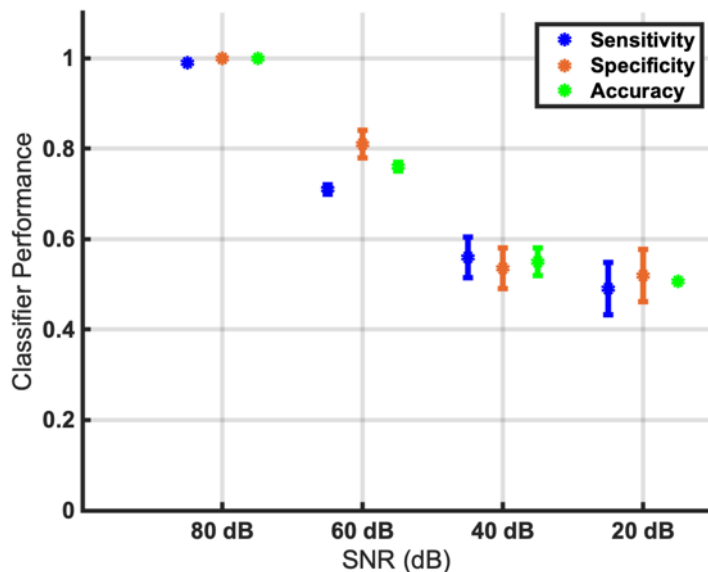


Figure 4.22: Performance of the RBF-SVM using sub-frame means as input features. Each dot on the plot denotes the mean classifier performance across the 10-fold testing, with the error bars representing the standard deviation range at the respective noise level. The performance at 80 dB SNR is near the ideal of 1 ± 0 for all metrics, comparable to the performance achieved when using the complete frames. However, performance falls off quickly at lower SNRs, with all metrics below 0.85 at 60 dB and at approximately 0.5 at 40 dB and 20 dB.

4.5.2.2 Near and Far Sub-Frame Channels

In this section selected channels from each measurement sub-frame are examined as classifier input features. These channels are selected based on the physical locations of the measurement electrode pairs relative to the injection pairs. Specifically, classifier performance is analysed when using ‘near’ sub-frame channels and ‘far’ sub-frame channels. The near sub-frame channels are defined as the 7 measurement channels nearer in physical location to the injecting pair of a given sub-frame. The far sub-frame channels are defined as the 6 measurement channels further in location from the injecting pair. The complete set of near channels from each sub-frame are amalgamated and used as the input to the classifier with the same process performed to the far channels. This process reduces the input feature size to 112 features for the near sub-frame channels and to 96 features when using the far sub-frame channels, as compared to 208 for a full measurement frame. It is anticipated that the near sub-frame channels will be more informative due to their proximity to the injecting pairs.

The near and far subframe-channels, for one sub-frame (that of the 1-4 injection pair), are shown in Fig. 4.23. The injecting electrode pair is denoted by the red arrow, with the near sub-frame channels shown in orange, and the far sub-frame channels shown in green.

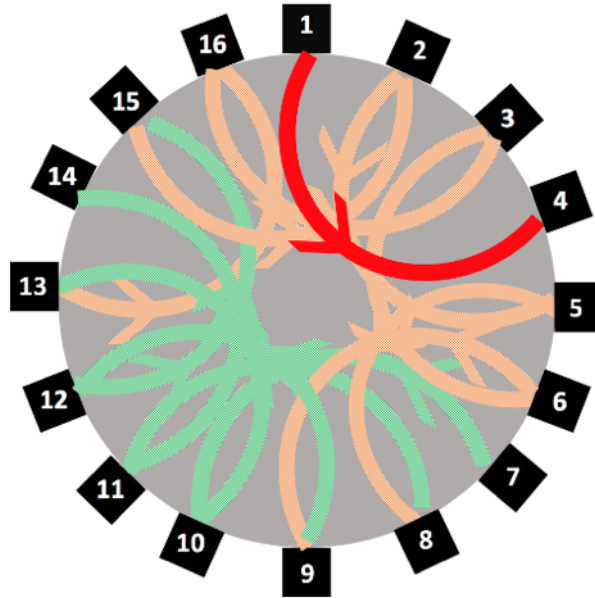


Figure 4.23: Near and Far Sub-Frame Channels. Here the injection pair of 1-4 is shown (red). The 7 nearest channels are shown in orange, with the 6 far channels shown in green. Channels involving the measurement pair are not considered. These near sub-frames and far sub-frames channels are then used as inputs to the classifier.

The performance of the RBF-SVM classifier using the near and far sub-frame channels are again reported at each SNR level as the mean \pm standard deviation of the sensitivity, specificity, and accuracy. These results are given in Fig. 4.24. The results show that both the near and far sub-frame channels offer perfect performance with sensitivity, specificity, and accuracy of 1.00 ± 0.00) at 80 dB SNR. A slight drop in performance is seen at 60 dB SNR, but all values at this SNR are still $\geq 0.99 \pm 0.01$. Further performance drops are seen at the 40 dB and 20 dB SNR levels.

Hence, the near sub-frame channels result in better performance than the far sub-frame channels. Performance at all SNR levels for the near sub-frame channels in particular is equivalent to that of using complete frames despite an almost 50% reduction in dimensionality.

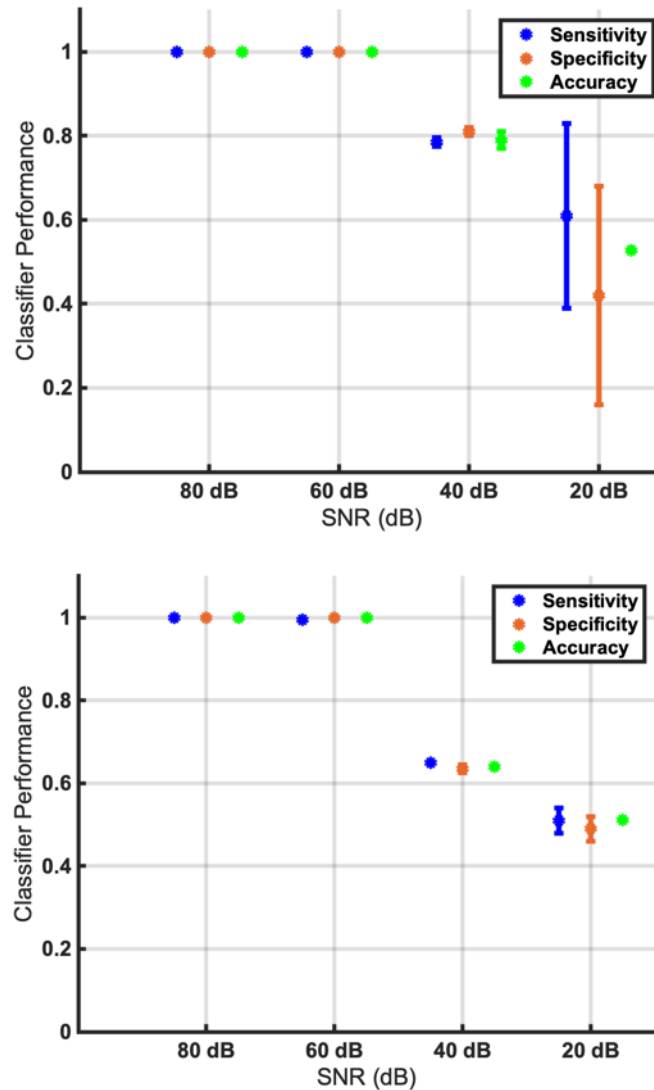


Figure 4.24: Comparison of RBF-SVM classifier performance with using the near (top) and far (bottom) sub-frame channels as input features. Both the near and far sub-frame channels results in perfect (1.00 ± 0.00) performance at 80 dB SNR, and near perfect ($\geq 0.99 \pm 0.01$) at 60 dB SNR. At lower SNR levels of 40 dB and 20 dB the near sub-frames outperform the far sub-frames. Of note, the near sub-frames result in equivalent performance to using full measurement frames at all SNR points.

4.5.2.3 Laplacian Scores

Laplacian Scores belong to a group of techniques used to select features referred to as filter-based methods [253], [254]. Filter methods work by analysing the data

before classification, giving a ranking to each feature. Then the number of ranked features that optimises performance can be chosen by the user. In the context of this work, features correspond to the measurement frame channels. Filter methods can be implemented as either supervised or unsupervised methods. Supervised filter methods require both the observations (inputs) and classes (labels) in order to rank the features. In order to avoid any bias or data contamination, it is important to carefully choose a subset of the entire data set for the feature selection process. Alternatively, unsupervised filter methods can use the entire dataset in order to rank the features without biasing the classification result. An unsupervised feature selection algorithm, the Laplacian Score algorithm [253], [254] was used in this study to rank the features on the measurement frames (datasets). Specifically, the Laplacian Score algorithm works on the assumption that if two data points are close as judged by a distance metric, then the data points most likely share a label. Further detail on the algorithm can be found in [253]. The distance metric used in this work to define the weight matrix of the algorithm was the Euclidian distance. The advantage of using the filter-based feature selection is that after determination of the optimal number of ranked features, the original data can be used as input for the classification. The only additional computational cost is the removal of unnecessary features.

The data was standardised, with the Laplacian score then calculated on each data set corresponding to each of the four SNR levels (80 dB, 60 dB, 40 dB, and 20 dB) to obtain a ranking of the 208 features at each SNR level. The optimal number of ranked features was then chosen through finding the number of features that lead to greatest generalised accuracy in the cross-validation training of the SVM classifier. In Fig. 4.25, the generalised accuracy is presented at each of the four SNR levels as the number of Laplacian score ranked features is increased. Based on Fig. 4.25 the optimal number of features can be determined, that is the best combination between the number of features and the best generalised accuracy. These optimal points are tabulated in Table 4.1.

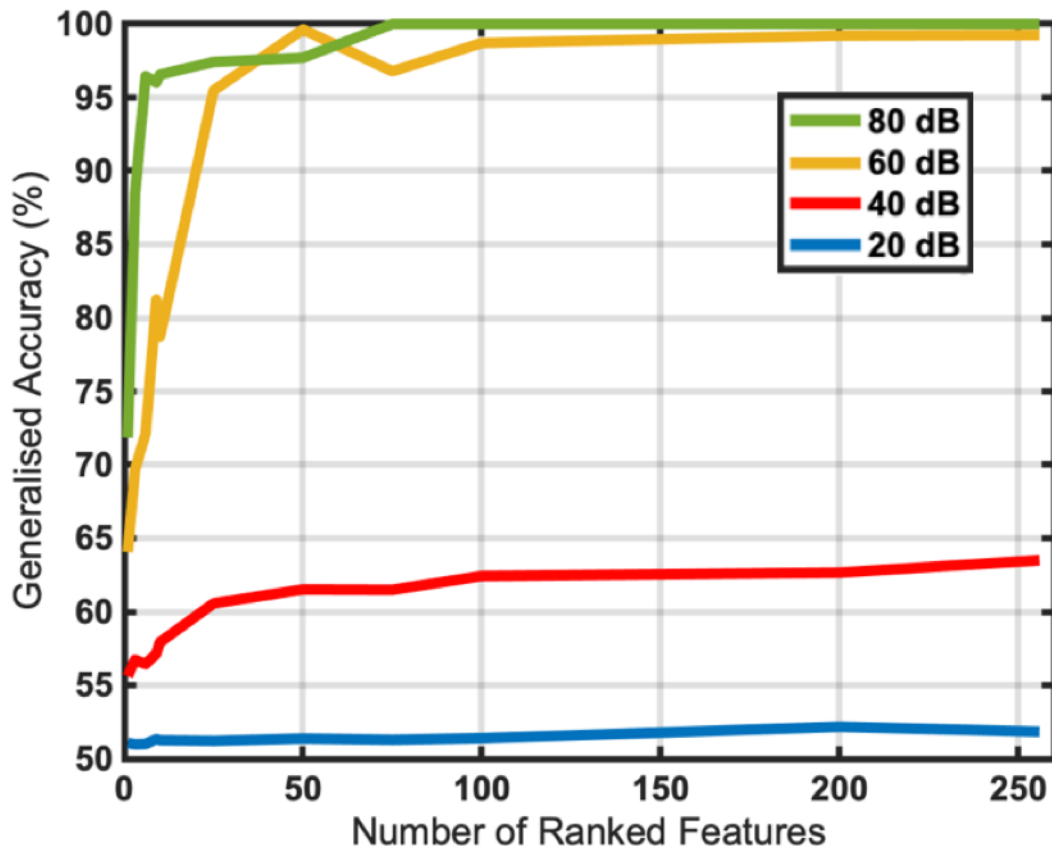


Figure 4.25: The performance of the RBF-SVM classifier using a different the number of ranked features, measured by the generalised accuracy. The ranked features were determined using the Laplacian Score. The optimal point at a given SNR is that offering the highest accuracy with the lowest number of features.

Table 4.1: The optimum number of ranked features at each SNR level (maximal accuracy with fewest number of features).

SNR	Number of Ranked Features	Generalised Accuracy (%)
80 dB	25	100
60 dB	75	100
40 dB	100	76
20 dB	208	53

The performance of the classifier at each SNR level was assessed with the pre-determined number of ranked features as given in Table 4.1. The results are shown

in Fig. 4.26. These results show that the accuracy, sensitivity, and specificity are perfect (1.00 ± 0.00) at 80 dB SNR. Further, all metrics exceed 0.97 ± 0.01 at 60 dB SNR. Thus, classification performance is preserved while significantly reducing the input feature size from 208 to 25 and 75 features for the 80 dB and 60 dB SNR levels respectively. Even at 40 dB SNR classifier performance was essentially unchanged compared to using full measurement frames while reducing the input data set to only 100 features. As with all previous analysis, as the SNR level decreased to 20 dB, classifier performance approaches that of a random guess (metric scores of 0.5).

Unsupervised filter-based feature selection allows preservation of the captured data to be used as inputs to the classifier in a reduced form. Transforming the data with variance techniques such as PCA may further enhance the results. The PCA approach is considered next.

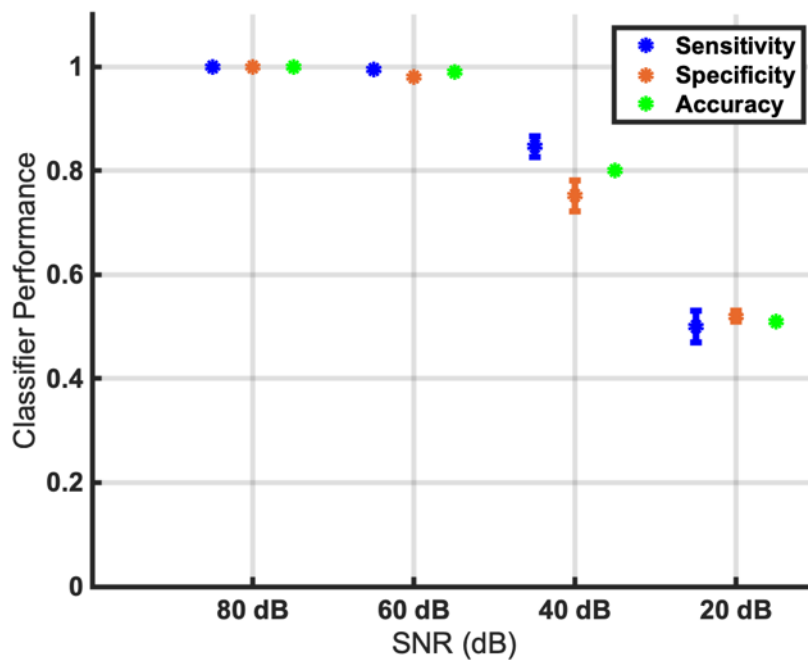


Figure 4.26: Performance of the RBF SVM Classifier at each SNR level using features based on Laplacian Scores. The number of ranked features offering maximal accuracy is predetermined with this feature set (selection of channels) used to train and set the classifier. Perfect performance is achieved at 80 dB SNR with 1.00 ± 0.00 in all metrics, with the use of only 25 features. In addition, an accuracy of ≥ 0.97 at 60 dB SNR is achieved using 75 features.

4.5.2.4 Principal Component Analysis

A commonly implemented feature extraction method is PCA [238], [239]. PCA is used to reduce the dimensionality of data by generating new variables that represent the original data. These new variables referred to as the principal components are created from a linear combination of the original variables with each successive component defining an orthogonal axis to the previous components. Thus, the entire set of principal components form an orthogonal basis for the space defined by the original data set. The data set can then be projected onto this new orthogonal basis in such a way that the variance in each axis is maximised allowing data to be potentially better discriminated [255], and only a select few principal components can be used to accurately represent the data.

Thus, PCA is used to both extract specific features and reduce the dimensionality of the data. The projection of the original data on specific principal components can be referred to as the ‘scores’. For every observation these scores are used as input features to the RBF-SVM classifier. As PCA is a variance based feature extraction algorithm, it is important to prevent any data contamination. When performing PCA it is necessary that there is no knowledge of the test data set. In this work PCA is performed on only the training data with the transformative coefficients stored and then applied to the test set data to obtain the projection onto the principal components. Thus, it is ensured that there is no knowledge of the test set data when performing PCA.

Similar to the previous section, a search for the optimal number of principal components was completed prior to assessing the classifier performance. The optimal number of principal components was established by finding the best generalised accuracy for each of the four SNR levels across the cross-validation training. In Fig. 4.27 a comparison of the generalised accuracy and the number of principal components for each of the four SNR levels is shown. From this graph, it becomes clear that for each SNR level there is a range of principal components when performance is maximised prior to a decrease of performance as more principal components are added. This is explained by the fact that each successive principal component explains less and less variance of the original data. Therefore, those final components are potentially just expressing the noise in the data set with no meaningful information contained. The optimal number of components chosen for the 80 dB, 60 dB, 40 dB, and 20 dB SNR levels is 10, 10, 11, and 31 principal components, respectively.

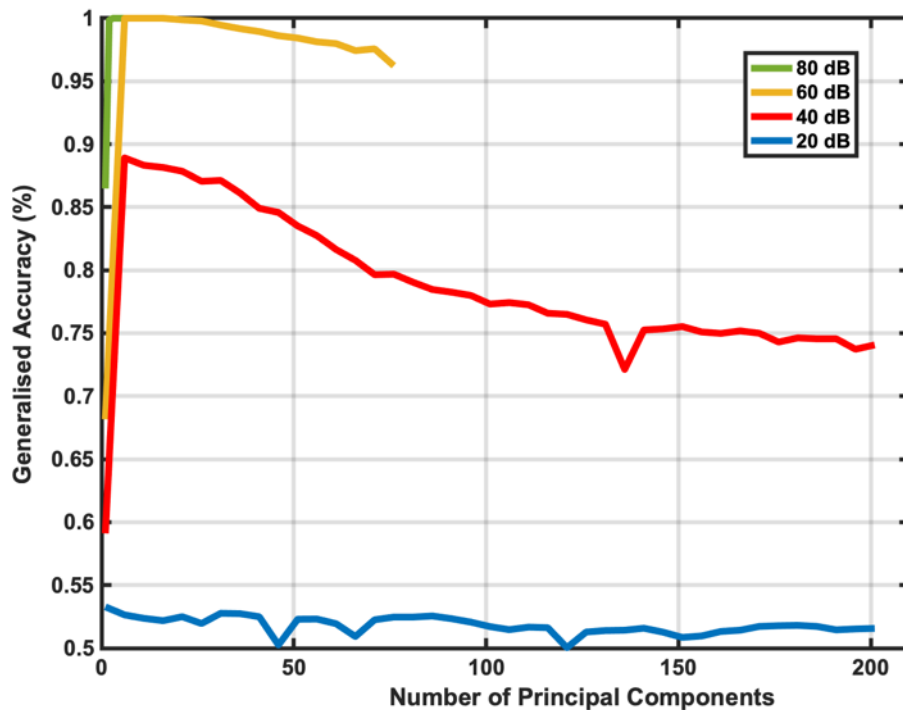


Figure 4.27: A comparison of the generalised accuracy at the four SNR levels as the number of principal components is increased. The optimal number of principal components at each SNR level is that number giving the highest generalised accuracy which is 10, 10, 11 and 31 principal components for 80 dB, 60 dB, 40 dB, and 20 dB SNR levels respectively.

The classifier performance was then assessed by projecting the test data set onto the principal components using the stored projection coefficients found in training. In Fig. 4.28, the performance of the classifier is compared at all four of the SNR levels. The use of PCA leads to a marked improvement in classification in comparison to using the entire raw data set (complete measurement frames), while also significantly reducing the input data set to at most 31 features. Most notably at 40 dB SNR there is an increase of almost 10% in the mean accuracy compared to using the complete measurement frames. A decrease in the input feature size from 208 features to only 11 features is also seen at the 40 dB SNR point. Also, significantly at 60 dB SNR perfect performance is achieved using only 10 components. However, as in all previous analysis, the classifier is no better than a random guess at 20 dB SNR.

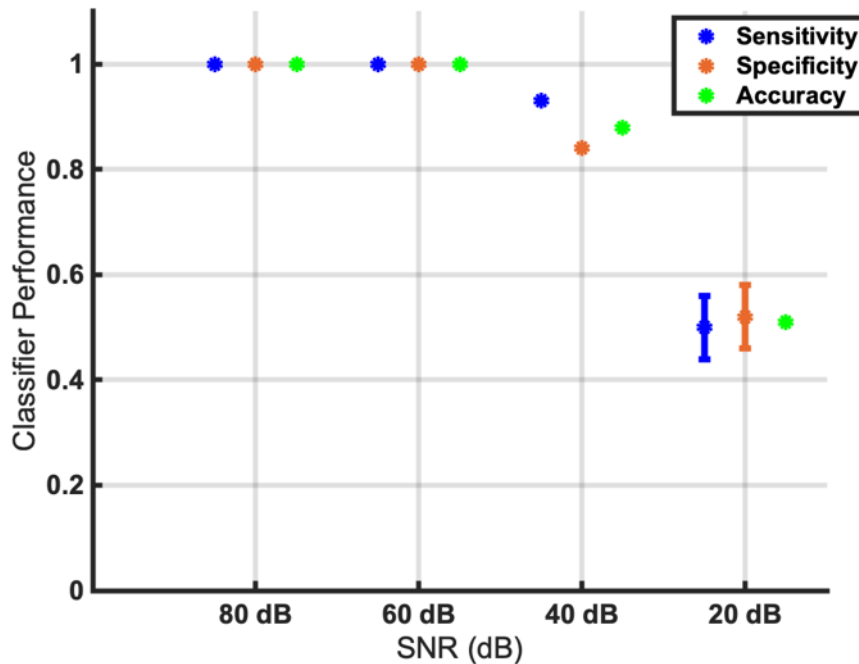


Figure 4.28: Comparison of the performance at each of the four SNR levels for the classifier after performing PCA. Perfect performance (1.00 ± 0.00 in all metrics) is given at the 80 dB and 60 dB SNR levels despite using only 10 components at each point. A near 0.1 (10%) improvement in accuracy is seen at the 40 dB SNR level compared to the full measurement frames, but performance is approximately 0.5 in all metrics at 20 dB SNR essentially representing a random classifier.

4.5.2.5 Ensemble Classifier

An ensemble classifier aims to make use of multiple classifiers to make an aggregate decision. Additionally, these classifiers allow for better control of the sensitivity and specificity of the classifier performance [256]. In this work an ensemble classifier was created by assigning a classifier to each of the 16 sub-frames from a given complete measurement frame. A voting scheme from each of the 16 classifiers was then used for the final classification decision. The design and implementation of this ensemble classifier is shown in Fig. 4.29. The operation of the ensemble classifier relies on each of the 16 classifiers separately classifying each case as ± 1 (bleed or normal). Next the sensitivity, specificity, and accuracy of the ensemble classifier at different threshold points was calculated. A threshold was defined here as the minimum number of separate classifiers needed to classify a case as a bleed for it to be classified as such, if the number was below this threshold then the case was classified as not bleed. The threshold was adjusted from 1 to 16 in steps of 1.

This control on the sensitivity and specificity allowed for the generation of a ROC curve. In Fig. 4.30 a comparison of the ROC curve at each of the four SNR levels for the ensemble classifier is shown. An analysis of the ROC curves indicates that the general trend is that for a low threshold (for example 1) the FP ($1 - \text{Specificity}$) rate will be high as the ensemble classifier is very sensitive to bleeds. This translates as a high sensitivity at a cost to specificity, if the system is not robust. At a high threshold (for example 16) sensitivity is reduced but specificity is maximised as the FN rate is high, with more classifiers needing to agree on labelling a case as a bleed before it is classified as a bleed. The accuracy will lie in between these two values of specificity and sensitivity at all threshold points.

The trade off in sensitivity and specificity is best illustrated at the lower SNR levels of 40 dB and 20 dB. For the higher SNR values of 80 dB and 60 dB there is a threshold (or set of thresholds) in the intermediate area where sensitivity, specificity and accuracy all are 1 ± 0 . For both the 80 dB and 60 dB SNR levels this area is centred at a threshold of 10. The ROC curve allows the user to select the operating point offering optimal performance, which for the proposed application of bleed detection is maximal sensitivity as justified in section 4.2.3. As shown in Fig. 4.30 the 80 dB and 60 dB SNR levels result in an operating point offering the perfect combination of sensitivity and specificity both equal to 1. At 40 dB SNR for example a maximal sensitivity of just over 0.9 is achieved with a reduction in specificity to 0.2, with a worse performance given at 20 dB SNR which has the performance of a random classifier.

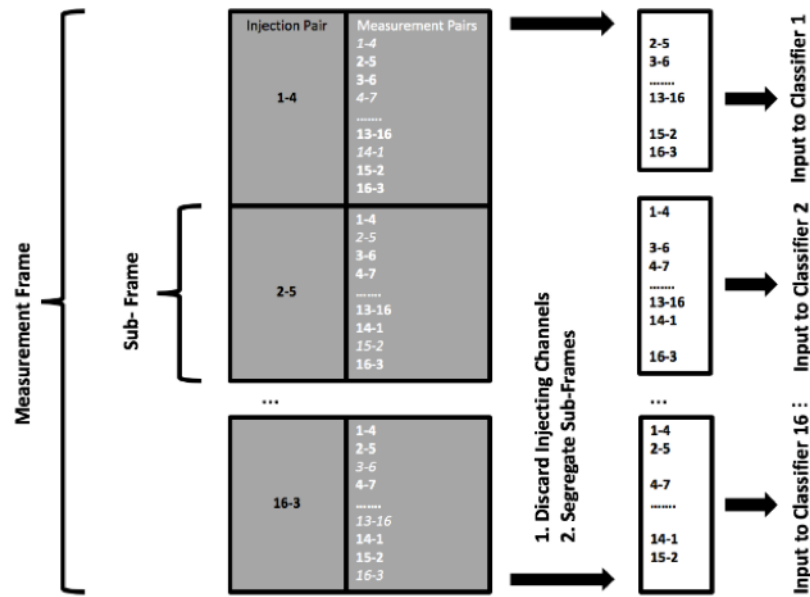


Figure 4.29: Example of the design and implementation of the ensemble classifier. The measurement frame for a given case can be divided into subframes with the channels from each subframe used as the input for a separate classifier. The complete set of frames are segregated in this way with 16 classifiers trained and tested. Each classifier separately labels a case as ± 1 with the aggregate result calculated according to a threshold which can be adjusted.

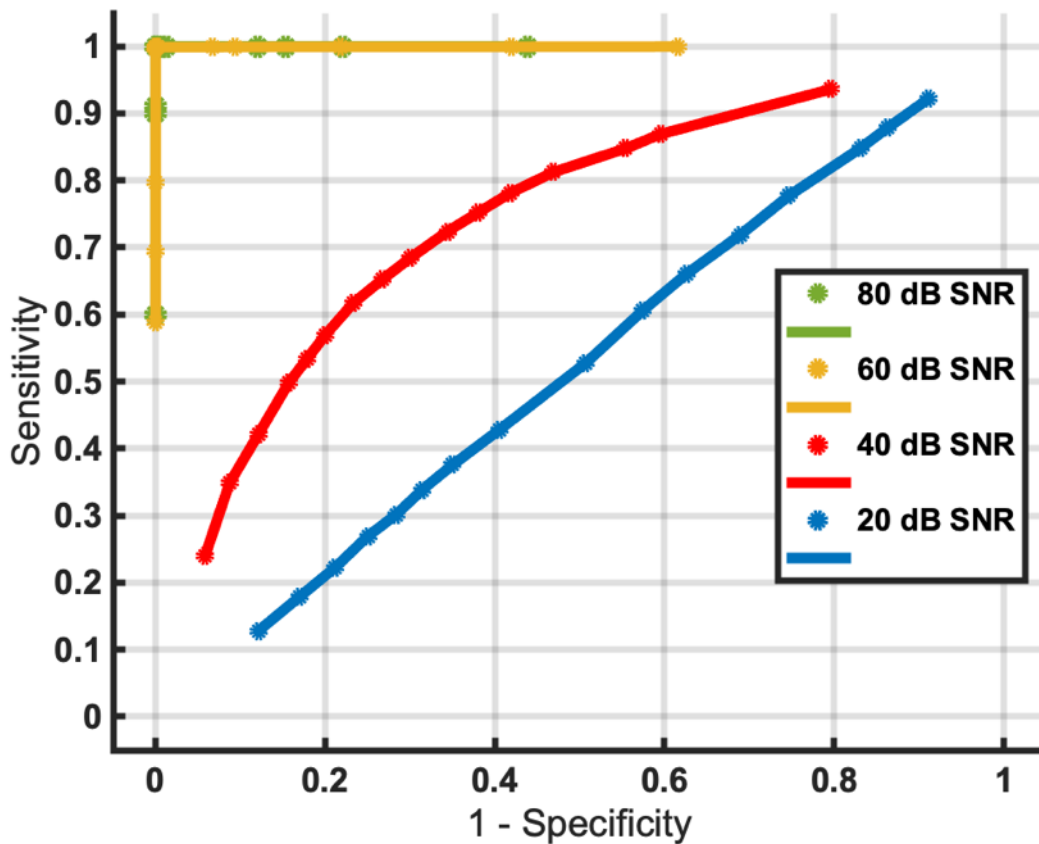


Figure 4.30: ROC curves for the Ensemble Classifier at each SNR level. The points on each curve correspond to each discrete threshold value between 1 and 16 from right to left, with the corresponding line interpolated between the points. The curves illustrate the trade-offs between sensitivity and specificity possible at each SNR level by changing the operating points. Both the 80 dB and 60 dB plots offer an operating point of perfect performance (0,1). Performance is reduced at 40 dB and is worst at 20 dB SNR as expected. The 20 dB line is approximately that of a random classifier, being a diagonal line passing through the points (0,0) and (1,1).

4.5.3 Investigations into Classifier Optimisation - Key Learnings

This section sought to investigate methods to improve classifier performance. These methods included first classifier selection, and then intelligent feature selection.

The simple replacement of the linear kernel with a Gaussian RBF kernel resulted

in improved performance. Although both the linear and Gaussian RBF kernels resulted in perfect sensitivity, specificity, and accuracy of 1 ± 0 at 80 dB SNR (with a NN classifier resulting in scores of 0.99 ± 0 in all these metrics), the benefit of the RBF kernel is seen at 60 dB and 40 dB SNR levels with an increase in the mean accuracy between approximately 3% and 9%, respectively relative to the performance of the linear kernel. This significant improvement in classifier performance highlights the need to explore options related to classifier choice and also the input feature selection process.

The next part of this section examines methods that changed the classifier input. Intelligent feature selection was applied to unsorted raw measurement frames. The aim was to reduce dimensionality with a view to increasing computational efficiency and without affecting classifier performance. Approaches used included pre-processing of the measurement frames to create sub-frame means, near and far sub-frame channels, using Laplacian scores and PCA to extract specific features, and examining an ensemble classifier with thresholding to control the sensitivity to bleeds. A summary of the performance of these different classifiers at the 60 dB and 40 dB SNR levels where performance was mostly impacted is shown in Table 4.2 and Table 4.3 respectively. For all classifiers, the 80 dB level yielded perfect classification results, whereas at 20 dB SNR all classifiers performed at essentially a guess level.

Table 4.2: Summary of different classifier performance at 60 dB SNR. All metrics reported as the mean \pm standard deviation of the sensitivity, specificity, and accuracy with a perfect score being 1.00 ± 0.00 . All classifiers used RBF kernel except when labelled ‘Linear’. Linear: Linear kernel with full measurement frames as the classifier input; RBF: RBF kernel with full measurement frames as the classifier input; Mean: Sub-frame means as classifier input; Near: Near sub-frame channels as input; Far: Far sub-frame channels as classifier input; Laplacian: Optimal number of ranked features as determined by Laplacian filtering used as classifier input; PCA: Optimal number of principal components used as classifier input; Ensemble: Ensemble classifier used. Results correspond to the threshold offering maximal sensitivity.

		Sensitivity	Specificity	Accuracy
Classifier Type	Linear	0.95 ± 0.01	0.96 ± 0.01	0.95 ± 0.01
	RBF	0.99 ± 0.00	0.97 ± 0.00	0.98 ± 0.00
	Mean	0.71 ± 0.02	0.82 ± 0.03	0.76 ± 0.01
	Near	1.00 ± 0.00	1.00 ± 0.00	1.00 ± 0.00
	Far	0.99 ± 0.01	1.00 ± 0.00	1.00 ± 0.00
	Laplacian	0.99 ± 0.01	0.97 ± 0.01	0.98 ± 0.00
	PCA	1.00 ± 0.00	1.00 ± 0.00	1.00 ± 0.00
	Ensemble	0.99 ± 0.00	1.00 ± 0.00	1.00 ± 0.00

CHAPTER 4. MACHINE LEARNING WITH EI MEASUREMENT FRAMES

Table 4.3: Summary of different classifier performance at 40 dB SNR. All metrics reported as the mean \pm standard deviation of the sensitivity, specificity, and accuracy with a perfect score being 1.00 ± 0.00 . All classifiers used RBF kernel except Linear. Nature of the classifier types is consistent with Table 4.2.

		Sensitivity	Specificity	Accuracy
Classifier Type	Linear	0.71 ± 0.02	0.70 ± 0.02	0.70 ± 0.01
	RBF	0.82 ± 0.02	0.76 ± 0.02	0.79 ± 0.00
	Mean	0.56 ± 0.04	0.54 ± 0.04	0.55 ± 0.03
	Near	0.75 ± 0.02	0.81 ± 0.02	0.78 ± 0.03
	Far	0.66 ± 0.01	0.65 ± 0.02	0.65 ± 0.01
	Laplacian	0.85 ± 0.02	0.75 ± 0.03	0.80 ± 0.01
	PCA	0.93 ± 0.00	0.83 ± 0.01	0.88 ± 0.00
	Ensemble	0.61 ± 0.04	0.77 ± 0.05	0.69 ± 0.01

Each of the intelligent feature selection methods significantly reduced the dimensionality of the input data to the classifier. Importantly such reductions did not overly affect performance. The key learnings from that work included the following:

- The sub-frame means approach reduced the input data size to only 16 features, however suffered from poor performance when the SNR levels dropped below 80 dB. A decrease in the mean accuracy of almost 25% in comparison to using all 208 features was reported even at 60 dB SNR;
- The near and far sub-frame channels gave an approximate 50% reduction in dimensionality. Using the near sub-frame channels preserved the classifier performance when compared to the full data set, whereas the far channels led to a reduction in the mean accuracy of almost 15% at 40 dB SNR. These results imply as was hypothesised that the near sub-frame channels are more important for classifier performance;
- Using the Laplacian scores to rank and choose features led to similar classifier performance to using all 208 features at all SNR levels. However at 80 dB, 60 dB, and 40 dB the input features were reduced to only 25, 75, and 100 features respectively;
- The use of PCA to extract and select features in combination with the RBF-SVM classifier lead to the best overall results with mean accuracy values of 100% and 88.26% at the 60 dB and 40 dB SNR levels. This marks a 1.25% and 8.91% improvement over using all 208 features while only needing the first 10 and 11 components at 60 dB and 40 dB SNR respectively;
- The ensemble classifier approach offered a trade-off between sensitivity and specificity depending on the threshold used. At 80 dB and 60 dB a wide region centred around a threshold of 10 offered perfect sensitivity, specificity, and accuracy. However, this method fails to match the performance of using all the input features at 40 dB.

Hence, sizeable improvements in classifier performance are possible from both classifier selection and intelligent feature selection.

4.6 Conclusions

This chapter sought to explore the feasibility of using a technique that used raw measurement frames designed for EIT as inputs to ML classification algorithms. The approach removes the image reconstruction steps which are challenging in static EIT scenes (Section 2.4.3.3, Section 2.4.6). An example of a static scene is a brain haemorrhage. The use of trained classifiers may be sufficient to identify the presence or absence of a haemorrhage, allowing the correct treatment path to be initiated.

A rationale for the use of ML for the proposed application was discussed initially in Section 4.2. In Section 4.3 the numerical and phantom experimental setups were described. Next, in Section 4.4 the effect of individual parameters on performance were examined when using a linear SVM. These parameters included the effect of noise in measurement frames, bleed location, bleed size, electrode positioning, and variations in anatomy. These parameters were examined in a comprehensive set of numerical models in Section 4.4.1. Then in Section 4.4.2 an analogous set of experiments were performed using the physical phantom model. The parameters studied using the phantom model included repeatability, lesion location, lesion size, electrode positioning, and anatomy. These phantom experiments gave results correlating with those of the numerical experiments. The phantom experiments also added more variables associated with a more realistic platform highlighting challenges. In particular the need for a system with high SNR was highlighted. The conclusions drawn from these sections are:

- Good performance (sensitivity, specificity, and accuracy at or near 1) is achievable particularly at 80 dB SNR;
- Information on lesion location and size can be obtained directly from measurement frames without an image if the SNR is sufficiently high;
- The technique is sensitive to new bleed locations not seen in the training data although the simple pre-processing step of sorting the measurement values can improve this;
- The technique robustly detects bleeds larger than those trained on, but struggles with those smaller;
- The technique is robust to small (± 2 mm) changes in electrode positioning;
- The technique struggles with unseen anatomies, in this chapter modelled as deviations in the morphology of the head and brain FEM models. This result may suggest a need to train on a large number of different anatomies.

Options for improvement of performance were examined in Section 4.5. First classifier selection was examined. The results demonstrated that a RBF kernel can significantly outperform a simple linear kernel for SVM classification. This non-linear function is better suited to defining a hyperplane particularly for inputs with a large number of dimensions. Next intelligent pre-processing of the frames reducing the number of dimensions was studied. Encouragingly, each method selected reduced the dimensionality of the input without affecting performance. In all cases, results indicated a high SNR was desirable. Methods such as the use of an ensemble classifier can be used to trade-off sensitivity and specificity in cases where perfect classification cannot be achieved.

Thus this chapter has demonstrated promise in the approach of using EIT measurement frames as inputs into ML for bleed detection. The application of classifiers to EIT measurements is an emerging and novel approach that is worthy of further investigation. Another approach to detection of static lesions is considered in the next two chapters, as a novel algorithm and modality for lesion detection is introduced. This algorithm is based on the natural symmetry of the head being disrupted by the presence of a perturbation. This disruption is detectable in measurement frames taken from symmetric orientations. The algorithm is introduced in Chapter 5, and improved and extended upon in Chapter 6. As shall be seen, although image reconstruction is performed, ultimately by the end of Chapter 6 it is rendered unnecessary. Rather, it is the gross conductivity change on either side of the sagittal plane and the trend in that change over a frequency band that is of diagnostic interest. This pattern of conductivity change can be captured as a novel metric that renders precise reconstruction unnecessary. In Chapter 7, the use of this metric is calculated from human data. At this point ML techniques are reintroduced with the novel metric as the input. The work of Chapter 7 also extends the classification from normal versus bleed, to include ischaemic lesions. Thus the ML techniques and paradigms introduced in this chapter are integrated with the novel algorithm of the next two chapters to result in a final integrated approach for lesion detection and identification in Chapter 7.

Symmetry Difference EIT – A Novel Algorithm for Static Perturbation Detection

Work from this chapter was published in two peer-reviewed articles. An early description of the algorithm with results from numerical studies was published as part of Bioengineering in Ireland - Proceedings of the 24th Conference of the Section of Bioengineering of the Royal Academy of Medicine in Ireland, Dublin City University, Dublin, Ireland, 2018 in the conference paper entitled “Electrical Impedance Tomography with Exploitation of Symmetry” [257]. A more complete and thorough introduction to the algorithm with numerical and phantom studies performed was published as a journal article in the Institute of Physics publication Physiological Measurement entitled “Symmetry difference electrical impedance tomography—a novel modality for anomaly detection” [194].

This chapter introduces a new modality for EIT called sdEIT that can be used to detect and identify unilateral lesions in cases where a natural plane of symmetry exists in the region of interest. Using stroke as a model, the proof-of-concept of sdEIT is demonstrated and then efficacy evaluated through a series of numerical and phantom experiments that assess the effect of individual parameters on algorithm performance.

5.1 Introduction

Symmetry Difference Electrical Impedance Tomography represents a novel approach to the imaging of static scenes, an area of challenge in EIT discussed in detail in Section 2.4.6. The modality may be applied in regions featuring a plane of symmetry. For example in the head the sagittal plane represents a border between the near mirror image left and right sides. In a healthy patient the two sides are nearly symmetric within the spatial resolution of EIT. However, if there is a unilateral lesion present then the symmetry is disrupted. It is this disruption in symmetry that sdEIT aims to detect. Work from Seone *et al.* have demonstrated

this principle with respect to EIS measurements whereby measurements across the sagittal plane were different in stroke patients but not healthy patients [202]. Hence in this chapter an approach to imaging static scenes using EIT through the exploitation of symmetry is described.

This chapter describes sdEIT using the example of stroke as a model. Hence, the head is the region of interest and the goal is two-fold:

- First to **detect** the presence of a lesion;
- Second to **identify** the detected lesion as haemorrhagic or ischaemic.

The layout of this chapter is as follows. First, in Section 5.2 an overview of the sdEIT algorithm is given. Next, Section 5.3 demonstrates a proof-of-concept of sdEIT by illustrating the steps involved in applying the modality to a simple numerical head model. Then Section 5.4 outlines an anatomically accurate numerical model, and a tank phantom model. These models are subsequently used in a series of experiments in Section 5.5 designed to both validate the sdEIT algorithm and to assess performance in scenarios with differing test parameters. These parameters include differences in the size, location, type of lesion as well as cases where measurement frames are contaminated with noise, and when the FEM models have errors in anatomy and assumed conductivity. Section 5.6 concludes the chapter by highlighting the significance and limitations of this new modality for EIT.

5.2 Symmetry Difference EIT - Algorithm Overview

In this section, the theoretical basis of the sdEIT is described. The sdEIT algorithm comprises two distinct steps summarised in Fig. 5.1, both resulting in an image and quantitative metrics:

1. Detection of Deviation from Normal Symmetry.

A ring of electrodes is placed across the plane of symmetry. The electrodes are arranged in an orientation that can be assigned as clockwise and then counter-clockwise orientations. These are symmetrically equal but opposite configurations. Measurement frames from each of these configurations are used to generate a difference image. The presence of a unilateral lesion ideally results in the imaging of the lesion as well as a confounding anti-lesion. The latter has opposite conductivity and position to the true lesion. A quantitative metric, the index of symmetry objectively evaluates the difference image to help the clinician decide if a lesion is detected.

2. Identification/ Disambiguation of Lesion Type.

A simulated model of the normal case is generated using *a priori* information. A measurement frame from this “pseudo normal model” is used to create a difference image with one of the measurement frames from Step 1. This “pseudo normal difference image” along with additional applied robust quantitative metrics described later in Section 5.3.2.2, are used to disambiguate if the lesion is a clot or a bleed. Alternatively this step may indeed return a result that indicates that disambiguation is not possible.

The proposed technique is reliant on an aggregate approach, with the outcomes from Steps 1 and 2 combined to strengthen the overall outcome. In this work the comprehensive results including image and metrics from both steps are reported for select illustrative examples. These cases demonstrate the strengths and limitations of the technique in a number of scenarios. However, in most cases only the metrics are reported as these metrics are sufficient to interpret the result. Thus reconstructed images are not required. This move away from a reliance on reconstructed images, and towards using robust quantitative metrics is a theme permeating through this thesis. The theme has been discussed for example in Section 2.5, and in all of Chapter 4 where ML was used directly with measurement frames without a reconstructed image.

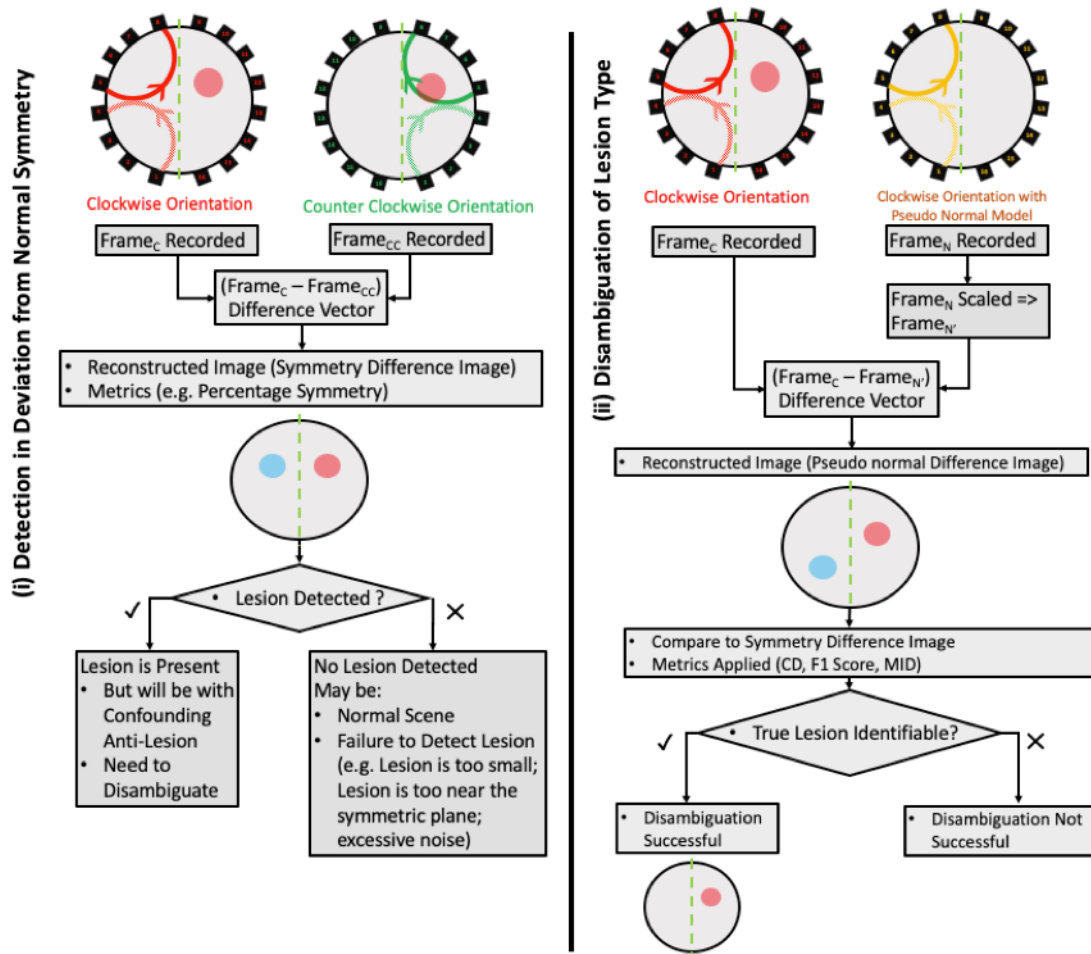


Figure 5.1: Summarised version of the two steps comprising the sEIT algorithm. In Step 1 the outcome is the detection or no detection of a lesion. After Step 2 the conclusion is either no lesion detection or lesion detection with disambiguation resulting in identification (bleed or clot in this application), as well as localisation. Further details and a thorough description are provided in Section 5.3.

In the case of stroke a definitive diagnosis of haemorrhagic or ischaemic is required to initiate treatment [2], [258]. These two lesion types have opposite electrical conductivity relative to brain parenchyma [205]. Hence for a haemorrhage the confounding symmetrical mirror image would appear as an ischaemic lesion and vice-versa. This result renders stroke a particularly challenging application for EIT. Thus, there is a need for both steps in sEIT when applied to stroke. The first detects an abnormality while the second disambiguates between the true lesion and the false mirror image. Significantly this technique could allow for

successful EIT detection of static or quasi-static lesions, such as those in stroke that cannot be detected using aEIT and with limited success using fdEIT (Section 2.4.6).

This section has given an overview of the sdEIT algorithm. In the next section sdEIT is further introduced using a simple example.

5.3 Symmetry Difference EIT - Initial Development and Proof-of-Concept

In this section, sdEIT is introduced through a basic example. This example employs a simple numerical head model with no added noise, and a large lesion far from the line of symmetry. This example is designed as both a proof-of-concept study, and as an introduction to guide the reader through the application of sdEIT. Numerical modelling and simulations were largely performed using MATLAB [173] and EIDORS [170], with other packages noted where relevant. A description of the simple numerical model is initially provided. Next the electrode layout required for sdEIT is introduced. The two-step sdEIT algorithm is then described in the final two subsections.

5.3.1 Modelling Techniques

In this section, the modelling techniques used to initially implement sdEIT are outlined. These included a simplified numerical model of the head, and a symmetrical electrode layout.

5.3.1.1 Symmetry Difference EIT Simplified Numerical Model

A simplified numerical model of the human head was created using the meshing tool Netgen [171] in conjunction with EIDORS [170]. The model was based on two concentric spheres:

- An outer sphere of diameter 160 mm which approximates the diameter of the head [130];
- An inner sphere of diameter 140 mm placed at a consistent depth of 10 mm, an average scalp-cortex distance [225].

Hence the surface of the inner sphere is 10 mm from the surface of the outer sphere. This arrangement results in an outer layer as the space between the spheres, and an inner layer represented by the inner sphere. The outer layer was modelled as an aggregate of all tissues external to the brain while the inner brain layer was modelled as an aggregate of the tissues comprising the brain, similar

to the numerical model previously described in Section 4.3.1. Based on work described in Section 3.3, conductivity values of 0.1 Sm^{-1} and 0.3 Sm^{-1} were assigned to the outer and brain layers respectively [205]. Spherical target lesions modelling haemorrhage and ischaemia, were also meshed in Netgen for placement in the brain layer. The conductivity was set at 0.7 Sm^{-1} for haemorrhagic lesions and at 0.1 Sm^{-1} for ischaemic lesions, which matched the properties of these tissues [259].

In this initial study, a single haemorrhagic target replicating a 30 ml lesion was placed far from the line of symmetry. The choice of 30 ml was based on research indicating that an ICH of volume ≥ 30 ml is an indicator of increased mortality [46]. As the proposed sdEIT algorithm is based on symmetry, the simplified numerical model described here used spherical geometry ensuring a high level of symmetry in the early developmental stage of the algorithm.

Next a ring of 16 electrodes was placed around the model at a height approximately half way between the apex and base of the outer hemisphere. The electrodes were placed symmetrically across the sagittal plane which is the natural line of symmetry for the head. The electrodes were modelled as having a diameter of 12 mm which is a typical commercially available size of EEG electrode [248].

The normal model of the head lacking lesions, and with electrodes arranged in a clockwise orientation was used to generate an inverse model using the GREIT algorithm [227]. Although designed for use in lung applications of EIT the GREIT approach was empirically found to work well in this initial development study of sdEIT [227]. The injection and measurement protocol used, based on empirical results, was a Pair Drive Skip 2 protocol [10]. The simplified numerical model is shown as part of Fig. 5.2.

5.3.1.2 Symmetry Difference EIT Electrode Layout

In sdEIT, two measurement frames from rings of electrodes in different orientations are differenced to generate an image. The electrodes are arranged around a plane of symmetry such that in a 16 electrode ring, Electrode #1 is the symmetric partner of #16, #2 is partnered with #15, and so on. In one injection/ measurement execution the measurement frame is recorded from the electrodes assigned in the clockwise orientation, while in the next a frame is collected with the electrodes assigned in the counter-clockwise orientation. Alternatively all channels can be collected simultaneously in one combined protocol with post-processing parsing out the clockwise and counter-clockwise channels and measurement frames. The setup of the clockwise and counter-clockwise orientations of the single electrode ring is shown in Fig. 5.2.

This layout ensures that the scene observed by a given channel in the clockwise case is the mirror image compared to the counter-clockwise case. The measurement frames produced from the two orientations comprise of these voltage measurements from mirror image channels. This layout enables the measurements recorded between these symmetric partner channels to be compared by differencing. If there is no abnormality in the region of interest, then a difference image produced from differencing the two measurement frames should be theoretically empty. Conversely the presence of an abnormality in the region of interest disrupts the inherent symmetry. This disruption is captured in the difference image produced. This comparison assumes that the setup for each electrode and its partner is the same, i.e. that the electrodes are identical in every way and the region they observe is effectively the same. This set of assumptions may not be valid in more challenging test cases. However, the assumptions enable simplification of the scenario for this proof-of-concept of sdEIT.

The case of a haemorrhagic lesion on the right-hand side in the plane of the electrodes is shown in the middle illustration of Fig. 5.2. It is noted that the lesion is near to Electrode #4 in the clockwise setup and near Electrode #13 in the counter-clockwise orientation. The first part of sdEIT is to detect this lesion, present as a mismatch in the two measurement frames.

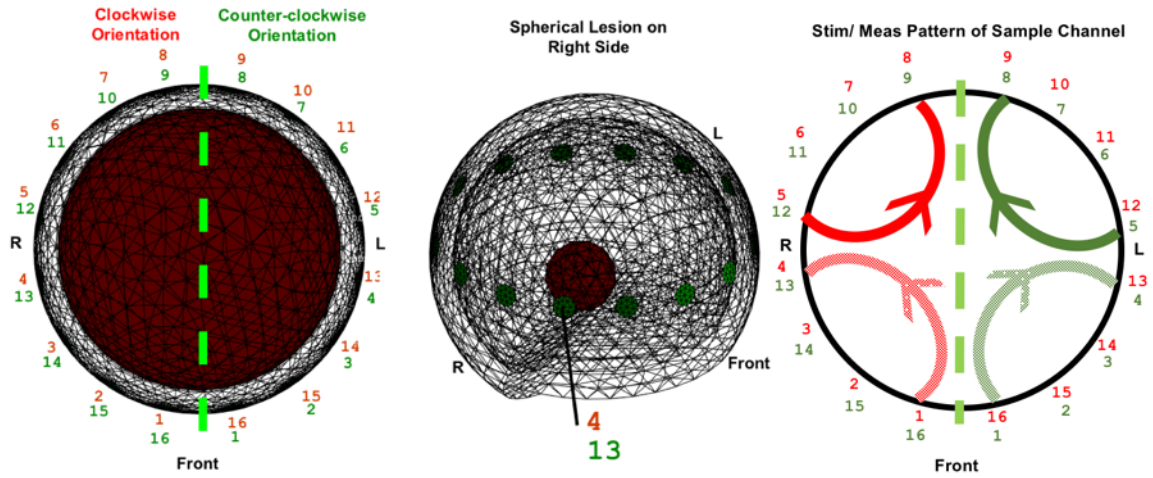


Figure 5.2: Left: sdEIT electrode layout on a simplified numerical model of the head (transparent) and brain (burgundy) based on spherical geometry where the natural plane of symmetry, the sagittal plane, is shown as a green dashed line. The view is from the top down with front, left, and right sides of the head marked. The clockwise electrode orientation are shown as red numbered electrodes. The counter-clockwise electrode orientation are shown as green numbered electrodes. Centre: A spherical haemorrhagic lesion inside the now transparent brain layer. The lesion is near to the clockwise orientation Electrode #4, which is the same as counter-clockwise orientation electrode #13. Right: The injection/ measurement pattern of a sample channel. The injection pair is shown in light colour, while the measurement pair is in a heavier tone. The clockwise orientation channel is in red while the corresponding counter-clockwise orientation channel is in green. The two respective channels of the same colour are symmetric partners.

This subsection has given a description of both simple the numerical model and symmetrical electrode layout. In the next section the two steps of the sdEIT algorithm are described.

5.3.2 Symmetry Difference EIT Algorithm and Quantitative Metrics

In this section, the sdEIT algorithm is applied to an example of the simple numerical head model with a large lesion far from the line of symmetry. The example clearly demonstrates the proof-of-concept of the algorithm and describes the two steps involved.

5.3.2.1 Symmetry Difference EIT Step 1 - Lesion Detection and Related Quantitative Metrics

A 30 ml simulated haemorrhage sphere is positioned close to clockwise Electrode #4 (counter-clockwise Electrode #13). EIT measurement frames from the Counter Clockwise (CC) and Clockwise (C) orientations are generated by solving the forward problem. The CC frame is taken as the baseline, with the C frame used as the update. The GREIT inverse model is used to reconstruct a difference image with the difference vector ($\text{Frame}_C - \text{Frame}_{CC}$) as input. This image is rendered as a slice through the electrode plane and is shown in Fig. 5.3. A symmetrical image is produced with a red (conducting) lesion seen near Electrode #4 as expected, but also the opposite blue (non-conducting) lesion seen near Electrode #13. Hence this symmetry difference image shows either a haemorrhage near Electrode #4 or an ‘anti-haemorrhage’ near Electrode #13. Fig. 5.3 also shows a surface plot of the symmetry difference image (on a 64 x 64 grid). The surface plot shows the intensity of the differences on the z-axis (arbitrary units).

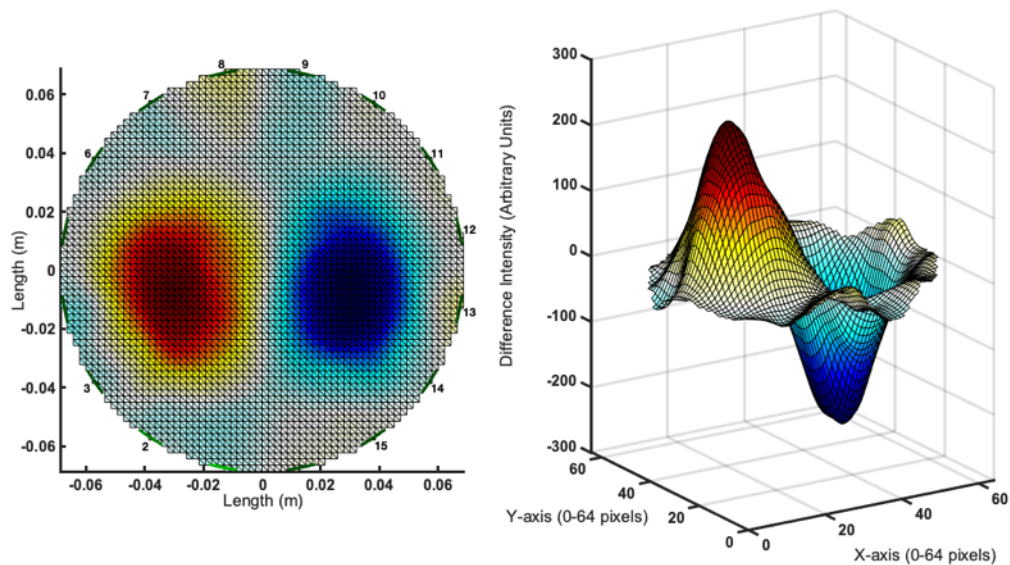


Figure 5.3: Left: Symmetry difference image showing a conductive target near Electrode #4 and a non-conductive target near Electrode #13. Right: Surface plot of the symmetry difference image. The z-axis of the surface plot (64 x 64 grid) shows the intensity values of the differences detected (arbitrary units). The topology is dominated by the symmetrical peak and trough caused by the presence of the lesion.

To quantitatively assess the symmetry difference image, thresholding is performed to create a binary image with the top and bottom 10% of pixels by intensity assigned as ‘1’ and all others ‘0’. The 10% value was empirically selected. Thresholding is performed to isolate the extreme regions of difference. These are Region of Interests (ROIs) which are where any potential lesion will be. The quantitative metric the index of symmetry is applied to the image, defined as:

- Index of Symmetry (IS): With the midline as the line of symmetry, the Left (L) and Right (R) pixels labelled ‘1’ have their locations compared to each other relative to the line of symmetry. If every pixel on the left has a corresponding pixel on the right, the score is +1 indicating perfect symmetry. If no pixels on one side have a partner in the same location on the other side, then the image is perfectly asymmetric with a score of -1 .

Ideally, the symmetry difference image with a lesion present would give a high IS, theoretically +1 in the ideal case. In this example, the IS score was +0.85. If the IS score is low then sdEIT should be deemed incapable of detecting a lesion in that particular case. While there is no exact threshold for this low value, empirically it was found that a $IS \leq +0.2$ corresponds to a poorly symmetric image with lesion detection not reasonable.

The IS is also low if there is in fact, no lesion present. A symmetry difference image and surface plot of a scene with no lesion present which should ideally have no difference is found to produce an image with differences, as seen in Fig. 5.4. However the surface plot of the normal case is effectively low-magnitude noise, and demonstrates poor symmetry ($IS = +0.14$). In the case of a true lesion as seen in Fig. 5.3, a peak and symmetric trough pair dominate the topology giving a IS score approaching +1 with the magnitude of the differences being dramatically larger than in the normal case.

Theoretically the normal image should be empty, i.e. noise-free with a constant zero magnitude. In practice this ideal result is not achievable due to the inevitable presence of noise from imperfect modelling and software. For example, increasing the number of voxels in the model resulting in a higher resolution model reduces these imperfections in assumed geometry but increases computational time. In the case of the anatomically accurate head and brain models described later, the assumption of symmetry is an approximation and will be an inevitable source of noise. The electrode modelling is imperfect with the size, shape and location of the electrodes limited by the resolution of the FEM model. Finally, the inability of the software to create infinitely precise measurements for the clockwise and

counter-clockwise electrode layouts is also an unavoidable source of noise. Despite these deviations from the ideal scenario, the normal case is clearly differentiable from the case in which a lesion is present, both from examination of the image itself and the IS metric.

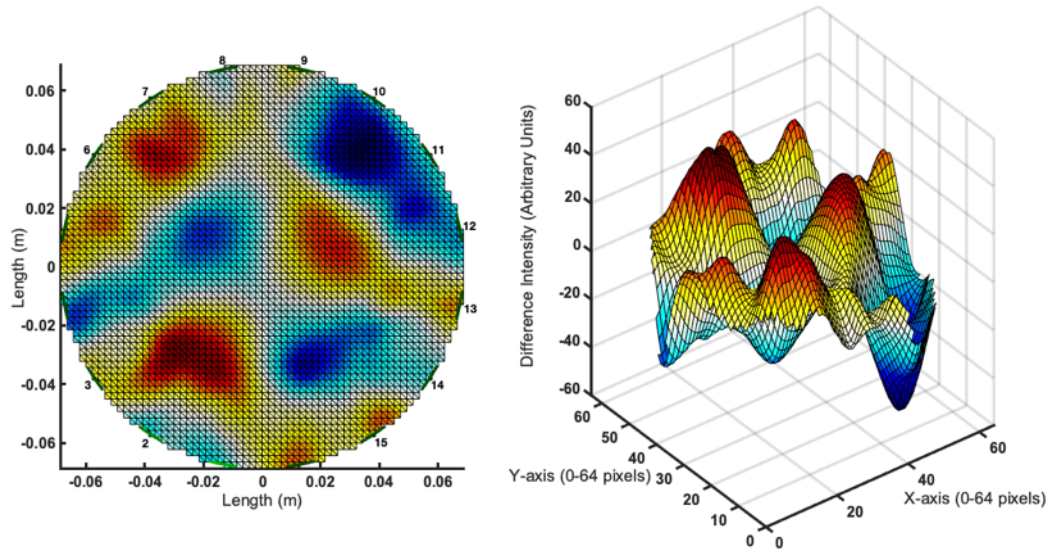


Figure 5.4: Symmetry Difference Image of the normal (no lesion) case is shown on the left with a surface plot (64 x 64 grid) shown on the right. The z-axis of the surface plot shows the intensity values of the differences detected (arbitrary units). The topology is chaotic and of low intensity as compared to the case where a lesion is present and dominates the topology, as shown in the surface plot in Fig. 5.3. The IS metric of +0.14 in the normal case suggests that a lesion likely not present.

It is noteworthy that in the lesion case, the anti-haemorrhage detected is not the same as an ischaemic sphere of the same size as the haemorrhagic sphere. This is as a result of a greater contrast existing between the background brain parenchyma ($\sigma = 0.3 \text{ Sm}^{-1}$) and haemorrhage ($\sigma = 0.7 \text{ Sm}^{-1}$) than exists between the former and an ischaemic lesion ($\sigma = 0.1 \text{ Sm}^{-1}$). Hence the magnitude of the red and opposite blue regions produced on the symmetry difference images are greater for the case of a haemorrhage than would be the case for an equivalent ischaemic lesion. However, this cannot be used to disambiguate and correctly identify the lesion as being a haemorrhage. A larger ischaemic sphere could also have produced this same result with the increase in lesion size compensating for the lower contrast. Hence, another approach is required to disambiguate the nature of the true lesion which could

either be a haemorrhage or a larger (relative to the haemorrhage) ischaemic lesion. This disambiguation comprises Step 2 of the sdEIT technique.

5.3.2.2 Symmetry Difference EIT Step 2 - Lesion Identification and Related Quantitative Metrics

The first step of sdEIT detects the presence of a lesion, with the second step designed to identify the type of lesion. The second step involves creating an approximate measurement frame of the normal (N) head from a model developed from *a priori* information along with a measurement frame taken with the lesion present. These measurement frames are used to generate a ‘pseudo normal difference image’, i.e., an artificially fabricated time difference image of the lesion relative to the normal. This artificial construction of a normal measurement frame is needed since a true normal measurement frame in stroke patients is rarely available [174]. The image produced from this step will not be perfect, but is sufficient when used in conjunction with the symmetry difference image from the previous section along with quantitative metrics, to disambiguate the lesion type and location.

First a forward model of the normal head is produced as accurately as possible using *a priori* information. This process is trivial in this example as the computer model of the head and brain are known exactly. In a real case a patient specific mesh is required for better reconstructions [163], [260]. While a specific mesh is unlikely to be available, recent work suggests a generic mesh maybe sufficient for good reconstruction in applications such as stroke [174]. A measurement frame from this *a priori* model with the electrodes in the C orientation can be produced to approximate the normal case. This measurement frame of the approximated normal can be used with the C measurement frame with the lesion present to produce a simple difference image. This image should detect the location and nature of the lesion if the model used to generate the normal is sufficiently accurate. However, in order to generate a high quality measurement frame of the normal, it is found that the accuracy must be very high in terms of anatomy and assigned conductivity (See Section 5.5.1.5). In more realistic cases this level of accuracy may be not possible. As the C measurement vector with the lesion present is largely normal except for the presence of a lesion, the normal measurement vector can be scaled using the measurement vector with the lesion present to result in a more robust normal measurement vector. This scaling technique is similar to that used in fdEIT [261]. Hence, the normal measurement frame (Frame_N) is adjusted by scaling its values according to the curve of best fit between Frame_N and the clockwise measurement (Frame_C). This scaling is described in the following piece of MATLAB code:

```
p = polyfit(FrameN, FrameC, 2);
```

$\text{Frame}_{N'} = \text{polyval}(p, \text{Frame}_N);$

Then, the pseudo normal difference image is generated using the scaled Frame_N ($\text{Frame}_{N'}$) and Frame_C as input data: $(\text{Frame}_C - \text{Frame}_{N'})$. ROIs as described in the previous section are generated, and compared to those from the symmetry difference image. The true lesion is a haemorrhage which should be commonly located in both images. The confounding regions will not be the same in both images due to the difference in how the images were produced. While both images use Frame_C with the true lesion location encoded in this measurement frame, they differ in the second frame used which has the lesion location encoded in a different location (Frame_{CC}) or not encoded (Frame_N). The resulting images are shown in Fig. 5.5. Three quantitative metrics are applied to the high and low intensity ROIs from both images:

- Centroid Difference (CD): The centroid (centre of gravity) of the ROIs on each image is calculated. The Euclidean distance between these centroids is then calculated. This distance is measured in pixels, with each complete image occupying a 64 x 64 square pixel grid. If the ROIs from the two images are similar then this distance should be small, ideally 0;
- F1 Score (F1): This metric measures the accuracy of the image and represents the harmonic mean of precision and recall, as described in Equation 5.1 [262], [263]:

$$F1 = \frac{2(Precision)(Recall)}{(Precision + Recall)}, \quad (5.1)$$

where,

$$Precision = \frac{TP}{(TP + FP)}, \quad (5.2)$$

$$Recall = \frac{TP}{(FP + FN)}. \quad (5.3)$$

The ROIs from the pseudo normal difference image are taken as the expected pixels and the symmetry difference image result the actual pixels. Hence the actual pixels are compared to the expected pixels to calculate the number of TP, FP, and FN pixels. The F1 score ranges from 0 – 1. If ROIs from the two images are similar then the F1 score should approach 1, if dissimilar the result will be close to 0;

- Mean Intensity Difference (MID): The mean intensity of the pixels in the respective ROIs are calculated. The difference between these mean intensities

is divided by the mean intensity in the pseudo normal difference image to normalise the result from 0 – 1, where 0 indicates the mean intensities are identical. The mean intensity difference is ideally 0 for the true target and 1 for the false target.

These metrics complement visual analysis of the images and objectively help identify the true target. The metrics should be considered collectively when deciding on the lesion type. The results of this simple head model case are listed in Table 5.1. As can be seen from Table 5.1 it is probable that the high intensity ROIs in the two images (from Fig. 5.5) match, while the low intensity ROIs do not have any similarity. Hence, in this case the decision based on these metrics is that the high intensity ROI i.e., the conductive lesion near Electrode #4, is the true target, which is correct.

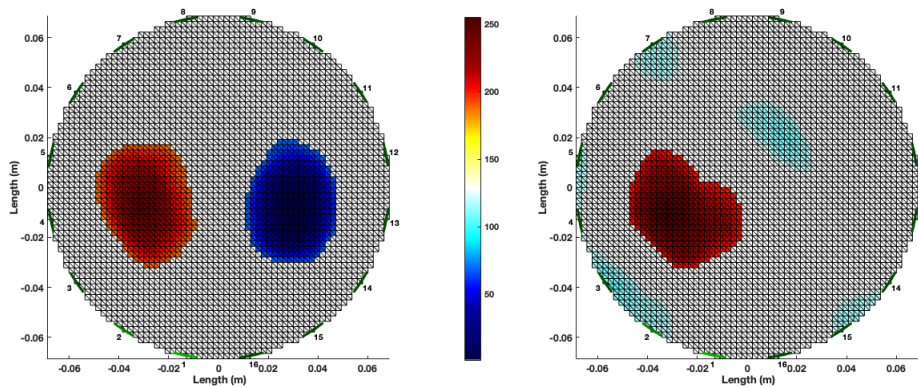


Figure 5.5: Thresholded images where the top and bottom 10% (by intensity) of pixels are kept. The difference intensities are mapped to a 0 – 256 scale, the colourbar of which is shown between the figures. Left: Symmetry difference image thresholded. From this thresholded image, the potential targets of a conductive target near Electrode #4 or non-conductive target near Electrode #13 are isolated. Right: Pseudo normal difference image thresholded. The largest high intensity and low intensity regions of interest in both images are compared quantitatively to assess if the high conductivity or low conductivity targets match. It is evident that the true lesion is the high intensity target near Electrode #4.

Table 5.1: Results of the Quantitative Metrics applied to the top (high intensity) and bottom (low intensity) ROIs compared from the two images.

Disambiguation Metric	High Intensity ROI	Low Intensity ROI	<i>Ideal Match for True Target</i>	<i>Ideal Result for False Target</i>
CD	2.25 pixels	15.5 pixels	<i>0.0 pixels</i>	<i>>> 0 pixels</i>
F1	0.84	0.07	<i>1.0</i>	<i>0.0</i>
MID	0.05	0.67	<i>0.0</i>	<i>1.0</i>

5.4 Modelling Techniques

In the next section sdEIT is applied to a comprehensive set of numerical experiments. In these cases an anatomically accurate numerical model is used. The design of this numerical model and the related experiment setup is now described. In addition, related experiments are performed in a tank phantom. This phantom and the experimental setup are also described in this section.

5.4.1 Numerical Models and Experimental Setup

The numerical model was developed as described previously in Section 4.3.1 (the ‘base numerical model’). Briefly, an anatomically accurate head model was developed from STL files of a human head [222], and brain [223]. The STL files were imported into EIDORS and meshed into a FEM model using Netgen [171] and GMSH [172]. When creating the FEM model a ring of 16 electrodes were placed on the surface symmetrically across the sagittal plane, with the mesh refined in the area of the electrodes [162]. The electrodes could be assigned in either clockwise or counter-clockwise orientation when taking measurements. The final FEM model comprised 268,240 elements in a 2-layer model, with this number of elements being a compromise between level of refinement and computation time.

As this study is intended as a proof-of-concept work the numerical model was kept relatively simple as a 2-layer model with the outer layer an aggregate of scalp, skull and the CSF layer of the meninges, and the inner layer an aggregate of the tissues of the brain. However, this simplification should not affect the underlying concept of the symmetrical comparison as the technique can be applied to any symmetric region regardless of number of layers or heterogeneities. The elements in the outer layer were assigned a conductivity value of 0.1 Sm^{-1} with the elements in the brain layer assigned as 0.3 Sm^{-1} as explained in Section 5.3.1.1 above [205]. The model is shown in Fig. 5.6.

The ‘normal’ model of the head, lacking lesions, and with electrodes arranged in a clockwise orientation, was used to generate an inverse model using the GREIT algorithm with the injection and measurement protocol a Pair Drive Skip 2 protocol (Section 5.3.1.1). The inverse model comprised of 6,846 elements, resulting in a fine resolution forward model and coarse inverse model (Section 2.4.3).

Spherical lesions of volume 2 ml, 10 ml, 20 ml, and 30 ml were created as STL files in Blender [177]. These volumes were chosen to replicate volumes typically seen in intracerebral haemorrhage where a median volume of 10 ml and mean of 17 ml is typical [47], while a volume of 30 ml is often the threshold before the prognosis deteriorates [46]. The selection of a sphere as the shape is a simplification: ICHs for example may be more ellipsoidal [226]. The lesions were assigned conductivity values of 0.7 Sm^{-1} when mimicking haemorrhage [205], and 0.1 Sm^{-1} when mimicking an ischaemic lesion [259]. The spherical lesions were positioned in five unique locations within the brain layer, in the plane of the electrode ring. In the following list the distance from the centre of the lesion to the indicated electrode is shown in brackets:

- (1) Near [16 mm] to Electrode #4 (Electrode #13 on counter-clockwise orientation);
- (2) Far [54 mm] from Electrode #4 (Electrode #13 on counter-clockwise orientation);
- (3) Near [40 mm] to Electrode #8 (Electrode #9 on counter-clockwise orientation);
- (4) Far [73 mm] from Electrode #8 (Electrode #9 on counter-clockwise orientation);
- (5) Midway [35 mm] from the sagittal plane and Electrode #13 (Electrode #4 on counter-clockwise orientation).

An image of these lesions demonstrating the sizes and locations is shown in Fig. 5.6. Further, in the subsequent results sections, all locations of lesions are with reference to Fig. 5.6.

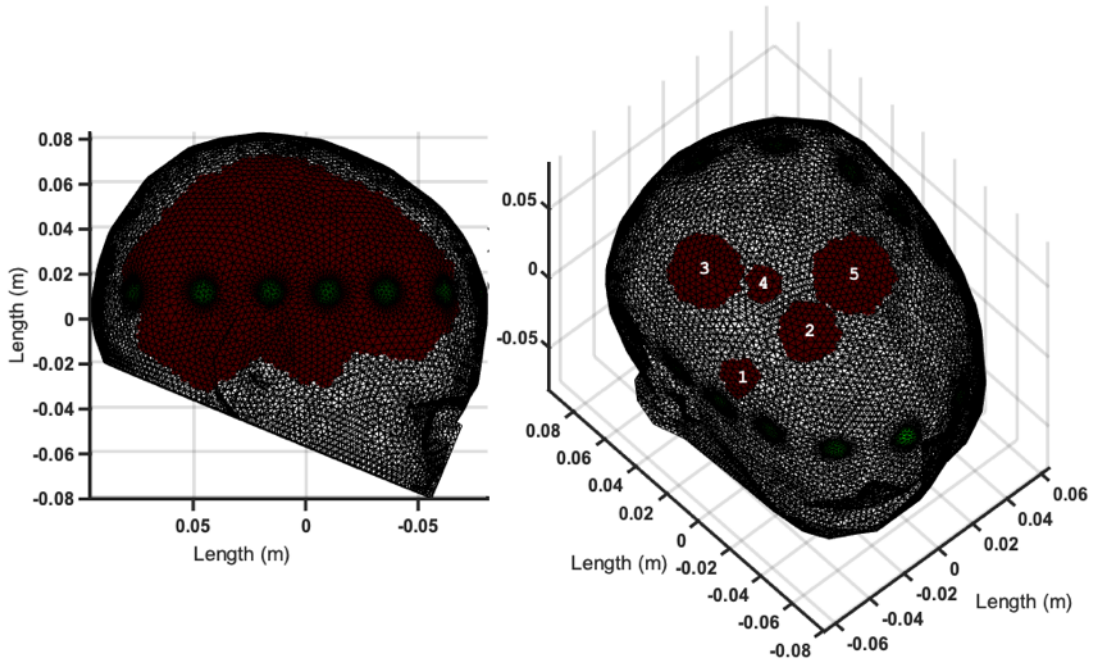


Figure 5.6: Left: Anatomically accurate 2-layer FEM model of head with brain and outer layer assigned conductivity values of 0.3 Sm^{-1} and 0.1 Sm^{-1} , respectively. A ring of 16 electrodes are represented as green circles. This electrode ring is placed symmetrically across the sagittal plane in a layout analogous to that shown in Fig. 5.2. Right: Locations and sizes of the phantom lesions used. The brain layer is removed for clarity. Locations: (1) near Electrode #4 (Electrode #13 on counter-clockwise orientation); (2) far from Electrode #4 (Electrode #13 on counter-clockwise orientation); (3) near Electrode #8 (Electrode #9 on counter-clockwise orientation); (4) far from Electrode #8 (Electrode #9 on counter-clockwise orientation); (5) midway from the sagittal plane and Electrode #13 (Electrode #4 on counter-clockwise orientation). Sizes: locations (1) and (4) are shown with 2 ml lesions, (2) has a 10 ml lesion, (3) has a 20 ml lesion and (5) has a 30 ml lesion. It should be noted that due to the method of assigning interior elements there is a pixellation effect and thus the lesion shapes are not perfect spheres in the FEM model.

These numerical models are used in Section 5.5.1, which reports the performance of sEIT in test scenarios designed to test hypotheses including:

- Effect of Lesion Location: sEIT is expected to perform best when a lesion is far from the plane of symmetry. A lesion near to or on the plane of symmetry would result in similar clockwise and counter-clockwise measurement frames since the two orientations overlap upon the plane. Such a lesion would hence be harder to detect. The further from the plane of symmetry the lesion lies the more divergent the clockwise and counter-clockwise measurement frames

should be. Therefore, Position (1) was expected to be the easiest lesion location to detect, with (2) and (4) being the more challenging;

- Effect of Lesion Size: sdEIT is expected to detect larger lesions more robustly than smaller lesions;
- Effect of Lesion Type: sdEIT should detect haemorrhagic lesions more easily than the equivalent ischaemic lesion as the contrast between blood and brain is greater than that between ischaemia and brain.

These hypotheses are tested in scenarios performed at different simulated noise levels: no noise (i.e. $\text{SNR} = \infty$), 80 dB, 60 dB, 40 dB, 20 dB, and 10 dB SNR. Noise was introduced into the measurement frames in an identical manner to that described in Section 4.4.1.1. Further, the effect of noise on performance is directly assessed, as well as the effect of imperfect modelling of the simulated normal on the second step of sdEIT.

5.4.2 Phantom Model and Experimental Setup

The phantom model consisted of a cylindrical Perspex tank of diameter 250 mm with 32 bolts equidistant and embedded in the tank wall. The bolts acted as electrodes. Only the odd numbered bolts were used, giving a 16 member evenly spaced ring. The Swisstom EIT-Pioneer set was used at a frequency of 100 kHz with a 0.5 mA peak to peak current. The conductivity of TMMs used in the setup were near identical across the 50 kHz–250 kHz band used by the Swisstom EIT-Pioneer (Fig. 3.7 and [153]) making the choice of 100 kHz arbitrary. The choice of 16 electrodes was used to match the setup of the numerical models described above in Section 5.4.1. The Swisstom EIT-Pioneer provides a 32 channel system which was used to define two co-located rings, one in clockwise orientation and the other counter-clockwise, attached to each of the 16 electrodes on the tank. Measurements frames were recorded for the 32 channel system and later the channels for both the clockwise and counter-clockwise rings parsed out. The line of symmetry was selected as the line joining the midway point between Electrode #1 and #16 to the midway point between Electrode #8 and #9. This line of symmetry is hence equivalent to that used in the numerical models.

Spherical haemorrhagic and ischaemic phantom lesions scaled so as to correspond to volumes of 2 ml, 10 ml and 30 ml in an actual brain were made from the solid TMMs as described in Section 3.3. The haemorrhagic lesions were of conductivity 0.7 Sm^{-1} and the ischaemic lesions of conductivity 0.1 Sm^{-1} at 100 kHz (Section 3.2.4.2). In addition cuboid shapes of size $50 \times 20 \times 20 \text{ mm}^3$ of the two phantom types were produced for initial testing of the material and the tank setup. The tank was filled to a depth completely submerging the electrodes with saline of

concentration 0.032 M, which had a conductivity of approximately 0.3 Sm^{-1} at 100 kHz thus emulating an aggregate of brain tissues [153]. Each spherical lesion was sequentially placed in positions equivalent to those used in the numerical simulations described in Section 5.4.1. These positions included near the exterior, near the line of symmetry, and midway from the exterior to the line of symmetry. For each lesion in each position 40 s (empirically chosen) of data was recorded, and analysed using the sdEIT algorithm. Photos of the setup are shown in Fig. 5.7 which shows the tank and electrode bolts with co-located red (clockwise) electrodes and black (counter-clockwise) electrodes. Also in Fig. 5.7 some of the spherical phantoms as well as cuboid test phantoms, and the support structure used to position the phantoms in the tank are shown. With sdEIT a direct symmetry comparison is made between the Left Hand Side (LHS) and Right Hand Side (RHS) of the tank.

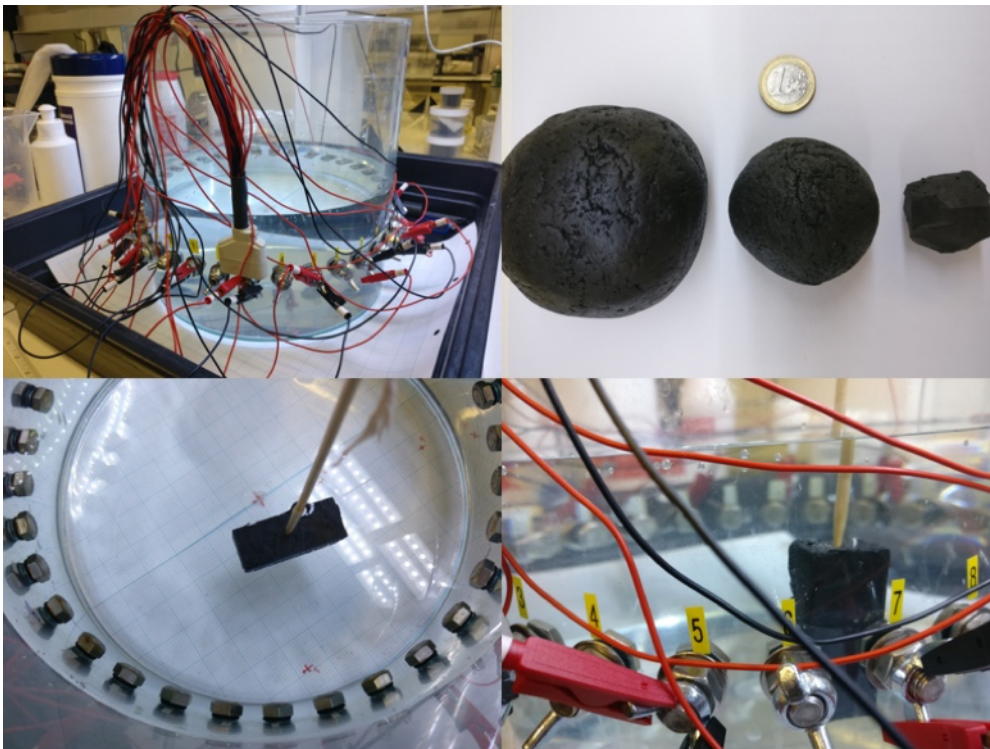


Figure 5.7: Tank experimental setup. Top left: Tank filled with saline and the two electrode rings. The clockwise electrodes are red, and odd numbered. The counter-clockwise electrodes are black, and even numbered. The electrodes from both orientations are co-located on the wingnuts of the bolts. Top right: Samples of the spherical phantoms used. These phantoms proportionally match 30 ml, 10 ml and 2 ml haemorrhages in a realistic-sized human brain. Bottom left: Wooden sticks are used to suspend a phantom at a fixed point in the tank with the aid of graph paper under the tank. Bottom right: Close up of a cuboid phantom next to Electrode #4 on the clockwise ring (Electrode #13 on the counter-clockwise ring).

The experimental setup used for the experimental implementation of sdEIT has been described in this section. A cylindrical saline filled tank model was used to emulate the brain, with phantom haemorrhagic and ischaemic lesions. The tank had an idealised geometry and near perfect symmetry as a result of the cylindrical shape. This geometry and the simple one-layer nature of the phantom was needed for this first application of sdEIT in a real world set-up. The results of the experimental implementation are reported in Section 5.5.2.

5.5 Investigations into Effect of Individual Test Parameters

In this section the effect of individual parameters on algorithm performance is assessed in both a series of numerical and phantom studies. The numerical studies are first described.

5.5.1 Numerical Studies

This section presents the application of sdEIT in a series of anatomically accurate numerical FEM models with a variety of lesions differing in location, size, and types. The performance of sdEIT is also examined in scenarios where measurement frames are contaminated with noise, and when the FEM models are have errors in anatomy and assumed conductivity. These test scenarios demonstrate the value of using the robust quantitative metrics along with images. Further, these scenarios both validate sdEIT and demonstrate the effect of individual test parameters on algorithm performance.

5.5.1.1 Study 1: Effect of Lesion Location

In Fig. 5.8, the reconstructed images of a 10 ml haemorrhagic lesion placed at Position (1) near the exterior, and at Position (4) near the midline, are presented. In Table 5.2 the quantitative metrics for these cases are reported. Both cases had an SNR of 20 dB. For the lesion near the exterior the IS is high (+0.56) and the disambiguation metrics clearly identify the high intensity ROI as the true lesion. When the lesion is near the midline however, the IS is -0.29 which indicates the inability of the method to detect a lesion. The analysis should be terminated at this point. However the disambiguation step if also applied also fails with no clear difference in the metrics from either the high or low ROI. This example demonstrates the challenge in detecting lesions near the line of symmetry.

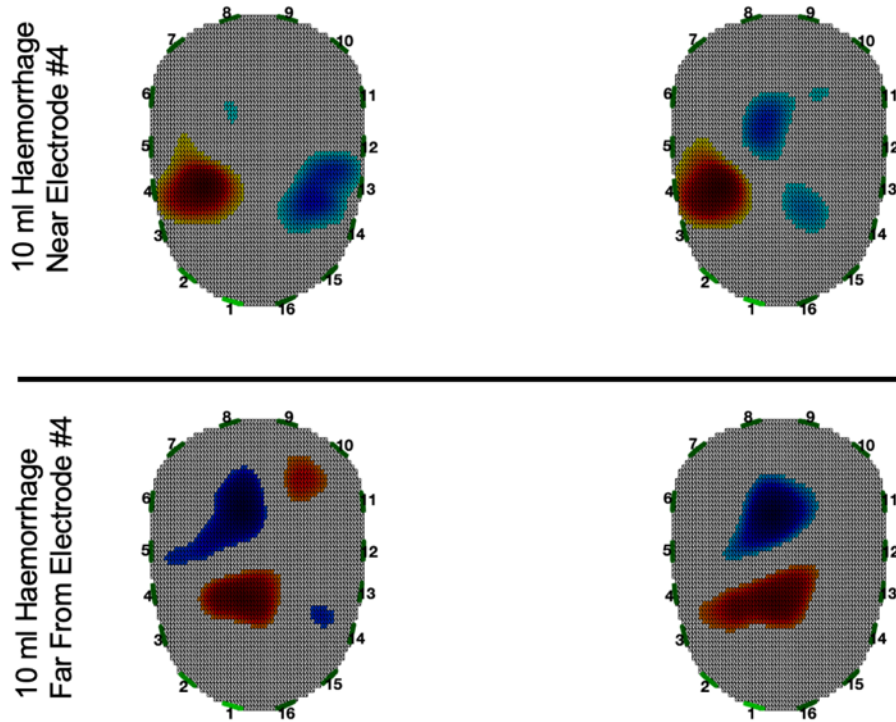


Figure 5.8: Symmetry difference images thresholded (left) and pseudo normal difference images thresholded (right) for 10 ml bleed near Electrode #4 (top) and 10 ml bleed far from Electrode #4 (bottom), both at 20 dB SNR. The lesion near the extremity shows a high IS and clear disambiguation favouring the high intensity ROI lesion. For the lesion far from the electrode near the midline of the head, symmetry is very poor. This result should lead to a decision at this point that a lesion cannot be detected. The results of the second step for the near midline lesion shows that ROI analysis fails to determine the true lesion. Quantitative metrics collating with these observations are reported in Table 5.2.

Table 5.2: sdEIT Quantitative Metrics for the separate cases of a 10 ml haemorrhage at 20 dB SNR positioned at (1) near the exterior, and at (4) near the midline.

Metric:	Case 1: At Location (1), Near Exterior		Case 2: At Location (4), Near Midline	
(i) IS	+0.56		-0.29	
(ii) Disambiguation Metrics	High Intensity ROI Analysis	Low Intensity ROI Analysis	High Intensity ROI Analysis	Low Intensity ROI Analysis
CD	2.3 pixels	26.5 pixels	0.8 pixels	6.7 pixels
F1	0.86	0.0	0.76	0.64
MID	0.02	0.02	0.02	0.18

5.5.1.2 Study 2: Effect of Lesion Size

The results of a 2 ml bleed, and 20 ml bleed at Position (5) with a 40 dB SNR are shown in Fig. 5.9. The reconstructed images give little or no indication of the size of the lesion, the largest red ROIs in all images are of similar size. Both lesions are strongly detected with the 20 ml lesion giving an extremely high IS metric of +0.92 and the smaller lesion reporting a IS of +0.48. Hence both IS scores are high indicating the lesion is clearly visible.

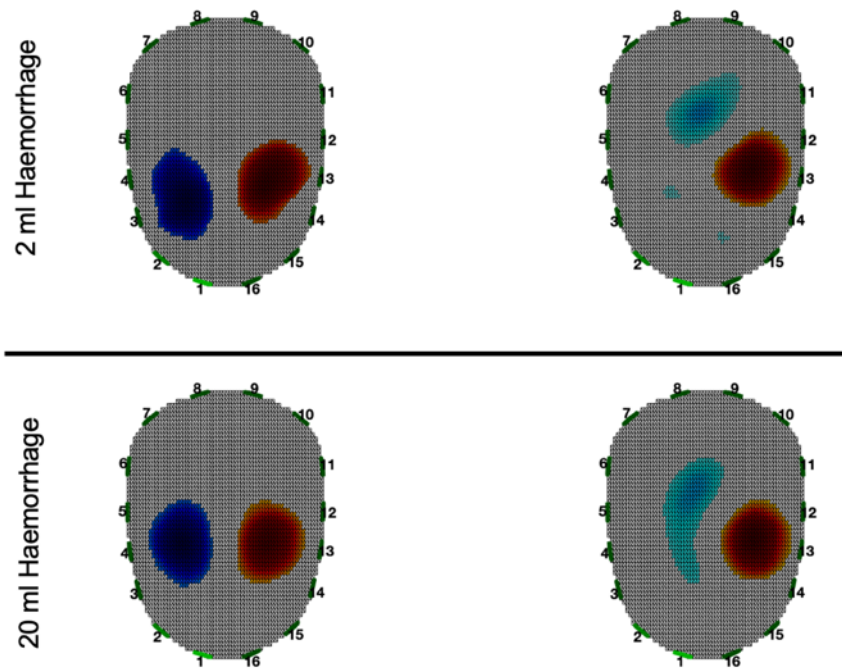


Figure 5.9: Symmetry difference images thresholded (left) and pseudo normal difference images thresholded (right) for small bleed (top) and large bleed (bottom), both at 40 dB SNR. In both cases the lesions are strongly detected, with both images sharing the high intensity ROI (i.e. haemorrhage), as quantified by the metrics reported in Table 5.3.

Table 5.3 reports the quantitative metrics from these cases. The disambiguation metrics calculated from comparison of the thresholded symmetry difference image and the pseudo normal difference image, strongly favour the high intensity ROI in both cases, with the CD, F1, and MID much closer to the expected case for a true match (near 0.0, +1.0 and 0.0 respectively) as compared to the low intensity ROI analysis. These results indicate that the high intensity ROI is the true lesion, which is a haemorrhage.

Table 5.3: sdEIT Quantitative Metrics for the separate cases of a 2 ml, and 20 ml haemorrhage positioned at (5) at 40 dB SNR.

Metric:	Case 1: 2 ml Haemorrhage		Case 2: 20 ml Haemorrhage	
(i) IS	+0.48		+0.92	
(ii) Disambiguation Metrics	High Intensity ROI Analysis	Low Intensity ROI Analysis	High Intensity ROI Analysis	Low Intensity ROI Analysis
CD	2.4 pixels	24.5 pixels	2.35 pixels	11.7 pixels
F1	0.84	0.0	0.85	0.35
MID	0.03	0.58	0.0	0.52

5.5.1.3 Study 3: Effect of Lesion Type

The contrast between brain (0.3Sm^{-1}) and an ischaemic lesion (0.1Sm^{-1}) is less than that between brain and haemorrhage (0.7Sm^{-1}). This difference in contrast implies that a haemorrhagic lesion should be more readily detectable than the equivalent ischaemic lesion. In Fig. 5.10 and Table 5.4 the sdEIT images and quantitative metrics for a 20 ml lesion of each type positioned at (5) with 40 dB SNR are presented. The results show that the true lesion is equally well detected in both cases, with the high ROI being favoured in the case of the haemorrhage and the low ROI being favoured for the ischaemic case. In both cases the CD, F1, and MID scores for the correct ROI are near the ideal score of 0 pixels, 1.0 and 0.0 respectively. The scores for the confounding lesion contrastingly are far from these ideal scores. In the case of the haemorrhagic lesion the IS score of +0.91 is coupled with disambiguation metrics favouring the high intensity ROI as being the true lesion. For the ischaemic lesion, an IS of +0.78 is followed by disambiguation metrics that indicate the low intensity ROI is the true target.

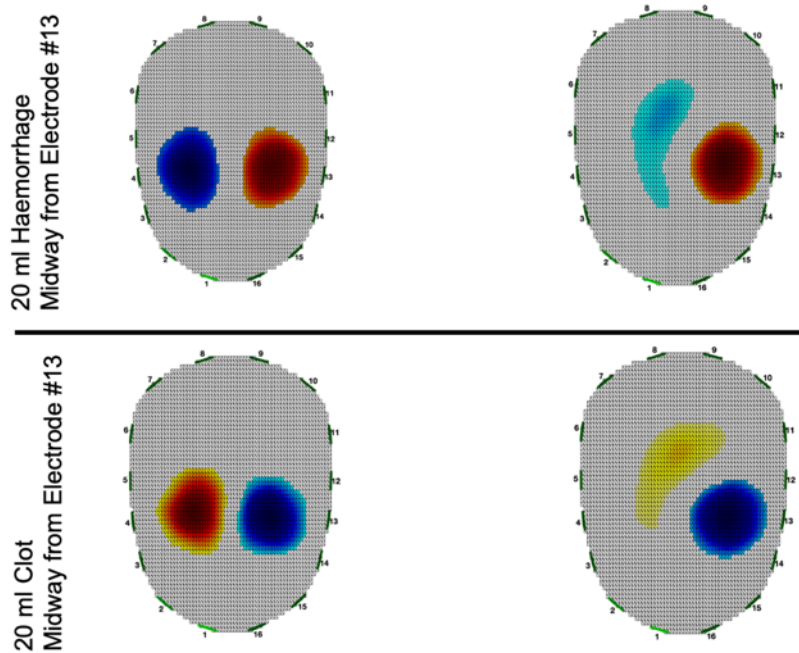


Figure 5.10: Symmetry difference images thresholded (left) and pseudo normal difference images thresholded (right) for equivalent haemorrhagic (top) and ischaemic (bottom) targets at 40 dB SNR. The symmetry difference technique detects both equally well.

Table 5.4: sdEIT Quantitative Metrics for the separate cases of a 20 ml lesion at 40 dB SNR positioned at (5), modelled as either a haemorrhage or an ischaemic lesion.

Metric:	Case 1: Haemorrhage		Case 2: Ischaemia	
(i) IS	+0.91		+0.78	
(ii) Disambiguation Metrics	High Intensity ROI Analysis	Low Intensity ROI Analysis	High Intensity ROI Analysis	Low Intensity ROI Analysis
CD	2.3 pixels	11.8 pixels	13.3 pixels	1.2 pixels
F1	0.85	0.34	0.35	0.91
MID	0.0	0.53	0.25	0.13

Surface plots of the symmetry difference image for each lesion type are shown in Fig. 5.11. These plots demonstrate that the haemorrhagic lesion results in a greater peak and trough than produced by the ischaemic lesion. This result is expected as there is a greater contrast in conductivity for a haemorrhage with respect to the healthy brain. It follows that a haemorrhage will be more readily detected than an ischaemia when approaching the limit of detection for the method (smaller lesion size, increased distance from the exterior, low SNR). This detectability is

demonstrated by considering the metrics from the case of a 10 ml haemorrhagic lesion at Position (1) at 20 dB SNR, and the equivalent ischaemic lesion also at Position (1) at 20 dB SNR as shown in Table 5.5. The haemorrhage is detectable and identifiable. The ischaemic lesion is also clearly detectable but the metrics are further from the ideal compared to the haemorrhage. For example a F1 score of 0.86 and CD of 2.3 pixels for the high intensity ROI in the case of the haemorrhage is reported compared to a F1 of 0.76 and CD of 4.6 pixels for the low intensity ROI in the case of the ischaemic lesion.

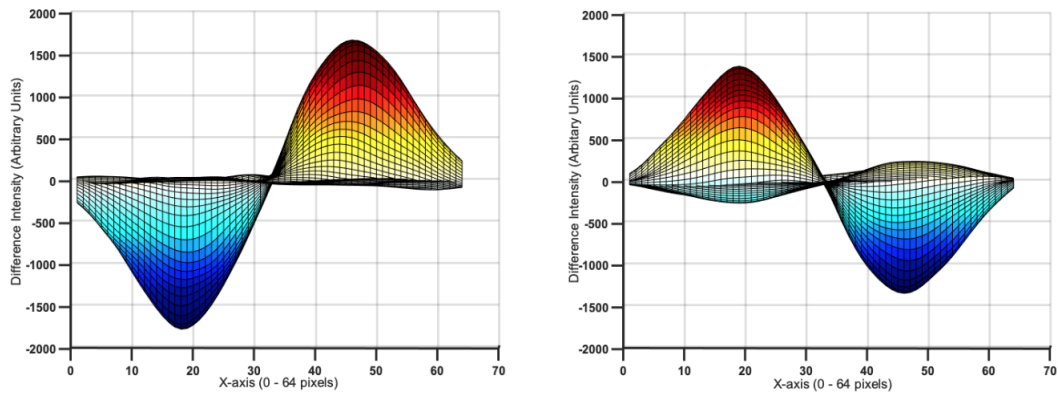


Figure 5.11: Surface plots of the symmetry difference images resulting from a haemorrhagic lesion (left) and ischaemic lesion (right) both of 20 ml located at position (5) with 40 dB SNR. The magnitude of the peak and trough corresponding to the haemorrhage and anti-haemorrhage lesion is 1669 (arbitrary units). For the ischaemic lesion this value is 1372 (arbitrary units). Hence the haemorrhagic lesion is easier to detect. However, the ischaemic lesion is still detectable.

Table 5.5: sdEIT Quantitative Metrics for the separate cases of a 10 ml haemorrhage at 20 dB SNR positioned at (1) near the exterior or a 10 ml ischaemic lesion at 20 dB also at position (1).

Metric:	Case 1: Haemorrhage		Case 2: Ischaemia	
(i) IS	+0.56		+0.53	
(ii) Disambiguation Metrics	High Intensity ROI Analysis	Low Intensity ROI Analysis	High Intensity ROI Analysis	Low Intensity ROI Analysis
CD	2.3 pixels	26.5 pixels	19.1 pixels	4.6 pixels
F1	0.86	0.0	0.21	0.76
MID	0.02	0.02	0.0	0.01

5.5.1.4 Study 4: Effect of Noise

Decreasing the SNR increases the noise in the measurement frames, and thus is expected to decrease the performance in sdEIT. This expectation is confirmed in Fig. 5.12 and Table 5.6 which present the images and metrics respectively for a 10 ml ischaemic lesion placed at position (3) under conditions of 80 dB SNR, 20 dB SNR and 10 dB SNR.

At 80 dB SNR the lesion is clearly detected and disambiguated. The IS is high with disambiguation metrics indicating the low intensity ROI as the true lesion as the low CD and high F1 scores are much closer to the ideal of 0 pixels and 1.0 respectively than the corresponding metrics from the high intensity ROI analysis. In this case, the MID results are practically the same for both ROIs rendering the metric of no value. It is emphasised that the metrics should be considered collectively when deciding on the result. Hence the failure of one metric should not lead to a conclusion that disambiguation is not possible. Good contrast in the F1 metric should lead to a decision in favour of the low intensity ROI being the true lesion. Contrastingly, at 20 dB SNR the lesion is barely detectable. The IS of +0.03 indicates a case on the limit of detection. The subsequent disambiguation metrics show a slight favouring of the low intensity ROI as evidenced by the marginally higher F1 score for the low intensity lesion. However it is suggested that this case be classified as inconclusive due to the low IS score and marginal difference in F1 scores. Finally, at 10 dB SNR the lesion is not detectable. The IS of -0.42 indicates extremely poor symmetry, confirming that detection of the lesion in this scenario is beyond the limits of sdEIT.

Existing EIT systems report SNR values typically of the order 80 dB and above [15]. Indeed a system developed specifically for use in EIT neurological applications including lesion diagnosis in stroke reported a SNR of 77.5 dB [15]. The strong performance of sdEIT at both 80 dB and 40 dB indicates that the modality could be promising for use in real world experiments.

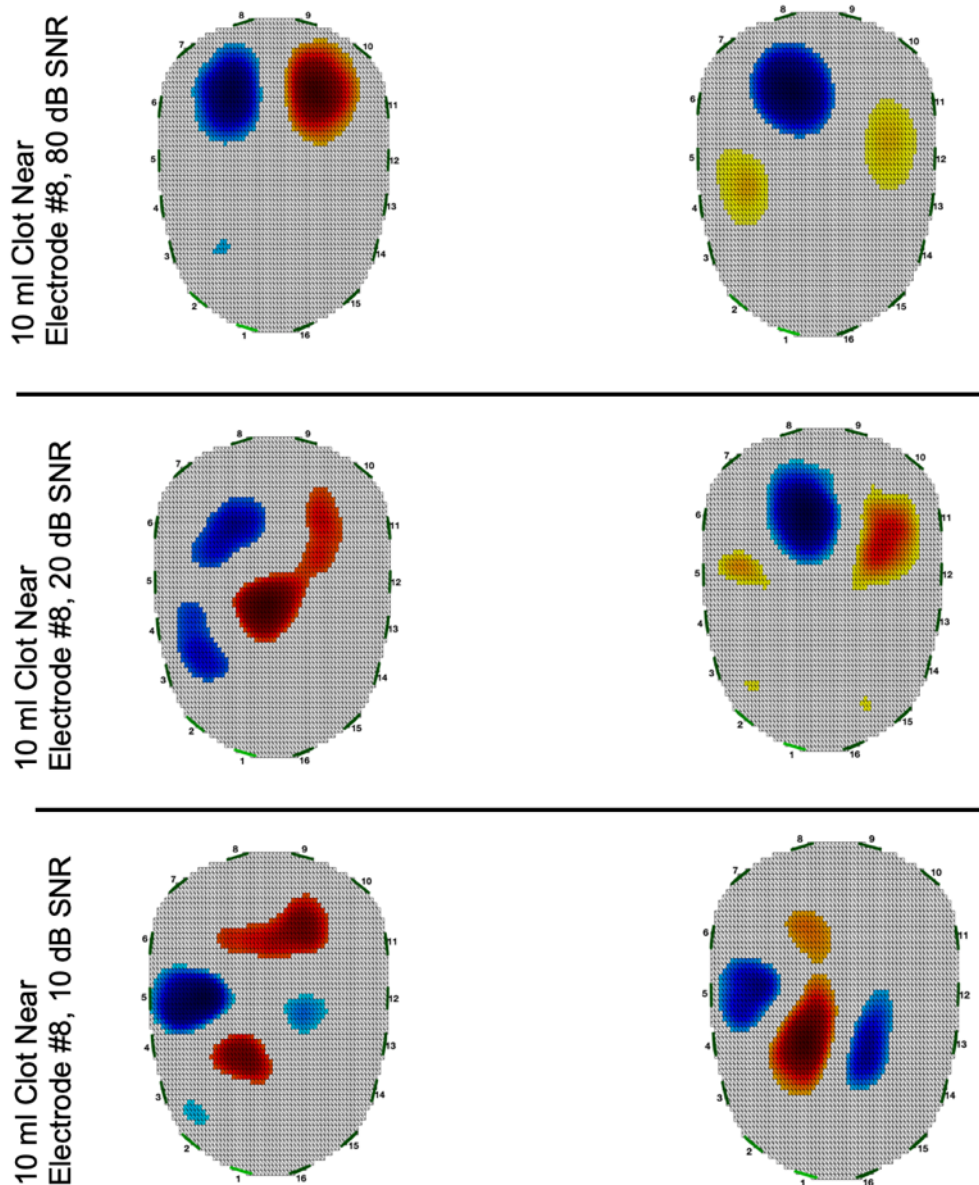


Figure 5.12: Symmetry difference images thresholded (left) and pseudo normal difference images thresholded (right) for in all the cases a 10 ml ischaemic lesion near Electrode #8: Top row images with 80 dB SNR, middle row images with 20 dB SNR, and bottom row images with 10 dB SNR. At 80 dB SNR the target is clearly detected and disambiguated. The lesion is barely detectable at 20 dB. At 10 dB SNR the lesion is undetectable. These visual analyses are quantified in Table 5.6.

Table 5.6: sdEIT Quantitative Metrics for the separate cases of a 10 ml ischaemic lesion at position (3) at 80 dB, 20 dB and 10 dB SNR.

Metric:	Case 1: 80 dB SNR		Case 2: 20 dB SNR		Case 3: 10 dB SNR	
(i) IS	+0.83		+0.03		-0.42	
(ii) Dis-ambiguation Metrics	High Intensity ROI Analysis	Low Intensity ROI Analysis	High Intensity ROI Analysis	Low Intensity ROI Analysis	High Intensity ROI Analysis	Low Intensity ROI Analysis
CD	13.1 pixels	6.2 pixels	13.1 pixels	7.1 pixels	24.2 pixels	1.2 pixels
F1	0.18	0.63	0.38	0.45	0.0	0.82
MID	0.24	0.20	0.15	0.14	0.01	0.2

5.5.1.5 Study 5: Effect of Modelling Errors

Creation of a good forward model of the normal lesion free head is the first part of Step 2 of sdEIT. As EIT is inherently sensitive to modelling errors, there is a need to keep the forward model of high quality [8], [10]. This section investigates the effect of modelling errors in the forward model of the normal case. These include errors in assumed brain anatomy, and conductivity. In order to study these errors the case of a 20 ml haemorrhagic lesion with no noise at Position (5) is considered.

In Table 5.7, the sdEIT results are reported. The results for the ideal forward model are displayed in the first row, and in following rows for non-ideal models. As Step 1 of the sdEIT process does not require use of the forward model of the normal head, the resulting IS metric has the same value (+0.88) for both ideal and non-ideal models. The results of the second step that uses the simulated forward model of the normal are now discussed.

The first row of Table 5.7 is the control case of the ideal forward model used to generate the simulated normal measurement set and subsequent image and metrics reported. Thus, the true lesion is clearly identified as the high intensity ROI (i.e. a haemorrhagic lesion) both from visual analysis and the clear disambiguation metric results of a CD of 0.5 pixels, F1 of 0.93 and MID of 0.01 for the high intensity ROI compared to 17.4 pixels, 0.17 and 0.57 respectively for the low intensity ROI.

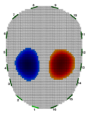
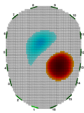
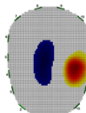
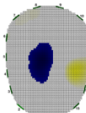
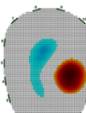
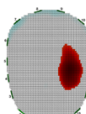
Errors in anatomical modelling are considered in the second and third row results of Table 5.7 where the effects of non-ideal anatomical modelling are shown. In the second row case a grossly asymmetric brain is used. In the third row case the brain is symmetric but reduced in volume by 10%. An intense blue artefact appears on the midline and the high intensity target although still detected is not

as obvious. The disambiguation metrics indicate this challenge in detection with results only slightly in favour of the high intensity ROI.

In the fourth and fifth rows of Table 5.7 errors in modelling of conductivity are presented. In the fourth row case the outer layer conductivity is set to 1 Sm^{-1} and the brain set to 3 Sm^{-1} . In the fifth row case the outer layer is set to 2 Sm^{-1} with the brain set to 4 Sm^{-1} . The correct conductivity values modelled for the outer layer is 0.1 Sm^{-1} and that of the brain layer is 0.3 Sm^{-1} . Hence, in the case of the fourth row the values are incorrect but the ratio is correct. In the fifth row case both the values and ratio of conductivity are incorrect. In these cases of the correct anatomy but incorrect conductivity values it is seen that if the ratio between layers is correct (fourth row) then the result is good, while incorrect ratio (fifth row) leads to deviations from the ideal control case.

It is hence seen from analysis of the results reported in Table 5.7 that having good *a priori* information to construct a forward model in terms of anatomical detail (in this case a 2-layer model) and ratio of conductivities between the layers is vital to achieving clear disambiguation between ischaemic and haemorrhagic targets. Poor anatomical detail appears to affect the results more than incorrect ratio of conductivities.

Table 5.7: sdEIT Quantitative Metrics and images for various forward models. In all cases the scenario is that of a 20 ml haemorrhage with no added noise. The first row shows the complete sdEIT result with the ideal forward model. Subsequent rows only show the output from step 2 (as the output of step 1 will be the same as in the first row) for various non-ideal forward models.

Metric:	Case 1: Ideal Forward Model		Symmetry Difference Image (Thresholded)	Pseudo Normal Difference Image (Thresholded)
(i) IS	+0.88			
(ii) Disambiguation Metrics	High Intensity ROI Analysis	Low Intensity ROI Analysis		
CD	0.5 pixels	17.4 pixels		
F1	0.93	0.17		
MID	0.01	0.57		
Case 2: Grossly Asymmetric Brain			Pseudo Normal Difference Image (Thresholded)	
(ii) Disambiguation Metrics	High Intensity ROI Analysis	Low Intensity ROI Analysis		
CD	7.0 pixels	10.9 pixels		
F1	0.59	0.31		
MID	0.19	0.17		
Case 3: Brain Shrunk in Volume by 10%				Pseudo Normal Difference Image (Thresholded)
(ii) Disambiguation Metrics	High Intensity ROI Analysis	Low Intensity ROI Analysis		
CD	8.5 pixels	9.6 pixels		
F1	0.48	0.42		
MID	0.49	0.15		
Case 4: Correct Brain Anatomy, Incorrect Conductivities but Correct Ratio				Pseudo Normal Difference Image (Thresholded)
(ii) Disambiguation Metrics	High Intensity ROI Analysis	Low Intensity ROI Analysis		
CD	1.8 pixels	11.5 pixels		
F1	0.89	0.37		
MID	0.0	0.39		
Case 5: Correct Brain Anatomy, Incorrect Conductivities and Incorrect Ratio				Pseudo Normal Difference Image (Thresholded)
(ii) Disambiguation Metrics	High Intensity ROI Analysis	Low Intensity ROI Analysis		
CD	7.1 pixels	17.9 pixels		
F1	0.62	0.0		
MID	0.19	0.61		

5.5.1.6 Study 6: More Challenging Lesion Models

In this section the performance of sdEIT is assessed in two additional cases:

- A lesion out of the plane of the electrode ring;
- Presence of multiple simultaneous lesions.

In Fig. 5.13 and Table 5.8 the images and metrics for the case of a 20 ml haemorrhage at Position (5) but raised out of the plane of the electrodes is shown for 80 dB SNR. The centre of the spherical lesion is raised by 25 mm out of the plane of the electrodes. The lesion is readily detected with sdEIT. Although the easiest detection scenario occurs when the lesion is in the electrode plane, a lesion out of the plane can still affect measurements due to the dispersive nature of current flow (Section 1.1). Any theoretical device based on a ring pattern of electrodes could be envisioned as consisting of a series of rings at different levels. Such a device by conducting readings at each level should result in any lesion present being in at least one of the planes under study and hence a maximal chance of detection.

Furthermore, it is possible that multiple lesions could be present simultaneously. For example one of the clinical conditions used to motivate this study, stroke does sometimes feature multiple lesions both in haemorrhagic and ischaemic cases [264], [265]. In Fig. 5.13 and Table 5.8 the images and metrics from the case of two haemorrhagic lesions presenting simultaneously, a 10 ml at Position (1) and 20 ml at Position (5) are reported at 80 dB SNR. The larger of the lesions is detected by sdEIT as expected, as the algorithm employs thresholds to isolate the extreme intensity regions of interest. Therefore, in the metrics the high intensity ROI is favoured.

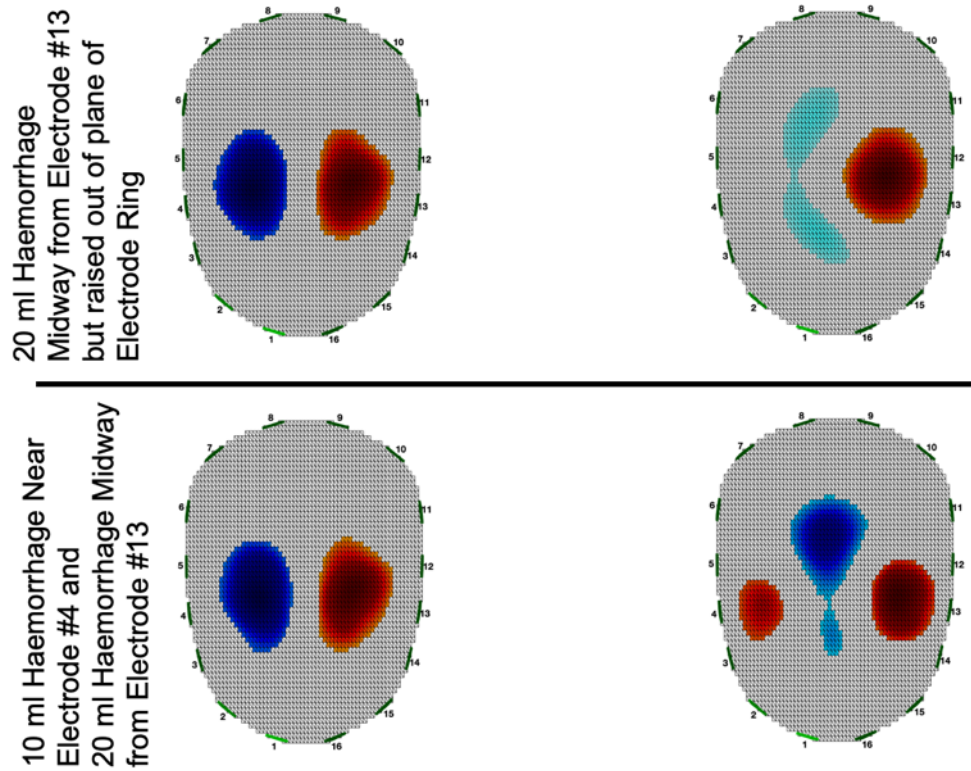


Figure 5.13: Symmetry difference images thresholded (left) and pseudo normal difference images thresholded (right) for the cases of (top row) a 20 ml haemorrhagic lesion at position (5) but raised out of the plane of the ring, and (bottom) the case where two haemorrhagic lesions are simultaneously present at both positions (1) and (5) of 10 ml and 20 ml volume respectively. The simulations are performed at a noise level of 80 dB SNR. In the case of the lesion outside the plane of the ring the haemorrhage is readily detected. For the case of two simultaneous lesions the larger bleed is detected. These visual analyses are quantified in Table 5.8.

Table 5.8: sdEIT Quantitative Metrics for the two challenging lesion cases: Lesion out of the electrode plane and multiple simultaneous lesions (both at 80 dB SNR).

Metric:	Case 1: 20 ml Haemorrhage at Position (5) but raised out of electrode plane		Case 2: Two Haemorrhagic Lesions: 10 ml at position (1), 20 ml at position (5)	
(i) IS	+0.91		+0.90	
(ii) Disambiguation Metrics	High Intensity ROI Analysis	Low Intensity ROI Analysis	High Intensity ROI Analysis	Low Intensity ROI Analysis
CD	1.5 pixels	6.8 pixels	5.6 pixels	13.4 pixels
F1	0.88	0.37	0.59	0.12
MID	0.0	0.64	0.04	0.35

5.5.2 Phantom Studies

This section details tank experiments of sdEIT using a model of brain tissue with dielectrically accurate haemorrhagic and ischaemic phantoms as described in Section 3.3.3. These phantoms differ in sizes, and are placed in various locations. Hence this section both validates sdEIT in a physical phantom, and assesses the effect of these test parameters on algorithm performance in the phantom.

5.5.2.1 Study 1: Effect of Lesion Location

The cases of the 10 ml haemorrhagic lesion positioned near the exterior of the brain at Position (1), and far from the exterior but near the midline at Position (4) are reported in Fig. 5.14 and Table 5.9. In both cases the lesions are readily identifiable. However, the case at position (1) shows stronger results as demonstrated by the higher relative IS and the disambiguation metrics which heavily favour the high intensity ROI. The increasing distance of the lesion from the electrodes reduces the quality of the result, and lesions near the line of symmetry are not as readily detectable with this technique. This matches the results from the equivalent simulation study in Section 5.5.1.1 where lesions further from the line of symmetry were easier to detect than those nearer the line of symmetry.

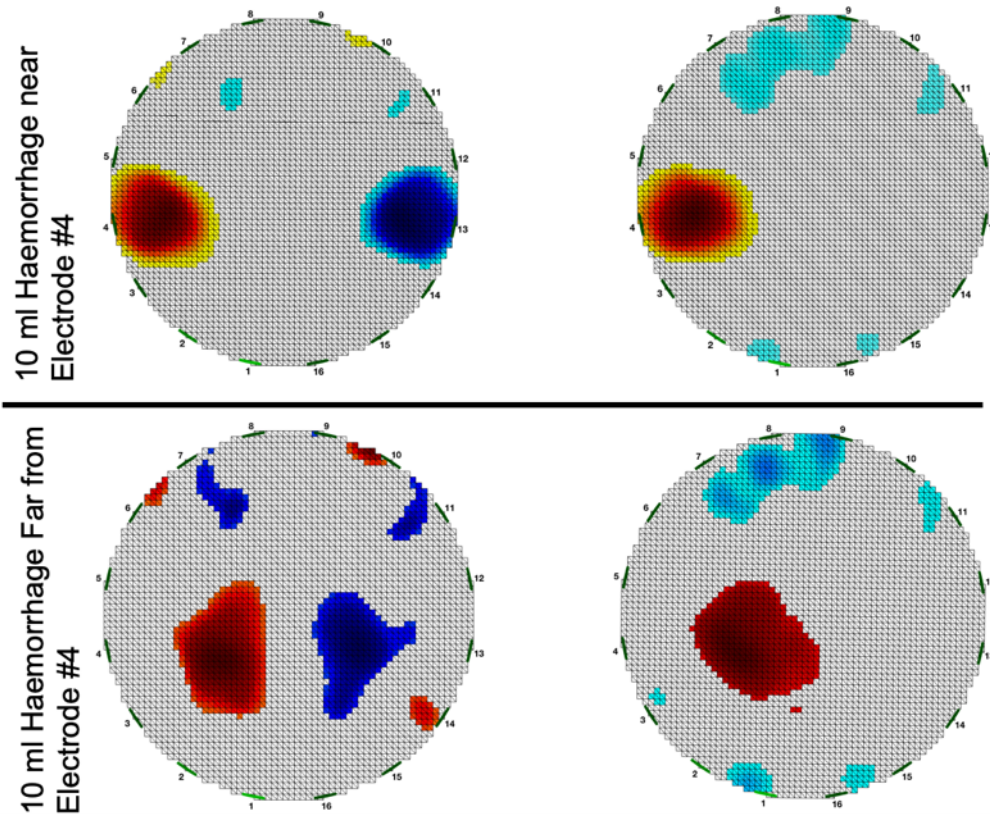


Figure 5.14: Symmetry difference images thresholded (left) and pseudo normal difference images thresholded (right) of haemorrhagic lesions of equal volume (10 ml equivalent) placed near to clockwise Electrode #4 (top row) and far from Electrode #4 (bottom row). As expected the scenario with the lesion near the electrode is more clearly detectable but the far from Electrode #4 case is also readily identified.

Table 5.9: sDEIT Quantitative Metrics for the separate cases of a 10 ml haemorrhagic lesion positioned at (1), near the exterior, or at (4), near the midline.

Metric:	Case 1: Near Exterior		Case 2: Near Midline	
(i) IS	+0.87		+0.36	
(ii) Disambiguation Metrics	High Intensity ROI Analysis	Low Intensity ROI Analysis	High Intensity ROI Analysis	Low Intensity ROI Analysis
CD	1.2 pixels	40.2 pixels	3.0 pixels	34.9 pixels
F1	0.91	0.0	0.75	0.0
MID	0.0	0.48	0.04	0.52

5.5.2.2 Study 2: Effect of Lesion Size

In Fig. 5.15 and Table 5.10 the images and metrics respectively for the 2 ml and 30 ml ischaemic lesion placed at the equivalent of position (5) in the tank are shown. The smaller lesion is not detectable, as evidenced by the negative IS score. The larger lesion is detectable as shown by a strong IS score and subsequent disambiguation metrics favouring the low intensity ROI. These results correlate with those from the corresponding simulation study (Section 5.5.1.2) where a larger lesion is more clearly identifiable compared to a smaller lesion.

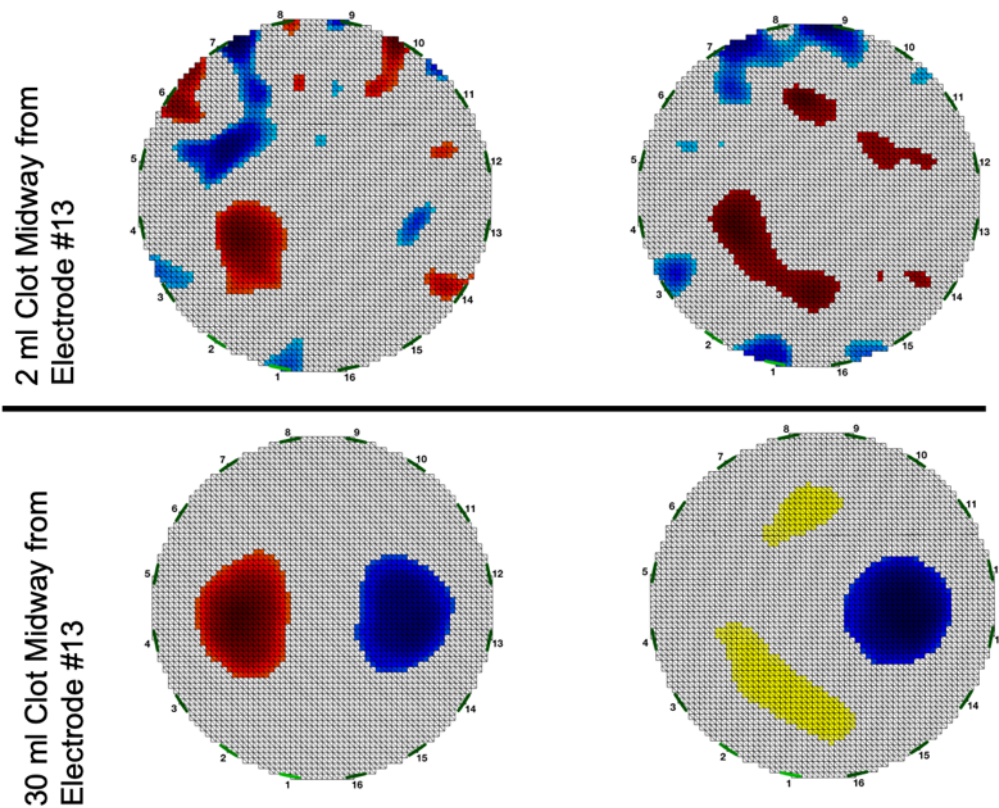


Figure 5.15: Symmetry difference images thresholded (left) and pseudo normal difference images thresholded (right) of small ischaemic lesion (top row) and large ischaemic lesion (bottom row) both positioned midway from Electrode #13. The small target, which is equivalent to a 2 ml lesion in a real brain is not detectable and the negative IS score is a clear indicator of this. The large 30 ml equivalent target is easily detectable and robustly disambiguated by the ROI disambiguation metrics.

Table 5.10: sdEIT Quantitative Metrics for the separate cases of a 2 ml and 30 ml ischaemic lesion positioned at (5).

Metric:	Case 1: 2 ml Ischaemic Lesion		Case 2: 30 ml Ischaemic Lesion)	
(i) IS	-0.39		+0.86	
(ii) Disambiguation Metrics	High Intensity ROI Analysis	Low Intensity ROI Analysis	High Intensity ROI Analysis	Low Intensity ROI Analysis
CD	4.1 pixels	15.5 pixels	15.3 pixels	1.2 pixels
F1	0.63	0.25	0.26	0.92
MID	0.07	0.07	0.36	0.31

To summarise, the sdEIT technique works successfully with experiments in the tank with the background medium representative of a homogenous brain and the targets emulating haemorrhagic and ischaemic stroke lesions. The experimental results also confirm those of the simulation and suggest that sdEIT has promise for real-world applications.

5.6 Conclusions

Clinical scenarios that are not time variant have few options for imaging with EIT as discussed in Section 2.4.6. This chapter proposes a new EIT modality to tackle these difficult imaging problems. sdEIT has the potential to develop into a stand-alone technique or as support tool for time static cases. This chapter comprehensively introduces the technique, describing its implementation and performance in a representative set of numerical and phantom experiments using the stroke clinical model as a vehicle.

Firstly, in Sections 5.2 an overview of sdEIT is given. This proposed technique can detect the presence of an abnormality where there is a natural line of symmetry in the region, and the presence of the abnormality upsets the inherent symmetry. The technique involves two distinct steps:

- Step 1: Detection of Deviation from Normal Symmetry;
- Step 2: Identification/ Disambiguation of Lesion Type.

Both steps result in images and robust quantitative metrics. These results collectively facilitate lesion detection and identification.

Next, in Section 5.3 sdEIT is introduced using a simple sample case of a large haemorrhagic lesion far from the plane of symmetry. This section initially describes the modelling techniques used, and the symmetric electrode layout implemented in order to generate two mirror image sets of measurement frames. The two steps

involved in sdEIT are then described along with the images and the quantitative metrics generated at each step.

Section 5.4.1 presents an anatomically accurate numerical model and experimental setup. These platforms are then used in a variety of test cases each investigating an individual test parameter. The results of these investigations are presented in 5.5.1, and have illustrated cases where sdEIT is successful and cases where sdEIT is inconclusive. Better, more robust performance is seen for:

- Lesions near the exterior;
- Larger lesions;
- Lesions of higher conductivity contrast;
- Situations where there is a higher SNR;
- Cases where the simulated normal is modelled accurately in terms of anatomy and conductivity profile.

Finally, a phantom tank model and corresponding experimental setup is presented in Section 5.4.2, with the results of experiments shown in 5.5.2. These phantom experiments validate sdEIT in the real world tank phantom model, with the results corroborating those seen in the numerical studies.

This chapter, in common with Chapter 4, attempts to develop a novel algorithm and modality for static imaging using EIT. In this chapter, the symmetry present in the head has been used for the first time as the basis for an algorithm with the results like those discussed in Chapter 4, showing strong promise for the application of EIT to such static and quasi-static problems. Next in Chapter 6, BFSD-EIT is introduced which builds upon sdEIT with improvements made to each part of sdEIT. These included improvements in the initial setup, modelling, image processing, and quantitative metrics. As shall be seen, this iterative algorithm moves forward the concepts and paradigms introduced in this chapter to the next stages of development, and ultimately application to human data in Chapter 7.

Bi-Frequency Symmetry Difference EIT - An Iterative Algorithm for Static Lesion Detection

Material described in this chapter was published in four peer-reviewed publications. Preliminary reports of the implementation of the algorithm in numerical models was presented as part of Bioengineering in Ireland - Proceedings of the 25th Conference of the Section of Bioengineering of the Royal Academy of Medicine in Ireland, University of Limerick, Ireland, 2019 in the conference paper entitled “Static Lesion Detection in Symmetric Scenes using Dual-Frequency Electrical Impedance Tomography” [266]. Subsequently the Institute of Physics publication Physiological Measurement entitled “Bi-Frequency Symmetry Difference Electrical Impedance Tomography – a novel technique for perturbation detection in static scenes” documented the full implementation and validation of the algorithm in both numerical and phantom models [193]. Next, the feasibility and limitations of the algorithm applied to the challenging case of stroke diagnosis was assessed and published first as a conference paper as part of the Proceedings from the 20th International Conference on Biomedical Applications of Electrical Impedance Tomography, University College London, London, England, United Kingdom, 2019 as a conference paper entitled “Bi-Frequency Symmetry Difference (BFSD) EIT in Stroke Diagnosis” [267], and then as a comprehensive journal paper entitled “Bi-Frequency Symmetry Difference EIT – Feasibility and Limitations of Application to Stroke Diagnosis” published in the IEEE Journal of Biomedical and Health Informatics [268].

This chapter presents BFSD-EIT as an iterative and improved algorithm over sdEIT (Chapter 5) for the detection of the presence, type and localisation of a perturbation with frequency-dependent conductivity in static scenes, with the implementation and validation using numerical and phantom models as well as assessment of the feasibility and limitations of the algorithm applied to the challenging stroke problem.

6.1 Introduction

In Chapter 5, sdEIT was introduced as an approach to perturbation detection, identification and localisation in challenging static scenes such as in stroke. In this chapter, an improved algorithm over that presented in Chapter 5 is proposed, called BFS-D-EIT, in order to advance the application of EIT to static lesion detection. This algorithm can be applied in situations featuring a plane of symmetry, where a perturbation causes a change in the symmetry of the scene, and where there is a known, frequency-dependent change in the conductivity of the materials in the region. Detection of changes in symmetry at two frequency points combined with *a priori* information of the expected tissues in the domain and the frequency-dependent conductivities of these tissues can be used to detect, localise and identify lesions using reconstructed EIT images and key metrics.

The chapter is laid out as follows. An overview of the BFS-D-EIT algorithm is given in Section 6.2. Section 6.3 presents the initial development and proof-of-concept of the BFS-D-EIT algorithm, while Section 6.4 considers the feasibility and limitations when applied to the stroke diagnostic problem.

With regards to the development and proof-of-concept, Section 6.3.1 details the numerical models and experimental phantoms used to collect data for this section. Section 6.3.2 describes the proposed BFS-D-EIT technique is described along with the resulting images, and quantitative metrics. A series of examples are also described to illustrate the algorithm. Next Section 6.3.3 reports results from numerical simulations with spherical bleed and clot lesions in a range of scenarios with differing sizes, locations, and SNR of the frames with select metrics used to illustrate where the technique performs well and where the technique fails. In Section 6.3.4, perturbations with frequency-dependent conductivity are examined in a variety of locations in a head-shaped tank phantom in order to validate the technique in a real-world situation (both with and without a skull layer). An overall discussion of the significance of the BFS-D-EIT technique is described in Section 6.3.5.

Section 6.4 tests the feasibility of BFS-D-EIT applied to stroke diagnosis, with the robustness of the algorithm assessed in relation to a range of limiting scenarios and modelling errors. Section 6.4.1 describes the numerical model (based on that from Section 6.3.1) developed as the test platform for this part of the chapter, and defines the quantitative metrics used in this feasibility section. Section 6.4.2 then details the test scenarios and results with performance assessed against test parameters including: measurement noise, electrode placement errors, contact impedance errors, deviations in assumed tissue conductivity, deviations in assumed anatomy,

and presence of a frequency-dependent background. The results are assessed using images and quantitative metrics, and discussed. These discussions help to defined tolerated ranges of error for the technique. Finally the technique is applied to a first human test case with data from a patient with a large clot in Section 6.4.2.8. A discussion of the section is given in Section 6.4.3 which describes the significance and limitations of the BFS-D-EIT technique applied to stroke diagnosis, and which also briefly compares the results of this work to the state-of-the-art in EIT for stroke diagnosis [17], [20]. The chapter is then concluded in Section 6.5.

6.2 Bi-Frequency Symmetry Difference - Algorithm Overview

The BFS-D-EIT algorithm is presented as an iterative improvement over sdEIT from Chapter 5. The sdEIT technique comprised of a two-step approach. The first step was detecting a deviation from normal symmetry if a unilateral lesion was present. This detection resulted in the imaging of the true lesion and a confounding anti-lesion of opposite conductivity in the mirror image position across the plane of symmetry. Then, in order to disambiguate between the true lesion and the confounding anti-lesion, the second step was to generate and analyse a pseudo time difference image using a simulated model of the normal. However, this second step required an accurate model of the normal, and as such, this is a limitation of the sdEIT technique that may hinder use in clinical applications.

Like sdEIT, the proposed BFS-D-EIT algorithm technique comprises two steps. However, BFS-D-EIT removes the need for a simulated model of the normal by instead using information from two different frequencies of measurement, combined with *a priori* information of the expected conductivity change in the tissues at the two selected frequency points. Unlike the specific information on each head shape and size that is needed for sdEIT, *a priori* information on the tissue conductivities is available from the literature (Section 2.4.2). These trends in conductivity are expected to be similar across people, albeit with an inherent degree of uncertainty in the quoted values (Section 2.4.2). For the work in this chapter, the conductivity values used are derived from studies specifically focused on the application of EIT to the stroke problem (Fig. 2.19 and [12], [139], [146]). Furthermore, in this chapter a 3D electrode layout is now used offering improved multi-dimensional information on the region of interest [139]. At each step, 3D images and customised quantitative metrics are produced and analysed. The steps involved in BFS-D-EIT are:

- First the **detection** of a deviation from normal symmetry;
- Second the **disambiguation** of the detected lesion type as haemorrhagic or

ischaemic.

The combined set of results of the two steps are used to identify the presence, type, and location of the lesion. Alternately, the results may also indicate the inability to detect a lesion.

The initial goal of this chapter is to introduce the BFS-D-EIT algorithm as a novel modality for tackling the imaging of static or quasi-static scenes. The stroke diagnostic problem is chosen as the motivating application, with the goal being the detection of the causative lesion and identification of the lesion as haemorrhage or clot (Section 2.2.2.2). These two lesion types are more conductive (haemorrhage) and less conductive (clot), respectively, than the surrounding brain tissue (Section 2.4.2, [12]). The two lesion types also differ in conductivity profiles with particular changes in conductivity seen in the low frequency range particularly between 25 to 100 Hz [12]. Thus, frequency-dependent changes in conductivity can be taken advantage of to support the differentiation of the lesion type. Therefore, the BFS-D-EIT algorithm is described in the numerical experiments (using a an anatomically realistic, 4-layer head model) through the sample application of stroke aetiology diagnosis. In the case of the phantom experiments, potato was used as a sample frequency dependent perturbation with a significant conductivity change in the range of operation (50 to 250 kHz) of the Swisstom EIT-Pioneer [12], [187].

Following this introduction of BFS-D-EIT, a thorough analysis of the feasibility of BFS-D-EIT when applied to the stroke diagnostic problem is performed by determining the limitations and examining the robustness of the algorithm with respect to a range of errors. Specifically, a series of numerical studies are conducted on the numerical model, that feature different limiting scenarios and modelling errors. The situations addressed include the effects of measurement noise, electrode placement errors, contact impedance errors, deviations in assumed tissue conductivity, deviations in assumed anatomy, and presence of a frequency-dependent background. While there may be additional possible situations, those investigated here comprise some of the most common and important errors and challenges of EIT [10], [20], [180], [181]. The result of these tests indicates where the BFS-D-EIT technique may be used, modifications that can be implemented to improve the outputs, parameter ranges that must be respected, and limitations of the algorithm when applied to stroke classification.

6.3 Bi-Frequency Symmetry Difference EIT - Initial Development and Proof of Concept

This section provides a thorough description of the BFS-D-EIT algorithm using the stroke diagnostic problem as a motivating sample application. Anatomically accurate computational models are used to demonstrate the proposed technique using different types, sizes, and locations of lesions with frequency-dependent or independent conductivity. Further, a realistic experimental head phantom is used to validate the technique using frequency-dependent perturbations emulating the key numerical simulations. The next subsection describes the models and phantom used, before subsequent subsections introduce the algorithm proper and report results of numerical and phantom experiments.

6.3.1 Modelling Techniques

In this subsection, numerical and phantom models used in the initial development of BFS-D-EIT are described. These include an anatomically accurate numerical 4-layer FEM model of the human head, as well as a phantom model based on the same anatomy. The numerical model is first described, followed by the phantom.

6.3.1.1 Numerical Models and Experimental Setup

The anatomically realistic head model described in [139] was the basis for the experiments of this study. This model was created from CT and MRI scans of an adult patient's head and is comprised of the tissues superior to a transverse plane along the level of inion-nasion line. In this model, 32 electrodes are positioned as described in [139], resulting in 4 electrodes positioned along the sagittal plane and the remaining 28 forming 14 symmetric pairs across the plane of symmetry. A CAD model was produced in Autodesk Fusion 360 [178], using the resources provided from [139]. For the work described in [139], the model comprised of 3 layers with brain, skull and scalp layers. However, in this study a CSF layer was added to the model, positioned between the skull and brain with a realistic thickness of 5 mm [225], [269]. This extra layer, resulting in a 4-layer model, is a more realistic representation of the anatomy of the head, inclusive of the resistive skull layer and conductive CSF layer surrounding the brain [6]. This 4-layer model was used in the numerical experiments.

Lesions were modelled in the numerical simulations as spheres of volume 10 ml and 50 ml and were assigned conductivity values representative of either a bleed or clot. The volumes were selected as being representative of small and large volume lesions, with the median volume of ICHs in the early stages of stroke reported as 17 ml [47],

[115]. A wide spectrum of lesion sizes is possible in stroke, with for example, the ICH volume in acute stroke reported in [47] as ranging from 1 to 101.5 ml (median 10.1 ml) and average infarction volume in acute stroke reported in [270] as $39.5 \text{ ml} \pm 84.9 \text{ ml}$. Three distinct positions were chosen for the perturbations: Position I: in the centre of the brain; Position II: on the left side of the mid-height transverse plane towards the exterior of the brain; Position III: on the right side, below the mid-height transverse plane in a caudolateral position. These positions and lesion sizes, along with a CAD model of the head including the electrode positions, are shown in Fig. 6.1.

A FEM model of the CAD model, comprised of 4,158,375 elements with refinement around the electrode positions, was subsequently created from this CAD model using COMSOL [179]. The 32 electrodes were modelled as being of diameter 10 mm, and contact impedance $1 \text{ k}\Omega$ were modelled on the scalp in a fashion similar to that described in [20]. This FEM model comprised the numerical model used in this work. The FEM model is sectioned into 4 discrete layers: brain, CSF, skull and scalp. The numerical experiments modelled the stroke aetiology differentiation problem, with focus on the conductivity of tissues between 25 to 100 Hz. As such the scalp, brain and CSF layers were assigned realistic conductivities of 0.25 Sm^{-1} , 0.1 Sm^{-1} , and 2 Sm^{-1} respectively [146], with the skull assigned a realistic conductivity distribution as a function of position ranging from 0.69×10^{-2} to $1.29 \times 10^{-2} \text{ Sm}^{-1}$ [139]. These values are considered constant across this band for the respective tissues, with in the case of skull the conductivity distribution as a function of position being constant across the band [139], [146]. However, the bleed and clot lesions were assigned conductivity values dependent on the frequency points selected, as described later in Section 6.3.2.1. The spherical lesions with assigned conductivities could be readily added to the FEM model, and measurement frames generated by forward solving of the FEM model [164].

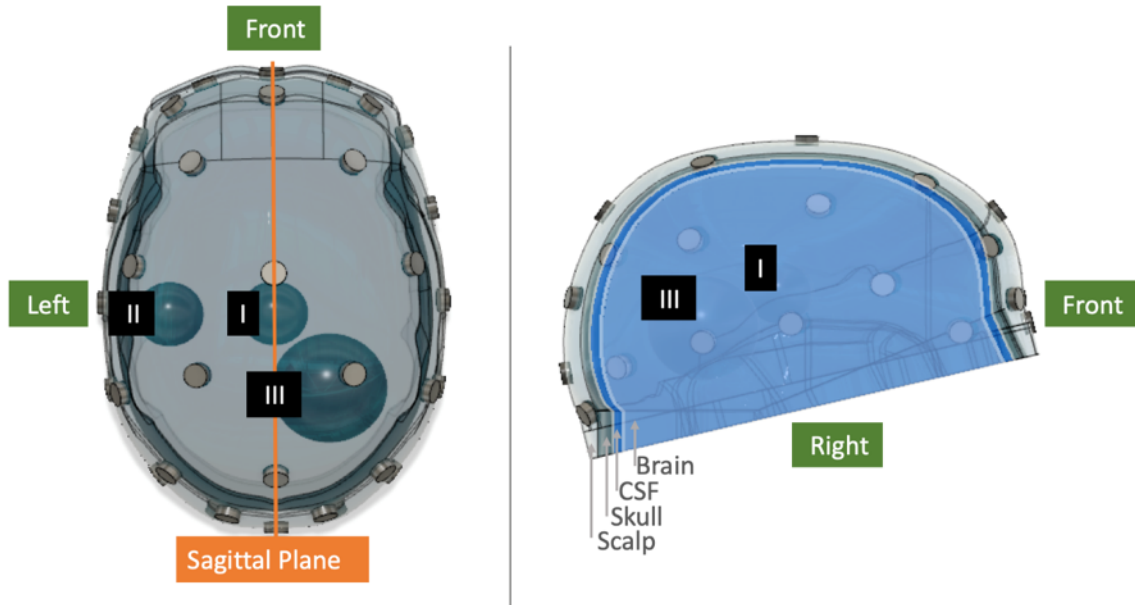


Figure 6.1: CAD model of the 4-layer head showing the scalp, skull, CSF and brain layers as well the position of the 32 electrodes. The sagittal plane represents a natural plane of symmetry in the head. Lesions in the numerical models were modelled as spheres of volume 10 ml and 50 ml positioned in one of Positions I, II or III. In this figure, 10 ml lesions are shown at Positions I and II, with a 50 ml lesion at Position III. In the phantom, cubic phantoms of equivalent volume were used at the same locations.

The proposed BFSD-EIT algorithm assumes symmetry about the sagittal plane. However a degree of tolerance to normal asymmetry must be present as the human head is not perfectly symmetric [271], [272]. As the head model used in this work and particularly the boundary (scalp), skull and brain layers are based on an actual human head, the model is not perfectly symmetric. Table 6.1 provides a metric of the degree of symmetry of the 4 layers of the numerical model. The percentage of voxels of a given layer from the RHS of the sagittal plane that if reflected across the plane fall within the boundary of that same layer as delineated by the LHS voxels is calculated. This calculation is repeated for the LHS reflected onto the RHS, with the average of the two used to quantify the percentage overlap (a proxy for the degree of symmetry). Further, Table 6.1 lists the distance error of the 32 electrodes as the distance between symmetric partners if each electrode is reflected across the sagittal plane onto the partner electrode. The electrode positions are selected largely from the EEG 10-20 system [139] which should result in a high degree of symmetry, although are positioned on a realistic imperfectly symmetric scalp.

CHAPTER 6. BI-FREQUENCY SYMMETRY DIFFERENCE EIT

Table 6.1: Degree of Asymmetry in the Head Model as (1) Mean \pm Standard Deviation of the Distance Errors of the 32 electrodes; (2) Percentage overlap between the tissues from both sides.

(1)	Mean (mm) \pm Standard Deviation (mm) Of Distances between Symmetric Pair Electrodes (if reflected across the sagittal plane)
	0.08 ± 0.13
(2)	Percentage Overlap Of voxels of each respective tissue (if RHS reflected across the sagittal plane onto LHS and then vice-versa)
Scalp	93.5%
Skull	90.1%
CSF	90.9%
Brain	98.3%

This subsection has detailed the design of numerical model, with the corresponding phantom based on the same geometry and anatomy now described.

6.3.1.2 Phantom Model and Experimental Setup

The phantom was developed by 3D-printing the adult tank described in [139]. The 3D print material was Accura ClearVue[®] polymer and it was printed using a 3D STL printer with a resolution of 4000 Dots per Inch (DPI). The resulting phantom is geometrically equivalent to the FEM numerical model, the exception being the absence of the CSF layer.

The skull layer consists of pores designed to divide identical saline brain and scalp layers while allowing the flow of current in such a manner (presuming that saline of conductivity 0.4 Sm^{-1} is used) that the effective conductivity of the skull is as modelled numerically with a conductivity ranging from 0.69×10^{-2} to $1.29 \times 10^{-2} \text{ Sm}^{-1}$ as a function of position [139]. In the phantom experiments, perturbations were cubes of potato with either 10 cm^3 or 50 cm^3 volume, positioned as described above. Potatoes constitute a readily available material that exhibit frequency-dependent conductivity over the range of operation of the EIT hardware system used in this study, the Swisstom EIT-Pioneer [12], [187]. The phantom is shown in Fig. 6.2 with electrodes attached and perturbation positioned. As is described in Section 5, phantom experiments were conducted with both a 1-layer model with the skull removed, and a 3-layer model with the skull in place. In all cases, 0.04 M saline was used in the phantom experiments, which has a conductivity of 0.4 Sm^{-1} [153].

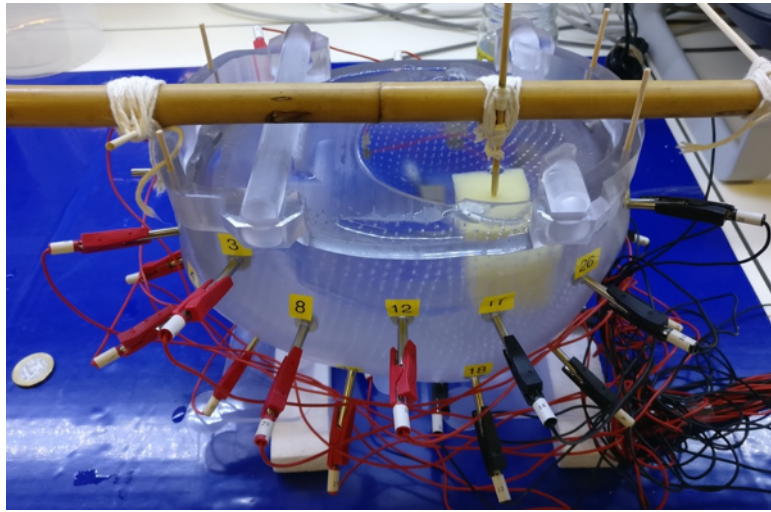


Figure 6.2: 3D printed phantom of the 3-layer head model with 10 cm^3 potato perturbation at Position III. The perturbations are suspended in place using a wooden pole and small stick as shown.

6.3.2 Bi-Frequency Symmetry Difference EIT Algorithm and Quantitative Metrics

In this section, the BFS-D-EIT algorithm is described in detail. The generation of both images and quantitative metrics using the technique, is now discussed step-by-step. Use-case examples, particularly of a 50 ml clot at Position III in the numerical model is described in subsection 6.3.2.1.

The algorithm can be summarised in two steps:

1. Detection of Deviation from Normal Symmetry.

The array of 32 electrodes on the scalp form 14 symmetric electrode pairs with the 4 electrodes on the sagittal plane forming symmetric pairs with themselves. There is also a 33rd electrode on the sagittal plane in the EEG Nz position that acts as a ground electrode. A protocol is developed that maximises the distance between electrode pairs, leading to more channels that traverse the brain, supporting detection of both deep and superficial lesions. This protocol is similar to the approach described in [20]. A measurement frame is taken in this “A-orientation” with a second frame taken in the mirror image “B-orientation”. The B-orientation is made up of electrodes each of which is the symmetrical partner of the corresponding electrode in A-orientation. The protocol used is the same in both orientations.

Data is collected with both orientations at frequency point 1 (f_1), where the

CHAPTER 6. BI-FREQUENCY SYMMETRY DIFFERENCE EIT

conductivity of the tissues is assumed as *a priori* information. A difference image is then produced using the frames from the two orientations. Detection metrics are also calculated. Deviations in symmetry between A-orientation and B-orientation are ideally detected. If a lesion is present on one side of the head, two objects will be detected: the lesion on the correct side of the head, and a confounding anti-lesion which has opposite conductivity and a mirror image position across the sagittal plane. If there is no lesion present, or if the lesion is positioned over the line of symmetry, no lesion will be detected.

2. Disambiguation of Lesion Type.

Step (2) involves comparing the results from performing Step (1) at f_1 , and again at a new frequency point (frequency point 2, f_2). Ideally, the conductivity of the tissues at f_2 is known. However, at minimum the trend in the change of conductivity of the tissues with respect to the first frequency point should be known. The results of this step, in combination with the results of step (1) and the *a priori* knowledge of the trend in conductivity values between f_1 and f_2 , can be used to disambiguate which type of lesion is the true pathology based on analysis of the images and the associated metrics. These steps are also summarised in Fig. 6.3.

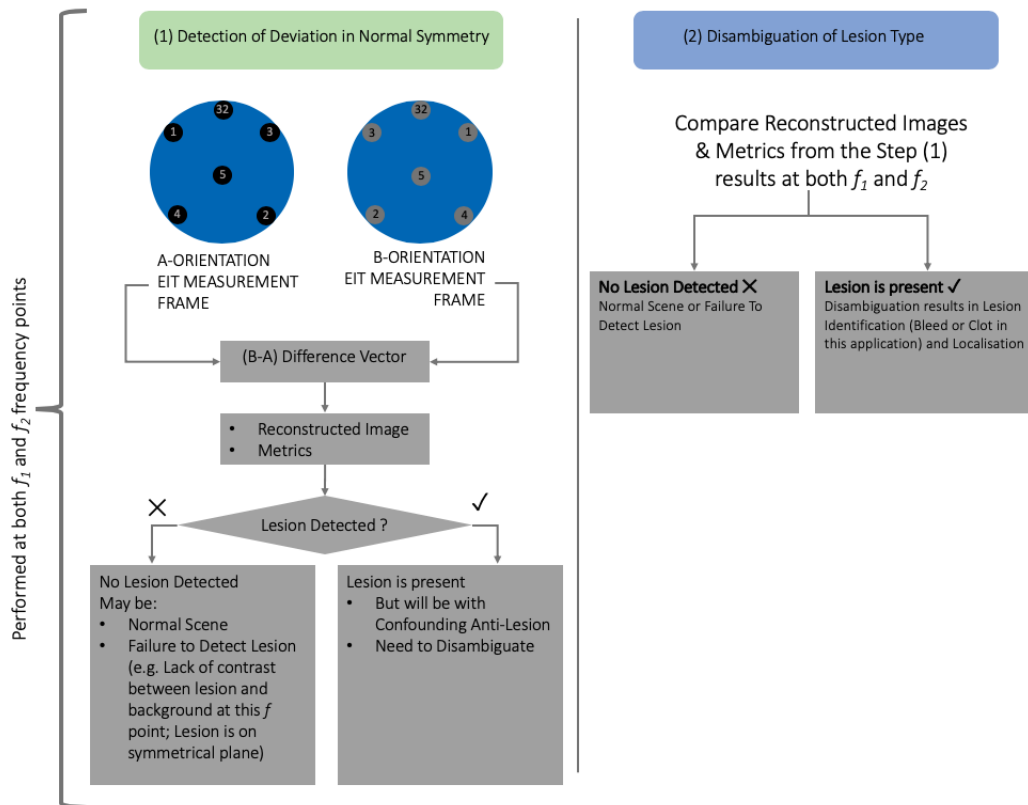


Figure 6.3: Summarised version of the two steps comprising the BFSD-EIT algorithm. In Step (1), the outcome is the detection (or lack thereof) of a lesion. After Step (2), the conclusion is either no lesion detection or lesion detection with disambiguation resulting in identification (bleed or clot in this application) as well as localisation.

For stroke, the two lesion types are more (bleed) and less (clot) electrically conductive than the brain [12]. Hence after Step (1) a bleed (if detected) would result in an image and metrics indicating the presence of a bleed with a confounding anti-lesion that is indistinguishable from a clot, and vice-versa. This inconclusive outcome necessitates Step (2) for disambiguation of lesion type.

Now that the technique has been described at a high level, the specifics are provided as follows. First, Pair Drive Skip 0 Protocol [10] was calculated which used the results from an inverse travelling salesman algorithm implemented using MATLAB [173], and maximised distances between electrode pairs. Forward models of the numerical FEM model without and with lesions (differing in conductivity, size, and location) were created. The protocol was used to generate measurement frames using the Parallel EIT Forward Solver (PEITS) algorithm as described in [20], [164]. The peak-to-peak current amplitude used was dependent on the selected

CHAPTER 6. BI-FREQUENCY SYMMETRY DIFFERENCE EIT

frequency according to that allowed by IEC 60601-1 [11], with measurements taken at different frequencies using different current amplitudes objectively compared using appropriate gain adjustments. For example at f values of < 100 Hz a current of amplitude $45 \mu\text{A}$ was used [13]. A measurement frame was generated for the A-orientation. This measurement frame was arbitrarily assigned as the ‘before’ and denoted as Frame_A . The protocol was repeated, and a frame was generated for the mirror image B-orientation. This measurement frame was arbitrarily assigned as the ‘update’ and denoted as Frame_B . Each electrode in A-orientation and the corresponding electrode in B-orientation are symmetrical partners. In this way, a given measurement pair from a given orientation represents information on the mirror image scene to what is seen by the equivalent measurement pair of the other orientation. This symmetry between orientations is illustrated in Fig. 6.4.

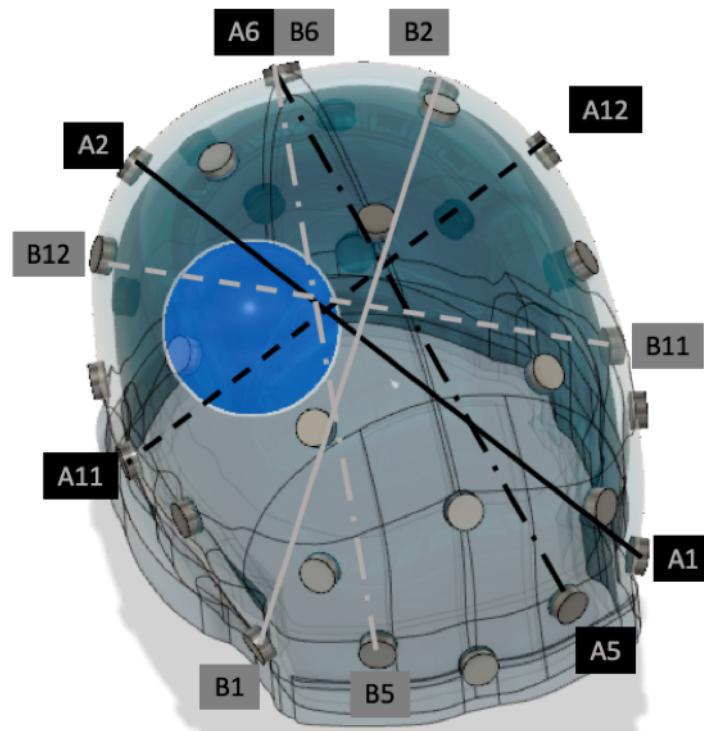


Figure 6.4: Six electrodes from A-orientation and the symmetrically equivalent B-orientation are shown along with 3 sample electrode pairs from each orientation. Any given pair from A-orientation is the symmetric equivalent of that from B-orientation (for example A11-A12 is the equivalent of B11-B12). In the absence of a perturbation or if there is a perturbation lying on the sagittal plane, the measurement recorded from a given pair should be identical to the respective symmetric partner pair. In this diagram, a 50 ml perturbation is in Position III (highlighted in blue). The perturbation will result in differences in the symmetric partner pair measurements. Also, it is seen that Electrode #6 from both orientations lies on the plane of symmetry (the sagittal plane) and so is its own symmetric partner. Finally, it can be seen that the algorithm used to design the Pair Drive Skip 0 pattern ensures that the distances between each electrodes pair constituting a channel is maximised.

The inverse problem of EIT is solved using 0th ordered Tikhonov reconstruction onto a coarse mesh corresponding to A-orientation (252,705 voxels), with the difference vector ($\text{Frame}_B - \text{Frame}_A$) as an input. A given voxel will be of positive intensity (arbitrary units) if the difference vector indicates the measurements from B-orientation are more conductive than those of A-orientation at that location. The size of the contribution of each measurement pair at that voxel depends on the reconstruction algorithm. Similarly, a voxel will feature negative intensity if the measurements from B-orientation are less conductive than those of A-orientation at that location. The magnitude of the intensity is proportional to the magnitude of the difference, with each voxel having an individual intensity value. Quantitative

CHAPTER 6. BI-FREQUENCY SYMMETRY DIFFERENCE EIT

metrics are produced from the set of voxel intensity values for each reconstruction performed at each f point (i.e. each of the two times Step (1) is performed). An image is also rendered for each reconstruction.

The first metric, the Global LHS & RHS Mean Intensity (GMI) is calculated based on the intensity of the collective set of voxels of on each side of the sagittal plane. Subsequently, thresholding is performed to focus attention on ROIs, which are candidate lesions, with further metrics applied to the detected ROIs. The GMI is defined as:

- GMI: The average intensity over all voxels on either side of the sagittal plane. Hence the GMI will be a two part number with a LHS and RHS value. In the presence of a lesion the values for RHS and LHS should be, ideally, of equal magnitude but opposite sign. In the absence of a lesion (or inability to detect a lesion), this “equal but opposite” pattern will not be present and further, theoretically, the values in such cases should be near zero. This metric alone can be used to detect, identify and to an extent localise a lesion (as explained further in Section 6.3.3). However, corroborative information from the images and other metrics is ideally also used before a diagnostic decision can be finalised. The GMI is given by:

$$GMI = \frac{\sum_{i=1}^{i=n_{LHS}} (VoxelIntensity)_i}{n_{LHS}} : \frac{\sum_{j=1}^{j=n_{RHS}} (VoxelIntensity)_j}{n_{RHS}} \quad (6.1)$$

Where n is the number of voxels on the LHS or RHS respectively.

Candidate lesions are then focussed on by thresholding to only show the highest and lowest 2% of voxels by intensity. This threshold value was chosen empirically. The thresholding process highlights contiguous ROIs. The ROIs are further filtered to remove ROIs < 5 ml in volume. This 5 ml value is deemed a threshold volume below which detection is unreliable [131]. A final filtering steps removes ROIs centred within 10mm of the mesh surface. ROIs within this proximity to the surface are deemed to be outside the brain layer and further, artefacts are often on the surface or around electrodes where EIT is sensitive to errors [8], [225]. The largest ROIs of both the high and low set of thresholded voxels are analysed (ROI_H , ROI_L) with further quantitative metrics including:

- Volume: The volume in cm^3 of the ROIs (i.e. the largest contiguous set of voxels in the thresholded image for both the ROI_H , ROI_L);
- ROI Mean Intensity (RMI): The mean intensity value (arbitrary units) of the ROI in the difference image per unit volume. Reported for both the ROI_H

and ROI_L . The value is (+) for an increase in conductivity, (-) for a decrease. The trend in this metric for both ROIs should reflect that of the GMI;

- **Difference in Centroid Location (DCL):** The difference in the centroid locations between the ROI_H and ROI_L for a given image. If one ROI is reflected across the plane of symmetry, ideally the two ROIs should superimpose perfectly resulting in a $\text{DCL} = 0$. A large deviation from zero indicates that the two detected ROIs are not symmetric and there is no lesion present, or that the technique cannot detect the lesion. Therefore, this is the first metric that should be analysed after the GMI.

In this section, the BFS-D-EIT algorithm has been described step-by-step, along with the images and quantitative metrics generated. In the next subsection, illustrative examples are given of the algorithm and results.

6.3.2.1 Bi-Frequency Symmetry Difference EIT Example Cases

A numerical example is now presented, of a noise-free case with a 50 ml clot at Position III. The clot is assigned a conductivity of 0.05 Sm^{-1} in step (1) (corresponding to a f_1 of 25 Hz) and then a conductivity of 0.09 Sm^{-1} in step (2) (corresponding to a f_2 of 100 Hz) [12], [146]. As described in Section 6.3.1.1, at these two frequency points, the other tissues (scalp, skull, CSF, brain) are considered to have constant conductivity. The scenario where background tissues change in conductivity between f points is considered later in Section 6.4.2.7. Reconstructed images at both frequency points, for the selected use-case example, are shown in Fig. 6.5. In this figure, voxels of intensity within the mean \pm one standard deviation of the voxels constituting each ROI (ROI_H and ROI_L) are depicted. Hence, the figure is of the two ROIs and any other voxels with intensities within the high and low thresholded ranges. Fig. 6.5 also provides the quantitative metrics associated with each frequency point.

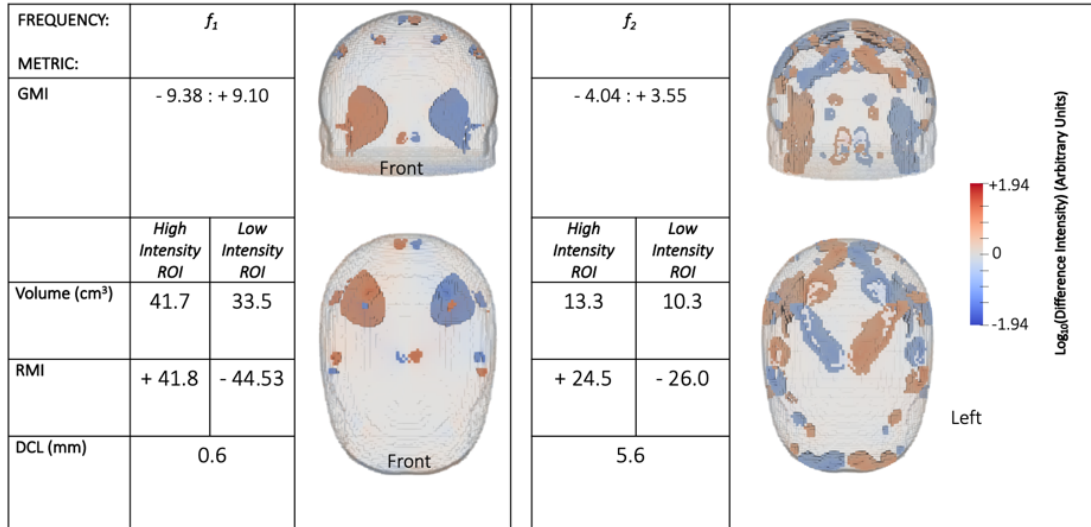


Figure 6.5: Reconstructed images and quantitative metrics for a 50 ml clot at Position III. At f_1 the lesion has a conductivity of 0.05 Sm^{-1} and the surrounding brain conductivity is 0.1 Sm^{-1} . The image for this frequency point shows ROIs suggestive of a conductive lesion in the true position and a confounding anti-lesion in the symmetrically opposite position. This result could be caused by a clot in Position III or a bleed in the symmetrically opposite position. Also, artefacts are seen near the mesh surface. At f_2 a clot has a conductivity of 0.09 Sm^{-1} while the brain conductivity is the same as at f_1 . The result is a much noisier image at f_2 than f_1 due to the reduced contrast. A clot is expected to produce this behaviour while the image of bleed at f_2 would give a result identical to the first image (at f_1). Hence the true lesion must be a clot, at Position III. The quantitative metrics support this conclusion with both the GMI and RMI having an “equal but opposite” pattern with larger magnitude in figures at f_1 than at f_2 as a result of more contrast between the tissues at f_1 than at f_2 . The enhanced contrast is also reflected in the increased volume of ROIs at f_1 and smaller DCL, relative to f_2 .

The image at f_1 shows a conductive lesion in the correct position and a confounding non-conducting anti-lesion in the mirror image position across the sagittal plane. Artefacts are also present in the image. These artefacts are largely localised towards the surface of the mesh, which is especially sensitive to errors in electrode position, and in this case imperfections in symmetry. Since the reconstruction is onto the mesh corresponding to A-orientation, the frame for A-orientation (the ‘before’) has encoded in it the information that a clot is at Position III. The remainder of the scene when considered from the view of A-orientation is normal. The frame for B-orientation (the ‘update’) indicates that the clot is in the mirror position to Position III, and the rest of the scene is normal. Hence, the difference vector indicates that Position III has changed from a relatively non-conductive clot in the ‘before’ to normal in the ‘update’. This is effectively an increase in conductivity from the

‘before’ to the ‘update’. The mirror position to Position III has had the opposite change. This result could occur either due to a clot at Position III or due to a bleed in the mirror image position. The image at f_2 indicates that the true lesion is that of a clot. This determination is evident from the images since at f_2 the image is noisier than at f_1 due to the decreased contrast between clot and brain conductivity at f_2 compared to at f_1 . If the true lesion was a bleed, then the conductivity contrast between the bleed and the brain is the same at both frequency points and hence the images would be effectively identical. This conclusion is supported by the metrics. With the GMI metric, an overall increase in conductivity on the LHS is seen, and a near equal but opposite decrease occurs on the RHS. The magnitude of GMI values decrease at f_2 compared to f_1 . This decrease is expected behaviour for a clot on the LHS as the contrast between the lesion and surrounding brain decreases at f_2 relative to f_1 . The ROI metrics correlate with a larger volume and RMI, with a smaller DCL, for the ROIs at f_1 compared to f_2 due to the improved contrast at f_1 .

For completeness, additional results are shown in Fig. 6.6 that examine the three other possible scenarios that may occur. While in Fig. 6.5 the data corresponds to a scenario in which there is a clot on one side of the brain, in Fig. 6.6, the results are for cases of:

- A bleed on one side of the brain, modelled by a 10 ml bleed at Position II;
- A bleed on the line of symmetry, modelled by a 50 ml bleed at Position I;
- A normal brain, with no lesions present.

CHAPTER 6. BI-FREQUENCY SYMMETRY DIFFERENCE EIT

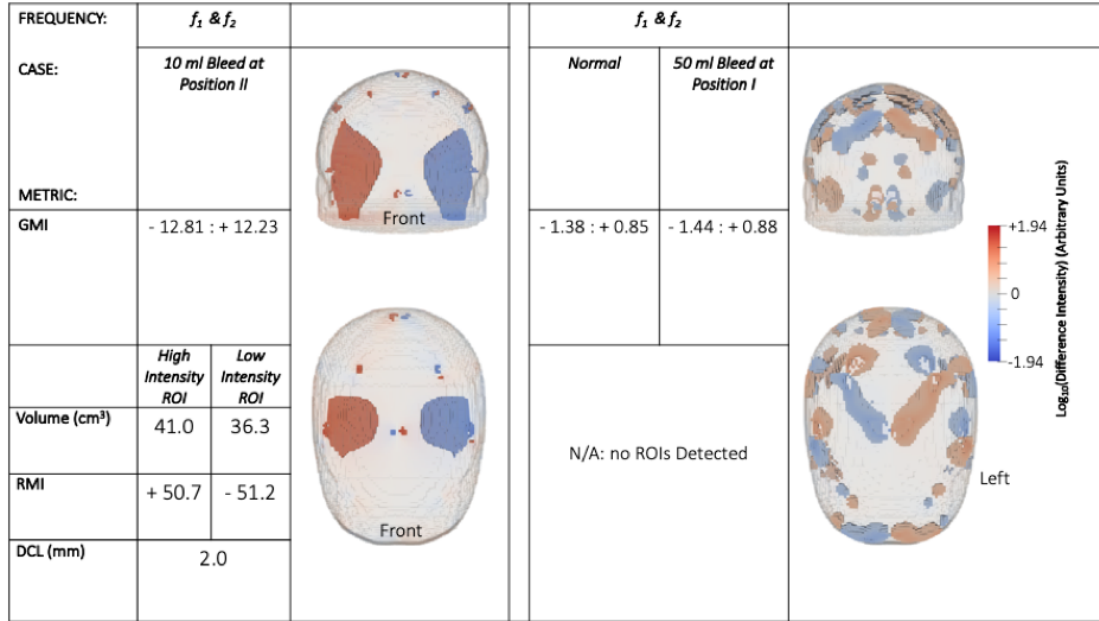


Figure 6.6: Reconstructed images and quantitative metrics for a 10 ml bleed at Position II (left) and for a case where no lesion is present (right). For both scenarios, the conductivities of the tissues are the same at both f_1 and f_2 , meaning the results are identical at both frequency points, hence only the results at one f point (arbitrarily f_1) are shown. The case with no lesion is near identical to the case where a 50 ml bleed is at Position I (not shown), since there is no deviation in symmetry between the two sides when a lesion lies on the plane of symmetry and hence no lesion is detectable. Artefacts are seen near the mesh surface but are not part of the brain layer.

A bleed is seen to give the opposite pattern of results to a clot. The reconstructed image of a bleed scenario has the ROI_L in the true location. At the two chosen frequency points, the conductivity of a bleed and the surrounding brain tissue are constant at 0.7 Sm^{-1} and 0.1 Sm^{-1} respectively. Hence, the two BFS-D-EIT steps give identical results. Therefore, if the repeat of Step (1) of the BFS-D-EIT technique leads to results identical to those of the first time Step (1) is performed, then the lesion can be identified as a bleed. In the case of a normal, there is no difference in symmetry between the sides, and theoretically an image of low (near zero) voxel intensity is produced. Artefacts at or near the mesh surface in the scalp and skull layers are seen in the image and result in a non-zero GMI. However, the magnitude of the GMI metric in the normal case is much smaller than if a lesion were present. The low magnitude of GMI means that more noisy voxels are visible as part of the 2% threshold. However, the image is clearly noise with no coherent ROI seen in the brain layer, and the filters described in Section 6.3.2 result in the artefacts

not being detected as ROIs. The case of a lesion evenly positioned across the plane of symmetry gives the same result as a normal, as there is no deviation in the symmetry of both sides. Hence, even a large lesion such as a 50 ml bleed is undetectable using BFS-D-EIT if it is positioned evenly across the line of symmetry.

This subsection has provided numerical example cases of the use of BFS-D-EIT in identification and detection of lesions. In the next section, a comprehensive set of numerical studies are performed examining the effect of lesion type, size, location, and SNR.

6.3.3 Numerical Studies

In this section, the BFS-D-EIT results are presented for a range of numerical simulations. In these simulations, the f_1 and f_2 values were chosen so that the conductivity of a clot changes from 0.05 Sm^{-1} (corresponding to a f_1 of 25 Hz) to 0.09 Sm^{-1} (corresponding to a f_2 of 100 Hz). Meanwhile the conductivity values of scalp (0.25 Sm^{-1}), skull (0.69×10^{-2} to $1.29 \times 10^{-2} \text{ Sm}^{-1}$, varying spatially), CSF (2 Sm^{-1}), brain (0.1 Sm^{-1}) and bleed (0.7 Sm^{-1}) are constant between the two f values [12], [139], [146]. The rationale for the selection of f_1 at 25 Hz and f_2 at 100 Hz values is the clear dichotomy in the trend of conductivity values of bleed and clot with respect to the background tissues in this range [12]. This divergence is necessary for BFS-D-EIT.

BFS-D-EIT results from 13 cases are reported:

- A normal (i.e. no lesion present);
- 10 ml and 50 ml lesions, of both bleed and clot, at each of Positions I, III, and III.

The BFS-D-EIT technique is applied to noise-free frames, and to frames with added noise at levels of 60 dB and 40 dB SNR. Due to the large size of the dataset reporting of all results (images and metrics) from all scenarios is not possible. Therefore, only the GMI, RMI, and DCL metrics are reported for brevity. Together, these metrics indicate when the technique works well and when it fails. However, ideally a full set of results with all images and metrics as given in Section 6.3.2.1, would be used for a firm conclusion to be reached regarding the presence, type, and location of a lesion. The notation for each case is described in Table 6.2. This notation is used throughout with the addition of ‘1’ or ‘2’ added indicating a case at f_1 or f_2 respectively. Fig. 6.7 shows the GMI results, while Fig. 6.8 gives the other quantitative metrics for various cases at the different noise levels.

CHAPTER 6. BI-FREQUENCY SYMMETRY DIFFERENCE EIT

Table 6.2: Notation for the numerical experimental setups (upper case – bleed; lower case – clot. Position I: centre of the brain; Position II: left side of the mid-height traverse plane towards the exterior of the brain; Position III: right side, below the mid-height traverse plane towards the exterior of the brain).

Case Notation	Case Description
N	Normal (No Lesion)
A/ a	10 ml, Position I
B/ b	50 ml, Position I
C/ c	10 ml, Position II
D/ d	50 ml, Position II
E/ e	10 ml, Position III
F/ f	50 ml, Position III

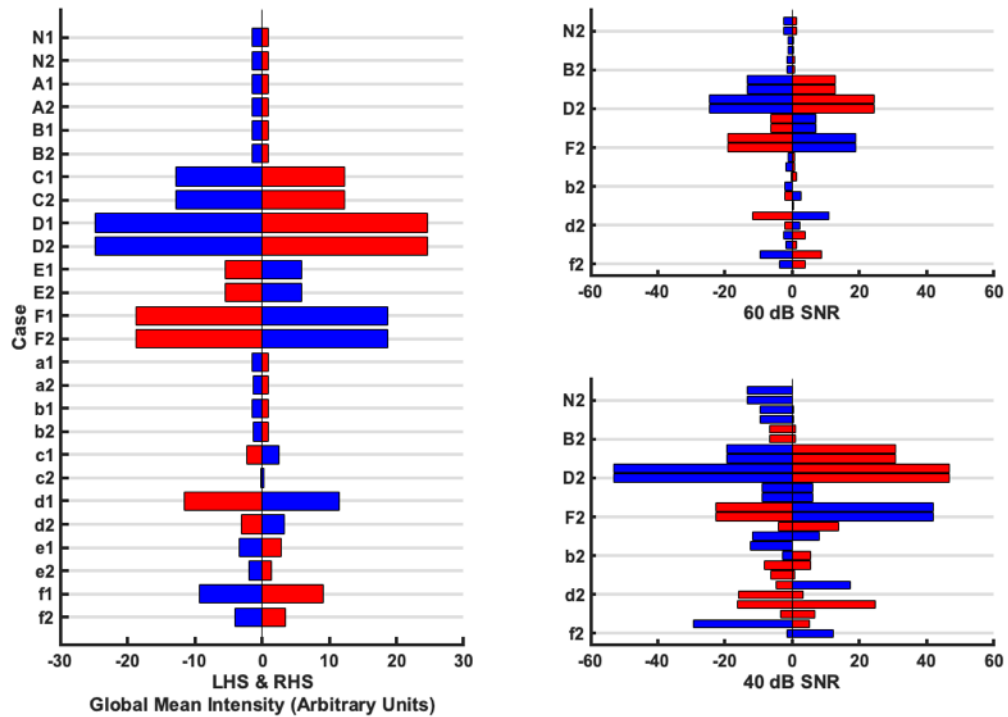


Figure 6.7: GMI metrics for each of the 13 cases at each of the noise levels. The notation used to describe each case is given in Table 6.2 with ‘1’ corresponding to f_1 and ‘2’ corresponding to f_2 . The blue bars represent a negative intensity value and the red bars a positive intensity value on either the LHS or RHS depending on the case. The normal case (N) and lesions on the sagittal plane (Position I, i.e., cases A/a and B/b) are expected to have near zero values. Bleeds away from the midline (Positions II and III, i.e., cases C-F) are expected to give identical results at each frequency. Clots away from the midline (i.e. cases c-f) will result in values of increased magnitude at f_1 relative to at f_2 as the contrast between clot and the background reduces. Left: Results with noise-free frames (i.e., $\text{SNR} = \infty$). Right: Results with 60 dB and 40 dB SNR. Note the axes correspond to those of the noise-free plot, with the grid lines grouping cases of the same location and nature. At 60 dB the results are still similar to the noise-free scenario, however now the “equal but opposite” property is compromised. At 40 dB, results become excessively noisy with only cases C, D, F clearly detectable. These plots indicate that the presence and disambiguation of a lesion is possible with this metric alone. Larger lesions should have values of greater magnitude than the corresponding smaller lesion. The localisation to the level of whether the lesion is in the LHS or RHS, is also possible to derive.

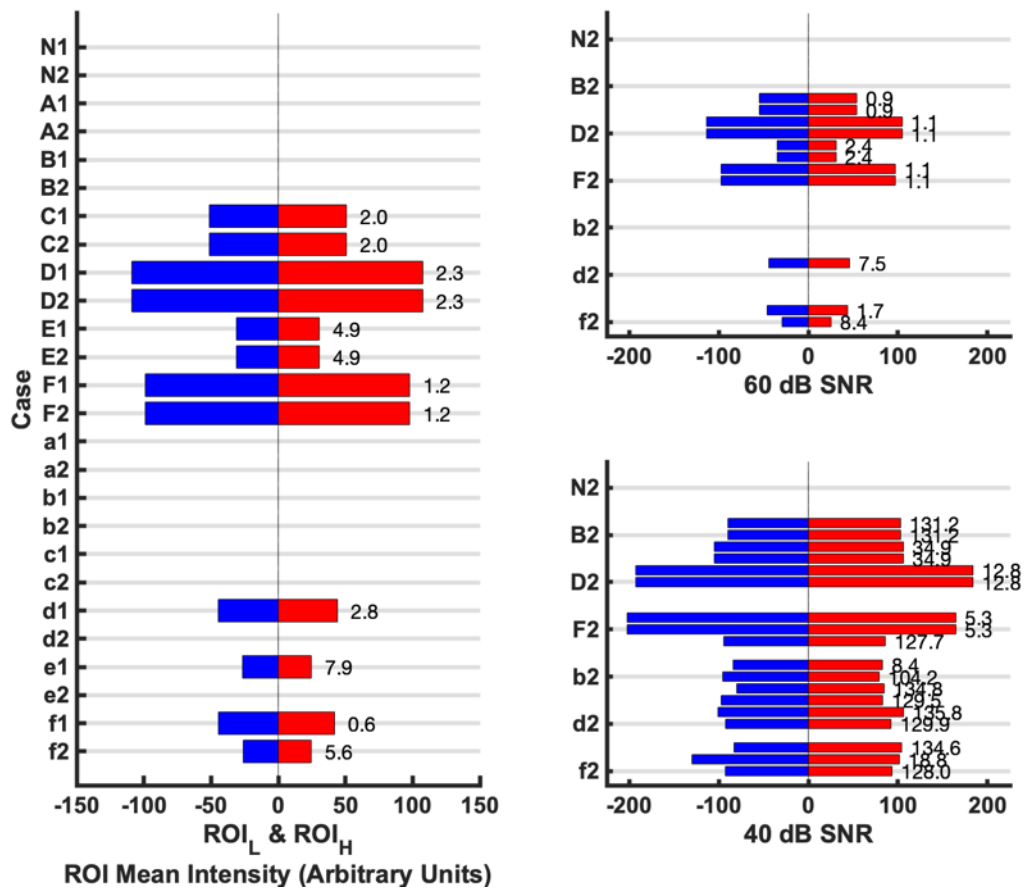


Figure 6.8: The Quantitative ROI metrics: RMI and DCL for the 13 cases at various noise levels. If no ROI is detected in a given case at a given frequency point, then no metric value is listed. Left: The noise-free scenario (i.e., $\text{SNR} = \infty$). Right: The results at 60 dB and 40 dB SNR levels (note the axes correspond to those of the noise-free plot, with the grid lines grouping cases of the same location and nature). The bars represent the RMI for the ROI_H (red bar) and ROI_L (blue bar). The DCL between a ROI_H and ROI_L for a given case is reported in mm to the right of the red bar. Ideally, DCL = 0; therefore, cases with high values indicate failed detection.

The GMI metric alone can detect, identify, and to an extent localise a lesion. Alternatively, this metric can indicate that there is no lesion or that there is a failure to detect a lesion. In Fig. 6.7, the GMI values should as a first feature, have theoretically “equal but opposite” values regardless of the case. The normal case and cases with a lesion at Position I (A-B, a-b) are seen to give near zero values. These near zero values indicate that both sides are symmetrically balanced and

hence no lesion is present, or the lesion cannot be detected as it lies on the plane of symmetry. For those lesions in Positions II (C-D, c-d) and III (E-F, e-f), the values of the mean intensities should deviate away from zero with larger values seen for larger lesions. This pattern is seen with the 10 ml lesion giving smaller mean intensities compared to the corresponding 50 ml lesion at the same location. A bleed will give identical results at both f_1 and f_2 while a clot will result in a larger magnitude intensity metric at f_1 compared to f_2 . A clot displays this pattern of results as a clot has a larger contrast compared to the background at f_1 relative to f_2 . These trends between f_1 and f_2 for bleed and clot which can be seen in Fig. 6.7 can be used to disambiguate the two lesion types. Finally, the side that the lesion is on can be derived from the mean intensities. For example, for the 50 ml clot at Position III (case ‘f’) the LHS mean intensity is negative and the RHS mean intensity metric positive (as explained in Section 6.3.2.1). A clot on the opposite side (for example, in case ‘d’) will have the opposite pattern. For measurement frames where noise is added it is seen that the algorithm performs well at 60 dB, with excessive degradation in performance at 40 dB SNR. Only cases C, D and F are detectable at the 40 dB SNR level. Notably, a bleed of the same volume and location as a clot (if away from the sagittal plane) always gives a larger magnitude of intensity as the contrast between bleed/ brain is larger than that of clot/ brain at f_1 and f_2 . Finally, lesions nearer the extremity give larger magnitude values than the equivalent lesion deeper in the brain. Consider D/d (nearer the exterior) compared with F/f (deeper in and nearer the sagittal plane) as an example of this final observation.

A study of Fig. 6.8 shows ROIs are detected in the noise-free reconstructions for the Position II and III cases C-F. No ROIs are detected as expected for the normal or Position I cases (N, A-B, a-b), with only artefacts or noise presenting in the images of these cases. This corresponds to the results seen in Fig. 6.6, right. Further, only case f has a ROI detected at both f_1 and f_2 with cases d-e only detected at the higher contrast f_1 . This result implies the ROI detection is less sensitive to lesions than the GMI metric. However, it is noted that the detection of the clot at f_1 and failure to detect at f_2 may be sufficient to disambiguate the lesion as a clot as the expected trend of conductivity change is followed, i.e. the expected reduction in contrast at f_2 leads to failure to detect. Quantitative metrics are applied to the cases where ROIs are detected. The RMI metric gives results and pattern similar to those of the GMI metric:

- Equal but opposite values;
- Larger values for bigger lesions: compare C versus D, and E versus F;
- Larger values for lesions nearer the exterior: compare C versus E, and D versus F.

The DCL metric, ideally zero for symmetric ROIs, is less than 6 mm in all cases where a lesion is detected except for the case of a 10 ml clot detected (case e1). The results at 60 dB are similar to the noise-free scenario with the exception of case e1 now not being detected. At 40 dB, cases D and F give reasonable results but with excessive noise present. This excessive noise is indicated by the often excessively large DCL and violation of the equal but opposite principle. Clearly better detection is achieved with a higher SNR. Some EIT applications, for example thoracic functional monitoring, can be successfully performed with systems offering an SNR of 30 to 40 dB [14]. However, more challenging applications, including those involving the head, usually require higher SNRs [14] with hardware capable of circa 80 dB available including the ScouseTom system [15].

This section has presented the results of using BFS-D-EIT for a range of numerical models differing in lesion type, size, location, and SNR. The purpose of this section was to examine scenarios where the algorithm is expected to perform well, and more challenging scenarios. In the next section BFS-D-EIT is further validated using the phantom model.

6.3.4 Phantom Studies

This section reports the application of the BFS-D-EIT technique to an experimental scenario using an anatomically realistic 3D-printed tank model of the head and skull, of identical geometry to the numerical model used in previous sections (but without a CSF layer), with frequency-dependent perturbations.

A full description of the head phantom is given in Section 6.3.1.2 [139]. All experiments were performed with both a 1-layer model with the skull removed, and a 3-layer model with the skull in place. In all cases, saline of conductivity 0.4 Sm^{-1} was used. A Swisstom EIT-Pioneer system was connected to the 32 electrodes used [187]. Before use, the system was allowed to warm up for one hour. The injection protocol followed the same Pair Drive Skip 0 pattern used in the numerical simulations. Potato cubes were used as frequency-dependent perturbations, with cubes of volume 10 cm^3 and 50 cm^3 .

As described in [12], potato represents a frequency-dependent material with a measurable change in conductivity occurring over the kHz range [12]. This range is within the operating range of the Swisstom EIT-Pioneer [187]. Measurements were taken at 80 kHz (f_1) and 100 kHz (f_2), capturing two frequencies across which potato features a significant increase in conductivity with respect to the saline background. Potato was found to be conductive with respect to the background at both f points, with enhanced contrast at f_2 compared to f_1 . These cubes were

CHAPTER 6. BI-FREQUENCY SYMMETRY DIFFERENCE EIT

placed in Positions I, II and Position III. The potato cubes were placed in the saline for an hour before taking recordings in order to ensure ionic equilibrium [12]. Then, measurements were taken for both A-orientation and B-orientations. The recordings were of 1-minute duration taken at 10 FPS and averaged. Recordings were for taken for each perturbation size, position, and also when no perturbation was present (normal case), at both f_1 and f_2 . The SNR of the hardware setup was calculated from the frames as the ratio of the mean to the standard deviation of the values for each measurement channel, then averaged for all channels across all frames at both frequency points. Using this method, the SNR was determined to be approximately 50 dB.

The BFSD-EIT method was applied, and results generated as in the previous sections. The results are reported in the same format as Section 6.3.3. The GMI metric results are given in Fig. 6.9, with the detected ROI analysis focussing on the RMI and DCL metrics shown in Fig. 6.10. The notation used for the phantom experiments is given in Table 6.3 with again the addition of ‘1’ or ‘2’ added indicating a case at f_1 or f_2 respectively. Sample reconstructed images of case ‘F’ for the 1-layer and 3-layer cases at both f points are shown in Fig. 6.11. It is again emphasised that a complete set of images and metrics is ideally used to assess a case but for brevity not all images are shown in this thesis.

Table 6.3: Notation for the phantom experiments (Position I: centre of the brain; Position II: left side of the mid-height traverse plane towards the exterior of the brain; Position III: right side, below the mid-height traverse plane towards the exterior of the brain).

Case Notation	Case Description
N	Normal (No Perturbation)
A	10 cm ³ , Position I
B	50 cm ³ , Position I
C	10 cm ³ , Position II
D	50 cm ³ , Position II
E	10 cm ³ , Position III
F	50 cm ³ , Position III

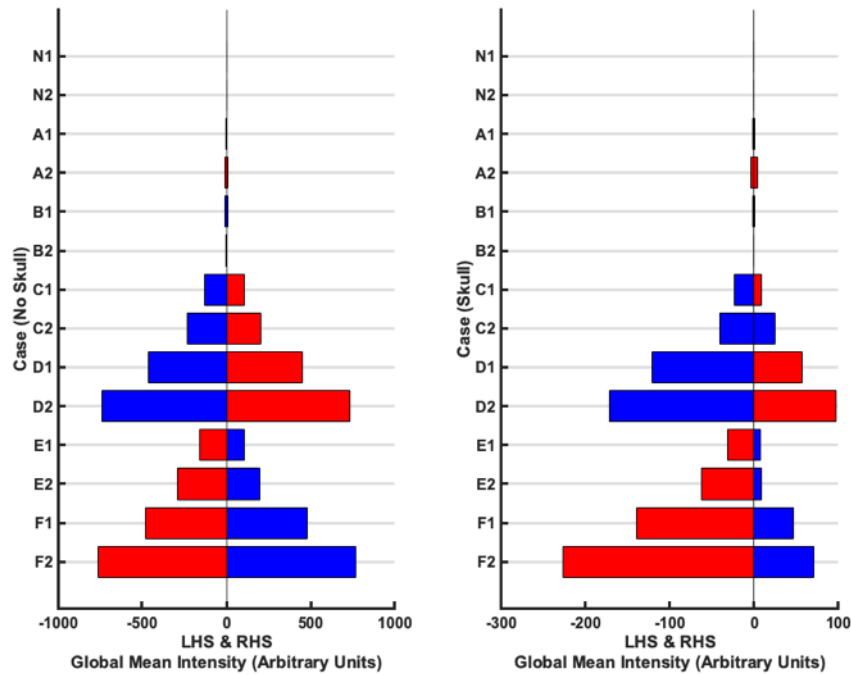


Figure 6.9: GMI results for each of the 7 cases with the 1-layer phantom (left) and 3-layer phantom (right). The notation used to describe each case is given in Table 6.3 with ‘1’ corresponding to f_1 and ‘2’ corresponding to f_2 . The blue bars represent a negative intensity value and the red bars a positive intensity value on either the LHS or RHS depending on the case. The potato perturbation is conductive with respect to the saline background at both f_1 and f_2 , with increased contrast expected at f_2 . The normal case (N) and perturbations on the sagittal plane (Position I, i.e., cases A and B) are expected to have near zero values. Position II and III cases (C – F) are expected to result in a negative intensity on the side the perturbation is truly on, with an equal but opposite positive intensity on the other side. Further the magnitude of intensities will increase for the Position II and III cases from f_1 to f_2 . The smaller perturbation will follow the same pattern as the larger perturbation in a given location but result in smaller magnitude of values (C compared to D, E compared to F). Finally, perturbations nearer the exterior (C, D) will give higher magnitude values compared to those further from the exterior (E, F). These expected patterns are borne out for the no skull (1-layer) set of results. *A priori* knowledge of the expected pattern of conductivity change for potato with respect to saline allows the detection, identification, and to an extent localisation of the perturbation. In the case of the 3-layer phantom, the presence of the skull which is a highly insulating layer dampens the signal, indicated with the lower magnitude of values compared to the 1-layer case. The results are as expected for cases D, E, F but the “equal but opposite” principle is violated.

CHAPTER 6. BI-FREQUENCY SYMMETRY DIFFERENCE EIT

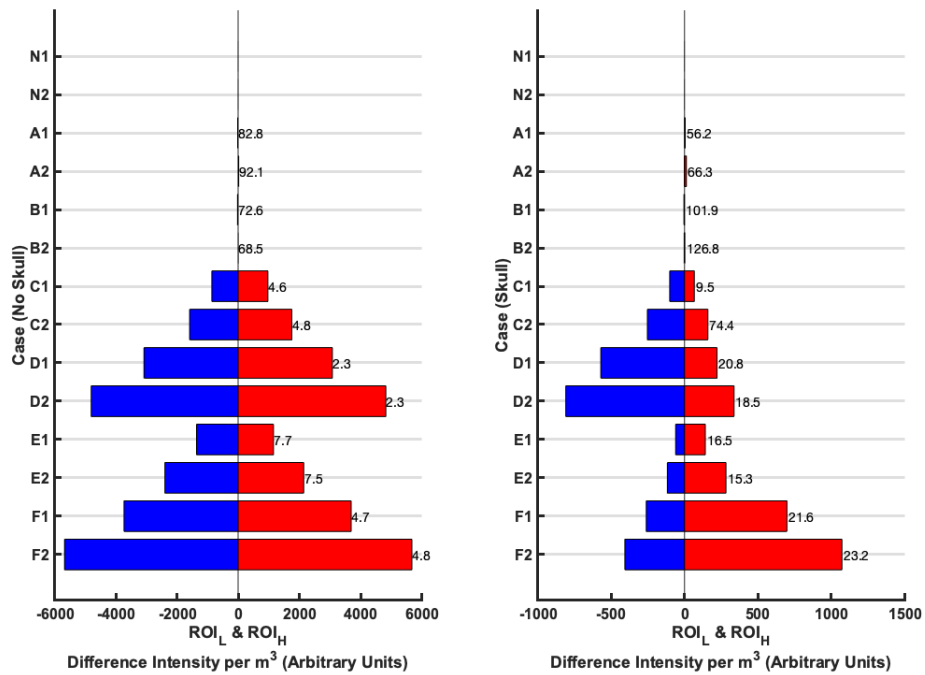


Figure 6.10: The Quantitative ROI metrics: RMI and DCL for the 7 cases with the 1-layer phantom (left) and 3-layer phantom (right). If no ROI is detected in a given case at a given frequency point, then no metric value is listed. The bars represent the RMI for the ROI_H (red bar) and ROI_L (blue bar). The DCL between the ROI_H and ROI_L for a given case is reported in mm to the right of the red bar. The results indicate that lesions are detectable with expected behaviour when no skull is present. However, detection suffers using these metrics when the skull is present.

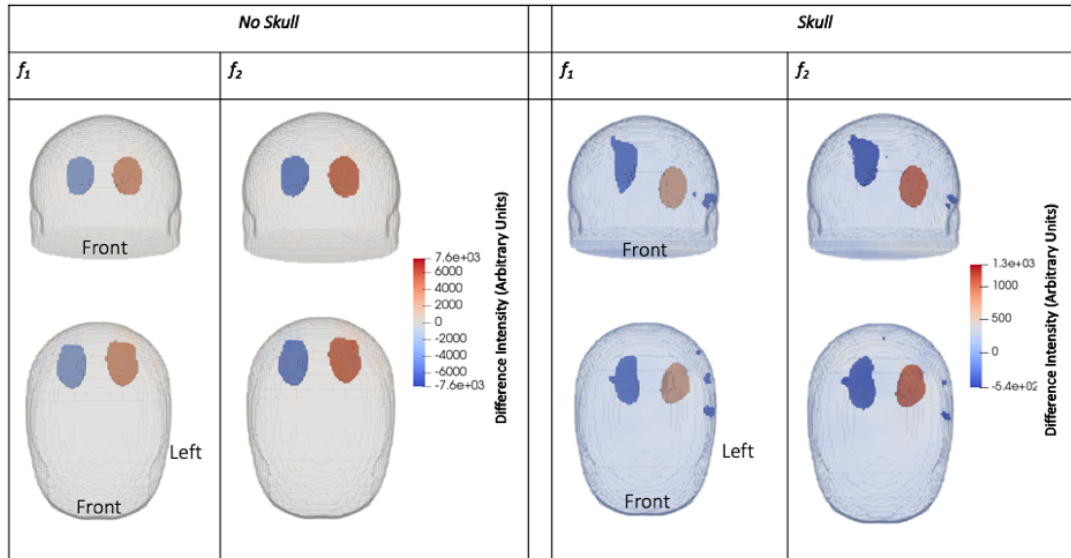


Figure 6.11: Reconstructed images for a 50 cm^3 cubic potato perturbation at Position III in the 1-layer phantom case (left) and the 3-layer case with the skull (right). The images at both 80 kHz (f_1) and 100 kHz (f_2) are shown. Potato is found to become more conductive with respect to saline from f_1 to f_2 with the enhanced contrast at f_2 evidenced by sharper ROIs and more intense ROIs at this point. The skull layer, being highly insulating, reduces the signal rendering images noisier when compared to the simpler 1-layer case. Further, the intensity of the voxels of the ROIs in the skull case is lower than in the no skull case.

The GMI metric for the 1-layer phantom case correlates with the results from the numerical simulations. The normal (N) and cases with the perturbations at Position I (A-B) give near zero results at both f points indicating no lesion is present or the inability to detect a lesion. For the other cases where the perturbations are away from the sagittal plane the following trends are observed:

- Equal but opposite values of GMI;
- Larger perturbations in the same location give larger magnitude results than smaller perturbations at a given f (C versus D, E versus F);
- Perturbations nearer the exterior result in larger magnitude values than equivalent lesions nearer the sagittal plane (C versus E, D versus F).

Potato is conductive with respect to saline at f_1 with this contrast enhanced at f_2 . This change results in the greater magnitude of GMI values for a detected case at f_2 compared to f_1 . Finally, the perturbation being conductive will result in a negative intensity on the side it is located with confounding positive intensity on the opposite side at a given f (as explained in Section 6.3.2.1). *A priori* knowledge of the expected pattern of conductivity change at the two selected f points of the materials involved which are saline and potato in this case, allows disambiguation

of the material as being potato. Hence, detection, identification and localisation on the left or right is demonstrated. With the skull, the signal is dampened as evidenced by the lower magnitude of intensities. The results are as expected for cases D, E, F but the “equal but opposite” principle is violated. It is hypothesised that slight asymmetry in the positioning of the skull may be responsible for this violation, with an asymmetry introduced as a result of this incorrect positioning even of the order of mm potentially causing an effect similar to the effect discussed later in Section 6.4.2.6.

In Fig. 6.10 the metrics relating to the detected ROIs are reported. ROIs detection in the 1-layer case gives results analogous to the GMI results. ROIs are detected for cases A, B but the low RMI values, and high DCL values (> 70 mm) should identify these as cases where no perturbation is detectable. For cases C-F where the perturbation is away from the sagittal plane:

- The “equal but opposite” principle applies;
- Smaller perturbations give results of lower magnitude of RMI compared to the corresponding larger perturbation;
- Perturbations nearer the exterior are better detected than those nearer the sagittal plane (evidenced here by the lower DCL of C versus E; D versus F).

The magnitude of RMI is larger for the f_2 result compared to f_1 as expected by the higher contrast at f_2 . For the skull cases, the trend of results seen in the metrics remains the same as for the corresponding 1-layer cases but violation of the “equal but opposite” principle, a lower magnitude of RMI, and an increase in the value of DCL are indicative of the challenge posed by the insulating skull layer.

The images of case F in Fig. 6.11 correlate with the metrics. The 1-layer model results in a sharper, less noisy and higher magnitude of intensity values for the detected ROIs compared to the 3-layer case. In both the 1-layer and 3-layer scenarios, the intensities of the ROIs at f_2 are higher compared to that at f_1 as expected by the enhanced contrast between potato and saline at f_2 .

Overall, the experimental results have demonstrated the proof-of-concept for using BFSD-EIT on symmetric regions with conductivity changes across frequency, as illustrated here with a realistic head-shaped tank.

6.3.5 Bi-Frequency Symmetry Difference EIT - Initial Development and Proof of Concept Discussion

The work in this section explores a novel EIT modality to facilitate imaging of scenarios that are static in nature. A range of scenarios fall into this category including important biomedical applications such as stroke diagnosis, where the identification of the aetiology as bleed or clot is vital. The BFSD-EIT technique is based on the selection of a frequency point (f_1) where *a priori* information on the conductivity of the tissues of interest, and the conductivity contrast between possible pathological tissue and normal background parenchyma is assumed. Next detection of deviations in symmetry across a natural symmetrical plane in the area of interest is performed by comparing EIT measurements from mirror image electrode pairs, and then reconstructing an image and calculating quantitative metrics based on the image. The image and metrics indicate detection of a lesion, as well as a confounding anti-lesion of opposite conductivity. Alternatively, no lesion may be detected indicating a normal scene or an inability of the technique to detect a lesion. In order to disambiguate a detected lesion from the anti-lesion, the technique is repeated at a 2nd frequency point (f_2) with again *a priori* information on the conductivity and contrast between the tissues. Analysis of the results from both steps, leads to either:

- Detection, identification, and localisation of the lesion;
- A conclusion that no lesion is present or detectable.

Stroke is an excellent sample application to demonstrate BFSD-EIT as the two aetiologies are effectively opposite in conductivity to each other with respect to the background. However, other conditions may only have one aetiology or aetiologies that do not have this conductivity profile. In these cases the disambiguation process is redundant, and Step (2) is not required or applicable. In stroke the possibility of two aetiologies, and that the aetiologies possess differing conductivity profiles means the full BFSD-EIT algorithm is applicable.

After performing BFSD-EIT a final result may be interpreted from some key metrics alone in particular the GMI metric. In addition for the detected ROI_H and ROI_L the RMI and DCL metrics can be applied to add additional surety to the result. Care must be taken in the selection of f_1 and f_2 . The trend in conductivity changes of the tissues at the two selected frequency points should be such that the contrast between the differing confounding perturbations and the background at f_1 and f_2 display a different pattern of change in order to achieve disambiguation. In the case of stroke values of f_1 and f_2 that allow disambiguation are documented as described in Section 6.3.3. At a f_1 of 25 Hz and a f_2 of 100 Hz the contrast between blood and brain is constant whereas the contrast between clot and brain decreases

from f_1 to f_2 .

This initial study demonstrates the effectiveness of the BFS-D-EIT technique in a variety of numerical and experimental scenarios using anatomically accurate models of the head. In the numerical models, a 4-layer head model is used in the implementation of BFS-D-EIT with spherical bleeds and clots at a variety of different locations, at two volumes (10 ml and 50 ml), with realistic conductivity values at a variety of SNR levels. These models demonstrate the effectiveness and limitations of the technique. Detection of lesions is stronger with higher SNRs, larger lesion sizes, and lesions nearer the exterior away from the plane of symmetry. In clinical applications, the use of two f points would result in further technical challenges particularly in terms of the maximal current amplitude allowed, which is 100 μ A RMS (141 μ A peak) at frequencies below 1 kHz as set out in the IEC 60601-1 guidelines [11]. However, robust EIT data has been collected from stroke patients at these frequencies [13] supporting the potential feasibility of the algorithm in real world scenarios given the appropriate hardware such as the ScouseTom [15] used in [13].

The technique was also validated experimentally in a 1-layer and 3-layer phantom model. These models are identical except for the absence or presence of a skull layer respectively. Cubic potato perturbations were used of 10 cm³ and 50 cm³ volume. Potato has a significant increase in conductivity from 80 kHz (f_1) to 100 kHz (f_2) which is within the frequency range of the Swisstom EIT-Pioneer. These perturbations were set against a saline background with detection, identification and localisation possible. Detection with the phantom skull in place was as expected more challenging than without. The selection of this experimental setup was driven by the relatively easy commercial availability of the Swisstom EIT-Pioneer system [187] opposed to for example the ScouseTom, and the significant change in the conductivity of potato in the operating range [12]. This hardware would not however be suitable for clinical application to the stroke problem as the range of operation (50 to 250 kHz) is outside that of where significant change in tissue conductivity is seen [12], [146]. Further, the SNR calculated as approximately 50 dB would not be suitable for head applications [14]. Importantly, the BFS-D-EIT algorithm is not dependent on a particular frequency *per se* but rather on there being a detectable conductivity change in the tissues or materials at the two selected frequency points. For the phantom setup this conductivity change was in the range 80 to 100 kHz while for the numerical setup the significant change was in the range 25 to 100 Hz. It is emphasised that the goal of this part of the chapter is primarily the introduction of the BFS-D-EIT algorithm with feasibility of clinical application of the technique considered in the next section.

6.4 Bi-Frequency Symmetry Difference EIT - Feasibility and Limitations of Application to Stroke Diagnosis

This section tests the viability and robustness of BFS-D-EIT applied to stroke diagnosis. The realistic 4-layer FEM model described in Section 6.3.1 is used as the basis to model anatomical scenarios with and without the presence of bleed and clot lesions. Performance is assessed with test parameters including:

- Measurement Frame Noise;
- Electrode Positioning Errors;
- Contact Impedance Errors of Electrodes;
- Errors in Assumed Conductivity of the Tissues (including at a voxel level and whole tissue level);
- Errors in Assumed Anatomy of the Head (including skull, brain and scalp boundary);
- A Frequency-Dependent Background.

These error situations comprise some of the most common and important errors and challenges of EIT [10], [20], [180], [181]. The result of these tests indicates where the BFS-D-EIT technique may be used, modifications that can be implemented to improve the outputs, parameter ranges that must be respected, and limitations of the algorithm when applied to stroke diagnosis. As a final test, BFS-D-EIT is applied for the first time to data from a human ischaemic stroke in order to assess performance in a real-world scenario.

In Section 6.4.1, the 4-layer numerical models are described, as well as the method of data generation, and the key quantitative metrics used to assess performance in this feasibility study. In Section 6.4.2, the various test scenarios and results are reported, and discussed.

6.4.1 Numerical Model, Data Generation, and Quantitative Metrics

This section details the numerical models used as well as the methods for data generation using EIT, and the quantitative metrics applied to the reconstructions to then assess performance.

Throughout Section 6.4 an ideal (‘correct’) model without errors is used to generate a set of results which are considered the ground truth. The performance of the algorithm applied to models with added errors (‘deviation’ models) are compared

to the results generated from this ideal model. Further, the model and methods described in this subsection describing this ideal model are the basis of the deviation models. The 4-layer CAD model described in Section 6.3.1.1 was used to generate FEM models of a 4 million tetrahedron fine mesh, and a 250,000 tetrahedron coarse mesh. The fine mesh was used to solve the forward problem and generate measurement frames, with reconstruction performed onto the coarse mesh. The electrode layouts (A-Orientation and B-Orientation), protocol used, process of measurement frame generation, and reconstruction method used is as described in Section 6.3.2. A key difference to the work done in Section 6.3 was that in this section there is the absence of electrode refinement for the models used in order to facilitate a variety of errors models with minimal alterations to the underlying mesh. Further, in all cases, comparison was made to results generated from the ideal model also without mesh refinement. Three test cases are considered for the studies of Section 6.4:

- N: no perturbation present;
- B: 10 ml bleed at Position II;
- C: 50 ml bleed at Position III.

These lesion locations are shown in Fig. 6.12.

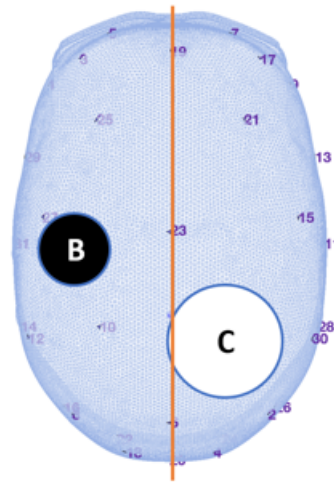


Figure 6.12: The fine FEM model used in Section 6.4 viewed from above. This FEM has electrodes in A-Orientation. The sagittal plane is shown as an orange line. The positions of the two model lesions, a 10 ml spherical bleed ('B') and 50 ml spherical clot ('C') are shown. In a given case only one or neither of the lesions are present.

Importantly, unless noted, the single f point of 25 Hz is used in the studies presented in Section 6.4. At this f point the tissues are assigned the conductivity

CHAPTER 6. BI-FREQUENCY SYMMETRY DIFFERENCE EIT

values of 0.23 Sm^{-1} , 0.69×10^{-2} to $1.29 \times 10^{-2} \text{ Sm}^{-1}$, 0.1 Sm^{-1} , 2 Sm^{-1} , 0.7 Sm^{-1} and 0.05 Sm^{-1} for scalp, skull, brain, CSF, bleed and clot respectively as described previously in Sections 6.3.1.1 and 6.3.2.1. While BFS-D-EIT compares results from two f points, accurate results from each f point is usually required for success. Hence, in this section the results at only a single f point are used to assess the feasibility of the algorithm. The high contrast between tissues at 25 Hz motivates the use of this f point. The limitations and robustness of the algorithm to errors at one f point is representative of the robustness at both.

The reconstructions for the three tests cases as illustrated in 6.13 are used to derive several quantitative metrics that are used in this section to support stroke diagnosis. The GMI, RMI, and DCL have been described already in Section 6.3. In this section the magnitude values of the GMI and RMI are calculated to the Log_{10} . The use of a log scale is for clarity when comparing the effects of the assessed parameters in the deviation models, as the differences in metric values can be quite pronounced. In addition, the following quantitative metrics are also used:

- Image Noise (IN): A measure of the number of thresholded voxels contained in the ROI compared to those in the entire thresholded image, averaged for the high (H) and low intensity (L) voxel sets. Ideally $\text{IN} = 0$, with range $0 - 1$. The IN is given by:

$$\text{IN} = 1 - 0.5 \left(\frac{\Sigma(\text{Voxels})_{\text{ROI}_H}}{\Sigma(\text{Voxels})_H} + \frac{\Sigma(\text{Voxels})_{\text{ROI}_L}}{\Sigma(\text{Voxels})_L} \right) \quad (6.2)$$

- Morphology Deviance (MD): The degree of overlap between ROI_H and ROI_L , if one ROI is reflected across the sagittal plane. Ideally $\text{MD} = 0$ (when perfect overlap occurs). The range of MD is $0 - 1$.

Where applicable, each test situation is iterated 10 times, each time with random variation of the error parameter within a chosen range (discussed in more detail in Section 6.4.2). The mean and standard deviation of each of the above metrics are reported across the iterations. For iterated test situations, the ROI Detection Rate (RDR) is calculated as:

- RDR: The percentage of times from the 10 iterations that ROIs are detected. Ideally the RDR is 0% for the N cases where no lesion present, and 100% for the B and C cases where a lesion is present.

This section has described the ideal ('correct') model without errors. The results described for this model are used to compare the performance of the algorithm applied to models with added errors ('deviation' models). Further, the model and

methods described in this section are the basis of the deviation models. The GMI, RMI, DCL, IN and MD results for the ideal model cases are used to compare with subsequent deviation models with modelling errors. For brevity, deviation model metric results, and not reconstructed images, are reported in the following sections.

6.4.2 Numerical Studies and Investigations into Effect of Individual Test Parameters

In this section the results of the ideal model test situations are reported followed by the results of the various deviation models. In total, 3 simulations were conducted for the ideal model tests with 265 simulations for the deviation models. A final test is also performed using human data.

6.4.2.1 Study 1: Ideal Model Results

The reconstructed images and quantitative metrics from the ideal model for a simulation at a f point of 25 Hz are shown in Fig. 6.13. The reconstructed image for the N case is largely composed of artefacts at or near the mesh surface. The images for the B and C cases show a significant reduction in these artefacts with the detected ROIs due to the presence of a lesion dominating the image as expected. The GMI metric values have theoretically “equal but opposite” values regardless of the case. The N case give near zero values for GMI (LHS -0.33 ; RHS $+0.38$), indicating that both sides are symmetrically balanced and hence no lesion is present or, if present cannot be detected. The presence of a lesion deviates the GMI value away from zero with the magnitude a function of the size of the lesion, the lesion position, and the contrast between the lesion and brain. Case B (LHS -1.19 ; RHS $+1.19$) gives a higher GMI score compared to C (LHS -1.03 ; RHS $+1.04$) despite the smaller volume due to the closer proximity of B to the exterior and the greater contrast between blood and brain compared to clot and brain. Both lesions cause a mean negative intensity on the LHS and a mean positive intensity on the RHS demonstrating the need for disambiguation.

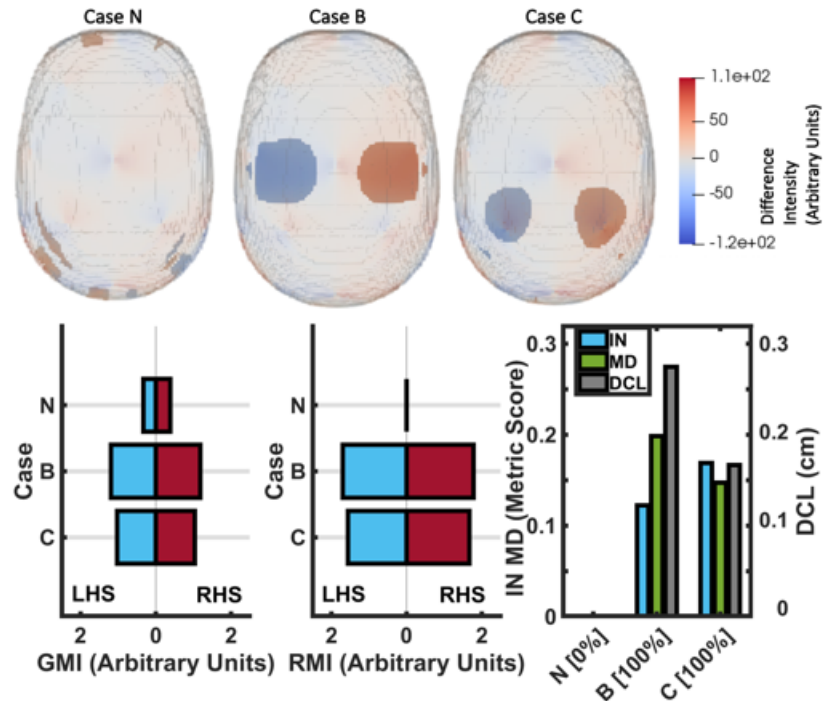


Figure 6.13: Top: Reconstructed images of the ideal model for the three cases at an f point of 25 Hz: No lesion present (N); 10 ml spherical bleed at Position II (B); 50 ml clot at Position III (C). The N case shows noisy artefacts towards the exterior of the FEM whereas when a lesion is present the ROIs corresponding to the perturbation are the dominant feature. Bottom: Quantitative metrics corresponding to the reconstructed images. GMI: The blue bars represent a negative intensity value and the red bars a positive intensity value on either the LHS (negative x-axis) or RHS (positive x-axis). RMI: If no ROI is detected in a given case at a given frequency point, then no metric value is listed, the bars represent the RMI for the ROI_H (red bar) and ROI_L (blue bar) on either the LHS (negative x-axis) or RHS (positive x-axis). IN, MD and DCL are reported if ROIs are detected. The RDR for each case is reported on the x-axis of the IN, MD, DCL plot.

For calculation of all metrics other than GMI, the ROI detection process is applied. In the N case, no lesion is present and no ROIs are identified, as expected. For both B and C, ROIs are successfully detected. In these cases, the RMI score gives the mean intensity of each of ROI_H and ROI_L with the pattern of values similar to the GMI (larger if larger lesion, nearer the exterior, larger contrast compared to brain). The DCL metric is < 3 mm for both cases indicating a high degree of overlap between the ROIs. The IN and MD values for the ideal cases (all < 0.2) can be used to compare to deviation models.

6.4.2.2 Study 2: Effect of Noise

In this test scenario, the measurement frames for each case at the f point of 25 Hz in each orientation were contaminated with additive Gaussian White Noise at levels of 80 dB, 60 dB and 40 dB SNR before reconstruction. Illustrative quantitative metrics are shown in Fig. 6.14 for the 80 dB and 60 dB tests, with the RDR results shown for all noise levels.

The GMI results at 80 dB are comparable to the ideal results (i.e., $\text{SNR} = \infty$) from 6.13. However, the MD and DCL now increases for both cases B and C. At 60 dB, further degradation in performance is seen with deviations in GMI from the ideal, and increases in the size of the standard deviations which are reported as error bars. In addition there are large IN, MD, DCL metrics, detection of ROIs in the N case, as well as failure to detect ROIs in the B and C cases. This failure to detect ROIs is particularly evidenced by the 10% RDR for C. At 40 dB, excessive noise results in a common failure to detect lesions.

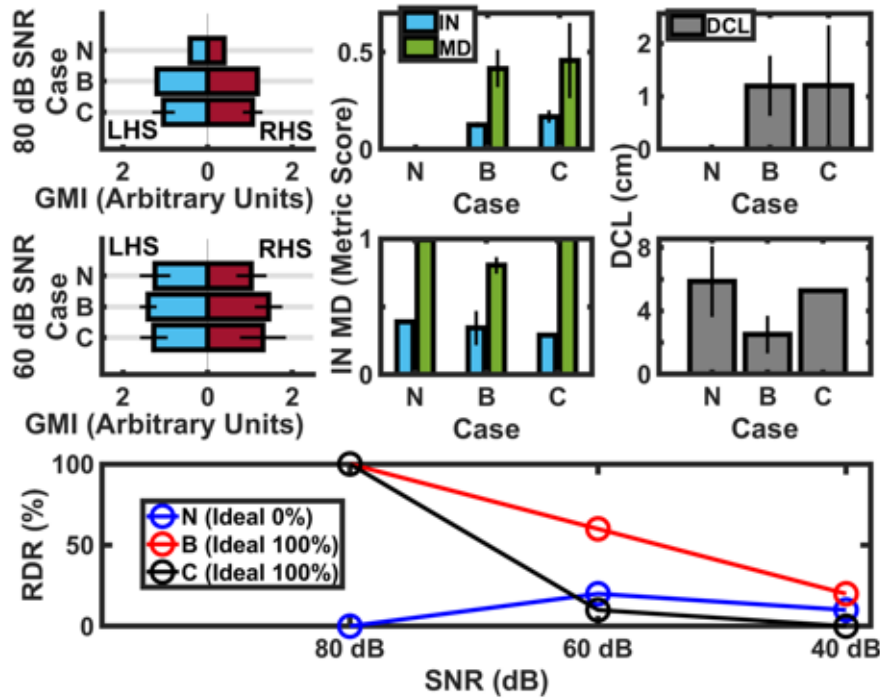


Figure 6.14: Quantitative Metrics for models where noise of 80 dB, 60 dB and 40 dB SNR is added to the measurement frames prior to reconstruction for cases N (no lesion present); B (bleed); C (clot). GMI: The blue bars represent a negative intensity value and the red bars a positive intensity value on either the LHS (negative x-axis) or RHS (positive x-axis). IN, MD and DCL are reported if ROIs are detected. The RDR for each case is reported at each noise level. For the 40 dB models, the RDR is shown, but the excessive noise hinders the ability to detect ROIs.

6.4.2.3 Study 3: Effect of Electrode Positioning Errors

Two scenarios of erroneous electrode positioning are analysed. These scenarios have errors present in the forward model relative to the inverse model and either:

- Symmetry is not maintained between symmetric electrode pairs;
- Symmetry is maintained between symmetric electrodes pairs.

In both scenarios the goal was to find and surpass the point where the integrity of the results is maintained.

6.4.2.3.1 Electrode Positioning Errors with Symmetry Lost The electrode centres are positioned randomly within a given radius of the ideal centre

position. No attempt is made to keep electrode pairs symmetric. The tested deviations in electrode positions were assigned with error radii of 1 mm, 2 mm, 5 mm, 10 mm, and 20 mm. The error radius for a model is the maximum distance an electrode can be positioned from the correct position on the mesh surface. Table 6.4 lists the distance error of the 32 electrodes in each model averaged over the 10 repetitions. These distance errors are with respect to the ideal position and between electrode pairs. The quantitative metrics resulting from these test cases are provided in Fig. 6.15 (top). The results indicate reliable performance (i.e. similar to the results achieved with the ideal model) for error radii of up to ± 5 mm if considering the GMI. This reliability is only up to ± 1 mm for the other metrics, with no ROIs reliably detected beyond this error radius as shown by the steep drop off in RDR for cases B and C.

6.4.2.3.2 Electrode Positioning Errors with Symmetry Maintained In this series of test scenarios, the electrodes centres are positioned randomly within a given radius away from the ideal position. However, unlike in the previous section now electrode pairs are kept symmetric with respect to each other across the sagittal plane (i.e. if reflected across the sagittal plane the electrodes map onto their partner exactly). The deviations tested were error radii of 2 mm, 5 mm, 10 mm, 20 mm, 30 mm, 40 mm, and 50 mm. Hence electrodes are positioned at or within these error radii from the ideal position on the mesh surface. Table I lists the distance error of the 32 electrodes in each model from the ideal position; the corresponding quantitative metrics are presented in Fig. 6.15 (bottom). The results indicate integrity of the BFS-D-EIT algorithm is maintained (i.e. are largely similar to the ideal model) up to the ± 20 mm error radius if considering the GMI. Integrity for the other metrics is maintained only up to ± 5 mm, with no or erroneous ROIs detected beyond this error radius. Both results are improvements over the situation where symmetry is not maintained, suggesting that the BFS-D-EIT algorithm can tolerate larger errors in expected electrode location if electrode pairs are kept symmetrical across the sagittal plane. Maintaining such a symmetry should be feasible to this degree in a clinical case, for example using an EEG cap for electrode placement [20].

CHAPTER 6. BI-FREQUENCY SYMMETRY DIFFERENCE EIT

Table 6.4: Mean \pm standard deviation of the distance errors of the 32 electrodes (Symmetry Lost or Symmetry Maintained).

Error (mm)	Radius	Mean (mm) \pm Standard Deviation (mm) of Electrode Positions with respect to the Correct Positions	Mean (mm) \pm Standard Deviation (mm) of Distances between Symmetric Electrode Pairs (i.e. if reflected across the sagittal plane)
<i>Symmetry Lost</i>			
± 1		0.47 ± 0.34	0.64 ± 0.45
± 2		1.34 ± 0.21	1.52 ± 0.65
± 5		3.31 ± 0.34	3.88 ± 1.59
± 10		6.39 ± 0.78	7.84 ± 3.15
± 20		13.19 ± 1.41	15.64 ± 6.51
<i>Symmetry Maintained</i>			
± 2		1.21 ± 0.24	0 ± 0
± 5		3.21 ± 0.52	0 ± 0
± 10		6.33 ± 1.05	0 ± 0
± 20		13.39 ± 2.19	0 ± 0
± 30		19.03 ± 3.77	0 ± 0
± 40		24.39 ± 3.36	0 ± 0
± 50		31.32 ± 5.29	0 ± 0

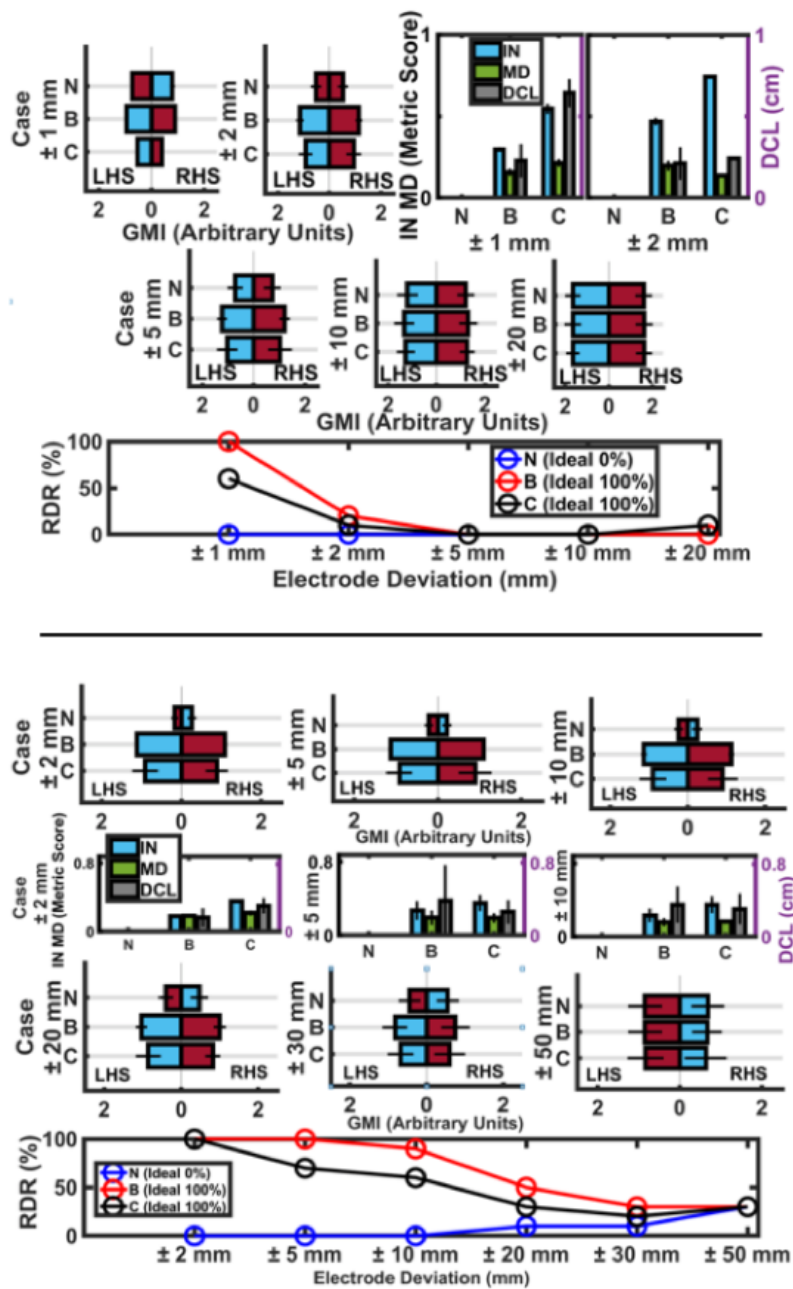


Figure 6.15: Quantitative Metrics for erroneous electrode position models with symmetry lost (top), and symmetry maintained (bottom) between electrode pairs. This study is performed for cases N (no lesion present); B (bleed); C (clot). GMI: The blue bars represent a negative intensity value and the red bars a positive intensity value on either the LHS (negative x-axis) or RHS (positive x-axis). IN, MD and DCL: These metrics are calculated if ROIs are detected and are shown for these situations. The RDR for each case is reported at each electrode deviation.

6.4.2.4 Study 4: Effect of Electrode Contact Impedance Errors

In this section, the impact of an inaccurate electrode contact impedance is investigated. In the ideal model, the electrode contact impedance is $1\text{ k}\Omega$. Here, the impedance on each electrode is randomly set between 800 to $1,200\ \Omega$ ($1\text{ k}\Omega \pm 0\text{-}20\%$) for a first test, and then within 500 to $1,500\ \Omega$ ($1\text{ k}\Omega \pm 0\text{-}50\%$) in a second test. Further, each of these tests is conducted in two different ways, either with:

- Symmetry not maintained between electrode pairs - i.e. all electrodes have random contact impedances within the range;
- Symmetry maintained - i.e. electrode pairs have the same erroneous impedance.

The resulting quantitative metrics for all of these scenarios are shown in Fig. 6.16. As can be observed from the figure, the results show that the lesion detection is effectively equivalent to that of the ideal scenario, for both impedance error levels, and regardless of whether symmetry is maintained or not.

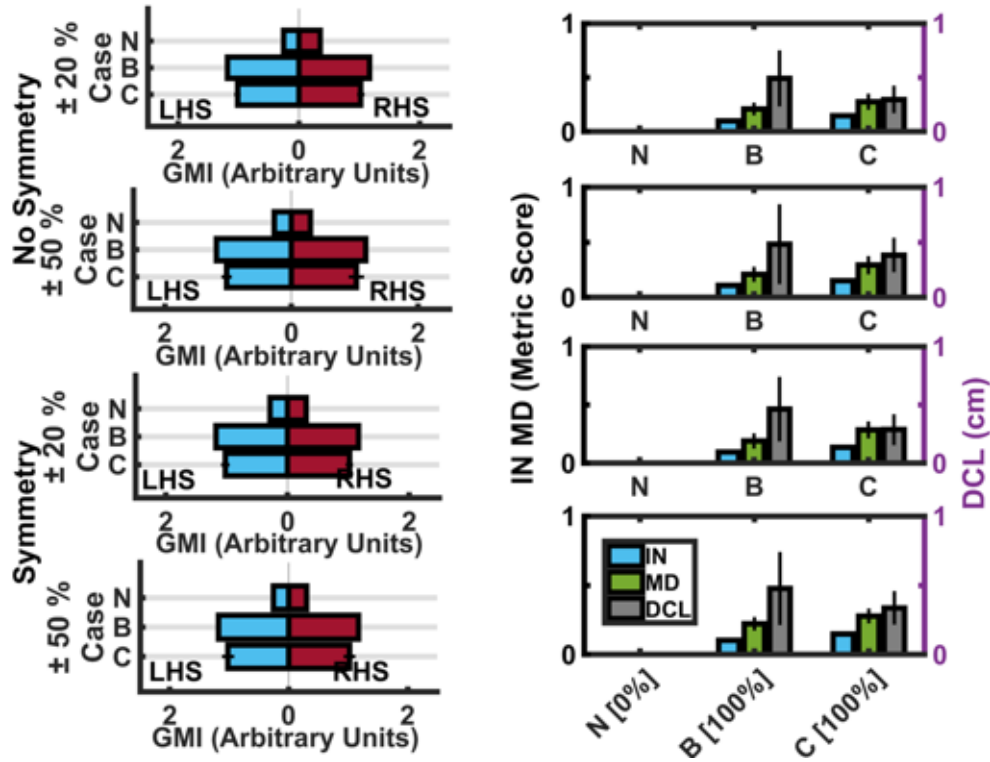


Figure 6.16: Quantitative Metrics for erroneous electrode contact impedance models. No Symmetry (top two rows): all electrodes have random contact impedances within the range $\pm 20\%$ or $\pm 50\%$. Symmetry (bottom two rows): symmetrical partner electrodes have the same (but erroneous) contact impedance within the range $\pm 20\%$ or $\pm 50\%$. Cases are N (no lesion present); B (bleed); C (clot). GMI: The blue bars represent a negative intensity value and the red bars a positive intensity value on either the LHS (negative x-axis) or RHS (positive x-axis). IN, MD and DCL: These metrics are reported if ROIs are detected. The RDR for each case is reported on the x-axis of the bottom-most IN, MD, DCL plot and was identical (and ideal) in all deviation models tested.

6.4.2.5 Study 5: Effect of Errors in Assumed Conductivity of Tissue

This section explores the impact of error in the assumed conductivities of the tissues. In the ideal model, the conductivities of the tissues are assigned as 0.23 Sm^{-1} , 0.69×10^{-2} to $1.29 \times 10^{-2} \text{ Sm}^{-1}$, 0.1 Sm^{-1} , 2 Sm^{-1} , 0.7 Sm^{-1} and 0.05 Sm^{-1} for scalp, skull, brain, CSF, bleed and clot, respectively, at the f point of 25 Hz. Here, errors of $\pm 5\%$, $\pm 20\%$ and $\pm 50\%$ are added to each of these conductivity values in separate deviation models. These deviation models incorporate these errors on either:

- A voxel level;

- A whole tissue level.

There is evidence in the literature that the conductivity of the tissues of the head may be largely symmetric in the absence of pathology [132], [273]. However, the dielectric properties of tissues have a band of uncertainty around the reference values and may vary inter- and intra-patient (Section 2.4.2). Many factors such as natural heterogeneity in tissue, precise location, age, metabolic activity, pathology and the measurement method affect the measured conductivity of a tissue and result in a degree of variability in the assumed reference value [147], [151]. This uncertainty is even more pronounced in the region of interest for EIT at frequencies under 1 MHz with significant variability in the dielectric properties of tissues, for example $\pm 24\%$ for fat and $\pm 35\%$ for blood [153]. The choice of error values up to $\pm 50\%$ of the ideal value was motivated by these reported variability ranges from the literature.

6.4.2.5.1 Voxel Level Errors in Assumed Conductivity of Tissue In this test scenario, each voxel, corresponding to a discrete tissue, has a conductivity value assigned as the ideal conductivity of the tissue \pm an error which is up to 5, 20, or 50%, depending on the model. Each tissue is thus made heterogeneous while the ideal model assumes them to all be homogenous. The results are effectively identical to the ideal model results even up to and including an error of $\pm 50\%$ of the assumed tissue conductivity values. The GMI results of the $\pm 50\%$ error model are shown in Fig. 6.17.

6.4.2.5.2 Whole Tissue Level Errors in Assumed Conductivity of Tissue In this test scenario, the complete set of voxels constituting a discrete tissue has a conductivity value assigned as the ideal conductivity of the tissue \pm an error which is up to 5, 20, or 50%, depending on the model. Each tissue is thus made homogenous but with an error in the conductivity compared to the ideal model. The results are effectively identical to the ideal model results even up to and including an error of $\pm 50\%$ of the assumed tissue conductivity values. The GMI results of the $\pm 50\%$ error model are shown in Fig. 6.17.

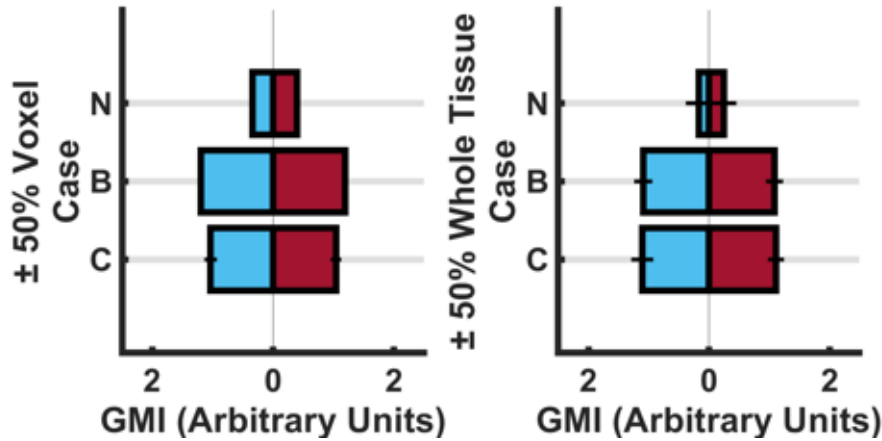


Figure 6.17: Quantitative Metrics for models with errors in assumed conductivity of tissues. Each individual voxel corresponding to a given tissue (left) or the whole tissue (right) is assigned a conductivity corresponding to the ideal conductivity of that tissue \pm up to a maximum of 50% error. The tissues include scalp, skull, brain, CSF, bleed or clot. Cases are N (no lesion present); B (bleed); C (clot). GMI: The blue bars represent a negative intensity value and the red bars a positive intensity value on either the LHS (negative x-axis) or RHS (positive x-axis).

6.4.2.6 Study 5: Effect of Errors in Assumed Anatomy of the Head

BFSD-EIT must be robust to a degree of anatomical asymmetry across the sagittal plane as well as deviations in the geometries of the fine (forward solved) and coarse (reconstruction) FEM meshes. In this section, two scenarios of anatomical deviations are considered:

- Excess skull or brain on one side of the head with respect to the other;
- Deviations in the geometry of the scalp (i.e. the boundary) between the fine and coarse meshes.

In both scenarios, fine meshes are created with the altered anatomy, with reconstruction onto the ideal coarse mesh.

6.4.2.6.1 Unilateral Excess of Skull or Brain As described in Section 6.3.1.1, the ideal model is based on an actual human head and is thus not perfectly symmetrical. The overall global symmetry of the head across the sagittal plane is calculated as the average percentage of voxels from each side that, when reflected across the sagittal plane, overlap with the voxels of that tissue type on the other side. For the ideal model, the global symmetry ranges from 90.1% for skull tissue to 98.3% for brain tissue. However, the ideal model does not have any gross

asymmetry that may resemble a lesion. Previous works have quantified the typical degree of asymmetry found in the skull [271] and brain [272]. An Asymmetry Index (AI), defined in [271] as:

$$AI = \frac{RHS - LHS}{RHS} \times 100, \quad (6.3)$$

where RHS and LHS are the distances of a series symmetrical points on the RHS and LHS to a point on the sagittal plane, can be used to quantify the level of symmetry. The AI varies depending on person, cohort and anatomical location, but values of 3 to 6 % have been reported [271].

For this study, an arbitrary location was selected on the left-hand side of the skull or brain at the approximate midpoint of the boundary between the frontal and temporal bones or lobes on the left lateral interior surface or exterior surface for the brain. Centered at this point, spheres of radii 10 mm, 20 mm, and 50 mm were projected out with any voxels designated as CSF within the radius reassigned as skull or brain depending on the scenario, with all other layers left untouched. Hence, in one scenario the skull is increased in volume by varying amounts at one point with the brain unchanged while in the other scenario the opposite is the case. Removal of the full thickness of CSF at a given point resulted in an AI of approximately 6%. The increase in skull (or brain) tissue, with reciprocal decrease in CSF, for the different deviation models are shown in Table 6.5. The corresponding quantitative results presented as only the GMI metric for brevity, are shown in Fig.6.18.

The results indicate that the BFS-D-EIT technique is very sensitive to deviations in anatomy. The replacement of CSF on the LHS by either skull or brain effectively places a low conductivity target at that location with even the smallest radius sphere compromising results compared to the ideal model. The smallest radius sphere results in $< 1 \text{ cm}^3$ tissue imbalance on the LHS. If ROIs are detected, these ROIs correspond to the excess skull or brain, meaning that no lesion is detectable.

However, it is noted that the GMI for a given lesion case is the arithmetic sum of the GMI for the erroneous N case and the GMI for the ideal lesion case. This finding may give the algorithm a degree of robustness to anatomical deviations, as will be discussed in more detail in Section 6.4.3.

CHAPTER 6. BI-FREQUENCY SYMMETRY DIFFERENCE EIT

Table 6.5: Volume of the increase in Skull or Brain Layer (with reciprocal decrease in CSF Layer) on the LHS with varying sphere radii.

Sphere Radius mm	Volume Increase of Skull		Volume Increase of Brain	
	cm ³	% of Total Voxels	cm ³	% of Total Voxels
0	0	0	0	0
10	0.86	0.06	0.84	0.06
20	3.70	0.17	3.56	0.17
50	24.67	1.14	24.35	1.12

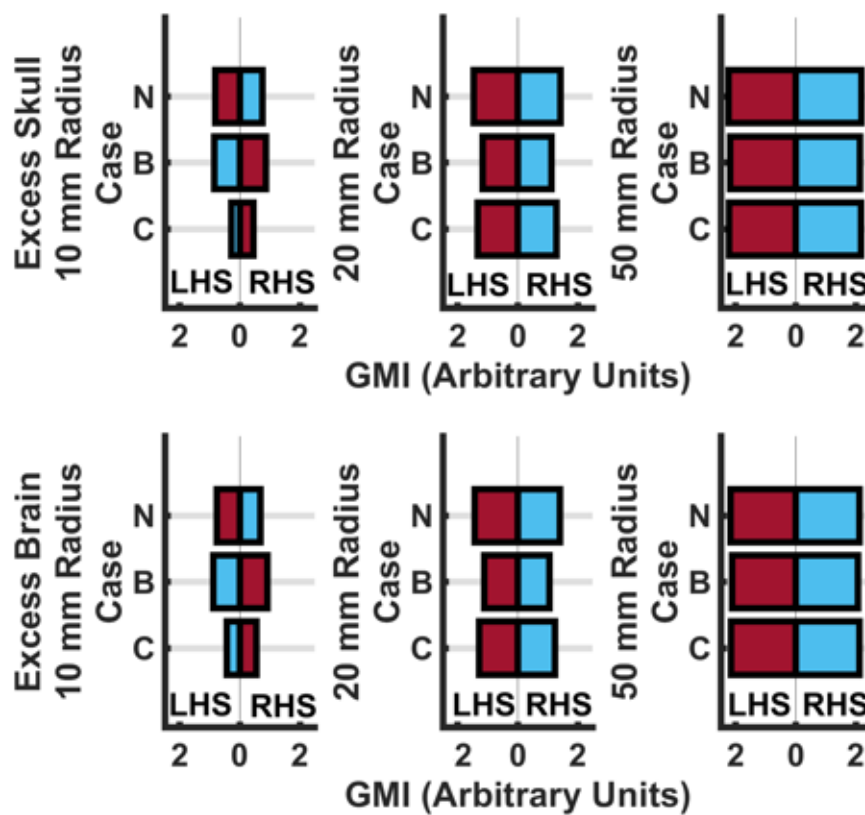


Figure 6.18: Quantitative Metrics for models with excess skull (top row) or brain (bottom row) on the LHS compared to the RHS. In each model, the CSF encompassed by a sphere of radius 10 mm, 20 mm or 50 mm centred at a point on the LHS of the skull (or brain) is re-assigned as skull (or brain). Cases are N (no lesion present); B (bleed); C (clot). GMI: The blue bars represent a negative intensity value and the red bars a positive intensity value on either the LHS (negative x-axis) or RHS (positive x-axis).

6.4.2.6.2 Altered Boundary - Shrunk or Dilated Scalp Two fine meshes were developed where the scalp layer was shrunk or dilated to 97% and 105% respectively of the original volume. The electrode positions were then translated onto the new boundaries. No other layers were affected. The 97% value represented a shrinking factor that maintained a layer of scalp over the skull (any further reduction in volume resulted in skull layer being exposed to the exterior). The 105% value was chosen as a complementary dilation factor. The work of [274] demonstrated that the external geometry of the head varies between people with various models predicting head circumference based on height and weight and an inter-model variance of about 10%. Hence assuming a “best guess” generic head mesh based on a patient’s height and weight would be available for reconstruction purposes, a 97 to 105 % variance in volume should be achievable. The results from these models, shown in Fig. 6.19, are comparable to the results from the ideal model.

The magnitude of the GMI are greater for the 97% model and less for the 105% model compared to ideal due to the reduction and dilation in scalp volume rendering the perturbations ‘bigger’ and ‘smaller’ compared to the whole head compared to ideal. The IN, MD and DCL metrics are all larger in value (but comparable) to ideal. The RDR is perfect in all cases (0% for N, 100% for B,C). Therefore this result suggests that the BFSD-EIT algorithm can tolerate small variances in symmetric head circumferences.

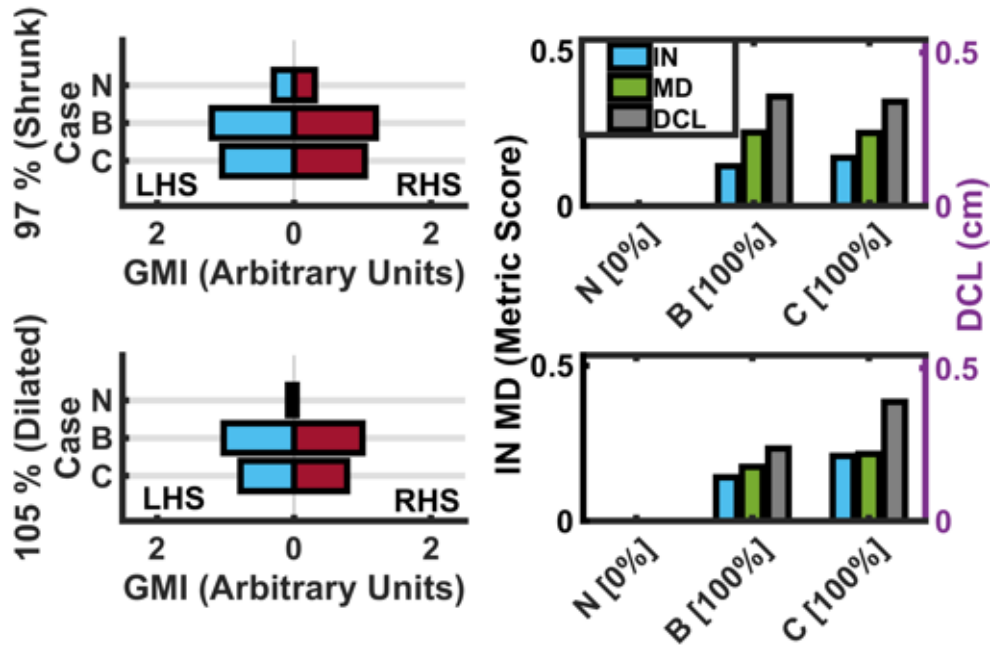


Figure 6.19: Quantitative Metrics for models where the scalp layer is shrunk to 97% of the original volume (top row) and dilated to 105% of the original volume (bottom row). Cases are N (no lesion present); B (bleed); C (clot). GMI: The blue bars represent a negative intensity value and the red bars a positive intensity value on either the LHS (negative x-axis) or RHS (positive x-axis axis). IN, MD and DCL are reported if ROIs are detected. The RDR for each case is reported on the x-axis of the IN, MD, DCL plot.

6.4.2.7 Study 6: Effect of a Frequency Dependent Background

The disambiguation step of BFS-D-EIT is dependent on a difference in the pattern of conductivity contrast between the bleed or clot and brain at the two different f points. At a f_1 of 25 Hz the conductivities of brain, clot and bleed are 0.1 Sm^{-1} , 0.05 Sm^{-1} , and 0.7 Sm^{-1} respectively. Re-application of the algorithm at a f_2 of 100 Hz where these respective tissue conductivities are 0.1 Sm^{-1} , 0.09 Sm^{-1} , and 0.7 Sm^{-1} , will result in theoretically identical metrics for a bleed as the contrast does not change, while for a clot the decrease in contrast will result in metrics more like a normal case. Hence disambiguation is achieved, aided by the assumed frequency-independent brain background.

This section investigates whether disambiguation is possible if the conductivity of brain also changes from f_1 to f_2 , and the change in contrast patterns are similar for lesion types. To investigate this, the GMI for the three cases (i.e., N, B, C) was computed for a f_1 of 25 Hz and then a f_2 of 25 kHz. At 25 kHz

the conductivity of brain, bleed and clot are 0.13Sm^{-1} , 0.7Sm^{-1} and 0.11Sm^{-1} as shown in Fig. 2.19. Crucially the brain conductivity has changed, and the contrast for both clot and bleed with respect to brain is less at f_2 compared to f_1 . The results are shown in Fig. 6.20. For both lesion cases, the GMI metric decreases in magnitude from f_1 to f_2 as both lesion types have decreased in contrast with respect to brain. Although the scale of decrease is greater for clot than bleed, the fact that both decrease confounds disambiguation. In order to achieve disambiguation, therefore, the selection of f points can be improved. For example, f_1 of 25 Hz and f_2 of 100 Hz, as used in Section 6.3, could be chosen due to the differing patterns in contrast change for bleed and clot with respect to brain.

However, a more robust technique would be a multi-frequency approach where the overall contrast pattern over a series of points can be used to identify the lesion type. In Fig. 6.21, the GMI patterns for the three cases over five f points from 25 Hz to 100 Hz is plotted. This is the band of most significant conductivity change between brain, bleed, and clot tissues. The results show that the GMI on both sides are equal but opposite at a given f point and importantly the pattern for a given case mirrors the contrast between lesion and background across the band:

- The GMI of case N is near zero and approximately constant;
- For case B the GMI is large in magnitude with a slow decrease across the band as the conductivity of brain slowly increases to reduce the contrast between the brain and the bleed;
- Case C shows a significant reduction in magnitude of GMI from 25 to 100 Hz mirroring the reduction in contrast between clot and brain across that frequency range.

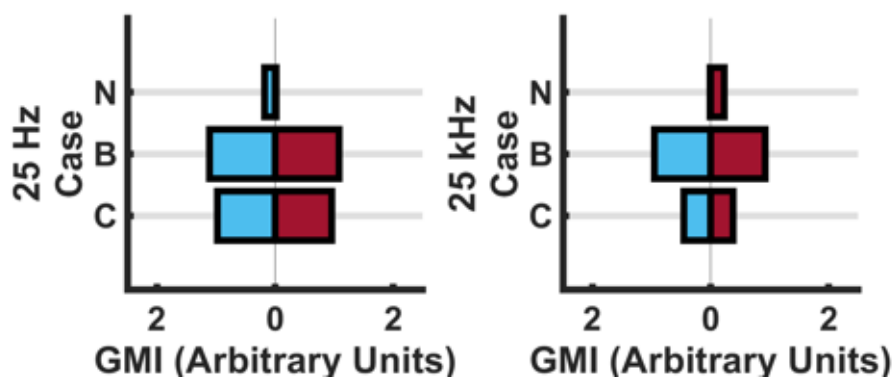


Figure 6.20: GMI metric results for the 3 cases at f_1 of 25Hz and then a f_2 of 25kHz, demonstrating the effect of a frequency-dependent background.

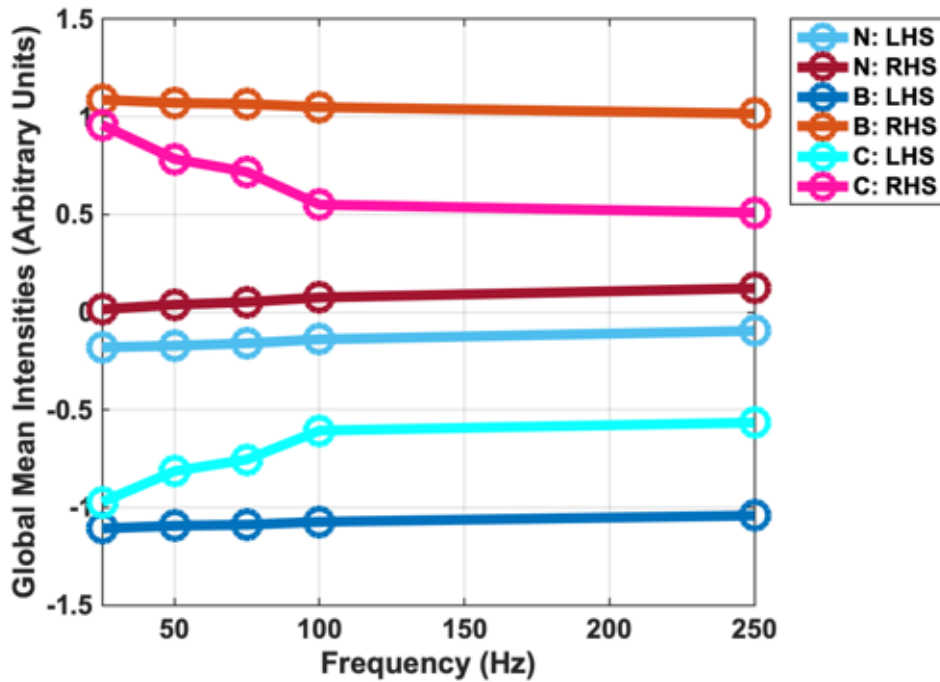


Figure 6.21: GMI metric results (LHS and RHS) for the 3 cases (N, B, C) across the 25 to 100 Hz band.

6.4.2.8 Study 7: Application to Human Data

As a final test, the BFS-D-EIT algorithm was applied to human data collected from stroke patients as part of a clinical trial with the Hyper Acute Stroke Unit (HASU) at University College London Hospital (UCLH) [13]. The SNR of the data was approximately 48 dB. A patient was selected with a right-sided ischaemic lesion occupying 13.7% of the brain volume ('P26' in the dataset). The measurement frames collected from this patient were reconstructed onto a coarse mesh derived from neuroimaging from the patient (mesh 'A'). Reconstruction was also performed onto two other coarse meshes derived from two other randomly selected patients 'P9' and 'P11' (meshes 'Y' and 'Z' respectively). This approach was performed to compare the effect of patient specific and non-patient specific meshes on the result. Further, as the measurement frames are from a human patient the 'forward model' is of a real human head inclusive of complete anatomy and inherent asymmetries. The results are shown in Fig. 6.22, as the GMI at four points in the 5 to 100 Hz band. This band corresponding to the f points used in [13]. Noise-free simulated measurement frames generated using fine FEM models of the lesion and head from patient P26 were reconstructed onto mesh A and used to represent the 'ideal' result,

shown as trace C on Fig. 6.22.

The results for reconstruction using the patient data and the patient specific mesh A is the nearest to the ideal of trace C, with a high magnitude GMI at the lower end of the band reducing over the band to 100 Hz. Further, for trace A the sign of the GMI matches at all points (positive on the RHS, and negative on the LHS) that of trace C. When reconstruction is performed onto the non-specific meshes, the result deviate from the ideal result. For the reconstruction onto mesh Y, the GMI sign of trace Y match trace C but the reduction in magnitude of GMI across the band is less. For the reconstruction onto mesh Z, the rate of reduction of magnitude is similar to trace A but the GMI sign is opposite (i.e. the clot is detected on the wrong side). The trend in GMI reduction associated with a clot across the band hence appears in both patient specific and non-patient specific meshes, with better results in the patient specific case.

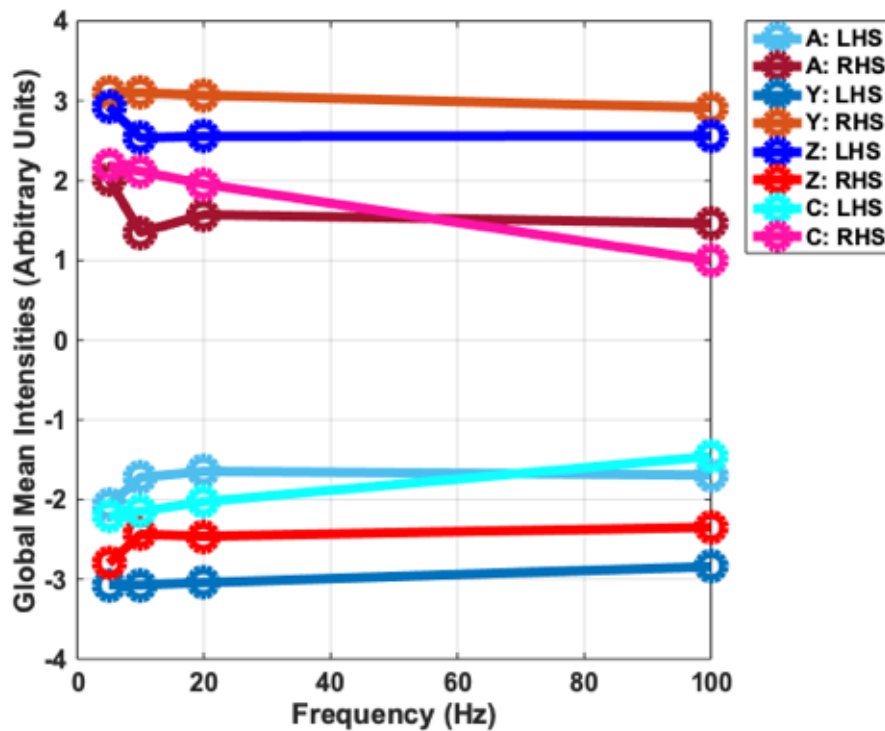


Figure 6.22: GMI metric results (LHS and RHS) human ischaemic stroke patient across the 5 to 100 Hz band. Reconstruction is performed onto a patient specific mesh (A), and two patient non-specific meshes (Y and Z). The results from using simulated data onto the patient specific mesh is also shown (C), and represents the ideal case.

6.4.3 Bi-Frequency Symmetry Difference EIT - Feasibility and Limitations of Application to Stroke Diagnosis Discussion

This section has considered the feasibility and limitations of applying BFS-D-EIT to the stroke diagnosis by assessing the performance of the algorithm with respect to a range of parameters. These scenarios encompass common and important challenges of EIT.

Algorithm performance is unsurprisingly better at higher SNR levels as shown in Section 6.4.2.2. The results suggest a SNR of 80 dB or higher is required for accurate lesion detection, with application of BFS-D-EIT for stroke detection still feasible down to a SNR limit of about 60 dB. Beyond this SNR level degradation of results means lesion detection is not reliable, but is possible. This detection at lower SNR levels is seen with the results from the human patient where measurement frames at 48 dB were used albeit with a large lesion, with the results comparable to the equivalent simulated lesion as shown in Fig. 6.22. While some EIT applications may be feasible at lower SNR levels, use of EIT applied to more demanding neural applications that may involve smaller changes and issues such as the skull and CSF dampening signals generally require systems capable of 80 dB and higher [14], [15], [275], [276]. It should be noted that the nominal rating of a system is usually higher than that achieved with patients. For example, the human data was recorded using the Scousetom system with a SNR rating of 77.5 dB [15]. Hence, as well as improvements in the core hardware, tackling of other hardware based noise sources such as wires, electrodes, connections, and movements of these during recording will be needed in order to improve the quality of data recorded from patients.

Electrode positioning errors are considered in Section 6.4.2.3. EIT is sensitive to errors in electrode positioning [10], with inaccurate electrode positions a major cause of artefacts due to the ill-posed nature of the reconstruction problem [180]. BFS-D-EIT assumes symmetric placement of electrode pairs. Moreover, these placement positions are assumed to be in agreement with the ideal model. These assumptions led to the investigation of the effect of two related potential error sources in BFS-D-EIT:

1. Electrode Positioning Errors with Symmetry Lost.

In this case, electrode pairs are not symmetric with respect to each other and are not correctly positioned relative to the ideal model. A severe effect on algorithm performance is seen in this situation with BFS-D-EIT tolerant to errors in electrode positioning within only a ± 1 mm radius of the positions expected by the ideal model. Unreliable ROI detection with a steep decline

in RDR from ideal is seen at radii beyond ± 1 mm. The GMI metric is more robust, with reliability seen up to about ± 5 mm error radius.

2. Electrode Positioning Errors with Symmetry Maintained.

Here symmetry between electrode pairs is maintained despite incorrect positioning with respect to the ideal model. The results are found to be improved relative to the case in which electrode pairs are not symmetric. The robustness of the GMI is evident with reliable results of up to ± 30 mm error radius. Acceptable results are only reported up to ± 5 mm for the other metrics with no or erroneous ROIs detected beyond this.

While the ± 30 mm limit is encouraging, it is only applicable if symmetry between electrode pairs is maintained. Without this condition being achieved the ± 5 mm value is a limitation, however this tolerance is still an order of magnitude of that achieved in [20]. Nevertheless, techniques to improve electrode placement accuracy are essential in order to further improve the robustness of the algorithm. The electrode positioning used is largely based on the EEG 10-20 system, and as such EEG caps may be used in the first instance to aid electrode positioning with a specific hat for BFSDEIT a possible improvement. Other aids include the use of image guidance technology [277], automated algorithms to calculate EEG positions [278], and devices to generate quick precise 3D models of patients' heads for use in EEG electrode placement [279]. Hence, electrode positioning while a challenge for EIT may be one that is surmountable.

Changes in the electrode contact impedance are studied in Section 6.4.2.4. The results show such changes have little or no effect on the BFSDEIT algorithm performance. Notably, the contact impedance ranges chosen ($\pm 20\%$ and $\pm 50\%$ of the ideal value) correspond to suboptimal and unacceptable variances in impedance as described by [20]. Therefore, realistically, variations in contact impedance will be below these ranges and are thus unlikely to impact the algorithm outcomes. As further explained in [20] changes in the impedance of the electrode have little effect on the current flow pattern within the head as the conductivity of the electrode is large even with the modelled errors compared to that of the tissues of the head.

Errors in assumed conductivity of the tissues were examined in Section 6.4.2.5. The uncertainty and variability in conductivity values of tissues, especially in the EIT range [153] means that the algorithm must be robust to errors in this parameter both at the voxel and whole tissue levels. At the voxel level, assigning each voxel a value of the ideal conductivity value for the respective tissue with an error of up

to ± 0 to 50% had little or no effect on the result compared to ideal. This result is attributed to the reconstruction onto a coarse mesh which has approximately $\frac{1}{16}$ th the number of voxels compared to the fine mesh. This “averages out” the heterogeneous nature of the tissue voxels in the erroneous models.

At the whole tissue level, assigning each tissue a value of the ideal conductivity value for the respective tissue with an error of up to ± 0 to 20% had little effect on the result compared to ideal. The reason for this result is the differencing of measurement frames from symmetrically opposite orientations resulting in error suppression and the contrast (proportional to the difference) between the tissues largely being maintained despite errors in assumed conductivity. Lesion detection is still achieved but the GMI results for the two different lesions are similar for an error of ± 0 to 50%. Lesion detection is the goal of the algorithm at a single f point. Identification of lesion type requires the disambiguation step but this step is dependent on lesion detection at both f points. Hence, this convergence of values for both cases is not of concern as the pattern of contrast change will differ for the two lesions between f points allowing disambiguation. Overall, at both voxel and tissue levels, these results are significant. As the true conductivity of a tissue is uncertain, the fidelity of the algorithm even with variability in tissue conductivity of up to 50% is strongly encouraging.

Errors in the assumed anatomy of the head were studied in Section 6.4.2.6. Two scenarios were examined with geometries different to that of the coarse reconstruction FEM mesh:

1. Unilateral Excess of Skull or Brain.

In the first scenario which examines the unilateral excess of tissues, the effect of reassigning the CSF as skull or brain on the left side is examined. This change is effectively the thickening of the skull or brain with a reciprocal thinning of the CSF. At the chosen f point, this modification effectively places a low conductivity target on the LHS compared to the RHS as the conductivity of skull or brain is less than that of CSF. The presence of this low conductivity LHS target compared to the CSF in the symmetric RHS location is seen in the GMI. The GMI reports a high intensity value on the LHS, and low intensity value on the RHS which are equal but opposite. Further, the magnitude of the GMI values increase as the volume of skull (or brain) tissue increases. The results are near identical for both sets of models, however the magnitude of the values from the skull models are slightly larger than those of the brain models as the contrast between skull and CSF is larger than that between brain and CSF.

In terms of the metrics based on ROIs, the isolation of the largest candidate ROIs results in the excessive skull (or brain) ‘lesion’ being detected instead of the bleed or clot in all cases. In the smallest 10 mm radius model, the lesion is removed by the filtering as it lies too near to the exterior, resulting in no ROI detection. When ROIs are detected the result is near identical metrics for all cases in the excess skull or brain models. The size of a ROI is a function of the volume of the lesion but also the contrast between the tissues on either side. The contrast between skull or brain and CSF results in larger ROIs than those produced for the 50 ml clot or 10 ml bleed (which are both contrasted with brain).

These results indicate that BFS-D-EIT is extremely sensitive to asymmetry in normal anatomy with an excess skull or brain tissue of $< 1 \text{ cm}^3$ on one side capable of masking the presence of true lesions. The excess tissue confounds the ROI analysis. However, the GMI results indicate that asymmetric anatomy may be tolerated by BFS-D-EIT if results are gathered at multiple frequencies the arithmetic sum property used. At a second f point where the conductivity of the tissues is different, analysis of the results would identify the presence of a lesion based on the known changes in tissue conductivities between the f points selected. For example, at 100 Hz the decreased contrast between brain (0.1 Sm^{-1}) and clot (0.09 Sm^{-1}) will result in a noticeable difference in the GMI result for case C at 100 Hz (closer to the N result) compared to 25 Hz where the enhanced contrast of clot compared to brain deviates the GMI result away from the N result more. If the conductivities do not change with frequency then disambiguation would not be possible. In the models used, neither skull, bleed nor CSF change in conductivity over the range considered [12], [146] meaning disambiguation of bleed from normal in the presence of asymmetric excess skull would be challenging.

2. Altered Boundary - Shrunk and Dilated Scalp.

It is unlikely that a patient-specific mesh would be available in acute stroke cases. However, it would be possible to have a generic “best guess” mesh for reconstruction that approximated the external head geometry based on non-invasive measurable parameters. These parameters could include for example circumference and nasion-inion distance. The shrunk (97% of original volume) and dilated (105% of original volume) scalp models gave strong results comparable to ideal. Of note, the GMI results were greater in magnitude for the 97% model as less scalp results in a larger effective presence of the lesions. The GMI values were smaller in magnitude for the 105% models for the opposite reason. In [174], it was argued that although images reconstructed

onto a correct mesh are of superior quality those from using a generic mesh, using the correct mesh did not improve stroke detection rates and thus a generic mesh may be sufficient. For stroke, lesion detection and lesion-type identification are crucial whereas image quality may not be as vital. As such, a generic best guess mesh may be sufficient for the feasibility of BFS-D-EIT in this application.

The alterations in boundary studied are uniform decreases or increases in the geometry of the original boundary. Non-uniform changes in the boundary would result in the challenges discussed in the previous section (unilateral excess of skull or brain) as well as resulting in changes in the symmetry of electrode positioning.

A frequency-dependent background has the ability to confound lesion detection if the pattern of contrast change between the possible lesion types (bleed or clot) and background is the same from f_1 to f_2 . This is examined in Section 6.4.2.7. However, if care is taken in the selection of f points then this potential problem can be avoided. In Section 6.3 the f points of 25 Hz and 100 Hz are used as there is a significant decrease in contrast between clot and brain at f_1 compared to f_2 , while there is effectively no change in contrast between bleed and brain at the same two f points. An alternative, and more robust method may be to assess the pattern of contrast change at multiple f points across a band, this method will be explored in more detail in Chapter 7.

The BFS-D-EIT algorithm was applied to human data for the first time in this chapter. The dataset from the UCL study represents the most comprehensive EIT stroke data currently available but also suffers from limitations including an SNR of 48 dB, and uncertainty over error sources such as electrode positioning [13]. Despite this, the use of human data represents measurement frames from a real human stroke patient as opposed to the controlled environment of numerical models used in other parts of the study. As found in Section 6.4.2.8, the trend in GMI associated with a clot appears in both patient specific and non-patient specific meshes. These important results point to the strong promise of BFS-D-EIT in stroke diagnosis. However, the results must be treated with caution as the data was taken from a patient with a large ischaemic lesion. Also while the results from using non-patient specific meshes were promising, best results were achieved for the mesh modelled on the anatomy of the patient which may not be available in acute scenarios [174]. The results give an indication that BFS-D-EIT may be feasible in true clinical scenarios. The GMI results for the ischaemic lesion generally following the expected ideal pattern for a clot, but not yet of adequate diagnos-

tic value with further studies with more patients and algorithm development needed.

In summary, BFS-D-EIT compares favourably to the state-of-the-art algorithm involving EIT applied to stroke problem which is the fdEIT algorithm of Malone *et al.* [20]. BFS-D-EIT shares the same challenges with regards anatomical variation, but shows superior tolerance to electrode positioning errors. While BFS-D-EIT was tolerant of errors of up to 30 mm, in [20] errors of 0.5 mm resulted in failure to detect lesions. BFS-D-EIT also shares the robustness to contact impedance seen in [20]. BFS-D-EIT shows advantages over the algorithm presented in [20] in terms of computational efficiency with 5-6 hours needed for image reconstruction in [20] compared to approximately 5 minutes for BFS-D-EIT. Further, as BFS-D-EIT compares measurement frames at each frequency point from mirror image orientations at that frequency point, it avoids a direct comparison of measurement frames taken at different frequency points. Hence, BFS-D-EIT avoids sources of error associated with fdEIT techniques resulting from the fact that different errors are present at different frequencies [12], [17], [193]. This latter point also explains the superior haemorrhage detection of BFS-D-EIT over a fdEIT algorithm such as that in [20]. In BFS-D-EIT the contrast in conductivity between haemorrhage and brain is leveraged at each f point for detection, and does not rely on a change in conductivity across frequencies which is absent for bleed and brain. Finally, the results in this study were achieved without mesh refinement at electrode contact points which was required in [20]. This lack of electrode refinement aids in the computational efficiency of BFS-D-EIT. While BFS-D-EIT has limitations and is currently not fit for consideration in clinical use as a stand-alone diagnostic device, the technique shows strong promise when applied to stroke diagnosis provided that the error tolerances listed above are respected.

6.5 Conclusions

This chapter has presented the BFS-D-EIT algorithm which represents an iterative, but substantial, improvement over sdEIT (Chapter 5). The BFS-D-EIT algorithm is capable of detecting lesions where the presence of the lesion disrupts a normally symmetrical scene. BFS-D-EIT identifies and quantifies these disruptions in symmetry, with localisation and identification possible through the use of two frequency points. An algorithm overview was presented in Section 6.2 which demonstrates the improvements over sdEIT. The use of two frequency points removes the need for an accurate numerical model of the normal scene to disambiguate lesion types. Further, this work has advanced upon sdEIT through the usage of a 3D electrode layout and has introduced more robust metrics.

CHAPTER 6. BI-FREQUENCY SYMMETRY DIFFERENCE EIT

Next, Section 6.3 has provided an initial development and proof-of-concept of the BFS-D-EIT algorithm with successful application in numerical models, and validation in phantom experiments. From Section 6.3 it can be concluded that BFS-D-EIT is seen to perform best for:

- Larger lesions;
- Lesions further from the plane of symmetry;
- Setups where there is a relatively high SNR.

In terms of SNR the results of Section 6.3 indicate hardware offering ≥ 60 dB SNR is needed for robust detection with respect to the sample stroke diagnostic application.

Next Section 6.4 studied the feasibility and limitations of BFS-D-EIT applied to stroke diagnosis through a variety of realistic numerical simulations. Scenarios designed to test the robustness and limitations of the algorithm were examined, with the conclusions that:

- Electrode positioning errors severely affect performance. However, tolerance of up to ± 30 mm from the expected position is seen if symmetry is maintained between partner electrodes;
- Contact impedance errors of electrodes (up to $\pm 50\%$ of the assumed impedance) have little effect on performance;
- Errors in assumed conductivity of tissues (up to $\pm 50\%$ of the reference value) whether at a voxel or whole tissue level have little effect on performance;
- Errors in assumed anatomy affect the performance of the algorithm. Asymmetrical anatomy across the sagittal plane can be detected as false positive lesions and mask true lesions. The GMI metric may be used to overcome this limitation, if the tissues have a frequency-dependent change in conductivity. Errors in the assumed boundary of the head with a 10% variance only slightly decreases performance;
- A frequency-dependent background can confound disambiguation if f points are not carefully chosen. A multi-frequency approach may be a more robust way to deal with frequency-dependent background with assessment of the overall contrast pattern across a band;
- An absolute limitation of BFS-D-EIT is an inability to detect lesions that lie perfectly across the plane of symmetry due to the basis of the algorithm being detection of differences in symmetry if present [193].

In particular, use of the GMI metric and a multi-frequency approach can result in a robust stroke detection method with promising results seen in the application of the algorithm to data from a human ischaemic stroke patient. The next chapter further investigates the GMI metric and a multi-frequency approach, and examining the

CHAPTER 6. BI-FREQUENCY SYMMETRY DIFFERENCE EIT

integration of this approach with the ML principles from Chapter 4 using both numerical and human data.

Multi-Frequency Symmetry Difference EIT with Machine Learning for Human Stroke Diagnosis

Material from this chapter appeared in two peer-reviewed works. A conference paper entitled “Stroke Diagnosis Using Multi-Frequency Symmetry Difference EIT with SVM Classification” was part of the published Proceedings from the 21st International Conference on Biomedical Applications of Electrical Impedance Tomography, National University of Ireland Galway, Ireland [280]. This conference paper was comprehensively extended upon, and published as the journal paper “Multi-Frequency Symmetry Difference Electrical Impedance Tomography with Machine Learning for Human Stroke Diagnosis” published in published as a journal article in the Institute of Physics publication Physiological Measurement [281].

This chapter advances on the utility of BFS-D-EIT by increasing the number of frequency points considered. This resulting Multi-Frequency Symmetry Difference Electrical Impedance Tomography (MFSD-EIT) algorithm is used to produce GMI metrics at each frequency as Multi-Frequency Global LHS & RHS Mean Intensity (MF-GMI) data from both simulated and human patients. This MF-GMI data in turn is used as the input for SVM classification algorithms to identify and differentiate between normal, haemorrhagic stroke, and ischaemic stroke.

7.1 Introduction

The effective application of EIT to lesion detection in static scenes is a core theme of this thesis. In Chapter 4, ML algorithms were applied to electrical impedance measurement frames. Significant promise was shown in the use of SVM classifiers in numerical and phantom studies with regard to the detection and differentiation of normal from static haemorrhagic lesions. Next, a novel modality of EIT suitable for static scenes featuring symmetry was presented in Chapter 5. This modality

focuses on detection of unilateral perturbations causing a change in this inherent symmetry. This modality was iterated upon in Chapter 6 with analysis of disturbances in symmetry in a scene at each of two frequency points, and an investigation of the frequency related changes. The resultant BFS-D-EIT algorithm was tested specifically in regard to application in stroke. The robustness of the technique, including maximal allowances with respect to errors, and techniques to improve the efficacy was established. The use of a quantitative metric called the GMI was found to enhance the robustness of the algorithm. Use of the GMI combined with a Multi-Frequency (MF) approach in the band of greatest change in conductivity of the tissues (≤ 100 Hz [12], [146]) in particular aided in maximising robustness.

In this current chapter, the areas explored in these preceding chapters are combined and integrated. Specifically, BFS-D-EIT is further developed by increasing the number of frequency points used. This new algorithm is referred to as MFSD-EIT. After applying the algorithm, GMI metrics are generated at each frequency. The human dataset collected by Goren *et al.* in UCL is used as the primary data source [13]. Realistic four-layer FEM models constructed from the CT scans of patients are used to generate simulated EIT measurement frames, as well as reconstruct and analyse the real measurement frames collected from these patients [13]. To the simulated and real frames, the MFSD-EIT algorithm is applied and the GMI results collected across a band from 5 to 100 Hz. This MF-GMI data is then used as input features for SVM classification to assess if differentiation between stroke types is possible.

The layout of the chapter is as follows: In Section 7.2, an overview of the UCL stroke dataset is given. Next, a summary of the MFSD-EIT algorithm is provided along with the definition of the MF-GMI metric. The rationale for application of the proposed technique in stroke is presented as well as the theoretical ideal results for normal, haemorrhage, and clot cases. Then, the numerical models used to generate simulated measurement frames, and to reconstruct the human frames are described in Section 7.3. This section ends with an overview of the MF-GMI data generation. In Section 7.4, this MF-GMI data is used as an input to a SVM classification algorithm. In this section the classification protocol is outlined before the results from various classification scenarios are reported. The results of these scenarios for both numerical and human data sets are discussed in Section 7.5. The chapter is concluded in 7.6.

7.2 Multi-Frequency Symmetry Difference EIT Applied to Stroke Diagnosis

In this section, the UCL dataset is presented, as well as a summary of the MFSD-EIT algorithm including the GMI metric. The rationale for the use of this proposed algorithm in stroke is described, and theoretical ideal results for normal, bleed and ischaemic patients are discussed.

7.2.1 The University College London Multi-frequency EIT Human Stroke Dataset

MF EIT measurement frames were collected by the EIT group in UCL as part of a clinical trial with the HASU at UCLH [13]. This dataset is the most comprehensive collection of human EIT data related to stroke. EIT measurement frames were collected at 17 frequency points from 5 Hz – 2 kHz, with maximal current adjusted according to IEC 60601-1 guidelines [11]. Data was collected from $N = 10$ healthy volunteers, and $N = 23$ stroke patients. In the published dataset, the measurement frames from the $N = 10$ healthy volunteers are provided along with that from $N = 18$ of the patients. The data from the remaining patients was rejected due to various reasons, but mainly poor-quality of frames. Of the remaining 18 patients, $N = 6$ had two sets of recordings taken at different time points resulting in a final dataset comprised of measurement frames from $N = 10$ healthy volunteers, and $N = 24$ sets of recordings from patients. Of the patients, $N = 10$ had haemorrhagic stroke and $N = 14$ ischaemic stroke.

The frames were recorded using the ScouseTom EIT system [15], with 32 EEG electrodes placed on the patient according to EEG 10-20 system with some variants as described in [195]. The electrode layout was identical to the layout described in Section 6.3.1.1. In most cases (16 of the 24 patient sets) recording was performed within 48 hours of stroke onset [13]. The injection/ measurement protocol provided 930 separate voltage measurements in a measurement frame at each frequency, with the protocol selected to maximise the magnitude of recorded voltages and the number of independent measurements. The recorded measurement frames had a mean reported SNR of approximately 45 to 50 dB, which is lower than the recommended minimum 60 dB from the feasibility study described in Section 6.4. However, care was taken to maximise quality of recording with removal of voltages excessively contaminated, filtering and other post-processing techniques performed by the UCL investigators [13].

Importantly the electrode layout was symmetric and so the electrodes could be

considered as two mirror image orientations, and thus suitable for MFSD-EIT. The protocol used in the UCL dataset was not a MFSD-EIT protocol, but the resultant measurement frames could be post-processed for input in to the MFSD-EIT algorithm. In addition to the EIT measurement frames, diagnostic imaging with CT and/or MRI scans of the 18 patients is provided in the dataset [13]. These images were collected at a different time point than the EIT recording session, and contain the diagnostic report of the radiologist. These neuroimages were used to generate FEM models, described in Section 7.3.1.

7.2.2 Multi-Frequency Symmetry Difference EIT Algorithm and Multi-Frequency GMI

MFSD-EIT is an extension of BFS-D-EIT with the use of multiple f points instead of two resulting in a more robust disambiguation of lesion type. A thorough presentation of BFS-D-EIT is given in Chapter 6. Briefly, the proposed MFSD-EIT algorithm can be considered as consisting of two steps:

1. **The Detection of a Deviation from Normal Symmetry.**

The electrodes are arranged on the body of interest as symmetric pairs with respect to a plane of symmetry. In the case of the head, the sagittal plane divides the head into symmetric LHS and RHS sides. Any electrode on the symmetric plane is considered its own pair. A measurement frame is taken from an ‘A-orientation’ and then from a mirror image ‘B-orientation’. A sample channel from both orientations is illustrated in Fig. 7.1. These frames are differenced and reconstructed using 0th order Tikhonov regularization [166] onto a FEM model corresponding to A-orientation. Each voxel in the reconstruction has a conductivity change assigned. For a given voxel, a positive conductivity change intensity indicates the measurements from B-orientation are more conductive than that from A-orientation at that location. The magnitude of the intensity is proportional to the magnitude of the difference in measurements. If a unilateral perturbation is present, symmetry will be disrupted at the location of the perturbation with an equal but opposite disruption in terms of conductivity change at the symmetric location.

2. **The Disambiguation of Lesion Type.**

In the case of stroke, the two causative lesions of haemorrhage and clot are more and less conductive than the brain respectively. This difference in conductivity results in ambiguity as to which of the disruptions detected from Step (1) is the true perturbation. The disambiguation step involves repeating Step (1) at a different frequency point where there is a known change in the pattern of conductivity of the tissues from the original frequency

point. The change in contrast translates as a proportional change in the conductivity difference detected at the candidate perturbation locations. *A priori* knowledge of the change in contrast of the tissues allows identification of the lesion as haemorrhage or clot. The use of multiple frequency points results in a more robust analysis since the pattern of change over a band can be considered as opposed to at only two points (Section 6.4.2.7). The voxel intensity values in the reconstructions can be analysed and used to generate robust quantitative metrics. The GMI metric has been shown to be particularly robust to errors and can alone be used to identify perturbations (Chapter 6).

The GMI metric was defined in Section 6.3.2 as the average intensity over all the voxels on each side (LHS and RHS) of the sagittal plane. The intensity will have magnitude and negative or positive sign. At each frequency point the resultant GMI is reported as two separate values: a LHS and a RHS value. If the body under consideration is perfectly symmetrical and no perturbation is present, then the result should be a LHS and RHS GMI of 0 at any frequency point. The presence of a unilateral perturbation moves the GMI away from 0, with equal but opposite values for LHS and RHS proportional to the contrast between the perturbation and the background brain at that frequency point. The GMI results for all frequency points considered are referred to in this chapter as MF-GMI data sets.

The UCL stroke dataset includes measurements taken at 5 Hz, 10 Hz, 20 Hz, and 100 Hz with these used as f points in this study, and the GMI calculated at each of these discrete frequencies.

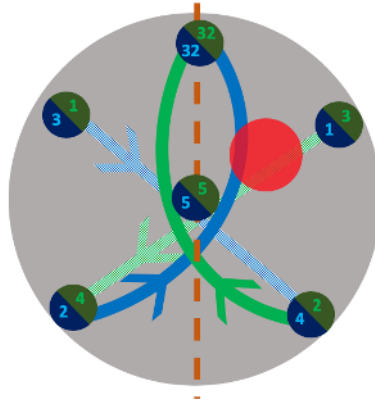


Figure 7.1: Illustration of an equivalent channel from A- (green) and B- (blue) orientations. The plane of symmetry is shown as an orange line, with electrodes simultaneously part of A- and B- orientations (for example Electrode #1 in A-orientation is also Electrode #3 in B-orientation). In the sample channel, current is injected between Electrode #2 and #32, with voltage measured between Electrode #3 and #4. The ‘green’ channel represents this channel when A-orientation is used while the ‘blue’ channel is this channel for B-orientation. The channels are equivalent and theoretically give the same voltage measurement in the absence of a perturbation. However, the presence of a perturbation (illustrated as a red circle) upsets the symmetry with this disruption seen as a difference in the voltages recorded between the green and blue channels.

7.2.3 Rationale for Application in Stroke

Stroke is a pathology of brain tissue, with the causative lesion either a bleed or clot [1]. Bleed is more conductive than brain at a given f point, with clot less conductive in the 5 to 100 Hz range [20], [195]. The pattern of change in conductivity contrast between bleed versus brain and clot versus brain shows most divergence below 100 Hz [20], [195]. These conductivity spectra from 5 to 100 Hz are shown in Fig. 7.2. The contrast in conductivity between ischaemia and brain shows a significant change in across the 5 to 100 Hz band with a high contrast at 5 Hz and low contrast at 100 Hz. Bleed shows an approximate constant contrast with respect to brain across the same band. Hence, theoretically, performing Step (1) of MFSD-EIT across this band at multiple f points should result in the same GMI result if the brain is normal or if a bleed is present. If a clot is present the GMI will be maximal at 5 Hz and reduce to the normal (perturbation free) value as 100 Hz is approached and the contrast reduces with respect to the background brain.

The other tissues of the head (scalp, skull, CSF) have approximately constant conductivity values in this frequency band [12], [146].

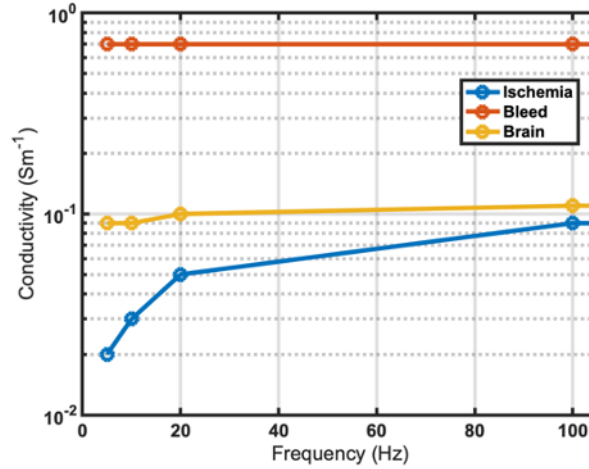


Figure 7.2: Conductivity spectra of ischaemia, bleed and brain across the 5 to 100 Hz band (data from [12], [146]). Ischaemia and bleed are respectively less and more conductive than healthy brain. However, across this band the contrast profile in conductivity between ischaemia and brain is significantly different than that of bleed and brain facilitating disambiguation using MFSD-EIT. The UCL stroke dataset includes measurements taken at 5 Hz, 10 Hz, 20 Hz, and 100 Hz.

7.2.4 Theoretical Ideal Results

The ideal results for a perfectly symmetrical head in three cases are shown in Fig. 7.3:

- N: Normal, i.e. no lesion present;
- B: Bleed present;
- C: Clot present.

In Fig. 7.3, the GMI is calculated at four f points (5 Hz, 10 Hz, 20 Hz, and 100 Hz). In all cases, the LHS and RHS components of the GMI at a particular f point are equal but opposite, while across the band the trend in GMI matches the change in contrast between the lesion tissue and background brain. In the normal case, the GMI is theoretically zero at all f points, while for bleed and clot the trends mirror those of the conductivity spectra seen in Fig. 7.2. As the patterns for bleed and clot differ, differentiation of these two lesion types should be possible. The magnitude of the GMI for lesions is a function of lesion location and size (with the sign a function of location), but the pattern is unaffected by these properties. In reality these ideal results are confounded by many factors, which are discussed in detail in Section 6.4.

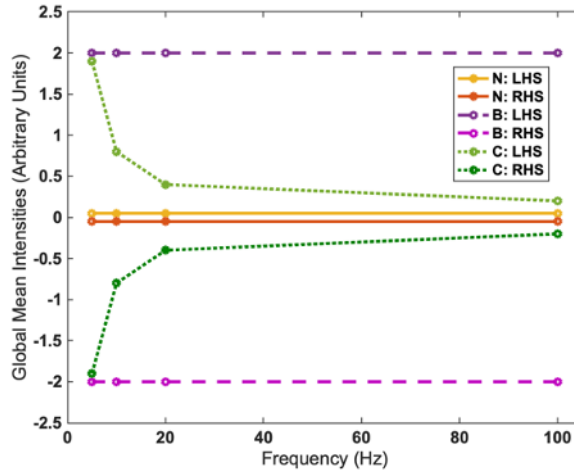


Figure 7.3: Theoretical MF GMI results for normal (N), bleed (B), and clot (C) cases across the 5 to 100 Hz band at four f points (5 Hz, 10 Hz, 20 Hz, 100 Hz). The GMI for a given case is ideally equally but opposite at each f point and the trend follows the contrast of the tissue with respect to background brain across the band. In the N case the results approach zero as there is no lesion present. The pattern for B differs to that for C leading to differentiation being possible.

7.3 Modelling Techniques and Data Generation

In this section a description of the FEM models used in the creation and reconstruction of simulated measurement frames and the reconstruction of human frames is presented. The section ends with a description of the MF-GMI data obtained from the numerical models and the human frames.

7.3.1 Numerical Models

The UCL dataset includes neuroimaging studies of the 18 stroke patients. These neuroimages were used to create four-layer CAD models of the anatomy of the head of each patient above the inion-nasion line [139] using 3D Slicer to segment out the scalp, skull, CSF, and brain layers from CT images before using Autodesk Fusion 360 CAD software to refine and convert the layers to STL files [178], [282]. Next, each of these four-layer STL models were converted into a fine tetrahedral mesh (~ 1 million elements each) with refinement around the electrode positions, with the electrodes modelled as 10 mm diameter and 1 k Ω contact impedance [162]. From each of these fine meshes, a coarse mesh ($\sim 200,000$ elements each) was created with the electrodes in A-orientation for use in reconstruction of both simulated and

human measurement frames.

Importantly, these patient specific meshes are not exact representations of the true anatomy due to inevitable approximations in the segmentation and meshing process. Further, it is likely that the electrode positioning may not have been in the theoretically exact location when recording patient voltages. These errors, and others such as assumed electrode contact impedance are likely unavoidable in practice where patient specific anatomy will not be known at the time of stroke onset and perhaps not required [174] [27]. Electrode placement will need to be performed with a degree of haste, and other compromises made due to the urgency of the condition. It is important that any technology and any algorithm can cope with these types of errors with an adequate degree of tolerance. As discussed thoroughly in Section 6.4, MFSD-EIT is robust to a variety of errors within certain limits.

In order to generate the simulated data, numerical models of anatomy are required. In order to increase the size of the data set as is recommended for ML [237], each of the 18 fine meshes were distorted to generate new anatomies. Each layer was dilated to 105% and shrunk to 97% of the original volume, which along with the normal geometry generates three possible anatomies for each of the four layers (Section 6.4.2.6.2). Combining every permutation of these layers results in 81 four-layer (i.e. 3^4 possible combinations) anatomies generated from each original patient STL model set and hence 1,458 simulated anatomies (18 x 81) overall, each made into a fine mesh. Into each of these meshes, spherical perturbations were placed in one of four different locations (north-east, north-west, south-east, south-west), and as 20 ml or 50 ml volume. These volumes are representative of a small and large lesion size (Section 6.3.1.1). In total, 1,458 normal simulated anatomies, and 11,664 lesion simulated anatomies were created, each as fine FEM models. A representative FEM model is shown in Fig. 7.4 with a 50 ml lesion in the north-east location along with a sample slice of the CT image that the model is derived from. In addition, a set of simulated anatomies was developed with lesions in a fifth location lying on the sagittal plane. These extra 2,916 lesion simulated anatomies with central lesions were solely used in one study to analysis the effect of central lesions on classifier performance (Section 7.4.2.6).

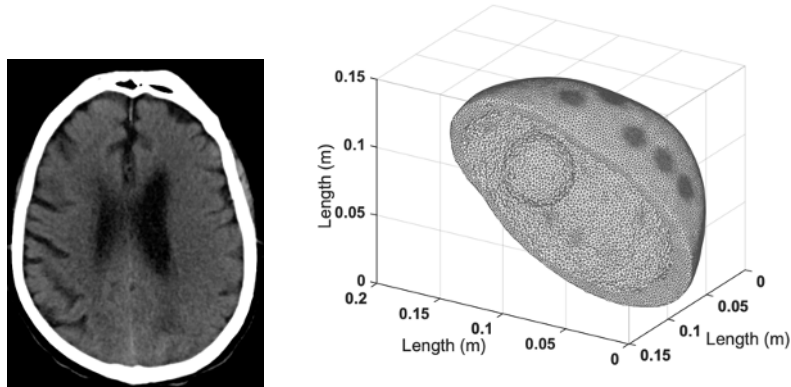


Figure 7.4: Left: All the simulated anatomies are derived from CT neuroimaging of stroke patients. A sample CT slice of the anatomy used to create the fine mesh is shown (from resources supplied in [13]). Right: Fine mesh with 50 ml simulated spherical lesion in the north-east position (where the front of the head represents north). The brain layer has been removed in order to show the lesion. The electrode refinement on the scalp layer is also clearly seen.

7.3.2 Multi-Frequency GMI Data Generation

This section describes the generation of MF-GMI data from the simulated anatomies and from the human measurement frames.

Simulated measurement frames were generated from the simulated anatomies. The fine FEM models corresponding to the perturbation free (i.e. normal) models were assigned conductivity values to the voxels of each of the four layers: scalp 0.23 Sm^{-1} , skull 0.05 Sm^{-1} , CSF 2 Sm^{-1} , brain 0.1 Sm^{-1} . These conductivity values are those of these tissues across the 5 to 100 Hz band [12], [146]. These models were then forward solved using the PEITS solver in order to generate measurement frames in both A- and B-orientations [164]. Noise was added to these frames at a level of 48 dB SNR. This noise level matched the average levels in the clinical human dataset [13]. The inverse problem of reconstruction was then performed onto the coarse mesh corresponding to the patient from which the simulated anatomy was derived (i.e. the original undistorted mesh). This choice of mesh for reconstruction emulates a real-world scenario where exact anatomy will be unknown and a best guess mesh may be needed for reconstruction. The GMI data was then computed. This process was repeated three additional times to simulate the generation of MF-GMI data at each of the four selected frequency points. Theoretically the GMI data generated at each f point will be identical in the normal case as the conductivities of the tissues are constant across the 5 to 100 Hz band, but will in

fact differ as a result of noise.

Next, the perturbation models were assigned 0.7 Sm^{-1} to those voxels where the perturbation is located. This value is the conductivity of a bleed across the band (Fig. 7.2). MF-GMI data was generated in the same manner as the normal models to result in simulated data of bleed cases. The perturbation models were next modelled as clots. The clot voxels were assigned conductivity values of 0.02, 0.03, 0.05, 0.09 Sm^{-1} in separate forward solves representing the clot at the four frequency points (Fig. 7.2), generating MF-GMI data for each case. Finally, the procedure for the normal models was repeated in order to provide sufficient sets of normal MF-GMI data to balance the number of perturbation (bleed and clot) sets. Due to the addition of noise to the measurement frames, each MF-GMI data from these normal cases was unique.

With regards the human data, the 18 coarse meshes used for reconstruction were derived from neuroimaging studies that were provided for the patients only [13]. Neuroimaging was not provided for the normal healthy volunteers. In order to reconstruct and generate MF-GMI data from the healthy volunteer measurement frames, each of these measurement frames were reconstructed using each of the 18 coarse meshes. Hence, 180 normal MF-GMI result sets were created. Further, in order to extend the amount of patient data, each of the 18 patient measurement frame sets were individually reconstructed and used to generate MF-GMI results from each of the 18 coarse meshes. The result was 180 MF-GMI result sets from bleed cases and 252 result sets from clot cases. Hence in most cases the mesh used to reconstruct and generate data was not anatomically related to the subject the measurement frame was derived from – the measurement frame from each patient is reconstructed onto each of the 18 possible coarse meshes, with only one of these related to the patient. This mismatch is a further error source, and a further test as to the robustness of the overall approach proposed in this paper.

These MF-GMI data sets are then used as features for SVM classifiers, described in the next section.

7.4 Machine Learning Applied to Multi-Frequency GMI Data

In this section, a ML classification algorithm is applied to the MF-GMI data derived from simulated and human measurement frames. Section 7.4.1 starts with a brief summary of SVM classifiers, the type of classifier used in this study. Next the

manner in which classification was carried out is outlined. In Section 7.4.2 the results of the various data sets in binary classifications and multi-class classification are reported, with the results discussed. In addition, consideration is given to the effect of lesions lying on the sagittal plane, and different levels of simulated noise on classifier performance.

7.4.1 Support Vector Machine Classifiers and Classification Protocol

SVMs were discussed in detail previously in Section 4.2. Briefly, SVMs are a group of ML algorithms often used for binary classification but can be adapted for use in multiclass classification [237]. SVM classification has been used in previous biomedical applications including the use of microwaves for detection of breast cancer [238], [239], [249], impedance spectroscopy for the detection of prostate cancer [243], and work reported in Chapter 4 on EIT measurement frames for the detection of brain hemorrhage. The SVM is trained with features from labelled observations (supervised learning) generating a trained model. This model is used to classify observations previously unseen with unknown labels (test or validation set). The features in this work are the MF-GMI data across the four f points. Hence the observations have 8 features or dimensions.

The basis of SVM classification is the creation of a hyperplane with margins that optimally separates observations within the classes as shown in Fig. 4.1. When training the model, the hyperplane and margins are defined and applied to future observations to classify them as class -1 or class $+1$ (in binary case). The kernel used by a SVM defines the function used in hyperplane generation. In this study a RBF is used which offers a flexible and robust hyperplane compared to simpler kernels such as linear kernels (Section 4.5).

The classification problems considered are the binary classification of normal versus lesion (bleed or clot), as well as all binary combinations of normal, bleed, and clot. Further, a multiclass classification of normal, bleed, and clot is performed. The labels (-1 or $+1$) correspond to the classes under investigation in a given binary classification task (e.g. ‘normal’ versus ‘lesion’; ‘bleed’ versus ‘clot’; ‘normal’ versus ‘bleed’; ‘normal’ versus ‘clot’). In the multiclass case, the labels 0, 1, 2 are used for ‘normal’, ‘bleed’, and ‘clot’ respectively.

The performance of the classifier can be reported in terms of the confusion matrix which tabulates the numbers of TP, TN, FP and FN classifications made by the trained model on a test or validation set. These metrics can be summarised as

sensitivity, specificity, accuracy as previously shown in Equations 4.1 - 4.3. In addition the metrics of Positive Predictive Value (PPV), and Negative Predictive Value (NPV) of the classifier are used to summarise the metrics, and are defined in Equations 7.1 and 7.2:

$$PPV = \frac{TP}{TP + FP}; \quad (7.1)$$

$$NPV = \frac{TN}{TN + FN}. \quad (7.2)$$

These metrics are reported in the results sections of this chapter, with the confusion matrices reported for the multiclass classification.

Next, the the processing of the MF-GMI data before use in the classifier is described as well as the procedure for training and testing a SVM classifier. The implementation used MATLAB, and in particular resources provided in the statistics and machine learning toolbox [173].

For each of the scenarios discussed in the following sections, the MF-GMI data sets from the simulated data at 48 dB, and the human data (~ 48 dB) are used in separate classifications with separately trained and tested classifiers, with the results for each set reported. For a given classification, the MF-GMI data corresponding to the scenario under investigation is used as the input features to the SVM classifier. Each observation has 8 features, and is labelled by class. In the case of the simulated data sets, the number of cases used are balanced between classes, whereas in the case of the human data set all the data is used due to the relatively small size of the available data.

Nested cross-validation is described in [283] and used in Section 4.5 as well as studies such as [249]. This method provides a generalized robust indication of classifier performance and helps mitigate against bias. This technique is used in this study to optimise SVM classification performance. The data is separated into $k = 10$ separate folds. Each of these outer folds is divided into a unique training set and test set made up of 90% and 10% of the total data set, respectively. The training set is used to select the optimal SVM classifier hyper-parameters (the box constraint and kernel scaling factor) using a Bayesian optimisation procedure in a $m = 10$ fold cross-validation process. The performance of the final classifier is assessed using the excluded test set. This process is repeated for each of the $k = 10$ folds with the final overall performance reported as the mean \pm standard deviation across the ten iterations. This approach is summarised in Fig. 7.5.

When calculating the performance results using Equations 4.1 - 4.3, and 7.1 - 7.2, incidents where the denominator term was zero was ignored for the purpose of calculation. Such a case happened once when calculating the NPV in the case of Normal versus Lesion using the human data where no negative cases were predicted. In each case, z-normalisation of the training set features is performed. The test set is z-normalised using the mean and standard deviation from the training set. This process ensures that there is no data contamination between the training and test set from the z-normalisation process [284]–[286].

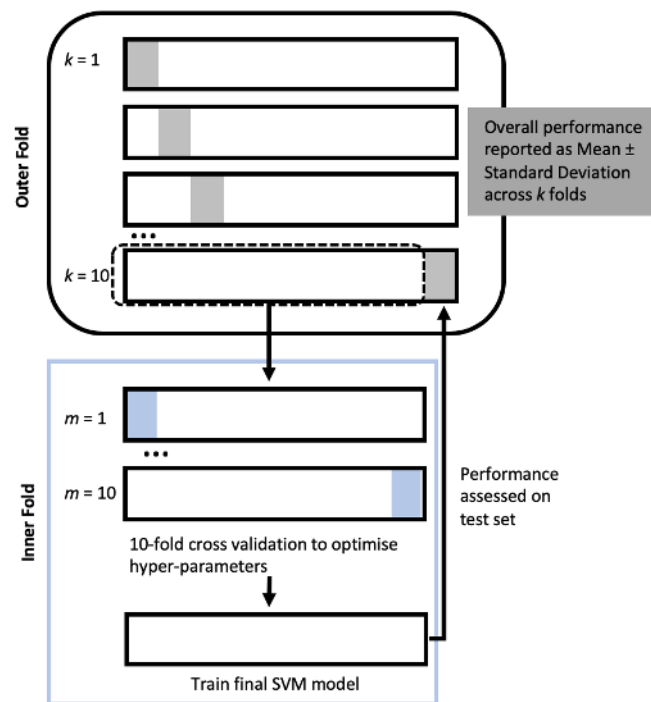


Figure 7.5: Nested cross-validation. The complete data set is separated into $k = 10$ folds with 90% as a training set (white) and 10% as a test set (grey). The training set from each of these outer folds is itself divided similarly into $m = 10$ inner folds divided into training (white) and test (blue) sets, with 10-fold cross validation performed on the inner fold to optimise hyper-parameters. These hyper-parameters are then used to train a final SVM model on the entire training set, with performance assessed on the held out test set. This repeated over the k folds with a final overall performance reported as the mean \pm standard deviation.

In the following sections, four cases of binary classification are considered followed by a multiclass classification problem. The multiclass problem uses an Error-Correcting Output Code (ECOC) classifier to effectively deal with the multiclass problem by combining multiple SVM binary classifiers [287]. Aside from using a

ECOC approach, the multiclass classification is treated identically to the binary classifications with nested cross-validation used.

7.4.2 Numerical and Human Classification Studies

In the following sub-sections, classification problems using both simulated data, and human data are studied with the results reported. These include all binary classification permutations of normal, bleed, clot, as well as a multiclass classification of the three classes. Finally the effect of lesions lying on the sagittal plane, and the effect of noise are examined.

7.4.2.1 Study 1: Normal versus Lesion (Bleed or Clot)

This study examined the binary classification of normal (assigned as the negative class) and lesion (assigned as the positive class). Lesion referred to either bleed or clot. The simulation data sets comprised of 10,064 simulated normal cases and 10,064 simulated lesion cases (with an even number of bleed and clot cases). The human data set comprised of 180 normal cases and 432 lesion cases (180 bleed, 252 clot cases).

The classifier performance for each data set is presented in Fig. 7.6. The results of the human data indicate strong lesion detection with a mean sensitivity of 88% and PPV of 81%. Detection of normal cases however proved challenging leading to poor mean specificity of 51% (NPV 66%). The mean accuracy was 77%. In the case of the simulated data set (48 dB SNR), all metrics are $\geq 89\%$, with a mean accuracy of 92%.

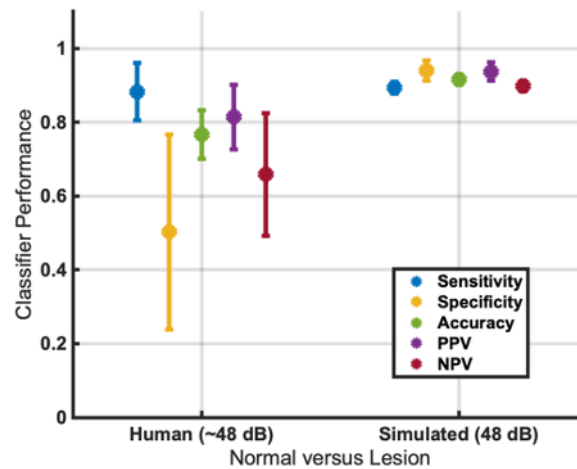


Figure 7.6: Classifier performance for normal (negative class) versus lesion (positive class) for human (~ 48 dB SNR), and simulated (48 dB SNR) data sets. A mean accuracy of 77% is seen for the human data, with a mean sensitivity of 88% and PPV of 81% indicating strong detection of lesion while the mean specificity (51%) and NPV (66%) indicative of a low rate of accurate detection of normal cases. In the case of the simulated results strong performance is indicated by an accuracy of 92% at the 48 dB SNR level.

7.4.2.2 Study 2: Bleed versus Clot

In this study, binary classification of bleed (negative class) versus clot (positive class) is considered. This scenario may be the most relevant to the clinical case where the patient is known to have a stroke and so the crucial diagnostic step is the identification of the lesion as a bleed or clot. The simulated data sets have an even number of bleed and clot cases with a total of 10,064 cases. The human data set is made up of the 180 bleed and 252 clots. The results are shown in Fig. 7.7. A mean accuracy of 85% is reported for the human data, with a mean sensitivity of 90% and PPV of 85% indicative of strong correct clot detection. Bleeds are slightly less well detected with a mean specificity of 77% and NPV of 86%. With regards to the simulated data set (48 dB SNR), all metrics have a mean of $\geq 99\%$

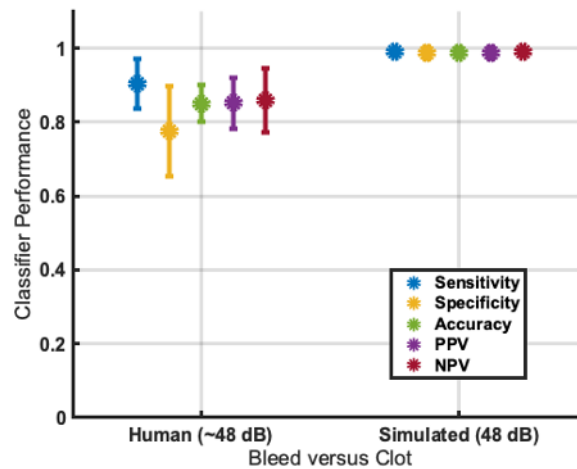


Figure 7.7: Classifier performance for bleed (negative class) versus clot (positive class) for human (~ 48 dB SNR) and simulated (48 dB SNR) data sets. A mean accuracy of 85% is seen for the human data, with clots strongly detected (mean sensitivity 90% and PPV 85%). Bleeds are slightly less well detected with a mean specificity (77%) and NPV (86%). The simulated results are strong at the 48 dB SNR level, with no metric with a mean less than 99%.

7.4.2.3 Study 3: Normal versus Bleed

The results for normal (negative class) versus bleed (positive class) are shown in Fig. 7.8. The simulated data sets have an even number of normal and bleed cases with a total of 10,064 cases. The human data set is made up of the 180 normal and 180 bleed cases. A mean specificity of 90% and NPV of 85%, with a mean sensitivity of 85% and PPV of 90% is reported for the human data (overall mean accuracy of 87%). In the simulated data, the mean accuracy of the 48 dB data set is also 87%. As well as being of value in the stroke diagnostic pathway, intracranial bleeds are an important feature in other conditions such as TBI (Chapter 4). Thus, a diagnostic modality that can robustly differentiate normal from bleed would be of significant value when applied to such cases.

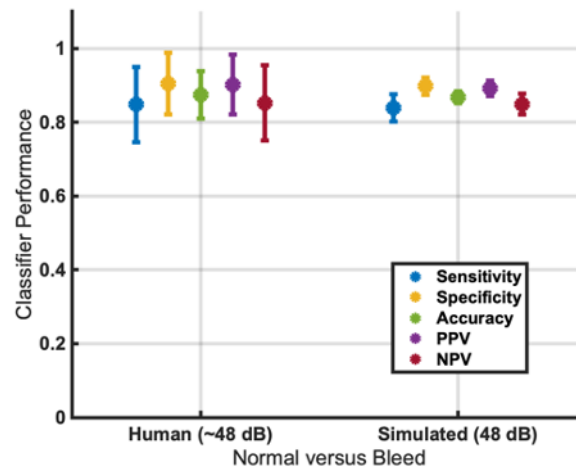


Figure 7.8: Classifier performance for normal (negative class) versus bleed (positive class) or human (~ 48 dB SNR), and simulated (48 dB SNR) data sets. The classifier performs with a mean accuracy of 87% in both the human and the simulated 48 dB SNR sets.

7.4.2.4 Study 4: Normal versus Clot

The results of the final binary classification combination of normal (negative class) versus bleed (positive class) are shown in Fig. 7.9. The human data set is made up of the 180 normal and 252 bleed cases, with the simulated data sets have 10,064 cases with equal numbers of both case types. In the simulated results, all metrics for the 48 dB SNR set are $\geq 91\%$. The human data set results have a mean accuracy of 74%, with the strongest result being a PPV of 79%.

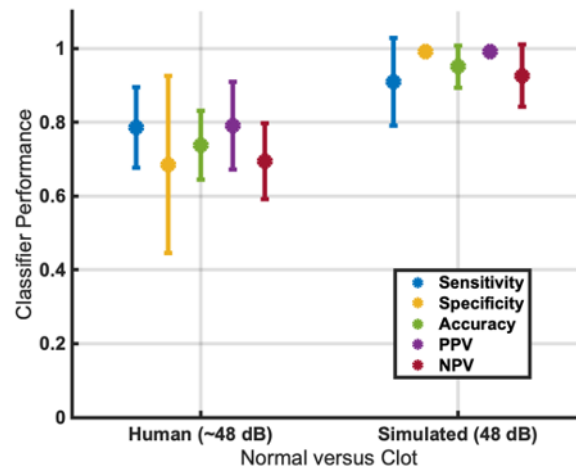


Figure 7.9: Classifier performance for normal (negative class) versus clot (positive class) for human (~ 48 dB SNR), and simulated (48 dB SNR) data sets. The classifier performs with a mean accuracy of 74% with the human data, with a mean accuracy of 95% in the simulated 48 dB SNR set.

7.4.2.5 Study 5: Multi-Class Classification

In this study, multiclass classification is performed with 6,290 each of normal, bleed, and clot cases (18,870 cases in total) in the simulated data sets (at 48 dB SNR level). The human data set is made of the 180 normal, 180 bleed, and 252 clot cases. The results are presented as confusion matrices of the average \pm standard deviation percentages of the classification results of the nested cross-validation in Tables 7.1 and 7.2. The mean overall accuracy of the classifier with the human data set is 68.0%, and for the simulated set is 90.1%. This discrepancy in results between the human and simulated data is speculated to be a result of sources of uncertainty and error in the human dataset, not present in the simulated dataset. This issue is discussed further in Section 7.5.1.

CHAPTER 7. MFSD-EIT WITH ML FOR HUMAN STROKE DIAGNOSIS

Table 7.1: Results as Confusion Matrices of Multiclass Classification for Human Data Set (~ 48 dB SNR). The results are the average \pm standard deviation over 10 iterations as percentages. The cells with bold text are correct classifications, with other cells incorrect. The cells on the rightmost column are the PPV results (dark blue), and the cells on the bottommost row are the sensitivity results (light blue). The cell in the bottom right is the overall classification accuracy (red).

Human Data Set							
Output Class		Target Class					
		Normal	Bleed	Clot			
		Normal	17.9 \pm 7.6	3.6 \pm 2.9		7.9 \pm 4.2	61.0 \pm 26.1
		Bleed	2.2 \pm 2.2	19.8 \pm 6.3		3.0 \pm 2.7	79.3 \pm 25.3
		Clot	9.3 \pm 7.4	6.1 \pm 5.5		30.3 \pm 5.6	66.3 \pm 12.9
60.9 \pm 26.0	67.2 \pm 21.5	68.4 \pm 13.3	68.0 \pm 19.9				

Table 7.2: Results as Confusion Matrices of Multiclass Classification for Simulated Data Set (48 dB SNR). The results are the average \pm standard deviation over 10 iterations as percentages. The cells with bold text are correct classifications, with other cells incorrect. The cells on the rightmost column are the PPV results (dark blue), and the cells on the bottommost row are the sensitivity results (light blue). The cell in the bottom right is the overall classification accuracy (red).

Simulated Data Set 48 dB SNR							
Output Class		Target Class					
		Normal	Bleed	Clot			
		Normal	29.7 \pm 1.6	4.4 \pm 1.0		1.5 \pm 1.1	83.4 \pm 4.5
		Bleed	3.3 \pm 0.9	28.6 \pm 1.5		0.1 \pm 0.2	89.3 \pm 4.8
		Clot	0.2 \pm 0.2	0.3 \pm 0.4		31.7 \pm 1.6	98.4 \pm 4.9
89.3 \pm 4.9	86.0 \pm 4.6	94.7 \pm 4.7	90.1 \pm 4.7				

7.4.2.6 Study 6: Effect of Centrally Lying Lesions

It is of interest to consider the effect of lesions lying on the sagittal plane on classifier performance. The use of such centrally lying lesions are not included in the datasets of the studies performed in the previous sections of this Chapter. As described in Chapters 5 and 6, an absolute limitation of the symmetry based algorithm is the inability to detect lesions lying perfectly on the plane of symmetry, since there is effectively no difference in the scene presented on either side of the plane. Simulated data sets at 48 dB noise levels are used to study the effect of centrally lying lesions using normal versus lesion and bleed versus clot binary classification problems. In both cases, an even number of each class are used with the number of cases the same as described in Sections 7.4.2.1 and 7.4.2.2. For the

data sets with no centrally lying lesions, the four locations and two volume sizes as described in Section 7.3.1 are used. For the data sets with centrally lying lesions, 20% of the cases have centrally lying lesions of the two volume sizes with the other 80% made of the non-centrally lying lesions. The results are shown in Fig. 7.10. In both cases considered, the results indicate a drop in classifier performance when central lesions are present in the data set. For example, the mean accuracy drops from 92% to 81% in the normal versus lesion case, with a drop from 99% to 88% in the bleed versus clot case.

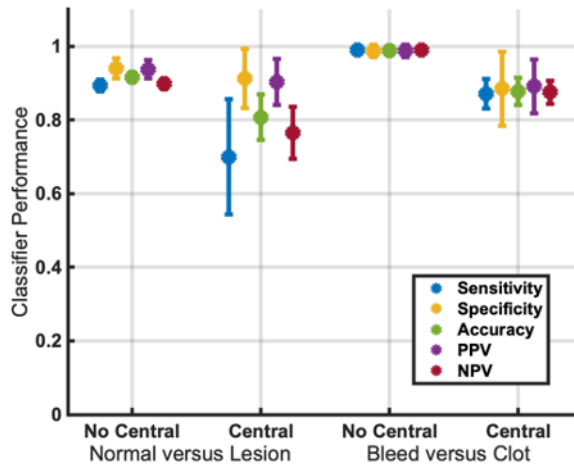


Figure 7.10: Central lying lesions effect on classifier performance for normal (negative class) versus lesion (positive class), and bleed (negative class) versus clot (positive class) for simulated (48 dB SNR) data sets. The classifier performance is consistently reduced in all metrics when centrally placed lesions are included in the data set compared to when absent.

7.4.2.7 Study 7: Effect of Noise on Classification Performance

In this work, the simulated data had noise added at a level of 48 dB SNR in order to match the SNR of the clinical data [13]. However, the simulations were also performed at noise levels of 80 dB and 20 dB in order to study the effect of noise. The mean accuracy from the simulated sets at each SNR level for each binary classification problem is shown in Table 7.3. Performance drops off at 20 dB compared to at 48 dB as expected, while the 80 dB level out performs the 48 dB. However, these results indicate only minor differences between the 48 dB and 80 dB sets, suggesting that perhaps 48 dB is adequate for accurate results if no other error sources are present.

Table 7.3: Results as Performance Accuracy reported as the average \pm standard deviation over 10 iterations as percentages for each Binary Classification Problem for the Simulated Data at 80 dB, 48 dB, and 20 dB SNR Noise Levels.

SNR Level		Binary Classification Problem							
		Normal Lesion	vs.	Bleed Clot	vs.	Normal Bleed	vs.	Normal Clot	vs.
	20 dB	67.2 \pm 3.1		74.4 \pm 5.3		76.7 \pm 2.3		60.6 \pm 3.5	
	48 dB	92.7 \pm 1.0		99.3 \pm 1.4		87.7 \pm 2.3		95.4 \pm 5.6	
	80 dB	93.8 \pm 0.0		99.4 \pm 4.1		90.8 \pm 3.7		99.5 \pm 2.3	

7.5 Multi-Frequency Symmetry Difference EIT with Machine Learning for Human Stroke Diagnosis Discussion

This section presents discussions of the classification results from the various scenarios considered in Section 7.4.2. These include binary classifications problems, a complete multiclass classification, and the effect of centrally lying lesions. A subsection considers some factors related to the UCL MF EIT stroke dataset which was the basis for the data generated in this chapter.

The binary classification problem of normal versus lesion was first examined in Section 7.4.2.1, with a lesion being a bleed or a clot. In the stroke diagnostic pathway, the initial diagnosis of stroke is not usually done using neuroimaging, relying instead on preliminary diagnostics that can be performed by the first responders including physical examination protocols such as ROSIER [54]. The results of these are used to label a patient as a potential stroke patient with neuroimaging subsequently performed [54]. Although initially thought to have a relatively high sensitivity and specificity (92% and 86% respectively), there is now evidence the specificity of these tests is possibly as low as 15% when performed by first responders [58]. As such there is value in a technology that could be replace such preliminary tests or be used in conjunction. The results seen in Fig. 7.6 show that with human data a mean accuracy of 77% was achieved for the classification of normal versus lesion (bleed or clot). Although the specificity (mean 51%) and NPV (66%) were lower than the sensitivity (mean 88%) and PPV (mean 81%), these former metrics show a significantly higher performance at identifying normal (negative) patients than the current preliminary diagnostics used. This encouraging result is supported by the results from the simulated data sets, where no metric is $<$ 89% when 48 dB SNR noise is added.

Next in Section 7.4.2.2, bleed versus clot was examined. Timely neuroimaging using CT or MRI is needed to differentiate between the lesion types before treatment for stroke can start [1]. It is this differentiation of lesion type that is the primary motivation of the work of this chapter. The fundamental idea being of MF-GMI data being capable of differentiating between bleed and clot as a result of differing conductivity profiles discussed in Section 7.2.3 and shown in Fig. 7.3. As shown in Fig. 7.7 the results are encouraging with the classifier performance on the human data set showing a mean accuracy of 85%, with a similar mean NPV and PPV values. While these results demonstrate significant promise on human data, there is evidence that further improvements are possible when the results of the simulated sets showing all metrics with mean values $\geq 99\%$ are considered.

The problem of normal versus bleed is analysed in Section 7.4.2.3. As discussed in Chapter 2, a related pathology to stroke is TBI, which may or may not feature intracranial haemorrhage. Initially physical examination protocols are used to triage a patient and decide on case severity with haemorrhage correlated with worse outcomes and a need to perform neuroimaging. The ability to rule in or out haemorrhage early in the triage process would result in better use of CT resources and patient outcomes and is another potential application for the presented algorithm. Although the conductivity of bleed does not change appreciably across the EIT band [12], [146], the presence of a bleed results in a significant change in the recorded EIT measurement frame and MF-GMI data compared to the normal case due to a disturbance in symmetry (Chapter 6). This change in MF-GMI should be distinguishable from the normal, as shown in (Section 6.4.2.1). Hence, the presence of a bleed should be detectable as a lesion from Step (1) as a result of the disturbance in symmetry, and further can be identified as a bleed in this case as no other lesion type is considered in this classification problem. However, the presence of asymmetric anatomy in the normal case can confound this detection as studied in Section 6.4.2.6. The results from the simulated and human data is shown in Fig. 7.8 with an overall accuracy of 87% in both cases.

The final binary classification problem of normal versus clot was considered in Section 7.4.2.4. Similar to the classification problem of bleed versus clot, normal versus clot is theoretically well suited to the MF-GMI approach due to the differing conductivity profile of clot across the band compared to no change for the normal case (Fig. 7.3). The results as shown in Fig. 7.9 confirm this with an accuracy of 74% reported for the human data, and all metrics $\geq 91\%$ for the simulated data at 48 dB. When considering the classifier performance results of the simulated data sets scenarios where there is a divergence in conductivity profiles across the

band between the two classes considered result in better classifier performance. For example, in the simulated data sets the mean accuracy is 95% for normal versus clot and 99% for bleed versus clot, compared to 92% for normal versus lesion and 87% for normal versus bleed.

The results from the simulated data shown in Fig. 7.8 when compared to the corresponding results in Fig. 7.9 (normal versus clot), imply challenge in classifying normal versus bleed compared to normal versus clot. The classifier results in Fig. 7.8 have a lower mean value compared to those in Fig. 7.9 for the simulated data. The classifier in the case of normal versus clot has the advantage of the change in conductivity featured by clot across the band. However, the results are still strong for normal versus bleed with mean accuracy of 87% for both the human and the simulated data sets. These results imply the MFSD-EIT with classification approach may indeed have application in areas such as TBI and build upon the work of Chapter 4 where ML was applied to EIT measurement frames in detecting intracranial haemorrhage. The lower accuracy in the human results for normal versus clot (74%) compared to normal versus bleed (87%) contradicts this expected trend. It is hypothesised that this discrepancy may be a result of the delay in ischaemic tissue becoming established after a stroke, as compared to a bleed which is instantaneously present may result in some ischaemic lesions being too alike the original 'normal' when EIT recordings.

A complete stroke diagnostic workup would comprise of classification as normal, haemorrhagic stroke, or ischaemic stroke. Currently, an initial detection is performed of normal versus lesion (not stroke or probable stroke), before neuroimaging is performed in the patients with a lesion to decide if the causative lesion is bleed or clot [54]. The multiclass results from Section 7.4.2.5 reported in Tables 7.1 and 7.2 give an indication as to the effectiveness of MFSD-EIT with SVM classification applied to such a one-step diagnosis. An overall accuracy of 68.0% is achieved with the human data, and 90.1% with the simulated data at 48 dB. Analysis of the confusion matrices show that in the simulated data set, the most common misclassification is normal as bleed and vice-versa. This misclassification is a consequence of the lack of contrast change in these tissues across the band. The change in conductivity of clot results in a consistently high performance as evidenced by sensitivity $> 94\%$, and PPV $> 98\%$.

Centrally lying lesions are considered in Section 7.4.2.6. Such lesions do not disturb the symmetry of the scene and so inclusion of such lesions in a data set should theoretically show worse performance compared to a set without. This prediction is confirmed by the results shown in Fig. 7.10, where a consistent

drop in performance is seen when the data sets that include the centrally lying lesions are included. While a causative stroke lesion can occur anywhere within the network of blood vessels in the brain, it is the case that vasculature is largely duplicated on either side of the sagittal plane with the major arteries serving the brain (middle, anterior and posterior cerebral arteries) all having left and right hand sides [27]. As such it would be unlikely for a stroke patient to have a sagittally positioned lesion (for example no lesion in the human data set was on the midline [13]) but such lesions would be challenging to detect with this technique.

A final study in Section 7.4.2.7 looked at the effect of noise on performance. As shown by the results in Table 7.3 although the accuracy at 80 dB is better than at 48 dB as expected, the performance is similar. These results suggest that while the higher SNR is desirable, perhaps stroke detection may be possible at lower SNR levels if other errors sources such as electrode placement are controlled.

7.5.1 UCL MF EIT Stroke Dataset - Other Remarks

The UCL MF EIT dataset is currently the most comprehensive collection of human stroke data available to researchers [13]. The dataset does however have some limitations.

The size of the dataset is relatively small, especially for use in machine learning applications where sets as large as possible are desirable and often numbering into the thousands (Chapter 4). The $N = 18$ neuroimaging studies were used to form 18 unique coarse FEM models for reconstruction. The $N = 10$ healthy, $N = 10$ haemorrhagic, and $N = 14$ ischaemic human EIT measurement frames were then reconstructed onto each model to give $N = 180$ normal, $N = 180$, and $N = 252$ sets of MF-GMI data. While this approach increased the data by a factor of 18, it remains a relatively modest number of observations.

Further, the data is biased in terms of classes with more cases of ischaemia than normal or bleed. Such imbalances in data can skew the performance results in classification. In this study, the simulated data sets were kept balanced in terms of numbers of observations from each class but all the human MF GMI data was used due to the limited pool available. Metrics such as accuracy, PPV and NPV are sensitive to imbalanced data, while sensitivity and specificity are not [288], [289]. Further, the dataset provides information on the location and nature of the lesions, but not precise information on size beyond qualitative terms such as ‘small’, and ‘large’. Although imaging is provided, interpretation of the images can be challenging. There are however examples of small and large lesions of both types in the set.

The work of Section 6.4 presented an analysis of the effect of error sources on the quality of GMI data. These errors included measurement frame noise, electrode contact impedance errors, and electrode positioning errors. While care was taken to maximise the quality of the protocol and data recorded, inevitably these sources of error are present in the human data and have an effect on the collected measurement frames. Of particular interest is electrode positioning errors where differences greater than ± 5 mm in the assumed location of electrodes can severely affect the GMI data (Section 6.4). The actual locations of electrodes are not reported in the dataset, and when placing electrodes on patients, placement error in the order of ± 5 mm is likely.

Other sources of uncertainty also exist in the dataset. For example, the delay from stroke onset to EIT recording ranged from hours to days while neuroimaging was performed at different timepoints which could lead to errors in data interpretation. Further, measurement noise is present in all recordings, with an average SNR of 48 dB across the frequency band despite the use of the ScouseTom which has a theoretical rating of 77.5 dB [13], [15]. The higher SNR was achieved when in use with a resistor phantom, highlighting the challenge in moving from ideal phantom models to human [15].

These limitations must be kept in consideration when considering the results of the study particularly with respect to the human data. Further, these limitations may explain the discrepancy in performance between the results from the human and simulated data sets. In the simulated cases while noise at a level of 48 dB SNR was added to the frames, no other modelling errors were present (for example electrode positioning).

7.6 Conclusions

This chapter reported on work applying the novel MFSD-EIT algorithm to both human and simulated stroke data for the first time. The important GMI metric summarises symmetrical differences on either side of the brain, with analysis of the GMI across multiple frequencies allowing the detection and identification of normal, haemorrhagic and clot cases. This principle is used for the first time with ML techniques used to achieve classification of normal, haemorrhagic and clot cases.

Firstly in Section 7.2 the UCL stroke data set is presented. While this is the most complete collection of human stroke EIT data available, limitations exist. These limitations include the small size of the set and possible errors in important parameters such as electrode positioning affecting achievement of accurate MF-GMI

data. Next the MFSD-EIT algorithm, and the MF-GMI metric are described which are an extension of the BFS-D-EIT algorithm and GMI metric respectively from 6. The rationale for application to stroke, and theoretical ideal results for the no lesion (normal), bleed and clot cases are then shown which leverage the differing conductivity profiles of the tissues across a frequency range.

Next in Section 7.3 the FEM models created from the UCL stroke data set are described, as well as the generation of MF-GMI data from these models. Both simulated data from these anatomically accurate models, and the human EIT data are used in subsequent sections.

In Section 7.4 the precise classification protocol which uses a robust nested cross-validation approach to generate trained RBF kernel SVM classifiers with the MF-GMI data as input features is described. Next a range of binary classification problems are considered. In the binary classification problems, better classification results are generally seen when the tissues under investigation differ in the pattern of conductivity change across the frequency band. Importantly this divergence in conductivity pattern is the case for bleed versus clot, with differentiation of these lesion types in stroke the main application proposed in this work. Strong results are also reported for more challenging clinically important classification problems such as normal versus bleed, and bleed versus clot. A mean accuracy of 87% and 85% are respectively reported for the human data in these cases. A complete one-step diagnostic modality for stroke is also considered as a multiclass classification of normal versus bleed versus clot. Here, classification had a mean accuracy of 68% with the human data.

As discussed limitations exist in the human data. These limitations are all issues that can be improved upon with future work, with indications from the simulated data that improvements in human data would result in better performance. In simulated datasets, mean accuracy is always $\geq 87\%$ for the measurements with 48 dB SNR, and $\geq 90\%$ for measurements with an 80 dB SNR noise level.

Hence there is ample evidence in the results presented that the proposed approach of using MFSD-EIT with ML algorithms is an exciting and promising approach to diagnosing human stroke and other related applications.

Conclusions

This chapter summarises the research objectives, experimental methods and results of this thesis. The motivation and main findings of this thesis are summarised in Section 8.1. Appropriate future work to further develop and extend the findings of this thesis are presented in Section 8.2 which concludes this thesis.

8.1 Summary and Conclusions

Important medical conditions such as stroke and TBI feature causative lesions which are essentially static in nature [1]. In the case of stroke, the sudden loss of neurological function due to an interruption in blood flow is the result of either a bleed (haemorrhagic stroke) or a clot (ischaemic stroke) [1]. An essential part of the work-up in stroke is the timely differentiation of the patient as a haemorrhagic or ischaemic stroke case in order to facilitate appropriate treatment which is highly divergent depending on the cause [1]. There is a need for rapid and definitive aetiology diagnosis in all stroke patients [13]. Currently the gold standard for diagnosis of stroke type is CT and MRI scans. However, challenges with availability of CT and MRI result in delayed imaging and treatment rates as low as 4% [13]. The example of stroke diagnosis in particular highlights the urgent need for a technology that can rapidly differentiate between the two causative lesion types and facilitate early initiation of correct treatment.

EIT may represent such a technology. EIT is a low-cost, portable and safe imaging technology which generates profiles of the electrical conductivity of the interior of a body of interest through the use of electrodes placed on the surface [6], [7], [10]. When applied to biomedical scenarios, EIT has to date enjoyed most success when used in areas featuring a time change [10]. Such applications allow the use of time differencing of the measurement frames and a cancellation of errors to which EIT is highly sensitive [7], [10], [19], [180]. However, in static scenes such as in stroke, time differencing is not possible and alternate techniques are required. Further challenges exist specifically in regards applying EIT to stroke including the attenuation of current due to the highly resistive skull, the shunting effect of the highly conductive CSF layer inside the skull, and the safety limitations on the

amplitude of current that can be used (for example a maximum current of 100 μA root mean square for frequencies up to 1 kHz) [6], [11]. As such, the effective application of EIT to static scenes is challenging. However, it is an area where development and innovation is needed. The work presented in this thesis represents progress towards achieving this innovation.

Chapter 1 introduces the motivation for this thesis, and presents the overarching clinical need for an efficient, robust, cost effective, sensitive and specific device for the detection and identification of brain lesions. EIT may have the potential to meet this need. Therefore the main contributions of this thesis are the provision of novel phantom test platforms for use in EIT, and the development of a novel algorithm and EIT modality designed to detect and identify static lesions.

Chapter 2 presents a comprehensive background of the normal and then abnormal anatomy and physiology involved in conditions with brain bleeds and clots. A comprehensive analysis of the patient pathways are presented for stroke and TBI, before a consideration of the requirements for a technology that meets the clinical need is discussed. Candidate technologies are then outlined. Finally EIT is selected from these candidates as a technology that shows significant promise. The technology of EIT is then comprehensively described.

Chapter 3 describes the development of a novel solid TMM for use in the fabrication of EIT test platforms. These TMMs were found to have accurate conductivity profiles across the frequency range of interest in EIT, and could be tailored to emulate tissue or tissue aggregates. Head phantoms were developed from this TMM, with phantom lesions also fabricated. These formed the basis of reconfigurable test platforms that could be incorporated into EIT experimental setups and used to generate data. Further, a pilot investigation into the use of 3D-printing as a way to further improve on the fabrication of solid phantoms was explored. The work of Chapter 3 helped address a primary objective of this thesis which was to develop a test platform for better acquisition of real world EIT data. These platforms were used in subsequent chapters, particularly Chapters 4 and 5.

Chapter 4 investigates the use of electrical impedance measurement frames used as inputs to ML classification algorithms. The frames are used without image reconstruction removing a challenging part of the usual EIT workflow. A series of numerical and phantom studies are presented investigating the use of a SVM classifier based approach to predict the presence or absence of a brain haemorrhage. The phantom studies are performed with the test platforms developed in Chapter 3. The results suggest this approach shows promise with better detection achieved

at higher SNR, better detection with lesions equal to or larger than those trained with, the possibility of eliciting information on the location and size from the frames, and robustness to small changes in electrode positioning. Challenges are seen with smaller lesions, and particularly unseen anatomies. Improvements in the performance of classifiers are further demonstrated through the use of non-linear SVM kernels, and the possibility of using intelligent pre-processing of frames to reduce dimensionality without a drop in performance. Since perfect classification is unrealistic, the use of trade-offs in sensitivity and specificity is also demonstrated.

Chapter 5 presents a second novel approach to static lesion detection using EIT. In this chapter, sdEIT is introduced which compares EIT measurement frames from symmetrically opposite orientations. In the case of the brain and head, the sagittal plane represents a natural plane of symmetry. sdEIT is shown in Chapter 5 to be capable of lesion detection and identification in cases where the presence of a lesion causes a disturbance in the symmetry across across the sagittal plane. A series of numerical and phantom studies are performed demonstrating better performance for lesions nearer the exterior, larger lesions, lesions of higher contrast, and setups with a high SNR. An area of challenge in sdEIT is the use of a simulated model of the normal which must be generated with a high level of accuracy for successful use of the algorithm.

Chapter 6 extends and iterates on sdEIT, resulting in the BFS-D-EIT algorithm. This algorithm removes the need for a simulated normal by comparing EIT measurement frames from symmetrically opposite orientations at two distinct frequencies. A complete feasibility study of the use of BFS-D-EIT in lesion detection and identification in stroke is then presented. This feasibility study examined the limits of use of BFS-D-EIT when presented with errors in test parameters such as electrode positioning and assumed anatomy that usually challenge EIT. The result is a defining of limits in these test parameters that is tolerated with BFS-D-EIT. Also the GMI quantitative metric is defined which is particularly robust to modelling errors. Finally, a successful application of BFS-D-EIT to human stroke data was performed for the first time.

Finally Chapter 7 consolidates the approaches presented in Chapter 4, and Chapters 5 and 6. In Chapter 7, MFSD-EIT extends the number of frequency points used, and extends the GMI metric over these frequency points as MF-GMI. This MF-GMI is used as input into ML classification algorithms and the performance in a range of binary classification cases of normal, bleed, and clot is studied as well as in the use of multi-class classification. Significantly these tests are performed both with simulated and human stroke data. The promise of this approach combining

MFSD-EIT with ML is seen by a mean classification accuracy of 87% and 85% for normal versus bleed, and bleed versus clot in the human stroke data. This work in this thesis thus represents the first time EIT has been successfully used to detect and identify brain lesions using real human data.

8.2 Future Work

This thesis sought to advance the application of EIT to static brain lesion detection and identification. Two areas in particular were focussed on for improvement as discussed in Chapters 1 and 2:

- The design of a better test platform for real world data acquisition;
- The development of a novel algorithm and modality for the detection and identification of static lesions.

The work in Chapter 3 sought to address the first area of test platform development and data acquisition. The solid TMMs and associated phantoms described in that chapter were successfully used in Chapters 4 and 5 to record data as part of a series of phantom studies. However, improvements in both the materials used and the fabrication process could be achieved in the future. In particular high percentages of graphite (30 to 45 %) and CB (3.5 to 5.7 %) were needed to cover the biological range with the TMMs. The higher percentages also led to challenges in mixing and ensuring of homogeneity. The ranges used were also relatively narrow leading to sensitivity in conductivity profiles. The work of Section 3.4 was a proof of concept study seeking to achieve such improvements through the use of 3D-printing. The use of a novel base composite mixture of ABS and SEBS, and a highly conductive grade of CB was found to cover the biological range with lower concentrations of CB required (5 to 11 %). Further the use of a twin screw co-axial extruder ensured homogenous mixing and the use of a 3D printer facilitated accurate fabrication. The exploratory study in Section 3.4 is an area of significant promise for future work. The use of 3D-printing in the development of phantoms is a relatively unexplored area. Phantoms based on 3D printed materials exist but primarily as a container for liquid based TMMs [290]. The relative lack of phantoms based on solid TMMs is in part due to issues such as complexity of fabrication [208]. Innovation and research into the areas of base composite design, use of conductive filler, and machinery for filament production may result in an increase in the ease of production of phantoms aided by the continuous development in 3D-printing technology.

The use of ML techniques in Chapter 4, and the development of the symmetry based algorithms in Chapters 5 and 6 represent important steps forward in the translation of EIT for use in static brain lesion detection and identification.

Ultimately the final approach used in Chapter 7 combined the novel symmetry based approach developed in Chapters 5 and 6 with the ML techniques from Chapter 4. However improvements are possible in the constituent parts of the algorithm. In terms of the symmetry based approach, improvements are possible in the frequencies used, measurement protocols adopted, and the data analysis performed.

In Chapter 7 the frequencies used were selected based on frequency bands where the pattern of conductivity change in bleed and clot were most divergent within the EIT band. Work on better characterisation of the conductivity of these tissues of interest within this frequency band (≤ 100 Hz) would improve the accuracy of computational and phantom models before moving to human data. The conductivity values used come from the work of Packham *et al.* [12], Horesh *et al.* [16], and the IT'IS database [148]. However as noted in Section 2.4.2, significant variance and uncertainty exists in such conductivity values reported in the literature. These uncertainties are worse at the frequencies of interest in EIT [153]. Hence improved dielectric characterisation of the tissues of the head at EIT frequencies would help refine the frequencies used in MFSD-EIT as well as improve the accuracy of computational and phantom models.

In terms of injection/ measurement protocols, the work of Chapters 6 and 7 adopted a protocol that maximised the distance between electrode pairs while also achieving the maximum number of independent measurements. This protocol was based on the work of Malone *et al.* [20]. In contrast, Skip Protocols are commonly used in other biomedical applications of EIT [10]. Indeed different types and quality of information is derived depending on the injection/ measurement protocol used in an EIT study [157], [291]. For example adjacent measurement patterns tend to be less sensitive to targets in the interior, while opposite measurement patterns tend to have a reduction in independent measurements [157]. An investigation as to what injection/ measurement protocol is optimum for the combined MFSD-EIT and ML approach was not considered in this thesis. Such a study has considerable merit and would be an area of interest in the future.

In this thesis and particularly in Chapters 6 and 7 a number of quantitative metrics were derived which sought to robustly summarise the output of the symmetry based algorithm. Ultimately the GMI metric and the related MF-GMI metric were found to be the most robust to errors while still identifying and detecting the presence of lesions. Further, these metrics were suitable for use as inputs to ML classification algorithms. Future work could study other quantitative metrics that exceed the performance of GMI related metrics.

With regards the use of ML techniques, the work of Chapter 4 analysed the effect of discrete parameters on classifier performance, choice of classifier, and intelligent pre-processing of classifier input. Each of these are areas with scope for future investigation and study. For example a study dedicated to classifier choice and optimisation should also be undertaken, and may lead to further performance improvements. A future study may look at the use of such classifiers in a cascade, with the aggregate result perhaps being of value. Many other pre-processing possibilities exist for investigation such as filtering to reduce noise, weighting of data from select channels, and so on.

Future work will also need to consider better numerical and phantom platforms in terms of realism, complexity of test scenarios and hardware. An example of an area that could be explored for test scenarios is a Monte Carlo simulation varying lesion location and size extending the simulation studies performed in Chapters 4 and 7. Finally, successful translation of a technology ultimately needs to move from computational and phantom models to humans. Hence, there is a need for future work to gather more EIT data from patients. The UCL human data set is a valuable resource for researchers. However the limitations associated with this data set as described in Section 7.5.1 outline important areas that could be improved in future work. For example the small size of the data set, and the imbalance of bleed and clot patient data are aspects that could be extended upon. The work presented in Section 6.4 has helped define boundaries on the tolerance of BFS-D-EIT and by extension MFSD-EIT to a variety of errors. These errors included measurement frame noise, electrode contact impedance errors, and electrode positioning errors. Care in minimising these error sources could be considered in future human data collection studies. Additional techniques could also be used to help minimise these errors. For example, errors in electrode placement were found to have to be within ± 5 mm for strong GMI data. As discussed in Section 6.4.3 this tolerance is an order of magnitude above that achieved in [20] but could be improved upon using a variety of techniques including the use of specialised hats for electrode placement, image guidance technology [277], electrode placement algorithms [278], and quickly generated computational models of patients' anatomies [279].

EIT is already a valuable technology in some biomedical applications. The work in this thesis has shown that EIT has significant potential to be a valuable diagnostic aid even in challenging scenarios such as static brain lesion detection and identification. Future work can and should further drive successful clinical translation, moving EIT from being a promising technology to a truly lifesaving technology.

Bibliography

- [1] G. A. Donnan, M. Fisher, M. Macleod, *et al.*, “Stroke,” *The Lancet*, vol. 371, no. 9624, pp. 1612–1623, May 2008.
- [2] B. Lee and A. Newberg, “Neuroimaging in traumatic brain imaging,” *NeuroRX*, vol. 2, no. 2, pp. 372–383, Apr. 2005.
- [3] NICE (National Institute for Health and Care Excellence). (2016). “Acute stroke,” nice.org.uk, [Online]. Available: <http://pathways.nice.org.uk/pathways/stroke/acute-stroke> (visited on 10/19/2016).
- [4] —, (2016). “Investigation for clinically important brain injuries in patients with head injury,” nice.org.uk, [Online]. Available: <https://pathways.nice.org.uk/pathways/head-injury#path=view%3A/pathways/head-injury/investigation-for-clinically-important-brain-injuries-in-patients-with-head-injury.xml&content=view-index> (visited on 10/19/2016).
- [5] T. Dowrick, C. Blochet, and D. Holder, “*In vivo* bioimpedance measurement of healthy and ischaemic rat brain: Implications for stroke imaging using electrical impedance tomography,” *Physiological Measurement*, vol. 36, no. 6, pp. 1273–1282, Jun. 1, 2015.
- [6] D. Holder, Ed., *Electrical impedance tomography: methods, history, and applications*, Series in medical physics and biomedical engineering, Bristol; Philadelphia: Institute of Physics Pub, 2005, 456 pp.
- [7] B. Brown, “Electrical impedance tomography (EIT): A review,” *Journal of Medical Engineering & Technology*, vol. 27, no. 3, pp. 97–108, Jan. 2003.
- [8] A. Adler, B. Grychtol, and R. Bayford, “Why is EIT so hard, and what are we doing about it?” *Physiological Measurement*, vol. 36, no. 6, pp. 1067–1073, Jun. 1, 2015.
- [9] I. Frerichs, M. B. P. Amato, A. H. van Kaam, *et al.*, “Chest electrical impedance tomography examination, data analysis, terminology, clinical use and recommendations: Consensus statement of the TRanslational EIT developmeNt stuDY group,” *Thorax*, vol. 72, no. 1, pp. 83–93, Jan. 2017.

BIBLIOGRAPHY

- [10] A. Adler and A. Boyle, “Electrical impedance tomography: Tissue properties to image measures,” *IEEE Transactions on Biomedical Engineering*, vol. 64, no. 11, pp. 2494–2504, Nov. 2017.
- [11] International Organization for Standardization, *International electrotechnical commission. medical electrical equipment: Part 1: General requirements for basic safety and essential performance*. Geneva, Switzerland, 2002.
- [12] B. Packham, H. Koo, A. Romsauerova, *et al.*, “Comparison of frequency difference reconstruction algorithms for the detection of acute stroke using EIT in a realistic head-shaped tank,” *Physiological Measurement*, vol. 33, no. 5, pp. 767–786, May 1, 2012.
- [13] N. Goren, J. Avery, T. Dowrick, *et al.*, “Multi-frequency electrical impedance tomography and neuroimaging data in stroke patients,” *Scientific Data*, vol. 5, no. 180112, pp. 1–10, Jul. 3, 2018.
- [14] W. Hun, H. Sohal, A. L. McEwan, *et al.*, “Multi-frequency electrical impedance tomography system with automatic self-calibration for long-term monitoring,” *IEEE Transactions on Biomedical Circuits and Systems*, vol. 8, no. 1, pp. 119–128, Feb. 2014.
- [15] J. Avery, T. Dowrick, M. Faulkner, *et al.*, “A versatile and reproducible multi-frequency electrical impedance tomography system,” *Sensors*, vol. 17, no. 280, pp. 1–20, Jan. 2017.
- [16] L. Horesh, O. Gilad, A. Romsauerova, *et al.*, “Stroke type differentiation by multi-frequency electrical impedance tomography - a feasibility study,” in *Proc IFMBE*, vol. 11, 2005, pp. 1252–1256.
- [17] E. Malone, G. S. dos Santos, D. Holder, *et al.*, “Multifrequency electrical impedance tomography using spectral constraints,” *IEEE Transactions on Medical Imaging*, vol. 33, no. 2, pp. 340–350, Feb. 2014.
- [18] S. Ahn, T. I. Oh, S. C. Jun, *et al.*, “Validation of weighted frequency-difference EIT using a three-dimensional hemisphere model and phantom,” *Physiological Measurement*, vol. 32, no. 10, pp. 1663–1680, Oct. 1, 2011.
- [19] E. Malone, G. S. dos Santos, D. Holder, *et al.*, “A reconstruction-classification method for multifrequency electrical impedance tomography,” *IEEE Transactions on Medical Imaging*, vol. 34, no. 7, pp. 1486–1497, Jul. 2015.
- [20] E. Malone, M. Jehl, S. Arridge, *et al.*, “Stroke type differentiation using spectrally constrained multifrequency EIT: Evaluation of feasibility in a realistic head model,” *Physiological Measurement*, vol. 35, no. 6, pp. 1051–1066, Jun. 1, 2014.

BIBLIOGRAPHY

- [21] M. Persson, A. Fhager, H. D. Trefna, *et al.*, “Microwave-based stroke diagnosis making global prehospital thrombolytic treatment possible,” *IEEE Transactions on Biomedical Engineering*, vol. 61, no. 11, pp. 2806–2817, Nov. 2014.
- [22] M. F. Jehl, “A novel framework for head imaging with electrical impedance tomography,” Ph.D. dissertation, University College London, Feb. 2016, 166 pp.
- [23] P. Yock, “Needs-based innovation: The biodesign process,” *BMJ Innovations*, vol. 1, no. 1, pp. 3–3, 2014.
- [24] P. Yock, S. Zenios, J. Makower, *et al.*, *Biodesign: The Process of Innovating Medical Technologies*. Cambridge: Cambridge University Press, 2010, 806 pp.
- [25] J. Valentin, “Basic anatomical and physiological data for use in radiological protection: Reference values: ICRP publication 89: Approved by the commission in september 2001,” *Annals of the ICRP*, vol. 32, no. 3, pp. 1–277, 2002.
- [26] T. Hines. (2016). “The anatomy of the brain,” Mayfield Brain & Spine, [Online]. Available: <https://www.mayfieldclinic.com/PE-AnatBrain.htm> (visited on 10/20/2016).
- [27] S. Standring, N. Ananad, and H. Gray, Eds., *Gray’s anatomy: the anatomical basis of clinical practice*, 41. ed, OCLC: 935913598, Philadelphia, Pa.: Elsevier, 2016, 1562 pp.
- [28] Edoarado. (2012). “Cranial bones,” Wikimedia Commons, [Online]. Available: https://commons.wikimedia.org/wiki/File:Cranial_bones_en.svg (visited on 08/10/2020).
- [29] E. Widmaier, H. Raff, and K. Strang, *Vander’s Human Physiology*, 14th. McGraw-Hill Education, 2016, 784 pp.
- [30] D. Slater. (2016). “Middle cerebral artery stroke,” Medscape, [Online]. Available: <http://emedicine.medscape.com/article/323120-overview> (visited on 10/20/2016).
- [31] A. Wessmann, K. Chandler, and L. Garosi, “Ischaemic and haemorrhagic stroke in the dog,” *The Veterinary Journal*, vol. 180, no. 3, pp. 290–303, 2009.
- [32] V. Velayudhan. (2018). “Stroke imaging: Overview, computed tomography, magnetic resonance imaging,” Medscape, [Online]. Available: <http://emedicine.medscape.com/article/338385-overview> (visited on 10/19/2016).

BIBLIOGRAPHY

- [33] S. B. Coutts, “Diagnosis and management of transient ischemic attack,” *CONTINUUM: Lifelong Learning in Neurology*, vol. 23, no. 1, pp. 82–92, Feb. 2017.
- [34] NICE (National Institute for Health and Care Excellence). (2016). “Transient ischaemic attack,” nice.org.uk, [Online]. Available: <https://pathways.nice.org.uk/pathways/stroke#path=view:/pathways/stroke/transient-ischaemic-attack.xml&content=view-index> (visited on 10/19/2016).
- [35] —, (2020). “NICE pathways,” nice.org.uk, [Online]. Available: <https://pathways.nice.org.uk/> (visited on 03/20/2020).
- [36] IHF (Irish Heart Foundation), “Irish national audit of stroke care (INASC),” Apr. 2008.
- [37] O. Saka, A. McGuire, and C. Wolfe, “Cost of stroke in the united kingdom,” *Age and Ageing*, vol. 38, no. 1, pp. 27–32, Nov. 13, 2008.
- [38] ESRI (Economic and Social Research Institute) and RCSI (Royal College of Surgeons in Ireland), “Cost of stroke in ireland (COSI): Estimating the annual economic cost of stroke and TIA in ireland,” Sep. 2010.
- [39] electronic Medicines Compendium. (2018). “SPC actilyse,” [Online]. Available: <https://www.medicines.org.uk/emc/medicine/308> (visited on 12/27/2018).
- [40] L. Lisabeth and C. Bushnell, “Stroke risk in women: The role of menopause and hormone therapy,” *The Lancet Neurology*, vol. 11, no. 1, pp. 82–91, Jan. 2012.
- [41] P. Appelros, B. Stegmayr, and A. Terent, “Sex differences in stroke epidemiology: A systematic review,” *Stroke*, vol. 40, no. 4, pp. 1082–1090, 2009.
- [42] D. Liebeskind. (2016). “Hemorrhagic stroke,” Medscape, [Online]. Available: <http://emedicine.medscape.com/article/1916662-overview> (visited on 10/19/2016).
- [43] J. Gomes and A. M. Wachsman, “Types of strokes,” in *Handbook of Clinical Nutrition and Stroke*, M. L. Corrigan, A. A. Escuro, and D. F. Kirby, Eds., Totowa, NJ: Humana Press, 2013, pp. 15–31.
- [44] R. Domingues, C. Rossi, and C. Cordonnier, “Classification of intracerebral haemorrhages,” *European Neurological Review*, vol. 9, no. 2, pp. 129–135, 2014.

BIBLIOGRAPHY

- [45] E. Auriel, M. E. Gurol, A. Ayres, *et al.*, “Characteristic distributions of intracerebral hemorrhage-associated diffusion-weighted lesions,” *Neurology*, vol. 79, no. 24, pp. 2335–2341, 2012.
- [46] J. C. Hemphill, D. C. Bonovich, L. Besmertis, *et al.*, “The ICH score: A simple, reliable grading scale for intracerebral hemorrhage editorial comment: A simple, reliable grading scale for intracerebral hemorrhage,” *Stroke*, vol. 32, no. 4, pp. 891–897, Apr. 2001.
- [47] J. B. Fiebach, P. D. Schellinger, A. Gass, *et al.*, “Stroke magnetic resonance imaging is accurate in hyperacute intracerebral hemorrhage: A multicenter study on the validity of stroke imaging,” *Stroke*, vol. 35, no. 2, pp. 502–506, 2004.
- [48] F. M. Siddiqui, S. V. Bekker, and A. I. Qureshi, “Neuroimaging of hemorrhage and vascular defects,” *Neurotherapeutics*, vol. 8, no. 1, pp. 28–38, 2011.
- [49] E. Jauch. (2017). “Ischemic stroke,” Medscape, [Online]. Available: <http://emedicine.medscape.com/article/1916852-overview> (visited on 10/01/2017).
- [50] J. Zhang, Y. Yang, H. Sun, *et al.*, “Hemorrhagic transformation after cerebral infarction: Current concepts and challenges,” *Annals of Translational Medicine*, vol. 2, no. 8, pp. 1–7, Aug. 2014.
- [51] American Stroke Association. (2017). “TIA (transient ischemic attack),” www.strokeassociation.org/STROKEORG/AboutStroke/TypesofStroke/TIA/%20TIA-Transient-Ischemic-Attack_UCM_310942_Article.jsp#.WBxRMuGLR0c (visited on 05/01/2017).
- [52] J. S. Balami, R. L. Chen, and A. M. Buchan, “Stroke syndromes and clinical management,” *QJM*, vol. 106, no. 7, pp. 607–615, Jul. 1, 2013.
- [53] A. M. Nor, J. Davis, B. Sen, *et al.*, “The recognition of stroke in the emergency room (ROSIER) scale: Development and validation of a stroke recognition instrument,” *Lancet Neurology*, vol. 4, no. 11, pp. 727–734, 2005.
- [54] NICE (National Institute for Health and Care Excellence). (2016). “Stroke overview,” [nice.org.uk, \[Online\]. Available: https://pathways.nice.org.uk/pathways/stroke](https://pathways.nice.org.uk/pathways/stroke) (visited on 10/19/2016).
- [55] D. Flynn, G. A. Ford, H. Rodgers, *et al.*, “A time series evaluation of the FAST national stroke awareness campaign in England,” *PLoS ONE*, vol. 9, no. 8, C. M. Schooling, Ed., e104289–e104289, Aug. 2014.

BIBLIOGRAPHY

- [56] L. Mellon, F. Doyle, D. Rohde, *et al.*, “Stroke warning campaigns: Delivering better patient outcomes? a systematic review,” *Patient Related Outcome Measures*, vol. 6, pp. 61–61, Feb. 2015.
- [57] H. L. Jiang, C. P. Y. Chan, Y. K. Leung, *et al.*, “Evaluation of the recognition of stroke in the emergency room (ROSIER) scale in chinese patients in hong kong,” *PLoS ONE*, vol. 9, no. 10, pp. 1–7, 2014.
- [58] R. T. Fothergill, J. Williams, M. J. Edwards, *et al.*, “Does use of the recognition of stroke in the emergency room stroke assessment tool enhance stroke recognition by ambulance clinicians?” *Stroke*, vol. 44, no. 11, pp. 3007–3012, 2013.
- [59] V. Nadarajan, R. J. Perry, J. Johnson, *et al.*, “Transient ischaemic attacks: Mimics and chameleons.” *Practical neurology*, vol. 14, no. 1, pp. 23–31, 2014.
- [60] National Stroke Association. (2016). “Transient ischemic attack (TIA) - ABCD2 score,” [Online]. Available: <https://www.stroke.org/sites/default/files/resources/tia-abcd2-tool.pdf>.
- [61] S. Kumar, M. Selim, S. Marchina, *et al.*, “Transient neurological symptoms in patients with intracerebral hemorrhage,” *JAMA Neurology*, vol. 73, no. 3, pp. 316–320, Mar. 2016.
- [62] D. Birenbaum, L. W. Bancroft, and G. J. Felsberg, “Imaging in acute stroke,” *The Western Journal of Emergency Medicine*, vol. 12, no. 1, pp. 67–76, Feb. 2011.
- [63] J. J. Perry, I. G. Stiell, M. L. A. Sivilotti, *et al.*, “Sensitivity of computed tomography performed within six hours of onset of headache for diagnosis of subarachnoid haemorrhage: Prospective cohort study,” *BMJ*, vol. 343, no. d4277, pp. 1–10, 2011.
- [64] N. M. Dubosh, M. F. Bellolio, A. A. Rabinstein, *et al.*, “Sensitivity of early brain computed tomography to exclude aneurysmal subarachnoid hemorrhage: A systematic review and meta-analysis,” *Stroke*, vol. 47, no. 3, pp. 750–755, 2016.
- [65] D. J. Miller, J. R. Simpson, and B. Silver, “Safety of thrombolysis in acute ischemic stroke: A review of complications, risk factors, and newer technologies,” *The Neurohospitalist*, vol. 1, no. 3, pp. 138–147, Jul. 2011.
- [66] (Jul. 2009). “Brain CT scan,” Wikimedia Commons, [Online]. Available: https://en.wikipedia.org/wiki/File:Brain_CT_scan.jpg.
- [67] (May 2013). “The hemorrhagic stroke,” Wikimedia Commons, [Online]. Available: https://commons.wikimedia.org/wiki/File:1602_The_Hemorrhagic_Stroke-02.jpg.

BIBLIOGRAPHY

- [68] (Feb. 2017). “CT brain MCA infarct,” Wikimedia Commons, [Online]. Available: https://commons.wikimedia.org/wiki/File:CT_Brain_MCA_Infarct.jpg.
- [69] J. A. Chalela, C. S. Kidwell, L. M. Nentwich, *et al.*, “Magnetic resonance imaging and computed tomography in emergency assessment of patients with suspected acute stroke: A prospective comparison,” *The Lancet*, vol. 369, no. 9558, pp. 293–298, Jan. 2007.
- [70] G. B. Chavhan, P. S. Babyn, B. Thomas, *et al.*, “Principles, techniques, and applications of t2*-based MR imaging and its special applications,” *RadioGraphics*, vol. 29, no. 5, pp. 1433–1449, Sep. 2009.
- [71] H.-S. Song, J.-H. Back, D.-K. Jin, *et al.*, “Cardiac troponin t elevation after stroke: Relationships between elevated serum troponin t, stroke location, and prognosis,” *Journal of Clinical Neurology*, vol. 4, no. 2, p. 75, 2008.
- [72] D. Liebeskind. (2016). “Hemorrhagic stroke treatment & management,” Medscape, [Online]. Available: <http://emedicine.medscape.com/article/1916662-treatment> (visited on 11/03/2016).
- [73] K. R. Lees, E. Bluhmki, R. von Kummer, *et al.*, “Time to treatment with intravenous alteplase and outcome in stroke: An updated pooled analysis of ECASS, ATLANTIS, NINDS, and EPITHET trials,” *The Lancet*, vol. 375, no. 9727, pp. 1695–1703, May 2010.
- [74] NICE (National Institute for Health and Care Excellence). (2016). “Alteplase for treating acute ischaemic stroke,” nice.org.uk, [Online]. Available: <https://www.nice.org.uk/guidance/ta264> (visited on 10/19/2016).
- [75] L. R. Wechsler, “The 4.5-hour time window for intravenous thrombolysis with intravenous tissue-type plasminogen activator is not firmly established,” *Stroke*, vol. 45, no. 3, pp. 914–915, Mar. 1, 2014.
- [76] J. L. Saver, “Time is brain—quantified,” *Stroke*, vol. 37, no. 1, pp. 263–266, Jan. 2006.
- [77] C. McCabe, K. Claxton, and A. J. Culyer, “The NICE cost-effectiveness threshold: What it is and what that means,” *PharmacoEconomics*, vol. 26, no. 9, pp. 733–744, 2008.
- [78] C. E. Tung, S. S. Win, and M. G. Lansberg, “Cost-effectiveness of tissue-type plasminogen activator in the 3- to 4.5-hour time window for acute ischemic stroke,” *Stroke*, vol. 42, no. 8, pp. 2257–2262, Aug. 1, 2011.
- [79] L. Ehlers, G. Andersen, L. B. Clausen, *et al.*, “Cost-effectiveness of intravenous thrombolysis with alteplase within a 3-hour window after acute ischemic stroke,” *Stroke*, vol. 38, no. 1, pp. 85–89, Jan. 1, 2007.

BIBLIOGRAPHY

- [80] H. Lutsep. (2016). “Mechanical thrombolysis in acute stroke,” Medscape, [Online]. Available: <http://emedicine.medscape.com/article/1163240-overview> (visited on 10/19/2016).
- [81] NICE (National Institute for Health and Care Excellence). (). “Mechanical clot retrieval for treating acute ischaemic stroke,” nice.org.uk, [Online]. Available: <https://www.nice.org.uk/guidance/ipg458> (visited on 10/19/2016).
- [82] R. G. Nogueira, A. P. Jadhav, D. C. Haussen, *et al.*, “Thrombectomy 6 to 24 hours after stroke with a mismatch between deficit and infarct,” *New England Journal of Medicine*, vol. 378, no. 1, pp. 11–21, Jan. 4, 2018.
- [83] L. Derex and T.-H. Cho, “Mechanical thrombectomy in acute ischemic stroke,” *Revue Neurologique*, vol. 173, no. 3, pp. 106–113, Mar. 2017.
- [84] B. Lapergue, R. Blanc, B. Gory, *et al.*, “Effect of endovascular contact aspiration vs stent retriever on revascularization in patients with acute ischemic stroke and large vessel occlusion. the ASTER randomized clinical trial,” *Journal of Vascular Surgery*, vol. 66, no. 6, pp. 443–452, Dec. 2017.
- [85] D. Sacks, B. Connors, and C. M. Black, “Society of interventional radiology position statement on endovascular acute ischemic stroke interventions,” *Journal of Vascular and Interventional Radiology*, vol. 24, no. 9, pp. 1263–1266, Sep. 2013.
- [86] IHF (Irish Heart Foundation), “Stroke thrombolysis guidelines,” Mar. 2015.
- [87] J. E. Fugate and A. A. Rabinstein, “Absolute and relative contraindications to IV rt-PA for acute ischemic stroke,” *The Neurohospitalist*, vol. 5, no. 3, pp. 110–121, Jul. 2015.
- [88] I. Dzialowski, M. D. Hill, S. B. Coutts, *et al.*, “Extent of early ischemic changes on computed tomography (CT) before thrombolysis: Prognostic value of the alberta stroke program early CT score in ECASS II,” *Stroke*, vol. 37, no. 4, pp. 973–978, Apr. 1, 2006.
- [89] S. Kumar, M. H. Selim, and L. R. Caplan, “Medical complications after stroke,” *The Lancet Neurology*, vol. 9, no. 1, pp. 105–118, Jan. 2010.
- [90] NICE (National Institute for Health and Care Excellence). (2016). “Stroke rehabilitation,” nice.org.uk, [Online]. Available: <https://pathways.nice.org.uk/pathways/stroke#path=view:/pathways/stroke/stroke-rehabilitation.xml&content=view-index> (visited on 10/19/2016).
- [91] K. M. Mohan, C. D. A. Wolfe, A. G. Rudd, *et al.*, “Risk and cumulative risk of stroke recurrence: A systematic review and meta-analysis,” *Stroke*, vol. 42, no. 5, pp. 1489–1494, May 1, 2011.

BIBLIOGRAPHY

- [92] S. T. Dawodu. (2016). “Traumatic brain injury (TBI) definition and pathophysiology,” Medscape, [Online]. Available: <http://emedicine.medscape.com/article/326510-overview> (visited on 10/28/2016).
- [93] J. J. Kim and A. D. Gean, “Imaging for the diagnosis and management of traumatic brain injury,” *Neurotherapeutics*, vol. 8, no. 1, pp. 39–53, 2011.
- [94] T. A. West and D. W. Marion, “Current recommendations for the diagnosis and treatment of concussion in sport: A comparison of three new guidelines,” *J. Neurotrauma*, vol. 31, no. 2, pp. 159–168, 2014.
- [95] Headway Brain Injury Services and Support. (2016). “Brain injury statistics,” headway.org.uk, [Online]. Available: <https://www.headway.org.uk/about-brain-injury/further-information/statistics/> (visited on 11/23/2016).
- [96] P. Lynch. (Dec. 23, 2006). “Contrecoup,” Wikimedia Commons, [Online]. Available: <https://commons.wikimedia.org/wiki/File:Contrecoup.svg> (visited on 08/04/2019).
- [97] H. Engelhard. (2016). “Subdural hematoma surgery,” Medscape, [Online]. Available: <http://emedicine.medscape.com/article/247472-overview> (visited on 10/28/2016).
- [98] J. Ullman. (2016). “Epidural hematomas treatment & management,” Medscape, [Online]. Available: <http://emedicine.medscape.com/article/1137065-treatment> (visited on 10/28/2016).
- [99] S. Tjoumakaris. (2016). “Fisher grade,” [Online]. Available: <http://emedicine.medscape.com/article/2172467> (visited on 11/10/2016).
- [100] H. E. Hinson, D. F. Hanley, and W. C. Ziai, “Management of intraventricular hemorrhage,” *Current Neurology and Neuroscience Reports*, vol. 10, no. 2, pp. 73–82, Mar. 2010.
- [101] NICE (National Institute for Health and Care Excellence). (2016). “Head injury overview,” nice.org.uk, [Online]. Available: <https://pathways.nice.org.uk/pathways/head-injury> (visited on 10/19/2016).
- [102] Mayo Clinic Staff. (2016). “Traumatic brain injury,” [Online]. Available: <http://www.mayoclinic.org/diseases-conditions/traumatic-brain-injury/basics/treatment/con-20029302> (visited on 11/03/2016).
- [103] J. E. Bailes and V. Hudson, “Classification of sport-related head trauma: A spectrum of mild to severe injury,” *Journal of athletic training*, vol. 36, no. 3, pp. 236–243, Sep. 2001.

BIBLIOGRAPHY

- [104] NICE (National Institute for Health and Care Excellence). (2016). “Observations of patients with head injury in hospital,” nice.org.uk, [Online]. Available: <https://pathways.nice.org.uk/pathways/head-injury#path=view%3A/pathways/head-injury/observations-of-patients-with-head-injury-in-hospital.xml&content=view-index> (visited on 10/19/2016).
- [105] G. Tsivgoulis, A. V. Alexandrov, J. Chang, *et al.*, “Safety and outcomes of intravenous thrombolysis in stroke mimics: A 6-year, single-care center study and a pooled analysis of reported series,” *Stroke*, vol. 42, no. 6, pp. 1771–1774, 2011.
- [106] S. M. Zinkstok, S. T. Engelter, H. Gensicke, *et al.*, “Safety of thrombolysis in stroke mimics: Results from a multicenter cohort study,” *Stroke*, vol. 44, no. 4, pp. 1080–1084, 2013.
- [107] T. D. Musuka, S. B. Wilton, M. Traboulsi, *et al.*, “Diagnosis and management of acute ischemic stroke: Speed is critical,” *Canadian Medical Association Journal*, vol. 187, no. 12, pp. 887–893, Sep. 8, 2015.
- [108] S. John, S. Stock, R. Cerejo, *et al.*, “Brain imaging using mobile CT: Current status and future prospects,” *Journal of Neuroimaging*, vol. 26, no. 1, pp. 5–15, 2016.
- [109] A. Itrat, A. Taqui, R. Cerejo, *et al.*, “Telemedicine in prehospital stroke evaluation and thrombolysis: Taking stroke treatment to the doorstep,” *JAMA Neurology*, vol. 73, no. 2, pp. 162–168, 2016.
- [110] S. S. Rajan, S. Baraniuk, S. Parker, *et al.*, “Implementing a mobile stroke unit program in the United States,” *JAMA Neurology*, vol. 72, no. 2, pp. 229–229, 2015.
- [111] S. Parker, R. Bowry, T.-C. Wu, *et al.*, “Establishing the first mobile stroke unit in the United States,” *Stroke; a journal of cerebral circulation*, vol. 46, no. 5, pp. 1384–91, 2015.
- [112] E. Fear, P. Meaney, and M. Stuchly, “Microwaves for breast cancer detection?” *IEEE Potentials*, vol. 22, no. 1, pp. 12–18, Feb. 2003.
- [113] N. Nikolova, “Microwave imaging for breast cancer,” *IEEE Microwave Magazine*, vol. 12, no. 7, pp. 78–94, Dec. 2011.
- [114] B. J. Mohammed, A. M. Abbosh, S. Mustafa, *et al.*, “Microwave system for head imaging,” *IEEE Transactions on Instrumentation and Measurement*, vol. 63, no. 1, pp. 117–123, Jan. 2014.

BIBLIOGRAPHY

- [115] A. T. Mobashsher, K. S. Bialkowski, A. M. Abbosh, *et al.*, “Design and experimental evaluation of a non-invasive microwave head imaging system for intracranial haemorrhage detection,” *PLOS ONE*, vol. 11, no. 4, e0152351–e0152351, Apr. 2016.
- [116] S. Candefjord, J. Wings, A. A. Malik, *et al.*, “Microwave technology for detecting traumatic intracranial bleedings: Tests on phantom of subdural hematoma and numerical simulations,” *Medical & Biological Engineering & Computing*, pp. 1–12, Oct. 2016.
- [117] G. Cosgrave and A. Cole. (2016). “Surgical treatment of epilepsy,” [neurosurgery.mgh.harvard.edu](http://www.embase.com/search/results?subaction=viewrecord&from=export&id=L369319870%5Cnhttp://dx.doi.org/10.1212/01.CON.0000431398.69594.97%5Cnhttp://sfx.library.uu.nl/utrecht?sid=EMBASE&issn=10802371&id=doi:10.1212%2F01.CON.0000431398.69594.97&atitle=Surgica), [Online]. Available: <http://www.embase.com/search/results?subaction=viewrecord&from=export&id=L369319870%5Cnhttp://dx.doi.org/10.1212/01.CON.0000431398.69594.97%5Cnhttp://sfx.library.uu.nl/utrecht?sid=EMBASE&issn=10802371&id=doi:10.1212%2F01.CON.0000431398.69594.97&atitle=Surgica> (visited on 09/27/2016).
- [118] NICE (National Institute for Health and Care Excellence). (2016). “Epilepsy overview,” [nice.org.uk](https://pathways.nice.org.uk/pathways/epilepsy), [Online]. Available: <https://pathways.nice.org.uk/pathways/epilepsy> (visited on 09/25/2016).
- [119] BrainScope. (2016). “BrainScope One System,” [Online]. Available: <http://brainscope.com/> (visited on 11/30/2016).
- [120] L. S. Prichep, A. Jacquin, J. Filipenko, *et al.*, “Classification of traumatic brain injury severity using informed data reduction in a series of binary classifier algorithms,” *IEEE Transactions on Neural Systems and Rehabilitation Engineering*, vol. 20, no. 6, pp. 806–822, Nov. 2012.
- [121] F. Gaillard. (2016). “Marshall classification of traumatic brain injury,” [Radiopaedia.org](https://radiopaedia.org/articles/marshall-classification-of-traumatic-brain-injury), [Online]. Available: <https://radiopaedia.org/articles/marshall-classification-of-traumatic-brain-injury> (visited on 11/30/2016).
- [122] L. S. Prichep, S. Ghosh Dastidar, A. Jacquin, *et al.*, “Classification algorithms for the identification of structural injury in TBI using brain electrical activity,” *Computers in Biology and Medicine*, vol. 53, pp. 125–133, 2014.
- [123] R. S. Naunheim, M. Treaster, J. English, *et al.*, “Automated electroencephalogram identifies abnormalities in the emergency department,” *American Journal of Emergency Medicine*, vol. 29, no. 8, pp. 845–848, 2011.
- [124] E. A. Michelson, D. Hanley, R. Chabot, *et al.*, “Identification of acute stroke using quantified brain electrical activity,” *Academic Emergency Medicine*, vol. 22, no. 1, pp. 67–72, 2015.

BIBLIOGRAPHY

- [125] L. S. Prichep, R. Naunheim, J. Bazarian, *et al.*, “Identification of hematomas in mild traumatic brain injury using an index of quantitative brain electrical activity,” *Journal of Neurotrauma*, vol. 32, no. 1, pp. 17–22, Jan. 2015.
- [126] HeadSense Medical Ltd. (2016). “HeadSense,” [Online]. Available: <http://www.head-sense-med.com/> (visited on 11/27/2016).
- [127] A. Levinsky, S. Papyan, G. Weinberg, *et al.*, “Non-invasive estimation of static and pulsatile intracranial pressure from transcranial acoustic signals,” *Medical Engineering and Physics*, vol. 38, no. 5, pp. 477–484, 2016.
- [128] A. N. Sen, S. P. Gopinath, and C. S. Robertson, “Clinical application of near-infrared spectroscopy in patients with traumatic brain injury: A review of the progress of the field,” *Neurophotonics*, vol. 3, no. 3, pp. 1–5, 2016.
- [129] InfraScan Inc. (2016). “InfraScan Handheld Brain Diagnostics,” [Online]. Available: <http://infrascanner.com/> (visited on 11/27/2016).
- [130] K. M. Bushby, T. Cole, J. N. Matthews, *et al.*, “Centiles for adult head circumference,” *Archives of Disease in Childhood*, vol. 67, no. 10, pp. 1286–1287, Oct. 1, 1992.
- [131] G. Boverman, T.-J. Kao, X. Wang, *et al.*, “Detection of small bleeds in the brain with electrical impedance tomography,” *Physiological Measurement*, vol. 37, no. 6, pp. 727–750, Jun. 1, 2016.
- [132] G. Bonmassar, S. Iwaki, G. Goldmakher, *et al.*, “On the measurement of electrical impedance spectroscopy (EIS) of the human head,” *International Journal of Bioelectromagnetism*, vol. 12, no. 1, pp. 32–46, Jan. 1, 2010.
- [133] T. Tang, M. D. Weiss, P. Borum, *et al.*, “In vivo quantification of intraventricular hemorrhage in a neonatal piglet model using an EEG-layout based electrical impedance tomography array,” *Physiological Measurement*, vol. 37, no. 6, pp. 751–764, Jun. 2016.
- [134] R. J. Sadleir, T. Tang, A. S. A. Tucker, *et al.*, “Detection of intraventricular blood using EIT in a neonatal piglet model,” in *2009 Annual International Conference of the IEEE Engineering in Medicine and Biology Society*, vol. 100, IEEE, Sep. 2009, pp. 3169–3172.
- [135] R. S. Naunheim, M. Treaster, J. English, *et al.*, “Use of brain electrical activity to quantify traumatic brain injury in the emergency department,” *Brain injury: [BI]*, vol. 24, no. 11, pp. 1324–1329, 2010.
- [136] E. Malone, “Multifrequency methods for electrical impedance tomography,” Ph.D. dissertation, University College London, Medical Physics and Biomedical Engineering, 2015, 170 pp.

BIBLIOGRAPHY

- [137] E. T. McAdams and J. Jossinet, “Tissue impedance: A historical overview,” *Physiological Measurement*, vol. 16, no. 3, A1–A13, Aug. 1, 1995.
- [138] M. Lazebnik, “Ultrawideband spectroscopy and dielectric properties-contrast enhancement for microwave breast cancer detection and treatment,” Ph.D. dissertation, University of Wisconsin-Madison, University of Wisconsin-Madison, 2008, 225 pp.
- [139] J. Avery, K. Aristovich, B. Low, *et al.*, “Reproducible 3d printed head tanks for electrical impedance tomography with realistic shape and conductivity distribution,” *Physiological Measurement*, vol. 38, no. 6, pp. 1116–1131, Jun. 1, 2017.
- [140] Jian-Bo Li, Chi Tang, Meng Dai, *et al.*, “A new head phantom with realistic shape and spatially varying skull resistivity distribution,” *IEEE Transactions on Biomedical Engineering*, vol. 61, no. 2, pp. 254–263, Feb. 2014.
- [141] M. Sperandio, M. Guermandi, and R. Guerrieri, “A four-shell diffusion phantom of the head for electrical impedance tomography,” *IEEE Transactions on Biomedical Engineering*, vol. 59, no. 2, pp. 383–389, 2012.
- [142] H. R. Gamba, R. Bayford, and D. Holder, “Measurement of electrical current density distribution in a simple head phantom with magnetic resonance imaging,” *Physics in medicine and biology*, vol. 44, no. 1, pp. 281–91, Jan. 1999.
- [143] L. Wang, W.-b. Liu, X. Yu, *et al.*, “Image monitoring for head phantom of intracranial hemorrhage using electrical impedance tomography,” in *Progress in Electromagnetic Research Symposium*, Shanghai, China, 2016.
- [144] A. Nissinen, J. P. Kaipio, and M. Vauhkonen, “Contrast enhancement in EIT imaging of the brain,” *Physiological Measurement*, vol. 37, no. 1, pp. 1–24, 2016.
- [145] C. Tang, F. You, G. Cheng, *et al.*, “Correlation between structure and resistivity variations of the live human skull,” *IEEE Transactions on Biomedical Engineering*, vol. 55, no. 9, pp. 2286–2292, Sep. 2008.
- [146] L. Horesh, “Some novel approaches in modelling and image reconstruction for multi-frequency electrical impedance tomography of the human brain,” Ph.D. dissertation, UCL, London, UK, 2006, 264 pp.
- [147] C. Gabriel and A. Peyman, “Dielectric measurement: Error analysis and assessment of uncertainty,” *Physics in Medicine and Biology*, vol. 51, no. 23, pp. 6033–6046, Dec. 7, 2006.
- [148] P. Hasgall, F. DiGennaro, C. Baumgartner, *et al.* (2015). “IT’IS database for thermal and electromagnetic parameters of biological tissues,” [Online]. Available: www.itis.ethz.ch/database (visited on 11/25/2016).

BIBLIOGRAPHY

- [149] C. Gabriel, S. Gabriel, and E. Corthout, “The dielectric properties of biological tissues: I. literature survey,” *Physics in Medicine and Biology*, vol. 41, no. 11, pp. 2231–2249, Nov. 1, 1996.
- [150] S. Gabriel. (1997). “Appendix c: Modelling the frequency dependence of the dielectric properties to a 4 dispersions spectrum,” [Online]. Available: http://niremf.ifac.cnr.it/docs/DIELECTRIC/AppendixC.html#Top_of_Page (visited on 12/05/2016).
- [151] C. Gabriel, “Dielectric properties of biological tissue: Variation with age,” *Bioelectromagnetics*, vol. 26, no. 7, S12–S18, 2005.
- [152] R. Pethig, “Dielectric properties of body tissues,” *Clinical Physics and Physiological Measurement*, vol. 8, no. 4, pp. 5–12, Nov. 1987.
- [153] C. Gabriel, A. Peyman, and E. H. Grant, “Electrical conductivity of tissue at frequencies below 1 MHz,” *Physics in Medicine and Biology*, vol. 54, no. 16, pp. 4863–4878, Aug. 21, 2009.
- [154] J. Zhang, B. Yang, H. Li, *et al.*, “A novel 3d-printed head phantom with anatomically realistic geometry and continuously varying skull resistivity distribution for electrical impedance tomography,” *Scientific Reports*, vol. 7, no. 4608, pp. 1–9, Dec. 2017.
- [155] I. G. Bikker, C. Preis, M. Egal, *et al.*, “Electrical impedance tomography measured at two thoracic levels can visualize the ventilation distribution changes at the bedside during a decremental positive end-expiratory lung pressure trial,” *Critical Care*, vol. 15, no. R193, pp. 1–8, 2011.
- [156] D. B. Geselowitz, “An application of electrocardiographic lead theory to impedance plethysmography,” *IEEE Transactions on Biomedical Engineering*, vol. BME-18, no. 1, pp. 38–41, Jan. 1971.
- [157] A. Adler, P. O. Gaggero, and Y. Maimaitijiang, “Adjacent stimulation and measurement patterns considered harmful,” *Physiological Measurement*, vol. 32, pp. 731–744, Jul. 1, 2011.
- [158] J. P. Avery, “Improving electrical impedance tomography of brain function with a novel servo-controlled electrode helmet,” Ph.D. dissertation, University College London, Jun. 2015, 253 pp.
- [159] J. Larsson, “Electromagnetics from a quasistatic perspective,” *American Journal of Physics*, vol. 75, no. 3, pp. 230–239, Mar. 2007.
- [160] R. S. Tavares, F. A. N. Filho, M. S. Tsuzuki, *et al.*, “Discretization error and the EIT forward problem,” *IFAC Proceedings Volumes*, vol. 47, no. 3, pp. 7535–7540, 2014.

BIBLIOGRAPHY

- [161] A. Adler, A. Boyle, and W. R. B. Lionheart, “Efficient computations of the jacobian matrix using different approaches are equivalent,” in *Proceeding of the 18th International Conference on Biomedical Applications of Electrical Impedance Tomography*, Thayer School of Engineering at Dartmouth Hanover, New Hampshire, USA, 2017.
- [162] B. Grychtol and A. Adler, “FEM electrode refinement for electrical impedance tomography,” in *2013 35th Annual International Conference of the IEEE Engineering in Medicine and Biology Society (EMBC)*, vol. 2013, IEEE, Jul. 2013, pp. 6429–6432.
- [163] A. Tizzard, L. Horesh, R. J. Yerworth, *et al.*, “Generating accurate finite element meshes for the forward model of the human head in EIT,” *Physiological Measurement*, vol. 26, no. 2, S251–S261, Apr. 2005.
- [164] M. Jehl, A. Dedner, T. Betcke, *et al.*, “A fast parallel solver for the forward problem in electrical impedance tomography,” *IEEE Transactions on Biomedical Engineering*, vol. 62, no. 1, pp. 126–137, Jan. 2015.
- [165] T. A. Khan and S. H. Ling, “Review on electrical impedance tomography: Artificial intelligence methods and its applications,” *Algorithms*, vol. 12, no. 88, pp. 1–18, Apr. 26, 2019.
- [166] J. L. Mueller and S. Siltanen, *Linear and Nonlinear Inverse Problems with Practical Applications*, ser. Computational science and engineering series. Philadelphia, PA: Society for Industrial and Applied Mathematics, Oct. 31, 2012, 349 pp.
- [167] B. Grychtol, W. R. B. Lionheart, M. Bodenstern, *et al.*, “Impact of model shape mismatch on reconstruction quality in electrical impedance tomography,” *IEEE Transactions on Medical Imaging*, vol. 31, no. 9, pp. 1754–1760, Sep. 2012.
- [168] W. R. B. Lionheart, “EIT reconstruction algorithms: Pitfalls, challenges and recent developments,” *Physiological Measurement*, vol. 25, no. 1, pp. 125–142, Feb. 1, 2004.
- [169] T. Li, D. Isaacson, J. C. Newell, *et al.*, “Adaptive techniques in electrical impedance tomography reconstruction,” *Physiological Measurement*, vol. 35, no. 6, pp. 1111–1124, Jun. 1, 2014.
- [170] A. Adler and W. R. B. Lionheart, “Uses and abuses of EIDORS: An extensible software base for EIT,” *Physiological Measurement*, vol. 27, no. 5, S25–S42, 2006.
- [171] J. Schoeberl, *Netgen*, version 6.1, Vienna, Austria.

BIBLIOGRAPHY

- [172] C. Geuzaine and J.-F. Remacle, “Gmsh: A 3-d finite element mesh generator with built-in pre- and post-processing facilities,” *International Journal for Numerical Methods in Engineering*, vol. 79, no. 11, pp. 1309–1331, Sep. 10, 2009.
- [173] *MATLAB 2019a*, version 2017A, Natick, Massachusetts, USA.
- [174] M. Jehl, K. Aristovich, M. Faulkner, *et al.*, “Are patient specific meshes required for EIT head imaging?” *Physiological Measurement*, vol. 37, no. 6, pp. 879–892, Jun. 2016.
- [175] A. Borsic, E. A. Attardo, and R. J. Halter, “Multi-GPU jacobian accelerated computing for soft-field tomography,” *Physiological Measurement*, vol. 33, no. 10, pp. 1703–1715, Oct. 1, 2012.
- [176] UCL EIT Group. (2018). “UCL EIT group - list of repositories,” EIT-team.github.io, [Online]. Available: <https://eit-team.github.io/> (visited on 03/20/2020).
- [177] Blender Foundation, *Blender*, version 2.78, Amsterdam, Netherlands.
- [178] Autodesk, *Fusion 360*, Mill Valley, CA, USA.
- [179] COMSOL Group, *COMSOL multiphysics*, Stockholm, Sweden.
- [180] M. Jehl, J. Avery, E. Malone, *et al.*, “Correcting electrode modelling errors in EIT on realistic 3d head models,” *Physiological Measurement*, vol. 36, no. 12, pp. 2423–2442, Dec. 1, 2015.
- [181] A. Boyle and A. Adler, “The impact of electrode area, contact impedance and boundary shape on EIT images,” *Physiological Measurement*, vol. 32, no. 7, pp. 745–754, Jul. 1, 2011.
- [182] L. Yang, M. Dai, C. Xu, *et al.*, “The frequency spectral properties of electrode-skin contact impedance on human head and its frequency-dependent effects on frequency-difference EIT in stroke detection from 10Hz to 1MHz,” *PLOS ONE*, vol. 12, no. 1, e0170563, Jan. 20, 2017.
- [183] H. McCann, S. Ahsan, J. Davidson, *et al.*, “A portable instrument for high-speed brain function imaging: FEITER,” in *2011 IEEE Annual International Conference on Engineering in Medicine and Biology Society (EMBC)*, Boston, MA: IEEE, 2011.
- [184] S. Khan, P. Manwaring, A. Borsic, *et al.*, “FPGA-based voltage and current dual drive system for high frame rate electrical impedance tomography,” *IEEE Transactions on Medical Imaging*, vol. 34, no. 4, pp. 888–901, Apr. 2015.

BIBLIOGRAPHY

- [185] X. Shi, D. Xiuzhen, F. You, *et al.*, “High precision multifrequency electrical impedance tomography system and preliminary imaging results on saline tank,” presented at the 27th Annual International Conference of the IEEE Engineering in Medicine and Biology Society, Shanghai, China, 2005.
- [186] Dräger AG. (2017). “Dräger: Ventilation and respiratory monitoring,” [Online]. Available: https://www.draeger.com/en_uk/Hospital/Productselector/Ventilation-and-Respiratory-Monitoring/ICU-Ventilation-and-Respiratory-Monitoring (visited on 12/13/2017).
- [187] Swisstom AG. (2017). “Swisstom EIT-pioneer set,” [Online]. Available: <http://www.swisstom.com/en/products/pioneer-set> (visited on 11/15/2017).
- [188] M. Yasin, S. Böhm, P. O. Gaggero, *et al.*, “Evaluation of EIT system performance,” *Physiological Measurement*, vol. 32, no. 7, pp. 851–865, Jul. 1, 2011.
- [189] Y. Mamatjan, B. Grychtol, P. Gaggero, *et al.*, “Evaluation and real-time monitoring of data quality in electrical impedance tomography,” *IEEE Transactions on Medical Imaging*, vol. 32, no. 11, pp. 1997–2005, Nov. 2013.
- [190] A. Boyle, “Geophysical applications of electrical impedance tomography,” Ph.D. dissertation, Carleton University, Ottawa, Ontario, Canada, Ottawa-Carleton Institute for Electrical and Computer Engineering, 2016, 280 pp.
- [191] S. J. Hamilton, “EIT imaging of admittivities with a d-bar method and spatial prior: Experimental results for absolute and difference imaging,” *Physiological Measurement*, vol. 38, no. 6, pp. 1176–1192, Jun. 1, 2017.
- [192] S. J. Hamilton and A. Hauptmann, “Deep d-bar: Real time electrical impedance tomography imaging with deep neural networks,” *IEEE Transactions on Medical Imaging*, vol. 37, no. 10, pp. 2367–2377, Oct. 2018.
- [193] B. J. McDermott, J. Avery, M. O’Halloran, *et al.*, “Bi-frequency symmetry difference electrical impedance tomography – a novel technique for perturbation detection in static scenes,” *Physiological Measurement*, vol. 40, no. 4, pp. 1–19, Feb. 20, 2019.
- [194] B. McDermott, E. Porter, M. Jones, *et al.*, “Symmetry difference electrical impedance tomography—a novel modality for anomaly detection,” *Physiological Measurement*, vol. 39, no. 4, pp. 1–20, Apr. 26, 2018.

BIBLIOGRAPHY

- [195] A. Romsauerova, A. McEwan, L. Horesh, *et al.*, “Multi-frequency electrical impedance tomography (EIT) of the adult human head: Initial findings in brain tumours, arteriovenous malformations and chronic stroke, development of an analysis method and calibration,” *Physiological Measurement*, vol. 27, no. 5, S147–S161, May 1, 2006.
- [196] V. Cherepenin, A. Karpov, A. Korjenevsky, *et al.*, “A 3d electrical impedance tomography (EIT) system for breast cancer detection,” *Physiological Measurement*, vol. 22, no. 1, pp. 9–18, Feb. 1, 2001.
- [197] M. H. Choi, T.-J. Kao, D. Isaacson, *et al.*, “A reconstruction algorithm for breast cancer imaging with electrical impedance tomography in mammography geometry,” *IEEE Transactions on Biomedical Engineering*, vol. 54, no. 4, pp. 700–710, Apr. 2007.
- [198] E. K. Murphy, X. Wu, and R. J. Halter, “Fused-data transrectal EIT for prostate cancer imaging,” *Physiological Measurement*, vol. 39, no. 5, pp. 1–15, May 25, 2018.
- [199] C. J. C. Trepte, C. R. Phillips, J. Solà, *et al.*, “Electrical impedance tomography (EIT) for quantification of pulmonary edema in acute lung injury,” *Critical Care*, vol. 20, no. 18, pp. 1–9, Dec. 2015.
- [200] A. Adler and A. Boyle, *Electrical impedance tomography*, in *Wiley Encyclopedia of Electrical and Electronics Engineering*, 1st ed., Wiley, Dec. 27, 1999.
- [201] F. Simini and P. Bertemes-Filho, *Bioimpedance in biomedical applications and research*. New York, NY: Springer Science+Business Media, 2018, 85 pp.
- [202] F. Seoane, S. Reza Atefi, J. Tomner, *et al.*, “Electrical bioimpedance spectroscopy on acute unilateral stroke patients: Initial observations regarding differences between sides,” *BioMed Research International*, vol. 2015, pp. 1–12, 2015.
- [203] S. Atefi, F. Seoane, T. Thorlin, *et al.*, “Stroke damage detection using classification trees on electrical bioimpedance cerebral spectroscopy measurements,” *Sensors*, vol. 13, no. 8, pp. 10 074–10 086, Aug. 7, 2013.
- [204] B. J. McDermott, E. Porter, M. Jones, *et al.*, “A novel tissue-mimicking material for phantom development in medical applications of EIT,” in *Proceeding of the 18th International Conference on Biomedical Applications of Electrical Impedance Tomography*, Thayer School of Engineering at Dartmouth Hanover, New Hampshire, USA, 2017.

BIBLIOGRAPHY

- [205] B. McDermott, B. McGinley, K. Krukiewicz, *et al.*, “Stable tissue-mimicking materials and an anatomically realistic, adjustable head phantom for electrical impedance tomography,” *Biomedical Physics & Engineering Express*, vol. 4, no. 1, pp. 1–13, Nov. 27, 2017.
- [206] J. Garrett and E. Fear, “A new breast phantom with a durable skin layer for microwave breast imaging,” *IEEE Transactions on Antennas and Propagation*, vol. 63, no. 4, pp. 1693–1700, 2015.
- [207] —, “Stable and flexible materials to mimic the dielectric properties of human soft tissues,” *IEEE Antennas and Wireless Propagation Letters*, vol. 13, pp. 599–602, 2014.
- [208] A. T. Mobashsher and A. M. Abbosh, “Artificial human phantoms: Human proxy in testing microwave apparatuses that have electromagnetic interaction with the human body,” *IEEE Microwave Magazine*, vol. 16, no. 6, pp. 42–62, Jul. 2015.
- [209] B. McDermott, E. Porter, A. Santorelli, *et al.*, “Anatomically and dielectrically realistic microwave head phantom with circulation and reconfigurable lesions,” *Progress In Electromagnetics Research B*, vol. 78, pp. 47–60, July 2017.
- [210] N. Makris, L. Angelone, S. Tulloch, *et al.*, “MRI-based anatomical model of the human head for specific absorption rate mapping,” *Medical & Biological Engineering & Computing*, vol. 46, no. 12, pp. 1239–1251, Dec. 2008.
- [211] E. Lüders, H. Steinmetz, and L. Jäncke, “Brain size and grey matter volume in the healthy human brain,” *Neuroreport*, vol. 13, no. 17, pp. 2371–2374, Dec. 3, 2002.
- [212] Smooth-On Inc. (2020). “Safety data sheet: VytaFlex 20,” [Online]. Available: https://www.smooth-on.com/msds/files/619A_1-619B_1.pdf (visited on 08/10/2020).
- [213] Thermo Fisher Scientific. (2020). “Safety data sheet: Graphite powder,” [Online]. Available: <https://www.fishersci.com/shop/msdsproxy?productName=G67500&productDescription=GRAPHITE+POWDER+500G&catNo=G67-500&vendorId=VN00033897&storeId=10652> (visited on 08/10/2020).
- [214] Alfa Aesar Chemical (Thermo Fisher Scientific). (2020). “Safety data sheet: Carbon black, acetylene, 50% compressed,” [Online]. Available: <https://www.alfa.com/en/msds/?language=EE&subformat=CLP1&sku=39724> (visited on 08/10/2020).

BIBLIOGRAPHY

- [215] A. Santorelli, O. Laforest, E. Porter, *et al.*, “Image classification for a time-domain microwave radar system: Experiments with stable modular breast phantoms,” in *European Conference on Antennas and Propagation (EuCAP)*, 2015.
- [216] D.-Y. Kim, R. Jung, H.-S. Kim, *et al.*, “Electrically conductive polymeric nanocomposites prepared in alcohol dispersion of multiwalled carbon nanotubes,” *Molecular Crystals and Liquid Crystals*, vol. 491, no. 1, pp. 255–263, Sep. 2008.
- [217] W. Franks, I. Schenker, P. Schmutz, *et al.*, “Impedance characterization and modeling of electrodes for biomedical applications,” *IEEE Transactions on Biomedical Engineering*, vol. 52, no. 7, pp. 1295–1302, 2005.
- [218] R. P. Suvarna, K. R. Rao, and K. Subbarangaiah, “A simple technique for a.c. conductivity measurements,” *Bulletin of Materials Science*, vol. 25, no. 7, pp. 647–651, 2002.
- [219] S. Panteny, R. Stevens, and C. R. Bowen, “The frequency dependent permittivity and ac conductivity of random electrical networks,” *Ferroelectrics*, vol. 319, no. 3, pp. 199–208, 2005.
- [220] K. Krukiewicz, M. Chudy, S. Gregg, *et al.*, “The synergistic effects of gold particles and dexamethasone on the electrochemical and biological performance of PEDOT neural interfaces,” *Polymers*, vol. 11, pp. 1–13, 67 Jan. 5, 2019.
- [221] *Parstat 2273 potentiostat/ galvanostat hardware user’s manual*, 2004.
- [222] Grozny. (2017). “Thingiverse - human head,” [Online]. Available: <http://www.thingiverse.com/thing:172348> (visited on 02/15/2017).
- [223] N. Dilmen. (2017). “NIH 3d print exchange- brain MRI,” [Online]. Available: <https://3dprint.nih.gov/discover/3DPX-002739> (visited on 02/15/2017).
- [224] Ultimaker. (2017). “Ultimaker 2 extended + specifications,” [Online]. Available: <https://ultimaker.com/en/products/ultimaker-2-plus/specifications> (visited on 11/23/2017).
- [225] M. G. Stokes, C. D. Chambers, I. C. Gould, *et al.*, “Simple metric for scaling motor threshold based on scalp-cortex distance : Application to studies using transcranial magnetic stimulation,” *Journal of neurophysiology*, vol. 94, no. 6, pp. 4520–4527, 2005.
- [226] J. R. Sims, L. R. Gharai, P. W. Schaefer, *et al.*, “ABC/2 for rapid clinical estimate of infarct, perfusion, and mismatch volumes,” *Neurology*, vol. 72, no. 24, pp. 2104–2110, 2009.

BIBLIOGRAPHY

- [227] A. Adler, J. H. Arnold, R. Bayford, *et al.*, “GREIT: A unified approach to 2d linear EIT reconstruction of lung images,” *Physiological measurement*, vol. 30, no. 6, S35–S55, 2009.
- [228] AkzoNobel. (May 24, 2018). “AkzoNobel chemical products. polymer chemistry. conductive blacks.” [Online]. Available: <https://polymerchemistry.akzonobel.com/products/polymer-additives/conductive-blacks/>.
- [229] Z. Weng, J. Wang, T. Senthil, *et al.*, “Mechanical and thermal properties of ABS/montmorillonite nanocomposites for fused deposition modeling 3d printing,” *Materials & Design*, vol. 102, pp. 276–283, Jul. 2016.
- [230] R. D. Deanin and K. R. Patel, “Carbon black embrittlement of ABS,” in *Toughness and Brittleness of Plastics*, R. D. Deanin and A. M. Crugnola, Eds., vol. 154, Washington, D. C.: American Chemical Society, 1976, pp. 256–262.
- [231] N. S. Karode, A. Poudel, L. Fitzhenry, *et al.*, “Evaluation of interfacial region of microphase-separated SEBS using modulated differential scanning calorimetry and dynamic mechanical thermal analysis,” *Polymer Testing*, vol. 62, pp. 268–277, Sep. 2017.
- [232] B. McDermott, M. O Halloran, A. Poudel, *et al.*, “3d printable solid tissue-mimicking material for microwave phantoms,” in *Proceedings of the 1st EMF-Med World Conference on Biomedical Applications of Electromagnetic Fields*, Split, Croatia, Sep. 10, 2018.
- [233] R. Ou, R. A. Gerhardt, C. Marrett, *et al.*, “Assessment of percolation and homogeneity in ABS/carbon black composites by electrical measurements,” *Composites Part B: Engineering*, vol. 34, no. 7, pp. 607–614, Oct. 2003.
- [234] B. McDermott, M. O’Halloran, E. Porter, *et al.*, “Brain haemorrhage detection using a SVM classifier with electrical impedance tomography measurement frames,” *PLOS ONE*, vol. 13, no. 7, e0200469, Jul. 12, 2018.
- [235] B. McDermott, M. O’Halloran, A. Santorelli, *et al.*, “Classification applied to brain haemorrhage detection: Initial phantom studies using electrical impedance measurements,” in *Proceeding of the 19th International Conference on Biomedical Applications of Electrical Impedance Tomography*, Edinburgh, Scotland, Jun. 2018.
- [236] B. McDermott, E. Dunne, M. O’Halloran, *et al.*, “Brain haemorrhage detection through SVM classification of electrical impedance tomography measurements,” in *Brain and Human Body Modeling: Computational Human Modeling at EMBC 2018*, S. Makarov, M. Horner, and G. Noetscher, Eds., Cham: Springer International Publishing, 2019, pp. 211–244.

BIBLIOGRAPHY

- [237] T. M. Mitchell, *Machine Learning*, ser. McGraw-Hill series in computer science. New York: McGraw-Hill, 1997, 414 pp.
- [238] A. Santorelli, E. Porter, E. Kirshin, *et al.*, “Investigation of classifiers for tumour detection with an experimental time-domain breast screening system,” *Progress In Electromagnetics Research*, vol. 144, pp. 45–57, 2014.
- [239] R. C. Conceição, M. O’Halloran, M. Glavin, *et al.*, “Support vector machines for the classification of early-stage breast cancer based on radar target signatures,” *Progress In Electromagnetics Research B*, vol. 23, pp. 311–327, 2010.
- [240] F. Golnaraghi and P. K. Grewal, “Pilot study: Electrical impedance based tissue classification using support vector machine classifier,” *IET Science, Measurement & Technology*, vol. 8, no. 6, pp. 579–587, Nov. 1, 2014.
- [241] D. Gur, B. Zheng, D. Lederman, *et al.*, “A support vector machine designed to identify breasts at high risk using multi-probe generated REIS signals: A preliminary assessment,” in *Medical Imaging 2010: Image Perception, Observer Performance, and Technology Assessment*, vol. 7627, SPIE, 2010, pp. 413–422.
- [242] S. Laufer and B. Rubinsky, “Tissue characterization with an electrical spectroscopy SVM classifier,” *IEEE Transactions on Biomedical Engineering*, vol. 56, no. 2, pp. 525–528, Feb. 2009.
- [243] M. A. Shini, S. Laufer, and B. Rubinsky, “SVM for prostate cancer using electrical impedance measurements,” *Physiological Measurement*, vol. 32, no. 9, pp. 1373–1387, Sep. 1, 2011.
- [244] T. Schlebusch, S. Nienke, S. Leonhardt, *et al.*, “Bladder volume estimation from electrical impedance tomography,” *Physiological Measurement*, vol. 35, no. 9, pp. 1813–1823, Sep. 1, 2014.
- [245] S. Khan, A. Mahara, E. S. Hyams, *et al.*, “Prostate cancer detection using composite impedance metric,” *IEEE Transactions on Medical Imaging*, vol. 35, no. 12, pp. 2513–2523, Dec. 2016.
- [246] E. K. Murphy, J. Amoh, S. H. Arshad, *et al.*, “Noise-robust bioimpedance approach for cardiac output measurement,” *Physiological Measurement*, vol. 40, no. 7, p. 074004, Jul. 30, 2019.
- [247] N. Cristianini and J. Shawe-Taylor, *An introduction to support vector machines: and other kernel-based learning methods*. Cambridge; New York: Cambridge University Press, 2000, 189 pp.
- [248] EASYCAP GmbH. (2017). “EasyCap EEG recording caps and related products,” [Online]. Available: <http://www.easycap.de/> (visited on 01/15/2017).

BIBLIOGRAPHY

- [249] B. Oliveira, D. Godinho, M. O'Halloran, *et al.*, “Diagnosing breast cancer with microwave technology: Remaining challenges and potential solutions with machine learning,” *Diagnostics*, vol. 8, no. 36, pp. 1–22, May 19, 2018.
- [250] Y. Li, A. Santorelli, O. Laforest, *et al.*, “Cost-sensitive ensemble classifiers for microwave breast cancer detection,” in *2015 IEEE International Conference on Acoustics, Speech and Signal Processing (ICASSP)*, South Brisbane, Queensland, Australia: IEEE, Apr. 2015, pp. 952–956.
- [251] C.-W. Hsu, C.-C. Chang, and C.-J. Lin, “A practical guide to support vector classification,” Department of Computer Science, National Taiwan University, 2003.
- [252] D. L. Hudson and M. E. Cohen, *Neural Networks and Artificial Intelligence for Biomedical Engineering*. Wiley-IEEE, 1999.
- [253] X. He, D. Cai, and P. Niyogi, “Laplacian score for feature selection,” *NIPS'05 Proceedings of the 18th International Conference on Neural Information Processing Systems*, pp. 507–514, Dec. 2005.
- [254] E. Dunne, A. Santorelli, B. McGinley, *et al.*, “Image-based classification of bladder state using electrical impedance tomography,” *Physiological Measurement*, vol. 39, no. 12, pp. 1–16, Oct. 9, 2018.
- [255] R. C. Conceição, M. O'Halloran, M. Glavin, *et al.*, “Evaluation of features and classifiers for classification of early-stage breast cancer,” *Journal of Electromagnetic Waves and Applications*, vol. 25, no. 1, pp. 1–14, Jan. 2011.
- [256] Y. Li, E. Porter, A. Santorelli, *et al.*, “Microwave breast cancer detection via cost-sensitive ensemble classifiers: Phantom and patient investigation,” *Biomedical Signal Processing and Control*, vol. 31, pp. 366–376, Jan. 2017.
- [257] B. McDermott, E. Porter, B. McGinley, *et al.*, “Electrical impedance tomography with exploitation of symmetry,” in *Bioengineering in Ireland 2018*, DCU: Royal Academy of Medicine in Ireland Section of Bioengineering, Jan. 27, 2018.
- [258] P. M. W. Bath, “ABC of arterial and venous disease: Acute stroke,” *BMJ*, vol. 320, no. 7239, pp. 920–923, Apr. 1, 2000.
- [259] M. Clay and T. Ferree, “Weighted regularization in electrical impedance tomography with applications to acute cerebral stroke,” *IEEE Transactions on Medical Imaging*, vol. 21, no. 6, pp. 629–637, Jun. 2002.
- [260] M. Vonach, B. Marson, M. Yun, *et al.*, “A method for rapid production of subject specific finite element meshes for electrical impedance tomography of the human head,” *Physiological Measurement*, vol. 33, no. 5, pp. 801–816, May 2012.

BIBLIOGRAPHY

- [261] A. Adler. (2012). “EIDORS mailing lists,” EIDORS Mailing Lists, [Online]. Available: <https://sourceforge.net/p/eidors3d/mailman/message/29588129/> (visited on 01/10/2018).
- [262] S. Mohammadi, F. Setti, A. Perina, *et al.*, “Groups and crowds: Behaviour analysis of people aggregations,” in *Computer Vision, Imaging and Computer Graphics Theory and Applications*, J. Braz, N. Magnenat-Thalmann, P. Richard, *et al.*, Eds., vol. 693, Series Title: Communications in Computer and Information Science, Cham: Springer International Publishing, 2017, pp. 3–32.
- [263] F. Thürk, A. D. Waldmann, K. H. Wodack, *et al.*, “Evaluation of reconstruction parameters of electrical impedance tomography on aorta detection during saline bolus injection,” *Current Directions in Biomedical Engineering*, vol. 2, no. 1, pp. 511–514, 2016.
- [264] J. Mauriño, G. Saposnik, S. Lepera, *et al.*, “Multiple simultaneous intracerebral hemorrhages: Clinical features and outcome,” *Archives of Neurology*, vol. 58, no. 4, pp. 639–642, Apr. 1, 2001.
- [265] A. E. Baird, K. O. Lövblad, G. Schlaug, *et al.*, “Multiple acute stroke syndrome: Marker of embolic disease?” *Neurology*, vol. 54, no. 3, pp. 674–678, Feb. 8, 2000.
- [266] B. McDermott, M. O’Halloran, and E. Porter, “Static lesion detection in symmetric scenes using dual-frequency electrical impedance tomography,” in *Bioengineering in Ireland 2019*, UL: Royal Academy of Medicine in Ireland Section of Bioengineering, Jan. 19, 2019.
- [267] —, “Bi-frequency symmetry difference (BFSD) EIT in stroke diagnosis,” in *Proceedings of the 20th International Conference on Biomedical Applications of Electrical Impedance Tomography*, University College London, Jul. 1, 2019.
- [268] B. J. McDermott, M. O’Halloran, J. Avery, *et al.*, “Bi-frequency symmetry difference EIT - feasibility and limitations of application to stroke diagnosis,” *IEEE Journal of Biomedical and Health Informatics*, pp. 1–14, 2019.
- [269] F. B. Haeussinger, S. Heinzl, T. Hahn, *et al.*, “Simulation of near-infrared light absorption considering individual head and prefrontal cortex anatomy: Implications for optical neuroimaging,” *PLoS ONE*, vol. 6, no. 10, e26377, Oct. 24, 2011.
- [270] S. Payabvash, S. Taleb, J. Benson, *et al.*, “Acute ischemic stroke infarct topology: Association with lesion volume and severity of symptoms at admission and discharge,” *American Journal of Neuroradiology*, vol. 38, no. 1, pp. 58–63, Jan. 2017.

- [271] P. P. Russo and R. L. Smith, “Asymmetry of human skull base during growth,” *International Journal of Morphology*, vol. 29, no. 3, pp. 1028–1032, Sep. 2011.
- [272] X.-Z. Kong, S. R. Mathias, T. Guadalupe, *et al.*, “Mapping cortical brain asymmetry in 17,141 healthy individuals worldwide via the ENIGMA consortium,” *Proceedings of the National Academy of Sciences*, vol. 115, no. 22, E5154–E5163, May 29, 2018.
- [273] L. Liu, W. Dong, X. Ji, *et al.*, “A new method of noninvasive brain-edema monitoring in stroke: Cerebral electrical impedance measurement,” *Neurological Research*, vol. 28, no. 1, pp. 31–37, Jan. 2006.
- [274] A. Nguyen, A. A. Simard-Meilleur, C. Berthiaume, *et al.*, “Head circumference in canadian male adults: Development of a normalized chart,” *International Journal of Morphology*, vol. 30, no. 4, pp. 1474–1480, Dec. 2012.
- [275] T. I. Oh, H. Wi, D. Y. Kim, *et al.*, “A fully parallel multi-frequency EIT system with flexible electrode configuration: KHU mark2,” *Physiological Measurement*, vol. 32, no. 7, pp. 835–849, Jul. 1, 2011.
- [276] J. Avery, T. Dowrick, A. Witkowska-Wrobel, *et al.*, “Simultaneous EIT and EEG using frequency division multiplexing,” *Physiological Measurement*, vol. 40, no. 3, pp. 1–21, Apr. 3, 2019.
- [277] S. Jeon, J. Chien, C. Song, *et al.*, “A preliminary study on precision image guidance for electrode placement in an EEG study,” *Brain Topography*, vol. 31, no. 2, pp. 174–185, Mar. 2018.
- [278] P. Giacometti, K. L. Perdue, and S. G. Diamond, “Algorithm to find high density EEG scalp coordinates and analysis of their correspondence to structural and functional regions of the brain,” *Journal of Neuroscience Methods*, vol. 229, pp. 84–96, May 2014.
- [279] G. Bonmassar and S. Iwaki, “The shape of electrical impedance spectroscopy (EIS) is altered in stroke patients,” in *The 26th Annual International Conference of the IEEE Engineering in Medicine and Biology Society*, vol. 4, San Francisco, CA, USA: IEEE, 2004, pp. 3443–3446.
- [280] B. McDermott, M. A. Elahi, A. Santorelli, *et al.*, “Stroke diagnosis using multi-frequency symmetry difference EIT (MFSD-EIT) with SVM classification,” in *Proceeding of the 21st International Conference on Biomedical Applications of Electrical Impedance Tomography*, National University of Ireland Galway, Jun. 2021.
- [281] B. J. McDermott, A. Elahi, A. Santorelli, *et al.*, “Multi-frequency symmetry difference electrical impedance tomography with machine learning for human stroke diagnosis,” *Physiological Measurement*, Jun. 18, 2020.

BIBLIOGRAPHY

- [282] A. Fedorov, R. Beichel, J. Kalpathy-Cramer, *et al.*, “3d slicer as an image computing platform for the quantitative imaging network,” *Magnetic Resonance Imaging*, vol. 30, no. 9, pp. 1323–1341, Nov. 2012.
- [283] G. C. Cawley and N. L. C. Talbot, “On over-fitting in model selection and subsequent selection bias in performance evaluation,” *The Journal of Machine Learning Research*, vol. 11, pp. 2079–2107, 2010.
- [284] Guodong Guo and S. Li, “Content-based audio classification and retrieval by support vector machines,” *IEEE Transactions on Neural Networks*, vol. 14, no. 1, pp. 209–215, Jan. 2003.
- [285] T. Jayalakshmi and A. Santhakumaran, “Statistical normalization and back propagation for classification,” *International Journal of Computer Theory and Engineering*, pp. 89–93, 2011.
- [286] B. Kumar Singh, K. Verma, and A. S. Thoke, “Investigations on impact of feature normalization techniques on classifier’s performance in breast tumor classification,” *International Journal of Computer Applications*, vol. 116, no. 19, pp. 11–15, Apr. 22, 2015.
- [287] S. Escalera, O. Pujol, and P. Radeva, “Separability of ternary codes for sparse designs of error-correcting output codes,” *Pattern Recognition Letters*, vol. 30, no. 3, pp. 285–297, Feb. 2009.
- [288] V. Garcia, R. A. Mollineda, and J. S. Sanchez, “Theoretical analysis of a performance measure for imbalanced data,” in *2010 20th International Conference on Pattern Recognition*, Istanbul, Turkey: IEEE, Aug. 2010, pp. 617–620.
- [289] A. Tharwat, “Classification assessment methods,” *Applied Computing and Informatics*, pp. 1–13, Aug. 2018.
- [290] N. Joachimowicz, B. Duchene, C. Conessa, *et al.*, “Reference phantoms for microwave imaging,” IEEE, Mar. 2017, pp. 2719–2722.
- [291] J. Hope, F. Vanholsbeeck, and A. McDaid, “Drive and measurement electrode patterns for electrode impedance tomography (EIT) imaging of neural activity in peripheral nerve,” *Biomedical Physics & Engineering Express*, vol. 4, no. 6, pp. 1–9, Sep. 21, 2018.